PB89-194039

Proceedings: Symposium on the Transfer and Utilization of Particulate Control Technology (7th). Volume 1

Radian Corp., Research Triangle Park, NC

Prepared for:

Environmental Protection Agency, Research Triangle Park, NC

May 89

U.S. Department of Commerce
National Technical Information Service

NTIS

PB89-194039

EPA/600/9-89/046a
May 1989

PROCEEDINGS: SEVENTH SYMPOSIUM ON THE TRANSFER AND UTILIZATION OF PARTICULATE CONTROL TECHNOLOGY
VOLUME 1

Susan R. Fields, Compiler

Radian Corporation
P.O. Box 13000
Research Triangle Park, NC 27709

EPA Project Officer:

Geddes M. Ramsey
Air and Energy Engineering
Research Laboratory
Research Triangle Park, NC 27711

EPRI Project Manager:

Ralph F. Altman
Air Quality Control Program
3412 Hillview Avenue
Palo Alto, CA 94304

AIR AND ENERGY ENGINEERING RESEARCH LABORATORY
OFFICE OF RESEARCH AND DEVELOPMENT
U.S. ENVIRONMENTAL PROTECTION AGENCY
RESEARCH TRIANGLE PARK, NC 27711

REPRODUCED BY
U.S. DEPARTMENT OF COMMERCE
NATIONAL TECHNICAL INFORMATION SERVICE
SPRINGFIELD, VA. 22161

TECHNICAL REPORT DATA
(Please read Instructions on the reverse before completing)

1. REPORT NO. EPA/600/9-89/046a
2.
3. RECIPIENT'S ACCESSION NO.
4. TITLE AND SUBTITLE Proceedings: Seventh Symposium on the Transfer and Utilization of Particulate Control Technology, Volume 1
5. REPORT DATE May 1989
6. PERFORMING ORGANIZATION CODE
7. AUTHOR(S) Susan R. Fields, Compiler
8. PERFORMING ORGANIZATION REPORT NO. EPRI GS-6208 (Volume 1)
9. PERFORMING ORGANIZATION NAME AND ADDRESS
Radian Corporation
P.O. Box 13000
Research Triangle Park, North Carolina 27709
10. PROGRAM ELEMENT NO.
11. CONTRACT/GRANT NO. NA (EPRI funded)
12. SPONSORING AGENCY NAME AND ADDRESS
EPA, Office of Research and Development
Air and Energy Engineering Research Laboratory
Research Triangle Park, NC 27711
13. TYPE OF REPORT AND PERIOD COVERED Proceedings; 3/87-3/88
14. SPONSORING AGENCY CODE **EPA/600/13**
15. SUPPLEMENTARY NOTES AEERL project officer is Geddes H. Ramsey, Mail Drop 61, 919/541-7963. Symposium held in Nashville, TN, March 22-25, 1988.

16. ABSTRACT
The proceedings document presentations from the 7th symposium on the transfer and utilization of particulate control technology, March 22-25, 1988, in Nashville, TN. Objectives of the symposium were to encourage the exchange of new knowledge in the particulate control field between designers, users, and researchers, and to stimulate new ideas that will lead to further technological improvements. Fabric filters (FFs) and electrostatic precipitators (ESPs) were the najor topics, but novel concepts and advanced technologies were also explored. Volume 1 contains 33 papers covering dust properties, power supplies and controls for ESPs, advanced SO2/particulate control studies, ESP performance evaluation and upgrading, and ESP modeling.

17. KEY WORDS AND DOCUMENT ANALYSIS

a. DESCRIPTORS	b. IDENTIFIERS/OPEN ENDED TERMS	c. COSATI Field/Group
Pollution	Pollution Control	13B
Particles	Stationary Sources	14G
Dust	Particulate	11G
Electrostatic Precipitators		13I
Sulfur Dioxide		07B
Mathematical Modeling		12A

18. DISTRIBUTION STATEMENT **Release to Public**
19. SECURITY CLASS *(This Report)* Unclassified
20. SECURITY CLASS *(This page)* Unclassified
21. NO. OF PAGES 557
22. PRICE

EPA Form 2220-1 (9-73)

NOTICE

This document has been reviewed in accordance with U.S. Environmental Protection Agency policy and approved for publication. Mention of trade names or commercial products does not constitute endorsement or recommendation for use.

ABSTRACT

These Proceedings document the presentations from the Seventh Symposium on the Transfer and Utilization of Particulate Control Technology, held March 22-25, 1988, in Nashville, Tennessee. The Symposium was sponsored by the U. S. EPA's Air and Energy Engineering Research Laboratory in Research Triangle Park, North Carolina, and EPRI's Coal Combustion Systems Division, in Palo Alto, California.

The objectives of the Symposium were to encourage the exchange of new knowledge in the particulate control field among designers, users, and researchers, and to stimulate new ideas that will lead to further technological improvements in the future. Fabric filters and electrostatic precipitators were the major topics, but novel concepts and advanced technologies were also explored. Topics discussed in each day's sessions are listed below:

Tuesday, March 22

- Plenary Session
- FF: Particulate Control for Incinerators
- ESP: Dust Properties
- FF: Full-Scale Fabric Filter Studies I
- ESP: Power Supplies and Controls for Precipitators

Wednesday, March 23

- FF: Full-Scale Fabric Filter Studies II
- ESP: Advanced SO_2/Particulate Control Studies I
- FF: Advanced SO_2/Particulate Control Studies II
- ESP: Precipitator Performance Evaluation and Upgrading I

Thursday, March 24

- FF: Advanced SO_2/Particulate Control Studies III
- ESP: Precipitator Performance Evaluation and Upgrading II
- FF: Fabric Filter Pilot-Scale Studies I
- ESP: Precipitator Modelling I

Friday, March 25

- FF: Fabric Filter Pilot-Scale Studies II
- ESP: Precipitator Modelling II

Volume 1 of the Proceedings contains 33 papers presented in the Dust Properties, Power Supplies and Controls for Precipitators, Advanced SO_2/Particulate Control Studies I, Precipitator Performance Evaluation and Upgrading I and II, and Precipitator Modelling I and II Sessions. These papers are primarily concerned with electrostatic precipitators for particulate control.

Volume 2 of the Proceedings contains 30 papers presented in the Particulate Control for Incinerators, Full-Scale Fabric Filter Studies I and II, Advanced SO_2/Particulate Control Studies II and III, and Fabric Filter Pilot-Scale Studies I and II Sessions. The papers in this volume cover a broader range of topics, but the emphasis is on the use of fabric filters for particulate control.

ACKNOWLEDGMENT

The assistance of Joan Ross, Radian Corporation, in compiling these Proceedings is gratefully acknowledged.

PREFACE

The Seventh Symposium on the Transfer and Utilization of Particulate Control Technology was held in Nashville, Tennessee, March 22 through 25, 1988. This symposium, the third of its kind to be jointly sponsored by EPA and EPRI, was devoted to the discussion of particulate emissions control. The Symposium's objectives were to promote the transfer of results of particulate control research to potential users of technologies, and to provide a medium for exchange of ideas among researchers in the particulate control field.

The symposium proceedings contain 63 papers presented by EPA and other Federal and State agency representatives, EPRI staff members, representatives of utility companies, equipment and process suppliers, university representatives, and research and development companies. Additionally, individuals from Australia, Canada, Denmark, Holland, Sweden, and Switzerland presented information on worldwide technological developments. Electrostatic precipitators and fabric filters were the major topics discussed during the Symposium. Other topics presented included system operation and maintenance, and integrated control processes.

Symposium cochairmen were Ralph Altman, Project Manager in the Air Quality Control Program of the EPRI's Coal Combustion Systems Division; and Geddes Ramsey, Project Officer in the Air Toxics Control Branch of the EPA's Air and Energy Engineering Research Laboratory. Welcoming remarks made for EPA by Geddes Ramsey, and for EPRI by Dr. George Offen, Program Manager in the Air Quality Control Program of EPRI's Coal Combustion Systems Division.

The Seventh Symposium broke new ground in presenting a panel discussion of particulate control issues at the beginning of the Symposium. Participants in the plenary session Panel Discussion on Particulate Control Issues were **Charles Altin**, Project Manager, Ebasco Services, Inc., **A. A. Arstikatis**, Client Manager, Combustion Engineering, **Peter Bibbo**, Vice President, Sales and Marketing, Research-Cottrell, **Gary Greiner**, Vice President, ETS, Inc., **Gerald Hollinden**, Branch Chief, Tennessee Valley Authority, **Richard McRanie**, Director of Utility Services, Kilkelly Environmental Associates, **Grady Nichols**, Director of Environmental Sciences Research, Southern Research Institute, **David Sloat**, Senior Engineer, Sargent and Lundy, **John Walton**, Deputy Director, Tennessee State Department of Health and Environment Division of Air Pollution Control, and **Jeffrey Williams**, Environmental Analyst, Rochester Gas and Electric. A summary of the discussion is included in Volume 1 of these Proceedings.

TABLE OF CONTENTS

VOLUME 1

PLENARY, DUST PROPERTIES, POWER SUPPLIES AND CONTROLS FOR PRECIPITATORS, ADVANCED SO_2/PARTICULATE CONTROL STUDIES I, PRECIPITATOR PERFORMANCE EVALUATION AND UPGRADING I, PRECIPITATOR PERFORMANCE EVALUATION AND UPGRADING II, PRECIPITATOR MODELLING I, AND PRECIPITATOR MODELLING II

Section Page

PLENARY SESSION

Ralph Altman, Chairman

Panel Discussion: Particulate Control Issues P-1

Session 1A: DUST PROPERTIES

Leslie Sparks, Chairman

Resistivity of Fly Ash/Sorbent Mixtures 1-1
R. P. Young*, J. L. DuBard, and L. S. Hovis

On-Line, In Situ Particle Measurements in Large-Scale Combustion Systems 2-1
P. L. Meyer*, D. J. Holve, L. J. Muzio, and G. H. Shiomoto

Session 2A: POWER SUPPLIES AND CONTROLS FOR PRECIPITATORS

Wallis Harrison, Chairman

Automatic Electrostatic Precipitator Control: Start-Up to Shutdown 3-1
P. G. Abbott*, T. C. Schafebook, and J. A. Brummer

Comparison Between Traditional and Modern Automatic Controllers on Full-Scale Precipitators 4-1
V. Reyes*

* Denotes Speaker

Section | Page

A Supervisory Computer Control for Smaller Industrial Electrostatic Precipitators 5-1
J. D. Riley* and F. Neulinger

A Total Energy Management System for Electrostatic Precipitators 6-1
S. F. Weinmann* and A. Russell-Jones

Expert Systems--Operator Advisors for Particulate Control Equipment 7-1
J. G. Musgrove* and P. N. DiDomenico

Electrostatic Precipitator Intermittent Energization Trials at Niles Generating Station 8-1
J. W. Hilborn* and R. Crynack

Session 3A: ADVANCED SO_2/PARTICULATE CONTROL STUDIES I

Ralph Altman, Chairman

Field Evaluation of Humidification for Precipitator Performance Enhancement 9-1
G. C. England*, B. A. Folsom, R. Payne, T. M. Sommer, P. J. Chappell, M. W. McElroy, and I. A. Huffman

Preliminary Test Results for Electrostatic Precipitator Performance with Furnace Sorbent Injection and Flue Gas Conditioning on a 300-MW Boiler 10-1
J. A. Arnott*, H. V. Krigmont, and E. L. Coe

Rapping Properties of Precipitated Ash/Sorbent Mixtures 11-1
M. G. Faulkner*, J. P. Gooch, R. Beittel, and J. L. DuBard

Precipitator Performance on a 130-MW Coal-Fired Atmospheric Fluidized-Bed Boiler Retrofit 12-1
T. Willkomm*, J. Larva, and T. Lugar

Full-Scale Demonstration of Flue Gas Desulfurization by the Injection of Dry Sodium Reagents into an Electrostatic Precipitator 13-1
R. G. Hooper*

Session 4A: PRECIPITATOR PERFORMANCE EVALUATION AND UPGRADING I

Grady Nichols, Chairman

An Unexpected Case of Back Corona 14-1
A. J. Ahern*

Overview of Keystone Station's Opacity Degradation and Subsequent Improvements 15-1
D. L. Strein*, D. W. Read, and A. Zarechnak

Flue Gas Temperature Mixing to Improve Electrostatic Precipitator Performance at Keystone Generating Station 16-1
J. Dudeck* and E. B. Bird

* Denotes Speaker

Section Page

Performance of the Dale Station Precipitators with Increased Plate Spacing 17-1
E. C. Landham*, J. M. Shipp, J. K. Neathery, and R. F. Altman

Experience with Pulsed Energization and Back Corona Supression of Electrostatic Precipitators 18-1
K. Porle* and K. Bradburn

Session 5A: PRECIPITATOR PERFORMANCE EVALUATION AND UPGRADING II

Bill McKinney, Chairman

Proof-of-Concept Testing of Electrostatic Precipitator Retrofit Technologies for Low and High Resistivity Fly Ash 19-1
G. Rinard*, M. Anderson, and R. F. Altman

Experimental Study of Ash Layer Detachment and Reentrainment Under Normal and Shear Rapping of Electrostatic Precipitator Collector Plates 20-1
D. H. Choi*, S. A. Self, M. Mitchner, and R. Leach

Analysis of the Performance of Multi-Stage Electrostatic Precipitators with Cooled-Pipe Precharger 21-1
L. E. Sparks*

Acoustic Sootblower Applications in Electrostatic Precipitators 22-1
J. L. Shelton*

A New Chemical Conditioner Together with a Special Feed System Keeps Plants on Emission Compliance at Low Treatment Costs 23-1
R. K. Sinha*

Session 6A: PRECIPITATOR MODELLING I

Phil Lawless, Chairman

Effect of Turbulence in Wire-Plate Precipitators 24-1
S. A. Self*, M. Mitchner, and K. D. Kihm

A New Concept in Electrostatic Precipitator Gas Distribution 25-1
A. G. Hein*

Structural Repair of Large Hot-Side Electrostatic Precipitators--An Update 26-1
C. A. Altin*, R. A. Schmidt, and K. K. Fatehpuria

A Self-Consistent Deutschian Electrostatic Precipitator Model 27-1
M. G. Faulkner*, J. L. DuBard, and L. S. Hovis

A Pilot Scale Study of Wide Plate Spacing for Precipitators 28-1
J. K. Horrocks, R. G. Corbin, and D.E. Towell
This paper was selected for presentation, but the speaker was unable to attend.

* Denotes Speaker

Section Page

Particle Charging and Collection Efficiency in a Laboratory Scale Electron Beam Precipitator 29-1
W. C. Finney, J. S. Clements, and R. H. Davis
This paper was selected for presentation, but the speaker was unable to attend.

Session 7A: PRECIPITATOR MODELLING II

James DuBard, Chairman

Calculation of Electric Field and Current Distributions Along Profiled Collecting Electrodes in a Wire-Plate Electrostatic Precipitator 30-1
C. E. Akerlund*

Three-Dimensional Secondary Flow and Electrohydrodynamics for Various Electrostatic Precipitator Configurations 31-1
T. Yamamoto, P. A. Lawless, N. Plaks, and L. E. Sparks
Presented by D. Ensor

An Interactive Model for Analysis of Electrical Conditions in Electrostatic Precipitators 32-1
P. A. Lawless*, N. Plaks, and L. E. Sparks

Improving ESP Performance By Reducing Losses............................ 33-1
P. A. Lawless*, T. Yamamoto, and L. E. Sparks

Appendix: ATTENDEES A-1

VOLUME 2

PARTICULATE CONTROL FOR INCINERATORS, FULL-SCALE FABRIC FILTER STUDIES I, FULL-SCALE FABRIC FILTER STUDIES II, ADVANCED SO_2/PARTICULATE CONTROL STUDIES II, ADVANCED SO_2/PARTICULATE CONTROL STUDIES III, FABRIC FILTER PILOT-SCALE STUDIES I, AND FABRIC FILTER PILOT-SCALE STUDIES II

Section Page

Session 1B: PARTICULATE CONTROL FOR INCINERATORS

Theodore G. Brna, Chairman

Characterization of Stack Emissions from Sewage Sludge Incinerators 1-1
R. M. Leuser* and L. A. Velazquez

Total Scrubbing of Incineration Air Pollutants--The EMCOTEK Approach 2-1
H. L. Marschall*, H. H. Elliott, and D. G. Jones

* Denotes Speaker

Section Page

Session 2B: FULL-SCALE FABRIC FILTER STUDIES I

Wallace Smith, Chairman

The Design, Start-Up and Operation of the Intermountain Power Project, Unit #2 Fabric Filter System 3-1
R. L. Miller*, J. J. Carnevale, T. L. Conkin, and D. O. Swenson

Monitoring of Start-Up and Operation of Intermountain Power Project Unit #1 Fabric Filter 4-1
P. V. Bush*, W. V. Piulle, J J. Carnevale, and T. L. Conkin

Fabric Filter Emissions, Study of Their Variability 5-1
W. R. Lane*

Fabric Filtration--Still a Black Art 6-1
R. M. Jensen*

Flue Gas Dust Extraction for the Slag-tap Pulverized Coal Firing at Brunswick Central Thermal Power Station, Using the "Superjet" Tubular Filter 7-1
W. Flatt*

Session 3B: FULL-SCALE FABRIC FILTER STUDIES II

Ramsay Chang, Chairman

Optimizing and Controlling Baghouse Operations at BG&E C.P. Crane Station 8-1
J. E. Sturtevant* and G. P. Greiner

Predicting Relative Drag for Baghouses from Coal Chemistry 9-1
T. R. Snyder*, P. V. Bush, W. B. Smith, and R. L. Chang

Lifetime Baghouse Costs 10-1
P. E. Frankenburg*

Recommendations for a Baghouse Design Change and for Some New Test Procedures 11-1
R. M. Jensen*

Australian Experience with Fabric Filters on Power Boilers--An Update for 1987 12-1
A. T. M. Vandewalle and H. F. Johnson
Presented by F. Thomson

Session 4B: ADVANCED SO_2/PARTICULATE CONTROL STUDIES II

George Offen, Chairman

EPRI High-Sulfur Spray Dryer/Fabric Filter Pilot Results 13-1
G. Blythe*, L. Lepovitz, R. Rhudy, and K. Cushing

* Denotes Speaker

Section Page

Particulate Control for a Combined Lime/Ammonia Spray Dryer for SO_2 Removal 14-1
W. T. Davis*, A. Pakrasi, G. D. Reed, T. C. Keener, and J. T. Lee

Operating Results of Several Baghouses in Dry FGD Service 15-1
M. Fiedler* and C. Barranger

Dust Collector Design Considerations for MSW Acid Gas Cleaning Systems 16-1
J. R. Donnelly*, B. Brown, T. D. Tarnok, and R. J. Triscori

A Study of a Reverse-Gas Fabric Filter Controlling Particulate Emissions from a 50-MW Atmospheric Fluid-Bed Combustor 17-1
C. C. Barranger*, H. Isaka, and Y. Matsui

Session 5B: ADVANCED SO_2/PARTICULATE CONTROL STUDIES III

David Ensor, Chairman

Analysis of the Performance of an Electrostatic Precipitator Operating Downstream of a Spray Dryer on High-Sulfur-Coal Flue Gas 18-1
M. D. Durham*, C. M. Huang, J. DeGuzman, B. F. Kee, and R. G. Rhudy

E-SO_x System for Combined Particulate and SO_2 Control 19-1
L. Hovis*, R. E. Valentine, J. L. DuBard, and J. C. S. Chang

Full-Scale Precipitator Experience Following a Lime Slurry Flue Gas Desulphurization System 20-1
K. Bradburn* and C. Mauritzson

Video-Based In Situ Droplet Concentration and Size Analyzer 21-1
J. D. McCain*

Session 6B: FABRIC FILTER PILOT-SCALE STUDIES I

John Mycock, Chairman

Fabrics Evaluation for Utility Baghouses on Coal-Fired Boilers 22-1
D. V. Giovanni*, L. G. Felix, C. J. Bustard, G. E. Kenniston, and W. B. Smith

Parametric Testing of Filtration Fabrics for Low-Sulfur-Western Coal Fly Ash 23-1
L. G. Felix*, C. J. Bustard, G. E. Kenniston, D. V. Giovanni, and R. L. Chang

Pulse-Jet Fabric Filters for the U.S. Electric Utility Industry 24-1
R. C. Carr*, A. T. M. Vandewalle, and W. B. Smith

Mechanisms of Fabric Filter Performance Improvement with Flue Gas Conditioning 25-1
S. J. Miller*, D. L. Laudal, and S. S. Kim

* Denotes Speaker

Section Page

Advances in Electrostatically Stimulated Fabric Filtration 26-1
N. Plaks* and B. E. Daniel

Session 7B: FABRIC FILTER PILOT-SCALE STUDIES II

Robert Jensen, Chairman

Using the Fabric Filter Gas Flow Model to Simulate the Operation of a Pilot-Scale Baghouse 27-1
D. H. Pontius*, C. J. Bustard, and R. L. Chang

Fabric Filter Options for Low-Sulfur Coal 28-1
K. M. Cushing*, C. J. Bustard, W. B. Smith, W. V. Piulle, and R. C. Carr

Fabric Filter Options for High-Sulfur Coal 29-1
R. F. Heaphy*, R. R. Wilson, R. P. Gehri, and R. F. Altman

Experience with High Temperature Filter Media in Envelope-Type Filters in Flue Gas Cleaning 30-1
E. Vogel*

Appendix: ATTENDEES A-1

* Denotes Speaker

PARTICULATE SYMPOSIUM

PANEL DISCUSSION

The plenary session of the Seventh Symposium included a panel discussion of issues likely to influence the nature of particulate control regulations and technology at utility plants in the future. Panel members were all experts in the particulate control field and represented all aspects of this technology from research and development to operation and maintenance. The panel was composed of the following members:

Mr. Charles A. Altin	Ebasco Services, Inc.
Mr. Arch Arstikaitis	Combustion Engineering, Inc.
Mr. Peter Bibbo	Research-Cottrell, Inc.
Mr. Gary Greiner	ETS, Inc.
Dr. Gerald A. Hollinden	Tennessee Valley Authority
Mr. Richard McRanie	Kilkelly Environmental Assoc.
Dr. Grady Nichols	Southern Research Institute
Mr. David Sloat	Sargent & Lundy
Mr. John W. Walton	State of Tennessee Air Pollution Control Program
Mr. Jeffrey Williams	Rochester Gas & Electric Corp.

Collectively, this group has more than 150 years of pollution control or utility experience. Dr. Ralph Altman of EPRI was moderator of the discussion.

Panel members were given the following list of questions to address:

1. What developments do you expect to affect fabric filter technology at utility plants in the future?

2. What developments do you expect to affect ESP technology in the future?

3. What generation technologies do you think will be adopted by utilities in the future (for instance, atmospheric fluidized-bed, gasification, or cogeneration) and what effect will these changes have on particulate control technology?

4. What do you think the chances of success are for developing combined SO_x, NO_x, and particulate control technologies, and what is your projected schedule for these technologies?

5. What effect will the PM_{10} or other new environmental regulations (for instance, toxics or acid rain) have on particulate control at utilities?

There was a general consensus among the panel members as to what the most significant future developments for both fabric filters and precipitators were likely to be. For precipitators, wide plate spacing, new electronic controls, gas conditioning with humidification or SO_3, and conversion to two-stage operation were identified as having potential. For fabric filters, advanced cleaning methods (particularly pulse-jet cleaning), improved fabrics, a better understanding of the formation of dustcakes (leading to better predictive tools) and gas conditioning were identified as technologies to watch.

There was a much wider diversity of opinion concerning the effect of future environmental regulations and generation technologies on particulate control. These questions, however, were the most interesting to the panel members and to the audience. Acid rain legislation was described as being eminent or distant by different panel members. There was a wide variety of views on how quickly, and to what extent, utilities would build or retrofit atmospheric fluidized beds. Surprisingly, there was general agreement that while the new ambient PM_{10} regulation could affect isolated utilities, its effect would not be very dramatic.

The discussion generated numerous positive comments, and the panel members deserve praise for the job they did preparing for, and participating in, the discussion. Plans are being made to have similar discussions at future particulate symposiums. A summary of the panel discussion follows.

Question 1: What developments do you expect to affect fabric filter technology at utility plants in the future?

Mr. Gary Greiner -

Mr. Greiner said that, given no major changes in the requirements of the utility application, there is no reason to expect change in the type of fabric filter technology currently employed; most users and regulators are comfortable with the status quo. However, in most applications, benefits can be derived from improved O&M (to reduce costs). He also sees a number of technical changes that may drive the industry to adopt pulse-jet baghouses, including:

(1) Increased application of acid gas controls, with resulting lower baghouse inlet temperatures, will allow lower temperature, felted fabrics, and smaller baghouses (both factors favor the pulse-jet).
(2) New power plants will be smaller, again giving the pulse-jet baghouse an advantage.
(3) With the growth of the use of AFBCs, which produce fly ash that makes it harder to maintain stable pressure drop, and pulse-jet baghouses may provide the necessary cleaning energy.

Dr. Grady Nichols -

Dr. Nichols identified a number of developments: new fabrics, optimized cleaning techniques, pulse-jets, modeling capability to predict/optimize selection and design, and gas conditioning (especially for high-sulfur coal applications).

Question 2: What developments do you expect to affect ESP technology in the future?

Mr. Peter Bibbo -

Mr. Bibbo stated that future developments which will be influenced by government regulations are uncertain. No one knows what regulations will be passed, such as more restrictive PM_{10} emission limits or acid rain controls. Possible technologies to meet new requirements include wide plate spacing, humidification for new plants, SO_3 conditioning for coal switching, pulse energization, and gas cooling.

Mr. Bibbo stated that some plants will opt for more SCA; but noted that specification in this new environment was an uncertain process.

Mr. Bibbo also stated that large pilot-scale experience with new developments is needed before going on to full-scale and finally, that reentrainment needs further study.

Dr. Grady Nichols -

Dr. Nichols agreed that acid rain legislation will be a driving force for technology changes. He sees significant technical developments in the following areas: catalytic SO_3, wide plate spacing, two-stage precipitation, pulse energization corona discharge for NO_x/SO_x, and high temperature-high pressure (HTHP) collectors for PFBC and IGCC.

Mr. Peter Bibbo -

Mr. Bibbo said the HTHP collectors have been tested, and the collection process worked; but several very different hardware problems remain to be solved.

Dr. Gerald A. Hollinden -

Dr. Hollinden stated that, with the likelihood of new regulations, increased attention will be placed on NO_x control. He posed the question: What effect will combustion modifications have on ESPs? Increased carbon in ash, different SO_3 levels, and different particle size distribution are a few potential changes that deserve attention.

Mr. David Sloat -

Mr. Sloat noted a problem of particulate carryover into flue gas desulfurization (FGD) systems which, in some applications, could interfere with efficient operation of the FGD system. This carryover problem could, for example, prevent application of energy management systems to some precipitators but encourage the use of intermittent energization as a means of reducing power consumption. He also stated that the conversion of hot-side ESPs to cold-side operation or to baghouses is an important problem that needs attention. For instance, on a unit where the hot-side precipitator has operated at over 750 degrees F for several years, structural damage could complicate conversion and affect resulting cold-side performance. There are now several such conversions, and the impact of structural deterioration can now be assessed and design changes made to account for any such problems.

Mr. Charles Altin -

Mr. Altin questioned the current approach to energy management systems that monitor opacity for ESPs which are required to meet a 0.03 lb/MBtu emission limit. Although some may believe that 20% opacity is in compliance with 0.03, some data on new generating units suggest that opacity may range between 5 and 10% to achieve 0.03. Therefore, energy management systems set to control opacity at the 16 to 18% range may, and probably will, cause violation of the 0.03 lb/MBtu emission standard where applicable. Utilities so affected need to reevaluate in-house data and develop new set points to assure the 0.03 is met all the time.

Mr. Peter Bibbo -

Mr. Bibbo stated that the compliance with fine particle standards may require more energy than compliance with total suspended particulate matter standards.

Dr. Grady Nichols -

Dr. Nichols questioned the last statement because he thinks intermittent energization works as well on fine particles as it does on total particulate.

Question 3: What generation technologies do you think will be adopted by utilities in the future (for instance, atmospheric fluidized-bed, gasification, or cogeneration) and what effect will these changes have on particulate control technology?

Mr. Charles Altin -

Combined-cycle/cogeneration now represents a significant portion of generating capacity in this country. Its role in power generation will substantially increase in the future. However, what will happen to the cost of electricity if natural gas prices dramatically increase? Will these facilities be abandoned? Does this generation of technology represent the best interest of the nation in terms of conserving a precious natural resource and development of a rational national energy policy? Mr. Altin also sees a number of AFBCs, especially for repowering of older units. He expects them to be in the 200-300 MW size range. Fabric filters will be used, but the potential for somewhat higher dust loading and altered particulate characteristics may have an impact on their operation.

He also sees a large growth in the use of municipal solid waste (MSW) as a fuel, but this development will require cooperation between the developer and local governments. Emissions from these systems will probably be controlled by spray dryers with ESPs or fabric filters. MSW may be a logical outgrowth of a national energy policy.

Dr. Gerald Hollinden -

The Tennessee Valley Authority doesn't see any new fossil development before the year 2000 due to 10,000 MW of nuclear power to come on-line. He stated that AFBCs are the best repowering option and may be the best choice for new capacity because of fuel flexibility, low NO_x (200 ppm) and low SO_x (90-95% reduction). TVA's experience shows that grain loading and size distribution are similar to that from a pulverized coal-fired unit, but resistivity is different by 1-2 orders of magnitude. However, their pilot ESP worked very well behind the pilot AFBC so fabric filters may not be needed.

Mr. Richard McRanie -

Mr. McRanie sees electrostatic precipitators and fabric filters as equally competitive for applications of moderate size (> 150 MW) so individual decisions will depend on the best bid (who the most aggressive bidder is at the time). Life extension will be the major goal of utilities for the next decade.

He questioned the wide-spread acceptance of phased, combined cycle/gasification (IGCC). If gas turbines are used for peaking and later converted to baseload with the addition of a gasifier, what will replace the peaking capacity?

Dr. Grady Nichols -

Dr. Nichols noted the interest in PFBCs as a generation technology but warned that there is no proven gas cleanup technology for this process.

Question 4: What do you think the chances of success are for developing combined SO_x, NO_x, and particulate control technologies, and what is your projected schedule for these technologies?

Mr. David Sloat -

Mr. Sloat said that there has been some success at pilot scale for a number of technologies, including dry sorbent injection combined with low NO_x burners, slagging combustors, fluid-bed collectors (CuO process), and E-beam. However, none have been demonstrated at large scale. Their utilization will depend, to some degree, on the timing of any acid rain regulations as well as the significant tightening of NO_x emission limits. Full-scale testing will not occur until the 1995 to 2000 period. If new environmental regulations require significantly greater reduction of SO_x/NO_x and if the reduction is required before the year 2000, then the success of the combined technologies is severely threatened.

He also believes that many of these technologies cost more than flue gas desulfurization combined with low NO_x burners or even flue gas desulfurization combined with selective catalytic NO_x reduction.

Dr. Gerald Hollinden -

Dr. Hollinden expressed concern about the development of these new technologies and referred to the experience of the 1971 New Source Performance Standards for SO_2, where emission limits and required technology were based on very short-term tests at Lawrence, without long-term knowledge of operational impacts. (That assessment was later questioned by Wade Ponder of the U. S. Environmental Protection Agency).

Dr. Hollinden went on to say that emerging technologies need to be demonstrated at a scale of greater than 100 MW at one site and then verified at 4 or 5 additional sites (deployment exercise) to show general applicability before they can be considered "commercially available". He sees the most optimistic schedule to be 1993 for completion of the first demonstration of a combined NO_x/SO_x system and 1995 for the start of the 4- to 5-year validation effort. Hence, there will be no commercially proven technology before the year 2000.

He also believes regulations and competitive forces may prevent the development and application of a combined NO_x/SO_x/particulate system. As developers improve the performance of controls for individual pollutants, regulations will be introduced at more stringent levels. Therefore, the simultaneous systems will probably be unable to compete with combinations of the best individual pollutant control systems and will never be able to catch up.

NO_x limits below 0.2-0.3 lb/MBtu will be hard to achieve with conventional pulverized-coal-fired boilers without the use of selective catalytic reduction (SCR) or other postcombustion processes. Also, if the limit is set at 0.1 lb/MBtu, it will probably require the use of postcombustion control for the bubbling-bed FBC. These facts suggest that limits should be set only after weighing the effects of these limits on currently available or developing combustion technologies.

Mr. Richard McRanie -

Mr. McRanie supported and emphasized Dr. Hollinden's comments on the need for a deployment step. As an example, he noted problems with too rapid acceptance of hot-side ESPs and supercritical boilers. The concern applies equally to advanced generation and pollution control technologies.

Question 5: What effect will the PM_{10} or other new environmental regulations (for instance, toxics or acid rain) have on particulate control at utilities?

Mr. John Walton -

At the state level, Mr. Walton sees no impact of the PM_{10} on utilities until or unless EPA sets corresponding stack limits. This is partly due to the fact that Tennessee has visible emission limits that are more restrictive than mass-based limits. Tennessee is working on the detached plume problem which is being controlled on a case-by-case basis.

He noted that air toxics regulation is more complex than other air pollutants because air regulators have to interact with Resource Conservation and Recovery Act (RCRA) regulators. He agreed that acid rain limits will become the biggest problem unless that issue is superseded by ozone concerns. He disagreed with a proposed change to a 30-day rolling average because the State of Tennessee now has a 24-hour standard based on Continuous Emission Monitoring (CEM) that is more restrictive.

Mr. Jeffrey Williams -

Mr. Williams stated that there are no ambient problems with PM_{10} in New York State, and no problems are anticipated in the future.

He doesn't see any acid rain legislation in the near future either. The biggest worry in the New York Area is NO_x and ozone which pose health problems. He sees the potential for lower ozone National Ambient Air Quality Standards (NAAQS) and the introduction of air quality transport regions. Therefore, concern should be with any impacts of NO_x controls on particulate control. He also expressed concern that scrubbing or fuel switching could have a negative effect on particulate control in the future.

Mr. Arch Arstikaitis -

PM_{10} is not an issue for the utility industry in the foreseeable future for several reasons.

First, by meeting New Source Performance Standards for particulate emissions the utilities are already below the projected limits proposed in PM_{10}, much less just for particulate emissions in the respirable range. This legislation would impact and be an issue for the industrial and commercial sectors rather than the utility sector.

Secondly, there is no accepted point source measurement technique for PM_{10}. A substantial effort has to first be expended in developing the measurement techniques before legislation can be affected.

The next pollution issue to confront the utility industry is therefore not PM_{10} but acid rain legislation All indications are than an acid rain bill will be passed relatively soon with the Waxman bill seemingly emerging as the leading contender. This bill would require compliance with newly mandated SO_x emissions level sometime between 1993-1995.

Compliance options for SO_x include fuel switching, sorbent injection and wet or dry scrubbing. With the possible exception of wet scrubbing, all the other compliance options will have a marked effect on the presently employed particulate control systems.

Mr. Richard McRanie -

Mr. McRanie stated that most fine particulate (PM_{10}) matter comes from nonstationary combustion sources or wood stoves. However, utilities could be implicated in fugitive emissions from coal piles, where there is a potential for PM_{10} emissions that are several times greater than the stack PM_{10}. He feels that toxics regulations are coming, but better test methods are needed. Some of the tests presently being used have a ± 50% accuracy.

He also stated that there is some chance of acid rain legislation being passed this year, prior to election, and a 90% chance by the end of next year. The Republicans would like to improve their environmental posture. The only remaining question in Congress is how the new control equipment and operation costs will be paid for.

Charles Altin -

Mr. Altin agreed that acid rain could be the driving force for new or improved controls. He cited a recent Ebasco study that showed acid rain retrofit costs would be higher than $3000/ton SO_2 removed for units having low capacity factors and/or short remaining lives (10-15 years). Thus, acid rain legislation could kill life extension or life continuation plans for many units.

RESISTIVITY OF FLY ASH/SORBENT MIXTURES

by: R. P. Young
J. L. DuBard
Southern Research Institute
Birmingham, Alabama 35255-5305

L. S. Hovis
Air and Energy Engineering Research Laboratory
U.S. Environmental Protection Agency
Research Triangle Park, North Carolina 27711

ABSTRACT

One method for reducing the emission of sulfur oxides by coal-fired utility boilers is to inject a calcium-based sorbent material into the furnace or combustion flue gas to capture these oxides. This results in a particulate which is a mixture of coal fly ash and partially spent sorbent. Applying the usual procedure for measuring resistivity of fly ash to these ash/sorbent mixtures results in erratic and inconsistent values of resistivity. However, by limiting the maximum temperature at which the measurements are made, the nature of these mixtures is preserved and accurate and reproducible values of resistivity are obtained. The resistivities of samples from four different sorbent injection methods were measured and correlated with their chemical composition.

This paper has been reviewed in accordance with
the U.S. Environmental Protection Agency's peer
and administrative review policies and approved
for presentation and publication.

INTRODUCTION

Methods for reducing the amount of sulfur oxides (SO_x) emitted from the smokestack of a coal-fired power plant by injecting calcium based compounds into the furnace or into the combustion flue gas downstream to absorb these oxides are the subject of intense research efforts. These processes result in a particulate which contains both coal fly ash and partially spent sorbent material which must be removed by the particulate collection system (such as an electrostatic precipitator). The presence of the sorbent causes the resistivity of the mixture to be significantly higher than that of the fly ash alone. And since the resistivity of the particulate influences the collection efficiency of the dust (higher resistivity dusts being more difficult to collect), it is important to be able to accurately measure the resistivity of the mixture to determine if the precipitator will operate within an acceptable efficiency range.

Application of the IEEE Standard 548-1984 procedure for measuring resistivity of fly ash to measuring resistivity of an ash/sorbent mixture resulted in inconsistent values of resistivity and an overall lack of repeatability, as well as large discrepancies between values measured using the ascending and descending temperature methods. This behavior was traced to large changes in the nature of the as-collected sample caused by heating to 450°C, as specified by the Standard. In order to preserve the nature of the as-collected sample, it was decided that the sample should not be exposed to temperatures in excess of 250°C during resistivity measurements. And to obtain the best repeatability, these measurements should be made in the descending temperature mode.

Experiments in which a large amount of charge was transferred across a sample were conducted to try to determine the charge carrying species in an ash/sorbent sample. However, no single ion or group of ions could be identified as the charge carriers for all the samples tested. Attempts to correlate the resistivities of the mixtures with their chemical composition were generally unsuccessful. However, comparisons of the resistivities of the ash/sorbent samples with those of the sorbents alone show good correlations between particular combinations of sorbent compounds and the ash/sorbent mixtures.

SAMPLE CHARACTERIZATION

The eight samples used in this work resulted from burning pulverized coal in either a pilot-scale combustion facility or a full-scale power plant and injecting the sorbent into the furnace or into the flue gas downstream of the regenerative air heater. The samples were then subjected to a battery of tests designed to characterize them as completely as possible. These tests included chemical analysis, particle size analysis, thermogravimetric analysis (TGA), scanning electron microscope (SEM) photographs, density, mercury porosimetry, and surface area measurements. Because the important qualitative features of the data were the same for all of the samples, the results reported here will focus on the sample generated by burning Pittsburgh coal and spraying Longview hydrated lime into a chamber in which the entering flue gas temperature was about 149°C (300°F). This sample is designated the "E-SOX sample" because one type of cool-side lime slurry injection process is the EPA E-SOX process.

SEM photographs of the E-SOX sample showed that it consisted of spherical, amorphous particles of coal fly ash, agglomerates of fly ash particles, and crystalline clusters of the sorbent material. In some cases, the crystalline clusters surrounded a few spherical fly ash particles. The dispersal of the spherical and crystalline particles appeared to be uniform.

Results of chemical analysis of the E-SOX particulate are shown in Table 1. The presence of the sorbent material in this sample is reflected in the relatively high value of calcium (reported, by convention, as CaO). Also included in the table are the mass median diameter (mmd), density, and porosity (ratio of the void volume in the sample to the total volume occupied by the sample) for this material.

Because calcium reacts readily with water, it was necessary to test the E-SOX sample for adsorption of moisture to see if the material remained in its as-collected state long enough to permit routine laboratory tests on a sample. As a simple test for the adsorption of water, the specific surface area of (a) a sample exposed to room air (relative humidity of about 60%), and (b) a sample continuously exposed to the flue gas conditions under which it was collected (67°C and 11% humidity by volume) was measured according to the theory of Brunauer, Emmett, and Teller (1) (the "BET area"). The changes in BET area during the 8 days of exposure to moisture were quite small for both samples. This indicates that, for reasonably short times (a few days) between acquiring the sample and transporting it to the laboratory, the change in BET area of the sample due to exposure to atmospheric humidity will be small.

RESISTIVITY MEASUREMENTS

The E-SOX sample was subjected to a resistivity test according to IEEE Standard 548-1984 (designed for testing fly ash only) at 9.6% water vapor by volume. Measurements were taken during both heating and cooling of the sample. The results of this test are shown in Figure 1. For most of the temperature range, the resistivity measured in the ascending phase is higher than that measured in the descending phase for a given temperature. In the low temperature limit, the resistivity measured in the descending mode is three orders of magnitude less than that measured in the ascending mode. Thus, this procedure for making resistivity measurements yields widely different results for ash/sorbent samples, depending on the method chosen for changing temperatures.

Another drawback to use of the IEEE procedure for ash/sorbent samples is the lack of repeatability in the data when a sample is "cycled" -- i.e., successive resistivity measurements made on the same sample and under identical conditions. Figure 2 shows data (using the descending temperature method) for a fresh sample (E-SOX 3), and samples tested once and twice previously (E-SOX 2 and E-SOX 1, respectively). In general, the resistivity of the fresh sample was always higher than that of the cycled samples. Sometimes this difference was as much as an order of magnitude for a given temperature. Therefore, the resistivity of these samples decreases when they are cycled using the IEEE procedure.

ANNEALING EFFECTS

Because of the differences in resistivity between the ascending and descending temperature methods, it seemed likely that heating the E-SOX sample to 450°C was somehow responsible for the discrepancy. Thermogravimetric analysis (TGA), which measures the change in weight of a sample as it is heated, can be used to detect the loss of one or more components of a sample during heating. Results for the E-SOX sample are shown in Figure 3. The initial decrease in weight of the sample is due to driving off adsorbed moisture. Weight loss which occurs between about 300 and 450°C has been identified as decomposition of calcium hydroxide in the sample. Therefore, heating to 450°C results in a fundamental change in the nature of the sample.

One possibility for the differences in the resistivity of fresh and cycled samples is partial decomposition of $Ca(OH)_2$ after the first heating and complete decomposition with subsequent heating. To test this hypothesis, TGA was run twice on several samples to see if any additional weight loss occurred during the second heating to 450°C. The weight changes for these second runs were less than 1%. It seems unlikely that such a small change could be responsible for the difference in resistivity shown in Figure 2 (an approximate order of magnitude difference at the lower temperatures).

The effect of temperature on the surface area of the E-SOX sample is shown in Figure 4. For this test, the sample was maintained in an atmosphere of dry air (measured water concentration of 0.21% by volume) at a temperature of 50°C. After 24 hours, a portion of the sample was removed for BET analysis. The temperature was then raised in increments of 50 degrees, to a maximum of 450°C, and the procedure repeated. A steady increase in the surface area with temperature up to 400°C was observed. Then when the sample was heated to 450°C for 24 hours, the surface area dropped sharply to a value which was a factor of 3 lower than the initial value. Thus, a large change in the surface area of the sample accompanies the decomposition of the $Ca(OH)_2$.

Because of the large change in the BET area, it was hoped that differences between the annealed and as-collected sample could be seen in the SEM photographs.

However, photographs of the two samples were indistinguishable, even up to a magnification of 10,000X. Bahco particle size classification of the annealed sample showed that the mmd increased from 6.3 μm for the as-collected sample to 7.7 μm for the annealed sample. Pursuing this further, the BET area of the size fractions collected in the Bahco machine was measured and is shown in Table 2. Although the surface area changed across the entire range of sizes, the percent change increased as the particle size increased. The density also increased from a value of 2.35 g/cm^3 for the as-collected material to 2.51 g/cm^3 for an annealed sample, while the porosity stayed relatively constant (77 and 74%, respectively).

An alternative explanation for the differences in resistivity between fresh and cycled samples is that the change in surface area of the sample is incomplete after one heating but completed after the second heating. BET measurements of cycled E-SOX samples confirmed this: the specific surface area of a fresh sample was 3.0 m^2/g and dropped to 1.9 m^2/g after one heating to 450°C. For subsequent heatings, this value became constant at 1.8 m^2/g. Therefore, the differences in the fresh and cycled resistivities probably result from changes in the surface area of the sample.

MODIFIED RESISTIVITY PROCEDURE

The preceding results indicate that, in order to avoid the large changes in BET area and the decomposition of $Ca(OH)_2$ induced by annealing the E-SOX sample at 450°C, it will be necessary to limit the upper temperature at which resistivity is measured. From the data of Figures 3 and 4, restricting the maximum temperature at which measurements are made to 250°C should avoid these changes. In addition, it was found that the descending temperature mode (beginning at 250°C and decreasing the temperature during the measurements) provided the best repeatability in the measurements.

CORRELATION OF RESISTIVITY AND SAMPLE CHEMISTRY

For the case of fly ash produced by burning coal only, correlations between ash chemistry and ash resistivity enabled Bickelhaupt (2,3) to construct a successful computer model for predicting the resistivity of fly ash from its chemical composition. Applying that model (3) to the eight samples used in this work yields predicted values of resistivity which are consistently lower than the measured values. Figure 5 shows an example of the failure of the computer model to predict the resistivity of the E-SOX sample. Not only do the magnitudes not agree in general, but the entire trend of the predicted data is wrong. This is not surprising since the samples used to obtain the model generally had far less calcium content than an ash/sorbent mixture. Also, the current conduction mechanism may be different for the two cases. Thus, a new correlation between ash/sorbent chemical composition and resistivity must be obtained.

The first step in searching for a correlation between chemical composition and sample resistivity is to identify the charge carrying species. An experiment was conducted in which six different ash/sorbent mixtures were placed between parallel plates at a temperature of 60°C in an environment containing 11% humidity by volume. An electric field of 2 kV/cm was continuously applied across the samples for a period of 1 month. At the end of that time, portions of the samples next to the electrodes were removed for chemical analysis. Unfortunately, the results of chemical analysis did not show any consistent pattern of ion migration. Since the amount of charge transferred in each test was on the order of 40 coulombs, it cannot be argued that the migration of an ionic species was too small to be detected. Instead, it must be assumed that the charge carriers were not included in the compounds tested for in the usual chemical analysis.

Since the primary difference between an ash/sorbent mixture and the fly ash alone is the large amount of calcium in the mixture, the resistivities of calcium-based compounds expected to be found in the mixtures are of interest. The resistivities of calcium hydroxide, calcium sulfite, calcium sulfate, and calcium carbonate are shown in Figure 6. The data were taken in an atmosphere containing 15% water vapor by volume. Calcium sulfite has the highest resistivity of the four compounds. The resistivity of calcium sulfate is about an order of magnitude lower for most of the temperature range. Magnitudes of the calcium hydroxide and carbonate curves are much lower than those of the sulfite or sulfate. Note that the peak resistivity values for the ash/sorbent mixtures studied ranged from 10^{12} to 10^{14} ohm-cm, so the data of Figure 6 seem to bracket the data for the mixtures.

Figure 7 compares the resistivity of the E-SOX sample with that of the two calcium compounds which have been shown to be dominant in the sample. The shape of the E-SOX data is very much like that of the calcium hydroxide, but its magnitude is nearer that of the calcium sulfite. Similarly, data for the other mixtures appear to be combinations of the data for the sorbent compounds. Stepwise multiple regression performed on the resistivity data of the mixtures and the calcium compounds showed that the resistivity of mixtures employing injection of the sorbent into the furnace could be expressed as the sum of the resistivities of $CaCO_3$ and $CaSO_4$. Mixtures utilizing sorbent injection in the downstream flue gas could be expressed as the sum of the resistivities of $Ca(OH)_2$ and $CaSO_3$. The correlation coefficients (r^2) for these regressions generally exceeded 0.97. An example is shown in Figure 8 for the E-SOX mixture. The predicted data were obtained from the correlation equation

$$\rho(\text{E-SOX}) = 1.80\text{E}12 + 24.62\rho[Ca(OH)_2] + 0.01\rho(CaSO_3)$$

where ρ is the resistivity and $r^2 = 0.98$. Therefore, it does appear that the resistivity of an ash/sorbent mixture is primarily determined by the resistivities of the calcium compounds present.

MODELING ASH/SORBENT MIXTURE RESISTIVITY

Although the precise dispersion of fly ash and sorbent particles throughout the mixture is not known, assume, for simplicity, that the layer consists of discrete particles of either fly ash or one of the sorbent compounds. In addition, assume that the resistivities of all fly ash particles are the same and those of all sorbent particles of a given compound are the same. Then a charge traversing the bulk of the sample through or along these resistive particles can be represented by an electrical circuit composed of resistors representing the fly ash and sorbent particles. Because the resistivities of the calcium compounds are so high (Figure 6) and no correlation between resistivity and chemical composition was found, the resistivity of the fly ash is expected to be negligible in comparison to that of the sorbent. Also, the results of multiple regression (e.g., Figure 8) suggest that only two calcium compounds are important for a given ash/sorbent mixture. Then, by the usual method of adding resistors in series, we could write:

$$R = n_1R_1 + n_2R_2 \tag{1}$$

where R is the equivalent resistance of the entire circuit, and n_1 and n_2 are the number of calcium compound resistors of type 1 and type 2, respectively, in the path of the charge.

Although the sample will be highly inhomogeneous on the local level, we would expect that, on the average, a charge would encounter the same number of resistors of type 1 and the same number of resistors of type 2 during any complete traverse of the sample. Therefore, the relative number of each type of resistor would be the important parameters in determining the contribution of each species to R, and we could rewrite equation (1) as:

$$R' = a_1R_1 + a_2R_2 \qquad (2)$$

where $R' = R/(n_1+n_2)$

$a_1 = n_1/(n_1+n_2)$

$a_2 = n_2/(n_1+n_2)$

and $1 = a_1 + a_2$.

Note that the resistance calculated from equation (2) will always be less than that of the larger resistor and greater than that of the smaller resistor. Moreover, if a_1 and a_2 are comparable and one resistance is much greater than the other, then the overall resistance will be essentially equal to this higher resistance. This is the type of relationship suggested by Figures 7 and 8. Determining the amounts of the particular calcium compounds present in these mixtures is complicated and the techniques for doing so need refinement. But preliminary evidence indicates that the coefficients obtained with multiple regression are related to the relative abundance of these compounds.

Of course, the true nature of an ash/sorbent mixture will be much more complicated than that assumed here. But the development of equation (2) can be easily extended to the case where more calcium compounds contribute to the overall resistivity of the mixture. Such a simple picture is intended to act only as a starting point for trying to understand the resistivity of the ash/sorbent samples.

CONCLUSIONS

Application of IEEE Standard 548-1984 (intended for measuring the resistivity of fly ash only) is not appropriate for use with fly ash/sorbent mixtures. This is due to decomposition of calcium hydroxide and large changes in the surface area of these samples which occur when they are heated above 300°C. In order to avoid the large changes in the sample caused by heating, the IEEE procedure should be modified to limit the upper temperature at which resistivity is measured to 250°C for these mixtures. And to obtain best repeatability of the resistivity measurements, the test should be conducted in the descending temperature mode. Measurements using this modified procedure have shown that the resistivities of ash/sorbent mixtures are primarily determined by the resistivities of one or more calcium compounds within the sample.

REFERENCES

1. Brunauer, S., Emmett, P.H., and Teller, E. Adsorption of gases in multimolecular layers. J. Amer. Chem. Soc., 60:309-19, 1938.

2. Bickelhaupt, R. E. A technique for predicting fly ash resistivity. EPA-600/7-79-204 (NTIS PB80-102379), 1979.

2. Bickelhaupt, R. E. Fly ash resistivity prediction improvement with emphasis on sulfur trioxide. EPA-600/7-86/010 (NTIS PB86-178126), 1986.

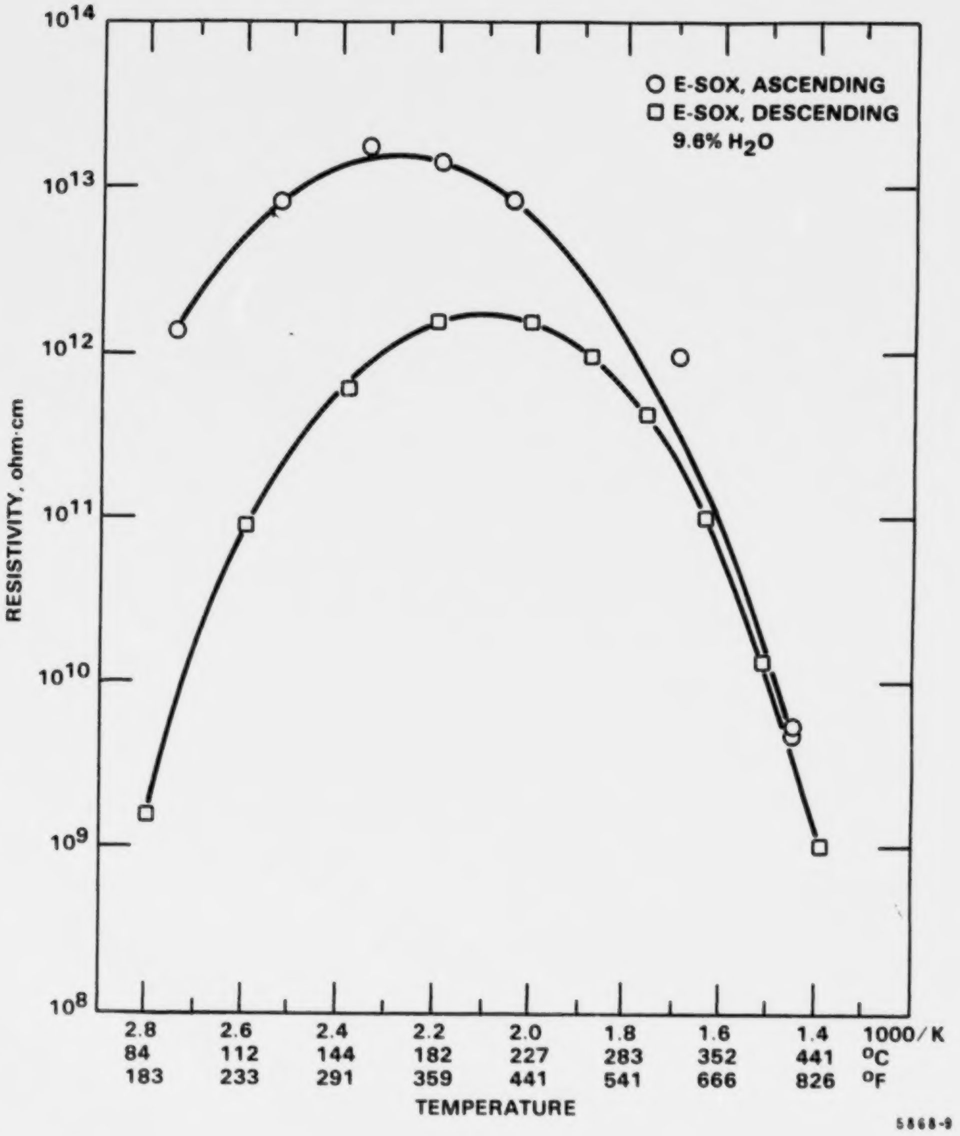

Figure 1. Resistivity of E-SOX sample obtained according to the IEEE Standard 548-1984 for resistivity measurements of fly ash.

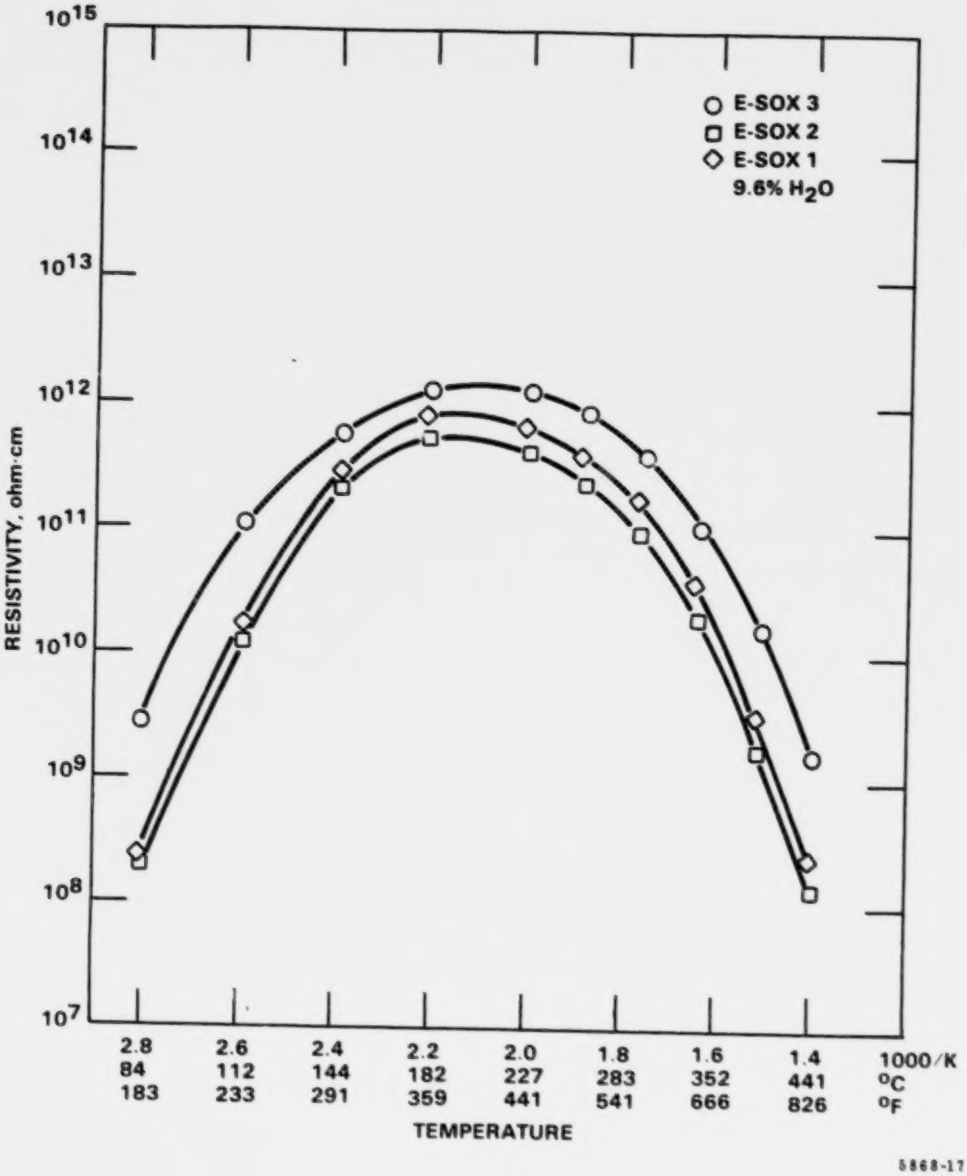

Figure 2. Comparison of resistivity data for a fresh E-SOX sample (E-SOX 3) and samples tested once and twice previously (E-SOX 2 and E-SOX 1, respectively).

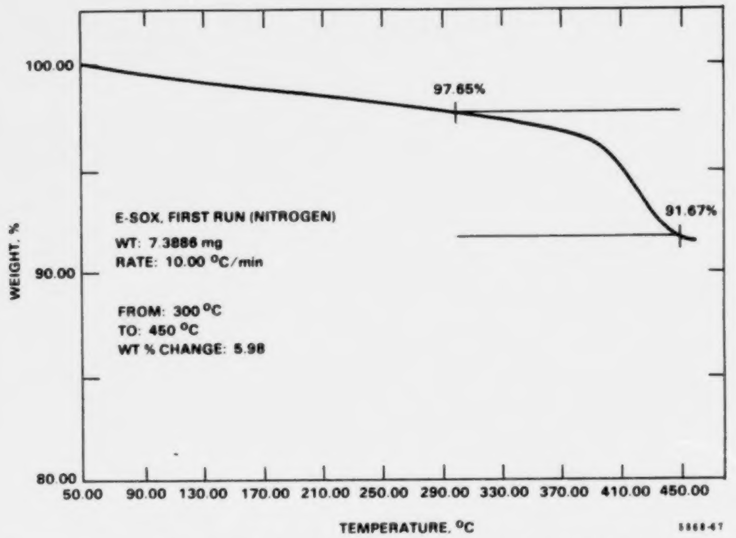

Figure 3. Thermogravimetric analysis (TGA) of E-SOX sample from 50 to 450 °C in a nitrogen atmosphere.

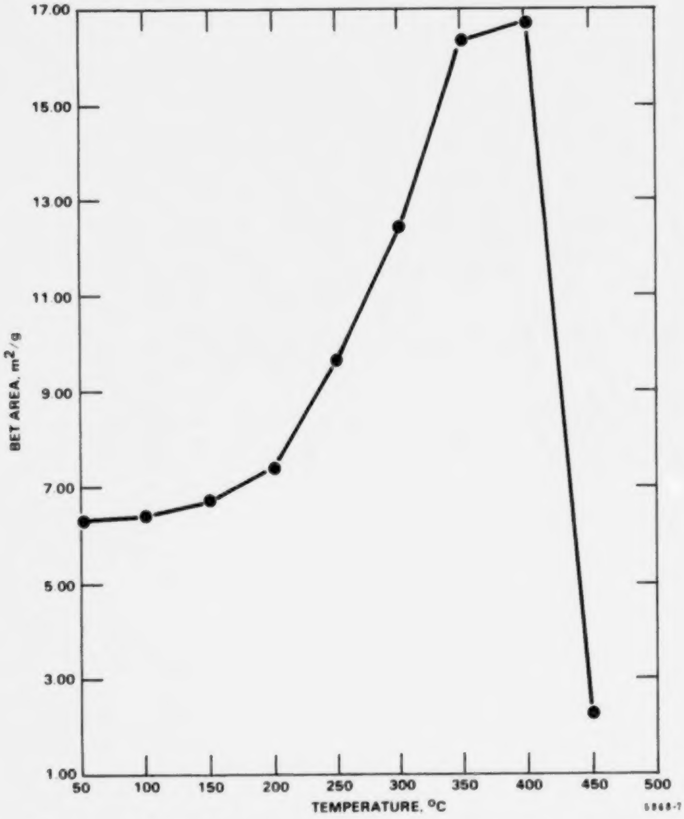

Figure 4. BET area of E-SOX sample as a function of annealing temperature in dry air.

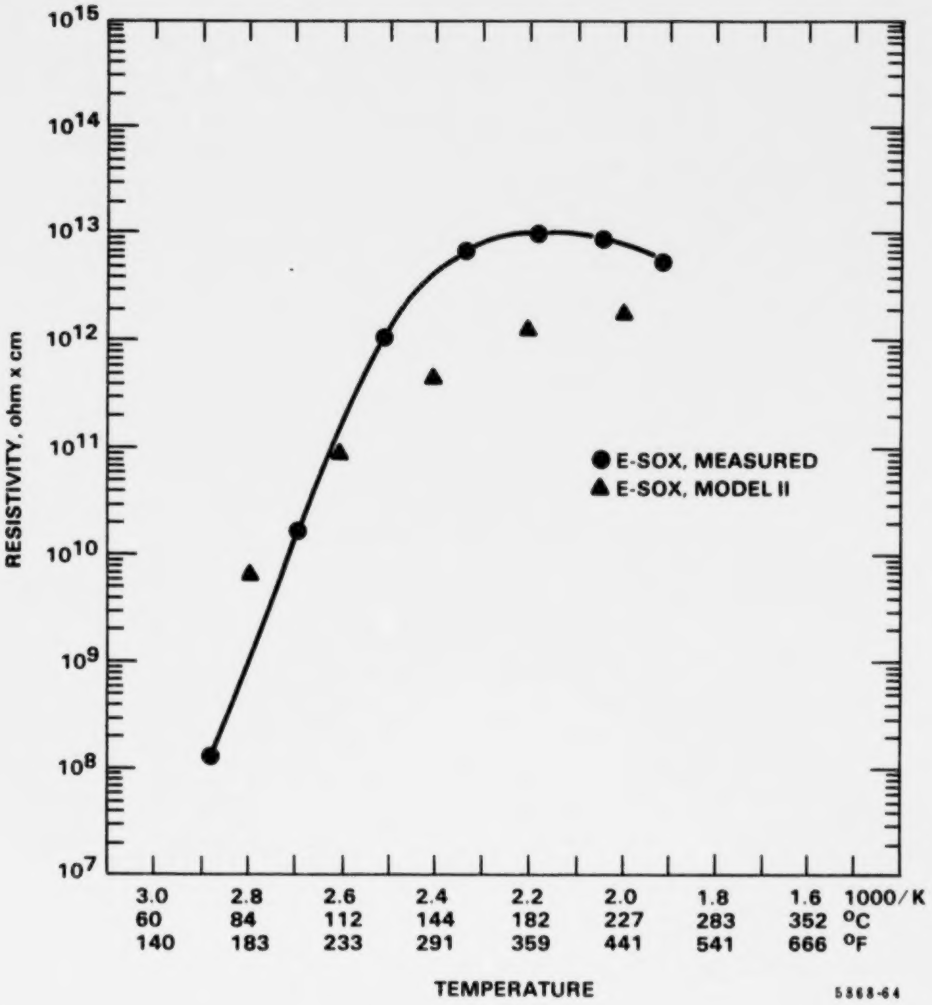

Figure 5. Comparison of measured resistivity values and those predicted by the Bickelhaupt computer (Model II, Reference 3) for an E-SOX sample in an atmosphere containing 15% water vapor by volume.

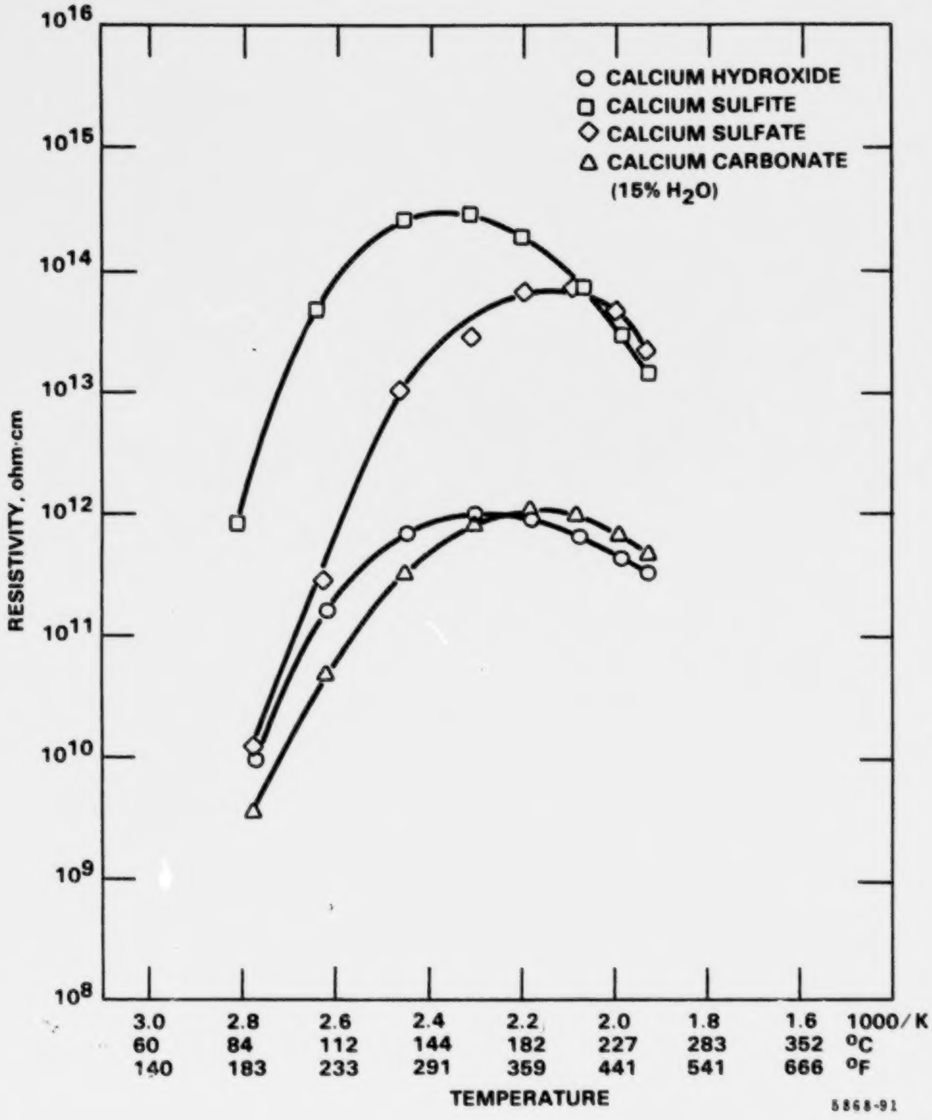

Figure 6. Resistivities of calcium compounds expected to be present in ash/sorbent mixtures.

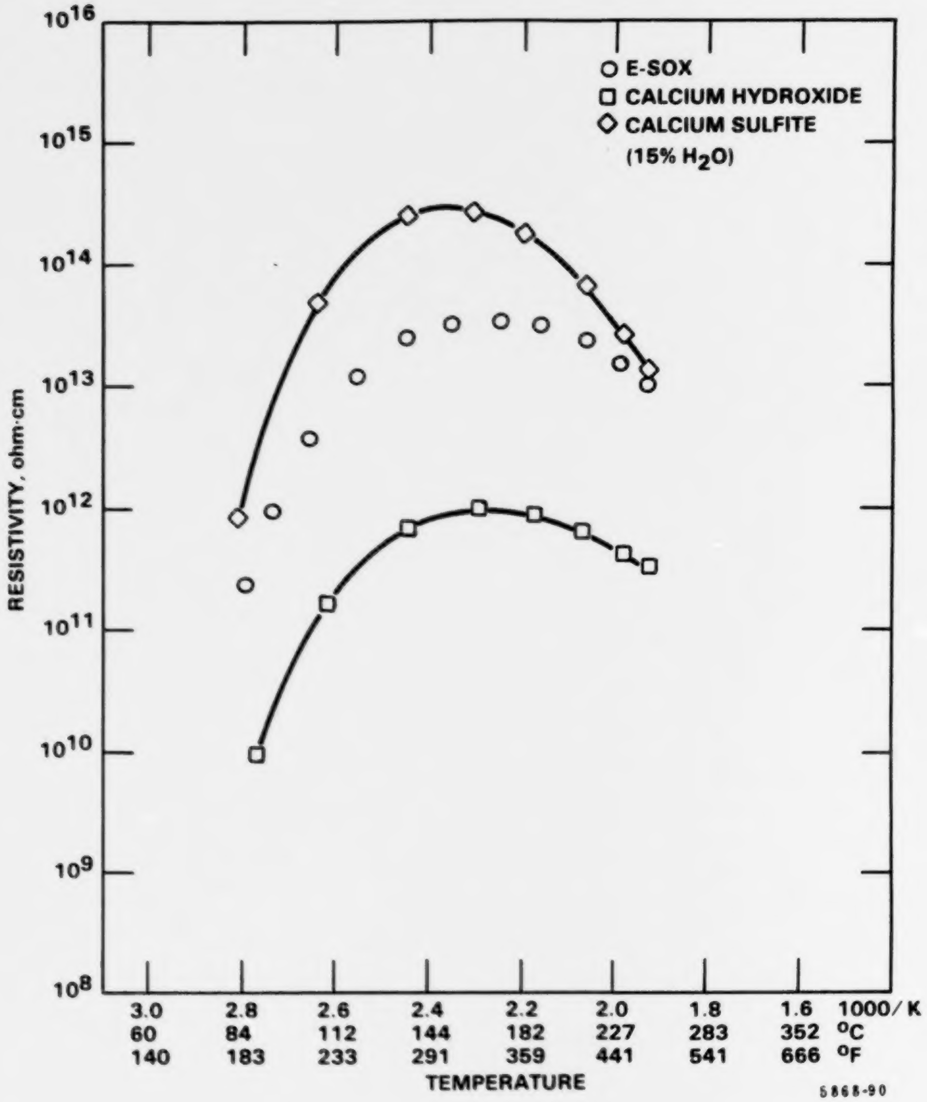

Figure 7. Comparison of the resistivities of an E-SOX sample, calcium hydroxide, and calcium sulfite.

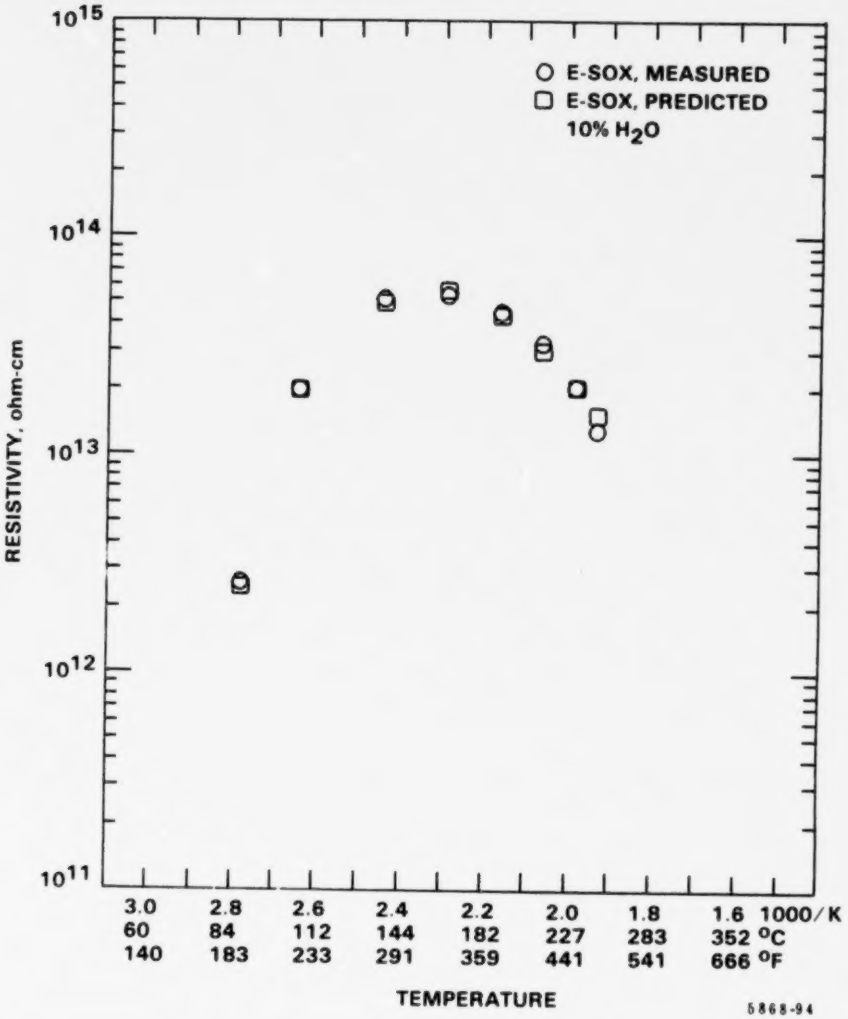

Figure 8. Comparison of the measured resistivity of an E-SOX sample and that predicted from a combination of the resistivities of $Ca(OH)_2$ and $CaSO_3$ in an atmosphere containing 10% water vapor by volume.

TABLE 1. CHEMICAL ANALYSIS OF E-SOX SAMPLE

Chemical Compound	Weight Percent
Li_2O	0.02
Na_2O	0.19
K_2O	0.87
MgO	1.0
CaO	32.4
Fe_2O_3	13.1
Al_2O_3	11.6
SiO_2	24.9
TiO_2	0.5
P_2O_5	0.12
SO_3	13.5
LOI	11.1
density (g/cm^3)	2.35
mmd (μm)	6.3
porosity (%)	77

TABLE 2. BET OF BAHCO FRACTIONS, AS-COLLECTED AND ANNEALED

BAHCO MODE (μm)	BET AREA (m^2/g) AS-COLLECTED SAMPLE	ANNEALED SAMPLE	% CHANGE
1.6	7.0	4.7	33
2.5	6.1	2.9	52
4.7	5.6	2.0	64
8.3	5.5	1.8	67
11.6	5.2	1.4	73
19.0	5.4	1.2	78
24.1	6.2	1.2	81
26.9	6.1	0.9	85
remainder	9.4	1.7	82

ON-LINE, IN SITU PARTICLE MEASUREMENTS IN LARGE SCALE COMBUSTION SYSTEMS

D. J. Holve, P.L. Meyer
INSITEC
2110 Omega Road, Suite F
San Ramon, CA 94583

L. J. Muzio, G. H. Shiomoto
Fossil Energy Research Corporation
23342 C South Pointe
Laguna Hills, CA 92653

ABSTRACT

A compact, optical probe (PCSV-P) was developed to provide on-line, in situ particle measurements in large scale combustors. Southern Company Services arranged for a demonstration of the probe at the Watson Power Plant. The PCSV-P made measurements of particle concentration, size, and velocity in the furnace (1330°C) and at the inlet and outlet of the electrostatic precipitator. A comparison of optical probe velocities with measurements made by pitot tubes showed consistent trends in velocity values as function of position in the duct. Cascade impactor and optical probe results were in good agreement for particle sizes up to 4 - 10 microns. The optical probe measures higher particle concentrations at larger particle sizes. Differences in the large particle results are believed to be due to the way in which large particle information is measured and analyzed by the two techniques. Optical probe measurements showed that the greatest variation in the velocity and particle concentration occurred at the ESP exit. While the small particle count rate was steady, the large particle count rates varied by a factor of six. These fluctuations are indicate that processes such as rapping periodically releases bursts of larger particulate. The most complex velocity flow field was also measured at the ESP exit.

INTRODUCTION

Research on new fossil energy processes and research directed at improving existing power plant operations requires instrumentation that accurately characterizes operational conditions. The availability of reliable data is crucial to basic research, design, and process control. In both conventional and advanced systems the problems of slagging, fouling, and erosion are primary limitations on the efficient use of coal (1). The ability to measure particle size, concentration, and velocity distributions is a key step in controlling these adverse effects.

Optical techniques, based on light scattering, have the capability to provide on-line, in situ measurements of particle-laden flows. Instruments incorporating these techniques can provide real time measurements of the process stream. Since this measurement technique is based on the analysis of light scattered by airborne particulate, it avoids the sample handling problems encountered by other techniques which must collect particle samples for analysis.

While optical techniques can provide the required particle measurements, there are problems applying such techniques to large scale, industrial operations. The key problems are due to beam steering and aerosol opacity effects. Thermal gradients in the process stream cause changes in the refractive index which deflect (or steer) the laser beam. Maintaining the alignment of an optical system becomes difficult when there are large refractive index variations over the laser beam pathlength. Aerosol opacity refers to the problem of transmitting the light signals through high particle concentrations over the long distances in industrial systems. It is difficult to maintain clean windows for optical access in particle-laden process streams. Also, it is difficult to avoid degradation of the light signals through secondary scattering by other particles in the flow. A third concern is that the measurement technique itself must minimize interference with the process flow. A device which causes a major disturbance in the flow will not accurately measure or represent the flow.

This paper presents our solution to these design problems. We present results from the successful application of our optical probe, the PCSV-P, in a large scale application. Southern Company Services arranged for the Jack Watson Power Plant in Gulfport, Mississippi to host tests of the PCSV-P in a 250 MW furnace and at the inlet and outlet of the ESP. Southern Company Services also funded Southern Research Institute to make cascade impactor measurements in parallel with the optical probe measurements. We compare data from the PCSV-P, a particle counting technique, with measurements made by cascade impactors, a particle mass measuring technique. The impactor data were collected and provided by Southern Research Institute.

PROBE DESIGN REQUIREMENTS

An optical, single particle counting instrument, the PCSV-E, has been previously developed and commercialized by Insitec. Measurements have been made in ambient and high temperature particle-laden flow streams (1). The measurements have been validated by mass balances and comparisons with other instruments (1, 2). One of the advantages of the forward light scattering technique used by the PCSV-E is that a wide range of particle types can be measured since the measurement technique is minimally affected by variations in particle material properties, such as shape or composition. The PCSV-E is laser-based instrument which can span ducts or flow streams up to 1.5 meters in diameter. This upper limit is imposed by beam stability requirements, beam attenuation in high density flow streams, and instrument alignment requirements.

In order to make measurements in larger scale combustion systems, it is necessary to place the optical measurement system in the end of a cooled probe, as shown in Figure 1. This configuration, known as the PCSV-P, was designed to meet the significant space and durability constraints on the optical system hardware. The hardware for the optical system must be compact and rugged to withstand high temperatures and the mechanical stresses due to thermal expansion. As outlined in the following points, the optical system also requires unique design solutions for the detector and for the optical alignment:

1. Space and durability requirements prohibit the use of photomultipliers or other temperature sensitive detectors in the probe.

2. Continuous in situ alignment is mandatory in order to maintain system alignment under changing thermal conditions.

Both of these design constraints are solved by using a large diameter (400 micron), multi-mode, fiber optic cable to transfer the scattered light signals from the optical probe to the signal processor for detection and analysis (3). The fiber optic system can be translated within the probe to ensure proper alignment of the optical system during measurements in hostile environments.

The design of the probe is also subject to the following constraints on its physical size:

1. Minimize perturbation of the aerosol flow in the region of the sample volume

2. Maintain lens temperatures below 80°C

3. Provide sufficient space to mount optics and translators

TECHNICAL APPROACH

Figure 1 shows a schematic diagram of the cylindrical end of the PCSV-P optical probe. The heat transfer and mechanical design requirements resulted in a "shutter concept" for the probe's Flow Access Region. The probe uses an external housing for thermal protection in harsh environments and to protect the windows when the instrument is not being used. The housing has a 10 x 4 cm slot, known as the Flow Access Region, for passage of the aerosol flow. The internal probe (which contains the windows and optical assemblies) also has a matching 10 x 4 cm slot. When the slots are lined up, the aerosol flow passes through the opening in the probe. Rotating the internal probe 90° closes off access to the aerosol flow. This action protects the window system from the mainstream flow environment when the instrument is not being used.

The laser light is focussed to form a sample volume located at the center of the Flow Access Region. Two independent laser beams are used to span two separate particle size and concentration ranges. Measurements are made sequentially by selecting a particular beam using a solenoid-driven shutter. Measurements are made over a total particle size range of 0.2 - 200 microns.

A window purge system is used to keep the system free from deposits. As shown in Figure 1, the windows are recessed to minimize the chance for window obscuration and to reduce the aerodynamic disturbance of the purge air on the primary flow through the Flow Access Region. The exposed windows are made of fused silica for reliability and stable optical quality at high temperatures. Purge air flowrates can be adjusted for the various measurement conditions to avoid perturbing the sample volume region.

The scattered light signals and the incident laser beam intensity are monitored by the fiber optic. The fiber is accurately positioned by motorized micrometer drives. Use of an optical fiber eliminates exposure of sensitive detectors to harsh environments. Following any deflections in the laser beam (caused by mechanical stresses or refractive index variations due to temperature gradients), the motorized drives reposition the fiber optic so that it is properly aligned to define an invariant sample volume.

The fiber optic transmits the signal from the optical probe to one of two detectors mounted in the signal processor unit. Since a fiber optic is used for signal transmission, the signal processor and computer may be located in a control room at some distance from the optical probe.

PRINCIPLE OF OPERATION

Like the PCSV-E, the PCSV-P is an optical, single particle counting instrument. The principle of operation of both instruments is based on the analysis of light scattered by particles passing one at a time through a focussed laser beam (2, 4, 5). A schematic diagram illustrating the optical technique is shown in Figure 2. The transmitter optics uses a low power laser to illuminate particles as they randomly and singly pass through the beam. On the receiver side, the fiber optic conducts the scattered light signal to a photomultiplier. It measures the scattered light from each particle passing through the sample volume and transfers a voltage pulse to the signal processor. The signal processor measures the amplitude and the width of each signal. The width of the signal is related to the particle speed while the amplitude and signal countrate provide the particle concentration and size distribution information.

Unlike sampling instruments which can control the particle trajectory through a certain region of the illuminating beam, all in situ techniques must address the problem of random particle trajectories through nonuniform sample volume intensity distributions. For in situ instruments, such as the PCSV-E and the PCSV-P, a particle trajectory through the center of the sample volume results in a much higher signal intensity than does a particle trajectory near the boundary. Therefore, the amplitude of the scattered light signal depends not only on the particle size but also on its trajectory. In addition, the sample volume variation with particle size must be taken into account if absolute particle concentrations are to be determined. For the PCSV instruments, an intensity deconvolution algorithm is used to solve the particle sizing ambiguity and the sample volume variation with particle size (6).

TEST SITE: JACK WATSON POWER PLANT, GULFPORT, MISSISSIPPI

Southern Company Services hosted a demonstration of the PCSV-P optical probe at Mississippi Power's Plant Watson Unit No. 4. The No. 4 boiler is an opposed wall, pulverized coal-fired unit manufactured by the Riley Stoker Company. It is rated at 250 MW and fires a high sulfur, eastern bituminous coal with an ash content of 8-9%. A Western Precipitator, rated at 154 SCA (specific collection area) is used for particulate collection.

The optical probe made particle measurements at three locations:

1. furnace (1330°C)
2. inlet duct to the electrostatic precipitator (125°C)
3. exit duct from the electrostatic precipitator (121°C)

FURNACE

PCSV-P measurements were made at the 112'3" port at the nose of the boiler. The optical probe was inserted at one foot intervals up to seven feet from the furnace wall. The local temperatures were in the range from 1315 - 1344°C.

ESP INLET

Before comparing the optical probe and cascade impactor results, it is important to understand the way in which measurements were made with each instrument. A diagram of the inlet duct to the ESP is shown in Figure 3. The inlet duct measured 23 feet across with a depth of 7 feet 10 inches. Seven 4-inch ports on the top of the duct provided access for the instruments. Probe and impactor measurements were made at ports 1 and 2.

PCSV-P: Measurements were performed over the depth of the inlet duct at one foot intervals. Separate measurements were recorded for each port at each depth. Each measurement required about two minutes.

Cascade impactor: Each measurement is a composite of data collected at three points for each port. Each impactor run spanned the duct by collecting data at depths of approximately 1, 3, and 5 feet. Each run required about 10 minutes to complete. The results are reported as a composite measurement representing a traverse across the duct at that port.

ESP OUTLET

Measurements at the exit of the ESP were done downstream of the induced draft fan at the transition to the stack. A diagram of this duct is shown in Figure 4. At the ESP exit, there are six 4-inch diameter ports located on the side of the duct. Port 3 was unavailable to either the probe or the impactor since it was being used for temperature measurements. An I-beam behind port 1 prevented the probe from accessing this port.

PCSV-P: Measurements were made at one-foot intervals across the duct at four different ports (2, 4, 5, 6). As was the case for the ESP inlet, separate measurements were reported for each position at each port. The measurements represent spatial and temporal information about the particle flow at the ESP exit.

Cascade impactor: Each measurement represents a composite of data collected across the whole plane at the ESP exit. Each measurement is a composite of data collected at 15 points: three different positions (about 2, 6, and 10 feet from the wall) at five different ports (1, 2, 4, 5, and 6). These composite measurements represent spatial averages over the plane at the precipitator exit. They also represent temporal averages over the 1-2 hours required to make the measurement.

EXPERIMENTAL RESULTS

INSTRUMENT DESIGN AND RELIABILITY

Throughout the test series, the probe's optical system proved to be reliable and sturdy under the hostile conditions encountered in the plant environment.

A series of heat flux tests was conducted to evaluate the probe's water cooling system in the high temperature furnace environment. The boiler load during these tests was fairly constant, varying between 244 to 250 MW. The results showed that heat absorption by the probe remained fairly constant at 62,000 Btu/hr-ft^2 for positions from 2 to 7 feet from the furnace wall. The design heat flux was 59,700 Btu/hr-ft^2, which is in good agreement with the measured values. The importance of this consistency between theory and practice is that probe performance can be accurately predicted in new applications.

There were no problems with window obscuration during the high temperature furnace tests (1330°C). The laser light transmission values remained constant throughout the four hours of exposure during the measurements. A small buildup of slag occurred on the outer probe, but this was easily removed at the end of the test.

Beam steering due to transverse thermal gradients was found to be negligible in the high temperature tests. Small fluctuations of approximately 5% were noted in the beam power and these are quite acceptable.

Particle size calibration checks were performed prior to and following the Plant Watson tests. The primary standards used for calibrating the optical system are a rotating reticle (for particles larger than 6 microns) and monodisperse latex spheres (for submicron particles). These sizing standards are used to check the instrument calibration at several points on the calibration curve. Table 1 compares the known and measured values of particle size before and after the tests at Plant Watson. These results show that the instrument calibration was maintained throughout the cross country shipment and the tests at the plant. The consistency of the calibration checks confirms the precision of measurements.

PARTICLE SIZE AND VELOCITY DISTRIBUTIONS

During the one week of tests at Plant Watson, particle measurements were made at the inlet and outlet of the ESP using both the optical probe and the cascade impactor and in the furnace using the probe. Over 100 separate measurements were made by the optical probe.

The following sections discuss some of the main features of the results.

Spatial Variations

Since the optical probe only measures particles passing through the sample volume of the instrument, it can be used to make spatially-resolved size and velocity measurements. The PCSV-P made particle velocity measurements in the furnace and at the ESP inlet and outlet. Southern Research Institute also obtained flow velocities at the inlet and outlet of the electrostatic precipitator using a Type S pitot tube. Both instruments report a wide range in velocity values at the ESP exit. Table 2 summarizes the results from each location.

The spatial variation of particle velocities at the ESP inlet is shown in Figure 5. The top figure compares the optical probe and pitot tube measurements for port 1. The lower figure compares the results for port 2. The two techniques show the same trends as a function of position in the duct. The optical probe, which measures the average particle velocity, reports lower velocity values than does the pitot tube, which measures the flow velocity head.

In general, we found that the velocities decreased near the wall. However, at the precipitator exit, velocity distributions were very complex, sometimes increasing closer to the walls. Figure 6 shows a three dimensional map of the particle velocity distribution at the ESP exit measured using the PCSV-P. Given the large bends in the duct and the proximity of the ID fan, recirculations in the flow stream may be responsible for this complex behavior.

Optical probe measurements in the furnace and at the ESP inlet and outlet showed that there is little spatial variation in the shape of the particle size distribution at each location. In fact, particle size distributions at all three measurement locations have the same characteristic shape. This finding is consistent with previous PCSV measurements of pulverized coal in small scale combustors (1). Both the optical probe and the cascade impactor reported a particle concentration peak at about 10 - 20 microns. This peak is preserved throughout the process flow stream from the furnace to the precipitator exit.

Temporal Variations

A unique feature of particle counting techniques such as the probe is the capability to show temporal variations in particle concentration. The probe required just two minutes for each measurement. Therefore, variations occurring over a several minute period could be detected. These variations cannot be measured by techniques such as the cascade impactor which makes measurements over much longer time intervals (e.g. 1-2 hours at the ESP exit).

The optical probe showed some variation in the number density as a function of time at all three measurement locations. However, the location exhibiting the largest variation in particle concentration was the outlet of the ESP. Figure 10 compares number density variations at the inlet and outlet of the ESP. These curves show the cumulative particle number concentrations per cubic centimeter of the local gas density. The cumulative number density curve represents the total concentration for all particles larger than the indicated diameter.

The upper set of curves in Figure 7 represents seven individual PCSV-P measurements made over a two-hour period. All measurements were at the same position in the same port at the ESP inlet (port 1, three-foot depth). The individual measurements each required about two minutes to make. The eight ESP outlet measurements were all taken at the same position in the same port (six-foot depth in port 5) over a period of 30 minutes.

The spread in the number concentrations curves represents variations in ESP inlet and outlet operating conditions over time. The outlet measurements show a wider variation in number density, especially for the larger particles. Figure 8 shows another way to represent the data at the ESP outlet. Particle countrate is plotted as a function of time for the small particles (0.3 - 2.1 microns) and the large particles (2.3 - 40 microns). The axis on the right also shows the average particle velocity during the 30 minute test period. While the small particle countrate fluctuates over a range of 11.5 to 15.5 kHz, much larger, cyclic variations are observed in the large particle countrate, from 2.9 to 19.2 kHz. We suspect that the wide spread in the number distribution curves and the fluctuations in the large particle countrate are related to rapping, the removal of collected particulate from the plates. Bursts of larger particles may be released during this process.

ESP Efficiency

Optical probe measurements of the precipitator as a function of particle size are shown in Figure 9. Penetration is defined as the ratio of the mass frequency at the outlet to the mass frequency at the inlet for a given size. PCSV-P mass frequencies were obtained by averaging the results from three runs and assuming a particle density of 2.48 g/cm^3. The results in Figure 9 are consistent with typical precipitator performance, showing that penetration increases with decreasing particle size.

Comparison of Probe and Impactor Measurements

Figure 10 compares the number and mass distributions measured by the probe and impactor at the inlet and outlet of the ESP. As discussed above, the impactor measurements represent averages over traverses of the duct at the ESP inlet and averages over the entire duct cross section at the ESP outlet. The optical probe data shown in these figures represent the average of three separate measurements made at different positions in the inlet and outlet ducts. The impactor and probe measurements were also made at different times during the one week tests at Plant Watson.

The number density data (plotted as number/dry normal cubic centimeter) and the mass density data (plotted as mg/dry normal cubic meter) show good agreement between the two techniques in the small particle size range. The optical probe and cascade impactor report similar number and mass frequencies for particle sizes up to 4 microns at the ESP inlet and for particle sizes up to 10 microns at the outlet. For particle sizes larger than 4 - 10 microns, the optical probe consistently reports higher particle concentrations than does the cascade impactor.

What explains the difference in the large particle measurements? Probe and impactor measurements were made at different times and at different points in the ducts. However, we believe that the primary factor explaining the difference in the large particle measurements is due to differences in the two measurement techniques. The optical probe measured particle number (or counts) directly over a size range with a lower limit of 0.3 - 0.8 microns (depending on the particle number density) to an upper size limit of 100 microns. The cascade impactor measured particle mass directly over a size range from < 0.24 microns to an upper size limit of 7 microns. All material > 7 microns was collected by a cyclone precutter and a curve fitting program was used to extend the measurements to particle sizes of 100 - 150 microns. The optical probe makes direct measurements of large particles. In contrast, the cascade impactor does not make direct measurements of this particle size range. Estimates of particle mass in the large size range are generated by a curve fitting program which assumes a given shape of the underlying particle distribution. Differences in the way in which large particle information is measured and analyzed by the two techniques undoubtedly contributes to the differences in the results.

Another factor which may contribute to differences in the mass-based results is the choice of particle densities used to calculate the optical probe's mass distributions. The mass distributions for the optical probe were obtained by multiplying the particle density by the particle volume distribution (computed from the number density assuming a spherical equivalent diameter). The particle density value which was used, 2.48 g/cm^3, may accurately reflect the density of the smaller particles in the flyash samples. However, it may be too high for the larger particles. Large pulverized coal particles can form hollow spheres (cenospheres) during the combustion process. These cenospheres will have a significantly lower apparent density than either the flyash or the feed coal. The next step in the analysis will be to analyze some collected samples to determine if there are a significant number of cenospheres in the size range above 10 microns.

CONCLUSIONS

The optical probe was successfully tested in a commercial power plant. The tests demonstrated the feasibility both the measurement technique and instrument design for large scale, high temperature, industrial applications. Over 100 data sets were collected at three locations within the power plant: the furnace (1330°C), and the inlet and the outlet of the electrostatic precipitator (121 - 125°C). The major findings from the initial analysis of the data are summarized here:

1. Comparison with pitot tube measurements.

Particle velocities measured by the probe and the pitot tube were consistent, showing the same trends as a function of position. The optical probe values, which are based on an average particle velocity, are consistently lower than the pitot tube values, which are based on measurement of the flow velocity head.

2. Comparison with cascade impactor measurements.

The cascade impactor and optical probe number and mass frequency measurements compared very well for particles up to 4 - 10 microns in diameter. For large particle sizes, the optical probe always measured higher particle concentrations than did the cascade impactor. While the measurements were made at different times, differences in the measurement techniques contribute to this discrepancy as well. The optical probe technique is based on the direct measure of particle counts for particles up to 100 microns in size, while the cascade impactor is based on the direct measure of particle mass for particles up to 7 microns in size. One factor affecting the results may be the curve fitting program used by the cascade impactor to extend the measurements to particle sizes larger than the seven micron upper limit of the impactor stages. A second factor affecting the mass-based results is that the optical probe used the same particle density value for the entire size range. While this value describes the dense, spherical small particles formed from molten ash, it is not appropriate to describe large particles such as cenospheres.

3. Spatial variations at the three measurement locations in the power plant.

Optical probe measurements at a number of different positions in each port at each location showed that there was no strong variation of particle size or concentration as a function of position in the duct.

4. Temporal variations at the ESP outlet.

The greatest variation in the velocity and the particle number distribution occurred at the ESP outlet. While the overall shape of the particle size distribution remained the same, the large particle countrate fluctuated rapidly. We expect that these fluctuations are indicative of the ESP operation. Rapping, or other processes which occur periodically, may release occasional bursts of larger particulate. The most complex velocity flow field was also measured at the ESP exit.

ACKNOWLEDGEMENTS

This work was performed under DOE SBIR Contract Number DE-AC03-86ER80230. We gratefully acknowledge the support and participation of David Gallaspy and Wallis Harrison of Southern Company Services, Inc. We also wish to thank Southern Company Services for contracting with Southern Research Institute to make the cascade impactor measurements. We also thank Plant Watson (Mississippi Power Co.) personnel for their assistance during the tests.

The work described in this paper was not funded by the U.S. Environmental Protection Agency and therefore the contents do not necessarily reflect the views of the Agency and no official endorsement should be inferred.

FIGURES

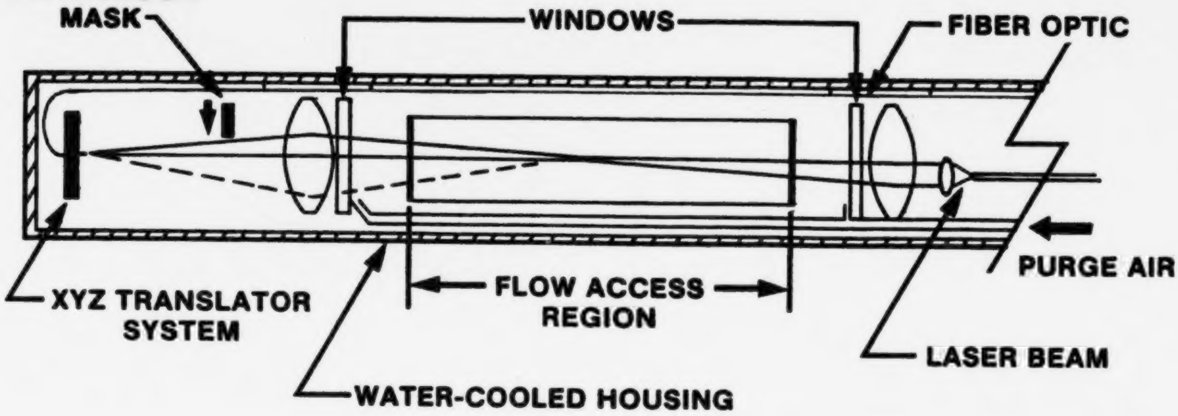

Figure 1. Schematic of the PCSV-P optical probe. The probe measures 9 cm OD with a 10 x 4 cm Flow Access Region.

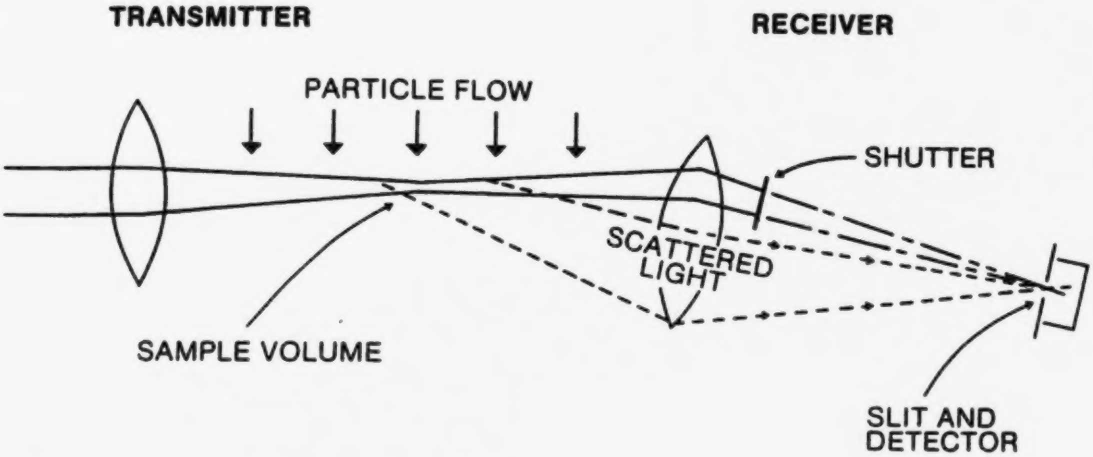

Figure 2. Detail of the PCSV-P optics showing the sample volume.

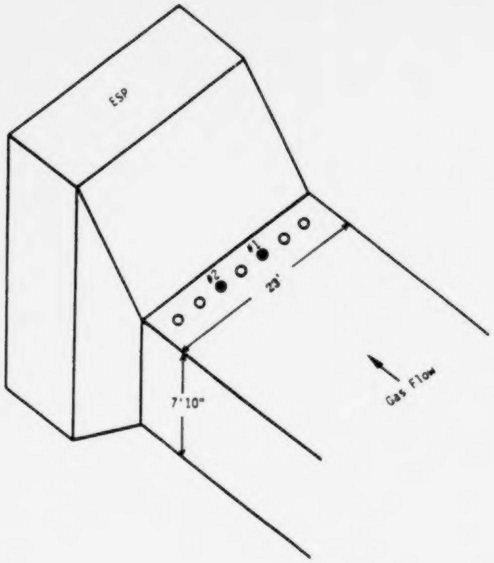

Figure 3. Schematic of the ESP inlet duct. Ports 1 and 2 were used for particle measurements by the optical probe and cascade impactor.

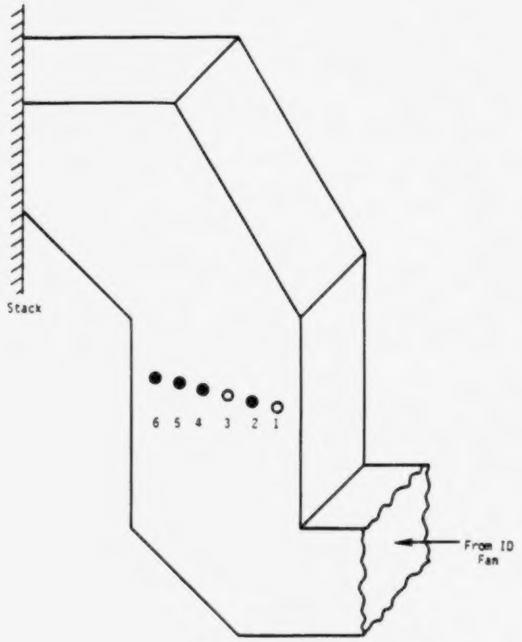

Figure 4. Schematic of the ESP outlet duct. Ports 2, 4, 5, and 6 were used for particle measurements by the optical probe. Ports 1, 2, 4, 5, and 6 were used by the cascade impactor.

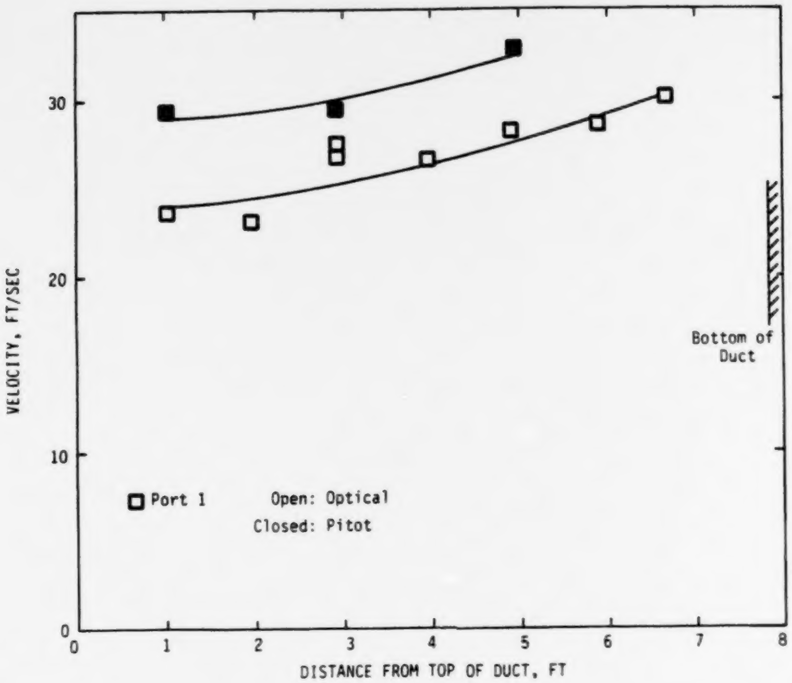

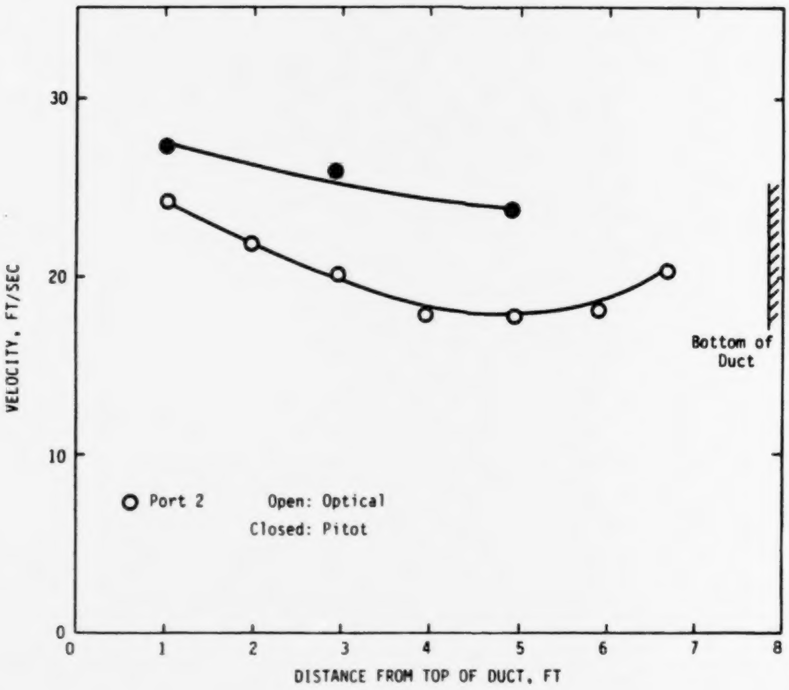

Figure 5. Velocity traverses made by the PCSV-P and pitot tube at ports 1 and 2 in the ESP inlet.

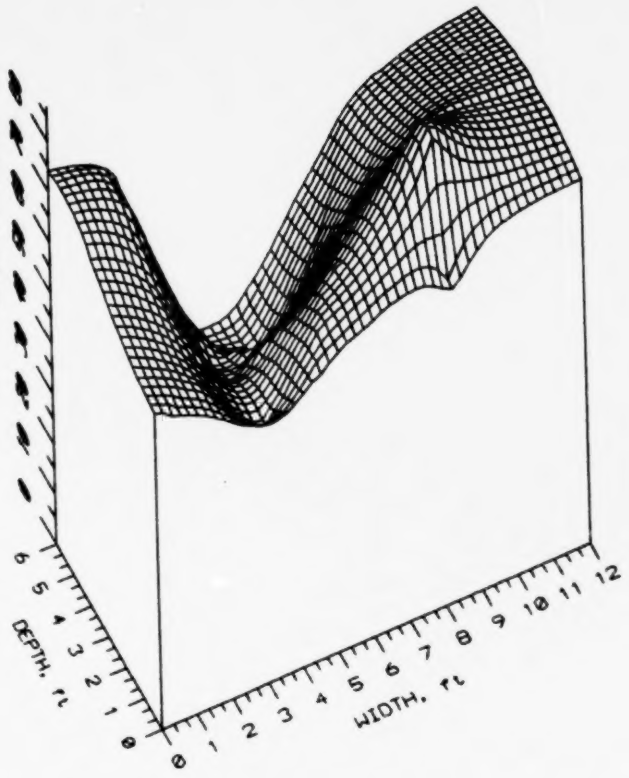

Figure 6. Velocity profile in the duct at the ESP exit as measured by the PCSV-P.

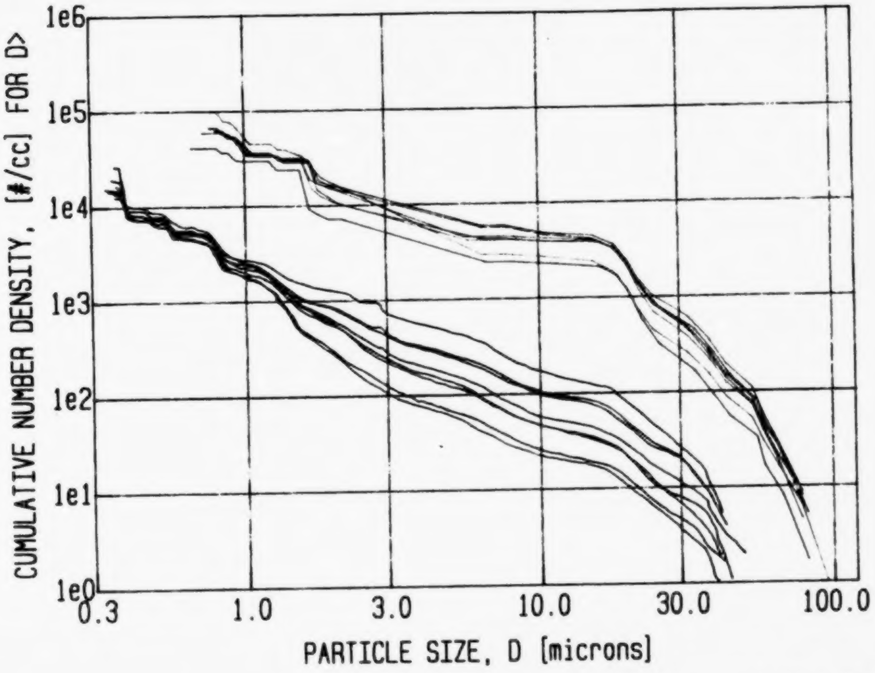

Figure 7. Cumulative number density variations with time at the ESP inlet and outlet as measured by the PCSV-P. Inlet measurements were made at a fixed location over a two-hour interval. Outlet measurements were made at a fixed location over a 30 minute interval.

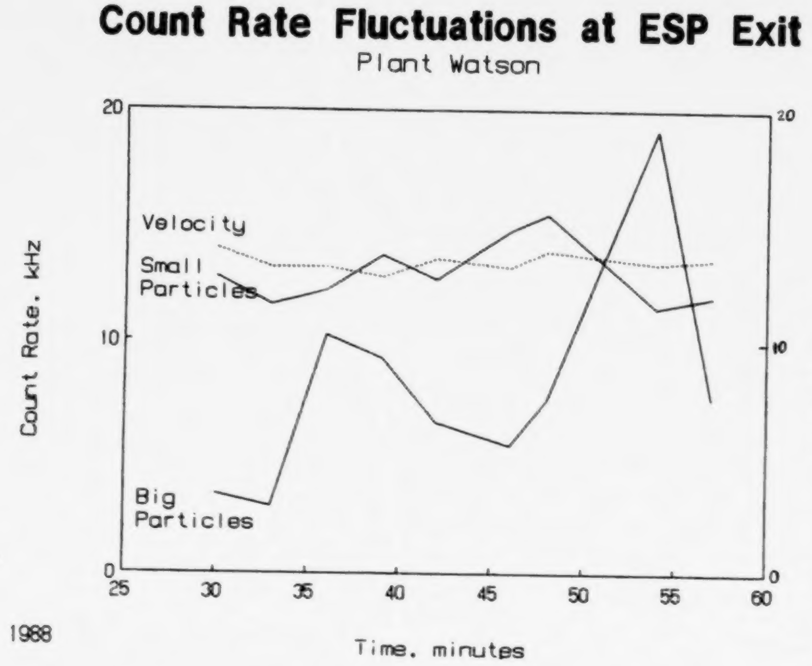

Figure 8. Temporal variation of the large and small particle countrates and the average particle velocity at the ESP outlet.

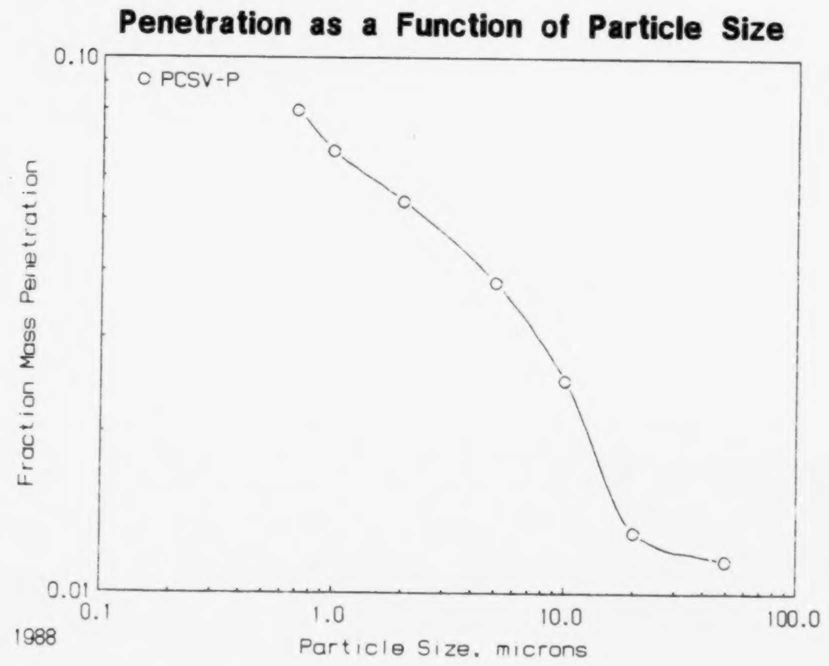

Figure 9. ESP efficiency as a function of particle size.

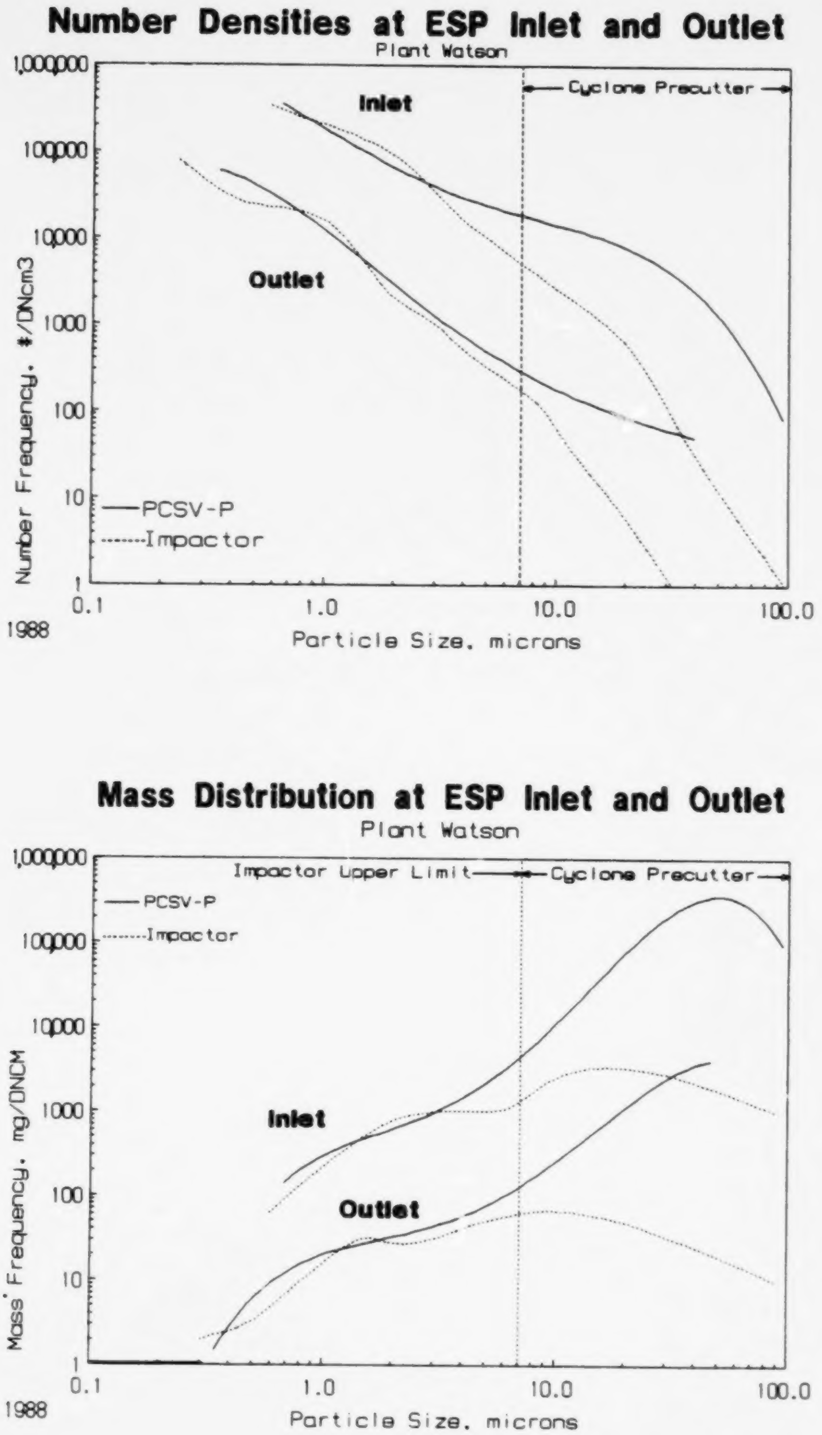

Figure 10. Comparing probe and impactor number and mass distributions at the ESP inlet and outlet. Probe data represent the average of three measurements taken at different points in the inlet and outlet duct. Impactor data are composites of traverses of the duct taken at the inlet and averages across the entire duct at the outlet.

TABLES

TABLE 1. PCSV-P PARTICLE SIZE CALIBRATION RESULTS BEFORE AND AFTER WATSON TESTS

Reticle Diameter* (microns)	Measured Diameter (microns) Before	After
6.0	4.7	6.1
9.0	8.5	
24.0	21.0	24.6

*Uncertainties in the reticle diameters are ± 1.0 micron.

TABLE 2. VELOCITY RANGES AT EACH MEASUREMENT LOCATION

	PCSV-P	Pitot Tube
Furnace	27 - 33 m/s	
Precipitator Inlet	5.7 - 7.8 m/s	7.3 - 10 m/s
Precipitator Exit	16 - 25 m/s	12 - 20 m/s

REFERENCES

1. Holve, D.J., "In Situ Measurements of Flyash Formation from Pulverized Coal," Combustion Science and Technology, 44, 269-288 (1986).

2. Holve, D. J., Self, S. A., "An Optical Particle-Sizing Counter for In Situ Measurements; Parts I and II," Journal of Applied Optics, 18(10) 1632-1652 (1979).

3. Holve, D. J., Milanovich, F. P., "A Hybrid Optical Probe for In Situ Particle Measurements in Large Scale Combustion Systems," The Combustion Institute Western States Meeting, Fall 1986, Tucson, AR, 1-33, WSS-86-14.

4. Holve, D. J., "In Situ Optical Particle Sizing Technique," Journal of Energy, 4(4), 176-183 (1980).

5. Holve, D. J., "Transit Timing Velocimetry (TTV) for Two Phase Reacting Flows," Combustion and Flame, 48, 105-108, (1982).

6. Holve, D. J., Annen, K., "Optical Particle Counting and Sizing Using Intensity Deconvolution," Optical Engineering, 23(5), 591-603 (1984).

AUTOMATIC ESP CONTROL: STARTUP TO SHUTDOWN

By: Paul G. Abbott
Theodore C. Schafebook
GE Environmental Systems
Lebanon, Pennsylvania

John A. Brummer
Metropolitan Edison Company
Reading, Pennsylvania

ABSTRACT

The current generation of electrostatic precipitator control systems literally provides operators with fingertip control of all operating functions. Computer-based central control consoles form the heart of a network of subsystem controls, containing their own degree of microprocessor "intelligence". The central control console can be placed in any environmentally controlled location which provides the utmost in operator control and monitoring. From the central control console the operator can execute a full range of operating functions such as individual component on/off, control setting adjustments, operation status, alarm notice and fault indication, conditions monitoring and implementation of specially programmed control strategies.

Another key feature of computer control is the data storage capability. With this function the operator can request reports automatically or on demand, generate graphs for trend analysis and problem solving, and maintain operating records automatically.

This paper identifies the hardware and software of a complete computer-based control system as incorporated on the Metropolitan Edison, Portland Unit No 2, retrofit ESP project which began operation in mid-1987. A summary of operator experience to date and how automatic, computer-based controls have benefitted this system will be provided.

INTRODUCTION

The proper operation, control and monitoring of electrostatic precipitators (ESP) has, in many cases, been limited by ESP controls, data acquisition instrumentation and equipment alarms being located in various remote areas of the plant. This arrangement makes it difficult for the operator to collect and coordinate all the information necessary to optimize precipitator operation for varying process conditions, to evaluate a particular operating problem, or to simply monitor operation to avoid problems before they develop. Even with the use of microprocessor based transformer-rectifier and rapper controls, which provide discrete state-of-the-art control, the plant operator still lacks a fully integrated control system which incorporates plant process or operating data as well as ESP and auxiliary equipment operating status and control all in one central location so that total system performance can be optimized.

Today's computer technology provides the opportunity to have a fully integrated computer-based system that provides complete remote control, automated control strategies, monitoring and diagnostic capabilities from one master control center. This type of system not only provides the utmost in operating convenience but, more importantly, provides the plant operator with a system that promotes confident, reliable and economic operation of the ESP.

This paper will review such a system at Metropolitan Edison Company's Portland Unit No. 2, installed as part of a complete electrostatic precipitator retrofit project, which began operation in May, 1987.

Unit No. 2 has a nominal gross generating capacity of 252 MW. The coal being burned in the boiler is an Eastern bituminous coal with a sulfur range of 0.95% to 2.00%.

Particulate emission guarantees are a maximum mass emission of 0.1 lb per million Btu of heat input to the steam generator and a maximum opacity of 20% at the stack outlet.

The GE rigid frame electrostatic precipitator is a two-chamber unit with each chamber containing six bus sections in depth and 47 - 12-inch gas passages in width. The unit has six electrical fields powered by six double outlet bushing 55 KV(DC) transformer-rectifiers and is designed to have five of the fields in operation to meet performance guarantee requirements, allowing one redundant field.

The control hardware local to the ESP is microprocessor based transformer-rectiifier controls, a single board computer-based rapping control system and several multiplexers for data collection and system control. These devices are continuously monitored by a microcomputer Host Workstation located in the main boiler control room. This Host Workstation gives the operator pushbutton control with a choice of manual operation or automatic control mode algorithm selections. This workstation also has multiple tools for trend analysis and troubleshooting such as automatic report generation and graphing of data.

HARDWARE SYSTEM

The hardware system has a Host Workstation located in the main control room with several communication links running throughout the plant to remote locations. Each remote location has some degree of intelligence to collect data and/or receive commands from the Host Workstation. The two most important remote devices, the transformer-rectifier (T-R) automatic voltage control and electrode rapping control, are microprocessor based systems which have stand-alone control capabilities and can be manipulated by the Host Workstation. There are also three remote interface controllers for converting hardware inputs and outputs to a digital serial communication link with the Host Workstation.

TRANSFORMER-RECTIFIER CONTROLLER

The transformer-rectifier automatic voltage controller (AVC) is a single board microprocessor control, which contains an 8 bit Intel 8031 microprocessor, 8K ROM, and a serial communication port. The controller continuously monitors precipitator T-R operating conditions and normally applies the highest possible power levels to maintain optimum collection efficiency.

The controller's main feature is a highly responsive spark detection circuit that can be set and adjusted for the particular process. Figure 1 shows the range of response the controller will perform. In the event of a low energy spark, the system does not reduce current to zero, but only reduces the current a small amount, enough to squelch the spark and keep the reduction of power to a minimum. A high energy spark causes a reduction to zero current on the next half-cycle, and stays off for one or two half-cycles. The unit then executes a recovery step function for an immediate increase to a specified level and a fast ramp for rapid power increase to a level just below the level of power where the last spark occurred. Finally, the system ramps up slowly attempting to increase power to T-R nameplate rating. The controller also monitors for alarm conditions which can cause equipment damage. A high primary voltage and low primary current indicate an open circuit and will trip the cabinet. A low primary voltage and high secondary current indicate a short circuit and the system cuts off power for 10 seconds and then attempts to reapply power. The system will attempt this retry nine times before tripping out the control cabinet. This is incorporated to allow time for the short to clear without operator intervention and avoid nuisance trips. The system also senses for a shorted silicon rectifier (SCR), RAM failure, ROM failure, and zero crossing synchronization.

The controller has several LED indicators for alarms and system conditions and a liquid crystal display for alarm information, meter readings, spark rate, and adjustment settings. Communication to the Host computer is through an RS422 serial port transmitting at 9600 baud. The Host can request status of any AVC and it will return primary voltage, secondary voltage, primary current, secondary current, spark rate, and alarm status. The Host can also request a T-R power set point change from 0 to 100% in 1% increments for total control from the remote Host location. The AVC has a fail-safe mode in that if it does not receive communication from the Host for a certain period of time, the AVC will revert to a stand-alone mode of operation.

RAPPING CONTROLLER

The rapping controller is a self-contained module with all control and power circuits for operating up to 256 electromagnetic impact rappers. The system is divided into a lower power area for control and a high power area for rapper energization isolated by optical couplers. There are four circuit boards to control the system that plug into a DEC Q-bus structure. The system has a DEC Falcon SBC-11/21+ microcomputer with 16K RAM, 4K ROM for program storage, and two serial communication ports. Parallel I/O communication is utilized between the microcomputer and a digital to analog conversion board for fast transfer of data.

When a rapper is to be energized, the controller follows this sequence:

- Determines if any other rapper is operating and if there is, will hold the request(s) until the present operation is complete.
- Chooses the appropriate row and column SCR to open a current path to the rapper to be energized. (The system uses a 16 row x 16 column matrix system to choose the rapper to be energized requiring only 32 SCR switches and wiring runs to energize 256 rappers.)
- Sends the proper number of phase controlled half cycles through this path for rapper energization.

The system senses the current feedback of each rapper energization and evaluates if it is the correct value for the corresponding rapper lift requested. If not, the controller will make the appropriate adjustment the next time that rapper is energized.

The system also provides alarm messages for individual rappers, consisting of short circuit, open circuit, high current and low current. If a short circuit should occur, the controller will de-energize the rapper within one-half cycle for circuit protection.

There is an alphanumeric display and push button terminal located on the front of the controller for local fault annunciation, operational information, and control of rapper timing and lift values. Normal operation is to control individual rows of rappers perpendicular to gas flow. The operator can enter a row round trip time or the time it takes to energize every rapper one time in a row, for either the collecting or emitting rappers. It is also possible to choose an individual rapper for discrete control of round trip time (RTT) and lift. The range of rapper control is 1 to 100 minutes for RTT in one-minute increments, and 0 to 20 foot-pounds of rapping force in one foot-pound increments.

Troubleshooting the system is simplified by utilizing local terminal feedback and internal cabinet indicators. The local terminal alerts the operator to individual rapper problems. The internal cabinet indicators show which row and column are energizing, if the power circuits are receiving gate pulses, blown fuse indicators, and computer failure. The system also does diagnostics on the CPU, RAM and ROM, and indicates any problems.

All control and display information at the local terminal is transmitted to the Host computer through an RS232c current loop at 2400 baud.

REMOTE CONTROL INTERFACES

There are numerous other inputs and outputs, in addition to the T-R and rapping controllers, that the Host Workstation uses for total precipitator control. The remote data acquisition and control signals are multiplexed to the Host Workstation through an RS422 serial communication line. The remote devices use 120 VAC input and output triac modules, 4 to 20mA input modules and Type J thermocouple input modules. These devices have a certain degree of intelligence such as setting time delays, latching inputs, and averaging analog inputs, and they also photo-isolate all I/O points. The multiplexures provide remote start/stop functions for the T-R and rapper controllers, status of hopper ash levels, hopper heaters, insulator heaters, and data acquisition of several operating parameters as shown in Figure 2.

HOST WORKSTATION

The Host Workstation is a dedicated microcomputer system specifically designed for precipitator control and data acquisition. The system is packaged in a desk arrangement, with a CRT and keyboard on top of the desk, microcomputer rack mounted under the desk drawer, and all wiring and power components located in the bottom compartment of the desk.

The CPU is a DEC Micro PDP11/23+ microprocessor with all circuit boards located on a DEC Q22 bus. The unit contains an integral power supply and two DC fans for board cooling. The system has 512K RAM, a 10M hard disk drive and two 400K 5-1/4" floppy drives. There are two four-channel asynchronous serial line interface modules configured and used for serial communication interface between the CPU and the remote hardware. The CRT and keyboard is a DEC VT241 color video graphics terminal for display and operator interface. Also included is a DEC LA210 graphics printer for generating hard copy reports.

When power is turned on, the unit automatically uses boot strap proms to perform a diagnostic check of the CPU and then accesses the 10M hard disk drive to load all program modules into memory. After the programs are loaded, they run automatically and access default operating set point values that have been saved to disk. Set point values such as T-R power, rapper lift, etc. can be changed by the operator and saved to disk, changing the original default set point values.

The software is divided into four parts: 1) the real time DEC RT11 operating system and library; 2) device drivers, coded in assembly language, used for controlling communication to all peripheral devices; 3) the foreground program modules, coded in Fortran and containing all the high level control algorithms; and 4) the background program, coded in assembly language to control all of the screen displays.

The Host Workstation hardware and software and the peripheral devices combine to form the elements of the GE Intelligent Precipitator (IP) control system.

OPERATOR INTERFACE

An important aspect of this equipment is that of providing a simple and straightforward method for the operator to use and interface with the system. The concept for the screen designs and operator interface is to have minimum inputs requiring one or two key strokes without alphanumeric command inputs.

The CRT display system is comprised of a series of screens which have data and operator control fields. Using the arrow keys, the cursor can be moved around the screen to any field that is a changeable field. There are three types of changeable fields:

- A select field is used to select another screen or choose a function. For example, there is a menu screen which lists all the possible screen displays that can be accessed. By pressing the arrow keys, the cursor will travel through the list of screens highlighting the one it is on. When the operator has placed the cursor on the screen title he wishes to select, he can push a function key and the CPU will retrieve the information and display the new screen.
- A toggle field allows selection from two or more preprogrammed states. When the cursor is properly placed on this type of field, pushing the function key causes the field to change states, such as ON/OFF.
- A numerical field displays and changes numerical set point values in the system. When the cursor is on the proper field, the numerical keys are used to change the value and when the function key is pressed, the system will accept the new set point value.

To ensure that only authorized personnel can change certain values in the system, some fields are under password control. Typically, changeable fields, such as opacity or temperature set points that control algorithm operation, are under password control while start and stop functions are not.

The bottom line of each screen is the same and has three specific functions:

- It displays the current date, time, stack opacity percentage, and the unit megawatt level.
- It has a simplified menu for selection of some of the most frequently used screens.
- When the operator enters incorrect data, such as a numerical value that is too high for the peripheral device to handle, the system will signal the error by an audible beep. By pushing the function key, an error message overwrites the bottom line to advise the operator of his error. (Example: 'set point out of range').

Figure 5 shows a screen dump to a printer with the bottom line displayed. Note that the print statement is in a reverse video mode which indicates the location of the cursor. The printout was produced by placing the cursor on this menu selection and pushing a function key.

Operation of the equipment during the last nine months has allowed optimization of operating set point values for all devices. Therefore, present normal operation of the system only requires the operators to use the cursor control keys and the one select function key to start or stop devices or to select a control mode.

AVAILABLE CONTROL AND MONITORING SCREENS

Transformer-Rectifier (T-R) and associated control data are located on one screen as shown in Figure 3. The first two columns show six designated T-R units and their associated KVA size. The next three columns are status fields which indicate if the communication link with the AVC is operating properly, cabinet alarm status, and power status. T-R 2-D is an example of the unit off due to an operator manually stopping the unit, while T-R 2-F is an example of the unit off due to an alarm trip. The next three fields are control fields that are used to make changes to the system. They allow start or stop of a T-R unit, reset of an alarm condition as the stop function is also an alarm reset function, and entering a percent of power from 0 to 100%. The remaining columns are data fields giving the following information for each T-R unit: actual observed set point, primary voltage, primary current, secondary current, secondary voltage, and sparks per minute. When the precipitator is in the manual mode of operation, all T-R operating set points are typically set at 40% power levels. At full boiler load, these settings have resulted in an average opacity of approximately 4%. A printout of actual T-R data in manual mode is shown in Figure 4.

The electrostatic precipitator has six double outlet bushing T-R sets. Each bushing is connected to a bus section in each of the two precipitator chambers. The rapper rows are configured to reference one row to one outlet of a T-R unit for a total of twelve rapper rows. Three types of screens are associated with the rappers:

- The main rapper screen lists the twelve rows of rappers with their round trip time and lift, per row of collecting or emitting rappers. The round trip times in minutes and lift in foot-pounds are numerical fields that can be changed by the operator. This screen also has a start/stop field for controlling power to the rapper cabinet, and indication if an individual rapper is not at the same set point value as its associated row value. Because an individual rapper can be set differently than the row value, the operator can select another screen which will give him information on the individual rappers in that particular row.

- An individual row screen allows the operator to observe and change any individual rapper set points. It also shows information of the rappers alarm status for short circuit, high current, low current or open circuit. Normally these screens are only used if there is a problem with an individual rapper. Up to this point in time, there have been no reports from the operators of these screens being used.

- There is also an overall rapper fault table for quick viewing of alarms for all rappers on one screen.

The system includes an event or log screen that shows the last 64 messages the system produced and includes all alarms and important events such as a T-R being de-energized by the operator. Messages are one-line long and indicate the date and time of occurrence. The messages are also sent to the printer for hard copy record of events.

There are three screens that show information graphically, similar to that shown in Figure 2. These screens help the operator to visualize the system and associated location where specific operating parameters are being measured. These are very helpful when reviewing the process, giving quick insight into parameters such as pressure, temperature, flow rate, ID fan amps, damper status and opacity.

The graphic information screens are the predominant screens used during normal operation of the unit.

The T-R control screen is used during boiler startup or is the initial screen accessed if any abnormal operation were to develop.

The remaining screens are typically accessed as required for additional information or to alter operation of the equipment.

CONTROL STRATEGIES

This paper previously reviewed how the operator can change operating set points manually from the Host Workstation. This section will review the higher level algorithm and control strategies where the system program automatically maintains control of the precipitator operation. The control strategies are Energy Management, Automatic Startup, Power Down Rapping, Rapper Optimization, Boiler Trip and Hopper Overfill.

These control strategies are standard options available with the system but have been customized for this particular site and Met-Ed specific requirements.

Each of the control strategies has a specific screen display associated with it for operator input of set point adjustments and monitoring its operation.

ENERGY MANAGEMENT

There are times in the operation of the precipitator that very high T-R power levels do not need to be maintained to achieve the required opacity and corresponding mass emission limits. In many cases, power consumption can be decreased substantially with little change in opacity.

The Energy Management control mode is a method of conserving T-R power consumption by automatically controlling T-R operating levels to maintain the stack opacity within an operator selected window of high and low opacity set points. When first selected, this routine will power down each T-R, one at a time, and record secondary voltage and secondary current in three percent increments as it is powered back up. This information is used to calculate the slope of a V-I curve, and along with the respective plate area and the current operating point, is used to calculate an energy-saving parameter for each T-R. The algorithm continually monitors the average opacity. If the opacity goes above the high set point limit, it will choose the optimum T-R to increase power and if below the low set point will choose the optimum T-R to decrease power with the optimum T-R being determined by the energy-saving parameter. In order to maintain accurate energy-saving parameters, new V-I curves are automatically measured every eight hours or whenever a significant shift of the T-R operating point from the V-I curve is detected.

There is a maximum opacity set point which is set at a level above the high limit. When opacity exceeds the maximum set point or there is an input indicating soot blowing, all T-R units are immediately increased to full power. This power level is maintained for a pre-set time period or abort time. After the abort time has elapsed and if the stack opacity is below the maximum set point level, the algorithm will resume controlling the T-R power levels to maintain the stack opacity within the high/low opacity set points.

The system has been operating with normal set point values of 4% low opacity set point, 6% high opacity set point, 12% maximum opacity set point and abort time of two minutes.

A graph of total T-R secondary power (KW-Avg.) versus time during Energy Management control mode operation is shown in Figures 5 and 6. Figure 5 shows the starting point of this control mode by the decrease and increase of T-R secondary power while V-I curve data for each T-R is completed. When the V-I data for all of the T-R's is completed, the control will begin reducing T-R power consistent with actual opacity and opacity set point limits. Figure 6 shows the total T-R power level while operating within the high and low set point opacity limits. Figure 6 also shows a point at which time the control mode is turned off with T-R's returned to manual mode at 40% power level set points and the resultant increase of total T-R power. The graphs do not show actual T-R primary power (KW-RMS), but do show relative amounts of power which can be saved by the control system during certain conditions. This particular case results in power savings of approximately 78%. The figures shown are actual printouts available from the system report generation capabilities, which are discussed later.

An item of interest regarding resolution of control strategy and field optimization was that of an opacity excursion during the V-I curve procedure of the outlet T-R unit. This occurred each time a V-I curve was attempted and the power was reduced below 5 to 10%. This was resolved by limiting power down on V-I curves to 10% for the outlet T-R.

AUTOMATIC STARTUP

Emission requirements dictate that the electrostatic precipitator must be in operation during boiler startup to maintain stack opacity within acceptable limits. In order to eliminate or minimize ESP problems that would result during low temperature operation, a specific operating procedure is followed for T-R units and rappers.

This system has an Automatic Startup algorithm which relieves the operator from having to monitor the ESP startup procedure, during a period when he is concerned with boiler startup operation, and also eliminates the requirement for personnel to manually turn on T-R units and adjust rapping parameters at the proper time.

Automatic Startup has three specific modes of operation which are Boiler Purge, Cold Startup and Hot Startup. The primary control parameters for these operating modes are precipitator outlet flue gas temperature and stack opacity.

The Boiler Purge is normally the first phase of startup where the draft fans are turned on to purge the boiler system prior to actual combustion in the boiler. This can create an opacity excursion due to re-entrainment of residual fly ash that has accumulated in the ductwork. The distinction between ESP Cold Startup and Hot Startup is whether or not the flue gas temperature is less than (cold) or greater than (hot) the anticipated acid dew point temperature.

During Boiler Purge mode, the T-R power levels are controlled to maintain a 20% opacity limit. The operator has a choice of operating in this mode for a time period from 0 to 30 minutes, selectable in six-minute increments. A zero purge is used when the system is off line a very short time and the ESP is still at an elevated temperature. It is assumed in a purge situation that it will be difficult to dislodge the dust from the plates. The rappers are therefore set for maximum intensity and a round trip time proportional to the purge time for the six total rapper rows in depth, with six round trip times in the first row to one round trip time in the last row. For example, if the purge is set for six minutes, the first row of rappers will be set at a one-minute round trip time, the second row will be at two minutes, the third at three minutes, etc. If the purge is set for 30 minutes the first row of rappers will be at a five-minute round trip time, the second row at 10 minutes, etc. At the start of the Purge Control, the T-R units are energized to a power level of 25%. The algorithm continuously evaluates opacity. If this opacity is above the high set point level, T-R power level will be increased until the opacity is below the high set point.

When the purge time is complete, the algorithm will evaluate the precipitator outlet flue gas temperature versus the set point temperature and will determine if there should be a cold or hot start up sequence.

When the Cold Startup mode is initiated, the T-R sets are energized and set to a 0% power level. Stack opacity is continually evaluated and if the opacity increases above a high set point opacity limit, the algorithm will increase power on the outlet T-R unit. If the outlet T-R unit is at maximum power, the next T-R closest to the outlet of the precipitator will be increased. This sequence continues through all T-R's or as may be required to maintain the maximum stack opacity limit. As the T-R power level is being increased, the algorithm continually monitors for sparking. If sparking is detected, the maximum limit for that T-R will be at a set point just below the sparking level. If the opacity goes below a low set point, the power of the T-R closest to the inlet of the precipitator, which is not at a zero power level, will be decreased.

The normal opacity limits presently being used for Automatic Startup are 6% for the high set point and 4% for the low set point.

During this control mode, the algorithm also sets rappers to maximum intensity and adjusts the round trip time based upon which T-R "looks" like the inlet T-R. For example, if all the T-R units are above 0% power level, the inlet rapper row round trip time will be five minutes, the second row 10 minutes, the third row 15 minutes, etc. If only the outlet two T-R units are above 0% power levels, then the second to last rapper row will be at a five-minute round trip time and the last rapper row at a 10-minute round trip time.

The unit is maintained in a Cold Startup mode, continually evaluating opacity and adjusting T-R power input and rapping parameters as required, until the flue gas temperature reaches the set point temperature. At that point the algorithm changes control to the Hot Startup sequence.

The Hot Startup mode can be initiated immediately after Automatic Startup is selected or at any time during Cold Startup dependent upon the flue gas temperature. This mode energizes all of the T-R sets in a set sequence, if they were not previously energized during the Cold Startup mode, and sets the T-R power levels and rapper parameters to default or operator set point values. After this sequence is completed, the unit will be on line and will operate in the manual mode until another mode of operation is selected.

POWER DOWN RAPPING

In some extreme operating cases, dependent upon fly ash properties and ESP operating conditions, it can be very difficult to remove fly ash from the collecting system, particularly while under the influence of an electrical field which can increase the holding or pinning force of the ash layer on the collecting electrode. Although there have been no indications of this problem at the Portland Station, a Power Down Rapping (PDR) control mode is available to use if it should occur. The concept of Power Down Rapping is not new and has been proven at many sites. The power of a T-R set is reduced to decrease the electrical holding force and at the same time increase the rapping force and decrease round trip time on that field for more effective ash removal.

The algorithm is designed to provide the operator with multiple adjustments which can be set for each electrical field. This allows the operator to optimize each field for the best results to alleviate the ash build-up problem.

The operator has the choice to select a single or multiple electrical field to operate in the PDR mode. When multiple fields are selected, the algorithm will allow only one field to be powered down at any one time. There is an adjustable time period of from 1 to 10 minutes between power down periods to allow the unit operation to settle between occurrences. When an electrical field is selected to be powered down, the T-R will not be instantaneously set to a lower power level, but will power down at an adjustable ramp rate from 0.2 to 2 minutes to minimize an opacity excursion. The reduced power level for PDR operation can be set for any value from 0% to 100% of rated power level for each T-R. This allows reduction of power to a point that enhances the plate cleaning, but still maintains a low electrical field for collection and minimizing re-entrainment as opposed to turning power off completely. The T-R will stay powered down for an adjustable time period of from 1 to 30 minutes. During this period the rappers associated with this T-R are set to operate at selected values for RTT and intensity which typically are set for faster RTT and higher intensity than normal. After the T-R off time is complete, the field will be returned to the normal rapping and T-R settings.

During PDR operation, the system is continually monitoring opacity and if it exceeds a maximum set point, the algorithm will temporarily abort, returning all rappers and T-R's to their normal settings. After the opacity excursion is over, the algorithm will continue at the point where it was interrupted.

RAPPER OPTIMIZATION

A detrimental change of fly ash on the collecting plate in the form of excessive buildup and/or greater electrical resistivity will normally result in reduced corona power input with increased sparking.

The Rapper Optimization control mode will monitor the corona power of each transformer-rectifier and if the power decreases below a set point level, it will vary rapper frequency, attempting to maintain optimum corona power input.

The system increases rapping RTT from an initial setting to a faster time, and after a period of time reevaluates the power levels. This procedure continues until the power level is improved to greater than the set point level or all optimization steps have been attempted. If power is not restored to the set point level, the system will determine which rapper settings were optimum and return to those settings. If, during rapping optimization, the T-R power level is restored to the set point level and maintains that level for 12 hours, the Rapper Optimization steps will be reversed in an attempt to return to original round trip times and to stay above the T-R power set point.

The operating conditions of this unit to date have not required the use of this control mode.

HOPPER OVERFILL

The hopper overfill algorithm is designed to reduce the possibility of precipitator damage and subsequent poor operation due to excessively filled hoppers.

When a full hopper is detected, and it persists for one minute, an alarm message is generated and a countdown clock is initiated. The countdown clock has a selectable time of 5 to 60 minutes and when this time has expired, the T-R unit associated with that hopper will be de-energized. If a second high hopper level is encountered and the countdown clock has expired, it will not turn off the associated T-R until the first alarm situation is cleared. The countdown time is normally set at 60 minutes, which allows the maintenance personnel time to empty the hopper. The operator also has the ability to override the T-R turn-off function if he deems it appropriate. There have been a few occurrences of full hopper alarms on the inlet hoppers and typically the problem has been resolved before a T-R unit is de-energized.

BOILER TRIP

When a boiler trip or flameout occurs, the ID fans will normally continue to run with the possibility of unburned combustibles going to the precipitator. Typically, there is a trip function which will turn off all the T-R sets immediately to prevent a hazardous condition. At the Portland Station, however, this occurrence has been approached somewhat differently. If the ID fans continue to operate during a boiler trip and the T-R units are turned off, there will be a possibility of a high opacity excursion. In order to prevent an opacity excursion, the T-R units are not turned off but are reduced in power to a level that will allow collection but not create any sparking in the ESP.

When a signal is received from the main boiler control that a trip has occurred, the system will immediately abort any operating control mode in use and set all T-R units to a power level set point of 25%. After the T-R units have been set to this low value of power, the system continually checks for sparking. If a spark is detected, that T-R unit will immediately be powered down in 5% increments until no sparking is detected. The precipitator will stay in this mode of operation until the boiler trip input signal is cleared and the operator clears the abort condition at the Host Workstation, at which time all T-R units are then turned off and the system is in a standby mode.

AUTOMATIC RECORD KEEPING

One of the advantages of the computer system is to store and manipulate information. There are four different methods in which information can be printed out and used to evaluate the process and aid in troubleshooting.

As reviewed previously in this paper, there is a screen display (log) that shows all alarm messages and important events with a date and time stamp. All these messages are also continuously being printed out as they happen so that there is a permanent record of events. The system alarms, such as high hopper level, T-R trip, and communication failure to a remote device, are obvious items to print out. Any change that is made to the system, such as a control mode selection or any change of set points such as a rapper lift value, are printed out. Status events are more difficult to define but are a very important tool for system evaluation. For instance, when in the Energy Management mode, T-R units will automatically power up and down at various times to collect data for V-I curves. To alert the operator that this occurrence is normal and is not a malfunctioning T-R AVC, messages are printed out when a T-R unit starts a V-I curve, when it has completed powering down, and when it has powered back up.

The second type of informational printout is a report on demand by the operator of a specific screen/data display. For example, if the operator is viewing the T-R data screen which has all the T-R meter readings, he can print it out obtaining an instantaneous report of data at the time it is selected, as shown in Figure 3. This is true for all screens that contain any changeable field or data conditions such as meter readings.

The third method of sending information to the printer is the automatic report generator. This feature has three selection fields. A start field defines the time a report will be outputted to the printer and is selected in hours and minutes. A cycle field will select how many hours after each report is generated the next report will be generated and this is selected from one to 24 hours in one-hour increments. The third field is a stop selection which closes the report generation window. At the Portland Station, the start and stop fields are set to 23:00 hours and the cycle field is set to 4 hours. A report will automatically be printed out at 23:00 hours, four hours later at 03:00, and again at 07:00, etc. With the stop field set at the same time as the start field, reports will be continuously generated every four hours. The automatic report generation capability relieves the plant personnel from having to take manual readings, assures that equipment and system operating information is available for recordkeeping purposes, and for review and evaluation should an operating problem develop.

The fourth method of obtaining information from the system is X-Y graphing of data which previously has been collected and stored. This has proven to be a very valuable tool in looking at trends in data versus time and also in troubleshooting problems in the system.

The graphs can be used with all the analog process values shown in Figure 2, the secondary current of each T-R unit, calculated T-R seconary power, and V-I curves of each T-R unit. The operator has the choice of reviewing one or two graphs on the screen at a time and also selecting several time periods. The choice of time periods can be for the past 10 minutes, 1 hour, 8 hours, 24 hours, 7 days and 28 days. For example, Figure 5 shows the total calculated T-R secondary power graphed for a one-hour period between 13:33 and 14:33, the most recent time being noted at the bottom of the graph to simulate a strip chart recorder printout.

DISCUSSION - SUMMARY

The Unit No. 2 electrostatic precipitator system has been operating successfully since startup. Performance tests conducted in July 1987, while firing a 1.0% sulfur coal in the boiler, resulted in average outlet emissions of 0.052 lb per million Btu and an average stack opacity of 8%. Tests conducted in September 1987, while firing a 1.9% sulfur coal, resulted in lower average outlet emissions of 0.029 lb per million Btu and a stack opacity of 5%.

The IP control system has been shown to be a reliable and valuable asset, contributing to the overall electrostatic precipitator system performance, as well as providing operating cost savings in electrical energy and in personnel manhours required to monitor, operate and record operation of the equipment.

Prior to the installation of this equipment, the operator relied upon a stack opacity recorder and one common precipitator trouble alarm. In the event of any operating difficulty, the operator was alerted to a problem but had no way of determing the cause of that problem. Plant personnel were required to observe and record T-R electrical data and auxiliary equipment operation at remote locations and then coordinate that information with system operating data in the control room, attempting to resolve the problem. Any necessary adjustments to the equipment operation again required plant personnel going to the remote location to make those adjustments. This was a very time-consuming trial and error method of operation requiring costly expediture of plant personnel manhours.

With the installation of the new IP computer-based control system, the operator now has the capability to monitor and control the complete electrostatic precipitator system from one central location in the boiler control room. He can therefore quickly respond to operating variables or equipment difficulties and optimize the precipitator operation and performance as required. Operating decisions can be made quickly and reliably based upon complete system operating information utilizing the real time screens or data logging capabilities provided by the control system.

The plant operators were provided with a completely new automated precipitator control system which presented totally new concepts of operation. Training was conducted in both the classroom and at the Host Workstation in actual operation. Initially, the operators were somewhat reluctant in the operation of the new system. However, the simple operation of the system, ease of operator keyboard entry and data access resulted in minimum training time for the operators to become proficient in the use of the equipment.

Because the system provided a great deal more information on the precipitator system operation, more training time was actually utilized on basic precipitator operation and control theory than on the operation of the control system itself. The operators have now learned to analyze and interpret system operation and problems, and have the knowledge and confidence to use the control system to modify or correct the operation for optimum performance.

The automated system control strategies, such as Automatic Startup and Energy Management, have provided reliable system control capabilities that relieve the operator and plant personnel from continually monitoring and controlling the precipitator system, thereby freeing their time to address operation of the main plant and not having to be concerned with the operation of the precipitator and stack opacity compliance.

The automatic report generation, event log and graphs have resulted in reduced manhours for recordkeeping and provided a working tool for system analysis. This feature has been used for continuous updating of the control algorithms, to resolve minor problems and fine tune the system for optimum operation.

Plans for the future include a continuing program to monitor system operation, particularly the automatic control modes, to possibly further refine and optimize the control parameters and operating set points, consistent with long-term operating trends.

There are also plans to install a new distributed boiler control system and the precipitator control system will become part of that system. This central plant computer system can provide the possibility of doing more detailed boiler-precipitator system trend analyses to evaluate feed forward parameters and new control strategies.

The work described in this paper was not funded by the U.S. Environmental Protection Agency and therefore the contents do not necessarily reflect the views of the Agency and no official endorsement should be inferred.

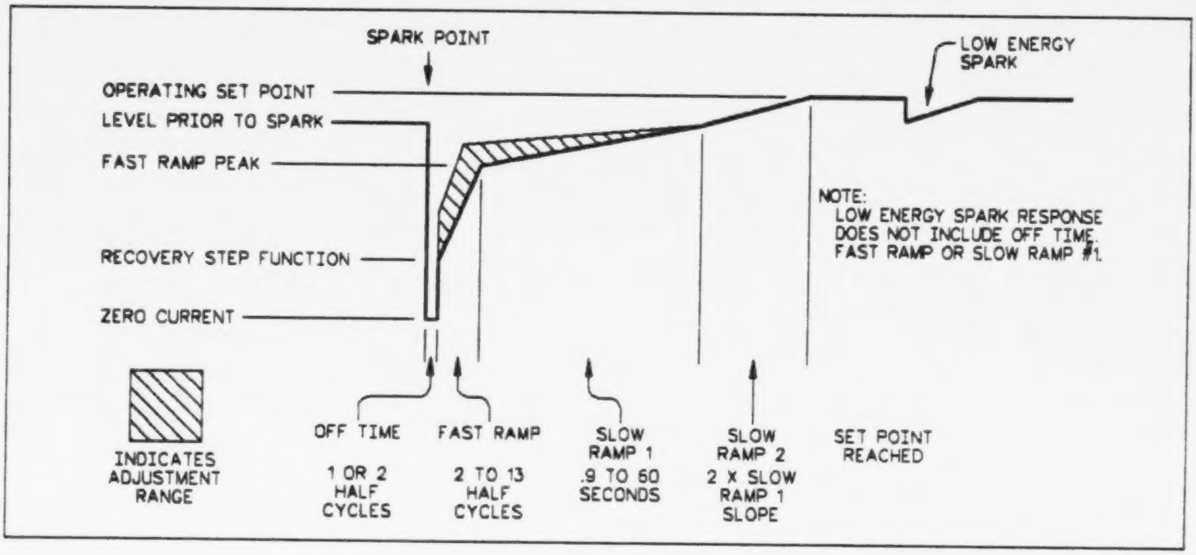

Figure 1. Typical T/R AVC Controller Operation And Spark Response.

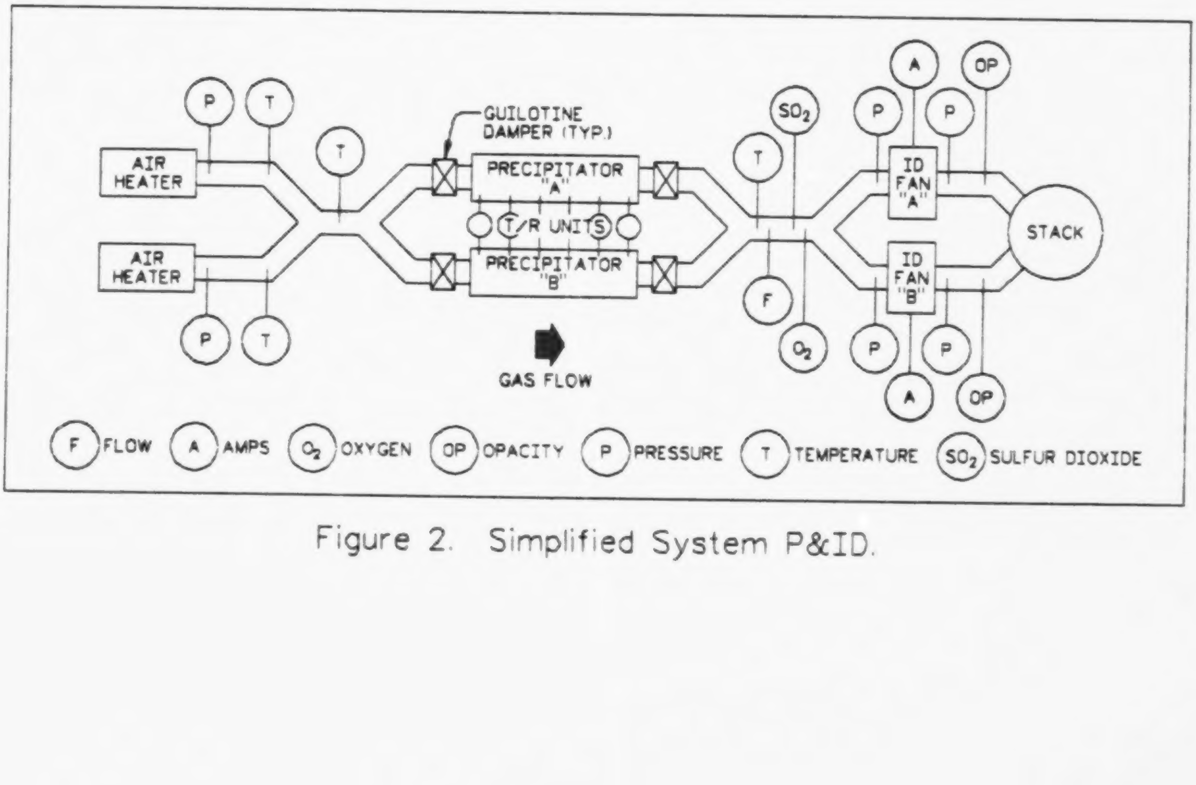

Figure 2. Simplified System P&ID.

T/R	KVA	STATUS			CONTROL			% MAX OBS	PRIMARY		SECONDARY		SPARKS PER MIN
		COMM LINK	ALARM	POWER	START	STOP	% MAX SET		VOLT	AMPS	mAMPS	KV	
2–A 2–B	50 50	ON ON	OK OK	ON ON	START START	STOP STOP	100 100	60 100	288 480	62 104	384 640	33 55	15 0
2–C 2–D	90 90	ON ON	OK OK	ON OFF	START START	STOP STOP	100 100	100 0	480 0	196 0	1155 0	55 0	0 0
2–E 2–F	115 115	ON ON	OK TRIP	ON OFF	START START	STOP STOP	100 100	100 0	480 0	250 0	1475 0	55 0	0 0

Figure 3. Transformer–Rectifier Control Screen.

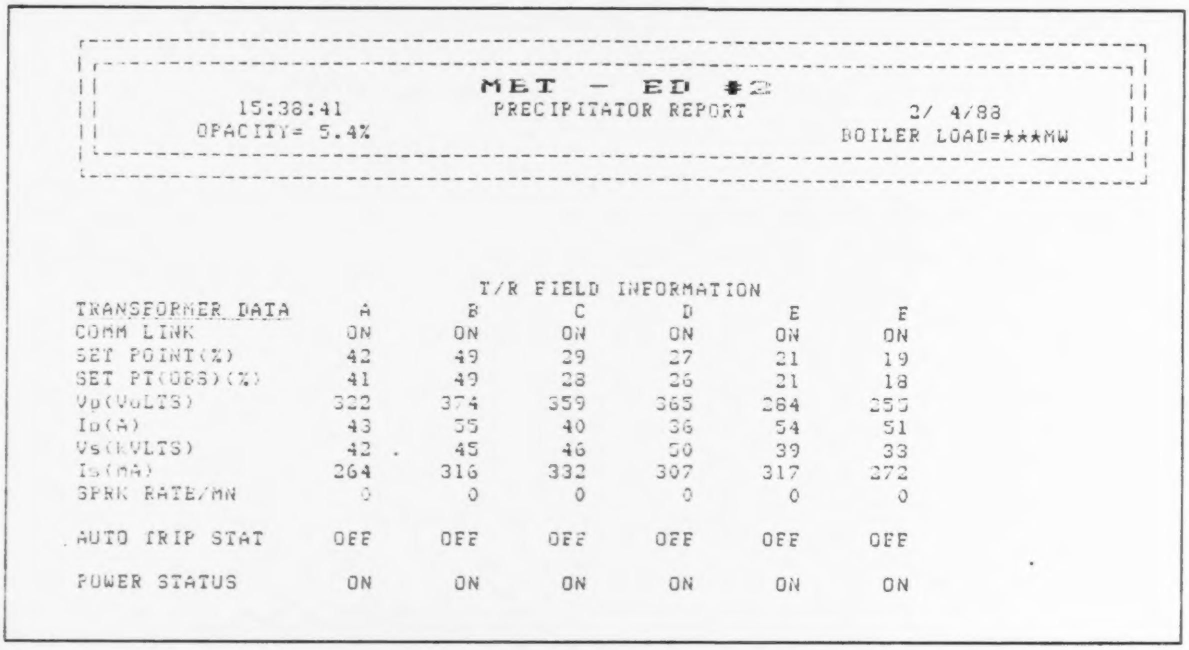

```
                          MET  -  ED  #2
      15:38:41           PRECIPITATOR REPORT                 2/ 4/88
     OPACITY= 5.4%                                      BOILER LOAD=***MW



                              T/R FIELD INFORMATION
TRANSFORMER DATA      A         B         C         D         E         F
COMM LINK            ON        ON        ON        ON        ON        ON
SET POINT(%)         42        49        29        27        21        19
SET PT(OBS)(%)       41        49        28        26        21        18
Vp(VoLTS)           322       374       359       365       284       255
Ip(A)                43        55        40        36        54        51
Vs(KVLTS)            42   .    45        46        50        39        33
Is(mA)              264       316       332       307       317       272
SPRK RATE/MN          0         0         0         0         0         0

AUTO TRIP STAT      OFF       OFF       OFF       OFF       OFF       OFF

POWER STATUS         ON        ON        ON        ON        ON        ON
```

Figure 4. Transformer–Rectifier Operating Data Printout.

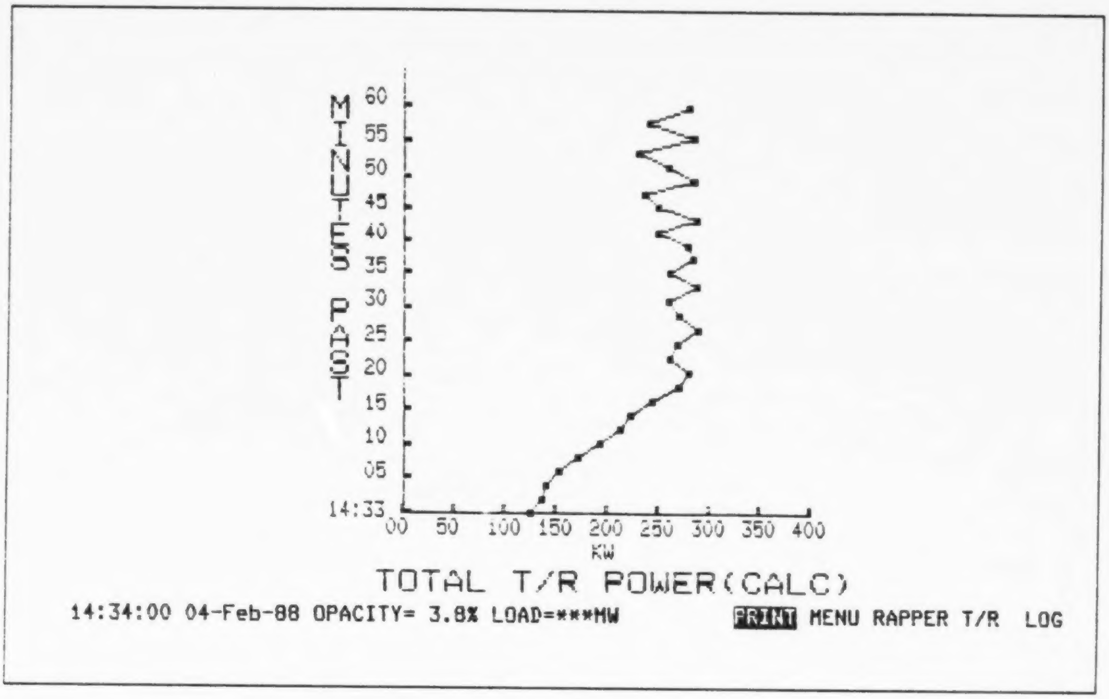

```
14:34:00 04-Feb-88 OPACITY= 3.8% LOAD=***MW
```

Figure 5. Total T/R Power At Beginning Of Energy Management Control.

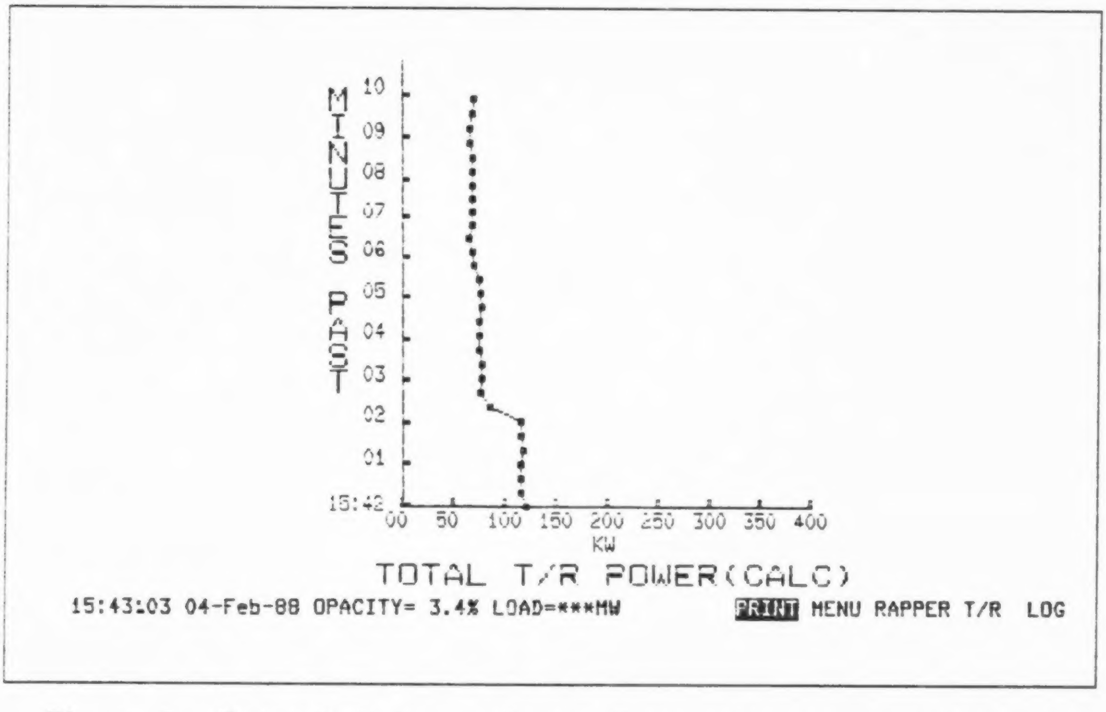

```
15:43:03 04-Feb-88 OPACITY= 3.4% LOAD=***MW
```

Figure 6. Total T/R Power During Energy Management Control.

COMPARISON BETWEEN TRADITIONAL AND MODERN AUTOMATIC CONTROLLERS ON FULL SCALE PRECIPITATORS

by

Victor Reyes
The F.L. Smidth Group, Copenhagen, Denmark

ABSTRACT

The advent of microprocessor based digital controllers with their inherent memory and computing capability has resolved some shortcomings of the traditional analog controllers, and has enabled introduction of new control strategies.

As an example an extremely fast voltage recovery after sparkover can be obtained at any precipitator current level without unnecessary blocking of the thyristors causing reduced efficiency, and without occasioning arcing or multiple sparking. The impact of this feature on precipitator efficiency is illustrated by field experiences from full scale precipitators.

Another important feature is an improved detection of back corona and a proper reaction when this phenomenon occurs. A back corona detector fulfilling these requirements is described. This detector makes it possible to change automatically from traditional DC energization to intermittent energization in case of back corona and vice versa. The influence on the performance of the precipitator is illustrated by field investigations on precipitators for different applications.

Finally, an efficient and low cost Energy Management Control System is presented, and its function is illustrated with an application example.

INTRODUCTION

The incorporation of the microprocessor in the automatic control unit of ESP's high voltage power supplies, replacing the traditional analog controllers, has opened a great number of new possibilities to the designer of power supplies and ESP vendors. The function of the control unit, as shown in Figure 1, is to deliver firing pulses to the control thyristors in every half period of the supply frequency, and the fundamental task of the controller is to deliver the pulses at the right moment according to the existing operating condition of the ESP.

The controller dealt with here is designed by FLS and used under the name PIACS-DC (Precipitator Integrated Automatic Control System for DC power supplies) for controlling the high power supplies from different manufacturers for use at FLS precipitator installations. Figure 2 shows the front plate of the controller.

The following chapters describe the most relevant features of the controller with respect to ESP collection efficiency, and performance results from full scale ESP are presented.

FAST REACTION TO SPARKS IN THE ESP

Without exception all manufacturers of high voltage power supplies for ESP's aim to achieve a fast reaction of the automatic control after a spark in order to maximize the voltage time integral of the precipitator voltage and thus keep a high precipitator efficiency.

A fast reaction to a spark is achieved by avoiding unnecessary turn-off time intervals of the control thyristors and by recovering the precipitator voltage to the highest possible level within few half periods of the mains frequency. This fast voltage recovery has to be performed without multiple sparking, i.e. a new spark should be avoided during the recovery period.

DETECTION AND CLASSIFICATION OF SPARKS

Most of the controllers used today classify the sparks in the ESP according to their intensity in 2 types:

a) The first type includes the sparks where the precipitator voltage rises instantaneously to a certain level after the spark within a very short period of time (light spark).

b) The second type includes the sparks where the precipitator voltage remains low after the spark for a certain period of time, or a current exceeding a preselected level is detected (severe spark). For such sparks most of the controllers introduce a turn-off time for the thyristors before the recovery of the precipitator voltage.

Figure 3 shows 2 oscillograms illustrating the 2 types of sparks, and the reaction of the PIACS-DC controller. Figure 3.b shows that, even in case of severe spark, the voltage can be raised to a level equal to the DC level before spark, without introducing a turn-off time.

The problem in connection with the use of a turn-off time is closely related to the detection method used and the way the recovery is performed. As known, primary current, primary voltage, precipitator current, precipitator voltage or a combination of these are used to sense the sparks.

Each method has advantages and disadvantages, but these will not be discussed in the present paper.

Nevertheless, a few words have to be mentioned about spark detection by means of current sensing. This method, used with a threshold level to detect a severe spark, may cause a wrong interpretation of the spark in many controllers. Figure 4 illustrates the typical problem.

In this case the spark takes place after the peak of the precipitator voltage, and at a point where the current has a relatively low value and the mains voltage is approaching its zero-crossing. Therefore, no overcurrent appears, and the controller does not block the thyristors, but raises the precipitator voltage in the next half period. This charging of the capacitance of the ESP results in a rather high capacitive current, which may be detected as severe spark and will be followed by a turn-off time.

As shown in Figure 4 this turn-off time may have a substantially long duration, which will degrade the precipitator performance. In this particular case it is clearly observed that the blocking period introduced by the controller is completely unnecessary. Similar observations and measurements performed with different controllers at several plants indicate the advantages of detecting sparks by sensing the precipitator voltage. After a spark detection the PIACS-DC tries to raise the precipitator voltage in the next 2 half periods and introduces a turn-off time, only in case the precipitator voltage is still low after this attempt. With the voltage raised as described in the next section, the controller can generally handle severe sparks without using a turn-off time.

RECOVERY OF THE PRECIPITATOR VOLTAGE AFTER SPARK

To keep the periods with low voltage at minimum, the precipitator voltage must be raised to the highest level permitted by operating conditions as quickly as possible.

This is not a simple problem, because the precipitator average current in most controllers is directly or indirectly controlled in a feedback closed loop. After a spark the firing angle is increased to perform a current setback. This firing angle will not be the right one to raise the precipitator voltage to a suitable level within a minimum of time. Figure 5 illustrates this problem.

Curve B shows the average voltage from a DC power supply and curve A the attainable peak voltage in the first half period after a spark versus firing angle. These curves show that the controller, operating in the afore-mentioned way, only gives the correct initial firing angle, if the power supply is operating around the point where the two curves cross each other.

The voltage will be raised to a level which is too high if the power supply is operating at a low firing angle. This will result in multiple sparking. If the power supply is operating at a high firing angle the voltage recovery will be too slow, see Figure 6.

This problem can be solved by using a microprocessor based controller, as this has memory and computing capabilities. The solution is to incorporate a curve similar to curve A in Figure 5 in the controller and to store information about precipitator field capacitance and short circuit impedance of the power supply.

With this information the right firing angle can be determined immediately after a spark, according to the present level of the precipitator voltage, and the thyristor is fired with this angle. The power supply is operated in an open loop during the recovery period.

Utilizing this method the reaction to a spark of a PIACS-DC controller is shown in Figure 7. The two oscillograms illustrate the voltage recovery after spark at high current operation (low firing angle) and at low current operation (high firing angle). In both cases the precipitator voltage can be raised to the the DC level before the spark within 3 half periods without using a turn-off time and without occurrence of multiple sparking.

INFLUENCE ON THE COLLECTION EFFICIENCY

Basically, it is not easy to make valid comparisons to determine the impact of a fast voltage recovery on the collection efficiency due to the difficulty in changing from one controller to the other without causing disturbances in the ESP operation.

Nevertheless, tests have been made at an ESP installation, dedusting a kiln and a raw mill at a cement works. The kiln has a rated output of 1500 metric tpd. The ESP consists of two chambers with two fields each and is designed for a collection efficiency of 99.47% with an SCA of 75 $m^2/m^3/s$ (381 ft^2/1000 acfm). The gas flow rate is 237,000 m^3/h (139,500 acfm) at 128°C (262°F). The ESP is energized by four high voltage supplies, each 70 kV (peak)/600 mA, controlled by PIACS-DC units.

The test was performed at one chamber, having its own stack, where an optical density monitor was mounted. For the purpose of the test the two controllers were programmed not only with their standard spark reaction, but further with a reaction similar to the one shown in Figure 6.b, and it was possible to change between fast and slow reaction without interruption of the power supply by means of pocket terminals connected to the controllers. The ESP was operating at normal and stable conditions at rated kiln production. Gas temperature was 157°C (315°F), and current levels were normal. The measured spark rates were around 20 sparks per minute.

By changing several times between the two types of reaction it was possible to obtain consistent results. These indicated reduction in the optical density from 0.29 with slow reaction to 0.28 with fast reaction. This corresponds to a reduction in the dust emission from 200 to 190 mg/m^3.

INTERMITTENT ENERGIZATION OF ESP

This form of operation is nowadays a standard feature in most DC high voltage power supplies, as it allows energy savings and, under certain operating conditions, improvements in collection efficiency. The PIACS-DC controller incorporates intermittent energization as standard under the name of Energy Control (EC). A fast reaction after spark is also required under this form of energization. Figure 8.a shows the voltage recovery after spark for operation with a cycle time of 30 ms, (three half periods of the mains frequency) compared with traditional DC operation (Figure 8.b). The cycle time is defined as the period between 2 current pulses.

BACK CORONA DETECTION AND CURRENT CONTROL

Most of the controllers used in the past detect back corona by sensing the slope of the V-I curve. When the slope changes sign and becomes negative, the detector indicates back corona, and afterwards the current is limited to a value around the "knee" of the V-I curve.

Field experiences indicate that this method is insufficient in a lot of cases. The example being discussed in the following is from a Danish power station, burning low sulphur (0.7%) coal from Petchora, USSR. The unit is a 300 MW (e) coal fired boiler, dedusted by an ESP designed for a collection efficiency of 99.45% with an SCA of 60 $m^2/m^3/s$ (305 ft^2/1000 acfm). The gas flow rate is 1,351,200 m^3/h (795,000 acfm) at 125°C (257°F). The ESP consists of two chambers with three fields each.

The four front fields are energized by COROMAX pulse systems and the two outlet fields by DC high voltage power supplies. The six power supplies are controlled by PIACS-COROMAX and PIACS-DC control units, respectively.

The current-voltage characteristic for the outlet fields is shown in Figure 9. This shows the trough voltage, i.e. the lowest point in the precipitator voltage waveform, appearing in one half period of the mains frequency, the average and the peak voltage versus average current. The average curve, which is the one normally used to detect back corona, does not give a clear indication of back corona, as no "knee" is found. However, the trough curve yielding a more sensitive detection shows back corona, as the trough voltage starts decreasing for an increasing current above a certain current level. The presence of back corona is confirmed by Figure 10, showing the dust emission versus the input power to the two outlet fields.

A controller with a back corona detector based on slope sensing of the average V-I curve will operate at point A, while a controller with a detector based on slope sensing of the trough curve will operate at point B with a lower emission and lower power consumption.

However, a further improvement can be attained by utilizing an even more sensitive back corona detection for control of the EC cycle time as indicated in point C.

The optimal operating point corresponds to a cycle time of 70 ms, but the operation with 50 ms cycle time selected by the detector represents a substantial improvement as compared to operation with the slope sensing detectors.

The results are summarized as follows:

Detection	Emission	Power consumption
A (average voltage)	160 mg/m³, NTP *)	155 kW
B (trough voltage)	115 mg/m³, NTP	48 kW
C (PIACS DC)	100 mg/m³, NTP	30 kW

*) The NTP conditions are defined as 0°C and 760 mmHg.

DETECTION PRINCIPLE

The used back corona detector senses the trough value of each half period of the precipitator voltage and compares the value before a spark with the corresponding value after the spark. Figure 11 shows the typical waveforms of the precipitator voltage and primary current when a spark takes place during back corona conditions. It is observed that the trough voltage, compared with its value before the spark, is increased during several periods of the mains frequency after the spark, thus indicating back corona.

The detector is activated at selected time intervals (typically every 15 min.) and performs the comparison described above. In case of back corona the controller changes from DC to EC operation, first to a cycle time of three half periods (30 ms), and subsequently the off-time is increased by two half periods (20 ms), as long as back corona is detected.

When the detector is activated the current of the power supply is increased towards its nominal value ignoring a possible current limit until spark occurs. If no spark takes place, a blocking interval is introduced by the controller, and the trough value of the voltage after the blocking interval is compared with the corresponding value before the blocking period in the same manner as described before in the case of sparks.

Figure 12 shows the detection of back corona based on such a blocking period. This example corresponds to the installation described in connection with Figure 10. Before the detection the power supply is operating in the EC mode with a cycle time of 30 ms, but the detector finds back corona and increases the cycle time to 50 ms.

OPERATION AT LOW RESISTIVITY CONDITIONS

Figure 13 shows dust emission versus input power from a precipitator installation for a 130 MW (e) coal fired boiler in Denmark, treating low resistivity dust from a blend of

British and Polish coals with medium sulphur content (1.1 - 1.4%). The ESP consists of two chambers, each with two fields with an SCA of 42 m²/m³/s (213 ft²/1000 acfm). The test was performed at one chamber, and each field is energized by one 80 kV (peak)/1200 mA high voltage power supply with PIACS-DC controller. The dust emission is determined by a calibrated monitor at the exit duct, measuring the optical density.

In this case the controller remained at DC operation, which is obviously the best energization mode for this application. By changing manually to EC operation with a cycle time of 130 ms the controller reverted automatically to DC operation after six back corona measurements.

ENERGY MANAGEMENT CONTROL SYSTEM (EMCS)

Apart from back corona conditions the ESP's high voltage power supplies must normally operate at the maximum of their capability to maintain a high collection efficiency. However, in periods with more favourable operating conditions like lower inlet dust concentration or lower dust resistivity, it may be possible to reduce the input power to the precipitator fields without exceeding the required emission level, and considerable energy savings can be obtained.

This function has to be performed automatically, and today several microprocessor based control systems incorporate this feature.

The system dealt with here consists of one printed circuit board to be included in one standard PIACS-DC controller, or PIACS-COROMAX, and capable of controlling a maximum of ten controllers independently. Figure 14 shows an example with an ESP with one chamber and three fields.

PRINCIPLE OF OPERATION

The EMCS unit receives an analog current signal from an opacity or optical density monitor. This signal is filtered and converted to a digital PWM signal (Pulse Width Modulated signal), which is sent via optocouplers to a digital input in each PIACS controller. In each controller this "emission signal", indicating the opacity or the optical density, is further filtered in a digital low-pass filter included in the software with a selected time constant.

The filtered "emission signal" is compared with 2 selected set values (S1 and S2), see Figure 15. If the emission is higher than S1, the current limit used by the controller is the normal set value. But if the emission falls in the range determined by S1 and S2, the current limit will be reduced according to the control characteristic curve until the "emission signal" begins to increase. If the emission becomes lower than S2 the current limit is kept at the selected "low value".

In the ESP with three fields, shown in Figure 14, the setpoints S1 and S2 have to be adjusted for each controller in such a way that the current reduction in each power supply influences the dust emission as little as possible. This may be characteristic for each ESP installation, but a preferred method is to start reducing the current limit at the inlet field, then the middle field, and finally the outlet field. Normally, the setpoint S2 will have a common value for the 3 controllers.

The EMCS unit can control the individual control units, irrespective of DC or EC operation (intermittent energization). Each controller is operated with a cycle time determined by its back corona detector, and the EMCS unit controls the current limit within this cycle time.

An EMCS unit is installed at the precipitator operating at low resistivity dust, described in the previous chapter (see Figure 13). The set values S1 and S2 are adjusted to maintain an average optical density of 0.3 equal to the level attained when the unit is running at rated load.

In Figure 16 is shown a sketch of the strip charts indicating the optical density and the average current in the inlet and outlet fields with the unit operating at about 50% load.

At t = 0 min. the EMCS function has been stopped from the keyboard, the optical density is approx. 0.1, an the power consumption of the chamber is 41 kW. At t = 9 min. the EMCS is activated and starts reducing the current levels. The average optical density rises after some time to approx. 0.3, and the current is kept at a low value in both fields. The spikes appearing in the optical density correspond to rapping losses. It can be noticed that the current in the outlet field is raised slightly when the spikes have a high amplitude. The power consumption in this case is 6 kW, and thus the energy saving is about 35 kW (7.6 W/m^2 collecting area).

At = 25 min. the EMCS is turned off, and the optical density and the current levels return to their original values.

CONCLUSIONS AND SUMMARY

The results obtained in relation to a fast recovery of the precipitator voltage after spark shows that the voltage can be raised very quickly after a spark without introducing unnecessary turn-off periods for the phase control thyristors. Further, the described method contributes to limit the current surges during recharging the precipitator field, in this way reducing the thermal effects in the power supplies, specially in case of operation at high spark rates.

A fast reaction to sparks is shown to give a minor improvement in the collection efficiency at operating conditions with a comparatively low spark rate.

Back corona detection by analyzing the V-I curve with average values of precipitator current and voltage has proven not to be sufficiently sensitive. Even the more sensitive method by analyzing the curve with trough voltage values and average current does not yield an optimum back corona detection in all situations.

An improved back corona detection based on comparison of the trough values of the precipitator voltage in the individual half periods before and after sparks has yielded excellent results when used to control the cycle time of the intermittent energization in order to keep the precipitator out of back corona.

Finally, a simple and low cost energy management control system has been described. This system may be utilized to attain substantial power saving without exceeding specified opacity limits during periods of low production, or otherwise easy precipitator conditions.

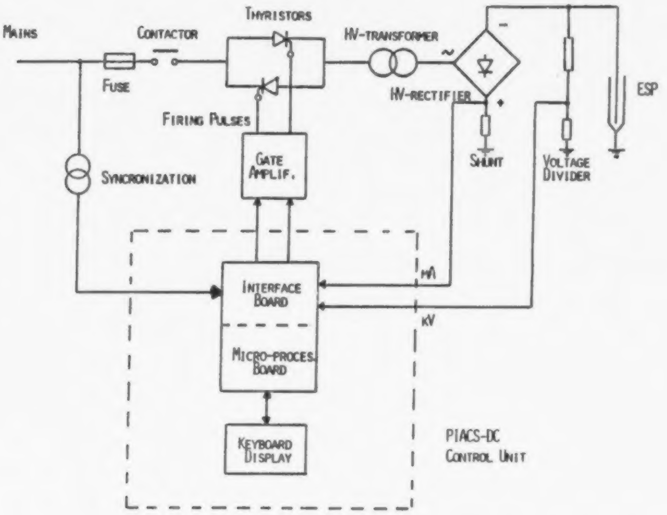

Figure 1. Block diagram of a high voltage power supply.

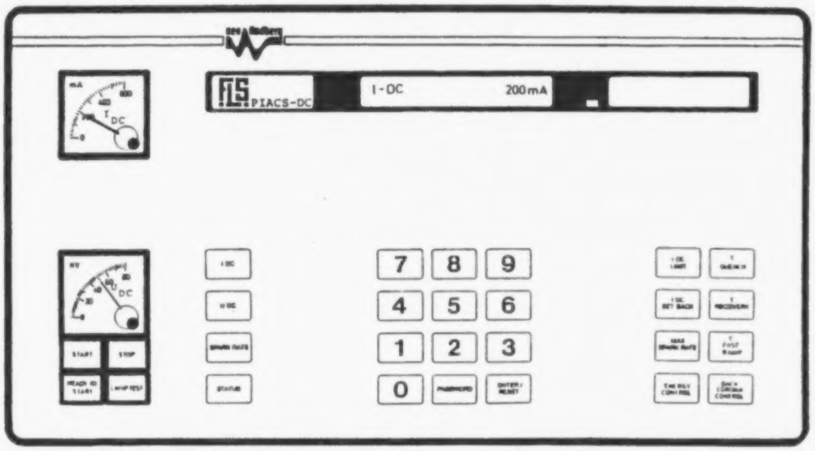

Figure 2. Control panel for the PIACS-DC controller.

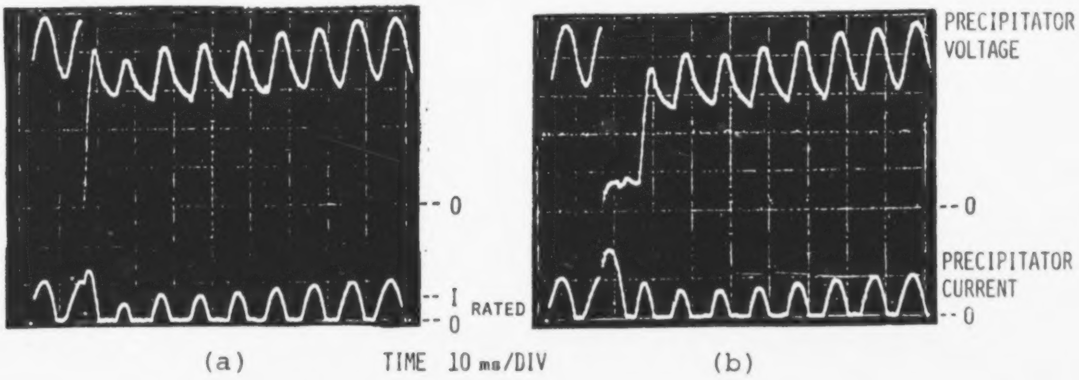

Figure 3. Classification of sparks according to their intensity. Ligth spark (a) and severe spark (b).

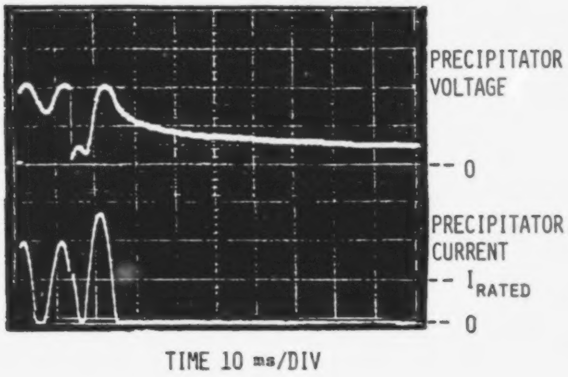

Figure 4. Spark detection by current sensing. Unnecessary use of a turn-off time.

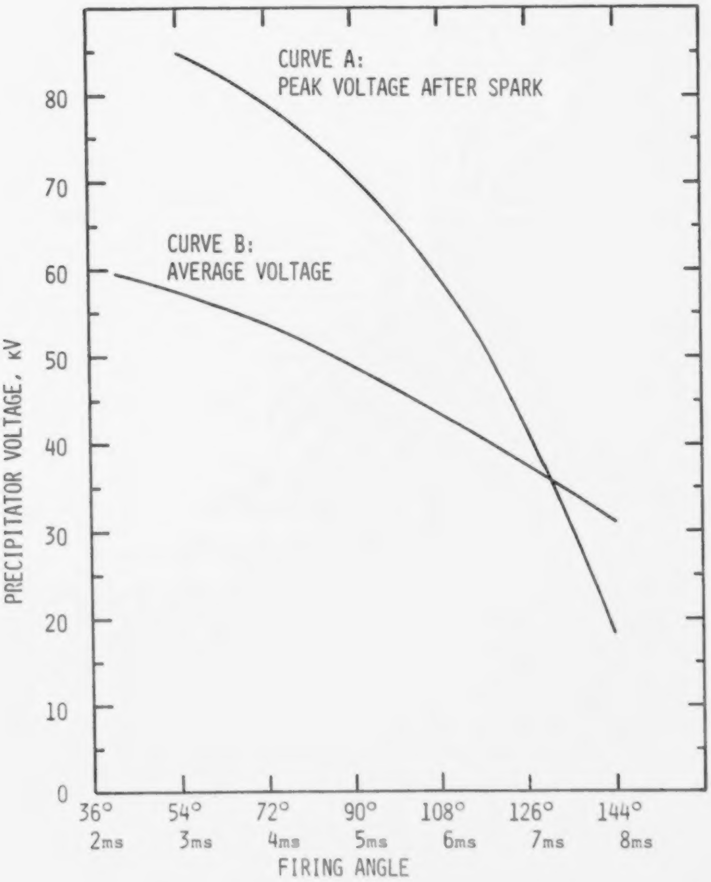

Figure 5. Average voltage (curve B) and attainable peak voltage after spark (curve A), as function of the firing angle.

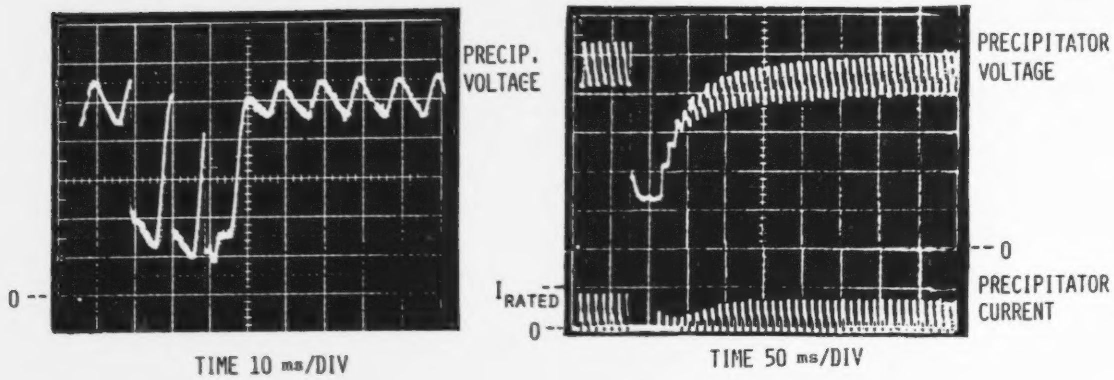

(a) (b)

Figure 6. Illustration of an analog controller reaction to some sparks. Too fast reaction (a) and too slow reaction (b).

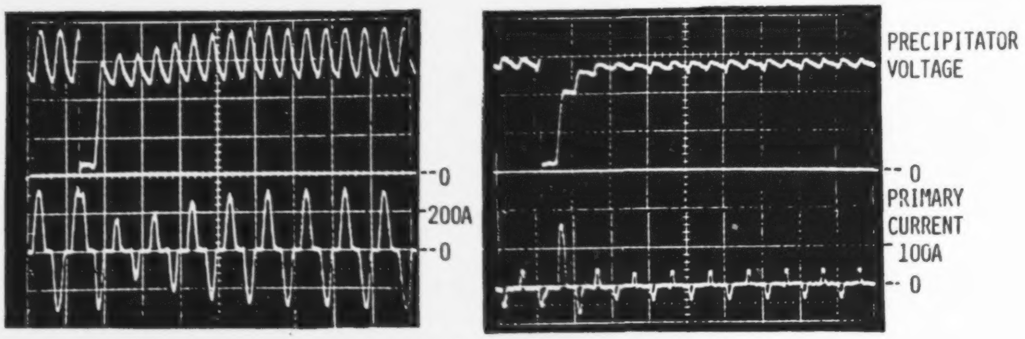

(a) (b)

Figure 7. Digital controller reaction to sparks when operating at high current (a) and at low current (b).

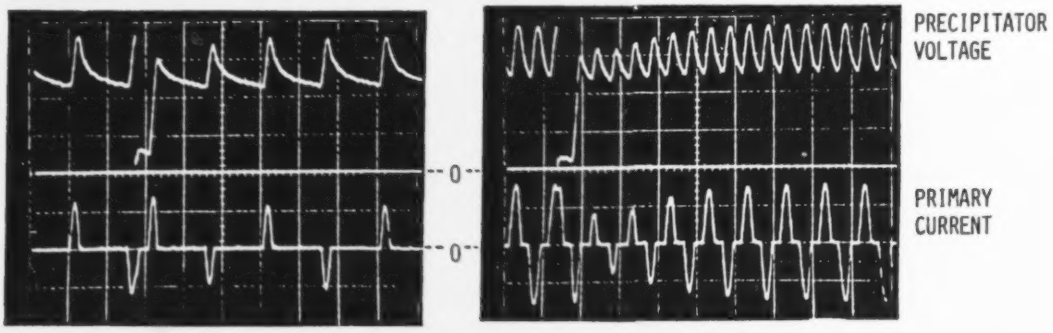

(a) (b)

Figure 8. Precipitator voltage and primary current at EC-operation (a) and traditional DC-operation (b). Reaction to spark.

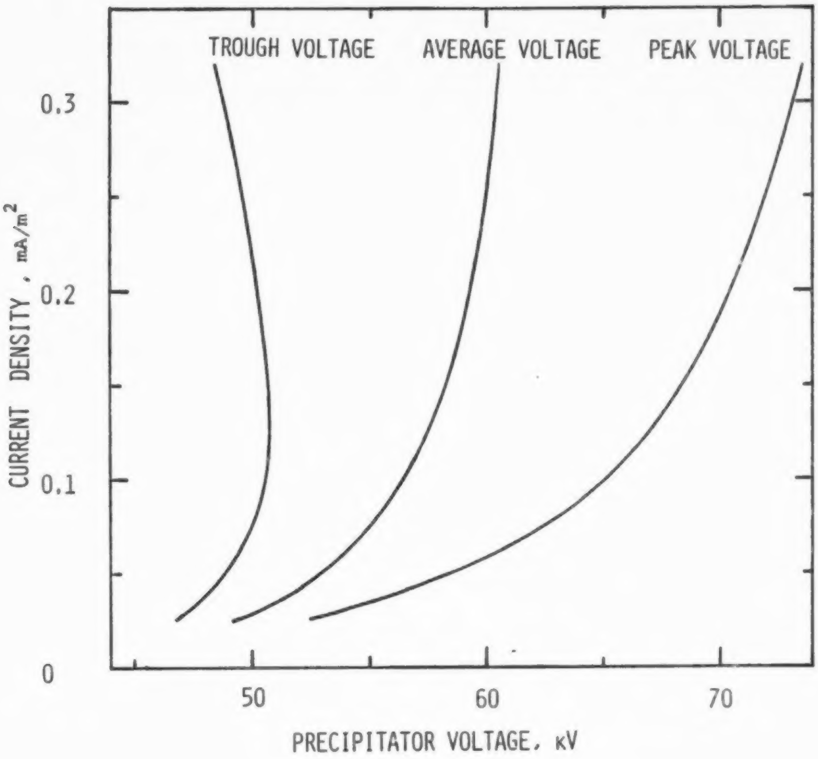

Figure 9. Current-voltage curves at back corona conditions.

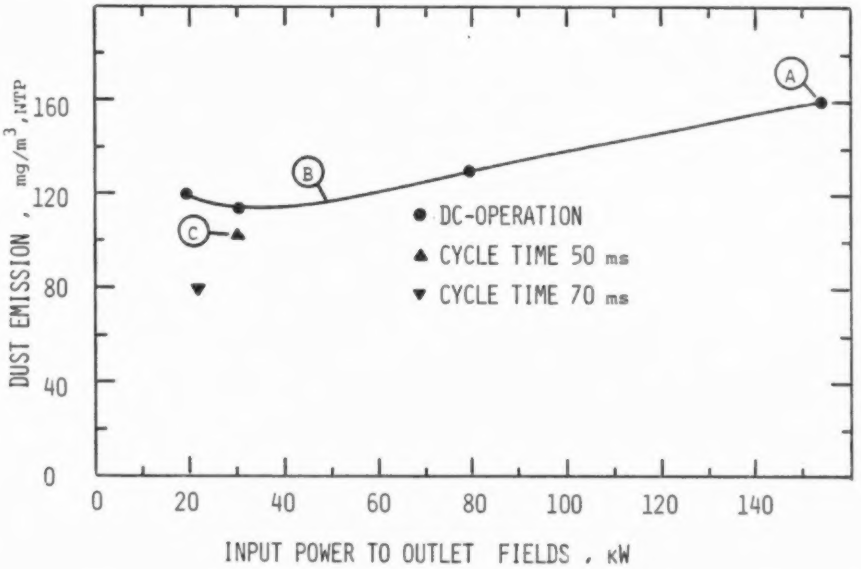

PRECIPITATOR: 2 CHAMBERS, 3 FIELDS, 3780 m² COLLECTING AREA/FIELD
POWER SUPPLY: 4 PULSE SYSTEMS AND 2 T/R SETS, 90kV/1200 mA

Figure 10. Dust emission versus power input at back corona conditions.

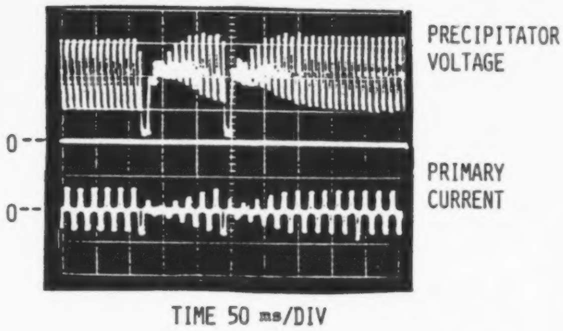

Figure 11. Reaction to spark in case of back corona.

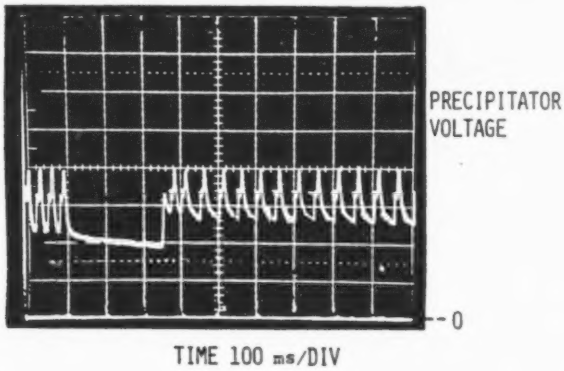

Figure 12. Back corona detection at EC-operation by using a blocking period. Automatic change from a cycle time of 30 to 50 ms.

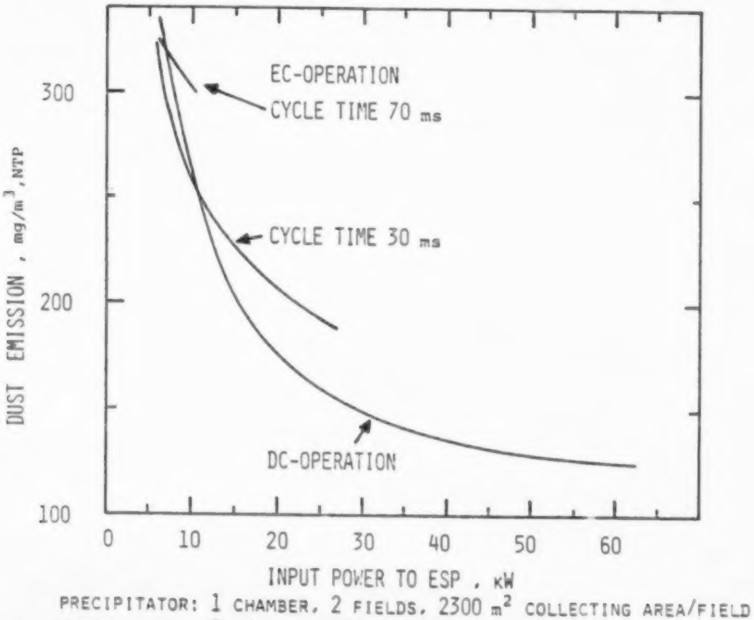

PRECIPITATOR: 1 CHAMBER, 2 FIELDS, 2300 m^2 COLLECTING AREA/FIELD
POWER SUPPLY: 2 T/R SETS, 80 kV/1200 mA

Figure 13. Dust emission versus power input at no back corona conditions.

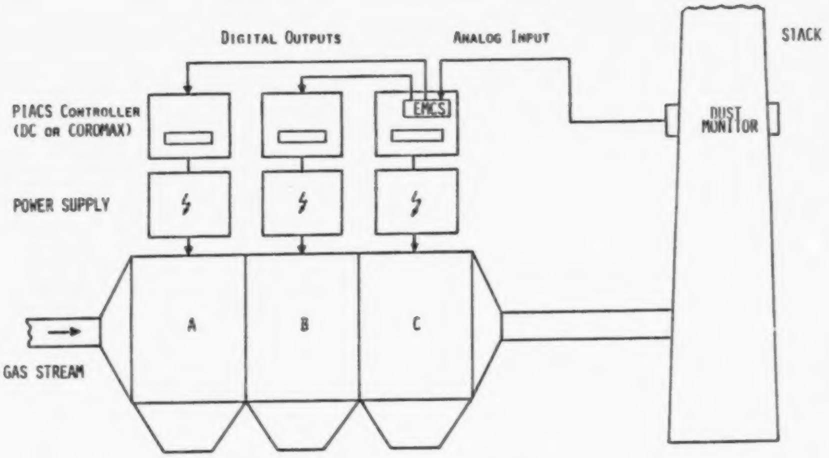

Figure 14. Principle of operation of the EMCS unit.

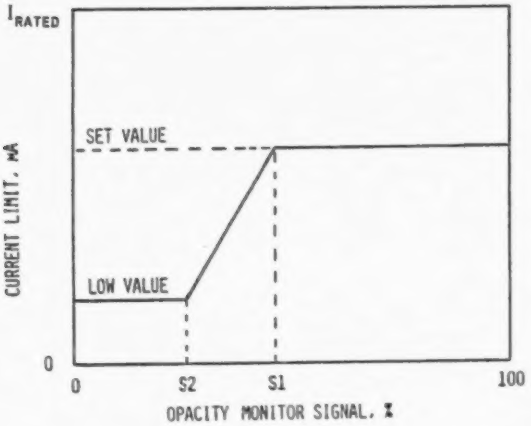

Figure 15. EMCS control characteristic for one controller.

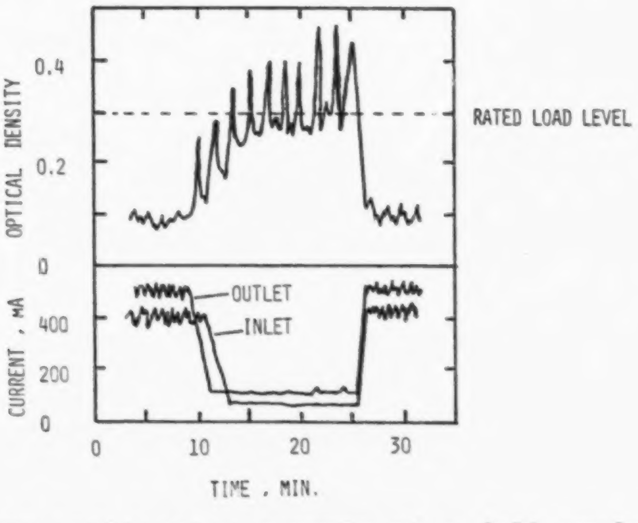

Figure 16. EMCS application example at a full scale ESP.

A SUPERVISORY COMPUTER CONTROL FOR SMALLER INDUSTRIAL ELECTROSTATIC PRECIPITATORS

by

J. D. Riley
Lurgi Corporation
River Edge, New Jersey

and

F. Neulinger
Lurgi GmbH
Frankfurt, West Germany

ABSTRACT

Attention has been given in the past to master computer controls used for monitoring, process control, and energy savings in conjunction with large electric utility sized electrostatic precipitators. Now such a computer control is available for smaller industrial sized precipitator installations, which have only 4 to 10 transformer-rectifier power supplies. As an example, the features and benefits of one actual installation are described.

INTRODUCTION

The electrostatic precipitator is one of the most economical means for collecting dust from industrial gases and waste gases; it is capable of reliably meeting even the most exacting environmental protection standards. However, increasing dust collection efficiency naturally entails higher power consumption. Thus, energy-saving methods have become a focal point of interest.

Maximum precipitator efficiency is achieved with the operating voltage in the individual zones of a precipitator as close as possible to the varying flashover voltage of the gas at all times. This task has traditionally been fulfilled by the automatic analog control system of the transformer-rectifier sets.

Employing the latest microcomputer technology, there has been developed a highly effective system for precipitator control and monitoring, excelling any analog control system so far installed. In addition, process optimization and energy minimization have been realized.

In previous papers we have discussed the use of such technology applied to electrostatic precipitators serving the electric utility industry and other industries having large precipitators. More recently, a comparable system has been developed making this technology cost effective for smaller industrial electrostatic precipitators.

SYSTEM OVERVIEW

The new concept consists of the microcomputer control systems for the individual transformer-rectifier sets and a superordinated process automation system which coordinates, monitors and optimizes the functions of the decentralized components, in accordance with the required clean gas dust content and important parameters of the preceding process (Fig. 1).

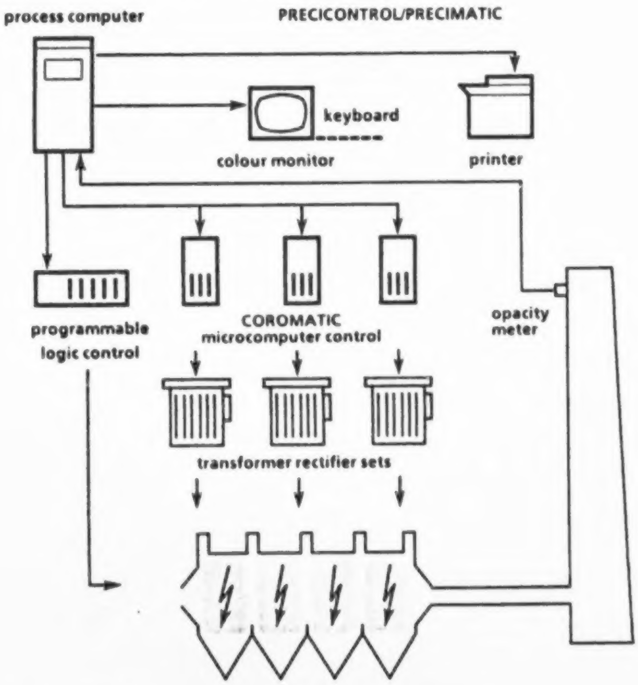
process computer
PRECICONTROL/PRECIMATIC
keyboard
colour monitor
printer
programmable logic control
COROMATIC microcomputer control
opacity meter
transformer rectifier sets

Figure 1. System Overview

Microcomputer Control System for T/R Sets

An important function of the microcomputer control system for T/R sets lies in the optimization of the voltage/time area and, thus, the optimization of the dust collection efficiency.

The microcomputer control adapts perfectly to varying operating conditions, since its memory permits the detection of rising, decreasing, or constant flashover limits and, hence, can control by applying variable scanning periods and steps.

Since the flashover limit varies constantly as a function of the process, and since the only criterion for validly determining this instantaneous limit is the flashover itself, extremely short operating voltage dead-times are an important factor for maintaining high precipitator operating efficiency.

Moreover, the reaction to a flashover is optimized by adjusting the dionization time and a curve of voltage increase after a flashover via a programmed learning algarithm, the optimization criterion being the avoidance of sequence flashovers.

Therefore, a comparison of conventional analog control systems with the microcomputer control shows clearly that optimum adaption of flashover reaction to the varying process conditions enables an improvement in the voltage/time area and thus in the dust collection efficiency (see Fig. 2).

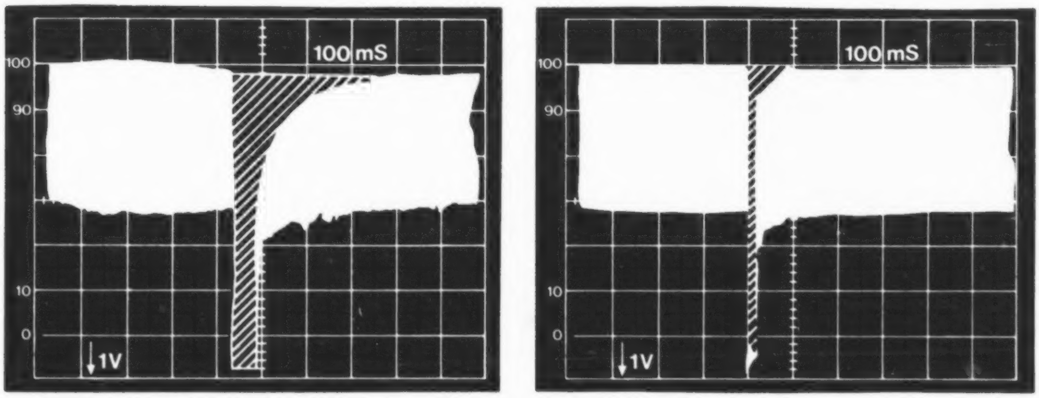

Analog Control

Coromatic Control

Figure 2. Comparison Analog Control/Coromatic Control Flashover Reaction

The dust deposited on the collecting electrodes of a precipitator is retained there, in part, by electric forces of adhesion. Another unique and highly advantageous feature of the microcomputer control is reduced voltage rapping. To ensure optimum cleaning of electrodes, the control automatically reduces the voltage in the section being cleaned during rapping and then restores it to its former value when the rapping cycle is complete (see Fig. 3). The improvement in the voltage/-time area is considerable. Dust puffing at the stack is thus reduced or even eliminated.

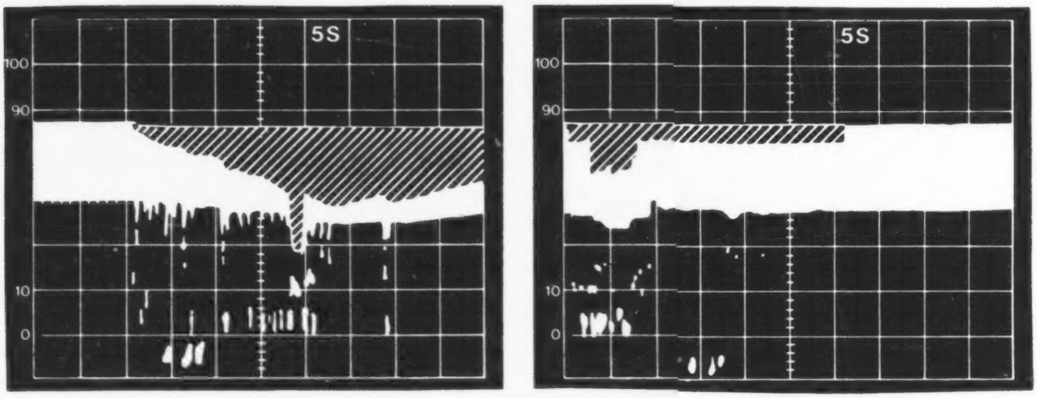

Analog Control

Coromatic Control

Figure 3. Comparison Analog Control/Coromatic Control Rapping Reaction

The current to voltage ratio, I/V, is a major factor concerning precipitator efficiency, and this ratio may vary over a wide range (see Fig. 4). To optimize precipitator efficiency, the microcomputer control records the I/V characteristics, calculates the plotted curve steepness and adjusts controller reaction to a flashover accordingly; if the characteristic is steep, control is accomplished by current steps, if it is flat, by voltage steps. If a characteristic exhibits a voltage maximum, the microcomputer adjusts to a value directly above the voltage maximum.

A further feature of the microcomputer control is the ability to provide millisecond pulsing or Variopulse operation (see Fig. 5). This feature is the subject of a previously presented paper which can be referenced for details. However, suffice it to say, this feature has been found to cause significant improvement in collection efficiency of certain precipitators and has the nice byproduct of considerable possible energy savings.

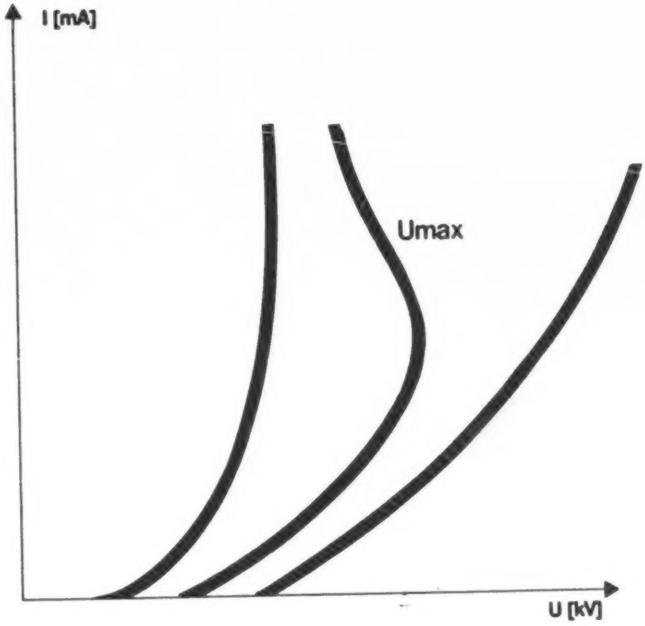

Figure 4. Various Current/Voltage Characteristics

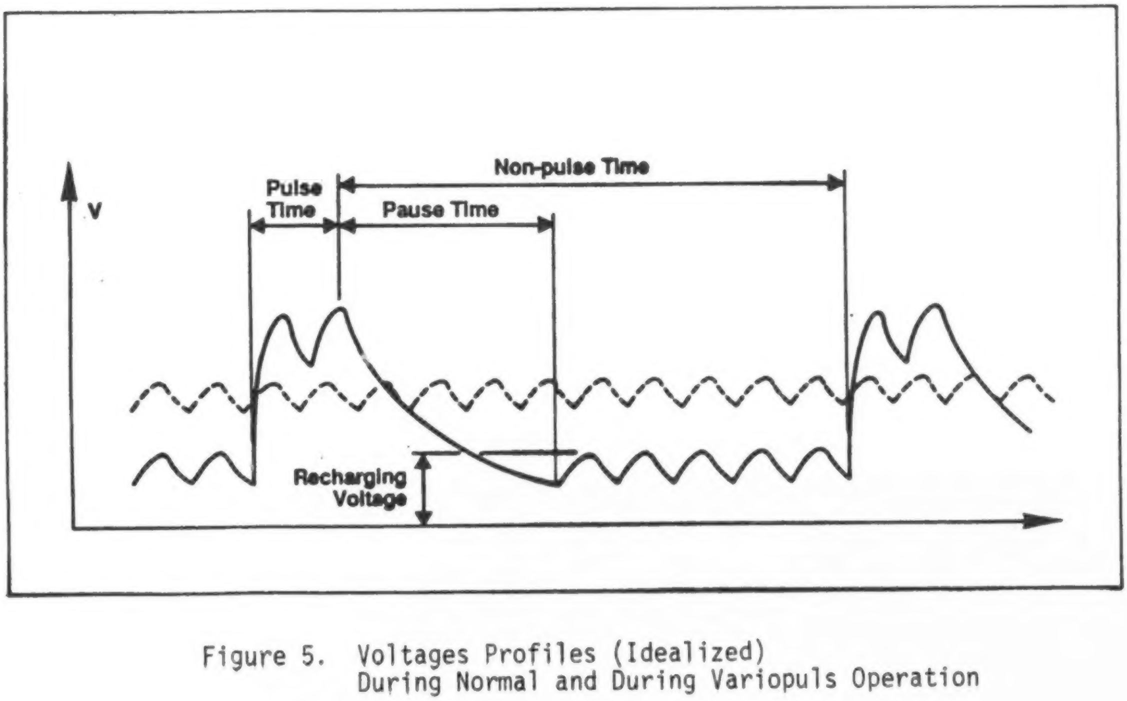

Figure 5. Voltages Profiles (Idealized)
During Normal and During Variopuls Operation

Superordinated Process Automation System

In order to perform its function, the process computer requires a variety of inputs.

From the process itself there are various inputs depending upon the process, such as fuel feed rate, mill output, gas temperature, etc., which will give an indication of gas volume and inlet dust loading.

In addition, the relevant input data from the individual microcomputers is required, such as current and voltage of the individual precipitator zones, the profile of the current and voltage curve, the rapping signal, and the electric power applied.

Lastly, there is required a signal from the opacity meter.

PROCESS OPERATION AND CONTROL

One main function of the process automation system is process operation and control. This function is handled through the use of a display unit which permits better organization, clearer representation of information and as a result, ease of operation as well as improved control of errors. Using a display unit also means that the space requirements of the control system, as well as the equipment and cable material required, can be reduced resulting in a corresponding reduction in costs.

Fig. 6 shows the compact, tabletop equipment installed for the operation of a small 2-field precipitator on a sinter plant process.

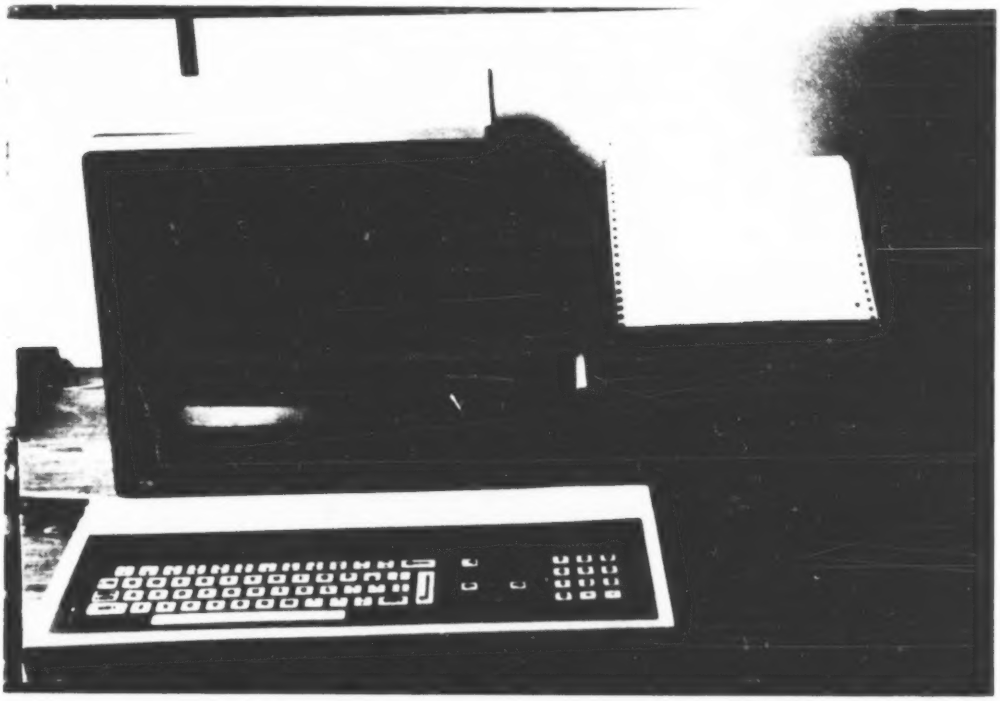

Figure 6. Tabletop Workstation

The keyboard is provided for process operation. A series of keys has a variable function which automatically adapts to the display.

Messages from the process are displayed on the monitor and recorded by a printer.

From this workstation, the operator can start or stop individual T/R's, make adjustments and monitor the central telegram traffic between the master automation system and the microcomputer control of the individual T/R sets.

The operating functions are activated by pressing the appropriate function key on the PRECIMATIC. Functions such as voltage increase or decrease of T/R sets, set-point pre-setting of the clean gas dust content, selection of overall display and monitoring of records.

Establishing records and data curves for monitoring requires filing of the data transmitted from the microcomputer controls of the T/R sets (e.g., precipitator voltage, precipitator current) and of the data of the clean gas dust content, the coordination of the monitor, processing of the monitor displays and/or the measured variable curves.

The various representations of measured variables give the shift personnel a quick survey of the entire "electrostatic precipitator" and inform the operator of the behavior of the electrostatic precipitator as a function of the different process parameters. Also, it permits any failure to be analyzed more quickly and more precisely resulting in easy correction.

Examples of data that can be displayed on the monitor include:

- Precipitator voltage;
- Precipitator current;
- Clean gas dust content;
- Power consumption of precipitator; and
- Boiler load.

This data can also be graphed versus time to show trends.

From the sinter plant previously referred to, you will note in Fig. 7 the basic precipitator data display taken from the monitor. In Fig. 8 is shown the display of information from one zone or bus section.

By use of the printer, relevant process prints can be recorded and provide a useful chronological history.

It is particularly useful to record when adjustments are made, when errors occur and when they are cleared.

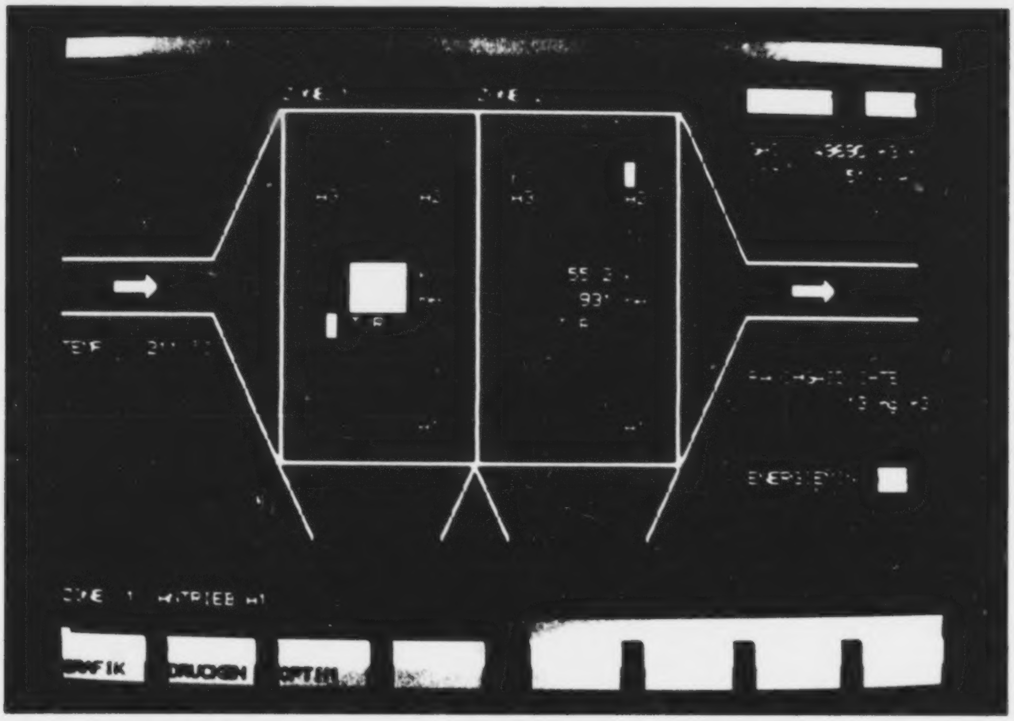

Figure 7. Monitor Display of Overall Precipitator

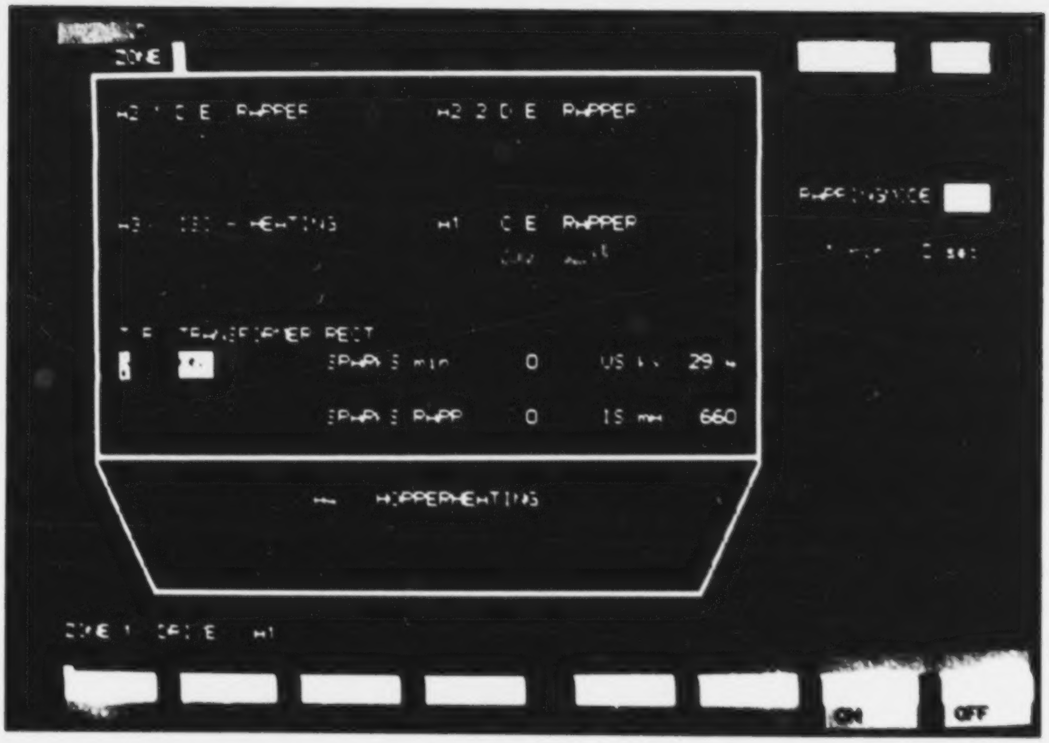

Figure 8. Monitor Display of One Precipitator Bus Section

PROCESS OPTIMIZATION

In addition to process control, the other basic advantage of the master automated process computer is process optimization.

Rapping optimization is important since the interval between rapping of the collecting electrodes influences the precipitator efficiency. If this rapping interval is too long, the dust deposit on the collecting electrodes might be so considerable, that the precipitator operation is impaired and the collection efficiency decreases. On the other hand, a too short rapping interval will, from experience, also lead to higher emissions.

The objective of rapping cycle optimization is to determine the best rapping cycle for each precipitator zone with the total dust emission from the precipitator being the lowest. This can be done by means of a complex mathematical function programmed into the automation system. This program takes various process variables into account which affect the required rapping cycle, such as boiler load.

The collection efficiency of electrostatic precipitators essentially depends on the amount of energy supplied. When the optimum precipitator efficiency is reached, additional energy consumption will not however lead to a further reduction of the clean gas dust content. The output signal from a smoke density measuring unit installed in a clean gas duct, as well as a corresponding programmed optimization strategy, serve to limit the energy consumption of the electrostatic precipitator to the extent necessary for optimum collection efficiency.

This optimization strategy is based on the availability of the corresponding precipitator current-voltage curves for each precipitator zone. An evaluation of this data by the computer makes it possible to control the current in the individual zones of the precipitator according to the dust emission. This results in a reduction of the precipitator currents combined with a better collection efficiency than called for and a corresponding reduction in energy.

This optimization strategy serves to reduce the entire energy consumption of the electrostatic precipitator by selectively reducing the current of individual T/R sets according to a pre-programmed plan.

Any interferences, such as failure of a transformer-rectifier set, load changes or rapping, etc., are, of course, taken into account. The energy savings resulting from this strategy have been confirmed by several tests.

For example, Fig. 10 shows results from the Bexbach Power Station in Germany. The top graph illustrates operation in the normal manner. The bottom graph illustrates the results after energy optimization has been implemented by the control. It can be noted that energy consumption was reduced 40% with no increase in emissions.

It should be emphasized that the cost savings will be far higher if the units in question are operated at partial load during nights, weekends, or other off-peak periods.

Results will vary from one installation to another. According to our experiences, gathered in Australia, West Germany, USA and elsewhere, energy savings of up to 90% can be achieved in this manner. With this kind of savings, the payback time of the process automation system will be a short one.

What other savings can be expected with the use of the process automation system? The installation costs will be much lower for the automation system than for conventional systems, since a large number of cables, switches, panel instruments, etc., can be dispensed with. Moreover, the user friendly design reduces the number of shift personnel required and thus labor costs.

a) WITHOUT ENERGY MINIMIZATION

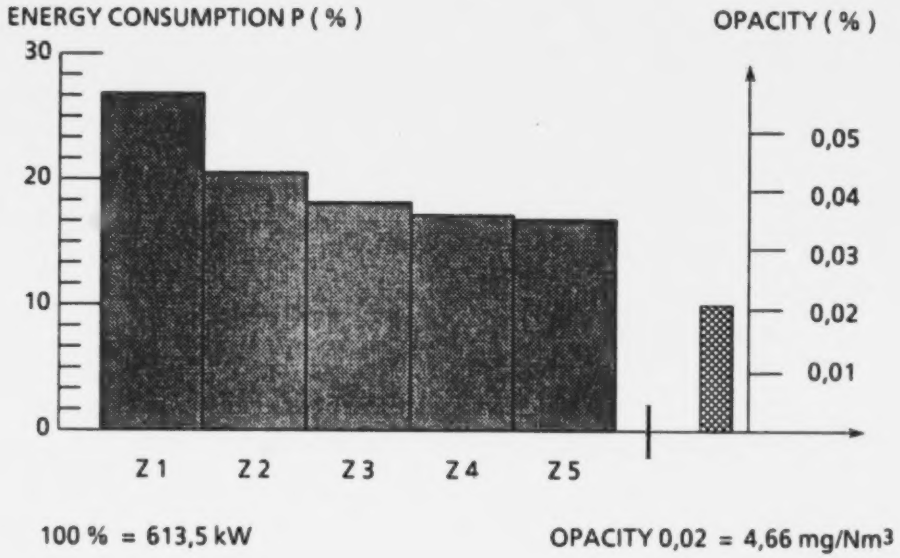

b) WITH ENERGY MINIMIZATION

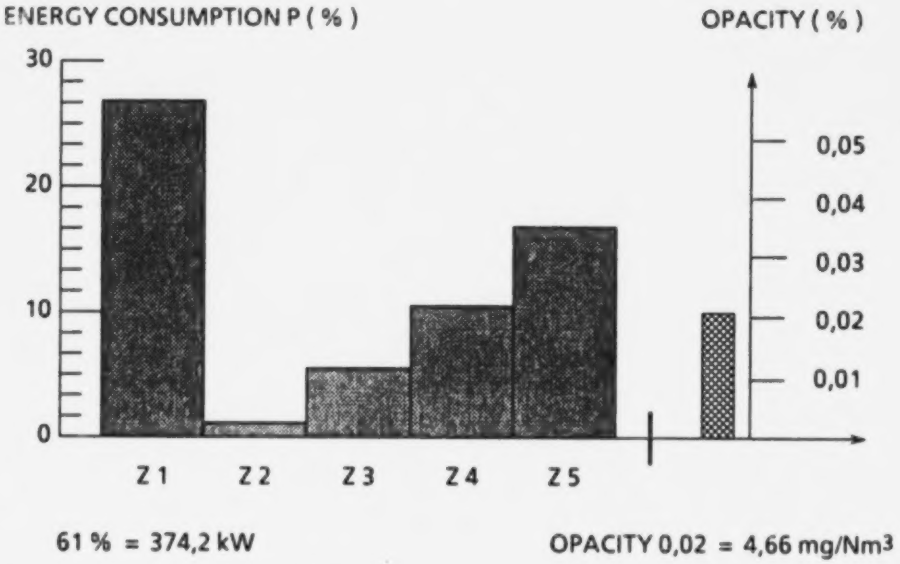

Figure 10. Energy Consumption of a Power Station ESP

AVAILABILITY

A final point on availability. In the event of a failure of one component, the star-type layout will prevent a breakdown of the entire system. Each component can continue operation independently. After a main power failure, the components will automatically restart and continue operation once the voltage has returned.

CONCLUSION

Finally, we can say that a useful process automation system now exists, which provides useful advantages to operators of small, as well as large, electrostatic precipitator installations.

The work described in this paper was not funded by the U.S. Environmental Protection Agency and therefore the contents do not necessarily reflect the views of the Agency and no official endorsement should be inferred.

A TOTAL ENERGY MANAGEMENT SYSTEM FOR ELECTROSTATIC PRECIPITATORS

by: Sanford F. Weinmann, P.E.
Lodge-Cottrell Operations
Dresser Industries, Inc.
Houston, Texas

Dr. Anthony Russell-Jones
Lodge-Cottrell Ltd.
Division of Dresser U.K. Ltd.
Birmingham, England

ABSTRACT

Until relatively recent times the sources of coal for a power plant were generally close to the plant, and almost certainly within the same country. The availability of lower cost coals from world markets, coupled with escalating alternative fuel costs, has changed this situation.

Electrostatic precipitators in many cases must be designed to cope with ash from a wide variety of coal types. If the precipitators are designed to provide a specific emission for the worst of the fuels fired, in terms of their ash precipitation characteristics, then when less demanding ashes are to be caught, the plant will behave as though it were over-specified. In these circumstances, required emission levels can be achieved with less than maximum power. It is in a situation such as this that a Total Energy Management System (T.E.M.S.) is essential.

The T.E.M.S. described here comprises intelligent remote terminal units (RTU's) in the form of automatic voltage controllers linked to a supervisory control and data acquisition (SCADA) computer. The latter can be optionally linked into the boiler plant's main computer network, or stand alone, to provide and derive useful information concerning plant operation. Precipitator power consumption is optimized and, provided the necessary signals can be obtained, T.E.M.S. can optimize a variety of operational parameters for the precipitator. Collecting electrode rapping sequences are also programmable to ensure minimized rapping re-entrainment should any field become de-energized. The system is designed for new plant or retrofit applications, and operating experience on power plants is presented.

The work described in this paper is not funded by the U.S. Environmental Protection Agency and therefore the Contents do not necessarily reflect the views of the Agency and no official endorsement should be inferred.

'ODGE COTTRELL'S - TOTAL ENERGY MANAGEMENT SYSTEM

I. Introduction

Lodge-Cottrell has designed and successfully implemented the **Total Energy Management System** (TEMS). **TEMS** is a master level supervisory control and data acquisition (SCADA) computer system. The **TEMS** computer acts as a second level control system for Lodge-Cottrell's **Series IV^{TM} AVC, AVC III,** and older **analog AVC** units (supplied by L-C and others). Figure 1 shows a block diagram of the system.

Many precipitators installed in U.S. power generating facilities have been designed for a variety of coals with varying amounts of redundancy to ensure environmental standards are met at all times. When burning coals with easily precipitated dust, or when the boiler is operating at less than 100% load, excess precipitation capacity is available. Under such conditions, required emission levels can often be met at less than maximum power.

Lodge-Cottrell engineers have run a number of comprehensive stack opacity versus power consumption tests. The data from these tests verifies that power consumption can be substantially reduced while still maintaining specified emission levels. For example, one year's data for power versus opacity is presented in Figure 2 for a coal-fired boiler in the Northeast U.S. With these test results in mind, Lodge-Cottrell can offer an opportunity to match precipitator power consumption with dust and boiler characteristics. In all, three different control algorithms have been installed and tested at various plants in the U.S. as well as in England. The algorithms include: 1) a set point control system, 2) a system referred to as Pulse Modulation^{TM}, and 3) a critical point control system. In each of these systems the **Total Energy Management System** automatically controls T/R set power levels using a feedback signal from the station stack opacity monitor.

This paper will attempt to focus on the energy saving results from the three different algorithms, as well as describe the advantages of each application. Additionally this paper will highlight many of the features of the **TEMS** product which approach the artificial intelligence aspects of the operator-machine interface software.

II. Energy Management Scheme 1 - The Set Point System (See Figure 3)

The **set point** control system for energy management requires that the operator enter a target set point for the opacity level. The target is generally determined by observing plant operation over a period of time and determining typical opacity levels at full boiler load. The user adjusts the set point to the typical opacity level plus an offset (offset levels are generally in the range of 1 to 4 percent).

The user adjustable target is bounded by a dead band (high and low limits). When the opacity is found to be outside the dead band area (and inside alarm limits) the TEMS computer automatically alters the energy levels to each automatic voltage controller. The amount of alteration (increasing or decreasing energy) is determined by the error between the current opacity signal and the set point. The correction factor applied to the AVC is "gained" via an adjustable multiplier (set by the operator). The controller action can be characterized as a **set point controller with gain and reset.**

The power adjustment to each T/R is made by means of secondary voltage regulation. Each T/R is manipulated in such a manner as to limit the secondary voltage within an operator defined range. The TEMS computer allows the user to set a maximum and minimum kV associated with each T/R set. The TEMS computer sends (via serial data link) the new maximum kV value to the appropriate AVC (or group of AVC's) each time a power step (increment or decrement) is required. Once a maximum or minimum kV level is met, TEMS will not attempt to exceed the limit.

The set point system is bounded by alarm limits (high and low opacity level alarms) which force the algorithm to return AVC's to the full power mode of operation if a problem is detected. The high end limit is based on a six minute average of the opacity signal. The high limit is always set at a point well below the predescribed limits of State, Federal, and Local EPA regulations.

The **set point** algorithm has been installed in many locations and has been proven to be effective in terms of a power savings tool at each of the sites in question. An example of this application may be found at a Midwestern coal fired, 550 MW station. The **TEMS** product applied at this location uses Lodge-Cottrell's analog controller as a base to control energy consumption. The precipitator at this location is a five field two box unit. There are four electrical bus sections per field. In all 40 T/R sets are used.

In August of 1985, and again in August of 1986, the **TEMS** product's energy savings abilities were tested at this location. These tests were run without adjustment to the existing AVC's, such as to bias the results. The results of these tests showed that the average power consumption of the precipitator could be lowered on an average of 450 kW (normally the 40 T/R's consumed 1,050 kW). This result is based upon boiler operation which cycled in each 24 hour period; highest loads were observed during the "business day", lower loads were in the evening and early morning hours.

Figure 4 shows the cyclic power consumption of the precipitator with and without the TEMS set point power control system in operation.

Note that the average power saving demonstrated is 450 kW. Figure 5 is a scatter diagram of opacity vs precipitator power consumption. This graphic provides a key piece of information. That is, the savings generated with the system were achieved with only a 3% average rise in stack opacity.

Figure 6 shows precipitator power consumption vs boiler load with and without the TEMS product in operation. It is important to note that the average power savings at low boiler loads is up to 70% (720 kW was saved at a boiler load of 360 MW) of normal consumption (1050 kW). At higher loads the average power savings was reduced to a level in the range of 400 kW.

The slope of the power consumption vs boiler load curve line with TEMS is reversed from that of the system running without the system. That is, that with the set point system running the precipitator requires less power at lower boiler loads and more power at higher boiler loads. Without the addition of the set point system more precipitator power is consumed at lower boiler loads, and less power is consumed at higher loads. By altering this basic relationship with the addition of the TEMS the efficiency of the precipitator's usage of power is greatly enhanced.

The payback of this system based upon fuel costs alone, is approximately $96,000 per year[1].

III. Energy Management Scheme 2 - Pulse Modulation^{TM}

The second method of energy management is **Pulse Modulation**. This algorithm is executed via the TEMS - AVC interface via the manual or automatic modes of operation. The stack opacity meter is normally used to provide feedback to the system to automatically regulate the **Pulse Modulation** settings for each AVC. Testing has been carried out on this system at the Central Electric Generating Board's (U.K.) West Burton Station (Unit #3). The unit under test utilizes four precipitators.

During testing gas volume ranged from 383,000 to 424,000 ACFM (180.6 - 200 AM^3/sec). Both boiler load and exit gas temperatures remained constant. Specific power readings were taken from kilowatt hour meters installed in the main feed to the rectifier sets.

Pulse Modulation was used at settings ranging between one of two pulses energized to one in six pulses energized. The graph in Figure 7 was generated as a result. The data indicates that at full power 47.4 kW per precipitator (255 kW/m^3/sec), the station achieved efficiencies in the range of 98.85%. With **Pulse Modulation** in use the plant could save as much as 29.7 kW (155 kW/m^3/sec) per precipitator and remain within local environmental guidelines.

The resultant power savings were in the range of 63% as the result of Pulse Modulation. The total savings across the four precipitators amounts to 118.8 kW. Based upon fuel costs the calculated payback associated with the system is approximately $20,000 per year.

---

[1] Payback is based upon fuel cost of $0.21 per kWH. It is assumed that the plant is operational 90% of the year.

IV. The Critical Point Control (CPC) Algorithm

The third power savings algorithm is called **Critical Point Control**™, or **CPC**. **CPC** regulates T/R power consumption based on stack opacity. However, it is not a set point system. The critical point is defined as the point on the opacity - power curve at which opacity rises due to a decrease in precipitator power input (Figure 8). **TEMS** automatically searches for the critical point. Searches can be initiated following boiler load changes, or operator initiation (Figure 9). When the critical point is detected, **TEMS** will increase power to selected T/R's until the stack opacity decreases to its original baseline. As a result of this algorithm the power which is saved is the power which has a minimum effect on opacity and efficiency levels.

When the CPC is inactive power levels are at 100%. Once the routine is activated the supervisor will reduce power to the AVC's in the order prescribed by the operator. The TEMS unit reduces power to the first through Nth group sequentially. Groups of AVC's are defined through operator input, and may be arranged in any fashion. Power is reduced first using Pulse Modulation (PM); the cutting out of a percentage of line cycles passed through each AVC's SCR pair, and then by reducing the maximum T/R secondary voltage by the use of each AVC's "MAXKV" parameter (see table 1).

After each power reduction step to a group of AVC's, the supervisor continues to monitor the opacity signal. If the opacity is seen to rise by more than the amount of the SLOPE parameter, the supervisor determines that a critical point has been located. If a CRITICAL POINT is located the supervisor reverses direction and increases power to the AVC's (in reverse order) for one step, and holds that power level. The Supervisor waits the prescribed period of time (dead time) between controller action.

Each time power is reduced to all units in a group, the opacity signal is examined to determine if a CRITICAL POINT has been located. If the CRITICAL POINT is found (or the routine is shut off) power is increased to the group under control in the reverse order from which it was decreased for one step only.

Once the opacity level stabilizes the supervisor will hold power level constant until;

1. The CRITICAL POINT CONTROLLER is shut off. When this occurs the CPC automatically restores 100% power levels to all AVC's.

2. The Opacity is seen to increase by the CRITICAL amount. When this event occurs, the CPC will increase power levels to the AVC's in reverse group order until the opacity is seen to fall to its original base level.

3. The Opacity is seen to decrease. When this event occurs the CPC will again begin reducing power and search for a new CRITICAL POINT.

The Critical Point Control algorithm has been purchased for application at two 850 MW boilers in the southeastern U.S. As of this date one of those control systems is being commissioned; the second unit will be commissioned circa July 1988. Testing on this system is due to take place in the near future. At this time no specific data is available. Based upon manual operation of the AVC units in a fashion which emulates the Critical Point Control algorithm, an approximate 40 percent of power was saved at a 720 MW (boiler) load.

Further testing on this system will be done in coming months.

V. Man - Machine Interface Features

In addition to the power savings opportunity, **TEMS** makes the man to machine (AVC) interface a much more tolerable task. Larger precipitators require numerous T/R control units. The sheer number of T/R sets makes it difficult to gather operational data and status information. **TEMS** provides a central operations console for the operator to determine the status of each AVC (off, manual, auto, etc.) as well as the data being returned from each T/R (volts, amps, mA, kV, and KW). The real time opacity is also displayed on a separate graphic along with the six minute average opacity figures for a one hour period.

Historical data is retained on disk. This "trends" data package includes: six minute, one hour, eight hour, and 24 hour averages and deviation figures for each T/R (volts, amps, kV, mA, and kW) as well as opacity, and total T/R power consumption. These data items are filed on the system's hard disk, and some files are retained for as long as 31 days. The analog data which is gathered may be printed upon demand.

The system menu also provides options for V-I curve generation, alarm logging (up to 3600 alarm occurrences are stored on disk and are available for review on demand) and a functional test of AVC-TEMS communication links. Alarms will include those normally associated with the T/R (low kV, current limit, etc).

The net effect of the features described above is that the operator will spend far less time logging precipitator data. The operator will be better informed of precipitator operation as a result of having instantaneous feedback instead of having to wait until the controls are inspected every four hours. Although not included in the payback figures mentioned earlier in this text, the data gathering and operator interface functions of the T.E.M.S. have an economic value. The dollar amount associated with this feature is difficult to assess. If, however, the operator can stay better informed as a result of the system's many capabilities, then perhaps problems can be solved when they are minor; real economic savings can amount to much larger numbers than mentioned in prior examples.

In summary, TEMS performs two very essential functions. First, the system provides the user with the opportunity to trim power consumption with regard to air pollution control. Second, it provides the needed function of a centralized data acquisition, display, and control device.

TEMS is based upon Digital Equipment's LSI 11/53 processor. The LSI 11/53 can support 128 AVC/TEMS interfaces, two independently functional color terminals, eight channels of analog data acquisition, a high speed printer and telephone modem (to Lodge-Cottrell's Houston based facility). Also included is a 16 channel analog-to-digital convertor module used to acquire analog signals such as opacity.

The operating system used in the Micro 11/53 is Digital Equipment's Micro RSX 11M+ (RSX stands for resource sharing executive). This operating system is a real time, multi-tasking, multi-user system which is capable of executing several tasks at one time. The primary advantage of this type of operating system and what sets it apart from personal computer type operating systems is that it can execute such functions as report generation and opacity monitoring and AVC control execution simultaneously. This operating system provides the flexibility needed to acquire data from the AVC's as well as report, trend, and execute control commands for the operator's ease. As a result operator interface does not "hog" the machine's resources, nor does any other background machine function. Instead all tasks are executed on a "share" basis giving equal time to important tasks. This is a distinct advantage in the precipitator control systems environment.

Data is clearly displayed on an a 19" high resolution graphics terminal. TEMS software is written such that the operator needs to do minimal typing. The menu driven software requires that the operator use primarily the cursor control (arrow) and select keys to view different pages of data as well as generate typed reports. The terminal has a built in audible alarm which alerts control room personnel when a problem arises within the precipitator's realm.

A 212A compatible (1200 baud) modem is also provided. The modem allows for remote access (by telephone) of the 11/53. This link is protected by password and account numbers for external security. The modem link can be used by Lodge-Cottrell personnel (at the request of Plant personnel) to assist with set-up or debugging of software on a timely basis. The cost of such assistance is greatly reduced since travel is not required.

A summary of the capabilities included in TEMS includes:

1. Acquisition and Display of:
    - Primary and secondary T/R signals value
    - Automatic voltage controller status and alarms
    - Stack opacity signals
2. Pertinent data items are graphed, printed, or displayed as follows:
    - opacity vs time
    - T/R power vs time
    - total precipitator power (128 T/R's) vs time
    - opacity and total power vs time
3. Stored data files include opacity, T/R signals, and power in the following format;
    - ten, 6 minute averages and deviations
    - eight, 1 hour averages and deviations
    - three, 8 hour averages and deviations
    - thirty, 24 hour averages and deviations

This data is stored on the system's hard disk, in formatted fashion for the purpose of generating reports.

4. Stored data files for events such as alarms, T/R control status changes, etc., are stored in an "event logger" file capable of holding 3600 discrete events. This file is stored on the system's hard disk for the purpose of generating reports. Hard copy reports include:

    - AVC alarms (tagged with time and date)
    - Opacity exception limit (EPA 6 min avg exceeded).
    - AVC or Supervisor mode changes (e.g., opacity control on or off tagged with time and date)

5. The RSX-11M+ operating system does not permit unauthorized personnel to gain access to programming source code. An account number and password are required. These items are made available to authorized personnel only.

6. TEMS executes energy management control. The controller uses the Critical Point Control™ algorithm, or any of the other algorithms described within the scope of this paper to save power.

7. The color CRT displays either kV, mA, volt, amp, or kW information for all T/R's on a single screen (the global display). An individual T/R data monitor and display are provided as well. The individual display contains options for command of the T/R (auto, manual, off, etc.) mimicking control functions available at the T/R's control cabinet.

8. The keyboard allows the operator to start and stop opacity control, place all T/R's off, in auto, in manual or startup from a single function key.

9. Acquisition and display of V-I curve data. V-I curve data is stored on the system hard disk.

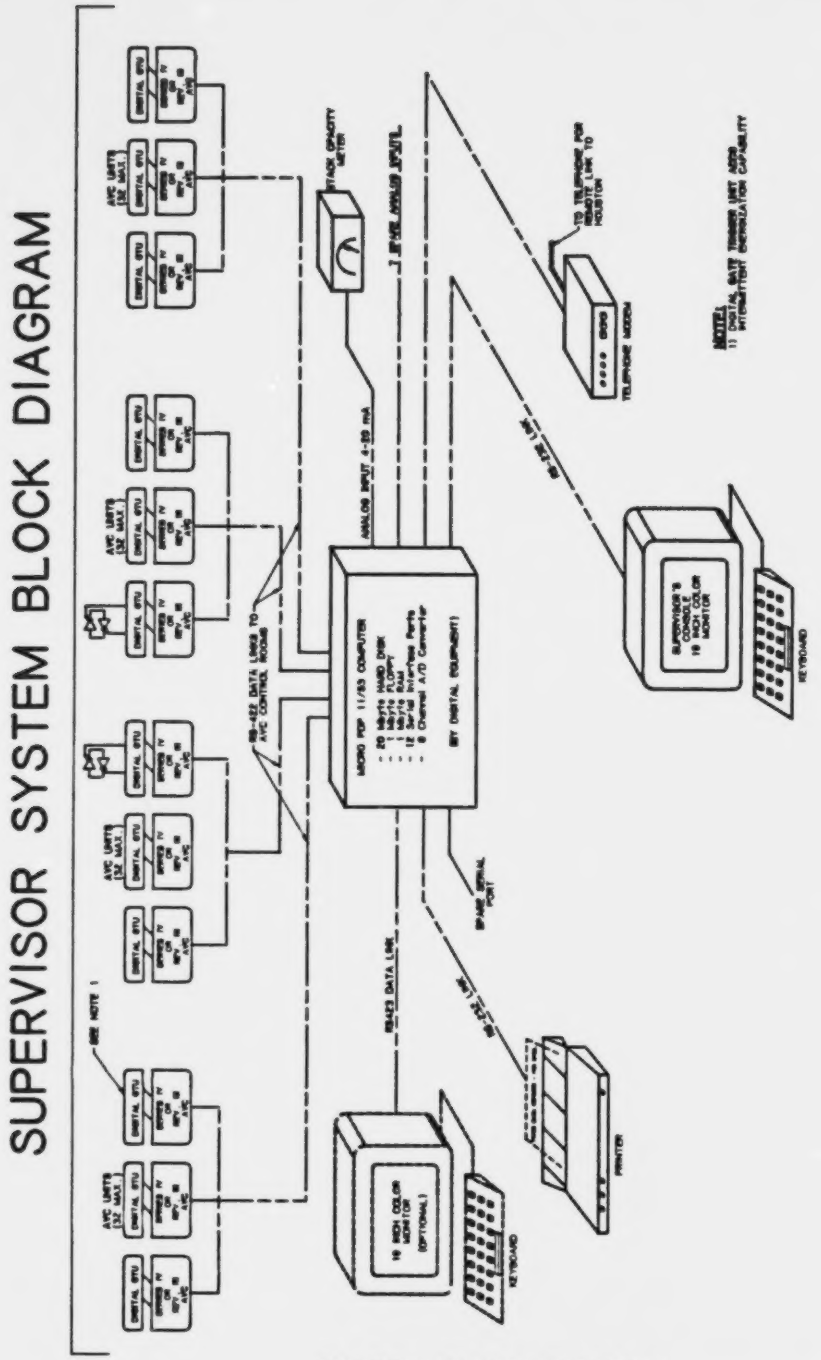
SUPERVISOR SYSTEM BLOCK DIAGRAM
AVC UNITS (32 MAX.)
SEE NOTE 1
DIGITAL GTU
SERIES IV OR REV. III AVC
RS-422 DATA LINKS TO AVC CONTROL ROOMS
MICRO PDP 11/53 COMPUTER
- 20 Mbyte HARD DISK
- 1 Mbyte FLOPPY
- 1 Mbyte RAM
- 12 Serial Interface Ports
- 8 Channel A/D Converter
(BY DIGITAL EQUIPMENT)
ANALOG INPUT 4-20 mA
STACK OPACITY METER
7 SPARE ANALOG INPUTS
RS423 DATA LINK
19 INCH COLOR MONITOR (OPTIONAL)
KEYBOARD
RS-232 LINK
SPARE SERIAL PORT
PRINTER
RS-232 LINK
SUPERVISOR'S CONSOLE 19 INCH COLOR MONITOR
KEYBOARD
TELEPHONE MODEM
TO TELEPHONE FOR REMOTE LINK TO HOUSTON
NOTE:
1) DIGITAL GATE TRIGGER UNIT ADDS INTERMITTENT ENERGIZATION CAPABILITY

SYSTEM BLOCK DIAGRAM

Figure 1

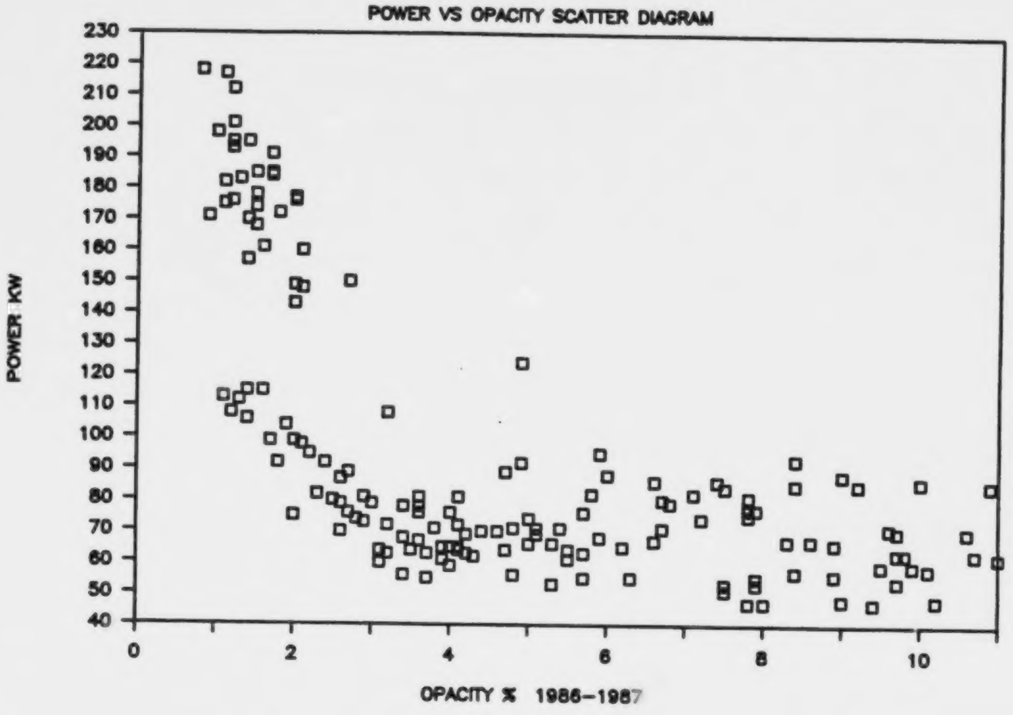

Figure 2

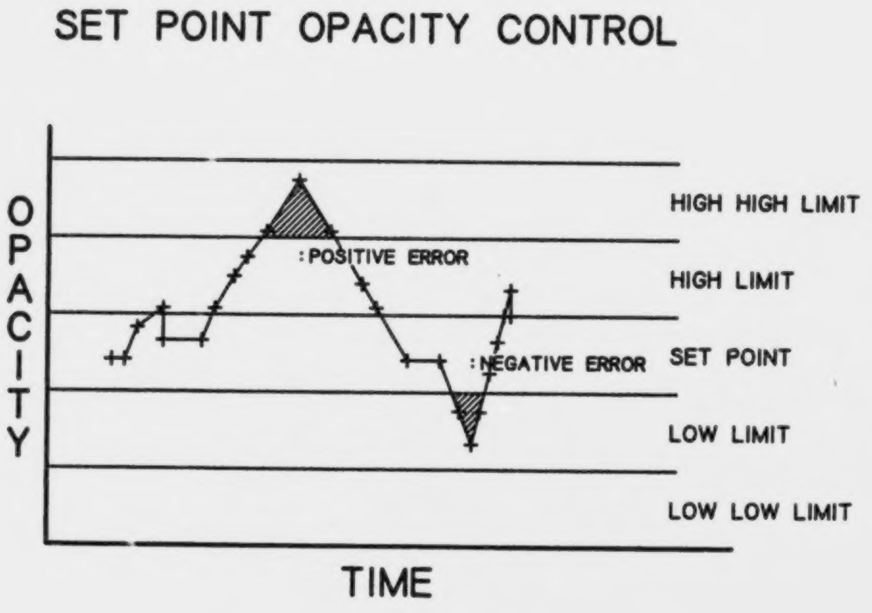

TIME vs OPACITY
Figure 3

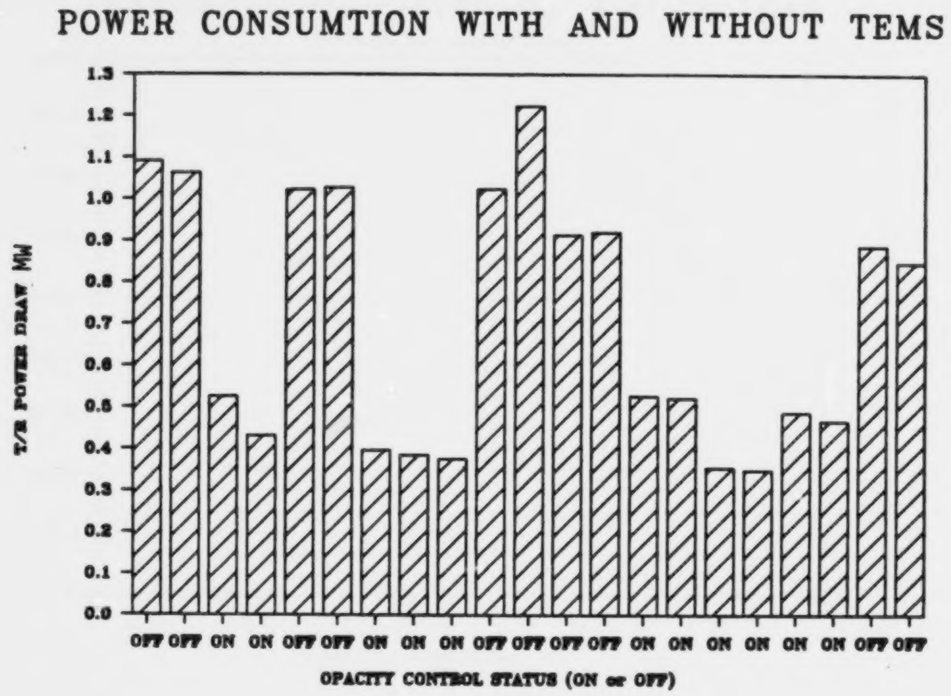

Figure 4

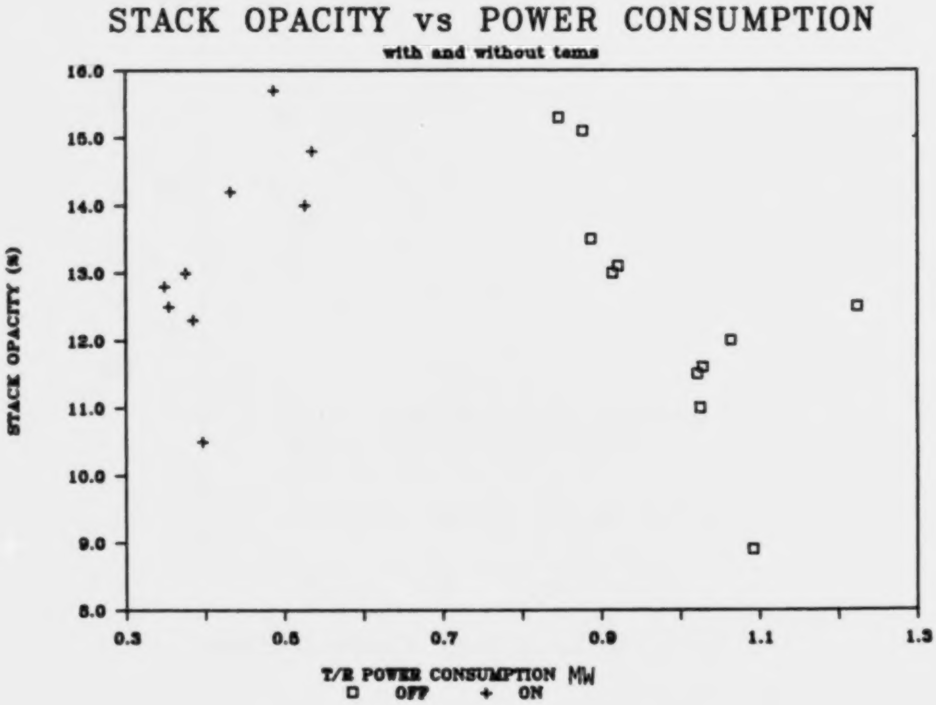

Figure 5

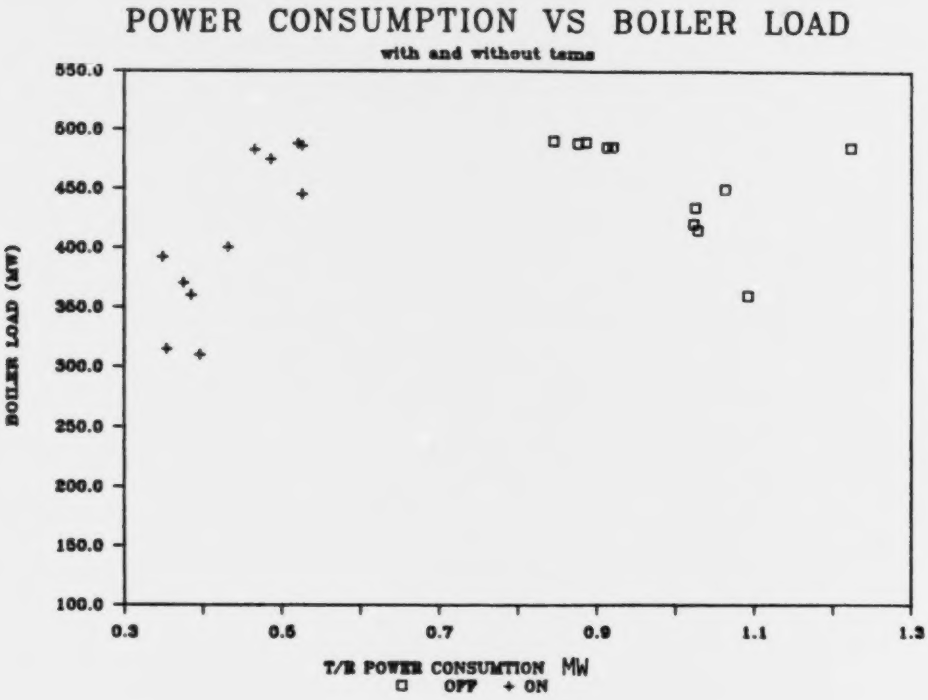

Figure 6

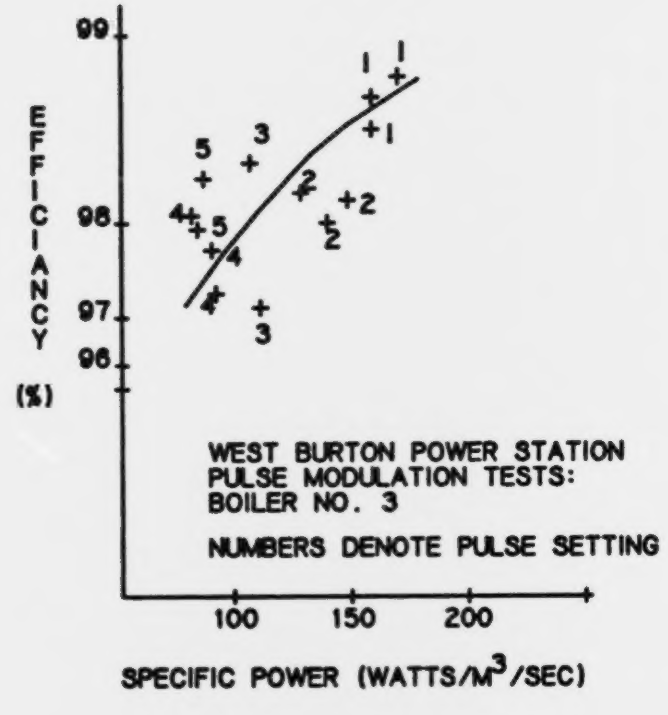

Figure 7

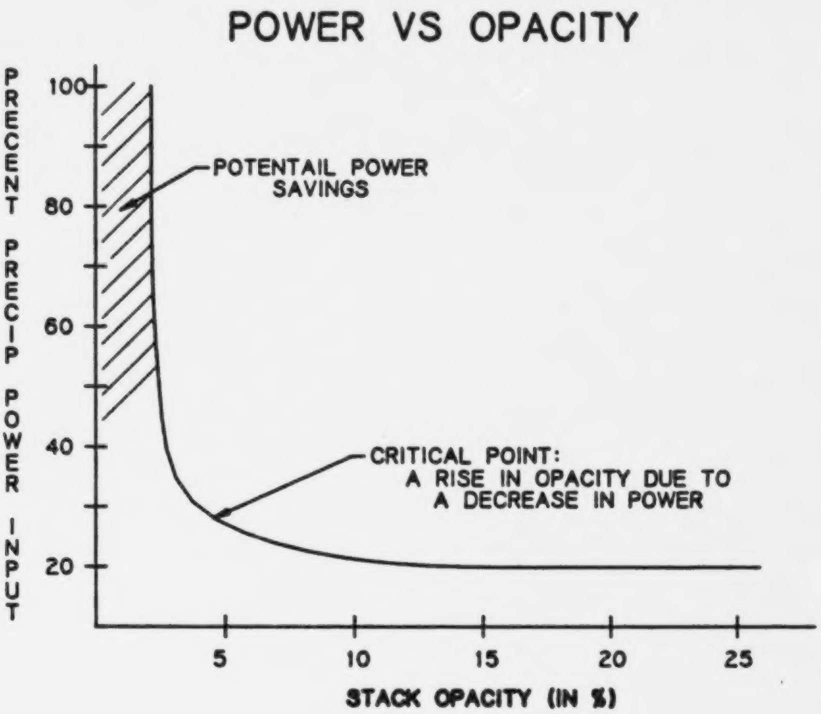

Figure 8

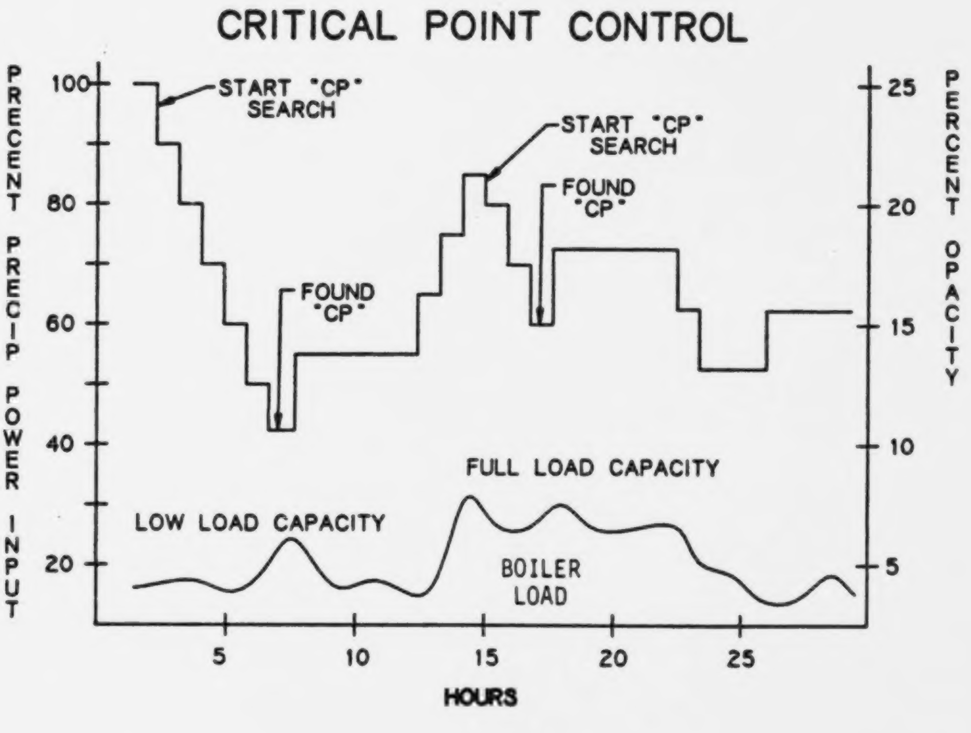

Figure 9

TABLE 1.

CRITICAL POINT CONTROL POWER REDUCTION STEPS

CONTROL STEP #	ACTION
1	Apply PM of 10% to all units in group
2	Apply PM of 20% to all units in group
3	Apply PM of 30% to all units in group
4	Apply PM of 40% to all units in group
5	Apply PM of 50% to all units in group
6	Apply PM of 60% to all units in group
7	Apply PM of 70% to all units in group
8	Reduce MAXKV parameter by 2.0 kV in all units
9-Nth	Repeat step 8 until MAXKV = MKV parameter stored on supervisor disk file.

EXPERT SYSTEMS - OPERATOR ADVISORS FOR PARTICULATE CONTROL EQUIPMENT

By: John G. Musgrove & Peter N. Di Domenico
Bechtel Western Power Company
Houston, Texas 77056

ABSTRACT

Electric utilities are using expert systems technologies for operator advisors in the diagnosis of rotating equipment maintenance problems. Particular attention has been focused on turbine generator maintenance. A brief discussion of expert systems is provided as an introduction to this presentation.

Applications for operations and maintenance advisors for air pollution control systems will be considered within the next few years. A discussion of the potential benefits to accrue to particulate control systems upon the incorporation of expert systems is presented. The kinds of operations advice and equipment alarms for baghouses and electrostatic precipitators will be presented. Approaches to implementation and incorporation of expert systems in air pollution control systems are discussed. Sample rules and their application to operator advisory systems will be given to enhance understanding of the advantages of applying expert system technologies to air pollution control systems.

THE RECENT HISTORY OF CONTROL SYSTEMS

The evolution of control systems for particulate control equipment has accelerated due to the availability of inexpensive integrated circuits and microcomputers. This presentation will begin with a brief history of recent advances in the control systems for baghouses and electrostatic precipitators in the electric utility industry before discussing the next step in control system improvements, the incorporation of expert systems. It will conclude with a suggestion about how control systems will be in the next decade.

In the early 1970's electrostatic precipitator control systems were manually set and adjusted based on a 'spark rate'(1). Similarly, baghouse operating parameters were observed and controlled manually. Toward the end of that decade the incorporation of electronic circuits permitted sophisticated electronic automatic voltage controllers (AVC) to be designed (2). Baghouse controls became more automated and reverse-gas cleaning sequences could be set to initiate either on high system delta P or on a preset time interval (3,4). Operator alarms could be set to initiate upon failure of the control system to maintain stable, compliant operation. Nonetheless, manual observations and recording of many of the operating parameters were still required (5). The only remote capability was the forwarding of a 'precipitator trouble' alarm contact to a local operator control room (3).

In the early 1980's, integrated circuits replaced circuit boards full of individual components. Replacement of precipitator AVCs and rapper control systems with more electronically advanced ones became an accepted method of improving precipitator performance (6,7,8,9). Equipment manufacturers and after-market manufacturers sold improved control systems to assist operators in returning their pollution control equipment to design performance. The next step in control system sophistication was the addition of centralized data logging systems. These systems permitted automatic recording and storage of operating data as well as the remote control of AVC operations from a single computer terminal or workstation (10,11,12,13,14,15).

All these improvements have greatly simplified the operators' job, permitting him to observe and change individual AVC parameters from a central control point and eliminating his function as a data recorder.

A primary advantage of the current supervisory controllers with their data logging functions is their ability to provide operating data for an expert to evaluate following a major emissions control upset or failure. Unfortunately, a particulate control domain expert is still required to review and examine what will now be volumes of data in order to detect and determine the cause of the failure. The benefit of an expert system in the control system can be described thus:

> "This sort of self-initiating system will help us identify problems while they can be easily fixed, rather than just making it easier to clean up after disasters".

Can expert systems be useful to electric utilities? I believe so. Last May, 138 utility personnel attended a 3-day program, "Seminar: Expert Systems Applications in Power Plants" (17). Seventy-six presentations were made by representatives of twenty-three utilities.

Ninety attendees were consulting engineers and computer specialists, and forty-three represented vendors of expert system hardware and software.

The remainder of this presentation will focus on the next level of improvement to be made in air pollution control systems, the incorporation of knowledge-based expert systems.

---

1. Chapman and Yeager, p.40. (Reference 16)

EXPERT SYSTEMS

WHAT THEY ARE

What, then, is an expert system? It is one of the currently active areas of commercialization of artificial intelligence (AI), Figure 1 (18).

What then is artificial intelligence?

> "Artificial intelligence is an attempt to program computers to perform tasks, which when they are performed by people are considered to be intelligent behavior - playing checkers, chess, backgammon, understanding sentences, finding mineral deposits, configuring a computer system, diagnosing diseases, and so on".

An expert system, therefore, can also be described as "a computer program using expert knowledge to attain high levels of performance in a narrow problem area." The importance of this is that "artificial intelligence programming focuses on verbal and graphic aspects of knowledge rather than mathematical aspects." To further appreciate this difference one must understand how these differences are implemented, Figure 2 (18).

WHAT THEY DO

With the advent of AI programming one now speaks of symbolic programming, and the separation of the knowledge, in a knowledge base, from the control structure, the inference engine. "This separation of knowledge from inference control is probably the most important concept to come out of AI research." It also permits the inference engine to be easily applied to different knowledge bases with equal success.

Expert systems are also providing new software tools that permit programming at the knowledge level, rapid system prototyping and iterative refinement of the program rather than programming to a specification. The new tools provide a powerful development environment with graphics, editors and debuggers. Object oriented programming environments exist. Explanation facilities can easily be built in to explain to a user how conclusions are being reached and thus justify an expert system's decisions at any point in the consultations. The programs can also deal with conflicting or incomplete data and can easily accept changes in variable values without having to re-execute the entire program, a 'what if' analysis for values of variables.

The simplest form of knowledge bases are found in rule-based systems, a collection of rules about elements of knowledge. Rules are syntactical expressions of the form: If A is True and B is True then C is True. But the significant difference is in the programming language. In algorithmic programs, such as BASIC, FORTRAN or dBASE III, a rule might be expressed as in Equation 1:

---

1. Chapnick, p 5.

2. Waterman, p 11.

3. Harmon, p 11.

4. Ibid, p 8.

```
If A = 100 .and. B = 35
Then C = 40
Else E = 65                                                 (1)
```

Even the well-known program Lotus 1-2-3 (21) permits similar information rules to be expressed, as in Equation 2:

```
@If(A5="Baghouse",B64*H11^2,G65*A12)                        (2)
```

Version 2.01 of that program even permits character string manipulation in its if-then statements. What symbolic programming has permitted is the use of character strings to be the symbols of the objects being addressed. A simple rule in VP-Expert, (22) an inexpensive expert system shell, could be expressed as in Equation 3:

```
If delta_P >= 0 AND
   mode = reverse_air_cleaning AND
   reverse_air_valve = open AND
   reverse_air_fan = on
Then valve_switch_operator = failed OR
   reverse_air_fan = failed                                 (3)
```

The difference is that variables are described by the objects for which they stand. More advanced programming environments permit programming knowledge frames that express information in forms that permit inheritance of data and information from 'parents' to 'children'. The classes have inheritance structures that greatly simplify data passing among the subobjects being represented.

WHY THEY ARE BETTER

The really significant aspect of expert system inference and control is that the program itself determines what is needed to be known to reach a goal. The program, not the programmer, then endeavors to get the necessary knowledge through searches of the knowledge base and questions to the user.

An expert system can also infer new facts from information it obtains during consultation with the user. If there exist rules such as Equations 4 and 5:

```
If A is True AND
   B is True
Then C is True                                              (4)
```

and

```
If C is True AND
   D is True
Then E is True                                              (5)
```

and if the goal is to determine if E is True, and if A and D are already known to be true, the program itself, through a process known as backward chaining, queries the user about the truth of B. If the user responds that B is True, the program 'knows' that C is True and therefore infers that E is also True.

Another important capability is that of explanation during a consultation. The user can, at any point in the consultation, ask the expert system why it is soliciting some specific information or how the system reached an intermediate conclusion. These features are very difficult, if not impossible, to implement in an algorithmic program.

Also, the user can ask 'what if A is not true' and the expert system will re-evaluate by a process known as recursion, the knowledge currently known, and seek to reach its goal by new or alternate means. More so than Lotus 1-2-3, expert systems permit the user to perform variable analysis with 'what if' statements without having to re-execute the entire program to establish a goal. The completion of a consultation does not result in the loss of variable values; they are retained for additional consultation if desired.

BENEFITS OF EXPERT SYSTEMS

GENERALIZED BENEFITS

With this brief introduction to expert systems and the potential benefits of symbolic programming, what is the benefit to plant operations? Quite simply, the transfer and utilization of expert knowledge from domain experts to control room operators. Expert systems can address the problems of variations in operators' skills and training by providing a consistent and continuous source of expertise. Expert systems can solicit an operator response by detecting a problem that could otherwise go unnoticed. They can monitor selected performance parameters on-line without regard to other demands being made of the human operators. They can help answer the important questions:

- What's Wrong - by identifying adverse trends leading to a failure;
- What's The Cause - by identifying probable causes and assessing probability of each, and by explaining the underlying reasoning of its decision;
- What To Do - by recommending operator actions to rectify the problem; and, advising success when the recommendation is carried out.

What are the advantages to operators of particulate control equipment? Table 1 presents seven advantages that can be addressed with these tools of artificial intelligence.

The real power and advantage of expert systems will be in conjunction with on-line process monitoring systems that will evaluate the data, in real time, as it is being recorded by the current generation of data logging supervisory controllers. The expert systems will conduct this evaluation in the background and issue low level or high level alarms as necessary. These expert systems will be embedded in the primary control system and be transparent to the user, monitoring the process data and advising the control operator as necessary to achieve the goals of low operating cost and high emission compliance. Individual expert control systems for particulate collectors and flue gas desulfurization systems may eventually be merged so that the optimum control will be achieved for the two devices together.

What will it cost to build these expert systems? The first ones, which may require some prototype developmental work in one expert system language and then delivery in a language compatible with the data logger, will be developed for approximately $250,000. Mature systems can then be added to existing control systems for less than $100,000 per installation.

ELECTROSTATIC PRECIPITATORS

Looking more closely, how might an expert system be applied to an electrostatic precipitator control system? From personal experience the following rule could prove valuable when too many AVCs are set in a manual control mode and the opacity limit is about to be exceeded:

```
If AVC_Sec_Volt < 70% AND
   AVC_Control = Manual AND
   Opacity > 18%
Then AVC_Control = Automatic OR
   AVC_Sec_Volt > 90%
```

The expert system would then advise the operator to increase manually controlled power to 90% or to switch to automatic operation. Similarly, a simple bit of knowledge regarding shutdown is to turn off the precipitator when the generating unit is off-line:

```
If Total_KV_Time # 0 AND
   Load_Time = 0
Then ESP_Control = Off
```

But an expert system could address more difficult problems which include: analyzing variations in control power among adjacent electrical sections in a field; detecting operation in back corona; detecting shorted electrical sections; analyzing opacity relationships to unit load and electrical power; and optimizing electrical load among all T/R sets. Maintenance procedures or recommendations, based on real-time data, could also be included in the expert control system. Suggestions for corrections for out-of-optimum performance could be included.

FABRIC FILTERS

How might such a program address fabric filter control? One important aspect of fabric filter startup is checking for bags with leaks or improper attachments. One case, which is depicted in Figure 3, (11) can be defined as "opacity drops significantly when a compartment is off-line for cleaning, then a bag leak in that compartment may be indicated". A procedure to perform this analysis was conducted manually on Intermountain Power Project Unit 1. A sample rule which could provide the same analysis might look like:

```
If Current_System_Delta_P < Prior_System_Delta_P AND
   Compartment_16 = Currently_Cleaning
Then Compartment_16 = Suspected_Bag_Failures
```

Another form of analysis is presented in Figure 4, (11). The trace of tubesheet delta P indicates that reverse-gas flow was initiated and that cleaning was effective. A sample rule to evaluate this situation and alarm if effective cleaning did not occur could be:

```
If Delta_P >= 0 AND
   Mode = Reverse_Air_Cleaning AND
   Reverse_Air_Valve = Open AND
   Reverse_Air_Fan = On
Then Valve_Operator_Switch = Failed OR
   Reverse_Air_Fan = Failed
```

For the simple case that greater numbers of compartments on-line should produce reduced system delta P, a rule for detecting an anomaly might be:

```
If Prior_Mode = Compartment_16_Cleaning AND
   Current_Mode = On AND
   Prior_System_Delta_P < Current_System_Delta_P
Then Check_Compartment_16_For_Leaking_Bags = True
```

FUTURE CONTROL SYSTEMS

What will the particulate control systems of the next decade look like? They will have embedded expert knowledge available to the operators continuously. Through incorporation of some of the other commercial aspects of artificial intelligence, Figure 1, they will have natural language capabilities and improved human interfaces that will allow an operator to ask the system questions in conversational syntax in English, Japanese, or other language specified by the customer. Their user-friendly interfaces will permit the operating staff to revise the knowledge base as necessary, customizing it for inclusion of knowledge unique to their own installation. As the aspects of speech synthesis and speech recognition improve and are commercialized the control systems will interact with operators with synthetic voices; alert operators by name, to anomalies in particulate control system operation; and state recommendations for correction just as some automobile manufacturers now use synthetic voices to alert drivers to fasten their seat belts or close a door that is ajar.

The work described in this paper was not funded by the U. S. Environmental Protection Agency and therefore the contents do not necessarily reflect the views of the Agency and no official endorsement should be inferred.

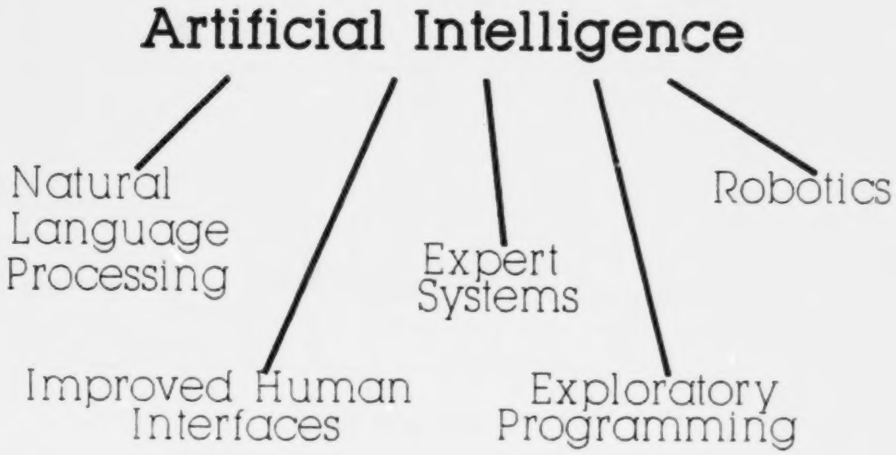

Figure 1. The Commercial Offspring of Artificial Intelligence

CONVENTIONAL PROGRAMMING	SYMBOLIC PROGRAMMING
Oriented toward numerical processing	Oriented toward symbolic processing
Numerically addressed data base	Symbolically structured knowledge base
Algorithms	Heuristics
Sequential, batch processing	Highly interactive processing
Mid-run explanation impossible	Mid-run explanation easy

Figure 2. Conventional vs Symbolic Programming

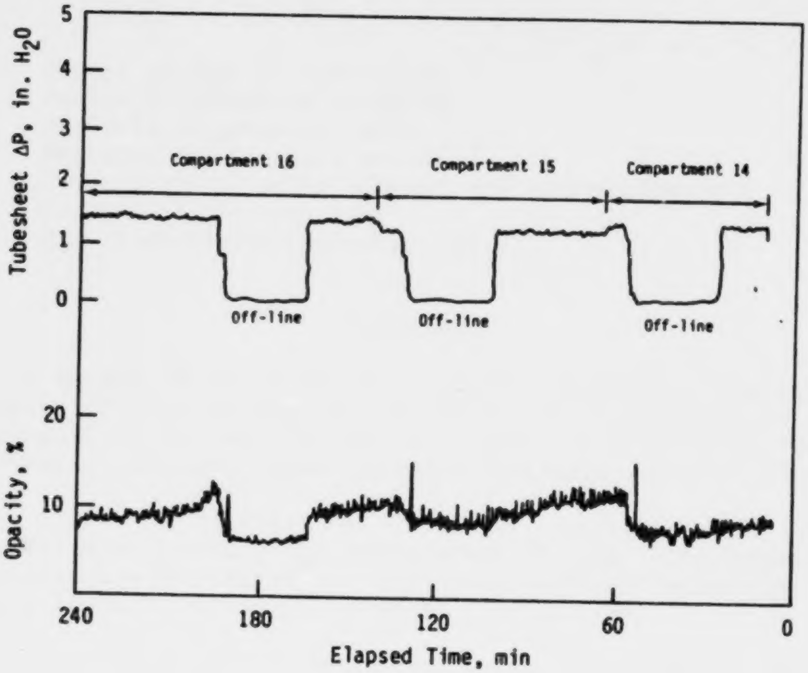

Figure 3. Strip Chart Tracing System Opacity and Tubesheet Pressure Drop for Three Compartments Over a 4-Hour Period

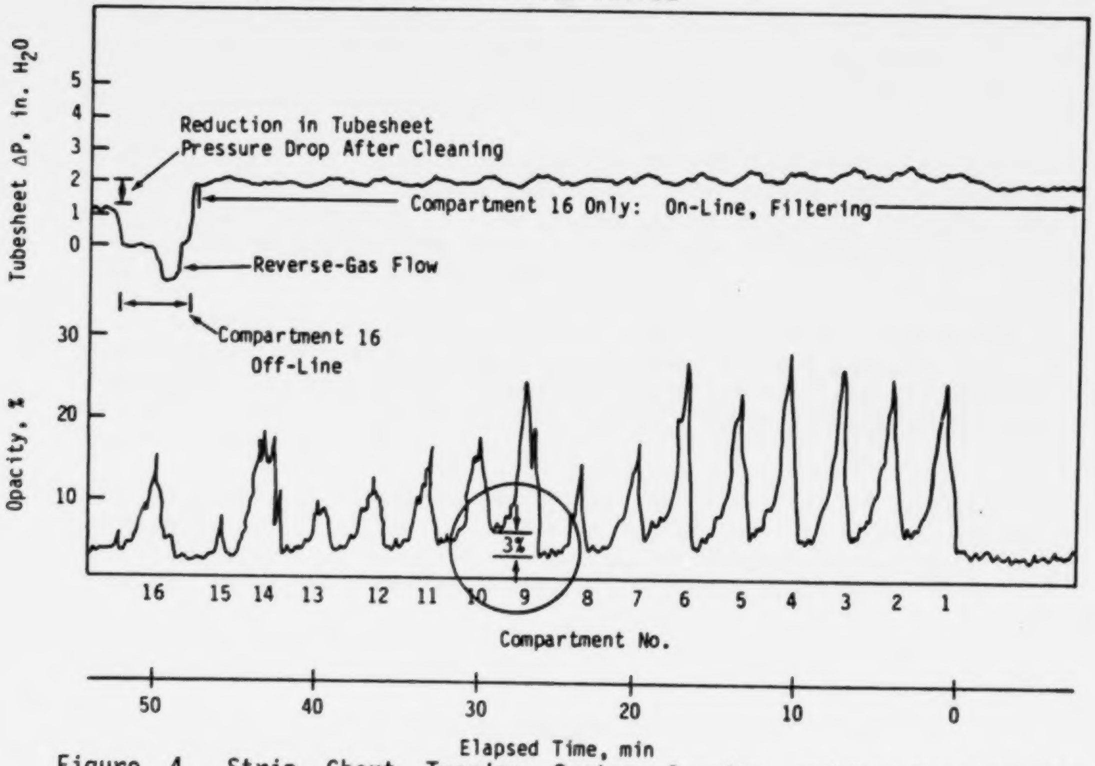

Figure 4. Strip Chart Tracing System Opacity and One Compartment's Tubesheet Pressure Drop Over a 55-Minute Period

TABLE 1 - EXPERT SYSTEM ADVANTAGES

Expert on-line 24 hours-a-day
Advice of operation anomalies
Analysis of graphical data
Messages about manual set points
Trend analysis among adjacent cells/compartments
Trend analysis with time
Reduction of startup/setup time

REFERENCES

1. K. J. McLean, et al. A New Microcomputer System and Strategy for the Control of Electrostatic Precipitators. In: Proceedings of the Third Symposium on the Transfer and Utilization of Particulate Control Technology. Electric Power Research Institute, Orlando, Florida, 1981.

2. N. Z. Shilling, R. Reese and J. Fackler. Impact of Intelligent Precipitator Controls. In: Proceedings of the Third Symposium on the Transfer and Utilization of Particulate Control Technology. Electric Power Research Institute, Orlando, Florida, 1981.

3. Kenneth S. Pope, et al. Design and Selection of the Air Quality Control System for Houston Lighting & Power Company's W. A. Parish Station - Unit 8. Paper presented at First Lignite Utilization Conference, Austin, Texas. February, 1980.

4. A. Reisinger and W. Theron Grubb. Fabric Evaluation Program at Coyote Unit #1 - Operating Results Update. Paper presented at Second Conference on Fabric Filter Technology for Coal-Fired Power Plants, Denver, Colorado. March 22-24, 1983.

5. P. Bibbo and P. Aa. Increasing Precipitator Reliability by Proper Logging and Interpretation of Operational Parameters - An Operator's Guide. In: Proceedings of the Second Symposium on the Transfer and Utilization of Particulate Control Technology. Electric Power Research Institute. Denver, Colorado, 1979.

6. J. T. Guiffre. Precipitator Upgrading and Fuel Control Program for Particulate Compliance at Pennsylvania Power & Light Company. In: Proceedings of the Second Symposium on the Transfer and Utilization of Particulate Control Technology. Electric Power Research Institute. Denver, Colorado, 1979.

7. John Musgrove, et al. Performance Improvement History of Inadequately Performing Precipitators. In: Proceedings of the Sixth Symposium on the Transfer and Utilization of Particulate Control Technology. Electric Power Research Institute, New Orleans, Louisiana, 1986.

8. M. B. Tuck. Dual Precipitators Rejuvenated; Curtain Warpage Solved. Power Engineering, November, 1986

9. Duane Swoboda. Upgrade Methods Improve Performance of Hot-Side Precipitators, Power Engineering, December, 1986

10. Gary Gawreluk. First Utility Application of a Micro-Based Distributed Control System for ESP's. In: Proceedings of the Sixth Symposium on the Transfer and Utilization of Particulate Control Technology. Electric Power Research Institute, New Orleans, Louisiana, 1986.

11. Walter Piulle. Diagnostic Monitoring System for Reverse-Gas-Cleaned Baghouses. EPRI ECS Update, No. 7,Winter 1987.

12. A. S. Viner and L. M. Finkel. Computer Monitoring of Pilot Baghouse Performance. In: Proceedings of the Sixth Symposium on the Transfer and Utilization of Particulate Control Technology. Electric Power Research Institute, New Orleans, Louisiana, 1986.

13. Victor Reyes. Comparison Between Traditional and Modern Automatic Controllers on Full-Scale Precipitators. Paper to be presented at Seventh Symposium on the Transfer and Utilization of Particulate Control Technology. Electric Power Research Institute, Nashville, Tennessee, 1988.

14. J. D. Riley. A Supervisory Computer Control for Smaller Industrial Electrostatic Precipitators. Paper to be presented at Seventh Symposium on the Transfer and Utilization of Particulate Control Technology. Electric Power Research Institute, Nashville, Tennessee, 1988.

15. Sandy Weinmann. A Total Energy Management System for Electrostatic Precipitators. Paper to be presented at Seventh Symposium on the Transfer and Utilization of Particulate Control Technology. Electric Power Research Institute, Nashville, Tennessee, 1988.

16. Bruce Chapman and Rick Yeager. Artificial Intelligence Applications in PWB Manufacturing. Texas Instruments Engineering Journal. 3:1 January-February, 1986

17. Seminar: Expert Systems Applications in Power Plants. Electric Power Research Institute, Boston, Massachusetts, 1987.

18. Paul Harmon, et al. Expert Systems Tools and Applications. John Wiley & Sons, New York, 1988.

19. Philip Chapnick. What is Artificial Intelligence. AI Expert. October, 1987

20. Donald A. Waterman. A Guide to Expert Systems. Addison-Wesley Publishing Company, Reading, Massachusetts, 1986.

21. "Lotus 1-2-3", Lotus Development Corporation, Cambridge, Massachusetts, 1986.

22. "VP-Expert", Paperback Software International, Berkeley, California, 1987.

ESP INTERMITTENT ENERGIZATION TRIALS
AT
NILES GENERATING STATION

John W. Hilborn
Ohio Edison Company
Akron, Ohio

Robert Crynack
Wheelabrator Air Pollution Control
Pittsburgh, Pennsylvania

ABSTRACT

The Niles Plant burns coal with a 2.9% to 3.3% sulfur and 11,600 to 11,900 Btu/pound from Ohio and Pennsylvania. Intermittent energization was added to the automatic voltage controls on Niles Unit No. 2 by Wheelabrator Air Pollution Control to determine how much, if any, power could be saved.

Niles Unit No. 2 has a B&W cyclone boiler, generates 108 NMW and is equipped with a 600 SCA precipitator. During normal operation, precipitator fields 1, 2 and 5 are energized at a low current setting resulting in an approximate particulate emission rate of 0.03 lb/mmBtu. During the baseline trials, without intermittent energization the average particulate emission rate was 0.021 lb/mmBtu with four fields energized. The average particulate emission rate then dropped to 0.012 lb/mmBtu with intermittent energization pulses varying from one cycle in five to one cycle in fifteen. The power savings during the trials was $53,250 compared to full power, but was $3,924 when compared to normal operation.

The results of the intermittent energization trials at Niles were surprising. The particulate emission rate dropped using intermittent energization with a good resistivity ash. This is contrary to other published data which has reported reduced emissions only with higher resistivity fly ash.

The work described in this paper was not funded by the U.S. Environmental Protection Agency and therefore the contents do not necessarily reflect the views of the Agency and no official endorsement should be inferred.

INTRODUCTION

The Niles Plant is located in Niles, Ohio, approximately 75 miles northwest of Pittsburgh, Pennsylvania. The Niles Plant is owned by the Ohio Edison Company which is headquartered in Akron, Ohio. The plant has two identical 108 NMW B&W coal-fired cyclone generating units that went commercial in 1953 and 1954. In 1981, new Wheelabrator precipitators with an design SCA of 520 were installed replacing mechanical dust collectors. Each precipitator is five-fields deep, two bus sections wide, and is powered by nine TR sets and has an operating SCA of 600.

The Niles Plant burns Ohio and Pennsylvania coal with a 2.9 to 3.3 percent sulfur content and a 11,600 to 11,900 Btu/pound content.

Wheelabrator Air Pollution Control contacted Ohio Edison in 1986 and asked if they could install intermittent energization on one of the precipitators at the Niles Plant to determine the power saving that could be achieved on a large precipitator with a cyclone-fired boiler burning medium sulfur coal.

The controls on the Niles Unit No. 2 precipitator are General Electric analog controls. Circuitry was installed on the General Electric controls in fields 2, 3 and 4 in order to intermittently energize these fields. Fields 1 and 5 were left normal.

TEST PROGRAM

A series of tests were performed on Niles Unit No. 2 from May 18-21, 1987, to determine the effects of cycle pulsing (intermittent energization) on the power consumption, opacity and the particulate emission rate. These tests included measuring the power consumption with a clip on KW meter, measuring the particulate emissions by performing stack emissions with a modified Method 17 procedure, and recording opacity, boiler, and precipitator data.

During all the tests, field No. 1 of the Niles No. 2 precipitator was out of service. Therefore, all the tests were performed with only four fields in service. Field No. 5 (last field) did not have intermittent energization capability and operated normally throughout the test series.

A total of 14 particulate emission tests were performed during the test period. Five of the tests were performed without intermittent energization and all the other tests were performed with fields 2 through 4 being intermittently energized with field No. 5 (last field) TR sets operating at 500 ma each. The steam flow was maintained between 700,000 lbs/hr to 740,000 lbs/hr for tests No. 1 through 10 and at 780,000 lbs/hr for test runs No. 11 through 14. The test data, results, and comments are shown on Tables 1 and 2.

The precipitator was baseline tested on May 18 and May 21 with field No. 1 out of service and fields No. 2 through 5 operating without cycle pulsing with the current limits set at their normal operating values. (Current limits set at 1/4 to 1/3 of maximum TR rating.) The results of both tests were essentially identical. The power consumption was 205 KW, the particulate emission rate was 0.021 lb/hr, and the opacity was 11%.

Two tests were performed at various times with fields No. 2 through 4 being cycle pulsed one-in-three cycle and field No. 5 TR sets operating normally at 500 ma each. These tests were in agreement. The power consumption was 264 KW, the particulate emission rate was 0.014 lb/mmBtu, and the opacity was 7%.

Two tests were performed on May 19 with fields No. 2 through 4 being cycle pulsed one-in-five cycles and field No. 5 TR sets operating normally at 500 ma each. These tests were in agreement. The power consumption was 197 kw, the particulate emission rate was 0.011 lb/mmBtu, and the opacity was 8%.

One test was performed on May 19 with fields 2 through 4 being cycle pulsed one-in-seven cycles and field No. 5 TR sets operating normally at 500 ma each. The power consumption was 140 kw, the particulate emission rate was 0.012 lb/mmBtu, and the opacity was 8%.

Four more tests were performed with field No. 1 out of service, fields No. 2 through 4 being cycle pulsed from one cycle in ten to one cycle in 20. At a cycle pulse ratio of one-in-ten cycles, the opacity started to increase and at a cycle pulse ratio of one-in-fifteen the emission rate and the opacity were increasing. The test results, data, and comments are shown on Tables 1 and 2.

DISCUSSION OF TEST RESULTS

It can be clearly seen from the test results that the particulate emission rate dropped dramatically with cycle pulsing rates between one-in-three and one-in-fifteen as shown on Graph No. 1. This is contrary to other published data which has reported reduced emissions only with higher resistivity fly ash. Although the resistivity of the fly ash was not measured during these tests, the tests without intermittent energization demonstrate that the resistivity of this fly ash was good. The emission rate of .021 with four fields energized in service could not have been achieved with a fly ash with a high or low resistivity. At this time, we do not understand why this drop in the particulate emission rate occurred. However, we considered that this was important and to let others know through this paper, in case it may be beneficial to their work in this area.

The power consumption for normal operation with three fields energized with the current limit set at one-fourth to one-third of the maximum rating was obtained by subtracting the power consumed by one field from the power consumed during the tests with four fields energized with the current limits set at one-fourth to one-third of the maximum rating.

The power consumption at a cycle pulse rate of one-in-seven was close to the power consumed during normal operation of this precipitator with three fields in service (usually fields 1, 2 and 5) with the current limit set at one-fourth to one-third of the maximum current limit. A cycle pulse rate of one-in-ten could save approximately $3,924 per year. This is reduction of approximately 35% of the normal power cost of $12,919 per year. The power saving was $53,250 per year when compared to full power (current limits set to maximum) operation. The power costs were based on 1.229 cents/kwh and the unit being on line 80% of the year.

CONCLUSION

The intermittent energization test program on Niles Unit No. 2 showed a power saving of approximately $3,924 per year versus the normal operation of the precipitators which is $12,919 per year. Normally, the first, second and fifth fields of this precipitator are energized at a reduced current limit and the emission rate is approximately 0.03 lb./mmBtu. However, the intermittent energization tests unexpectedly demonstrated a drop in the emission rate from 0.021 lb. particulate/mmBtu with four out of five fields energized without intermittent energization, to a particulate emission rate -- varying from 0.011 to 0.013 lb./mmBtu with a cycle pulse ratio varying from one-in-three to one-in-fifteen with a cyclone boiler burning a medium sulfur coal. Graph No. 1 shows the test results.

We do not have a clear understanding or explanation for this significant reduction in the particulate emission rate for good resistivity fly ash. The reduction may be related to the fact this unit is a cyclone-fired boiler, creating a finer particulate and a lower inlet particulate loading to the electrostatic precipitator. It, however, demonstrates that intermittent energization is not fully understood.

In 1988, Ohio Edison plans to perform tests with intermittent energization at the Gorge Plant in Akron, Ohio, which has marginal-sized electrostatic precipitators to determine if a gain in collection efficiency can be achieved under these conditions.

In addition, in 1987, Ohio Edison attempted intermittent energization at the Edgewater Plant in an effort to overcome a back corona problem that occurred while injecting lime into the boiler to remove sulfur oxides from the flue gas. Intermittent energization was of little or no help in this situation.

REFERENCES

1. Crynack, Robert R., Engelbrecht, Heinz L., and Graves, Neil D., "Saving Energy in Electrostatic Precipitator Operation."

2. Crynack, Robert R., "Improving Performance and Saving Energy with Intermittent Energization - A Case Study," APCA 78th Annual Meeting

ACKNOWLEDGEMENTS

The authors thank Dale Kurtz of Wheelabrator Air Pollution Control for the installation, and testing of intermittent energization at the Niles Plant, which gave the authors the opportunity to write this paper.

The authors thank Joe Dulovich, Steve Brown, Paul Phillips and all the other Niles Plant personnel that allowed intermittent energization to be installed on Niles Unit No. 2 and their help in performing the tests.

The authors also thank Morgan Jones and Adrian Cook, of Ohio Edison, who performed all the particulate emission tests.

Opacity Relationship with kW and Emission Rate

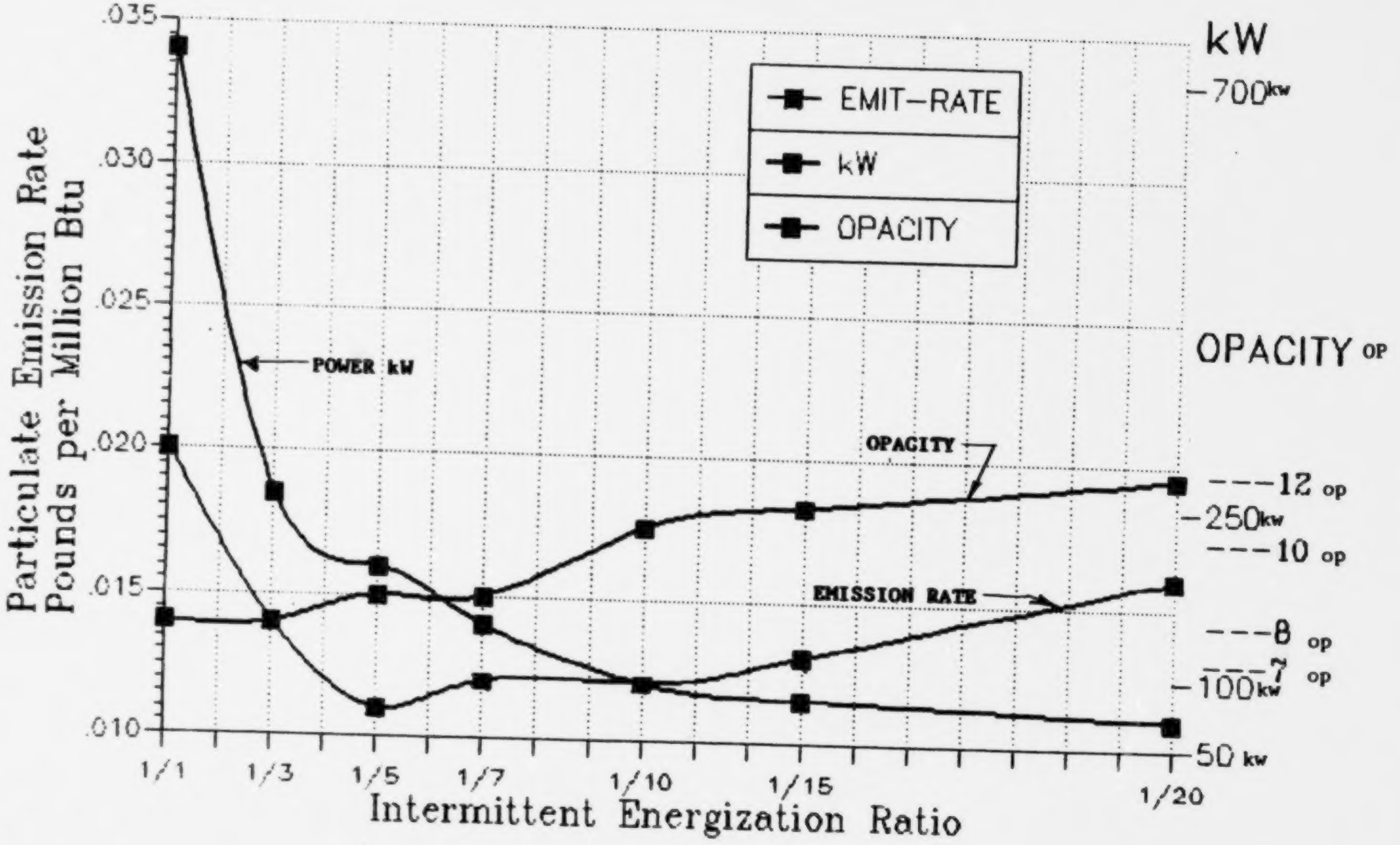

GRAPH NO. 1

TABLE NO. 1

CYCLE PULSE TEST RESULTS SUMMARY
NILES UNIT NO. 2

MAY 18-21, 1987

Mode of Operation	Power Consumption		Emission Rate	Opacity	Change in Power Consumption		Saving (6)	
	Meter Control Room (1)	Clip On Meter (2)			Meter Control Room (1)	Clip On Meter (2)	Per hr	Per Year
	KW	KW	$lb/10^6 Btu$	%	%	%	Dollars	Dollars
Normal (3 fields)	400	$150^{(4)}$	-	10	0	0	0	
Base (4 fields)	450	205	0.021	10	(12.5)	(36.7)	(0.67)	(4695)
Full Power	900	723	0.020	7	(225)	(383.0)	(7.04)	(49336)
Cycle 1/3	450	264	0.012 (0.016)*	$7(11^{(5)})$	(12.5)	(76.0)	(1.40)	(9811)
1/5	350	197	0.011	8	12.5	(31.3)	(0.58)	(4064)
1/7	325	140	0.012	8	18.8	6.7	0.12	840
1/10	275	104	0.012	10.5	31.3	30.7	0.56	3924
1/15	250	88	0.013	11.5	37.5	41.3	0.76	5326
1/20	250	77	0.016	12.5	37.3	48.7	0.90	6307
1/2 Normal	300	99	0.022*	$14.0^{(5)}$	25.0	34.0	0.63	4415
1/4 Normal	250	51	0.028*	$16.0^{(5)}$	37.5	66.0	1.22	8550

1. Includes all power consumed by precipitator and auxiliary equipment (hopper heaters, TR sets, rappers and etc.)
2. TR set power consumption only.
3. First field out of service during all tests.
4. Estimated by substarting power consumed by 4th field from results of data obtained for base test with 4th field in service.
5. Load 103 MW; all other tests performed with 91 to 98 MW load.
6. Saving based on coal cost of 1.229¢/KWH 1986 average and unit being on line 80% of the year.

TABLE NO. 2

CYCLE PULSE TEST DATA
NILES UNIT NO. 2

Date	Run No. 1 5/18/87	Run No. 2 5/18/87	Run No. 3 5/18/87	Run No. 4 5/19/87	Run No. 5 5/19/87	Run No. 6 5/19/87	Run No. 7 5/20/87
Steam Flow (1000 lbs/hr)	700	700	700	700	700	700	720
Air Flow (1000 lbs/hr)	740	740	740	720	710	710	740
Load NMW	91	91	91	91	92	92	94
Opacity %	10	7	7	8	8	8	10-11
ESP Temp F	290	290	290	280	280	280	280
Emission Rate (Lb/mmBtu)	0.022	0.020	0.021	0.011	0.012	0.012	0.012
kW (Panel)	450	900	450	350	325	350	275
Cycle Pulse Ratio	1/1	1/1	1/3*	1/5	1/7	1/5	1/10

Date	Run No. 8 5/20/87	Run No. 9 5/20/87	Run No. 10 5/20/87	Run No. 11 5/21/87	Run No. 12 5/21/87	Run No. 13 5/21/87	Run No. 14 5/21/87
Steam Flow (1000 lbs/hr)	720	740	720	780	780	780	800
Air Flow (1000 lbs/hr)	745	760	750	820	820	820	820
Load NMW	95	98	95	103	103	103	103
Opacity %	11-12	12.5	7	11	12	14	16
ESP Temp F	280	280	280	280	280	280	280
Emission Rate (Lb/mmBtu)	0.013	0.016	0.012	0.016	0.020	0.022	0.028
kW (Panel)	250	250	450	450	400	300	250
Cycle Pulse Ratio	1/15	1/20	1/3	1/3	1/1	1/1	1/1

*Field No. 2 only

FIELD EVALUATION OF HUMIDIFICATION FOR PRECIPITATOR PERFORMANCE ENHANCEMENT

by: G. C. England, B. A. Folsom, R. Payne, and T. M. Sommer
Energy and Environmental Research Corporation
Irvine, California 92718

P. J. Chappell
Air and Energy Engineering Research Laboratory
U.S. Environmental Protection Agency
Research Triangle Park, North Carolina 27711

M. W. McElroy
Electric Power Research Institute
Palo Alto, California 94303

I. A. Huffman
Richmond Power and Light
Richmond, Indiana 47313

ABSTRACT

This paper presents the initial results of a full scale utility boiler evaluation of flue gas humidification as a precipitator performance enhancement technique in conjunction with dry sorbent injection for SO_2 control. SO_2 emissions can be reduced substantially by injection of calcium based sorbents into the boiler furnace. However, the presence of partially spent sorbent in the fly ash degrades precipitator performance by increasing inlet dust loading, decreasing particulate size, decreasing SO_3, and increasing fly ash resistivity. Humidification offers a potentially simple and low-cost method of restoring precipitator performance and may also provide additional SO_2 removal. A sorbent injection/humidification system has been installed on a 61 MW tangentially fired utility boiler with a cold side precipitator. Short term test results obtained during system start-up indicate that opacity and precipitator electrical operation degrade rapidly with sorbent injection alone. Application of humidification during sorbent injection resulted in significantly improved precipitator electrical performance and lower opacity. No major operational problems have been observed to date; however, there is no experience with long term operation.

This paper has been reviewed in accordance with the U.S. Environmental Protection Agency's peer and administrative review policies and approved for presentation and publication.

INTRODUCTION

The injection of dry sorbents into the furnace of a coal fired boiler for SO_2 emissions control may prove to be a cost effective alternative to flue gas scrubbing in instances where moderate (e.g., <60%) SO_2 reduction is required. Critical issues affecting the commercial applicability of this technology are its adverse impacts on particulate control equipment and the effectiveness of countermeasures to offset these impacts. Since the technology is envisioned primarily for retrofit applications, it will most likely be used on boilers equipped with an electrostatic precipitator (ESP). Sorbent injection significantly alters the quantity and characteristics of the particulate matter entering the ESP. At cost effective calcium/sulfur ratios, the inlet precipitator dust loadings may increase by a factor of 2 or 3. Thus, even if the ESP maintained pre-sorbent injection collection efficiencies, there would be a corresponding increase in particulate emissions.

ESP operation involves three major processes:

1. Particle Charging - the particles are charged by passing the dust laden flue gas through an electric field generated by a high voltage DC corona. In modern power plant ESPs, the corona is formed around wires spaced in an array between plates, which are the negative and positive electrodes, respectively. The corona produces negative ions which flow toward the positive electrode, colliding with and thereby charging particles.

2. Particle Collection - the negatively charged particles migrate toward and attach to the positive electrodes (plates) due to coulomb forces resulting from the electric field.

3. Particle Removal - the particles collected on the plates are removed by rapping the plates. The particles are dislodged and move downward. Ash near the bottom of the plates then falls into hoppers, where it can be removed for storage or disposal.

Maximum collection efficiency is generally obtained by operating with the highest possible voltage drop and current density between the electrodes. This is generally limited by the onset of sparking, and voltage is maintained at or very near the sparking point by the ESP control system. The resistivity of the collected ash layer is a significant factor determining the maximum electric field strength. The voltage drop across a high resistivity ash layer can be significant and lead to formation of a positive corona on the surface of the ash layer (back corona). The back corona reduces the space charge due to the emission of positive ions and leads to excessive sparking. Sparking consumes power and severely limits the maximum operating voltage.

The deterioration of ESP collection efficiency with sorbent injection may be caused by several factors:

- The increased particulate loading, particularly the increased fraction of very fine particles, will increase electric space charge suppression of the corona current.

- The overall collection efficiency is reduced due to lower particle charging and greater sensitivity to turbulence of the very fine particles.

- The SO_3 in the flue gases is almost eliminated because of the presence of free CaO in the partially spent sorbent.

- The resistivity of the fly ash/sorbent mixtures increases by roughly 2 orders of magnitude over the fly ash alone due to the combined effects of SO_3 removal and increased CaO content (1,2,3). High fly ash resistivity degrades electrical operation due to formation of a back corona and premature sparkover.

- The ash layer on the discharge and collecting electrodes may increase in thickness and/or be more difficult to remove by rapping. This may increase reentrainment losses and further degrade electrical performance.

The application of ESP upgrades and performance enhancements has been considered in conjunction with sorbent injection (4). Potential ESP upgrades include increased precipitator size and electrical control upgrades (e.g., pulse energization). Potential performance enhancements include: 1) SO_3 conditioning, 2) indirect heat exchange to cool the flue gases, and 3) evaporative humidification of the flue gases. For the most part, previous applications of humidification to coal fired power boilers have included a large humidification tower to ensure complete evaporation of the water before the combustion products enter the ESP (5). A different approach to humidification has been taken for the present project which involves installation of an array of water spray nozzles in the existing flue gas duct immediately downstream of the air heater.

Energy and Environmental Research Corporation (EER) is evaluating sorbent injection on a 61 MW tangentially fired boiler. The project, sponsored by the U.S. Environmental Protection Agency (EPA) and the Electric Power Research Institute (EPRI), is being conducted at Richmond Power and Light's Whitewater Valley Generating Station Unit 2 in Richmond, Indiana. The boiler, a Combustion Engineering unit completed in 1972, is equipped with a Lodge-Cottrell cold side ESP. Design data for the ESP are given in Table 1. While the primary emphasis of the program is on the effect of sorbent injection process parameters on SO_2 removal in the boiler, a major objective is to establish that particulate emissions can be maintained at or below normal levels. However, during the start-up tests reported here, the goal was to maintain opacity under the regulated level of 40%. Flue gas conditioning by evaporative humidification has been selected as the approach for mitigating the impacts of sorbent injection on particulate emissions.

PROCESS DESIGN

Figure 1 illustrates the duct configuration between the air heater and ESP at Richmond. The duct layout is complicated by four turns. The ESP inlet contains turning vanes and baffles to distribute the flue gas evenly into the electrical section. Turning vanes are also located in turns 3 and 4 to improve the velocity profile entering the ESP. The total residence time in the duct at nominal full load conditions was calculated to be 2.2 sec between the air preheater outlet flange and ESP inlet flange. The design goals for the humidification system fitted to the RP&L unit were:

1. Cool the flue gases to $30^{o}F$ above the adiabatic saturation temperature.
2. Obtain complete evaporation of the water upstream of the ESP.
3. Minimize formation of deposits on the duct walls.

The location selected for installation of the water spray array in the existing flue gas duct was as close to the air heater outlet as possible to maximize the residence time for evaporation prior to the ESP.

There are three potential problem areas for deposition: the ESP electrodes, flow distribution plates, and the duct downstream of the water injection. Incomplete evaporation of the water sprays prior to the ESP could lead to water droplets being collected, wetting the ash layer on the collection plates. The unreacted sorbent injected into the boiler results in a high fraction of free CaO in the fly ash, which could form cementitious deposits on the plates. Such deposits might be difficult to remove by rapping.

Wet ash/spent sorbent deposits could also accumulate on the duct walls in the region downstream of the water sprays. Initial calculations of particle scavenging by water droplets suggested that water droplets and solid particles would not physically interact to a significant extent while in suspension. Therefore, problems would most likely occur because water droplets impact and wet the duct walls. Subsequent impaction of ash/sorbent particles could lead to the formation of heavy cementitious deposits which could necessitate shutdowns for removal or even threaten the structural integrity of the duct if uncontrolled. Therefore, the major objectives of the process design were to maximize evaporation of the water droplets prior to the ESP inlet, to minimize impingement of water droplets on the inner surfaces of the duct, and to provide for monitoring of duct surfaces during operation.

DROPLET EVAPORATION

One- and two-dimensional spray evaporation models were used to assess approximate droplet lifetimes under duct conditions as a function of spray droplet size distribution. Figure 2 illustrates calculated spray evaporation times as a function of the Sauter mean diameter (SMD) of the spray and approach to saturation. A droplet size distribution of 2.25 and typical flue gas conditions (temperature, water vapor, enthalpy) at the air heater outlet were assumed for the calculations. Figure 2(a) illustrates that sprays with 30 and 40 μm SMD will result in incomplete evaporation at the ESP inlet. A spray with a 20 μm SMD, however, would achieve complete evaporation prior to the ESP at 30°F approach to saturation. Figure 2(b) shows the impact of approach to saturation on spray lifetime. It can be seen that, if the specifications are relaxed, droplet lifetimes will be reduced significantly as the temperature above saturation increases. In the limit, if only a small amount of water were injected resulting in negligible cooling or humidification of the flue gas (223°F approach), the time required for complete evaporation decreases dramatically from approximately 3 to 0.8 sec.

DROPLET LIFETIMES

Droplet lifetimes are important because they control the amount of liquid droplets that could impact the duct surfaces. Inspection of the duct layout suggested that droplet impaction was most likely at the first duct turn downstream of the spray nozzle array. The data presented in Figure 2 show that much of the spray evaporates very rapidly, with over 75% of the spray completely evaporated within about 0.5 sec even for the larger SMD spray. This is because the smaller droplets evaporate very quickly. However, as the small droplets evaporate, the driving force for evaporation decreases, extending the lifetime of the very large droplets. Thus, although most of the spray evaporates prior to the first turn, a relatively large number of big droplets remain. Large droplets near the edge of the flow field will tend to separate from the gas flow at the turn due to their momentum and will probably impact on the wall.

NOZZLE DESIGN

The calculations indicate that nozzle performance is critical to the success of the humidification system. Nozzles which produce both a very fine SMD and a small fraction of oversize droplets are required. A survey of commercial spray nozzles was conducted to identify those with the most promising spray characteristics. The number of nozzles for the humidification system, and hence the individual nozzle capacity, was selected based on preliminary assessment of nozzle array requirements. Twin fluid nozzles were quickly identified as the only type capable of producing the desired spray quality and turndown requirements. The maximum air/water mass ratio was specified at 0.3 due to considerations of air compressor cost. Seven nozzles were selected for spray characterization tests using a Malvern droplet size analyzer and spray sampling for mass flux distribution. The results of spray characterization studies are summarized in Table 2. The nozzles produced SMDs ranging from 33 to 76 μm at 2 gpm. All of the nozzles produced a significant fraction of oversize droplets. Based on these tests, nozzle No. 7 was selected.

Additional calculations were carried out to refine the design of the nozzle array (e.g., evaluate nozzle-to-nozzle spray interaction) and to quantify the potential for wall deposits. Other humidification concepts (e.g., reverse sprays, steam atomization, and multiple staging) were also investigated, but did not show significant benefits over the initial concept of a single injection plane of nozzles aimed downstream, given the uncertainty of the design tools.

A physical model of the duct was constructed to evaluate gas flows in the evaporation region. Turning vanes were designed for the duct elbow (turn 1) at the air heater outlet to improve the gas velocity profile at the nozzle array.

SYSTEM DESIGN

The final design configuration was:

- An array of 31 nozzles on a triangular pitch located in the vertical section of duct near the air heater outlet.
- Nozzle to wall spacing of 1.4 ft.
- Commercial twin fluid nozzles with nominal 2 gpm capacity and utilizing compressed air as the atomizing fluid.
- Upstream turning vanes.

Although the system did not satisfy the original design goals, it was estimated that complete evaporation could be achieved at the ESP inlet down to a 70°F approach to saturation. Some wall wetting on the duct surfaces immediately downstream of the water sprays was predicted. However, it could be expected that the most serious deposition would occur at the top of the duct just downstream of turn 2 (refer to Figure 1).

Three 200 hp air compressors were required to supply the atomizing air to the spray nozzles. Plant circulating water was used for the humidification supply. The duct elbow was modified to incorporate the turning vanes at the air heater outlet. A programmable control system was designed and fabricated to control the humidification system based on coal flow and flue gas temperature. Provisions for monitoring system performance were installed including water flowmeters, temperature sensors in the gas stream and on the duct walls, load cells to monitor total duct weight, and many visual inspection ports throughout the ductwork.

BASELINE ESP PERFORMANCE

The ESP was inspected by the vendor and repaired prior to testing. A test was conducted without sorbent or humidification to establish baseline ESP performance. Table 3 summarizes the baseline performance results. Dust collection efficiency ranged from 97.6% to 99.2% over the range of test conditions evaluated. Fly ash resistivity, measured using a point-to-plane probe, ranged from 5.9×10^{10} to 1.13×10^{11} ohm-cm (depending on whether measured prior to or at the onset of sparking in the probe, respectively) for the nominal baseline coal and from 1.2×10^{10} to 5.1×10^{10} ohm-cm for the high sulfur coal. Based on the measured flue gas flow at the stack, the ESP specific collection area was 175 ft^2/1000 acfm at full load and 286 ft^2/1000 acfm at low load. The test results indicated that the ESP operation was nominally within design performance specifications.

PRELIMINARY HUMIDIFICATION PERFORMANCE

Preliminary test data were obtained during commissioning and start-up of the sorbent injection and humidification systems. The systems were operated for periods generally less than 4-6 hr, and operating conditions were varied during these periods as dictated by the start-up test requirements. Thus, only short term operation has been studied to date, and data acquisition was limited to normal plant and system operating parameters. For certain tests, limited ESP performance data were obtained in the form of secondary voltage-current readings.

It was readily apparent early during the start-up tests that opacity increased immediately upon sorbent injection, exceeding 40% opacity generally within less than 30 min. The opacity limit allowed by the State of Indiana for this test program is 40%; therefore, sorbent feed would be discontinued at this point. However, subsequent tests showed that humidification was effective in reducing opacity to below 40%.

Figure 3 illustrates the performance trends observed during a typical start-up test. Boiler load was 60 MW, coal sulfur was approximately 2.5%, and hydrated lime was used as the sorbent. Sorbent feeding commenced at 1413 hours. The feed rate was 3500 lb/hr, corresponding to a calcium/sulfur molar ratio of 1.0. There was an immediate increase in stack opacity from its initial level of 20%. As shown on the figure, this occurred coincident with a drop in the average ESP current density, indicating excessive sparking and/or back corona due to high dust resistivity.

At 1430 hours, the humidification water was started at 18 gpm, and the opacity increased briefly before falling to 25%. The opacity continued to decrease (but more slowly) to approximately 20%. Flue gas temperature decreased to approximately 285^{o}F, corresponding to approximately 165^{o}F approach to saturation. At 1515, the sorbent flow was increased to 6000 lb/hr (Ca/S = 1.7). The opacity initially continued to decrease but began to increase slowly shortly thereafter.

At 1600, the sorbent flow rate was increased further to 9000 lb/hr (Ca/S = 2.6). Opacity increased and stabilized at approximately 35%. At this time, flue gas temperature upstream of the humidification water sprays had risen to 355^{o}F, and the boiler operators indicated that fouling of the superheaters would require operation of the sootblowers. Previous experience indicated that an increase in opacity would accompany sootblower operation; therefore, at 1645 the water flow was increased slightly to compensate for the increased opacity. Approach to saturation decreased from approximately 175 to 165°F. The opacity slowly decreased from 35 to 30% following sootblower operation.

At 1740, the sootblowers were operated a second time. During operation of the sootblowers, opacity steadily increased and reached 40%. This was accompanied by a noticeable decrease in ESP current density. At 1810 the water flow was increased again. This restored current density to the level just prior to sootblowing and maintained opacity slightly below 40%. At approximately 1830, the sootblowers were operated again, and a slight increase in opacity was observed. Sorbent flowrate was reduced slightly just prior to sootblowing. Opacity slowly began to decrease after sootblower operation was completed. At 1940, sorbent injection was stopped.

ESP AND DUCTWORK INSPECTION

The above observations are typical of the general operation of the system during start-up. A complete inspection of the boiler, flue gas duct, and ESP was conducted after 75 cumulative hours of humidification and approximately 160 t of sorbent injected. No major duct or ESP deposition problems were identified. A very thin layer of deposits (approximately 1/4-1/2 in. thick) was found in the vertical duct section downstream of the water sprays. Only minor deposits were found on the ceiling at turn 2. There were also indications of clumps of agglomerated ash falling to the floor of the duct below the spray system; the ash had apparently built up on and was subsequently dislodged from the spray nozzles. Deposits in the ESP were considered normal, although there were distinct color stratifications (dark gray to very light gray) in the layer on the electrodes from the tests with sorbent injection.

DISCUSSION

Steady state operation with sorbent injection could not be achieved without humidification during these tests because of high opacity. Observation of ESP secondary voltage indicated that excessive sparking occurred when sorbent was injected without humidification. The ESP controls would adjust the secondary voltages downward to compensate for excessive sparking. This was particularly evident in the inlet field of the ESP. The resulting reduction in corona power leads to reduced collection efficiency, hence higher opacity.

The major benefit of humidification is that it allows the ESP to operate at increased power levels by reducing fly ash resistivity. Figure 4 shows current-voltage relationships for each field of the ESP with and without humidification. The data presented in Figure 4(a) were produced on the same day as the test discussed above, before operating the sorbent injection or humidification systems, by manually operating each field over a range of voltages. Each field has a unique maximum voltage limit prior to the onset of sparking or back corona. For example, the outlet field (field 4) secondary voltage was limited to approximately 45 kV, at which the current density was 8 nA/cm^2. Figure 4(b) illustrates the range of ESP operation in automatic mode during the test run. Humidification has eliminated sparking in field 4 and allowed secondary voltages of 48 kV and current densities of 16 nA/cm^2. This corresponds to more than double the effective corona power possible under normal operation, without sparking or back corona. Similar effects were observed for all but the inlet field, which showed only a mild improvement.

Although these results are site specific, the data collected during start-up illustrate the complex interaction of the processes occurring during sorbent injection/humidification which affect ESP performance. The influence of some of these are immediately apparent, while others have much longer response times. It has been suggested by others (2,4) that humidification acts by reducing resistivity because of a combination of reduced temperature and increased water content. This suggests that:

1. Addition of water should have an immediate effect on ESP performance because the gas temperature is reduced commensurate with water injection.

2. If sorbent injection causes boiler fouling and a reduction in heat absorption in the furnace, then ESP (flue gas) temperature will rise. This will degrade ESP performance without additional humidification.

3. Sootblowing will reduce boiler fouling, increase boiler heat transfer, and therefore reduce ESP temperature. This should improve ESP performance without additional humidification.

Support for the impact of boiler tube fouling on the performance of the ESP with sorbent injection is provided in Figure 5, which shows flue gas temperature at the air heater, upstream of the humidification sprays, and at the stack downstream of the ESP. It can be seen that stack temperature drops sharply when the water is turned on. However, during sorbent injection the air heater outlet temperature rises slowly due to boiler fouling, causing the stack temperature (and temperature in the ESP) to rise also. Sootblowing slows the rise in air heater outlet temperature. Each time the water flow is increased, the temperature drop between the air heater and the stack increases also. The overall impact of boiler fouling on ESP performance may take several days to develop.

A second long time constant phenomenon may also affect ESP performance. The properties of the steady state dust layer on the collecting electrodes will change with sorbent injection as the normal fly ash gradually is replaced by the fly ash/spent sorbent mixture. This could cause the effects of particle resistivity to increase and result in deteriorated electrical performance which may take place over a period ranging from hours to days. The short term tests conducted to date have not permitted this effect to be fully assessed, but an inspection of the ESP was conducted during a brief boiler outage, and no permanent buildup of material was observed on the electrodes.

Each time the humidification water was turned on or off the opacity would rise temporarily. This was attributed to shedding of material from the duct wall and ESP plates due to thermal contraction or expansion. Tests were conducted during a period when the plant was firing a low sulfur (1.5%) coal to assess wall wetting in the absence of sorbent. When sufficient water was added to decrease the flue gas temperature to about 235°F, the opacity suddenly increased. This may have been caused by acid condensation (no sorbent was injected during these tests); however the absence of a bluish color in the plume suggested that acid condensation may not be the cause. A second possible explanation is that the resistivity of the fly ash was reduced below about 2×10^8 ohm-cm, at which point ESP performance is known to deteriorate rapidly. Further tests are planned to evaluate possible consequences of over-humidification.

CONCLUSIONS

Limited performance results obtained during start-up suggest that humidification will enhance ESP performance during short term sorbent injection. Opacities were controlled to less than 40% at sorbent injection rates equivalent to Ca/S = 2.4. However, long term performance has not been demonstrated, and the system was not operated at close approach to saturation to establish the lowest achievable opacity when injecting sorbent. Stack opacity has been reduced at much higher temperatures than suggested by other workers (5). It is possible that the resistivity of the fly ash/spent sorbent mixture was reduced more than anticipated or that the impacts of high resistivity on collection efficiency were significantly reduced. Additional characterization of dust properties and ESP operation are required over longer term operation before performance can be assessed definitively. Additional tests are scheduled to be conducted later this year.

ACKNOWLEDGMENT

This work was sponsored jointly by EPA, EPRI, RP&L, and EER. The authors wish to acknowledge the efforts of E. Mecchia, R. Pennington, S. Bui, and N. Soelberg of EER for their efforts during the start-up and baseline testing. The authors also wish to acknowledge the outstanding cooperation and support from all the plant personnel at Richmond Power and Light, notably R. Ray, S. Rexrode, and D. Straight. J. DuBard and C. Landham of Southern Research Institute provided valuable discussions regarding the ESP operation and effects of humidification; these efforts are also appreciated.

REFERENCES

1. P. L. Case, et al. Testing of Wall-Fired Furnaces to Reduce Emissions of NO_x and SO_x Volume 1. Final Report, EPA 600/7-85-026a (NTIS PB85-224632/XAB) (1985).

2. R. S. Dahlin, et al. Effects of Furnace Sorbent Injection on Fly Ash Characteristics and Electrostatic Precipitator Performance. Proceedings: First Joint Symposium on Dry SO_2 and Simultaneous SO_2/NO_x Control Technologies, Volume 1, EPRI CS-4178, EPA-600/9-85-020a (NTIS PB85-232353) (1985).

3. F. E. Gartrell. Full Scale Desulfurization of Stack Gas by Dry Limestone Injection. Volumes I, II, III, EPA-650/2-73-019a,b,c (NTIS PB228447, 230384, 230385) (1973).

4. D. J. Helfritch, et al. Electrostatic Precipitator Upgrades for Furnace Sorbent Injection. Proceedings: 1986 Joint Symposium on Dry SO_2 and Simultaneous SO_2/NO_x Control Technologies, Volume 2, EPRI CS-4966, EPA-600/9-86-029b (NTIS PB87-120457) (1986).

5. G. Mayer-Schwinning and J. D. Riley. Conditioning of Power Station Flue Gases to Improve Electrostatic Precipitator Efficiency. Proceedings: Fifth Symposium on the Transfer and Utilization of Particulate Control Technology, Volume 2, EPRI CS-4404, EPA-600/9-86-008b (NTIS PB86-167160) (1986).

METRIC EQUIVALENTS

$$^{o}C = \frac{^{o}F-32}{1.8}$$

$kg = lb \times 0.454$

$m = ft \times 0.305$

$mm = in. \times 25.4$

$m^2 = ft^2 \times 0.0929$

$m^3 = ft^3 \times 0.0283$

$m^2/1000\ acmm = ft^2/1000\ acfm \times 3.28$

$kW = hp \times 0.7457$

$l/min = gpm \times 3.785$

$g/m^3 = gr/ft^3 \times 2.29$

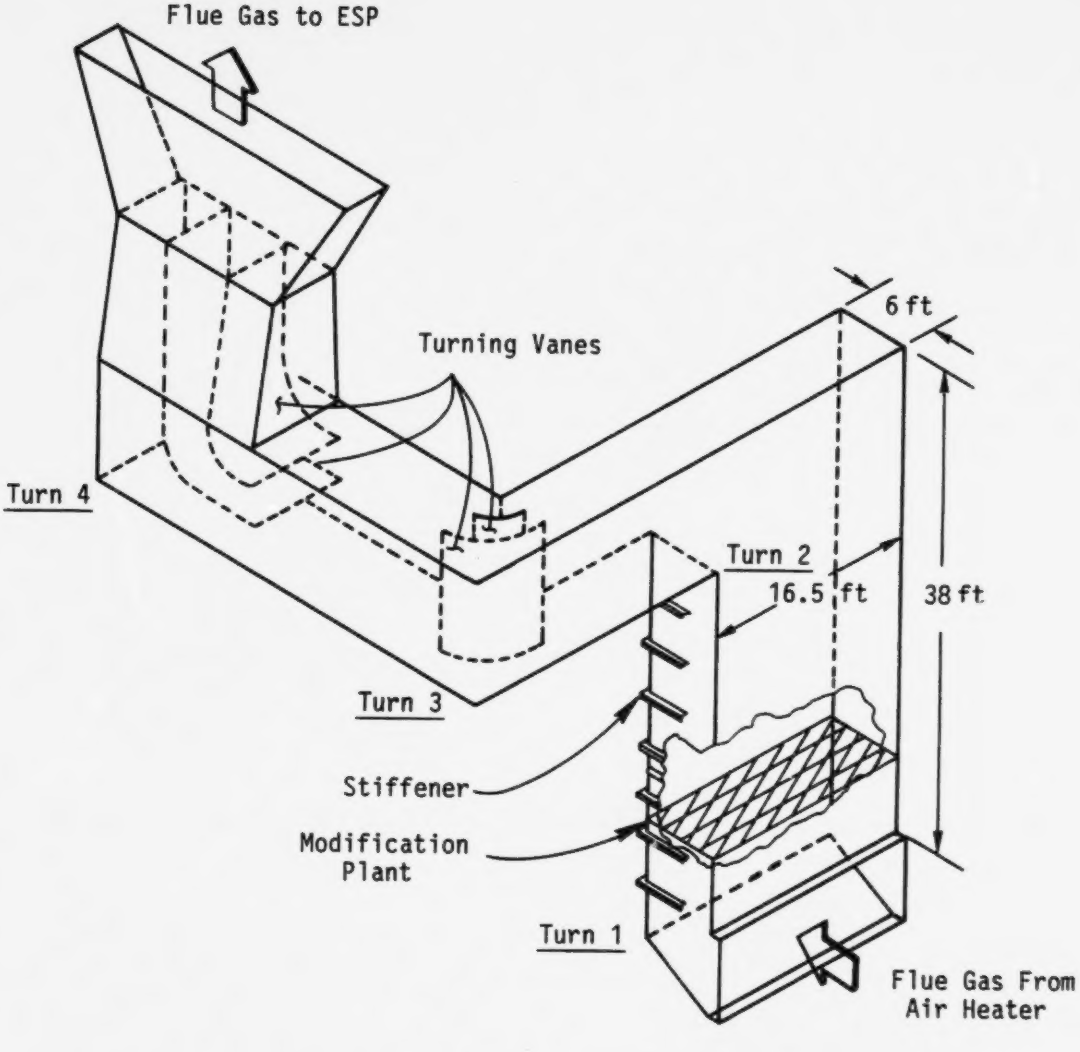

Figure 1. Flue gas duct layout between air heater and ESP.

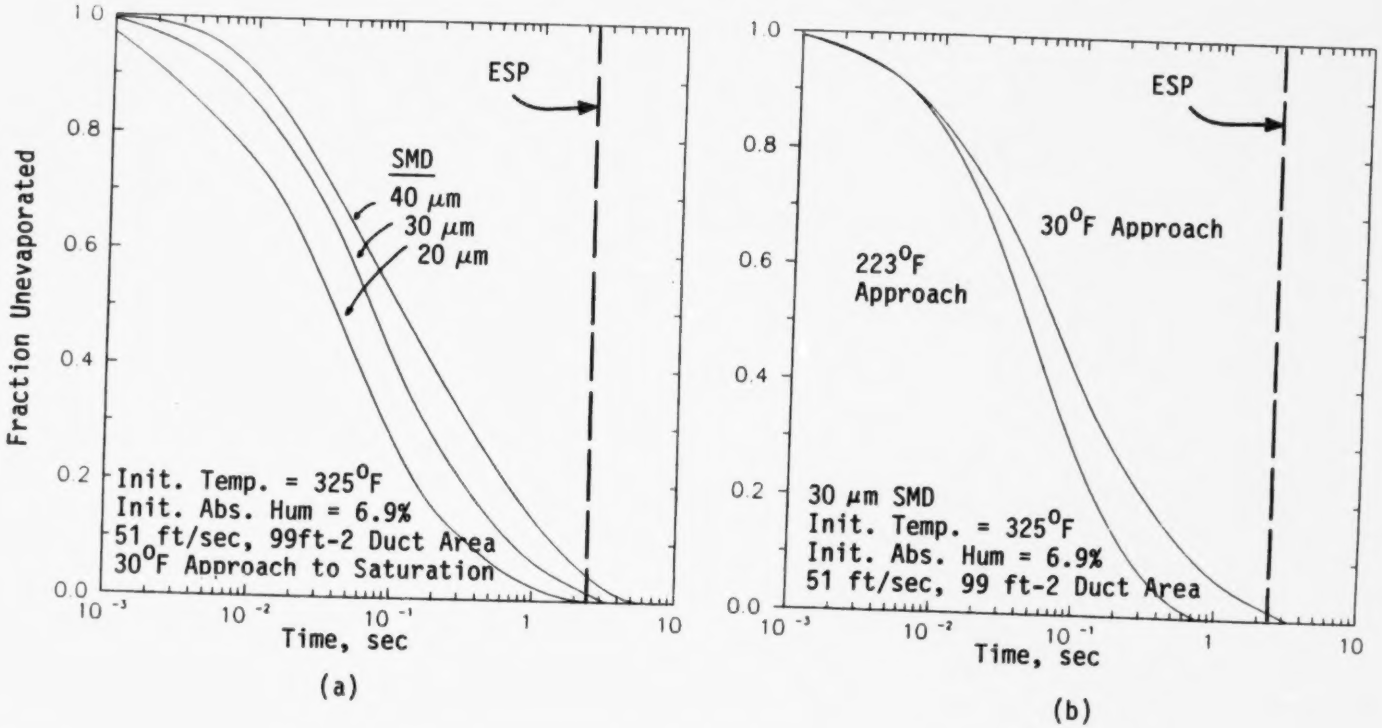

(a)

(b)

Figure 2. One-dimensional calculations of spray lifetime.

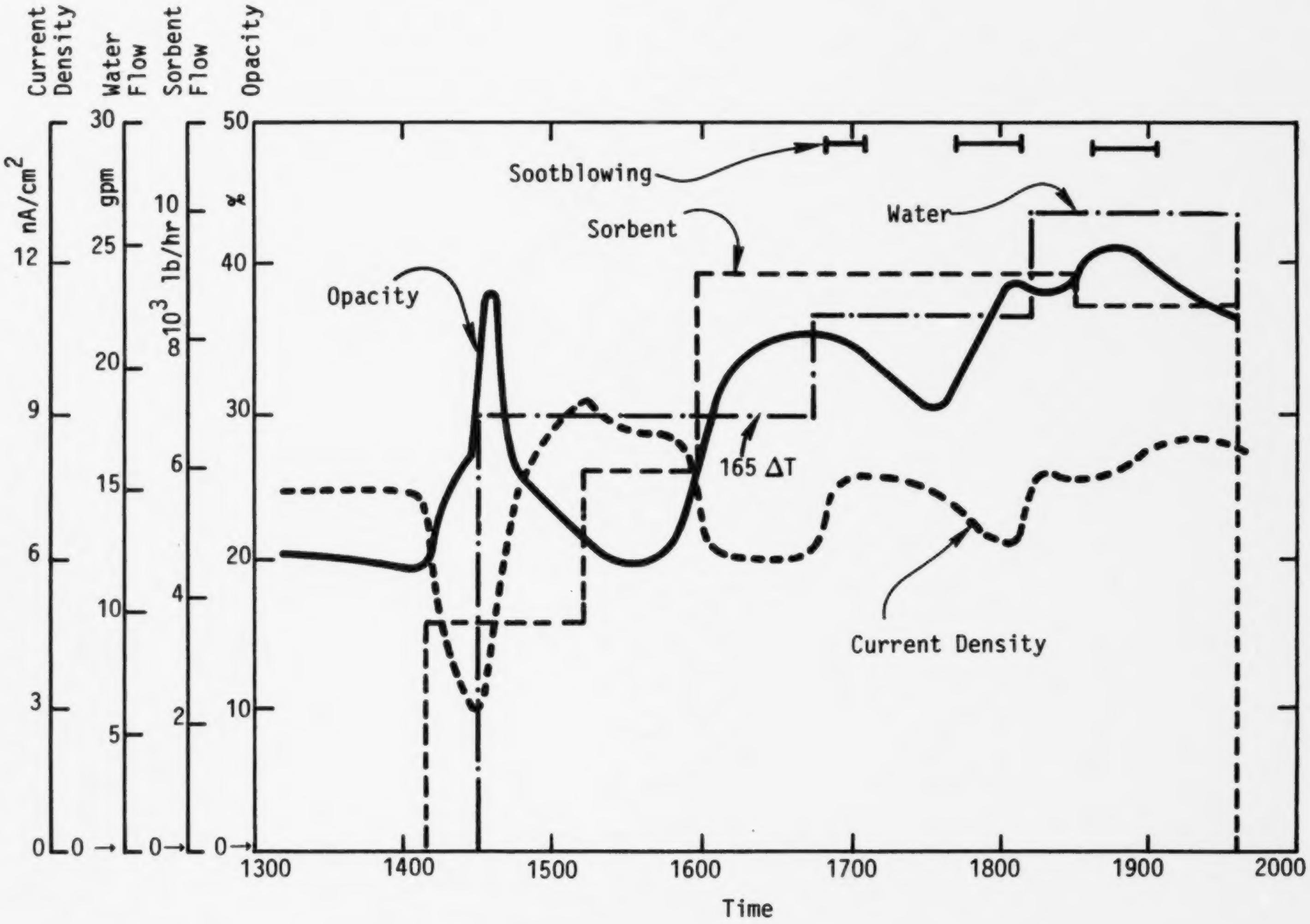

Figure 3. Humidification performance during start-up (60 MW load).

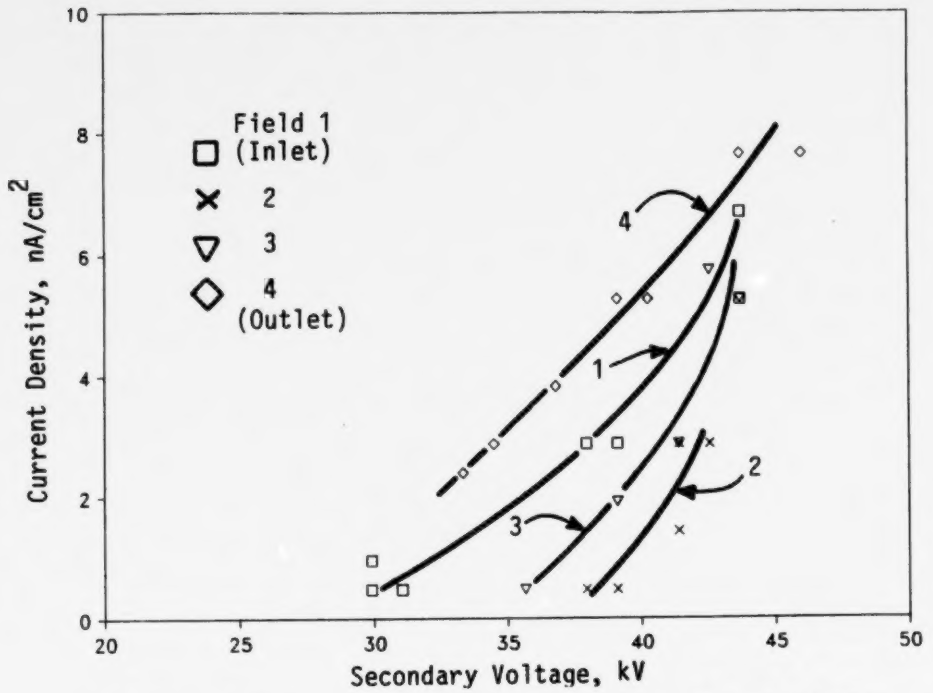

(a) Manual Mode, w/o Humidification or Sorbent Injection

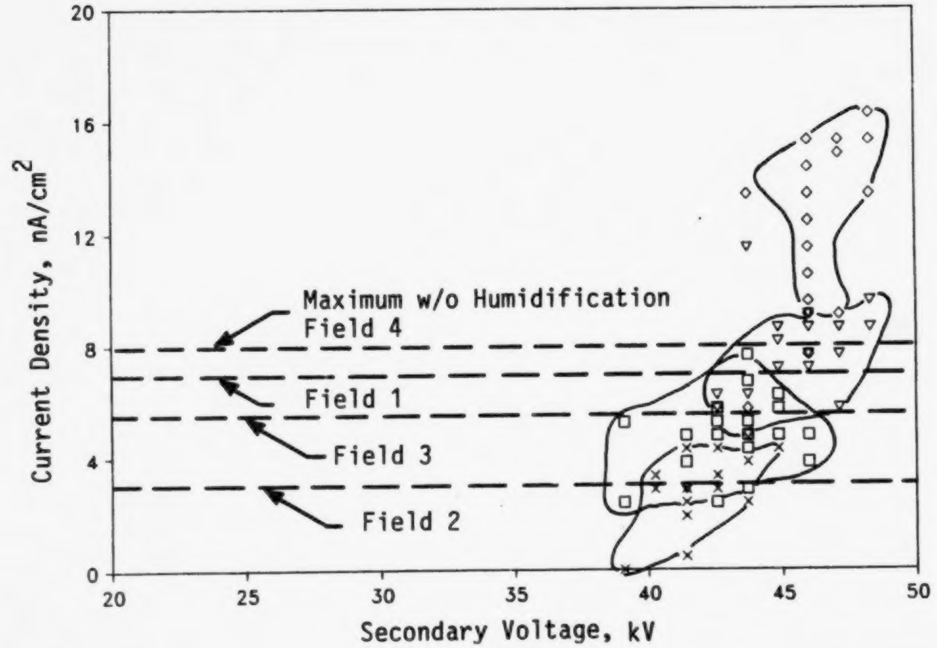

(b) Automatic Mode, Including Humidification and Sorbent injection

Figure 4. Effect of humidification on ESP operation.

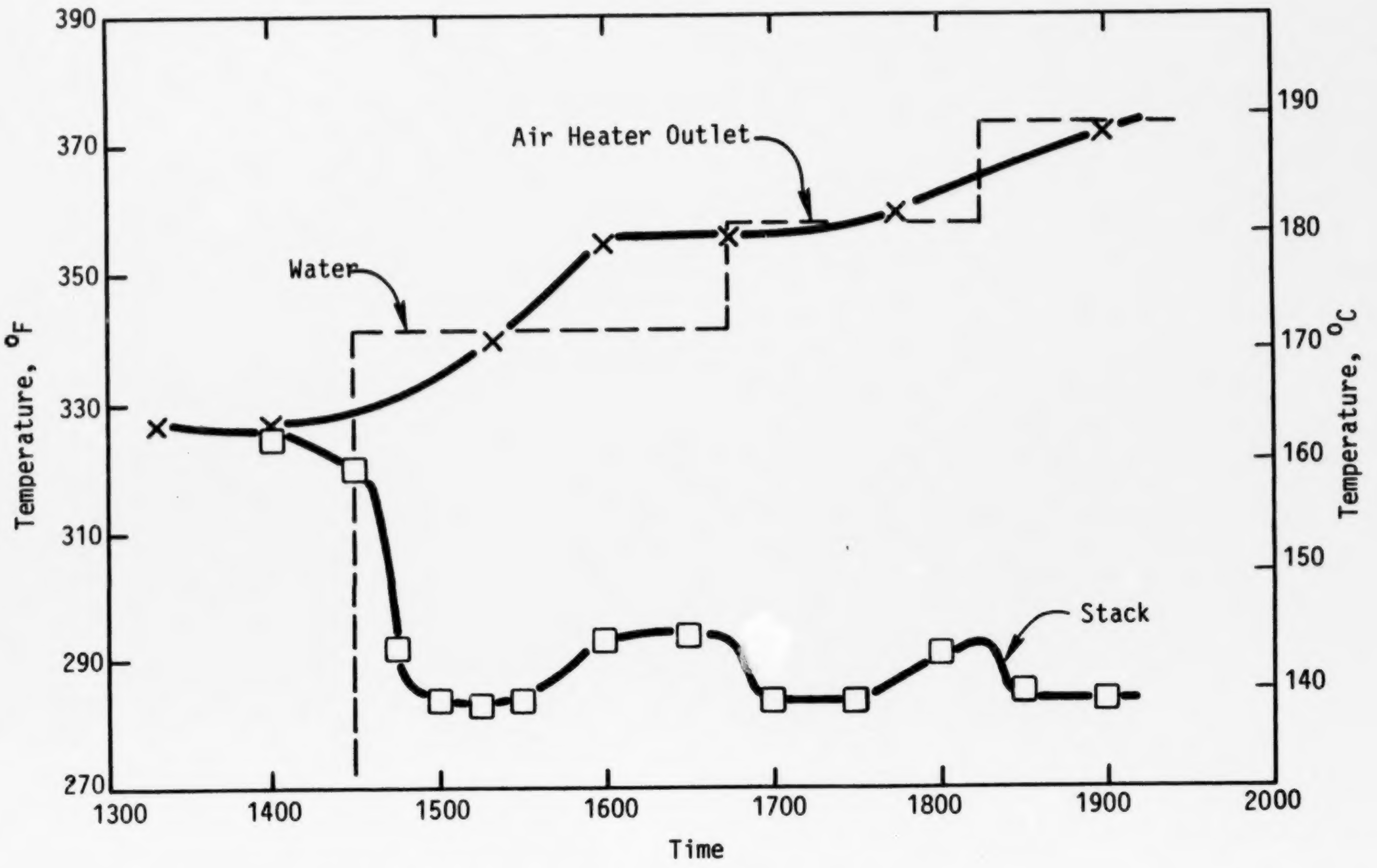

Figure 5. Effect of boiler fouling and water flow on ESP, temperature.

Table 1

ESP DESIGN CHARACTERISTICS

Parameter	Units	Design Value
Gas Volume	acfm	227,000
Gas Temperature	°F	285
Collection Area (Total)	ft^2	45,000
Specific Collection Area (SCA)	ft^2/1000 acfm	198
Inlet Fly Ash Flow	lb/hr	5,000
Inlet Fly Ash Loading	gr/ft^3	3.9
Gas Velocity	ft/sec	5.5
Residence Time	sec	5.46
Number of Fields (in Series)	--	4
Plate Length (Each Field)	ft	7.5
Plate Height	ft	3.0
Overall Aspect Ratio	--	1.0

Table 2

SPRAY CHARACTERISTICS AT 2 GPM

Nozzle No.	A/W (lb/lb) (kg/kg)	Avg. SMD[a] (μm)	Avg.>Oversize[a] (112 μm)
1	0.29	51	34
2	0.30	42	26
3	0.31	38	36
4	0.18	76	48
5	0.21	74	48
6	0.21	40	11
7	0.31	33	6

[a] Measured using laser diffraction method

Table 3

BASELINE ESP PERFORMANCE SUMMARY

Parameter	Units	Base Coal[a]			High Sulfur Coal[b]	
		64 MW_e	52 MW_e	40 MW_e	64 MW_e	40 MW_e
Inlet Particle Loading	gr/dscf	2.92	2.50	2.56	3.69	2.88
Stack Particle Loading	gr/dscf	0.0689	0.0204	0.0417	0.0799	0.0307
Collection Efficiency	%	97.6	99.2	98.4	97.8	99.0
Opacity (Average)	%	12	9	6	11	5
Fly Ash Resistivity - 1 μA	ohm-cm	5.9×10^{10}	--	--	5.1×10^{10}	--
- spark	ohm-cm	1.13×10^{11}	--	--	1.2×10^{10}	--
Fly Ash Particle Size						
Inlet - Mass Mean Diameter	μm	19	14	16	19	15
- Less Than 10 μm	wt %	39	44	41	35	44
Outlet - Mass Mean Diameter	μm	1.4	1.2	1.5	1.4	1.6
- Less Than 10 μm	wt %	100	100	100	100	100
Flue Gas Flowrate	acfm	257,700	199,500	157,600	249,600	151,600
SCA	ft^2/1000 acfm	175	226	286	180	297
Gas Temperature (Stack)	°F	325	311	300	328	302
Flue Gas SO_3 (dry)	ppm	1.2	--	--	15	--
Flue Gas SO_2 (dry, 3% O_2)	ppm	2369	--	--	4065	--
Flue Gas Moisture Content	vol. %	10.6	9.7	8.2	6.2	6.7

[a] Base coal: 2.0 - 3.0% Sulfur
[b] High Sulfur Coal: 3.5 - 5.3% Sulfur

PRELIMINARY TEST RESULTS FOR ESP PERFORMANCE WITH FURNACE SORBENT INJECTION AND FLUE GAS CONDITIONING ON A 300 MW BOILER

by: J. A. Arnott
Ontario Hydro, Power Equipment Department
Ontario, Canada

and

H. V. Krigmont and E. L. Coe, Jr.
Wahlco, Inc.
Santa Ana, California

ABSTRACT

This paper presents results of electrostatic precipitator (ESP) performance on a 300 MW boiler with a retrofit furnace sorbent injection system for SO_2 control. The boiler is equipped with a 1963 vintage ESP designed to handle fly ash from medium to high sulfur U.S. bituminous coal with a design efficiency of 99.0 percent and an SCA of 242 sq. ft/1000 ACFM.

In-situ resistivity data has been obtained and compared with theoretical calculations. Laboratory resistivity and calcium/SO_3 reactivity measurements were made on samples collected from the ESP hoppers.

Short term operational tests with SO_3 conditioning showed that unit opacity could be reduced to acceptable levels, and the precipitator could be made to operate satisfactorily. The relatively high SO_3 injection rates required suggest the latter could be influenced by calcium utilization factors.

The work described in this paper was not funded by the U.S. Environmental Protection Agency and therefore the contents do not necessarily reflect the views of the Agency and no official endorsement should be inferred.

BACKGROUND

Ontario Hydro is a provincially owned corporation established to provide electrical power for municipalities and direct customers throughout Ontario. In 1987 in Ontario there was a total of 31,000 MW of installed capacity, of which 9,000 MW was from pulverized coal fired boilers.

Ontario Hydro is required to reduce its overall SO_2 and NO_x emissions in stages, beginning in 1987 and decreasing to lower levels in 1990 and 1994. By 1994 overall SO_2 emissions must be reduced by more than 60 percent.

Since 1985, Ontario Hydro has conducted research and full scale testing of dry sorbent furnace injection to determine the suitability of this technology for reducing SO_2 emissions from coal fired stations. One of the major problems with this technology has been the inability of the existing electrostatic precipitators to handle the particulate produced during sorbent injection periods.

Studies are underway to evaluate potential SO_2 reduction technologies, and the dry sorbent furnace injection has been tested in three separate test programs on two different 300 MW boilers at the Lakeview Generating Station. Results from some of the earlier test programs have already been issued, (1)(2)(3).

Dry sorbent furnace injection involves the injection of powdered limestone, calcium hydroxide, or other sorbents directly into the upper furnace chamber of a boiler. At the high furnace temperature the sorbent is flash-calcined to lime. The sorbent particle then reacts with available SO_2 and oxygen to form calcium sulfate. The $CaSO_4$, and unreacted CaO are then collected along with the fly ash in the electrostatic precipitator (ESP).

During the sorbent injection the ESP is subjected to increased inlet dust loadings and the flue gas environment and ash characteristics are also altered considerably. Consequently, the stack opacity increases to unacceptable levels. The major cause is a large increase in fly ash resistivity and the consequent loss of power to the precipitator electrical fields. Following 1986 tests at Lakeview Unit 4, where semi-pulse energization was unsuccessful in controlling the opacity levels, it was decided to try to reduce the ash resistivity on Unit 5 with SO_3 flue gas conditioning. Wahlco, Inc. had approached Ontario Hydro previously suggesting use of SO_3 flue gas conditioning with dry sorbent furnace injection. A test program was developed and a test SO_3 injection system supplied by Wahlco was installed for evaluation on Unit 5 during sorbent injection testing in August and September of 1987.

This paper summarizes some of the results from the Unit 5 ESP tests with and without flue gas conditioning on two sorbent types; limestone and calcium hydroxide.

DESCRIPTION OF LAKEVIEW TGS UNIT 5

The Lakeview Thermal Generating Station is located on the outskirts of Metropolitan Toronto on the north shore of Lake Ontario. There are eight 300 MW pulverized coal fired boilers of varying design. Unit 5 is a front fired Babcock & Wilcox boiler and was selected for the Phase 3 test program. Phases 1 and 2 were performed on a tangentially fired Combustion Engineering boiler.

BOILER

The Unit 5 boiler was erected in the mid 1960's and is pulverized fuel fired, with water cooled division walls. The design secondary superheater outlet pressure is 2450 psi. Superheat and reheat outlet temperatures are rated at 1000°F with a steam flow of 2 x 10^6 lb/hr. The unit is equipped with 6 B&W type EL76 pulverizers, 18 burners, two Ljungstrom air preheaters, gas recirculating fan, two primary air fans, two induced draft fans and two forced draft fans.

The design fuel is a central U.S. bituminous coal with a maximum sulfur content of 3.5 percent, 7-14 percent ash, and a minimum calorific value of 12,300 BTU/lb. Typically this unit has been burning 1.7 percent sulfur coal with a 7 percent ash content and a calorific value of 13,000 BTU/lb from West Virginia and/or Pennsylvania.

PRECIPITATOR

The electrostatic precipitator (Figure 1) was manufactured by Joy Manufacturing Co. (Western Precipitation) and consists of one pair of twin collector units with a common division wall. It is three fields deep with 31 collecting curtains 12 ft x 24 ft per zone installed on 9 inch spacings. Collector plate area is 103,000 square feet per side. There are 12 45 kV silicon diode rectifier/transformers. The rated current of the first and second zone TR sets is 500 ma, the third zone is 700 ma. The ESP uses 0.1055 inch diameter discharge electrode wires with 20 lb. weights. Voltage control is automatic by saturable reactor, responsive to changes in rectified current flow.

Design gas flow per side is 425,000 cfm at 247°F for an SCA of 242 ft^2/1000 cfm. Normally however, the flue gas temperature entering the precipitator averages 280°F and the flue gas flow is higher than design by approximately 15 percent.

The wires and plates are cleaned by air driven vibrators. Over the years a number of these vibrators have become seized and during the test period 14 of the total of 65 were not operating.

The east and west precipitators have Lear Seigler opacity monitors installed on the ID fan outlets. Units 5 and 6 share a common stack, therefore a combined opacity is determined from a calculation using the Unit 5 and 6 east and west signals, and the known duct and stack diameters.

SORBENT INJECTION SYSTEM

The installed sorbent injection system for Lakeview Unit 5 disperses dry powdered limestone or calcium hydroxide into the upper section of the furnace. The sorbent fineness is 90 percent passing through #200 mesh, and it is supplied locally. Six nozzles are used for injection into the furnace in a 2200°F temperature zone.

The sorbent injection supply silo does not have sufficient capacity or automatic controls to allow for 24 hour injection of sorbent. Thus the sorbent injection runs were typically 3-6 hours in duration. To minimize the effect of constantly switching from sorbent laden fly ash to regular fly ash during the test period, the unit was taken off line or reduced in load when sorbent was not being injected. This could not always be accomplished due to system load demands.

DESCRIPTION OF THE FLUE GAS CONDITIONING TEST SYSTEM

A diagram of the liquid SO_2 based flue gas conditioning system similar to the one that was installed on Unit 5 is shown in Figure 3.

The system for generating SO_3 for flue gas conditioning consists of a liquid sulfur dioxide storage tank, a vaporizer, air heater, a SO_2 converter and a manifolded injection system.

Liquid sulfur dioxide is normally received in tank trucks and is pressure fed into the storage tank by means of a flexible transfer line. Sulfur dioxide is vaporized in the vaporizer and pressure fed to the system skid.

A centrifugal blower, located on the system skid, provides filtered process air which is heated to the required system temperature by thyristor controlled electric air heaters. Process temperatures are monitored, recorded and controlled to provide SO_2 to the converter at the proper temperature for catalytic conversion to SO_3.

The SO_2 is oxidized to SO_3 by means of a vanadium pentoxide catalyst. The oxidation is an exothermic reaction. The SO_3/air mixture from the converter is injected into the flue gas duct through a distribution manifold and injection probes. SO_3 production is adjusted automatically depending upon boiler load and the amount of SO_3 required to control the fly ash resistivity. The optimum injection rate of SO_3 could be determined by observing precipitator power levels and stack opacity.

The flue gas conditioning system was installed to treat the fly ash in 100% of the flue gas volume.

TEST SET-UP

Sampling ports were installed on the precipitator inlet and outlet ducting to allow for particulate sampling. Figures 1 and 2 show the location of the test ports with respect to the precipitator and the SO_3 flue gas conditioning nozzles that were installed for this phase of the test program.

The east precipitator inlet particulate loading, temperature and flow were measured in a duct 28'-6" x 5'-9" before the duct expansion to the precipitator inlet. Fly ash resistivity was measured at this location using a port that reflected the average flue gas temperature. The inlet particulate loading was measured with a modified BCURA sampling system. This is a high volume in-stack filter design similar to EPA Method 17.

The east precipitator outlet particulate loading and flue gas temperatures were taken at the dual pant leg ID fan inlet. The outlet particulate loading was measured with a high volume, custom designed, in-stack filter sampling system which utilizes Balston ceramic filters. Ash samples were collected from the ash hoppers, and from the inlet particulate sampling train.

The precipitator electrical panels were monitored throughout the tests. Unfortunately the indicating meters are limited to primary voltage, primary current and secondary current. Voltage-current curves were generated for several of the test conditions.

FIELD TEST RESULTS

In May 1987, prior to the Unit 5 outage for the installation of the sorbent injection system and the SO_3 conditioning equipment, precipitator tests were conducted to determine the premodification performance of the ESP. Only the east precipitator was tested and the efficiency was 99.4 percent at 235 MW. The average fly ash resistivity was 7 x 10^9 ohm-cm as measured with a Wahlco in-situ resistivity probe. The average opacity for these tests was 12 percent as measured by the Lear Seigler opacity monitor. In order to improve the precipitator performance in anticipation of the increased particulate loading, several warped curtains were replaced, and wires on the east side precipitator were cleaned.

Table 1 contains a summary of the east precipitator performance for all the precipitator tests. The "as-measured" resistivity for all tests is given in Table 2. It should be noted however that the resistivity figures "as-measured" with the SO_3 conditioning system in service may be influenced by the close proximity of the resistivity probe and the SO_3 injection probes. It was also noted that even when not injecting SO_3, the purge air system changed the flow pattern at the test ports and prevented inlet dust loadings from being measured. The inlet loadings were therefore calculated based on data obtained prior to the start-up of the SO_3 system.

Voltage - current curves were generated for several test conditions and are included in Figures 4-9. Precipitator inspections were performed throughout the test program. The precipitator performance will be discussed in the following sections for each of the test conditions.

BASELINE PRECIPITATOR TEST

The baseline tests were conducted prior to any addition of sorbent to the system. Cold air, voltage - current curves were generated prior to the unit start-up (Figure 5).

On July 15, 1987, Test 4 was performed shortly after the unit returned to service and showed an efficiency of 99.7 percent. However, it was subsequently discovered that 3 sections of rappers were not operating. A precipitator inspection showed that the middle field wires were building up and it was decided to increase the rapping intensity by changing the supply air pressure to the vibrators from 42 psig to 50 psig. The rapping sequence was also changed from 4:2:1 to 3:2:1 to assist in keeping the middle field cleaner.

On July 20th, a repeat test showed a precipitator efficiency of 99.4 percent. The opacity meters showed an opacity of 13-14 percent. This is higher than expected, and the east opacity meter alignment was suspected due to the indicated difference in opacity between the east and west ducts; also the "calibrated" eyeball indication of the stack opacity was reported as 6 percent. The east opacity meter was removed and recalibrated and when returned to service the average opacity on Test 11 at 235 MW was 7 percent (Figure 10). The outlet dust loading for Test 11 was 0.013 grain/acf. Fly ash resistivity "as-measured" in-situ for Tests 10 and 11 averaged 1.3 x 10^{10} ohm/cm. The precipitator electrical readings were steady and the east front field power level for Test 11 was 45.1 kVA. This was comparable to the premodification level of 43.2 kVA.

LIMESTONE INJECTION PRECIPITATOR TESTS

The addition of limestone as a sorbent to the furnace had a severe impact on the electrostatic precipitator performance. Shortly after the start of the injection the front field of the precipitator began to lose power. This reduced the effectiveness of the front field and shortly after it lost power, the following field exhibited the same behavior. The stack opacity increased with the time of injection and if allowed to continue the stack opacity could reach 50-60 percent even at the reduced loads at which the unit was operating (80 percent).

Figure 6 shows a typical voltage-current curve for tests with limestone injection. Severe back corona is exhibited at very low power levels. To maintain stack emissions to reasonable levels without flue gas conditioning, we were restricted to a short duration of limestone injection. Hence, the precipitators were never properly seasoned to the sorbent rich fly ash. Precipitator tests were performed shortly after injection and the results are probably better than true long-term efficiency, since the precipitator performance was just beginning to deteriorate.

Tests 31 and 32 at a 10 t/hr sorbent injection rate showed an average inlet dust burden of 2.76 grains/acf which is double the baseline inlet dust burden and consistent with calculated values. Unfortunately the outlet grain loading could not be measured due to a leak in the sampling train condenser. A retest (Test 47) showed an outlet dust loading of 0.288 grain/acf, for a precipitator efficiency of 89.5 percent with an average opacity of 60 percent. This test was conducted 5 hours after the initial injection of limestone. Fly ash resistivities varied from 6.6×10^{11} ohm-cm to 4×10^{12} ohm-cm.

CALCIUM HYDROXIDE BASELINE INJECTION PRECIPITATOR TESTS

The addition of calcium hydroxide as a sorbent caused even more severe problems to the electrostatic precipitator than limestone injection.

The fly ash resistivity of the calcium hydroxide sorbent injection was 2×10^{12} and significantly reduced the precipitator effectiveness. Two tests performed on the outlet gave an average outlet dust loading of 0.08 grains./acf. Calculating the inlet dust loading based on the coal ash content and sorbent injection rate, the outlet dust loading corresponded to a 96.8 percent precipitator efficiency and an opacity of 38 percent. However, these two tests were conducted only 30 minutes after injection started and the precipitator was in the process of losing power. Opacity charts showed a rise in opacity with time; opacity levels reached 50 percent less than 2 hours after the sorbent injection started (Figure 11). Thus the "as-tested" precipitator efficiency was again much higher than would be expected with long term running.

The fly ash analysis for the hydroxide injection test is contained in Table 3.

LIMESTONE INJECTION WITH SO3 FLUE GAS CONDITIONING

Test 92 was conducted with 8.8 tons of limestone being injected resulting in a 2.5:1 calcium to sulfur ratio. SO_3 was injected at a rate of 47 ppm. The stack opacity was reduced to 15 percent, as opposed to 60 percent without SO_3 injection. Outlet dust loading dropped to 0.021 grains/acf and based on a calculated inlet dust loading the precipitator efficiency improved to 99.3 percent from 89.6 percent without SO_3. The east front field electrical power was 25.3 kVA.

On the completion of Test 92, the SO_3 injection was shut off and there was a rapid rise in stack opacity (Figure 12), leaving little doubt as to the influence of the SO_3 injection under these conditions.

It was felt that further improvement in stack opacity could be possible by reducing the rapping intensity and lowering the SO_3 injection rate. Unfortunately, the lack of testing time prevented further evaluation of the SO_3 conditioning with limestone injection.

Test 94 was conducted at a limestone injection rate of 14 t/hr which was a 4:1 calcium to sulfur ratio. At this rate the SO_3 flue gas conditioning maintained opacity levels at 20 percent.

CALCIUM HYDROXIDE INJECTION WITH FLUE GAS CONDITIONING

SO_3 flue gas conditioning with calcium hydroxide injection also showed encouraging results. However, the lack of time again prevented the optimizing of the precipitator.

Test 99 was performed with an injection of 6 t/hr of calcium hydroxide (Ca/S ratio 2.1:1) and SO_3 injection set at approximately 70 ppm SO_3. The Units 5 and 6 combined opacity for the test period was 24 percent (Figure 14), and the outlet dust loading was measured at 0.0366 grains/acf. The precipitator efficiency based on a calculated inlet loading was 98.6 percent. Both the opacity and efficiency were much improved over the unconditioned flue gas performance. However, there was not the same level of improvement as was seen on the limestone sorbent runs with SO_3 injection. This is possibly due to initial higher resistivity levels when injecting calcium hydroxide and the more porous nature of the particles produced, or to the difference in the calcium utilization.

There did appear to be an increase in opacity and a decrease in first field power with time. As with the limestone tests, a dramatic increase in opacity was observed when the SO_3 injection was shut off. This was a much more rapid increase than was observed with the earlier tests injecting calcium hydroxide alone (Figure 14).

The voltage-current curve taken at the end of Test 99 (Figure 9), shows that the front field experiences back corona at a relatively low power level, with the following field undergoing back corona at a slightly higher level. This is still an improvement however, over the non SO_3 conditioned voltage-current curves in Figure 8.

Fly ash resistivity "as-measured" on Test 98 which had the same injection conditions as Test 99, showed an average value of 3×10^{11} ohm-cm (Table 2) as opposed to 2×10^{12} ohm-cm without SO_3 conditioning. However, the resistivity probe location close to the SO_3 injection probes may have biased the resistivity measurements obtained.

FLY ASH ANALYSIS

Selected samples from the sorbent injection tests were characterized with respect to ash chemistry, resistivity as a function of ascending and descending temperature, x-ray diffraction, and isothermal resistivity as a function of time in an air environment containing sulfur trioxide and water vapor. The samples are identified in Table 4 and the ash chemistry data are given in Table 5.

Ash Chemistry

The addition of sorbent obviously reduces the percentage of most of the other elements in the ash. The level of sulfur does not seem high for the sorbent test.

This could reflect ineffective injection or that sulfur may have been captured as a sulfite, or a sulfide and driven off when the ashes were ignited. Calcium carbonate seemed to be more effective than calcium hydroxide.

Resistivity/Temperature Data

Samples 8, 31, 34 and 94 were tested in accordance with IEEE Standard 548-1984 for resistivity as a function of temperature in an air environment containing 5.5% water vapor. The ascending and descending temperature modes were used. This series represents the baseline ash, sample 8; two levels of calcium carbonate injection, samples 31 and 34; and one case of calcium carbonate injection coupled with sulfur trioxide conditioning, sample 94. The results are shown in Figures 15 through 18.

In each case, the ascending temperature resistivity data are lower than the descending data. This is most pronounced in the case of samples 34 and 94. One can rationalize that this is due to the effect of absorbed and adsorbed moisture and acid. Note that above 400°C in the case of samples 34 and 94, the ascending data point for the highest temperature lies between the ascending and descending curves. Apparently the effect of the absorbed/adsorbed species is being destroyed at this temperature.

Using 150°C as a temperature of reference, it is noted that the resistivity for the baseline sample with 5.5% moisture in the gas phase and descending temperature is 2 E 12 ohm-cm.

At 150°C in the ascending mode, the sample that had experienced conditioning showed somewhat lower resistivity than the samples without conditioning.

The resistivity data for the series of tests involving the injection of calcium hydroxide, samples 72, 76 and 96 are given in Figures 19 through 21. With the exception of one sample, everything noted above for the calcium carbonate injection is applicable to the calcium hydroxide series. Since the water concentration in the calcium hydroxide series was 7.5% instead of 5.5%, the resistivity is slightly lower at 150°C but still in excess of 1 E 12 ohm-cm. The data for sample 96, calcium hydroxide injection and sulfur trioxide conditioning, were unusual in that the ascending resistivity data were greater than the descending values, and at the lower temperatures, the effect of water vapor on the resistivity was pronounced. This could be related to the high lime content especially if the lime were not reacted with the fly ash or gaseous species. In any event at 150°C in the descending mode, all the samples in this series had a resistivity value of about 2 E 12 ohm-cm.

Resistivity in an Environment Containing Sulfur Trioxide

An experiment was run to determine resistivity and exit gas sulfur trioxide concentration as a function of exposure time. The test conditions were an air environment containing 7.5% water vapor, an inlet sulfur trioxide concentration of 9 to 10 ppm and a temperature of 146°C (295°F). Samples selected for test included 8, 34 and 72. Sample 8 represents the baseline fly ash that had not been exposed to sorbent or conditioning. Samples 34 and 72 were produced from the same coal using similar injection rates of calcium carbonate and calcium hydroxide, respectively. The samples were annealed at 450°C in dry air and then thermally equilibrated at 146°C. Resistivity was determined after moisture was introduced to the environment. Sulfur trioxide was then injected at a concentration of 9 to 10 ppm. Resistivity and sulfur trioxide in the exit gas were then determined periodically as a function of time. Resistivity was measured at an electric field intensity of 4 kV/cm. After 92 hours of exposure, resistivity was determined as a function of electric field intensity. Resistivity and sulfur trioxide concentration as a function of exposure time are shown on Figure 22.

From experience with fly ash that does not contain large quantities of lime compounds one would expect the exit gas sulfur trioxide concentration to be equal to that of the inlet gas after ten hours. Obviously the lime suppresses the equilibration of the sulfur trioxide concentration. After ten hours of exposure the exit gas acid concentration was about 4 ppm. Even after 92 hours, the sulfur trioxide concentration in the exit gas was only approaching 7 ppm. After 92 hours, the resistivity of all samples was asymptotically approaching an equilibrium value that would have shifted to slightly lower values as the acid concentration finally reached 9 to 10 ppm. The resistivity of the ashes containing lime responded rapidly and significantly. After 20 hours and an exit gas sulfur trioxide level of about 5 ppm, the resistivity of both samples was 1 E 10 ohm-cm or less. After 92 hours with an acid concentration of about 7 ppm, the unadulterated fly ash (8) had a resistivity value of 1.1 E 11 ohm-cm.

The final step in an isothermal resistivity test involving an environment with sulfur trioxide present was the determination of resistivity as a function of electric field intensity. An electric field intensity of 4 kV/cm is normally used for resistivity tests. This value was used to acquire the data in Figure 10. The greatest field intensity used was 12 kV/cm. This level was used to establish the resistivity model and it often defines the breakdown value. In the present case, none of the samples broke down at 12 kV/cm. It is believed that resistivity values acquired at 12 kV/cm are reasonable because many precipitators are operated in a sparking mode. From Table 6, it is observed that the ashes without sorbent have resistivity values of about 4 E 9 ohm-cm at 12 kV/cm. This great attenuation of resistivity due to increased field intensity is not uncommon when the resistivity level is mainly controlled by sulfuric acid adsorption. Less attenuation occurs if the low-field-strength resistivity is low. Therefore samples 37 and 72 showed an attenuation factor of only about 2 as the field intensity was increased from 4 to 12 kV/cm. Under conditions for electrostatic precipitation, these ashes would have suitable resistivity levels when in equilibrium with a great deal less acid than that used in this experiment. In the case of the ashes containing sorbent, an equilibrium with only 1 ppm of sulfur trioxide measurable in the gas phase could be sufficient at 295°F. The ashes without sorbent would require slightly more.

X-Ray Diffraction

X-ray powder diffraction patterns were obtained for samples 8, 72 and 96, the baseline ash, the baseline ash plus calcium hydroxide sorbent, and the baseline ash plus calcium hydroxide sorbent that had been conditioned with sulfur trioxide, respectively (Table 6). Usually a fly ash generated in a pulverized coal boiler operating at 2200 to 2800°F consists of about 85% glassy material and 15% crystalline material excluding combustibles. Typically with sorbent injection, one might anticipate the crystalline concentration to be 50%. The x-ray data was acquired to determine which crystalline compounds were present. This information could influence opinions regarding resistivity and flue gas conditioning.

An unexpected result of the x-ray diffraction work was that the compound lime (CaO) was found and calcium compounds involving sulfur were not observed. The x-ray work was done using as-received samples so that thermal decomposition was not a factor. If all the sulfur were captured as calcium sulfate, one could roughly estimate that the fly ash/sorbent mixture might contain 25% of this compound. Usually if 2% by weight of a compound is present in a mixture, its presence can be detected by x-ray diffraction. If indeed there is a large percentage of free lime present in the fly ash/sorbent mixtures sulfuric acid conditioning could require large injection rates and long exposure time to satisfy the ash accumulated on the plates.

CONCLUSIONS

The Lakeview Dry Sorbent Furnace Injection Program provided a full scale demonstration of the effect of sorbent addition on electrostatic precipitator performance. The Wahlco SO_3 flue gas conditioning test facility enabled the evaluation of SO_3 injection in restoring precipitator performance during sorbent addition. The following conclusions have been reached on the work performed to date on Unit 5 at Lakeview TGS:

- The addition of sorbent causes an increase in fly ash resistivity on the Lakeview Unit from 1×10^{10} ohm-cm to 1×10^{12} ohm-cm for limestone addition, and to 1×10^{13} ohm-cm for calcium hydroxide addition. Back corona was evident at lower power levels on all fields.
- At a 3:1 calcium to sulfur ratio, the inlet loading to the precipitator is double the baseline loading. Calcium utilization was 10-20 percent during these tests.
- The existing electrostatic precipitator is unable to handle the sorbent-rich fly ash. Calcium utilization on the tests was low, and the combination of high resistivity fly ash and high inlet loading caused opacities to rise with time of injection.
- The use of SO_3 flue gas conditioning with limestone sorbent injection reduced the fly ash resistivity and suppressed the back corona. The SO_3 injection levels were higher than predicted, which is likely due to the low calcium utilization (10-20 percent) of the sorbent for these tests. Stack opacities were reduced to 15% and precipitator efficiency improved to 99 percent.
- The use of SO_3 flue gas conditioning with calcium hydroxide sorbent addition improved precipitator performance but not as significantly as with the limestone. SO_3 injection rates of 70 ppm greatly improved opacity, but was not sufficient to prevent a slow deterioration in precipitator performance.

ACKNOWLEDGMENT

The Laboratory Fly Ash Resistivity measurements were conducted by Dr. Roy E. Bickelhaupt.

REFERENCES

1. Cameron, D. and Arnott, J.A. — Design and Testing of Retrofit Dry Sorbent Injection System on a 300 MW Pulverized Fuel Boiler. Presented at the 1986 Joint Symposium on Dry SO_2 and Simultaneous SO_2/NO_x Control Technologies, June 2-6, 1986, Raleigh, North Carolina

2. Arnott, J.A. — Design and Testing of a Retrofit Dry Sorbent Injection System on a 300 MW Pulverized Fuel Boiler - Phases 1 and 2. Presented at Coal Technologies '86, Nov. 18-20, 1986, Pittsburgh, Pennsylvania

3. Mozes, M.S. et. al — Ontario Hydro's R&D on Sorbent Injection for SO_2 Control. Presented at EPRI Conference on Effects of Coal Quality on Power Plants, Oct 13-15, 1987, Atlanta, Georgia

4. E. L. Coe, Jr. and H. V. Krigmont — Prediction of SO_3 Injection Rates for Fly Ash Conditioning Systems. Presented at the Third International Conference on Electrostatic Precipitation, Abano, Italy, 1987

FIGURE 1
LAKEVIEW UNIT 5
PRECIPITATOR

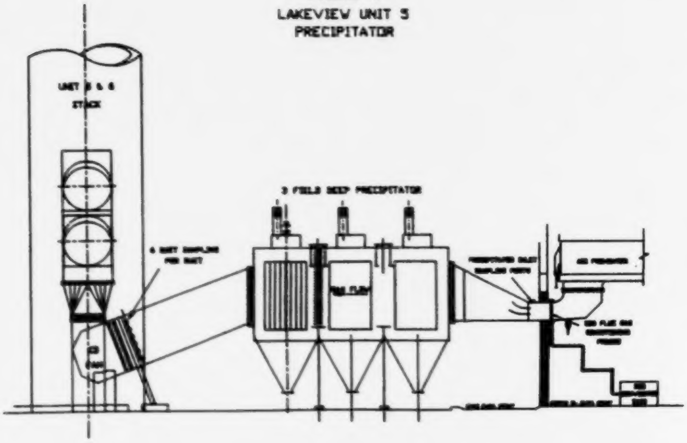

FIGURE 2
LAKEVIEW UNIT 5
SO3 CONDITIONING NOZZLE LOCATION

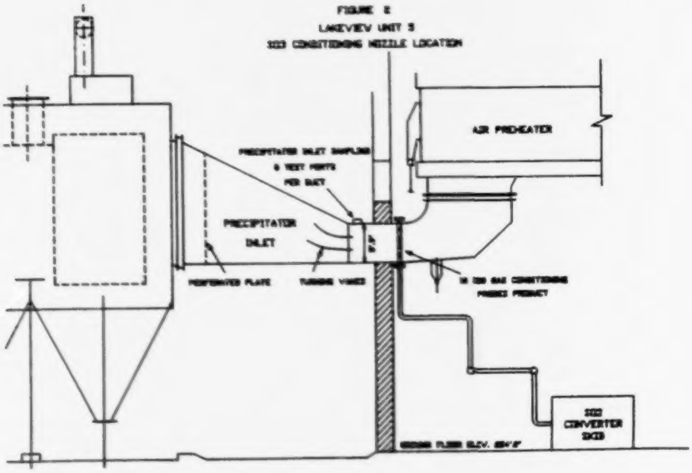

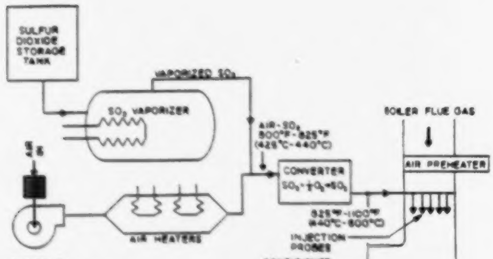

FIGURE 3
FLOW DIAGRAM
WAHLCO LIQUID SULFUR DIOXIDE
FLUE GAS CONDITIONING SYSTEM

FIGURE 4
VOLTAGE CURRENT CURVE
BASELINE TEST

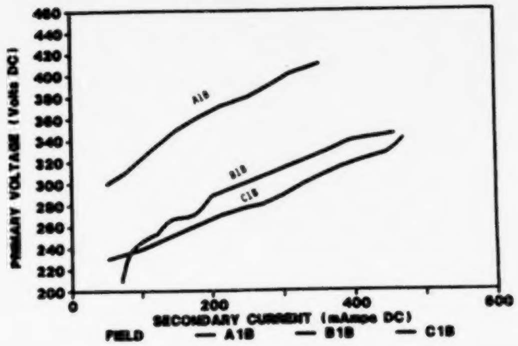

FIGURE 5
VOLTAGE CURRENT CURVE
COLD AIR TEST JULY 11, 1987

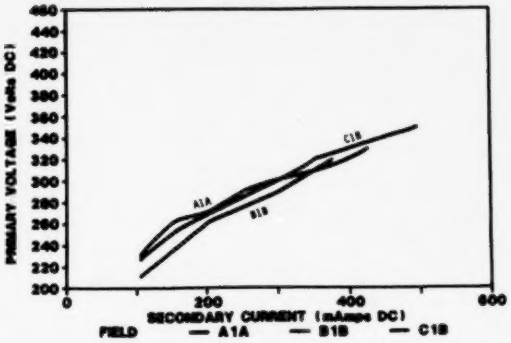

FIGURE 6
VOLTAGE CURRENT CURVE
TEST 93 8 t/h LIMESTONE

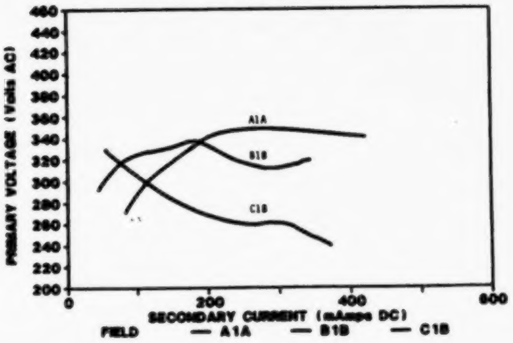

FIGURE 7
VOLTAGE CURRENT CURVE
TEST 92 LIMESTONE INJECTION WITH SO3

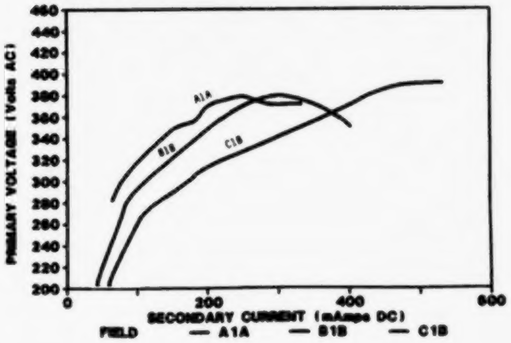

FIGURE 8
VOLTAGE CURRENT CURVE
TEST 70 Ca(OH)2 INJECTION 6 Tons/h

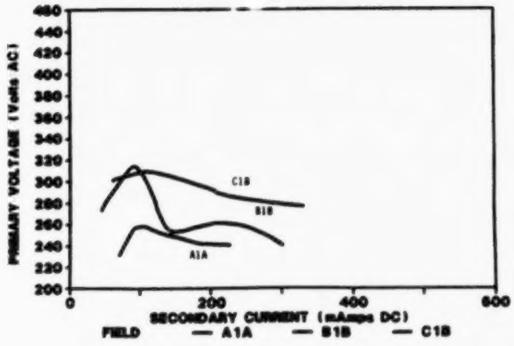

FIGURE 9
VOLTAGE CURRENT CURVE
TEST 99 Ca(OH)2 INJECTION AND SO3

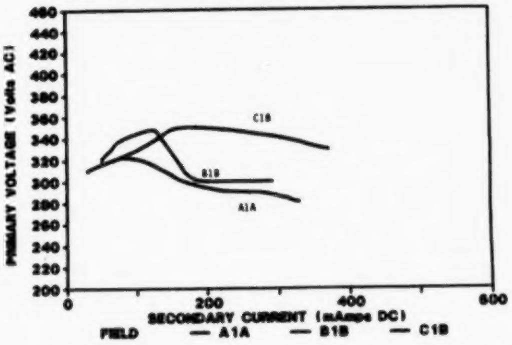

Figure 10

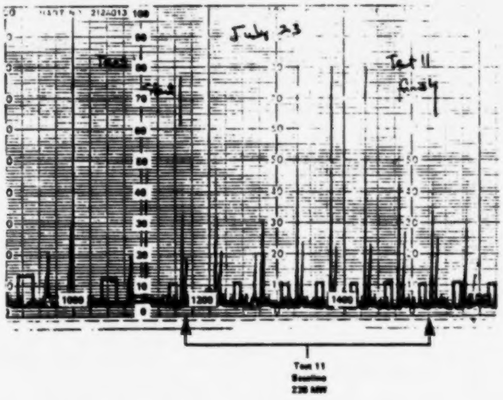

Figure 11

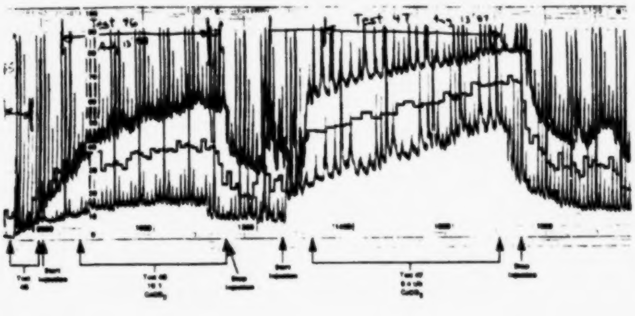

Figure 13

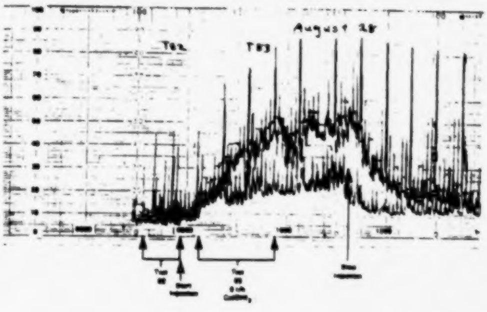

Figure 12

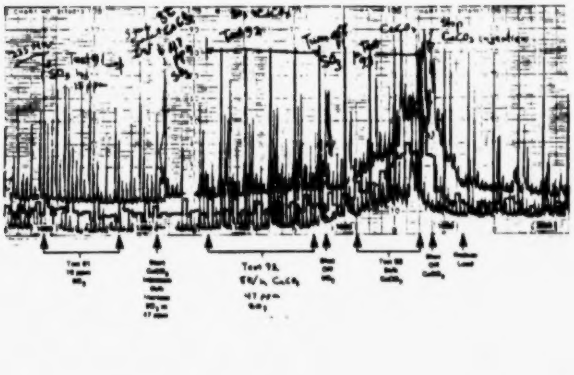

Figure 14

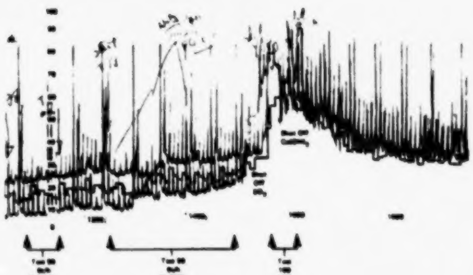

Figure 15 Resistivity in accordance with IEEE Standard 548-1984, ascending and descending modes. Lakeview Sorbent Injection Tests, Phase 3

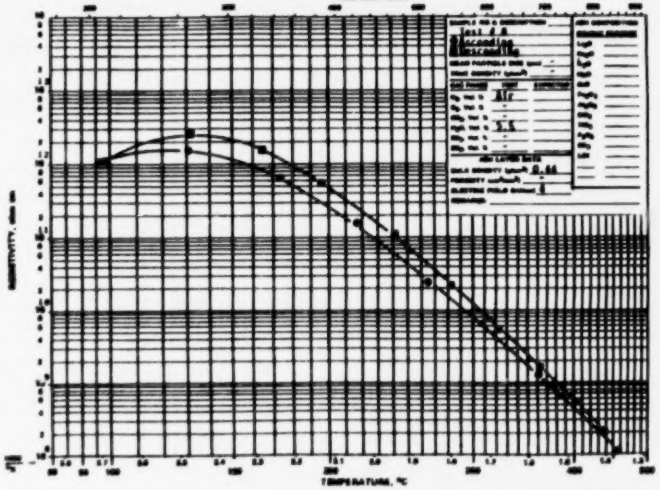

Figure 16 Resistivity in accordance with IEEE Standard 548-1984, ascending and descending modes. Lakeview Sorbent Injection Tests, Phase 3

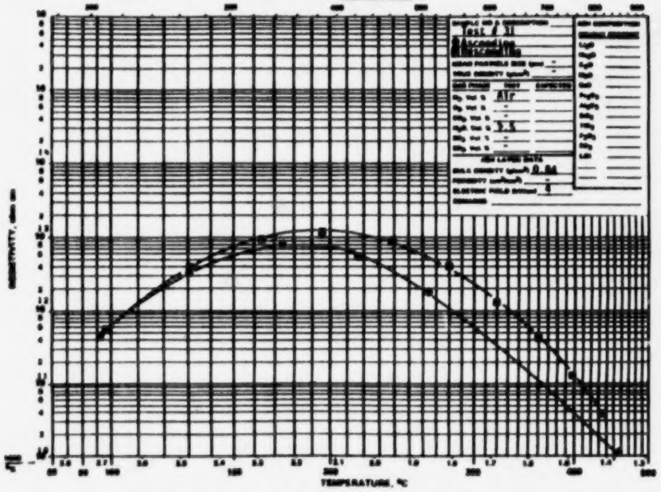

Figure 17 Resistivity in accordance with IEEE Standard 548-1984, ascending and descending modes. Lakeview Sorbent Injection Tests, Phase 3

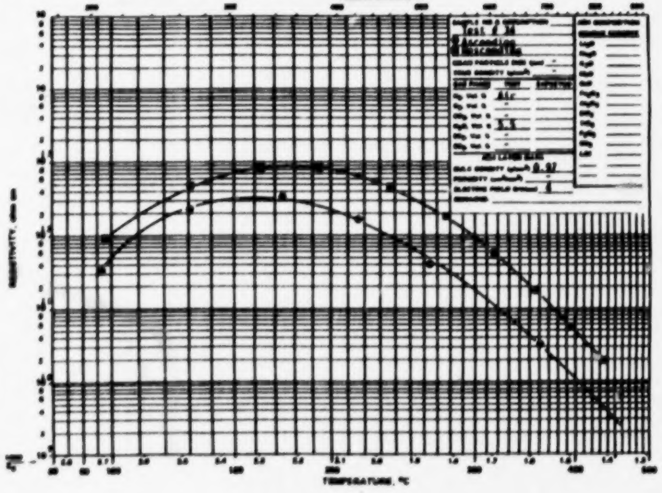

Figure 18 Resistivity in accordance with IEEE Standard 548-1984, ascending and descending modes. Lakeview Sorbent Injection Tests, Phase 3

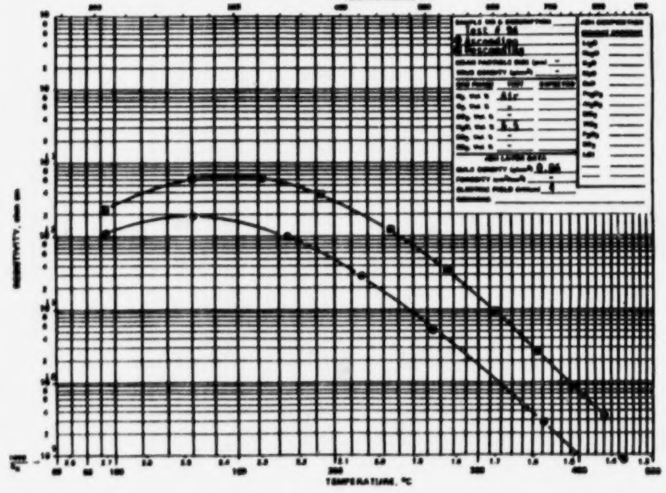

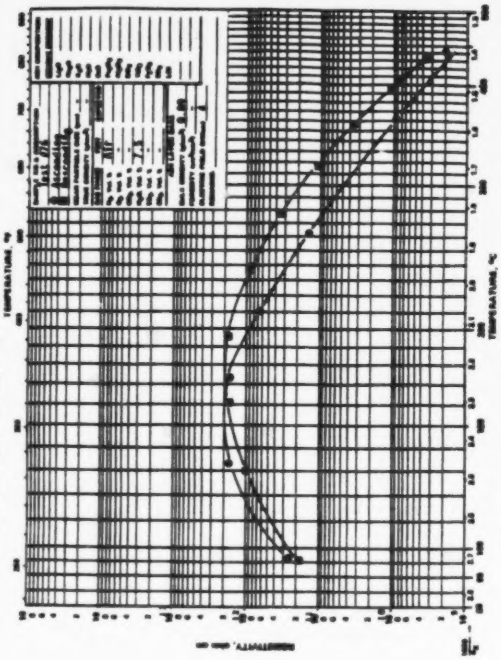

Figure 20 Resistivity in accordance with IEEE Standard 548-1984, ascending and descending modes. Lakeview Sorbent Injection Test, Phase 3.

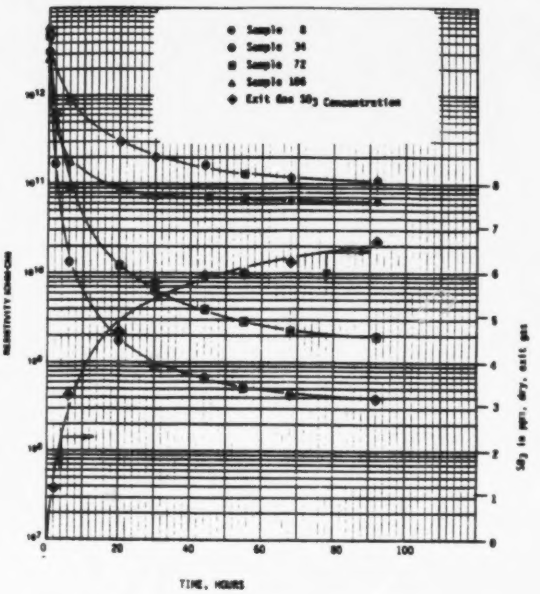

Figure 22 Resistivity as a function of exposure time to an air environment containing 7.5% water and an inlet concentration of 9 to 10 ppm sulfur trioxide.

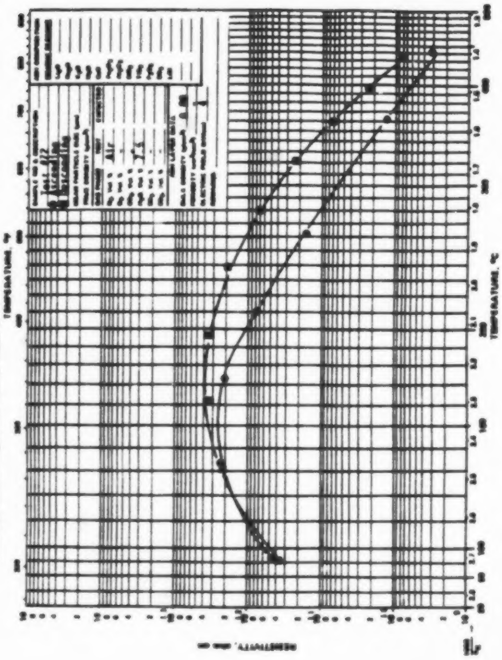

Figure 19 Resistivity in accordance with IEEE Standard 548-1984, ascending and descending modes. Lakeview Sorbent Injection Tests, Phase 3.

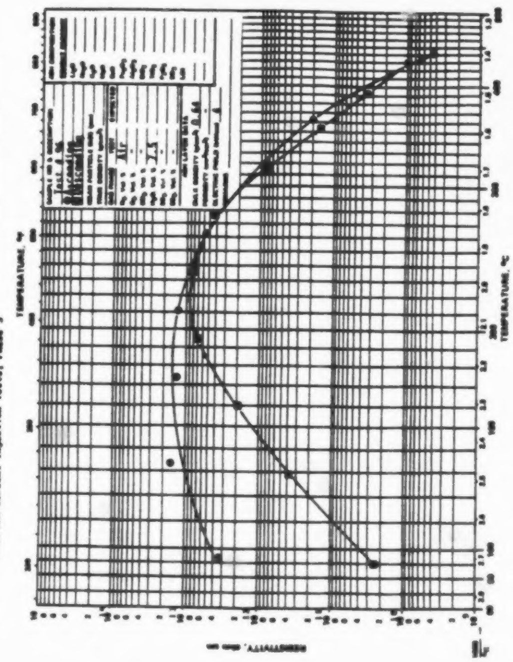

Figure 21 Resistivity in accordance with IEEE Standard 548-1984, ascending and descending modes. Lakeview Sorbent Injection Tests, Phase 3

TABLE 1
PRECIPITATOR RESULTS

	Inlet Dust Loading gr/scf	Inlet Flow acfm	Fly Ash Resistivity ohm-cm	Flue Gas Temperature °F	Carbon Ash (%)	Front Field Power (kVA)	Outlet Loading gr/scf	Stack Opacity (%)	Precipitator Efficiency (%)
Premodification									
1	1.34	480,400	4 x 10^9	290	4.1	–	.0087	11	99.45
2	1.38	442,800	9 x 10^9	284	4.4	–	.0072	13	99.48
3	1.4	464,600	–	281	4.7	43.2	.0087	–	99.38
Baseline									
4	1.28	414,000	–	282	11	32.7	.0034	13	99.7**
6	1.36	408,000	10^7 – 10^{11}	273	15	33.6	.0064	14	99.6**
7	1.37	408,000	–	275	8	38.7	.0087	14	99.4**
11	(1.36)	(400,000)	7 x 10^9	275	9	45.1	.0131	7	99.0
						27	.012	24	99.3
Limestone Injection									
31	2.75	388,000	1 x 10^{12}	288		24	–	33	–
32	2.78	367,000		274		18.7	–	34	–
47	(2.74)	(400,000)		288		30.8	.298	33	89.5
*62	(3.01)	(400,000)		288		25.3	.021	15	99.3
63	(2.89)	(400,000)		288		15	.046	28	98.4
Calcium Hydroxide									
80	(2.36)	(400,000)		270		10.9	.081	21	96.6
83	(2.52)	(400,000)		284		12.0	.077	44	97.0
*90	(2.58)	(400,000)		288		24.8	.0386	24	98.5

*SO_3 Injection **Rappers O/S ( ) Calculated Value

TABLE 2
SUMMARY OF RESISTIVITY MEASUREMENTS

Test	Date	Time	Temperature (°F)	Resistivity (ohm-cm)	Conditions	Coal Sulfur (%)	L.O.I. (%)
6	July 16	8:20	248	8.0*10**10	Baseline		
		9:00	240	2.2*10**11	Lakeview Coal	1.49	15
		10:30	241	4.6*10**7			
		11:00	241	4.5*10**7			
		11:40	290	1.4*10**11			
10	July 22	14:35	271	2.3*10**10	Baseline		
		15:05	270	2.0*10**10	Lakeview Coal	1.48	NA
		15:35	273	1.4*10**10			
11	July 23	9:15	273	6.5*10**9	Baseline		
		10:55	288	7.8*10**9	Lakeview Coal	1.47	9
20	July 27	13:05	288	1.7*10**12	8 t/h CaCO3		
		13:35	307	2.3*10**12	Lakeview Coal	1.41	9.8
21	July 27	14:10	288	4.0*10**12	6 t/h CaCO3		
		14:40	273	1.8*10**12	Lakeview Coal	1.41	NA
32	July 30	14:45	273	7.3*10**11	9.5 t/h CaCO3		
		15:10	281	8.7*10**11	Lakeview Coal	2.19	13.4
		15:40	288	8.8*10**11			
		16:20	288	3.1*10**12			
43	Aug 12	13:20	288	1.3*10**12	8 t/h CaCO3		
		13:45	287	1.9*10**12	Lakeview Coal	1.57	14.8
64	Aug 28	14:20	279	6.8*10**11	7 t/h CaCO3		
		14:45	280	3.8*10**12	Lakeview Coal	1.84	14.1
95	Sept 16	13:00	288	2.2*10**12	8 t/h Ca(OH)2	1.17	NA
96	Sept 16	14:30	275	6.8*10**12	8 t/h Ca(OH)2	1.6	NA
		14:55	280	5.8*10**10	Plus SO3		
97	Sept 17	9:25	291	4.7*10**10	6 t/h Ca(OH)2		
		9:40	294	6.2*10**11	Plus SO3	1.49	NA
		9:55	298	2.0*10**12			
		10:25	303	1.3*10**11			
98	Sept 17	10:40	288	4.8*10**11	8 t/h Ca(OH)2	1.33	NA
		10:55	285	3.8*10**11	Plus SO3		
		11:10	289	1.4*10**11			

TABLE 3
COAL ANALYSIS

	Ultimate As Fired								Proximate As Fired			
Sample	Moisture (%)	Carbon (%)	Hydrogen (%)	Sulfur (%)	Nitrogen (%)	Ash (%)	Oxygen (%)	C.V. (Btu/lb)	Moisture (%)	Vol. Matter (%)	Fixed Carbon (%)	Ash (%)
17	5.48	74.19	5.18	1.88	1.20	6.66	5.40	13,174	5.48	35.73	52.13	6.66
18	6.32	73.82	5.01	1.39	1.26	5.99	6.82	13,001	6.32	35.87	51.82	6.00
24	5.83	73.88	5.12	2.05	1.22	6.33	5.77	13,212	5.83	35.67	52.14	6.36
28	5.48	73.86	5.18	1.92	1.23	6.15	6.07	13,224	5.48	37.48	50.48	6.57
65	5.83	73.41	4.80	1.82	1.32	8.42	4.80	12,814	5.83	33.50	52.33	8.34
66	5.90	72.65	4.84	1.70	1.20	8.29	5.35	13,098	5.90	33.61	52.68	7.81
71&73	6.05	73.40	5.18	1.84	1.21	7.86	5.67	13,120	6.05	34.88	52.61	7.46
87	8.80	68.80	4.37	1.17	1.10	8.44	7.32	11,814	8.8	32.12	49.88	9.20
92	8.11	68.76	4.46	1.19	1.11	8.90	7.41	12,061	8.11	32.53	50.00	9.26

TABLE 4. IDENTIFICATION OF PHASE 3 LAKEVIEW SORBENT INJECTION TEST SAMPLES

Test Number	Date of Test (1987)	Load (MW)	Coal Sulfur (%)	Sorbent	Injection Rate (t/hr)	Ca/S Ratio	SO_3 Injection (%)
8	July 21	235	1.54	-	Baseline test		-
31	July 30	235	2.11	$CaCO_3$	10.0	1.75	-
34	July 31	185	1.83	$CaCO_3$	8.5	2.8	-
72	Aug 25	235	1.73	$Ca(OH)_2$	8.2	2.55	-
76	Aug 26	235	1.63	$Ca(OH)_2$	4.0	1.23	-
94	Sept 15	235	1.23	$CaCO_3$	13.7	4.05	95.5
96	Sept 15	235	1.50	$Ca(OH)_2$	8.6	2.85	93.8

TABLE 5. ELEMENTAL ANALYSIS IN WEIGHT PERCENT AS OXIDES

	#8	#31	#34	#72	#76	#94	#96
Na_2O	0.79	0.40	0.38	0.56	0.52	0.53	0.22
K_2O	1.81	0.76	0.84	1.16	1.18	1.17	0.83
MgO	0.88	0.81	0.94	0.81	0.77	0.87	0.68
CaO	1.20	39.45	32.10	20.31	16.57	17.79	41.75
Fe_2O_3	9.67	10.60	13.24	12.33	13.52	10.34	6.63
Al_2O_3	28.40	13.00	14.20	18.40	18.10	21.00	14.00
SiO_2	54.70	25.20	29.10	40.40	41.90	43.00	26.70
TiO_2	1.33	0.58	0.61	0.80	0.83	0.98	0.65
P_2O_5	0.30	0.30	0.28	0.27	0.41	0.28	0.23
SO_3	0.82	8.60	6.96	4.03	5.12	3.44	7.82
L.O.I.	7.47	8.90	9.29	5.68	5.30	4.18	5.36

Note: Ash analysis performed after L.O.I. test.

TABLE 6. CRYSTALLINE COMPOUNDS IDENTIFIED IN SEVERAL SAMPLES USING X-RAY DIFFRACTION

	8	72	96
Quartz SiO_2	60%	20%	15%
Mullite $3Al_2O_3 \cdot 2SiO_2$	30%	15%	15%
Magnetite Fe_3O_4	10%	10%	5%
Lime CaO		40%	55%
Calcite $CaCO_3$		10%	10%

RAPPING PROPERTIES OF PRECIPITATED ASH/SORBENT MIXTURES

by: M. G. Faulkner
J. P. Gooch
R. Beittel
J. L. DuBard
Southern Research Institute
Birmingham, Alabama 35255-5305

ABSTRACT

The addition of hydrated lime is being investigated as a method of reducing SO_2 in flue gas from pulverized coal combustion. In the case of furnace sorbent injection, the flue gas must be further conditioned to reduce dust resistivity and prevent back corona in an ESP. Prospective users must be able to anticipate the behavior of the collected ash layer when the ESP plates are cleaned by rapping. A study has been performed at Southern Research Institute to compare the rapping characteristics of fly ash and ash/sorbent mixtures on the basis of the rapping accelerations required to clean the ESP plates and of visual observations of the ash layer throughout the collection and rapping process. The measurements were made using a laboratory ESP to collect the dust generated in the SRI Coal Combustion Facility. Two of the tests involved furnace injection of hydrated lime with SO_3 or water conditioning. Another test involved lime slurry injection ahead of the ESP.

This paper has been reviewed in accordance with the U.S. Environmental Protection Agency's peer and administrative review policies and approved for presentation and publication.

INTRODUCTION

A technique currently undergoing investigation for the control of SO_2 in pulverized coal combustion generated flue gas is the addition of hydrated lime. The lime may be added by injection into the furnace (LIMB) or downstream. In either case, the collection of an ash/sorbent mixture in an electrostatic precipitator (ESP) is affected by the higher dust loading and smaller particle size distribution of the dust relative to untreated fly ash. The higher dust loading means more dust to collect which reduces ESP efficiency through space charge suppression of the corona. The smaller size distribution also reduces ESP efficiency as smaller sizes are more difficult to collect. These effects have been extensively studied. However, one of the properties of sorbent laden ash which is important to prospective users and which has not been well studied is the behavior of the dust layer in an ESP when the collection plates are cleaned by rapping. This paper compares the rapping characteristics of conditioned ash/sorbent mixtures to a baseline fly ash (no additives or conditioning) on the basis of the rapping accelerations required to clean the ESP plates and of visual observation of the dust layer throughout the collection and rapping process. The sorbents/conditioning agents tested were LIMB + SO_3, LIMB + water, and downstream addition of a slurry of hydrated lime in water. The measurements were made using a laboratory ESP collecting dust generated by Southern Research Institute's Coal Combustion Facility.

EQUIPMENT AND PROCEDURE

The laboratory ESP used in this work is a single lane ESP having two 66 x 122 cm (26 x 48 in.) collection plates with a total area of 1.6 m^2 (17.5 ft^2) and six corona wires on 15 cm (6 in.) centers. One collection plate was modified for the rapping measurements. As shown in Figure 1, the plate was rapped by dropping a sliding weight onto an anvil which passes through the ESP lid to the collection plate. The anvil contacts both the plate, which is 0.6 cm (1/4 in.) thick to provide rigidity, and the plate's frame. An accelerometer for measuring the rapping impulse is mounted on the outside of the plate in line with the anvil. At a corresponding point on the inside of the plate, two rubber blocks 0.3 and 0.16 cm (1/8 and 1/16 in.) thick are glued to the plate to act as dust depth gauges. The accelerometer and dust gauges were located 13 cm (5 in.) above the bottom of the plate between wires 5 and 6. This location was chosen for visibility from the observation windows located on the test port adaptor and the transition duct as shown in Figure 2. The rectangular windows on the test port adaptor were also used for plate illumination. These windows were kept clean by wipers which were operated from the outside of the ESP. The round window on the transition duct was cleaned by purge air and periodic removal and wiping.

The accelerometer used in this study is a tri-axial unit consisting of three separate uni-axial accelerometers imbedded on the x-, y-, and z-axes of a 2.5 x 2.5 x 1.25 cm (1 x 1 x 0.5 in.) aluminum block. The accelerometer weighs 36 g (1.28 oz). It is attached to the plate by three 4-40 bolts. The signal from each accelerometer axis is taken from the ESP by a co-axial cable and fed into a charge amplifier. The voltage output from the charge amplifier is displayed on a storage oscilloscope.

The relation between rapping weight drop height and plate acceleration was investigated by measuring the signal voltage as a function of drop height. The signal consisted of a damped, rapidly oscillating (1 kHz) voltage (Figure 3). The acceleration due to a rap was obtained by measuring the envelope of the displayed signal at its starting point, in volts, and converting this value to acceleration, in g's, using a calibration factor. The chief source of error in this procedure was irregular signals which required estimation to determine the shape of the envelope. The relationship between the weight drop height and the measured acceleration was fairly constant at a given temperature. However the relationship was very temperature sensitive, as shown in Figure 4. The signal variations due to temperature changes greatly exceeded the accelerometer's specifications and are assumed to be due to variations in the elasticity of the rubber bushings used to mount the plate. This temperature variation emphasizes the need to express the rapping data in terms of plate acceleration rather than in terms of some hardware dependent quantity such as rapper weight or weight drop height.

The ash used in these tests was generated by the Southern Research Institute Coal Combustion Facility. The combustor is a 300 kW (10^6 Btu/h) down-fired furnace which burns pulverized coal to produce fly ash which is very similar to the ash produced by a full-scale utility boiler. During these tests, the combustor burned Pittsburgh No. 8 coal at a rate of 39 kg/h (85 lb/h). Longview hydrated lime was used in all of the sorbent tests. The combustor test configurations for each of the tests are shown in Figure 5. Physical data on each of the tests are listed in Table 1. These are measured data with the exception of the dust loads, which were estimated based on previous tests, and the gas flow data, which were calculated.

The gas temperature at the ESP inlet was kept at about 135°C (275°F) for the baseline fly ash and LIMB + SO_3 tests to avoid variations due to temperature fluctuations. This corresponds to a plate temperature of 124°C (255°F), which is below the dew point of the SO_3. However, there was no evidence of H_2SO_4 condensation as the ash was dry and fragile rather than being wet and sticky. This implies that the SO_3 was entirely taken up by the LIMB ash. The temperature for the tests involving water were much lower at 74°C (165°F) at the inlet and 63°C (145°F) on the plate. Visibility for these tests was obscured by dust bearing condensation on the windows, but no condensation was evident on the collection plates. The difference in the temperatures was responsible for the change in the gas flow rates listed in Table 1.

During the collection of dust, only the last three corona wires were powered in order to increase the collection rate in the observed area of the ESP. When rapping, all six of the wires were powered to reduce the effects of dislodging dust from an unpowered upstream portion of the ESP. The wires were square with concave faces and during dust collection were powered to a negative 48 kV at about 0.5 mA for the baseline fly ash, 0.2 mA for LIMB ash (both SO_3 and water conditioned), and 0.1 mA for the slurry treated ash. The current reduction in the sorbent/ash tests is due to corona quenching caused by the high dust loads present when sorbent was added. As shown in Table 1, these dust loads were approximately triple the dust load for fly ash alone. Both collection plates were rapped clean of ash after each test. The wires were rapped every three to five tests except for the tests involving water, when the wires required rapping after every test.

Only single raps were investigated. The effects of multiple or continuous rapping were not studied in this work. For each rap, the rapping weight drop height and the plate acceleration were measured and the effect on the dust layer was estimated. The acceleration signal on the vertical axis (the direction of the rap) was used in these tests. The signals on the other axes were very similar to the vertical axis signal. The effect of the rap on the dust layer was determined by visually inspecting the plate after the large dust cloud caused by the rap had passed. The fraction of the collecting plate area which had been cleared of dust by the rap was estimated and recorded as the consequence of the rap. This estimation was hindered by the irregular shapes of the remaining dust. Another factor which affected estimation accuracy was nonuniform thickness of the remaining dust due to shearing within the dust layer. This occurred primarily with the LIMB ashes, resulting in greater inaccuracy in the LIMB ash data. The estimated error for evaluating the effects of a rap is 10 percent for the baseline fly ash or lime slurry data. The error for LIMB ashes may be much greater. The scatter in the LIMB data is significantly greater than in the baseline fly ash data.

OBSERVATIONS

BASELINE FLY ASH

Due to the light dust loading with fly ash, the visibility in the ESP with the power off was about 1 m (3 ft). Visibility improved considerably when the ESP was energized. The observation windows accumulated dust slowly and required wiping at roughly 1 min intervals. After 10 min of dust collection, the dust layer presented a mostly smooth appearance with infrequent reentrainment present. The reentrainment took the form of oblong patches of dust about 0.3 to 0.6 cm (1/8 to 1/4 in.) long which appeared to convert into streamers of particles which spewed out from the plate and were swept away by the airstream. This type of reentrainment left characteristic oblong pits in the dust layer. At 20 min, the surface was fairly rough, with pitting reentrainment occurring every few seconds. Dust layer thickness was about 0.16 cm (1/16 in.) at this point. The fly ash rapping tests were conducted after 20 min of dust collection.

When the collection plate was rapped, a dust cloud totally blocked vision of the interior of the ESP. It could not be observed whether any of the dust fell into the hoppers or was recollected. The hopper did accumulate a significant quantity of ash during a day of testing. (The gas velocity was 0.88 m/s (2.9 ft/s), not an unusually high value.) When the plates were visible again it was observed that the remaining fly ash layer had sharp edges and a uniform thickness. A small amount of continued reentrainment occurred around the edges of the remaining dust for several seconds after the plate was again visible, as flakes of dust measuring 0.6 to 1.2 cm (1/4 to 1/2 in.) powdered and spewed into the gas stream. A very thin film of dust was left on the plate after the rapping had removed as much of the dust as possible.

LIMB ASHES

The SO_3 and water conditioned LIMB ashes were very similar to each other. Due to the higher dust loading and finer particle size distribution of these ashes, the plates were not visible at all with the power off. With the power on, visibility was about the same as for the baseline fly ash with the power off. The observation windows accumulated dust quickly and required wiping at about 10 second intervals to maintain adequate visibility. After 10 min of dust collection, the dust layer showed many more pits than the baseline fly ash layer did at 20 min. These pits appeared every few seconds. In addition, fine flakes were blowing off of the surface. At 20 min, the surface appeared very eroded, with fine flakes continuously blowing off of the layer. The dust layer thickness appeared to be about 0.16 cm (1/16 in.) thick at 10 min but, due to the irregular surface produced by the reentrainment, the thickness could not be evaluated at 20 min.

As with the baseline fly ash, rapping the collection plate caused total obscuration of the interior of the ESP. After the rap, the dust remaining on the plate differed from baseline dust in that its surface was very irregular in shape and thickness. The residual dust layer appeared thinner and less rough than before the rap, suggesting that the layer had split rather than separating from the plate. The remaining dust patches were much more difficult to completely rap off of the plates than was the baseline fly ash.

Figure 6 compares the effects of rapping LIMB + SO_3 dust to the baseline fly ash. The estimated plate area which was cleared of dust by the rap is plotted as a function of the measured plate acceleration in the vertical direction. These data are compared on the basis of the same dust layer thickness, about 0.16 cm (1/16 in.), which required 8 to 10 min to accumulate for the LIMB + SO_3 test compared to 20 min for baseline dust. The straight lines in the figure are linear least-squares fits to the experimental data. A comparison of the rapping required for 50 percent dust removal shows that an SO_3 conditioned LIMB dust layer is easier to partially remove than an untreated fly ash layer. However, the figure shows that it is much more difficult to completely remove SO_3 conditioned LIMB ash from the plates than it is baseline ash. This suggests that, although a LIMB + SO_3 dust layer is more fragile than a fly ash layer, and consequently more prone to reentrainment, a more powerful rap will be required to clean the plates. This agrees with the observation that it was more difficult to completely clean the plates of LIMB + SO_3 ash in preparation for the next test.

Figure 7 shows the same data for LIMB + water. Although the behavior of this dust appeared to be the same as the LIMB + SO_3 dust (i.e., a tendency toward spontaneous reentrainment, layer splitting on rapping, and difficulty in completely cleaning the plate), the accelerometer data showed that this dust was easier to rap than the baseline dust. Compared to the LIMB + SO_3 dust, the LIMB + water dust was slightly less fragile (more difficult to rap less than 50 percent) but was easier to rap clean at the 90 percent level. The data do not reflect the difficulty of completely cleaning the plates, as the last few deposits required many hard raps to dislodge. The dust was collected for 8 min for a deposit thickness of 0.16 cm (1/16 in.). During the LIMB + water tests, mud formed on the uninsulated ESP windows. However no evidence of condensation within the ESP was observed.

The LIMB + water tests differed strongly from the baseline and LIMB + SO_3 tests in one respect: the wires rapidly accumulated a thick coating of dust. Wire deposits were not a problem during the baseline and LIMB + SO_3 tests, and the decision to rap the wires every three to five tests was made because some deposits were visible. The wires in the LIMB + water tests were completely coated in dust at the end of each 8 min test. By letting the wires go without rapping for 20-30 min, it was possible to build up very thick coatings, approaching 2 cm (3/4 in.) in diameter in some cases. The wire coating broke fairly easily but, due to the geometry of the ESP, was difficult to rap off. The coatings occurred only on the wires that were energized. The wires that were turned off showed no significant dust accumulation.

HYDRATED LIME SLURRY

The dust formed when lime slurry was used to condition the flue gas resembled the LIMB ashes in that visibility was poor and the collection rate was high due to the high dust load. This dust was also collected for 8 min for a 0.16 cm (1/16 in.) thick dust layer. However, the lime slurry dust layer differed from the LIMB dust layers in that it was very well behaved. The spontaneous reentrainment shown by the LIMB dusts was absent and the surface appeared smooth and free of pits. Chemical analysis showed that the dust collected on the plate was more uniform in composition than the LIMB dusts, being primarily calcium hydroxide. This may have contributed to the greater stability of this dust compared to the LIMB dusts, which were a mixture of calcium compounds. When rapped, the dust layer broke free without splitting and it was not difficult to rap the plate clear of all ash. The rapping efficiency data are shown in Figure 8, where it can be seen that this dust is uniformly easier to rap than the baseline fly ash. Like the LIMB + water dust, this dust collected on the wires very quickly, requiring wire rapping after each test. Also like the LIMB + water dust, mud formed on the uninsulated windows, although none was observed on the plate.

CONCLUSION

This study has compared the dust collection and rapping characteristics for a baseline fly ash and for the ash with the following additives: LIMB + SO_3, LIMB + water, and a slurry of hydrated lime in water. The comparison was made based on operator observations of the dust behavior and on rapping accelerations measured on the collection plate. Figure 9 shows the rapping efficiencies for all four test conditions. By comparing the curves, it can be seen that (for low accelerations) the LIMB ashes dislodge more dust than the slurry treated ash or the baseline ash. The curves do not show the manner in which the dust leaves the plate. The fragile LIMB ash layers split, leaving a thinner layer adhering to the plate while the outer portion was reentrained. By contrast, the more stable baseline and slurry treated dusts did not split but broke cleanly down to the plate, with portions of the dust either clinging to or leaving the plate. At the other end of the curves, it can be seen that the dusts which involve water addition require the least rapping to completely clear from the plate, followed by the baseline ash, and then by LIMB ash with SO_3, which was very difficult to clean from the plate. Some of the observations made on the dust layers are summarized in Table 2.

Based on this study, at least two observations can be made. 1) Unless the corona discharge in the ESP is severely suppressed, the higher dust loading with a treated ash will result in faster dust layer growth. 2) A conditioned LIMB dust layer is more fragile than an untreated or slurry treated fly ash layer, with the consequence that the LIMB dust layer tends to spontaneously reentrain more frequently. These observations suggest that sorbent treated ash needs rapping more often than fly ash.

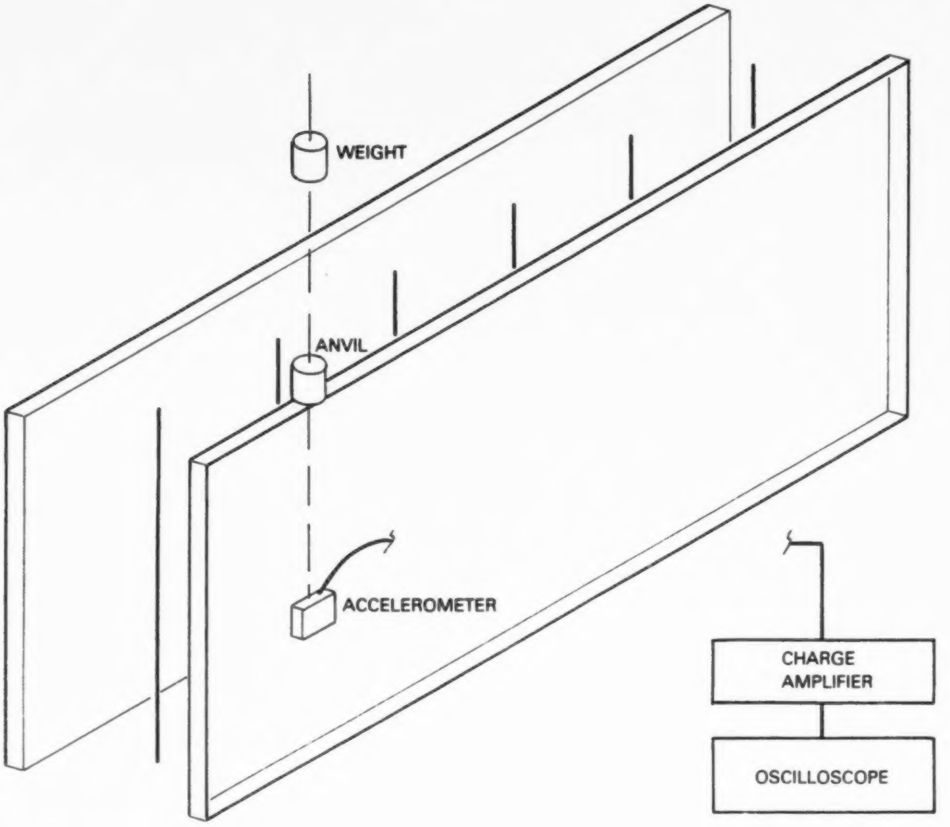

Figure 1. Schematic of ESP showing rapping weight and plate-mounted accelerometer. Signals from the accelerometer were amplified by a charge amplifier and displayed on a storage oscilloscope.

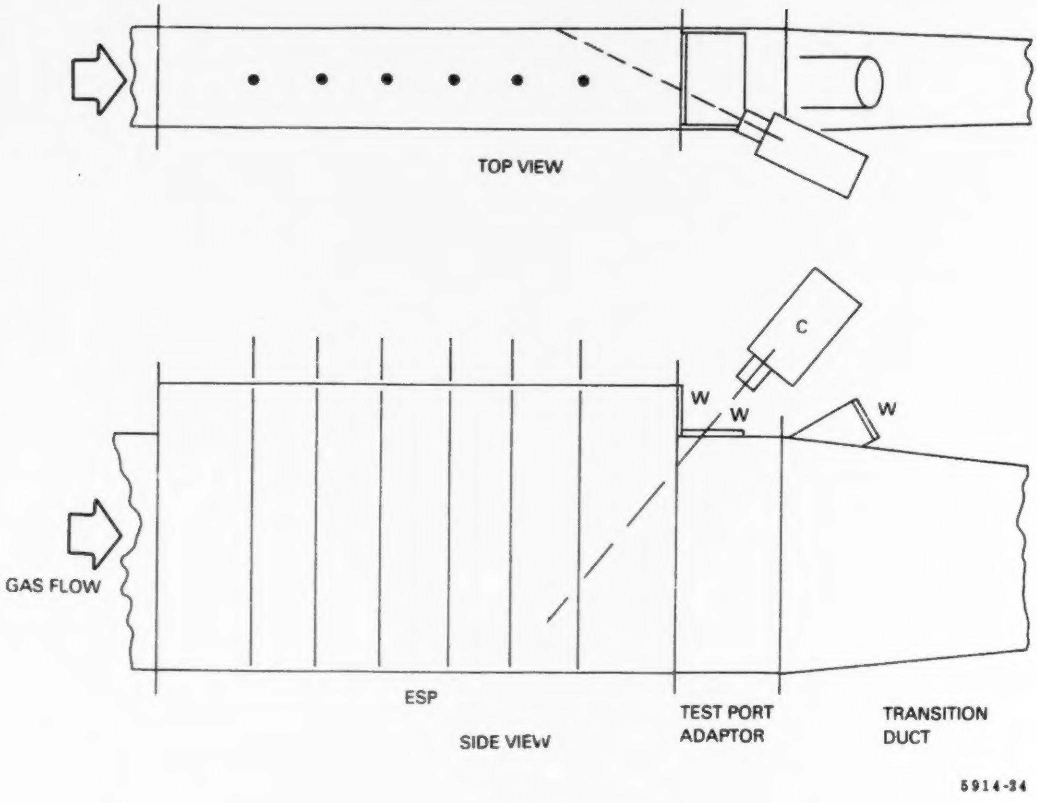

Figure 2. Schematic of ESP showing direction of viewing through rectangular and round windows W. For some tests viewing was by video camera C.

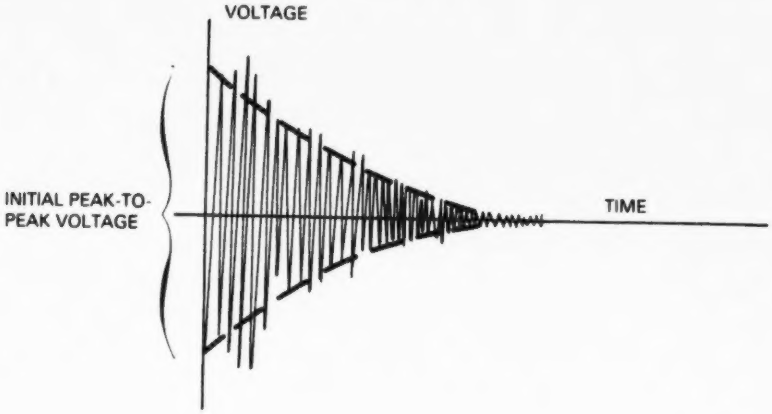

Figure 3. Simulated oscilloscope display showing the method of estimating the initial acceleration voltage.

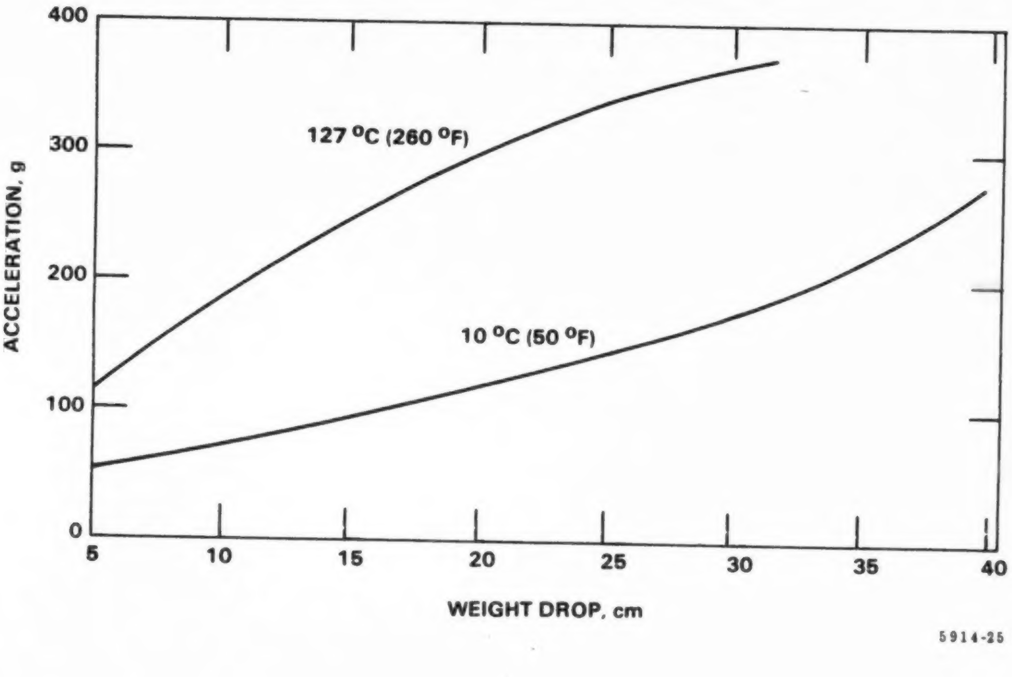

Figure 4. Plate acceleration as a function of weight drop distance at two temperatures.

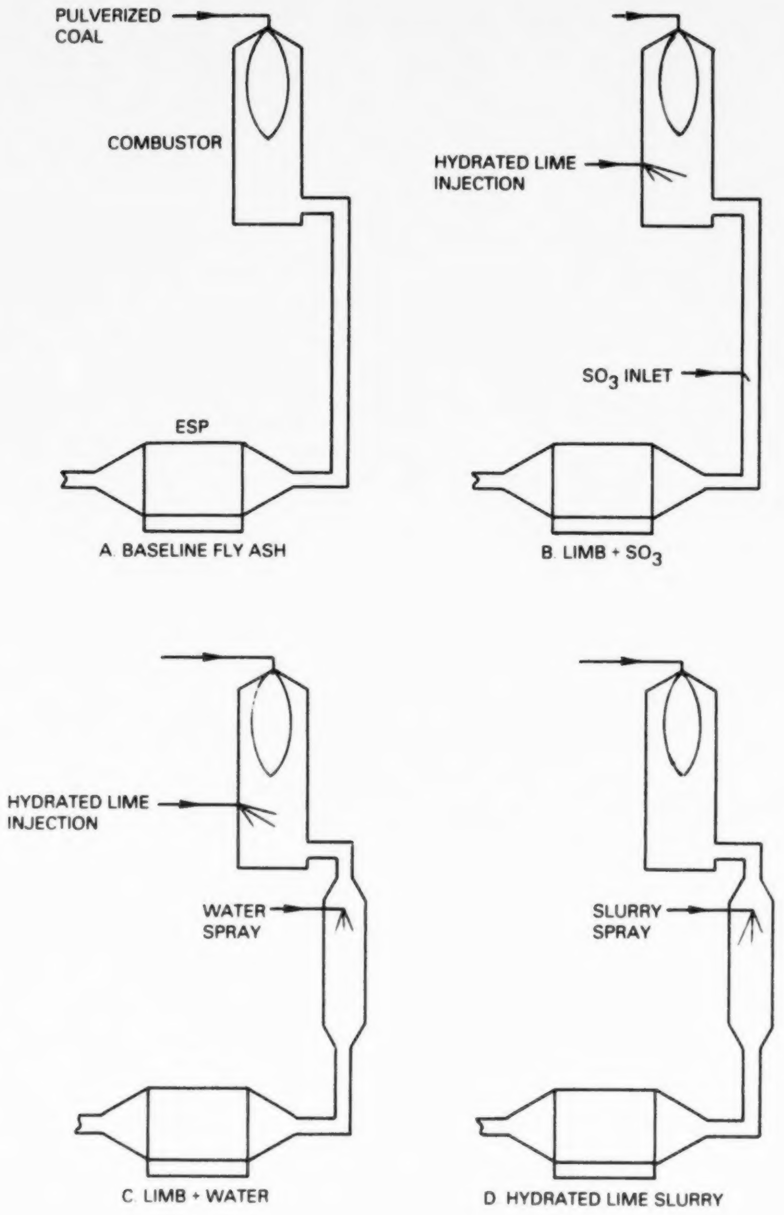

Figure 5. Coal combustor test configurations for plate rapping experiments using fly ash + sorbent + conditioner.

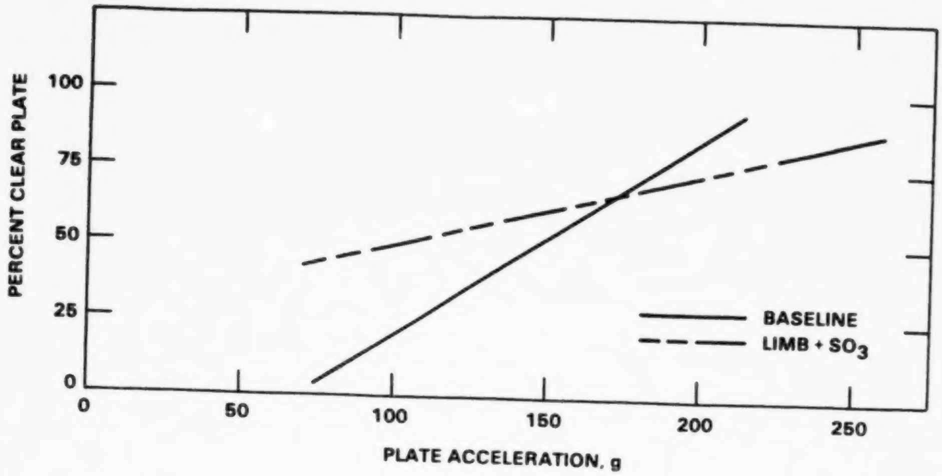

Figure 6. Rapping efficiency as a function of plate acceleration for SO_3 conditioned LIMB ash.

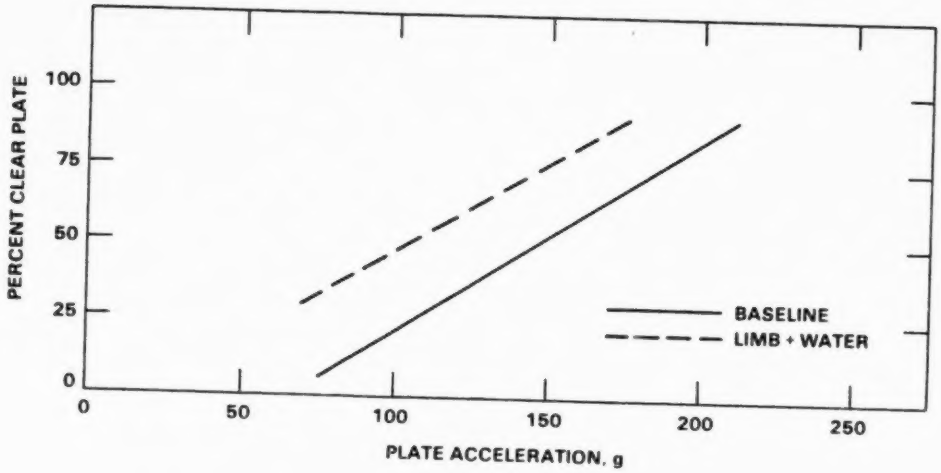

Figure 7. Rapping efficiency as a function of plate acceleration for water conditioned LIMB ash.

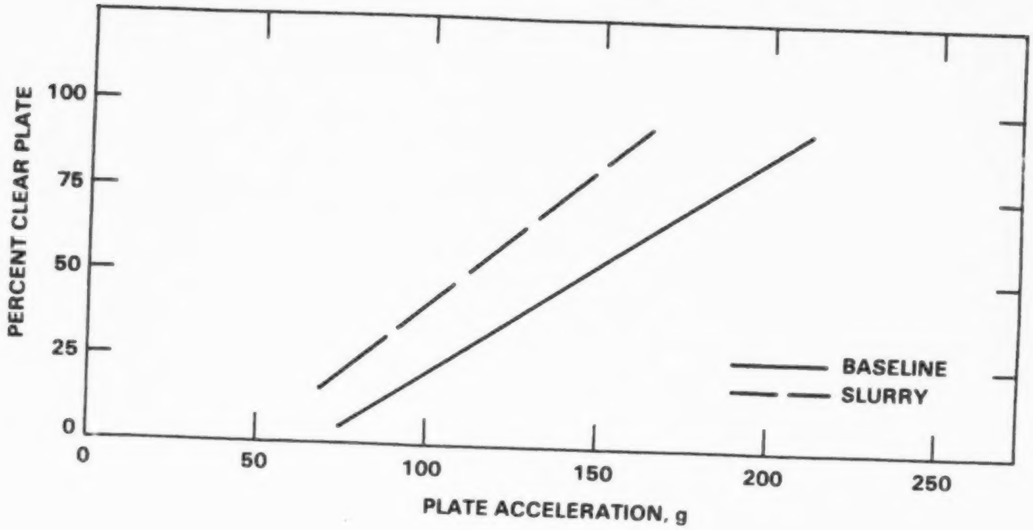

Figure 8. Rapping efficiency as a function of plate acceleration for hydrated lime slurry conditioned fly ash.

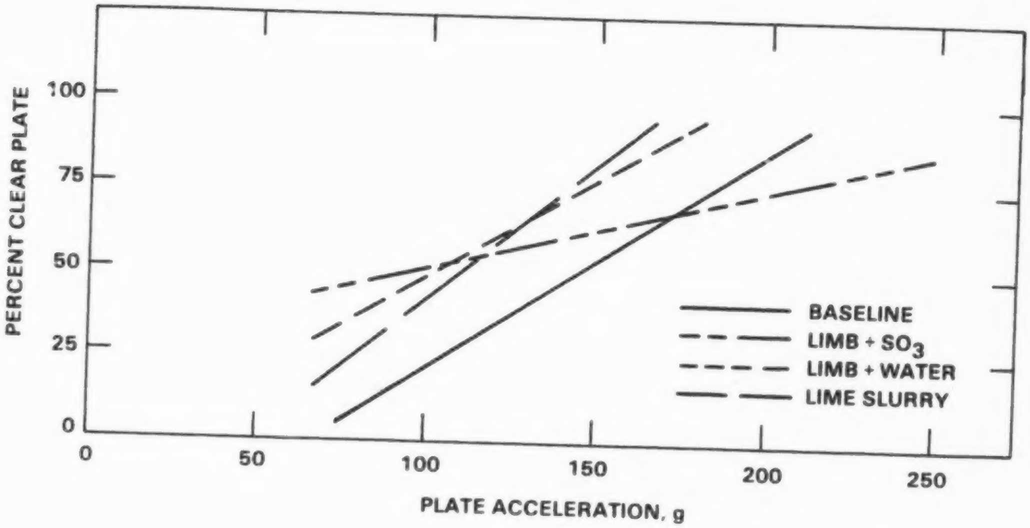

Figure 9. Rapping efficiency as a function of plate acceleration for four test conditions.

TABLE 1. TEST DATA

	Baseline	LIMB + SO_3	LIMB + water	Slurry
Sorbent feed rate, kg/h	--	5	4	4
(lb/h)	--	(11)	(8.8)	(8.8)
Ca/S ratio	--	2	1.5	1.5
Amount of conditioner, ppm	--	100	--	--
Approach to saturation, °C	--	--	22	22
(°F)	--	--	(40)	(40)
Estimated dust load, g/dscm	7	21	21	21
(gr/dscf)	(3)	(9)	(9)	(9)
In situ resistivity, ohm-cm	7×10^{10}	3×10^{11}	7×10^{11}	6×10^{10}
ESP gas flow rate, m^3/min	9.9	9.9	7.8	7.8
(acfm)	(350)	(350)	(275)	(275)
ESP gas velocity, m/s	0.88	0.88	0.70	0.70
(ft/s)	(2.9)	(2.9)	(2.3)	(2.3)

TABLE 2. OBSERVED PROPERTIES OF THE ASH LAYERS

Test type: fly ash +	Baseline (no additives)	LIMB + SO_3	LIMB + water	Slurry
Ash deposition rate	slow	fast	fast	fast
Ash layer stability	good	delicate	delicate	good
Reentrainment	moderate	much	much	little
Wire deposits	slow	slow	fast	fast
Rapping (1 = easiest, 4 = hardest)				
Partial rap	4	1*	2*	3
Complete cleaning rap	3	4	2	1

* Layer splitting was present.

PRECIPITATOR PERFORMANCE ON A 130 MW COAL FIRED ATMOSPHERIC FLUIDIZED BED BOILER RETROFIT

by: John Larva, Northern States Power
Thomas Willkomm, Northern States Power
Thomas Lugar, General Electric

Northern States power Company
Black Dog Plant
1400 Black Dog Road
Burnsville, MN 55337

General Electric Environmental Services, Inc.
Lebanon, Pennsylvania 17042

ABSTRACT

The Black Dog project is a 130 MW atmospheric fluidized Bed combustion (AFBC) boiler retrofit. Initial AFBC retrofit operation was in July of 1986. Particulate emissions control is with the original two sets of precipitators: 1954 and 1974 vintage. The paper describes the performance of the precipitators using various coal blends, bed material, and performance enhancements. Intermittent power supply timers, microsecond pulse energization and water injection were tested.

The work described in the paper was not funded by the U.S. Environmental Protection Agency and therefore the contents do not necessarily reflect the views of the agency and no official endorsement should be inferred.

INTRODUCTION

On March 2, 1988, Black Dog Unit 2 was operated at its maximum rating of 130 MW for the first time. In addition, the unit operated at maximum rating without excessive opacity excursions--the particulate emissions were estimated to be near the unit operating permit limit of 0.04 lbs/MBTU. The success of the high load operation came after a long list of ESP enhancements. This paper is mostly about pulse energization because that is what we have had the most success with.

Here's a partial list of the different areas the plant has pursued:

- Fired clay bed material
- Higher sulfur coal blends
- Ash recycle optimization
- Improved boiler operation (low excess air)
- Improved air heater thermal performance
- Improved rapper effectiveness
- Barbed wire electrodes
- Intermittent energization controls
- Pulse energization
- Water injection

Since the above list breaks down into either a boiler or precipitator related item, we have chosen to group and discuss them accordingly.

BOILER RELATED ACTIVITIES

CLAY BED MATERIAL

Initially the method of startup of the fluidized bed using limestone resulted in poor precipitator performance due to excessive inlet ash fouling and ash chemistry not conducive to effective particle charging and collection. This problem was eased somewhat by replacing limestone in the bed with fired clay, an inert bed material that would not effect the chemical composition of the flyash produced in the combustion process. Limestone would be added as needed to reduce sulfur dioxide emissions by injection during the coal combustion process rather than using a limestone bed. However, the fired clay injected just prior to and during startup was highly resistive and voltage-current characteristics indicated back corona was present even at low temperatures. See TABLE 1. After a few startups with clean ESP's, the precipitator V-I curves indicate back corona was very well established. See Figures 1 and 2.

HIGHER SULFUR FUEL BLEND

Since the other pulverized coal (PC) units in the plant also use ESP's and burn a 1.5 % sulfur coal blend, it was thought the higher sulfur coal blend may cause some improvement in precipitator performance. The first stack test was run with this blended coal. The results were not encouraging: almost 3 times the allowed particulate emissions at 78 % of maximum unit rating. See TABLE 4 which contains data from the 3-6-87 test. Later tests have shown that the plant's normal low sulfur,low cost coal (0.3 % sulfur) collects as well as the higher sulfur blend when fired in the AFBC boiler. No limestone addition is required to meet the plants sulfur emission limit when burning the low sulfur coal.

ASH RECYCLE OPTIMIZATION

Ash recycle is used at the plant primarily to improve combustion efficiency. The recycle system was not installed when the unit started up and its checkout lagged the boiler start-up by about a year. When the system was finally operated in 1987, it caused opacity problems. Later investigations showed the timing of the lock hoppers caused ash to be blown back into the boiler ducts from the ash hoppers. The timing problem was corrected and the recycle rate now significantly affects opacity to a large extent only during periods of soot blowing.

IMPROVED BOILER OPERATION

Since gas flow through the ESP is directly proportional to the boiler excess air, the plant was concerned when boiler problems caused greater than design excess air values to be used. Tramp air has been a problem with the unit since start up. Progress has been slow in reaching design conditions because equipment like dampers may require redesigning or replacement. In addition, the air flow measuring system has had some reliability problems and is presently being worked on. A project is presently underway to estimate various tramp air sources and take corrective action where possible in order to reduce air requirements to a minimum.

IMPROVED AIR HEATER PERFORMANCE

When the unit started up for the first time, the air heater gas outlet temperature at 85 % of maximum load, was 340° F. That is about 100° F more than the ESP was designed for, and many of the ESP problems have been caused by this higher temperature. A unit outage was taken early this year to plug hot gas bypass gaps around the air heater rotor baskets. An additional soot blower was also installed to clean the rotor from the top side. The gases leaving the air heater are now about 30° F cooler than before and the result is noticeable in ESP performance. The maximum load test run on 3-2-88 was largely the result of the improved air heater performance. The plant's goal still remains unchanged: to lower the air heater gas outlet temperature to its design value of 238° F and take advantage of the lower ash resistivity. See TABLES 1 and 2.

PRECIPITATOR RELATED ITEMS

IMPROVED RAPPER EFFECTIVENESS

Initial unit operation indicated the high resistivity ash was going to place heavy demands on the ESP plate and wire cleaning systems. Since even a small layer of ash causes lost performance, the plant wanted to assure itself that it was getting the best cleaning possible. Accelerometer tests were run on the plate and wire rapper system. Changes were later made based on these results. Inspection results are not yet conclusive, but it's likely more work will be required to provide acceptable long term cleaning.

BARBED WIRE ELECTRODES

Ash buildup on the wire electrodes has been identified with the (one start) voltage-current curves shown in Figure 1. The ESP voltage would be very high and the current very low. The barbed wires have largely eliminated this condition but they tend to operate at a lower voltage than normal wires. See Figure 10. Also, the barbed wire may not perform well with pulse energization, thus limiting their use to the inlet fields where pulse systems are less necessary.

INTERMITTENT ENERGIZATION

All twelve transformer/rectifier controllers were retrofit with intermittent energization timers. Based on opacity readings, the timers improved the ESP collection efficiency under the high resistivity ash conditions--6×10^{11} ohms-cm or greater. A comparison between pulse energization and intermittent energization (I/E)is seen in Figure 6. Because the unit's emissions were so much greater than desired, and the I/E showed so little improvement compared to the pulse energization system; no future testing with it is planned.

PULSE ENERGIZATION

PULSER TEST PROGRAM

Since the precipitator operating conditions fit the criteria for application of pulse energization to improve performance, NSP contracted with General Electric Environmental Services, Inc. (GEESI) to conduct a pulse energization test program with their mobile pulser system. The pulse energization data base (references (1) and (2)) indicated that the plant could expect to meet compliance conditions at a much higher maximum load using pulse energization.

THE CONCEPT OF PULSE ENERGIZATION

Pulse energization is a modification of a conventional precipitator power supply output whereby short high voltage pulses are superimposed on the existing precipitator power supply DC output. Pulsing addresses the problem of reduced ESP collection efficiency when collecting high resistivity particulate. If the resistivity is too great, back corona and premature spark-over at low applied voltages will occur due to the large relaxation time constant of the dust particles. The key to overcoming this condition is to decrease the current density to lower the voltage drop through the ash layer on the collecting electrode. This can be done by applying short high voltage pulses with a relatively long duration between the pulses. The pulses, approximately 150 microseconds in duration, are applied to a base DC voltage provided by the existing power supply. The existing power supply is maintained at a level just below the onset of sparking or back corona. The base DC voltage provides a constant electric field to maintain ion and particle migration toward the collecting plates. Between the pulses, the charge on the dust layer surface decays decreasing the average current density below a point where back corona would form. Thus the fundamental operating principle of pulse energization is an increased spark voltage level with back corona suppression by turning on and turning off the corona discharge at a predetermined rate. The superimposed pulse frequency and amplitude are adjusted for each particular application to achieve the highest pulse amplitude without the formation of back ionization.

Figure 3 is a basic schematic of the pulse power supply. A thyristor switch having a reversed conducting feedback diode supplies energy stored in C1 to the primary winding of a pulse transformer. The precipitator capacitance is reflected into the primary winding to act with inductor L1 as a series resonant, commutating circuit for the thyristor switch. The voltage is stepped up in the pulse transformer and is coupled to the precipitator through capacitor C2. A DC reference voltage is supplied by the existing DC power supply. The pulse voltage waveform and pulser output parameters are shown on Figure 3.

MOBILE PULSER DEMONSTRATION SYSTEM

Field testing of pulsing was accomplished using a specially designed mobile pulse demonstration system. Four pulse power supplies, mounted on a 48 foot (14.6 m) long flat bed trailer, are capable of energizing a total of 220,000 ft^2 (20,438 m^2) of collecting plate area. Also included on the trailer is a control room housing control cabinets for the pulsers and four 90 KVA transformer-rectifiers with linear reactors. The pulser trailer is shown in Figure 5. The mobile pulser system utilizes its own reference transformers instead of those on the precipitator due to the need for the pulser automatic controller to interface with the reference T/R controller. In retrofit applications the existing precipitator's transformers are used.

PULSE POWERING ARRANGEMENT

The conventional powering arrangement of Unit #2 is shown in Figure 4. Since the pulser trailer has four pulser systems, all three precipitators could not be pulse energized. Due to the enhanced collection of fine particulate with pulse energization, pulsing was applied to the downstream secondary precipitator. The upstream primary precipitators remained conventionally powered. After three months of successful pulser operation and optimization under a variety of precipitator operating conditions, additional pulsers were leased from GEESI. The additional pulsers power the primary precipitators to obtain additional performance enhancement for the state compliance tests. The pulse powering arrangement for the compliance tests is shown on Figure 4.

Tie in of the mobile unit pulsers utilized a dry high voltage insulated cable run from the output of each pulser to the precipitator electrical field at the existing transformer switch gear enclosure on the precipitator roof. Each pair of fields perpendicular to gas flow to be pulsed were linked together using short segments of dry insulated cable. The two leased pulsers were permanently mounted with pipe and guard connection.

PRECIPITATOR PERFORMANCE RESULTS WITH PULSING AND WATER INJECTION

Without pulse energization Unit #2 is unable to maintain ash emissions under 0.04 lbs/MBTU without drastic load reduction, i.e., to approximately 50MW. See TABLE 4. Low load tests indicated the collection efficiency was low even for relatively large particles. See TABLE 6. The results from the March 3, 1987 and the August 17,1987 tests indicate the pulsing reduced the emission rate from 0.117 to 0.036 lbs/MBTU at 100 MW's. Using pulse powering and water injection during the State of Minnesota compliance tests reduced emissions further to 0.027, 0.024, 0.022 lbs/MBTU at 106 MW. State compliance requires 0.04 lbs/MBTU. Based on prior tests (TABLES 7 and 8), the plant was not certain the unit would pass its emission test at full load so the unit was run at its present power pool rating of 106 MW. The test results are also significant due to the following test conditions:

- Eleven out of twelve recycle hoppers were in service during the testing.
- Due to air heater problems, precipitator flue gas temperatures and volumes were higher than design.

The effect on performance improvement with the primary ESP pulsed was significant. See TABLE 3. Prior to the addition of pulsers, the primary ESP's performance was severely degraded with low power levels and back corona. See TABLE 10. With pulse energization, the primary ESP is now performing as an upstream precharger with a much greater efficiency. The extra dust being collected in the fields of the primary precipitator also helps the downstream secondary precipitator operate at higher power level due to the lower dust loading.

WATER INJECTION

After startup, the plants greatest need was to bring the unit into compliance by offsetting the air heater design problems,i.e., the air heater gas outlet temperature being 100° F higher than expected at high loads. Although other AFBC plants have reported some success with their ESP's when operated at flue gas temperatures similar to the Black Dog plant's (reference (3)), the unit 2 precipitators were not working well at high loads and some conditioning was required. Several systems were considered before deciding on water injection. The requirement for over night shut downs on unit 2 limited the possible choices to a few systems. Also, the plant believes there will be no need for a flue gas conditioning system at full load once the final air heater is operating according to design--238° F air heater gas outlet at full load. The following are details on the original water injection system:

- 5 probes on each flue gas duct (two ducts)
- 5 spray nozzles on each probe (50 for two ducts)
- Normal spray rate at 100 MW: 40 gpm total
- Normal flow for the North and South probes: 15/25 gpm
- Air pressure at probe inlet: 110 psi
- Air flow rate: 2000-2500 SCFM for the whole system
- Sauter mean droplet diameter: 15 micrometers
- Direction of spray gas flow at point of nozzles: mostly vertical, located between flow straightener plates.
- Gas flow at spray nozzle location: upward

The plant has had problems with the above system. Wet ash began to build up on the duct walls and cross bracing. Gas distribution was affected, but the plugging was not complete enough to cause a high pressure drop and limit load. Some duct cross bracing has since been removed to prevent ash buildup. Future plans call for depending on the water injection only when there is no alternative. During an outage early in 1988, improvements were made to the air heater that increased its efficiency. The unit can now reach 130 MW (full load) with only 20 gpm of spray. A total of 4 out of a possible 10 probes were used during the test. A single 1000 SCFM air compressor supplied the atomization air requirement. See figures 8,9, 10 and TABLE 4.

SUMMARY AND CONCLUSIONS

Considering the capital requirements and the minimal risk associated with the on-site demonstration option, pulsers could be the ESP enhancement method of choice for many retrofit applications. If more ESP efficiency is needed at peak loads than pulsers can provide, a limited scale water injection system could be used in combination with the pulsers. Before the Black Dog unit was converted to an AFBC, it had a 100 MW rating. The plant's testing to date at 100 MW indicates the existing ESP's could be expected to meet new source performance standards under the following conditions: (1) no increase in maximum rated load is planned and (2) low sulfur coal is used--no limestone addition required. Additional testing will include using limestone with a higher sulfur coal blend and more air heater modifications.

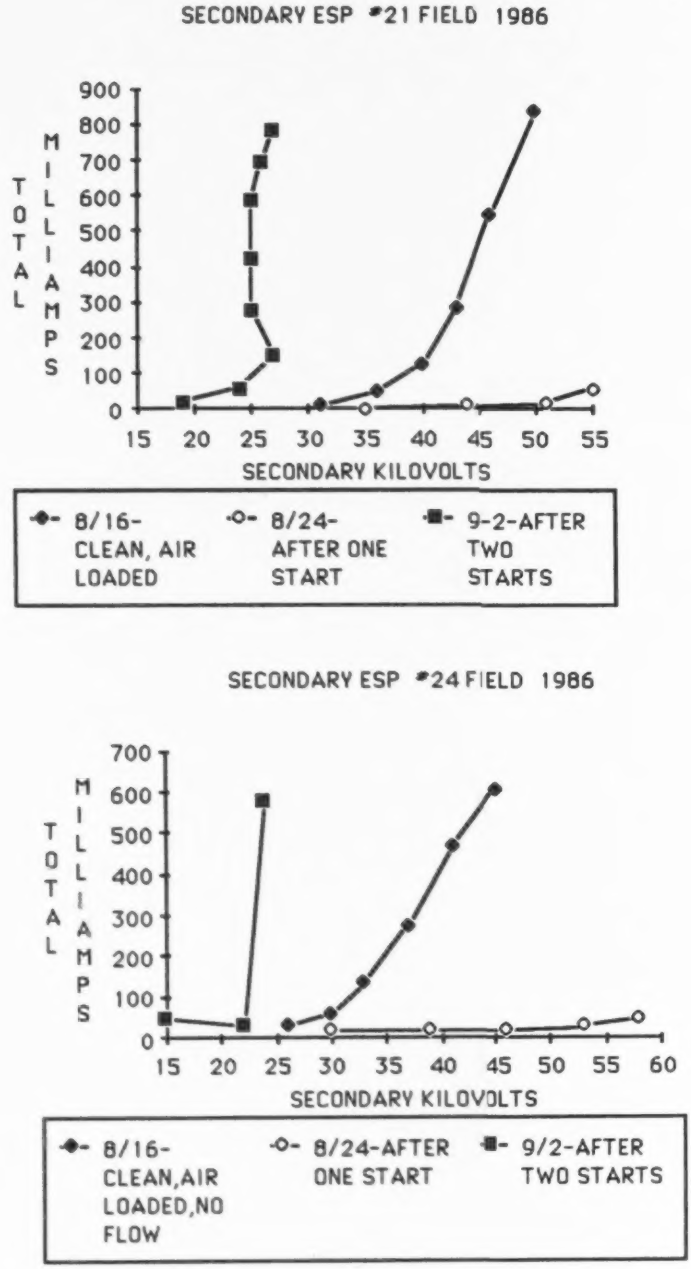

Figure 1. Voltage-current curves taken when unit was off line.

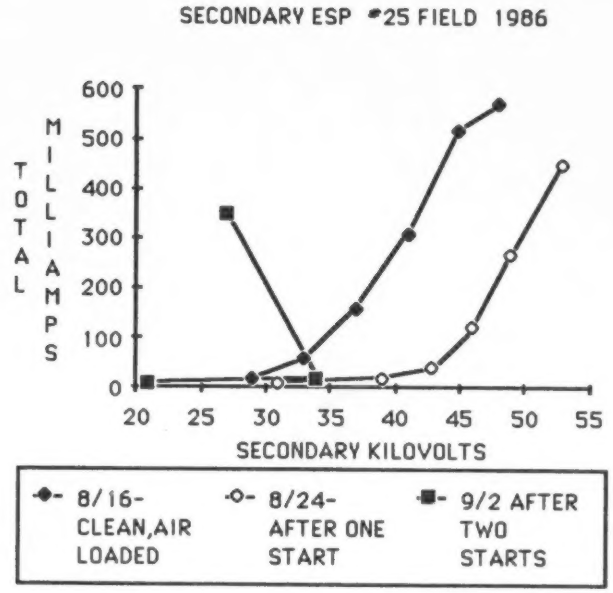

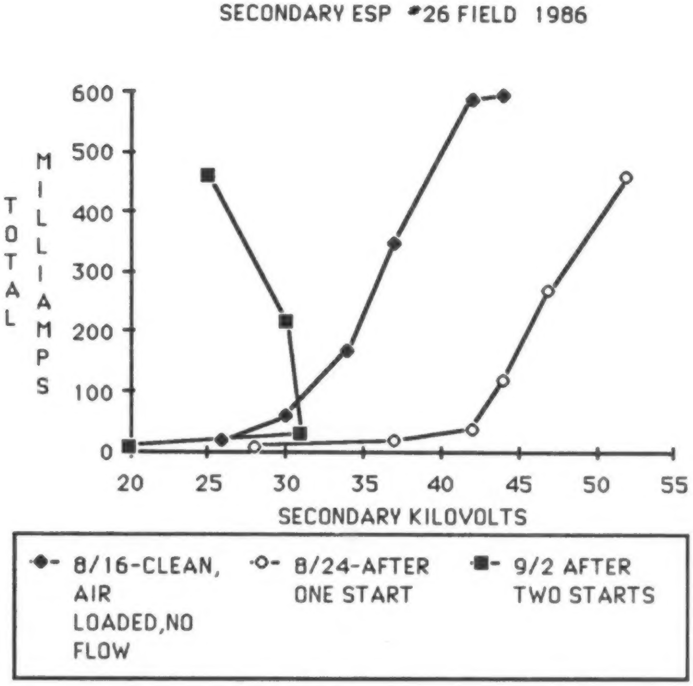

Figure 2. Voltage-current curves taken when unit was off line.

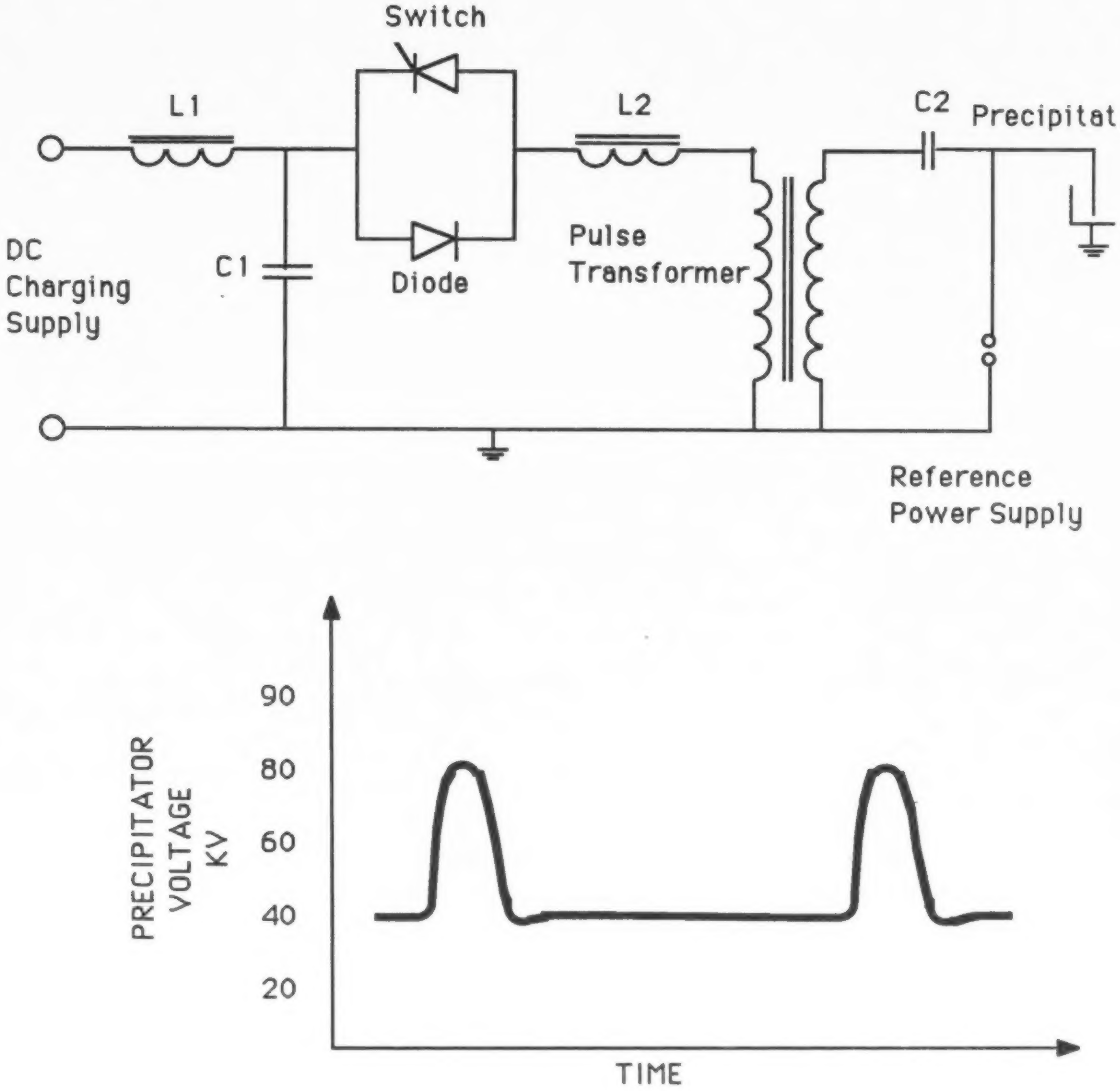

Power Capability	- to 55,000 sq. ft.
Pulse Width	- 120 to 500 microseconds
Pulse Repetition Rate	- 1 to 120 HZ
Maximum Pulse Voltage	- 50KV
DC Reference Voltage	- to 40 KVC
Maximum Combined Voltage (Pulse + Reference)	- 80 KV

Figure 3. Schematic diagram of pulser circuit and waveform.

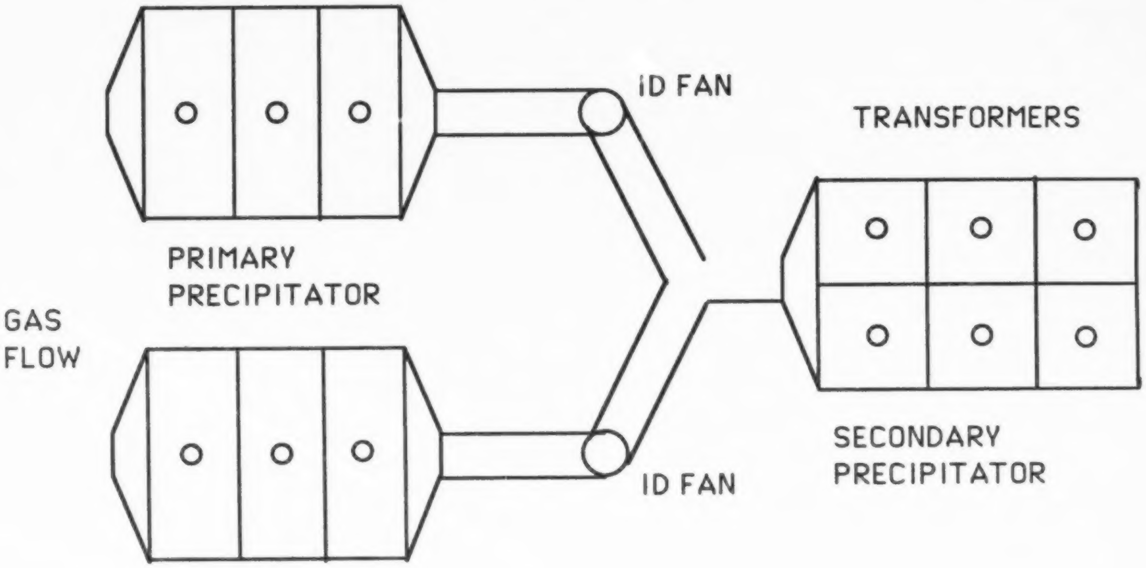

Research Cottrell Precipitator

Two Boxes, Three Fields/Box
Plate Height -20'
Total Plate Area - 62,000 sq ft
10,000 ft Plate Area/Field
SCA = 125
6 Transformers/Rectifiers
MIGI Rappers

Belco Precipitator

Three Fields In Depth, Three Cell
Plate Height - 30'
Total Plate Area - 97,000 sq ft

SCA = 194
6 Transformer/Rectifiers

Total SCA = 320

Figure 4. The original Black Dog Unit 2 precipitator configuration before the pulser system was added.

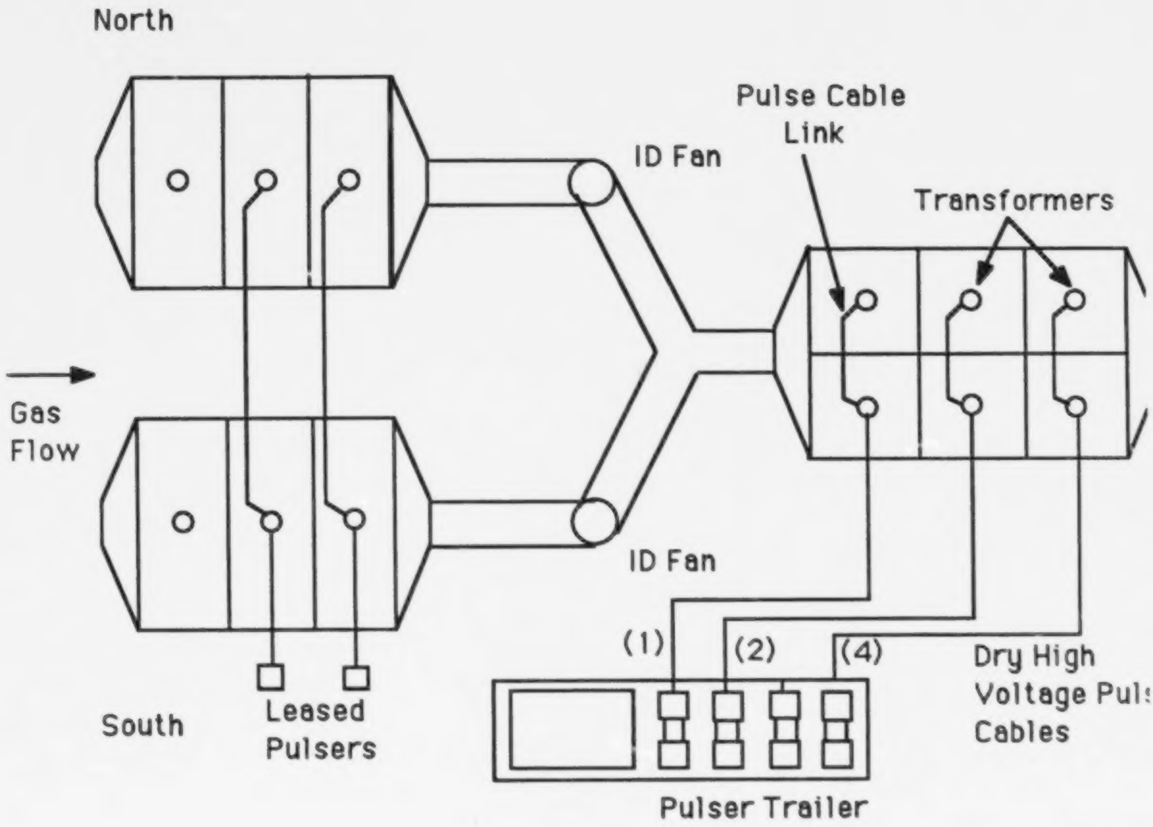

After The Test Program, The Pulse Trailer
Was Replaced With Three Leased Pulsers

Figure 5. Pulse powering arrangement during compliance testing.After the test program was complete, the pulse trailer was replaced with three leased pulsers.

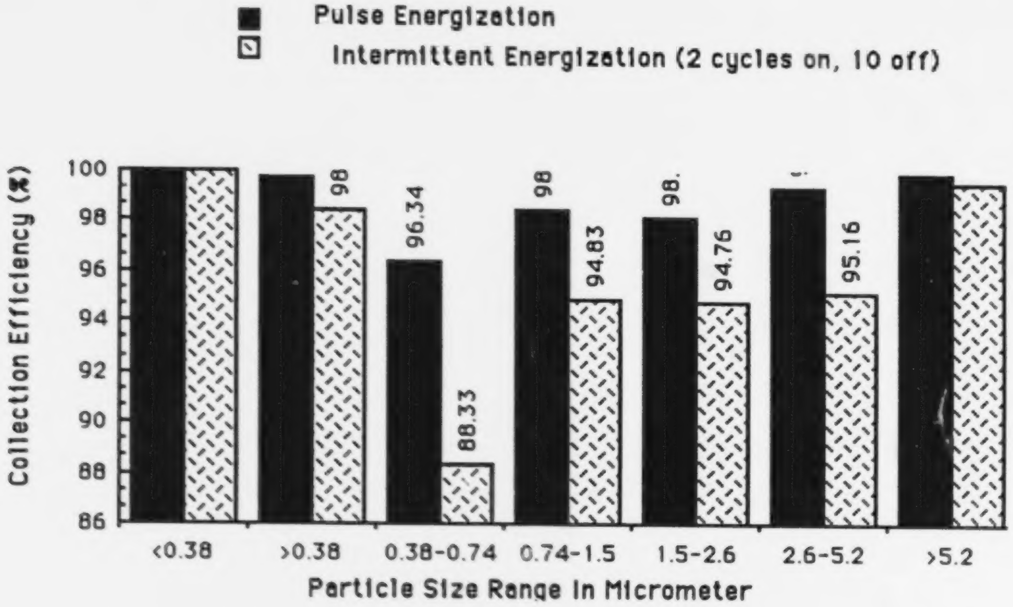

Figure 6. Particle size at ESP outlet during 50 MW operation operation with and without the pulser in service.

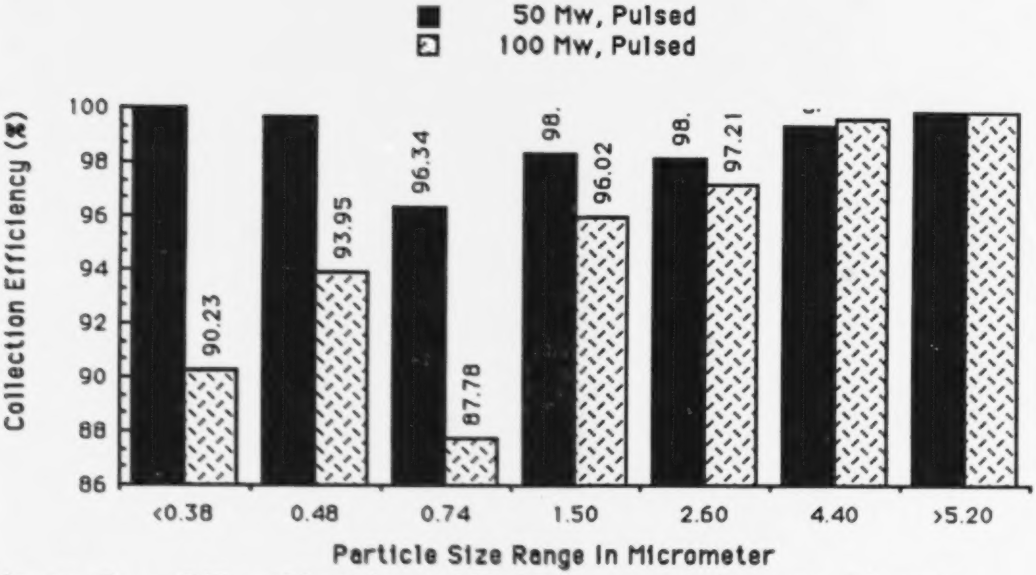

Figure 7. ESP collection efficiency comparison at 50 and 100 MW using the pulser supplies

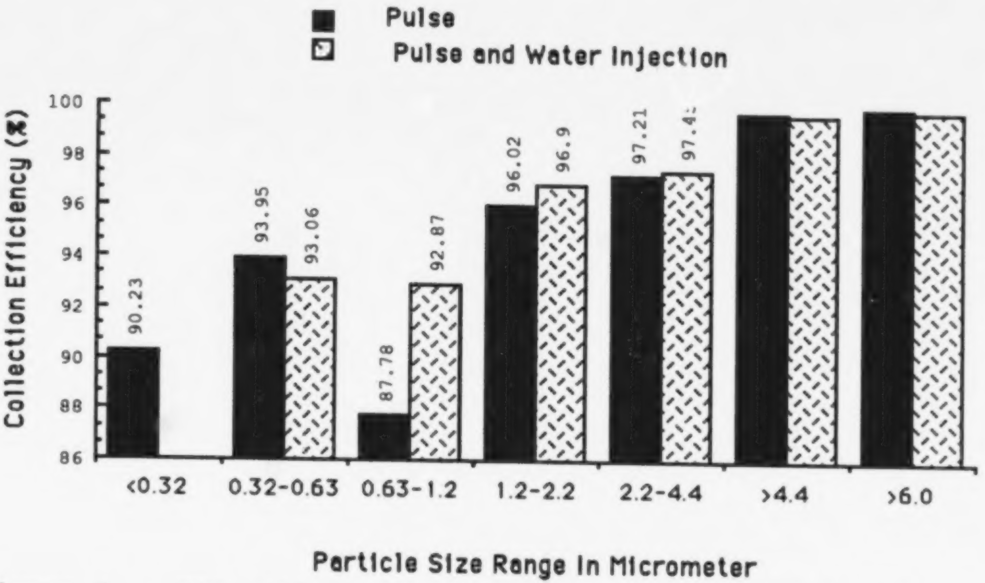

Figure 8. ESP collection efficiency at 100 MW with and with out 40 GPM spray water

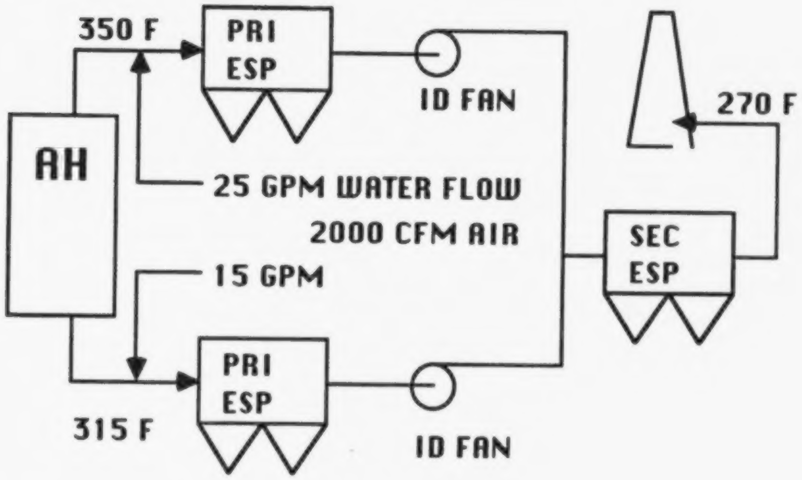

Figure 9. Schematic of the ESP spray water system operating at 106 MW load. Compressed air is supplied at 110 psi to the spray station.

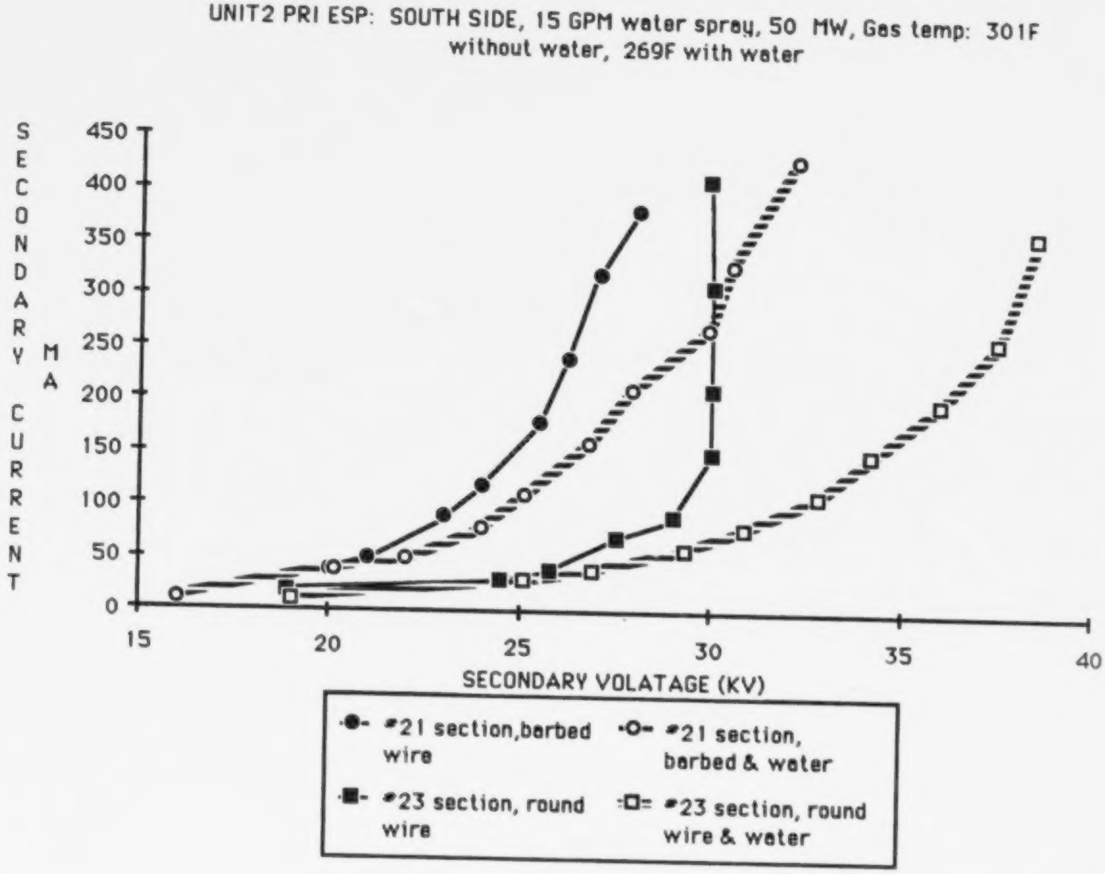

Figure 10. Voltage-current curves showing the effects of barbed wires and water injection.

Table 1. LABORATORY ASH RESISTIVITY (OHMS-CM) TESTS FOR ESP ASH

Gas Temp. (F)	Percent Moisture in Flue Gas 0*	6.2†	10.3†	15.6†
220	2.5×10^{14}	3×10^{11}	7×10^{10}	2×10^{10}
260	2.5×10^{14}	1.5×10^{12}	3.9×10^{11}	1.5×10^{11}
300	2.0×10^{14}	3×10^{12}	1×10^{12}	4×10^{11}
340	1.5×10^{14}	5×10^{12}	3×10^{12}	5×10^{11}
380	1×10^{14}	5×10^{12}	3.5×10^{12}	2×10^{12}

---

* Fly ash sample taken from ESP plates after using limestone.

† Fly ash sample from ESP ash hopper.

TABLE 2. IN-SITU RESISTIVITY PROBE MEASUREMENTS TAKEN IN THE AIR HEATER GAS OUTLET DUCT

Gas Temp. (F)	Resistivity (V-I curve) (ohm-cm)
274	8.0×10^{11}
291	6.5×10^{11}
305	1.2×10^{12}
318	2.3×10^{12}

TABLE 3. TYPICAL PULSER ELECTRICAL PARAMETERS[*]

Precipitator	Powering Mode	Secondary voltage
Primary ESP		
Inlet Field A	Conventional	39 KV
Inlet Field B	Conventional	37 KV
Center Field	Pulsed	Base - 30 KV, Pulse 44.0 KV[†]:74KV[§]
Outlet Field	Pulsed	Base - 30 KV, Pulse 40.5 KV :70 KV
Secondary ESP		
Inlet Field	Pulsed	Base - 30 KV, Pulse 46.5 KV:76 KV
Center Field	Pulsed	Base - 24 KV, Pulse 46.0 KV:70 KV
Outlet Field	Pulsed	Base - 28 KV, Pulse 48.5 KV:71 KV

---

[*] Taken during the November 19, 1987 emission test

[†] Pulse widths ranged from 140-155 microseconds and optimum pulse frequency was 30 pulses per second.

[§] Total charging voltage is sum of base and pulse voltages

TABLE 4. BLACK UNIT 2 PARTICULATE EMISSIONS TESTS: BEFORE AND AFTER ITS CONVERSION TO AFBC

Date	Boiler Type	Load (MW)	Emissions (lbs./MBTU)	Gas Temp. (F)	T/R POWER SUPPLY
7-21-83	PC	78	.048	306	Convent.
3-06-87	AFBC	100	.117	297	Convent.
7-15-87	AFBC	50	.042	280	Convent.

TABLE 4.Continued

Date	Boiler Type	Load (MW)	Emissions (lbs./MBTU)	Gas Temp. (F)	T/R POWER SUPPLY
7-15-87	AFBC	50	.009	280	66% pulsed 34% I/E*
8-17-87	AFBC	100	.036	297	66% Pulsed 34% I/E*
8-17-87	AFBC	100	.020†	297	66% Pulse 34%convent.
11-19-87	AFBC	106	.025†	--	66% pulsed 34%convent.
3-2-88	AFBC	130	----§	310	85% pulsed 15%convent.

---

* Intermittent Energization, 10 cycles on and 2 cycles off

† 40-50 GPM of water spray were in service during the test

§ 15-20 GPM of water spray, internal hot gas bypassing inside air heater was fixed. Common stack opacity was also subject to the effects of the gases from two other units at the time of the test. Opacity was indicating in the range of 12-17 percent.

REFERENCES

1. Turce, R.J. Electrostatic Precipitator Energization for the Collection of Highly Resistive Dusts. 86-JPGC-EC-3. Paper presented at the Jt. ASME/IEEE Power Generation Conference Portland, Oregon. October 19-23, 1986.

2. DuBard, J.L., Landham Jr., E.C. An Investigation of Precipitator Pulse Energization. EPRI CS-4717, September, 1986.

3. Altman,R. ESP performance with atmospheric fluidized-bed combustion. EPRI, Environmental Control Systems, Spring 1987, No.8, 2 pp.

FULL SCALE DEMONSTRATION OF FLUE GAS DESULFURIZATION BY THE INJECTION OF DRY SODIUM REAGENTS INTO AN ELECTROSTATIC PRECIPATATOR

by: Richard G. Hooper
CRSS, Inc.
Denver, Colorado 80202

ABSTRACT

This is the first full scale demonstration of dry sodium injection into the flue gas stream preceeding an electrostatic precipitator (ESP). The application of injecting dry sodium reagents for flue gas desulfurization (FGD) has been extensively studied in conjunction with fabric filters. This paper describes the integration of this effective FGD technology using sodium bicarbonate as the injected reagent and its impact on the electrical operating characteristics and the resulting particle collection efficiency of the ESP.

Results from the unique demonstration are described in terms of SO_2 removal, reagent utilization, ESP mass and particle size collection efficiency and the ESP electrical operating characteristics. Also included in the results is a discussion of the simultaneous NO/NOx removal occurring in conjunction with SO_2 removal.

The work described in this paper was not funded by the U.S. Environmental Protection Agency and therefore the contents do not necessarly refect the views of the Agency and no official endorsement should be inferred.

INTRODUCTION

Background

The subject of flue gas desulfurization by the injection of dry sodium based reagents has been extensively investigated in laboratory, pilot, and full scale applications since the 1960's. These investigations have provided the technical basis to evaluate the economic aspects of the technology and compare its advantages to the current and emerging calcium based technologies. The injection of dry reagents clearly is the least demanding of capital funds for both new and retrofit applications. The use of familiar hardware such as pulverizers, blowers, and silos permit the easy installation and operation of this simple technology.

Nearly all previous investigations have linked the injection of sodium based reagents with the use of a fabric filter for particulate control. However, as the results from this latest demonstration will show, the injection of dry sodium reagents is also easily linked with an electrostatic precipitator (ESP) for particulate control.

Figure 1 is a simplified flow schematic of a coal-fired power plant with dry sodium injection for SO_2 control. The dry reagent is pulverized and then pneumatically conveyed to the ductwork between the air heater and particulate control device (baghouse or ESP). The reagent is introduced into the ductwork through simple injection nozzles (pipe) in a manner that distributes the particles evenly throughout the gas stream. The products are then collected for disposal along with the fly ash.

Dry Injection Process Description

The reaction of the oxides of sulfur (SO_2,SO_3) in the flue gas occurs with sodium carbonate (Na_2CO_3), the product of the thermal decomposition of sodium bicarbonate ($NaHCO_3$). Therefore, when sodium bicarbonate is injected, the first step necessary for SO_2 removal is the decomposition into sodium carbonate:

(1) $2\ NaHCO_3$------- $Na_2CO_3 + H_2O + CO_2$

The rate of the decomposition of the bicarbonate controls the distance downstream of the injection location where the SO_2 reaction begins and the temperature of the flue gas at the injection location determines the rate of decomposition. Injection of bicarbonate into flue gas at temperatures greater than 275 F will assure that some sodium carbonate will be available for reaction within 0.4 seconds; this amounts to about 20 feet at typical gas velocity in the ductwork. The time/temperature relationship that the reagent experiences is critical to the efficiency of the SO_2 removal and the utilization of the reagent. Injection into higher flue gas temperatures (275-700 F) improves SO_2 removal and reagent utilization; injection into flue gas below 250 F significantly reduces reagent utilization because thermal decomposition is too slow and incomplete.

Once the decomposition has proceeded sufficiently to provide sites of sodium carbonate, the SO_2 then rapidly reacts according to the following overall reaction:

(2) $Na_2CO_3 + SO_2 + {}^1/_2\ O_2$ ------- $Na_2SO_4 + CO_2$

Dry sodium Injection offers several advantages over other FGD methods. These include:

Capital cost is significantly lower because of the comparative simplicity of the technology

Simultaneous NOx reduction occurs at minimal increase in cost

No liquids need be injected into the flue gas and only dry solids are handled as waste

Space requirements are minimal making the system easily retrofitted into existing particulate control devices.

Previous efforts relating to this technology were almost entirely focused on the injection of sodium reagents upstream of a baghouse. However, some pilot scale investigations have reported significant SO_2 removal and reagent utilization with injection upstream of an ESP. This project is primarily directed toward promoting this technology by demonstrating the full-scale application of the injection of sodium bicarbonate upstream of an ESP and then documenting the impact on the SO_2, NOx, and particulate emissions.

PROJECT DESCRIPTION

Objective

The objective of the project was to demonstrate the effective use of sodium bicarbonate as an agent for flue gas desulfurization when injected as a dry reagent into flue gas preceeding an electrostatic precipitator (ESP). Also considered a major factor in the project was the impact of the reagent on the performance of the ESP. A final objective was to demonstrate the effective use of the technology without plume coloration.

System Description

Figure 2 illustrates the equipment provided for this demonstration. Each of the two injection systems was capable of injecting the maximum rate necessary to complete the project. The reagent was introduced into the inlet ductwork of the south ESP through 2-inch pipe nozzles. Each system injected the reagent at two locations in the duct. It was most desirable to feed reagent through both systems so all four injection nozzles were used to distribute the reagent throughout the duct. However, at the lowest injection rate, only one feeder was used in order to assure more accurate control of the reagent feed.

The reagent was trucked to the site after pulverization to the desired particle size. Two 500 cubic foot capacity storage silos provided intermediate storage for the feeder hoppers.

The feed screw from the "Acrison" feeders delivered reagent into an air lock feed system that was connected to a 10-HP positive displacement blower. Reagent was conveyed pneumatically nearly 100 feet to the ductwork through 3-inch pipe. Both duplicate systems finally were split into two, 2-inch nozzles as the material was injected into the inlet ductwork. An illustration of the injection nozzle is shown in Figure 3.

Flue gas temperature and volume of gas flow were fixed by the plant operations. Flue gas temperature at the injection location ranged from 300-325 F. The location of the reagent injection and the flue gas velocity determine the distance and time within which the reagent must decompose and react with SO_2 before it is removed from the gas stream and collected by the ESP. It is estimated that the residence time of the reagent before the ESP is about 1.5 seconds.

Reagent was injected into one-half of the gas stream of the nominal 107 Megawatt generating unit. Injection into the inlet duct of the south ESP provided the opportunity to observe performance of the north ESP collecting fly ash only. The south ESP was referred to as the "treated side" and the north ESP as the "untreated side".

Project Structure and Participants

The funding for the project was shared between CRSS, Inc. (CRSS) and Industrial Resources, Inc. (IRI). IRI supplied reagent from its Nahcolite solution mining pilot plant.

IAM Consulting was contracted by CRSS to provide technical support and project coordination. GUS, Inc. was contracted to design, install and operate the feed equipment, and to supply operations and testing personnel. GUS also contributed personnel in the areas of project management and accounting.

KVB, Inc. was contracted to supply continuous monitors, sampling hardware and technical staff necessary to obtain data on a 24-hour, daily basis. Mullins Environmental Testing Co. (MetCo) was contracted to measure simultaneous mass and size dependent particle concentrations at the inlet and outlet of the ESP.

Project Chronology

Shown in Figure 4 is a time line illustrating the major periods of reagent injection throughout the demonstration. The width of the large blocks represents the time periods that reagent was injected and their height illustrates the nominal SO_2 removal during that period.

Delays in the start-up of the project that caused the initial test sequence to be altered and issues related to stack plume coloration were the primary considerations that resulted in the test sequence as shown.

One month following the initial demonstration, another test was performed to inject sodium bicarbonate plus an additive that prevented the occurrence of plume coloration and demonstrated the simultaneous removal of SO_2 and NOx. This test was conducted in a single day following several days waiting for satisfactory plant operations and consequential plant approval for the test.

COAL, ASH, AND REAGENT CHARACTERISTICS

Coal Characteristics

Operation of the boiler and consequential production of electrical power is the primary objective of plant management and operations staff. Fuel that is fired in the boiler must then be sufficient to produce the heat necessary to generate the desired electrical load. Small and seemingly insignificant differences in fuel can be tolerated and adjusted for by boiler operations personnel. However, these same fluctuations in fuel composition can create significant problems in the emission control device and ash handling systems.

In order to follow the trends or fluctuations in ash, sulfur, and moisture content of the fuel, GUS, Inc., sampled coal from the burner feed pipes.

Shown in Figure 5 is the ash content of the fuel from samples taken at approximately three hour intervals throughout the project. These results show ash content ranging from nominally 23 percent to greater than 30 percent; averaging 26.8 percent. Perhaps more significant is the trend that indicates the ash content rising steadily through the test period and finally decreasing near the end of the test period. This trend may be important because of the impact that the amount of ash has on the operation of the boilers. As shown in Figure 6, the boiler was not able to be operated at full load throughout the entire test. It appears that fuel ash quality and quantity changed during the trial, resulting in bottom ash problems. This operational issue was most apparent as the power demand was decreased substantially during the period of high ash content in the fuel.

Of course the increased ash content also has implications on the amount of ash that is carried through the boilers and to the ESP's for collection. Particulate mass measurements indicate that perhaps 20 percent of the total ash in the fuel is carried to the ESP's. The range of particle mass at the air heater inlet was evidence that the relative split of the ash between the boiler and ESP varied considerably. This was perhaps the greatest cause of varying outlet opacity.

The percent sulfur (dry basis) in the fuel varied from 1.31% to 1.51% without a particular pattern or trend throughout the test period. The as-fired fuel moisture content ranged from 1.4% to 3.0% without evidence of a trend.

Ash Characteristics

Ash samples were obtained from the first field hoppers of both the north (untreated) and south (treated) ESP's. Concentration of sodium (Na), sulfates (SO_4), carbonates (CO_3), and aluminum (Al) were determined by laboratory analyses and weight-loss-on-ignition (LOI) was measured for selected samples.

Baseline concentrations of the measured species are as follows:

Al; 11.2 + 0.6 weight percent (excluding sample 10)
Na; lower than detection limit for most samples
SO_4; 1.70 + 0.27 weight percent
CO_3; 5.34 + 0.84 weight percent

Weight-loss-on ignition (LOI) averaged 7.1 + 1.6 and ranged between 5.3% and 9.8%.

Average particle resistivity without reagent injection (fly ash only) was approximately 2.1×10^{10} ohm-centimeter (+1.58), and when measured during periods of reagent injection approximately 2.9×10^{10} ohm-centimeter (+1.34).

Reagent Characteristics

Chemical analysis of the sodium bicarbonate provided the basis to calculate the stoichiometric ratio (NSR) and percent utilization. During the demonstration, the reagent was sampled and evaluated for bicarbonate content. Brief on-site analysis indicated that the reagent was nearly 98% sodium bicarbonate. Subsequent laboratory analysis confirmed the purity of the reagent.

Particle size analysis of the sodium bicarbonate was performed on a selected sample collected during the demonstration. The sample was diluted in an organic liquid and particle size distribution was measured between 3um and 175um. The mass median diameter (MMD) of the reagent agglomerates (as received) was ~18um. A sample was then ultrasonically dispersed and the single particle mass median diameter (MMD) was ~7um.

TEST RESULTS

Description of Parameters

Because this technology was initially investigated as a flue gas desulfurization (FGD) method, it will perhaps always be considered in light of its effective removal of the oxides of sulfur (SO_2, SO_3). Consequently, SO_2 removal and reagent utilization were the primary parameters monitored during the demonstration. However, the injection of dry solids upstream of a particulate control device (in this case, an ESP), will predictably alter the operation of the device in some manner. Therefore, ESP performance and particulate emissions were also significant parameters monitored. Further, the possibility of NOx removal in conjunction with the SO_2 removal is an added benefit if the results are similar to those obtained with injection upstream of a baghouse. Therefore, measurement of the NO and NOx concentrations were also an important part of this demonstration.

Feed rate of the reagent was controlled both automatically and manually from the controls for the loss-in-weight feeders. Blowers provided a constant supply of ambient air that conveyed the reagent to the ductwork. SO_2 removal as a function of the amount of reagent injected (presented as Normalized Stoichiometric Ratio, NSR) is a measure of the effectiveness of the reagent and its distribution in the gas stream. The amount of bicarbonate injected was controlled to produce several levels of SO_2 removal that provide the basis to evaluate this specific installation.

Mass and particle size dependent emissions were monitored at the air heater inlet and the ESP outlet to provide some indication of the impact of the injection of the dry sodium bicarbonate on the collection efficiency of the ESP.

Throughout the project, coal samples were obtained every three hours and on-site analyses were made of ash, sulfur, and moisture content. In situ measurements of resistivity and current and voltage measurements were taken to document the impact of reagent injection on ESP operation.

Each parameter required individual consideration regarding the method and frequency of sampling and will be discussed according to the following list:

Gas Measurements
Particulate Measurements
Resistivity Measurements
Solid and liquid samples
Plant operating data

Gas Measurements

Sulfur dioxide (SO_2), nitrogen oxide (NO), total oxides of nitrogen (NOx), Oxygen (O_2), carbon dioxide (CO_2), and nitrogen dioxide (NO_2) were continuously sampled, monitored and recorded on analog strip charts. Calibration was conducted several times daily with standard bottled calibration gases. SO_2, NO or NOx, and O_2 were measured continuously at both inlet and outlet locations while NO_2 and CO_2 were measured for selected periods at one location and then switched to the other location for selected periods.

The continuous monitoring system used the analytical instruments as described below:

Flue Gas Component	Measurement Method
Sulfur Dioxide Nitrogen Dioxide	Ultraviolet, photometric
Nitrogen Oxides	Chemiluminescence
Oxygen	Electrochemical
Carbon Dioxide	NDIR, photometric

Particulate Measurements

Mass and particle size measurements were taken throughout the project to establish emission characteristics entering and exiting the south ESP. Mass measurements were also taken at the inlet and outlet of the North ESP for comparison.

Sampling methods for velocity, moisture, and particle mass concentration followed federal procedures of Methods 1, 2, 3, 4, and 17. Particle size distributions were obtained using standard Andersen cascade impactors.

Resistivity

Resistivity measurements before and during the injection of reagent were provided to evaluate the change in particle resistivity entering the south ESP. These measurements were made using the in situ, point-to-plane resistivity probe designed by Southern Research Institute.

Solid and liquid samples

Samples of the ash collected in the north and south ESP were collected for selected test periods throughout the project. These samples were sent to analytical chemistry labs for evaluation of selected components.

Plant operating data

Routine plant operating data including load, flue gas temperature at selected locations, and stack opacity were provided by plant engineers and operations personnel. Voltage and current for ESP operations were also collected.

Gaseous Emissions

Using the monitors described above, samples of flue gas were withdrawn through heated sample lines and analyzed for concentrations of SO_2, NO, NOx, NO_2, CO_2, and O_2. A manifold of three stainless steel, sintered filters was located across the ductwork at both the air heater inlet and ESP outlet. The three sample locations in each of the ducts provided some averaging of possible stratification of gas constituents. However, a comparison of the concentrations of SO_2 and NO from each of the three locations in the inlet and outlet ducts indicated no stratification from the boiler. Further, the manifolded sample provided much the same results as a single sample taken only from the middle of the ductwork. This was true for both the inlet and outlet locations.

Sodium Bicarbonate Utilization for SO_2 Removal

The injection of sodium bicarbonate to remove SO_2 in flue gas from fossil fuel fired boilers is a well documented technology. However, this project is unique because the injection of the reagent is upstream of an ESP and not a fabric filter. In the past it was perceived that the time necessary for the decomposition of the reagent and subsequent reaction with SO_2 were too great for significant SO_2 removal to occur in the ductwork preceeding the particulate control device. Therefore, it was perceived that the SO_2 primarily reacted with the decomposed reagent as it passed through the cake on the fabric filter surface. Measurement of SO_2 removal prior to the particulate control device often substantiated this belief. This, then, curtailed any effort to integrate the dry injection technology with an ESP for particulate control.

Recently, pilot plant efforts to integrate the dry injection of sodium reagent with an ESP have proved somewhat successful in terms of SO_2 removal and reagent utilization. This project expands these efforts to a full scale demonstration and broadens the horizon for the technology by evidence of the combination of SO_2 and NOx control that is achieved.

Shown in Figure 7 is the SO_2 Removal versus Normalized Stoichiometric Ratio (NSR) that was obtained during the project. The NSR is a measure of the amount of reagent injected relative to the amount theoretically required. For example, an NSR of 1.0 would mean that enough material was injected to theoretically yield 100 percent removal of the SO_2 in the inlet flue gas; an NSR of 0.5 would theoretically yield 50 percent SO_2 removal. The solid straight line indicates the theoretical use of the sodium bicarbonate. The curved line drawn through the data points indicates the actual SO_2 removal obtained. These results are the first of their kind at full scale and are extremely encouraging for the future of this application.

Percent utilization is a measure of the effective use of the reagent and is determined by dividing the percent SO_2 removal by the NSR. The percent utilization obtained during this project is shown in Figure 8. The low utilization of reagent at the higher NSR values is believed to result from uneven distribution of the reagent in the gas stream. This can be visualized as putting too much reagent in part of the gas stream (removing all the SO_2 in that space) and too little in the remaining space. There is too little time for the reagent to distribute evenly throughout the gas stream and react before it is collected by the ESP. Although utilization is expected to decrease with increasing NSR in all practical applications, the utilization as illustrated in Figure 8 could be improved with a redesign of the injection scheme.

Removal of the Oxides of Nitrogen (NO & NO_2)

As a consequence of the reaction(s) that produce SO_2 removal, subsequent removal of nitrogen oxide (NO) was measured during the project. This phenomenon has been observed (to a limited degree) by numerous investigators of this technology. However, never before have data been obtained to produce such an obvious correlation. The results shown in Figure 9 illustrate NO removal as a function of SO_2 removal. Although some data scatter is evident, it is clear that the change in NO concentration is directly a function of the amount of SO_2 removed.

The effect of NO removal with SO_2 removal is often associated with a coloration of the plume emitting from the stack. This and other studies have provided data that correlate the plume coloration to concentration of NO_2 in stack gas. This plume coloration is often described as a "brown plume"; NO_2 is a reddish-brown gas easily visible to the human eye. Most gases emitting from the stack are not visible to the human eye.

The NO_2 concentrations in the flue gas without the injection of reagent were measured to be about 20 ppm. As the reagent injection resulted in SO_2 removal, NO_2 concentrations at the ESP outlet increased as shown in Figure 10. All concentrations on this graph are corrected to zero percent (0%) O_2 levels, putting them on an equal basis. The dashed horizontal line estimates the minimum NO_2 concentration visible to the human eye.

> NOTE: The level of NO_2 visible to the human eye is dependent upon several site specific parameters. These parameters include stack dimensions, meteorology factors, position of the viewer, and perhaps the particulate concentration and size distribution exiting the stack. Plume coloration is not the same as stack opacity as measured by plant monitors. The relationship between visible NO_2 concentrations in the flue gas and stack opacity measured by conventional methods has not been established.

As shown in Figure 10 without injection of reagent, outlet NO_2 concentration is under the minimum necessary to cause plume coloration. However, with reagent injection and subsequent SO_2 removal, NO_2 concentration can rise significantly and thereby cause plume coloration. This plume coloration can be verified by the testimony of numerous plant and test personnel. This issue gave rise to the opportunity to extend the project and perform a test in which an additive was included in the reagent to eliminate the effect of the plume coloration.

Results from this final test are illustrated in Figure 10 in the darkened circles. Two effects should be noted: (1) the NO_2 concentration at the ESP outlet was considerably below the visible threshold. (2) SO_2 removal increased with the additive. Perhaps the most significant statement that can be made is that no plume coloration was visible during this test.

The result of including the additive with the reagent is shown in Figure 11. Again, the straight line is the theoretical maximum SO_2 removal and the curved lines are the results obtained without additive. The labeled triangle is the SO_2 removal obtained while injecting the additive and the labeled circle is the NOx removal. As shown the additive improved SO_2 removal and maximized NOx removal and resulted in NO_2 emissions far below the level that caused plume coloration. It is this test that encourages the pursuit of developing this technology as a simple, low cost method that will control SO_2 and NOx emissions in numerous applications.

Particulate Emissions

Once the dry reagent has been injected into the flue gas it must be captured by the particulate emission control device. This aspect of the technology is certainly no less important than its FGD capability because particulate emission regulations also must be obeyed. However, the challenge offered by the three field ESP collecting moderate resistivity ash was perhaps the most difficult project issue to adequately address. Before the project began. It was recognized that injecting more material into the south ESP might cause mass emissions to increase.

Inlet and Outlet Mass Measurements

Shown in Table 1 is the Percent Efficiency of the north and south ESP's calculated from mass measurements using EPA Method 17. The south ESP was the one with reagent injection and the north ESP was used for baseline comparison during periods of injection. In all cases measurements of fly ash concentrations were taken simultaneously at the air heater inlet and the ESP outlet. The amount of fly ash measured at the south air heater inlet ranged from 1624 pounds/hr to 8310 pounds/hr. (average = 3634 pounds/hr). These results illustrate that the reagent was collected at least as well as the fly ash (perhaps better) and that no immediate or short-term change in collection efficiency was experienced for these two reagent injection rates. Shown in Table 2, however, are total emission rates in pounds of particulate per hour. These results clearly show that emissions from the South ESP were greater during periods of reagent injection.

As shown in Figure 12, outlet mass emissions from the south ESP immediately increased following the initial injection period but did not increase with greater reagent injection rates throughout the test period. Outlet emissions from the north ESP were consistent each time tested. During periods of reagent injection, south ESP emissions were 64-100 percent greater than emissions from the north ESP. The reagent injection rates during these periods were 1450-6500 pounds/hour; this is 50-100 percent of the amount of fly ash at the injection location.

Inlet and Outlet Particle Size Measurements

Size distributions of the particulate were obtained at the south air heater inlet and ESP outlet during baseline conditions and during the first period of reagent injection (~25% SO_2). Average size distributions are shown in Figures 13 (inlet) and 14 (outlet). Outlet size distributions with and without injection are not significantly different and both are included in the average of Figure 14. As shown, a small peak is indicated at ~7um particle size range in the outlet emissions. This peak coincides exactly with the injected reagent particle mass median diameter; however, the peak is present for samples taken both during baseline and periods of injection. Unfortunately, there is not nearly enough size dependent data taken during periods of reagent injection to provide decisive evidence for a conclusion and this matter will need to be resolved during a long - term investigation of this technology. Figure 15 shows the fractional efficiency of the south ESP as determined from the average size distributions. Particles slightly less than 1 um (Log Dp = 0) in diameter were some of the least efficiently collected. This is very typical of ESP performance - unfortunately, it is particles in this size range that are most influential on stack opacity. Particles in the size range of ~7um were also less efficiently collected. This effect is likely a result of the large increase of particles at the ESP inlet due to reagent injection (MMD ~7um).

Dry Ash Analyses

A number of hopper fly ash samples was obtained from both the treated and untreated ESP's during the project. These samples were analyzed for sulfate (SO_4), carbonate (CO_3), bicarbonate (HCO_3), sodium (Na), and aluminum (Al) content. Selected samples were analyzed for carbon content by weight-loss-on ignition (LOI) analysis. In addition, a reagent sample was analyzed for carbonate, bicarbonate, and sodium content and was tested for particle size distribution.

Using the analytical results to produce Table 3, the following conclusions became apparent:

> Samples 25-1, 2, & 4, were not representative of the test. The ratio of sodium waste to fly ash is a good indicator of how well mixed are the ash and sodium wastes. The predicted and analytical ratios should match within ~20% to indicate a well mixed sample. These results indicate too much ash and not enough sodium waste in the sample. This was confirmed by the low sodium concentrations in the sample.

Sample 41-1 was not representative of the test. Too much sodium waste and not enough ash was in the sample. This was confirmed by the abnormal high sodium concentrations in the sample.

Samples 25-3, 55-1, and 63-1 are good representation of their tests. The agreement between predicted and analytical results indicted a well mixed sample.

For samples 25-3, 55-1, and 63-1, the weight percent of sodium measured by analytical means was substantiated when compared to weight percent sodium as predicted from the sodium content of the reagent and the average amount of ash to the ESP.

For samples 25-3, 55-1, and 63-1, the weight percent sodium predicted from the SO_4, CO_3, and HCO_3, is less than measured weight percent sodium. This indicates some unmeasured species are present.

DISCUSSION OF RESULTS

This project is the building block upon which longer term demonstrations and full-scale applications will begin. For this reason, conclusions drawn from the results will be carefully considered by analysts with wide backgrounds and special interests. For those who are looking for a low cost NOx removal technology, please be cautioned that this technology first requires SO_2 removal and then NOx removal follows as a consequence.

The project baseline values for gas and particulate concentrations began with great success. Between 1500 hrs., on day 2, and 0630 hrs., on day 5, reagent was injected for 85% of the time (54 hours) with the remaining 15% dedicated for baseline operation without injection. Once injected, the sodium bicarbonate immediately began to remove SO_2 from the flue gas. The effect was dramatic as outlet SO_2 concentration dropped to a steady level. The relatively steady boiler conditions facilitated the already simple operations. Controlling the amount SO_2 removed was a simple matter of injecting more reagent. However, it became clear at higher injection rates that reagent utilization decreased more rapidly than expected. At lower injection rates, SO_2 removal nearly equaled theoretical; yet, at the highest injection rates, it was obvious that reagent utilization decreased.

The design of the reagent injection system is believed to be the root cause of this decline in reagent utilization. While the nozzle design is sufficient to disperse reagent in the local area, additional design consideration for the number of nozzles and nozzle locations are believed necessary to improve reagent utilization at higher SO_2 removal levels.

Because the injection periods spanned only three consecutive calendar days, performance and emissions data should be considered only as an indicator of the first response of the ESP. Despite an increase in particulate loading caused by reagent injection, the electrostatic precipitator was able to retain its collection efficiency - this is an encouraging result!

During periods of reagent injection (without additive) when SO_2 removal was greater than 25 percent, NO_2 concentrations in the flue gas caused a visible plume coloration. The second test period using the same reagent (with additive) resulted in simultaneous removal of SO_2 and NOx from the flue gas without the visual plume coloration. The continuous monitoring instruments substantiated that NO_2 concentration in the outlet flue gas was below visual levels.

FIGURE 1

Schematic of a Coal-Fired Power Plant with Dry-Sodium Injection for SO_2 Control.

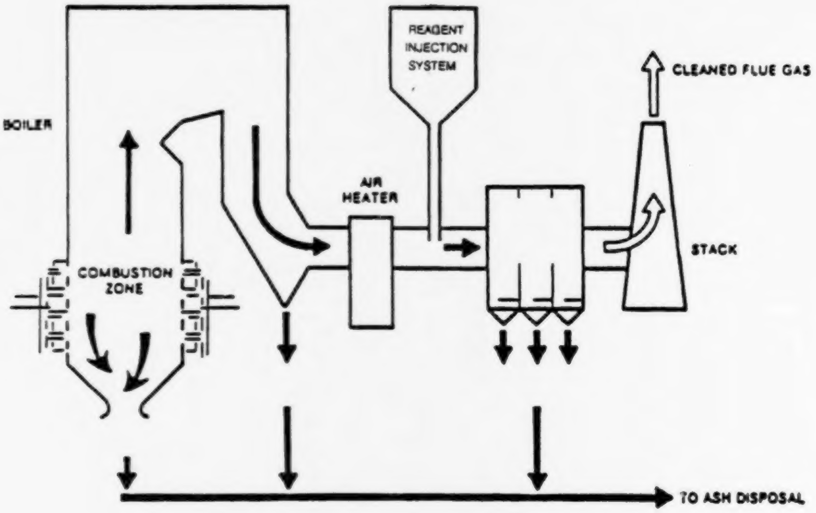

FIGURE 2

Layout of Dry Injection Equipment and Plant Configuration

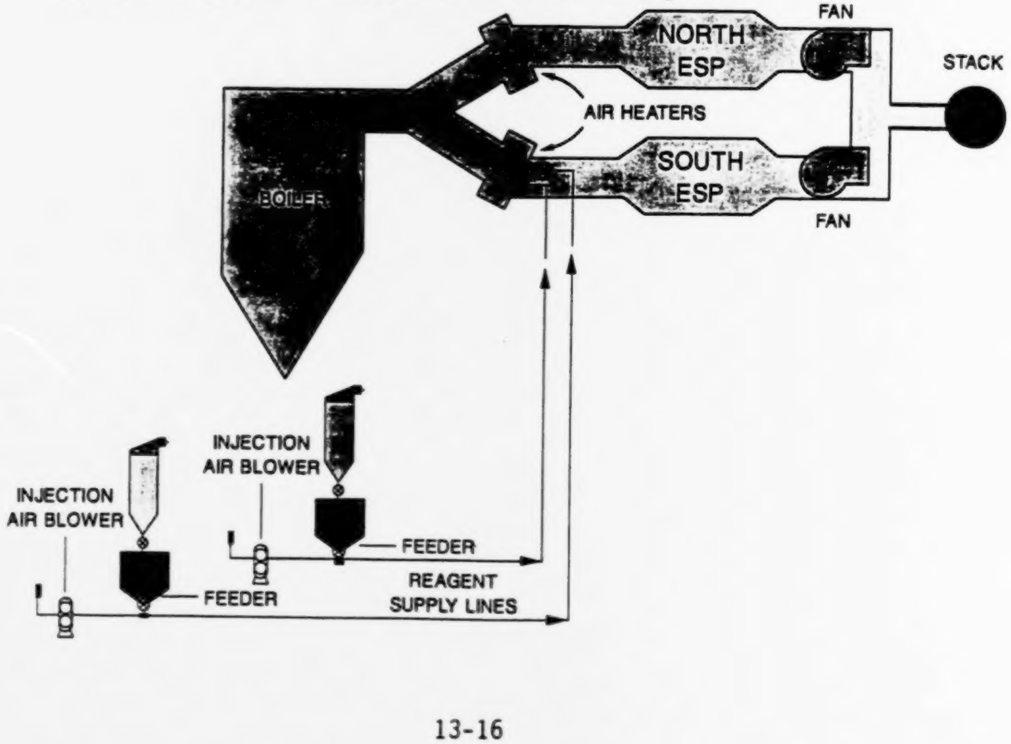

FIGURE 3

Injection Nozzle Scheme

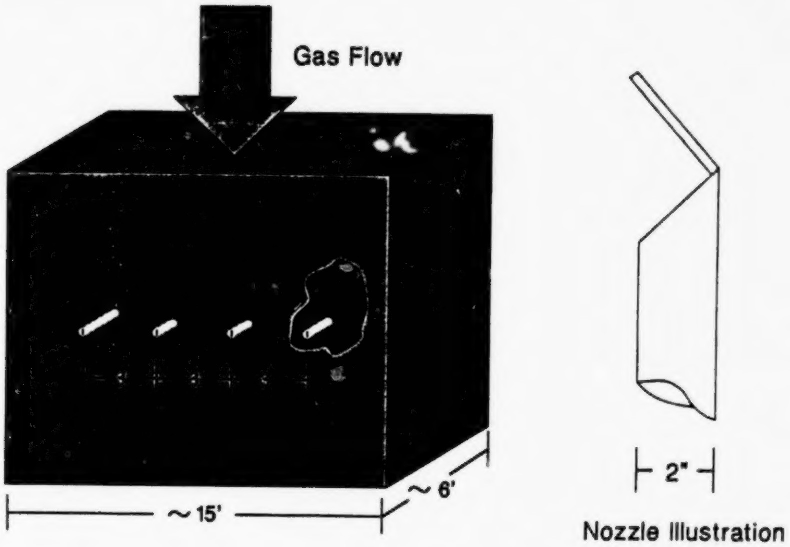

FIGURE 4

Project Timeline with SO_2 Removal

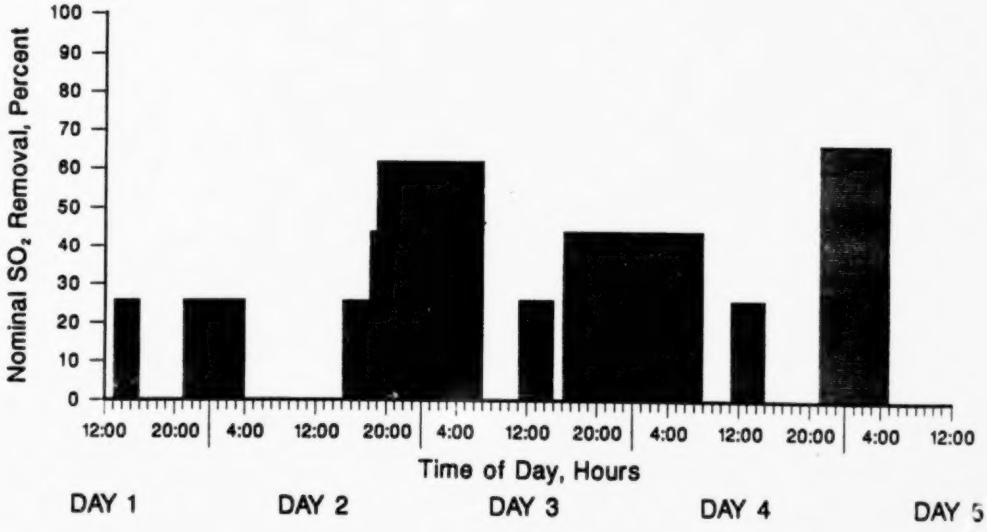

FIGURE 5

Percent Ash In Fuel vs Time

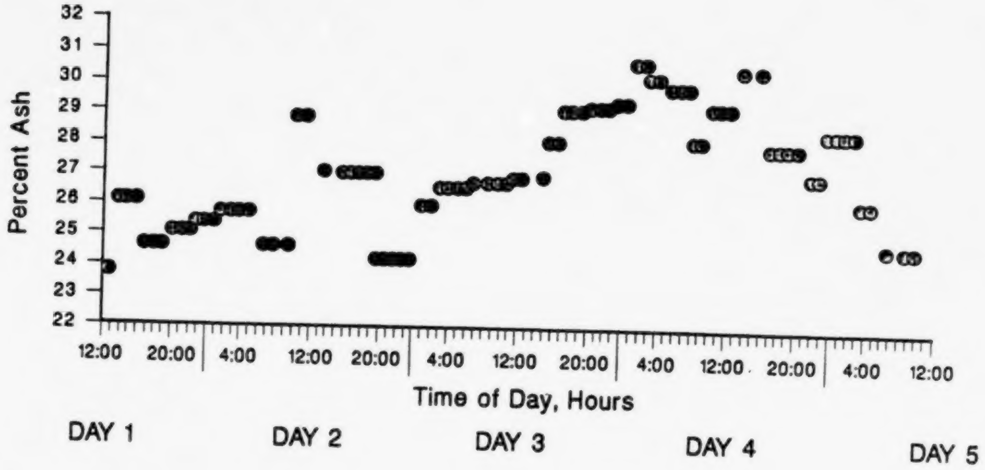

FIGURE 6

Load vs Time

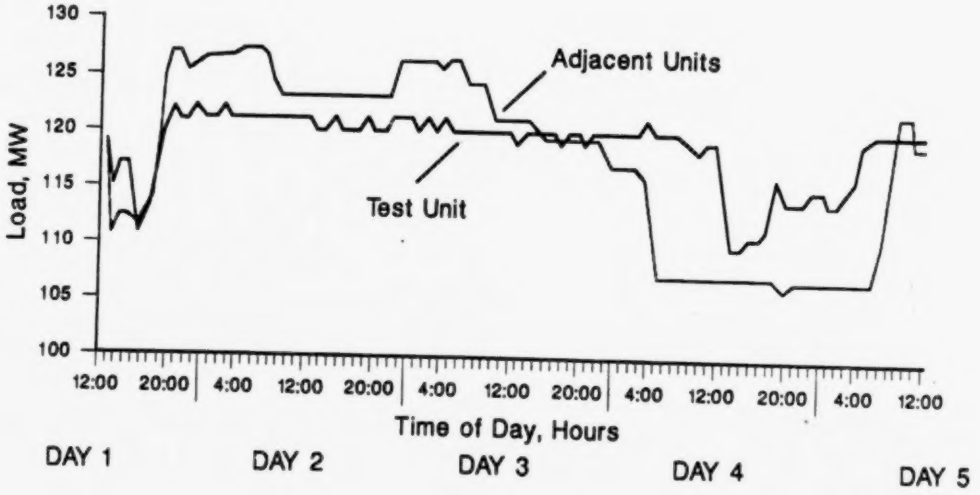

FIGURE 7

SO$_2$ Removal vs Normalized Stoichiometric Ratio (NSR)

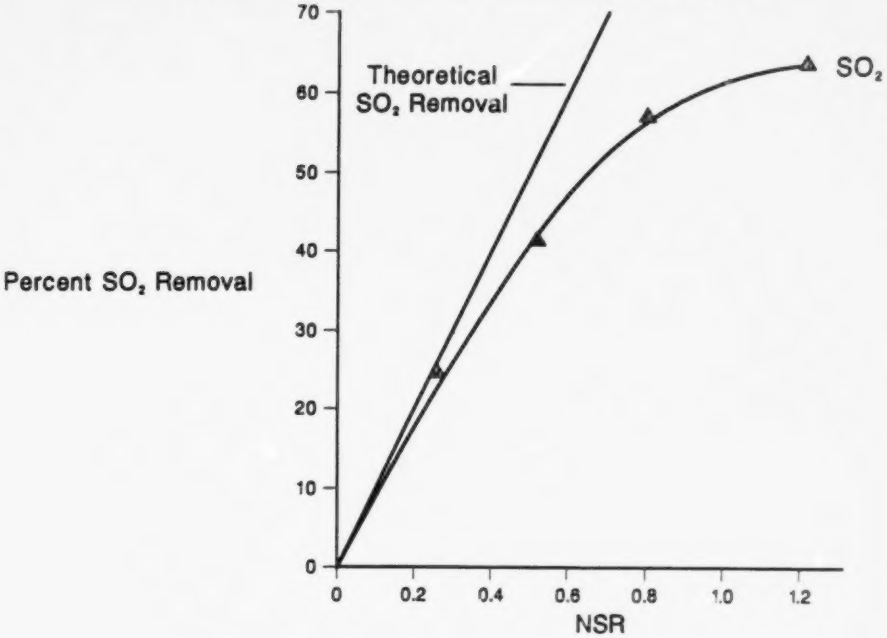

FIGURE 8

Average Reagent Utilization vs Normalized Stoichiometric Ratio (NSR)

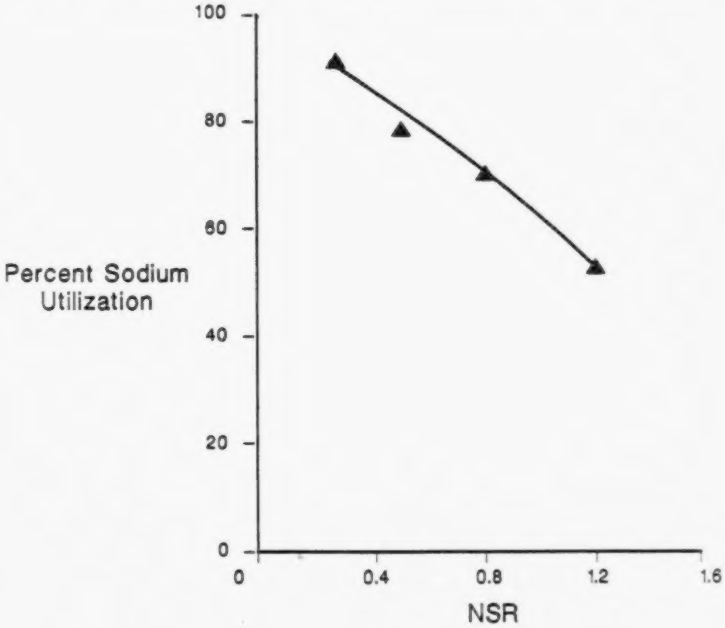

FIGURE 9

NO Removal vs SO_2 Removal

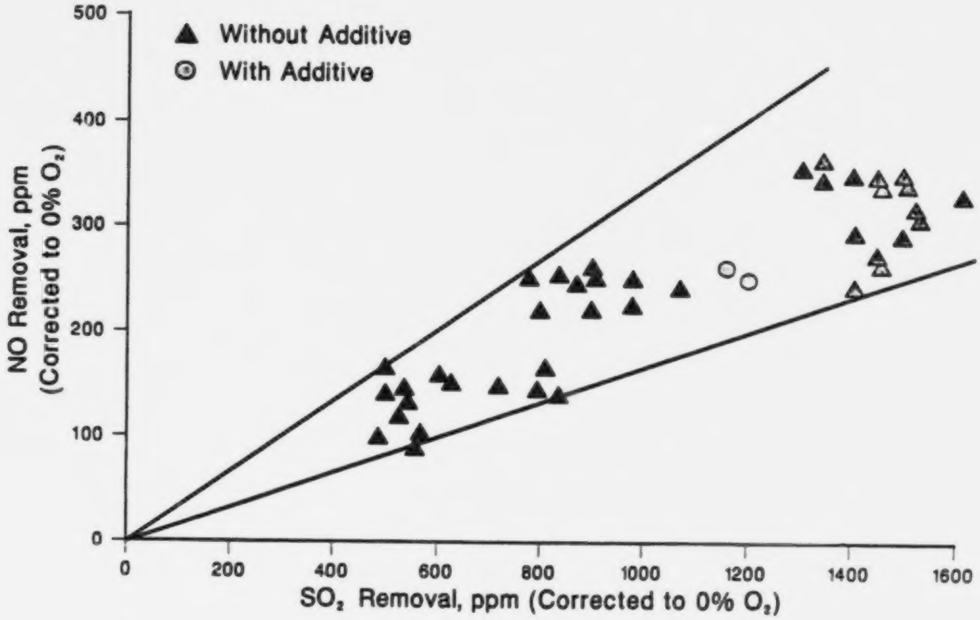

FIGURE 10

NO_2 Emissions vs Decrease in SO_2 Emissions

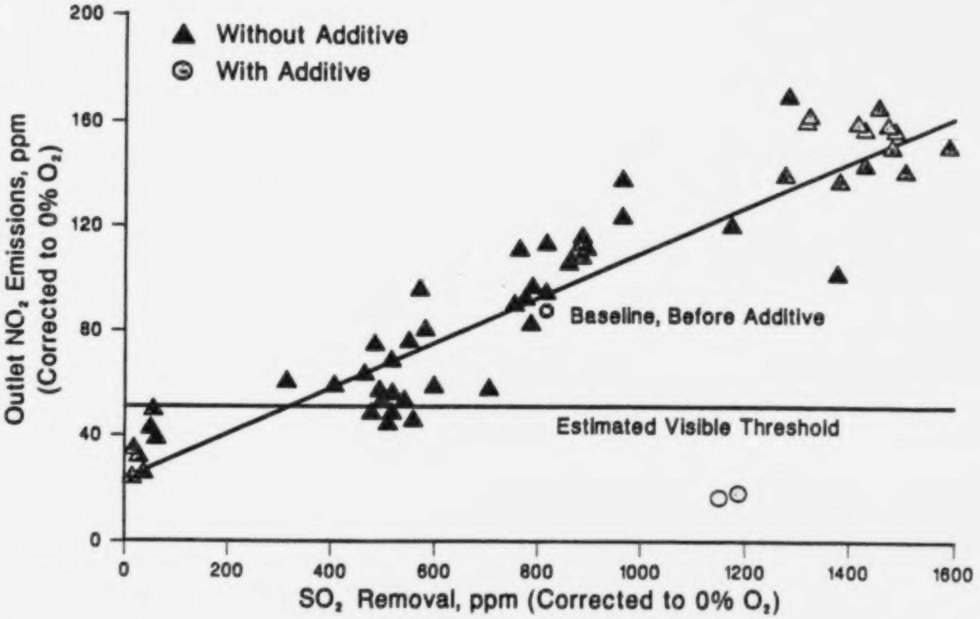

FIGURE 11

% Removal of SO_2, NO and NO_x vs Normalized Stoichiometric Ratio (NSR)

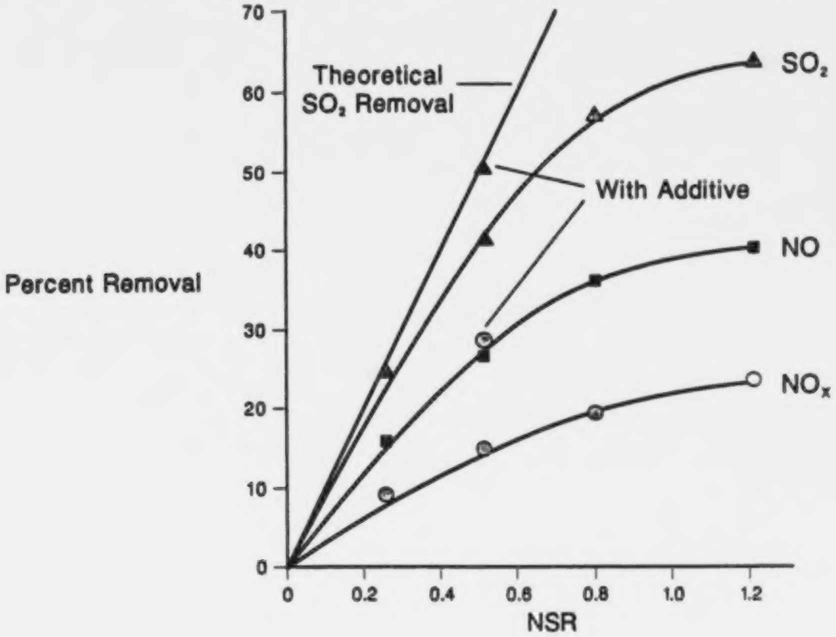

FIGURE 12

Outlet Mass Emissions vs Time

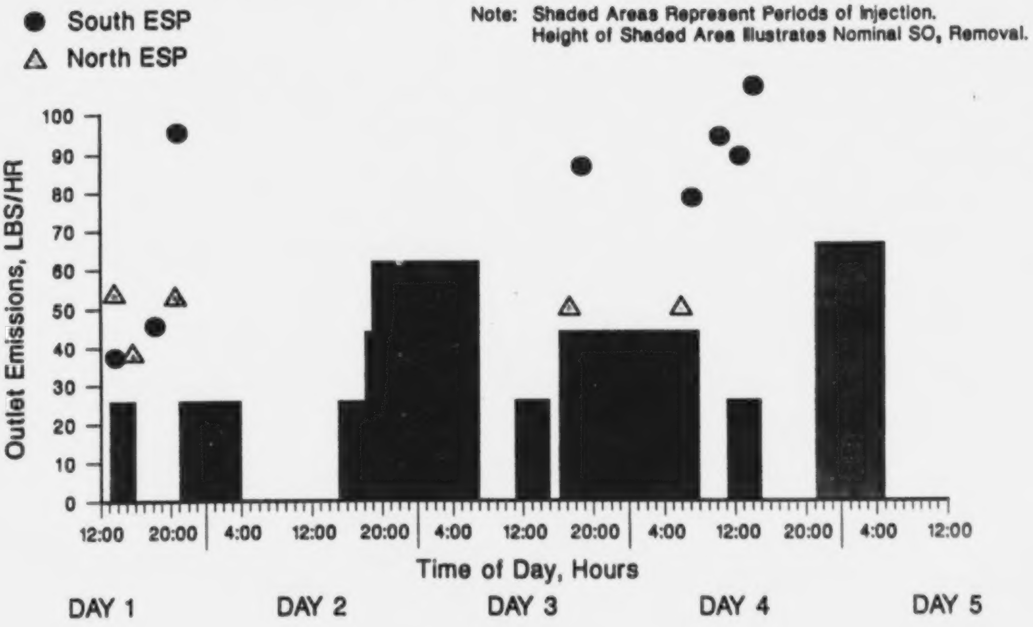

FIGURE 13

Air Heater Inlet Particle Size Distribution (Fly Ash Only)

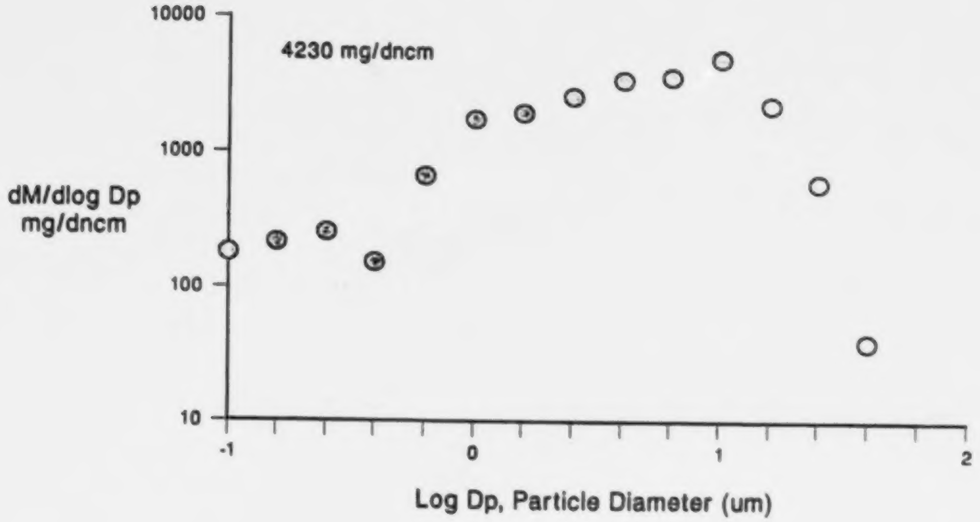

FIGURE 14

ESP Outlet Particle Size Distribution

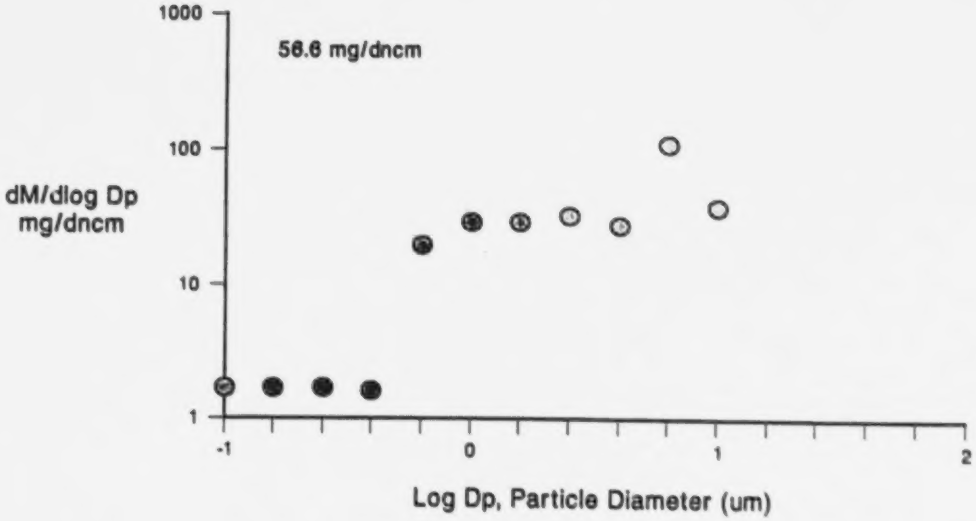

FIGURE 15

Fractional Efficiency vs Particle Diameter

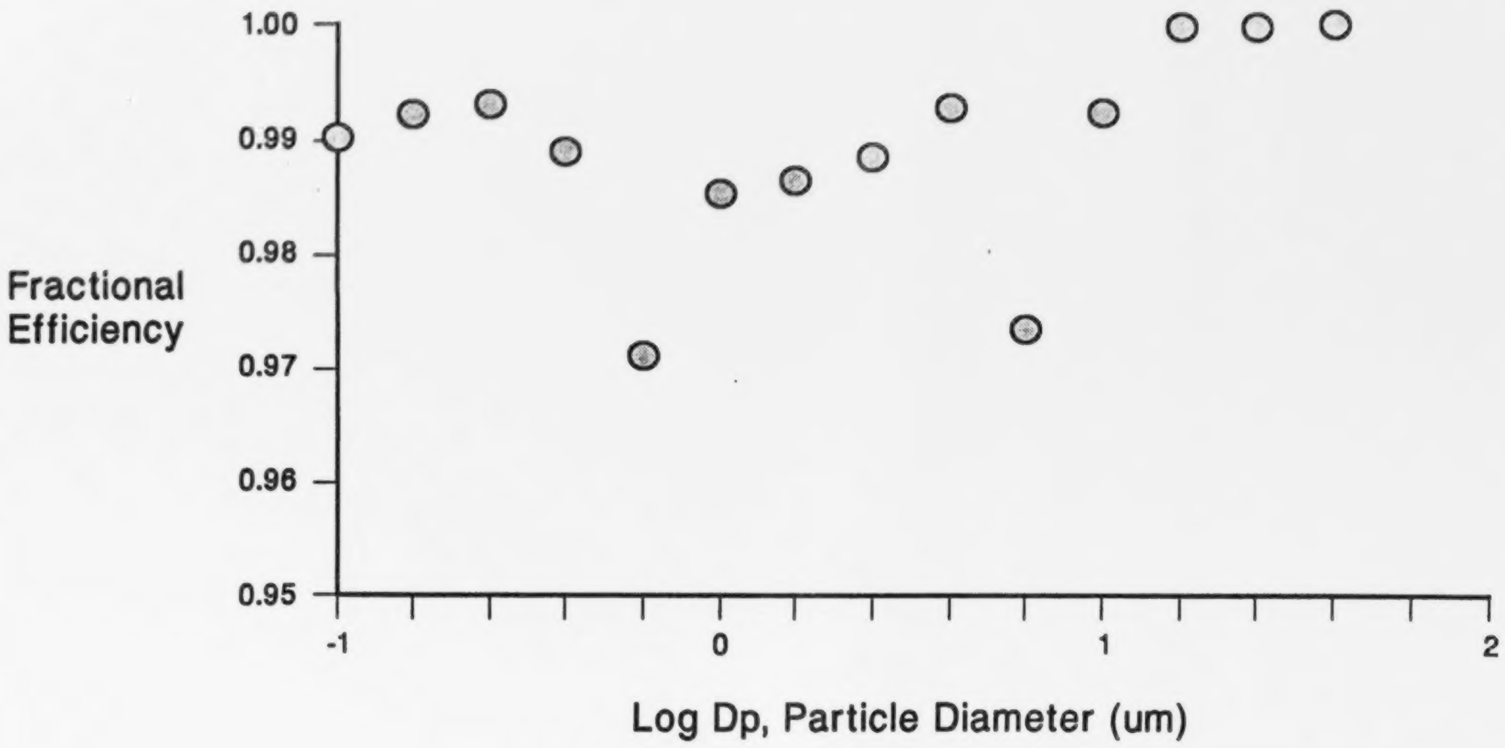

TABLE 1

ESP MASS COLLECTION EFFICIENCY

TEST CONDITION	ESP COLLECTION EFFICIENCY, % South	North (no injection)
Baseline (no injection)	99.10 - 98.60	
~25% SO_2 removal	98.30	98.30
~25% SO_2 removal	98.74	
~40% SO_2 removal	98.62	97.85
Average all data	98.60	98.15

TABLE 2

ESP OUTLET MASS EMISSIONS

TEST CONDITION	TOTAL EMISSIONS (Pounds/hr.) South	North
Baseline	39.4 + 2.7(3)	47.0 + 5.9(5)
~25% SO_2	94.1 + 10.0(3)	
~40% SO_2	77.4 + 4.9(2)	

() Indicates the number of replicate tests.

Table 3

SUMMARY OF FLY ASH ANALYSES

Sample I.D. (a)	Sodium Waste (b) Predicted, lbs/hr	Sodium Waste/Fly ash Predicted (c)	Analytical (d)	Weight Percent Sodium in Waste Analytical	Predicted (e)	Cation Balance (f)
25-1	1160	0.32	0.11	4.4	8.4	4.1
25-2	1195	0.33	0.13	5.8	8	5.8
25-3	1089	0.33	0.31	8.1	8.1	6.5
25-4	1225	0.34	0.19	5.7	5.3	6.1
41-1	2317	0.64	5.43	19.7	15.3	17.6
55-1	1046	1.11	0.91	17.8	18.4	14.5
63-1	5024	1.38	1.38	22.1	19.9	17.3

(a) Sample identified by nominal SO_2 removal for specific test.

(b) Based on amount of reagent injected and analytical ratio of cations $[SO_4]$, $[CO_3]$, $[HCO_3]$.

(c) Fly ash rate = 3634 lbs/hr; Average of nine inlet measurements on south ESP.

(d) Based on Aluminum concentrations.

(e) Based on reagent feed rate and fly ash concentration.

(f) Based on cation concentrations to calculate sodium weight percent.

AN UNEXPECTED CASE OF BACK CORONA

Anthony J. Ahern
American Electric Power Service Corporation
Columbus, Ohio 43216

ABSTRACT

The occurrence of high opacities and erratic power levels especially on an older and relatively small SCA precipitator where previously good performance was the norm indicates that a significant change has occurred. When the precipitator is a cold-side precipitator and the fuel is high-sulfur coal, the assumption that the root cause of the performance deterioration relates to the precipitator's mechanical condition appears to be reasonable. After being unable to account for the erratic electrical conditions based upon the mechanical conditions, a fresh examination revealed that back corona was responsible for the erratic power levels and high opacities. An intriguing facet of this case is that the back corona has been observed on the cyclone-fired units and not on the pulverized coal-fired units at the referenced plant. This paper is not a review of all the facts in this case and it does not provide answers as to why back corona is occurring. The purpose of this paper is to acknowledge that this unusual situation exists.

INTRODUCTION

The development of high opacities and erratic power levels is not a startling occurrence especially on an older and relatively small SCA precipitator. The root cause of the performance deterioration was found to be the development of back corona. This is not particularly unusual. What is unusual is to detect back corona when the precipitator is a cold-side precipitator and the bituminous eastern coal has a nominal sulfur content of 5%. This paper describes the situation where this unexpected case of back corona was found.

PLANT AND UNIT CHARACTERISTICS

The plant where unexpected back corona was found has five generating units. Units 1 and 2 are rated at 205 MWN and have wet-bottom pulverized coal-fired furnaces. Units 3 and 4 are rated at 215 MWN and have cyclone-fired furnaces. Unit 5 is rated at 585 MWN and has a dry-bottom pulverized coal-fired furnace. All five units receive a common fuel supply that comes from a mine located near the plant. The coal, an Ohio Meigs Creek number 9, is washed and after washing has a composition as indicated in Table 1.

Units 1-4 are each equipped with identical electrostatic precipitators having the specifications described in Table 2.

ELECTRICAL CONDITIONS

Many factors can be responsible for erratic precipitator power levels and opacity problems. Assessing electrical conditions can provide important insights into why erratic power levels are occurring. One diagnostic approach for assessing electrical conditions is to plot current density (J) versus the secondary voltage (V), the J-V curve, of individual bus sections. Figure 1 shows the J-V plots of the 4th field (outlet field) of Units 1-4, respectively. The "MIN", "AVG" and "MAX" curves denote plots of J versus V where "MIN" is the minimum of the pulsating voltage waveform, "AVG" is the average of the voltage waveform, and "MAX" is the maximum of the pulsating voltage waveform, respectively. Much to our surprise we found that Units 3 and 4 appeared to be operating in back corona. The assessment that back corona was occurring was based on the fact that the minimum voltage declined when the secondary current increased.

Figure 2 shows the J-V characteristics of the 1st, 2nd, 3rd and 4th fields, respectively, of the Unit 3 precipitator. Back corona is noted to be severe in the 3rd and 4th fields as opposed to the first two fields where back corona is either not occurring or is very slight.

Another means to identify that back corona is occurring is to observe the secondary voltage waveform after a spark has occurred and the T/R set controller shuts off the power and then reapplies it. Figure 3 is an oscilloscope photo of the secondary voltage and secondary current time traces as a spark occurred on Unit 3 when electrical conditions were poor. The upper trace is the secondary voltage and the lower trace is the secondary current inflow from the T/R set into the precipitator bus section. The horizontal time scale is 20 milliseconds per division. When the spark occurred, the discharge of the bus section voltage due to the short-circuit characteristic of a spark is evident. The T/R set automatic controller has sensed the spark and its algorithm of shutting off the current and then reapplying it is evident. Within a few half cycles after the spark, the minimum voltage is much higher than it was just prior to the spark even though the current has been significantly reduced. The minimum voltage then slowly begins to decline as more and more back corona develops.

OPERATIONAL CHARACTERISTICS

Since the early 1980's, Units 3 and 4 have experienced episodes of opacity exceedances and very erratic precipitator power levels. The condition of back corona has been observed to come and go. Typically, when Unit 3 or 4 is returned to service after an outage, no back corona is found and an opacity of 10% at full load is achieved. Figure 4 shows the secondary voltage and current time traces of an outlet field T/R set on Unit 3 within 24 hours after the unit returned to service. The voltage and current time traces at two different current densities, 5 and 50 milliamps per 1000 ft^2 of plate area, are superimposed on this one oscilloscope photo. The entire secondary voltage waveform at the higher current density is elevated above the lower current density voltage waveform.

Although not consistently repeated, the deterioration of electrical conditions on Units 3 and 4 follows a general pattern. When the unit returns to service back corona is not evident. The J-V curves usually appear similar to those on Units 1 and 2. Sometimes the corona initiation voltage is +20 KV instead of the 15 KV that would be expected. If the corona initiation voltage is 15 KV, within 1 to 3 days after returning to service it increases to +20 KV. A day or two later back corona is evident. Experience has shown that once back corona has developed, its severity increases with time. Back corona first appears in the fourth (outlet) field. In time (a matter of a few days usually) the secondary current levels decrease significantly and the peel back of the J-V curve becomes more pronounced. At this point the back corona usually has progressed to the third field. At full load the opacity would approach the 20% limit or load curtailments as much as 30% of full load would be necessary to not exceed the 20% opacity limit . The electrical conditions shown on Figure 5 would have developed. Superimposed on Figure 5 is the secondary voltage at two different current densities, 2 and 15 milliamps per 1000 ft^2 of plate area. The significant extent to which back corona drags down the secondary voltage when the current density is increased is evident.

Unit outages result in the unit returning to service with improved electrical conditions and without back corona. Even brief outages such as a hot restart of the unit immediately following a unit trip often result in the unit returning to service without back corona.

The unit is operated to maintain an air heater exit gas temperature of 320^oF. Due to duct thermal losses, the gas temperature entering the precipitator can be 300^oF. The temperature distribution across the precipitator inlet ranges from 280^oF to 315^oF. Experimentation for brief periods at lower gas temperatures showed that reducing the flue gas temperature by 20^oF usually either eliminated or reduced the severity of back corona. This, however, is not an acceptable operating condition because air heater pluggage develops at an unacceptable rate.

View ports were installed on the roof of the precipitator to visually observe plate and wire buildups during unit operation. No discernible differences in plate or wire buildups was observed with and without back corona occurring. Plate and wire buildups were typically less than 1/4" thick.

Precipitator records from the early 1970's, when the Unit 1-4 precipitators were installed, indicate that the 3rd and 4th fields operated without sparking at 50 milliamps per 1000 ft^2 of plate area. In the early 1980's washing of the coal to meet a reduced sulfur dioxide emission limit began. Erratic power levels on Units 3 and 4 were first observed coincident with the start of coal washing.

RESISTIVITY MEASUREMENTS

Southern Research Institute (SRI) was commissioned to measure in-situ resistivity on the inlet to the precipitator and the flue gas sulfur trioxide concentrations on both the inlet and outlet of the precipitator. The in-situ resistivity values were found to be quite normal for high sulfur coal. They ranged from 8.6×10^8 to 1.6×10^{10} ohm-cm. The sulfur trioxide (SO_3) levels were measured on the inlet and outlet of Units 1 and 3. All SO_3 concentrations were found to be within the range of 25-30 ppm.

In addition, lab measurements of resistivity were performed on ash deposits removed from Unit 3 collecting plates (within 12 hours after the unit was removed from service) and hoppers (when the unit was in service.) Figure 6 plots the lab measured resistivity as a function of temperature of the ash deposits taken from the 1st and 4th field plates and the inlet and outlet hoppers. The continuous curve data points were obtained without SO_3 in the gas environment and the solid points represent measurements with 28 ppm of SO_3 at two different temperatures. Figure 7 presents for the outlet field plate deposit the predicted resistivity using the Bickelhaupt resistivity model for a range of assumed SO_3 concentrations. SRI reported (1):

> Significant changes in fly ash resistivity occur over orders of magnitude rather than by factors of 2 or 3. Therefore, agreement within a half order of magnitude between different resistivity measurements, or between theory and experiment, is considered good agreement. Good ESP electrical operation is usually associated with fly ash resistivity values below about 5×10^{11} ohm-cm. Fly ash resistivity values above about 5×10^{11} ohm-cm usually result in electrical operating difficulties associated with back corona.
>
> It is immediately apparent from Figures 6 and 7 that ash samples taken from the outlet field collecting plates have unusually high resistivity compared to all other samples. The data points obtained with 28 ppm SO_3 indicate resistivity values low enough (< than 1×10^{11} ohm-cm) that back corona would not be expected to form. Nevertheless, there is a dramatic difference of almost two orders of magnitude between the resistivity values of inlet and outlet plate ash samples.
>
> It is also noteworthy that the resistivity values of outlet plate ash samples are very steep functions of temperature. A 15°F temperature drop, from 320°F to 305°F, causes an order of magnitude drop in resistivity.

FLY ASH ANALYSIS

The mineral analyses of fly ash samples taken from each of the four fields of Unit 3 precipitator are listed in Table 3. SRI reported (2):

> The very high iron content of the fly ash presumably results from the very high pyritic sulfur content of the coal. Also noteworthy, are the very high values of loss on ignition (LOI) and soluble sulfates with the values increasing from inlet to outlet of the ESP. These unusual results led to further attempts to identify the sulfate compound contained in the plate ash samples.

> Very significant differences between soluble sulfate concentrations in unignited ash and total sulfate concentrations in ignited ash were observed in many of this plant's ash samples. High LOI values were also associated with these samples, suggesting that a sulfur compound was being lost during the ignition procedure. For example, a previously obtained sample from the outlet field of Unit 3 precipitator contained 19.9% soluble sulfate in the unignited ash, 2.2% total sulfate (reported as SO_3) in the ignited ash and had an LOI of 22.6% at 750°C.
>
> The chemical composition of this ash suggested that the bulk of the sulfur had to be either in the form of free sulfuric acid or as an iron salt that would decompose at or below 750°C. Although the ash lacked the "stickiness" usually associated with the presence of free sulfuric acid, two tests were run to confirm the hypothesis of an iron salt. In one test, an unignited sample was conditioned at 350°C, a temperature sufficient to volatilize sulfuric acid. A weight loss of 6.1% was observed, but a subsequent analysis indicated no loss of sulfur. Observation of initial pH changes in distilled water on the addition of an unignited sample further confirmed the absence of free sulfuric acid.
>
> Next, an unignited sample was placed in a Pyrex tube and heated while a slow stream of air was drawn over the sample into a series of bubblers. Strong SO_3 fumes were observed in the water bubblers when the sample was heated to about 500-600°C. Analysis of all bubblers showed that SO_3, rather than SO_2, was evolved. Recovery of sulfur was 92% of theoretical.
>
> On the basis of the above tests it seems likely that the bulk of the sulfur is present as an iron salt rather than free sulfuric acid. The evolution of SO_3, but not SO_2, at a decomposition temperature in the range of about 500-600°C is consistent with the presence of ferric sulfate, $Fe_2(SO_4)_3$. The thermal decomposition of ferric sulfate yields $3SO_3$ + Fe_2O_3.
>
> It should be noted that the presence of 19.9% soluble sulfate in the form of ferric sulfate would require only 11.0% iron in the ash mineral analysis, reported in weight percent as the oxide Fe_2O_3, as compared with the measured value of 28.9%. Thus, there is an abundance of iron in the fly ash that is available for the formation of ferric sulfate.
>
> The formation of ferric sulfate in an ash layer that remains a long time on the collecting plates would be greatly enhanced by any temporary temperature excursion though the acid dew point.

The conclusion SRI drew, which was circumstantial, is that a time delayed chemical reaction occurs in the plate ash deposits which causes the growth and spread of back corona.

DISCUSSION

Why episodes of back corona occur on Units 3 and 4 is unclear. The conventional answer is that a high resistivity ash deposit is developing. Why this would happen on just the cyclone-fired units, Units 3 and 4, and not on the pulverized coal-fired units, Units 1, 2 and 5, is puzzling since they all burn the same fuel. It certainly appears that the combustion characteristics of the cyclone-fired units are a key element in the mechanism responsible for the back corona. The coincidence of the erratic power levels and the washing of the coal raises interesting questions about how washing could effect coal chemistry or the combustion characteristics of the coal.

The unconventional answer is that the back corona is not the result of a high resistivity deposit. Perhaps the electrical breakdown strength of the ash is unusually low such that corona is produced in the collecting plate ash layer at a very low electric field gradient. This would not explain why the corona initiation voltage is increased to +20 KV.

Also puzzling is why back corona is occurring when +25 ppm of SO_3 is present since SO_3 conditioning at levels well below 25 ppm has successfully eliminated back corona on other cold-side precipitators.

CONCLUSIONS

The detection of back corona on a cold-side precipitator with high-sulfur coal is quite unsettling in view of the fact that this phenomena is unreported for any other installation. It would appear that the combustion conditions of the cyclone-fired units are a key ingredient since Units 1 and 2 at the same plant, with identical precipitators, have never been observed to have either back corona or erratic power levels. One conclusion that can be drawn from this experience is that the industry still has some things to learn regarding the interrelationship of fuel, combustion conditions and our ability to predict precipitator performance.

The work described in this paper was not funded by the U.S. Environmental Protection Agency and therefore the contents does not necessarily reflect the views of the Agency and no official endorsement should be inferred.

REFERENCES

1. J. L. DuBard, E. C. Landham, Jr., W. R. Dickson. "Evaluation of ESP Operating Difficulties at Muskingum River Units 3 and 4" (SRI Project 6346). January 4, 1988. p 5-10.

2. J. L. DuBard, E. C. Landham, Jr., W. R. Dickson. "Evaluation of ESP Operating Difficulties at Muskingum River Units 3 and 4" (SRI Project 6346). January 4, 1988. pp 5-2, 5-9.

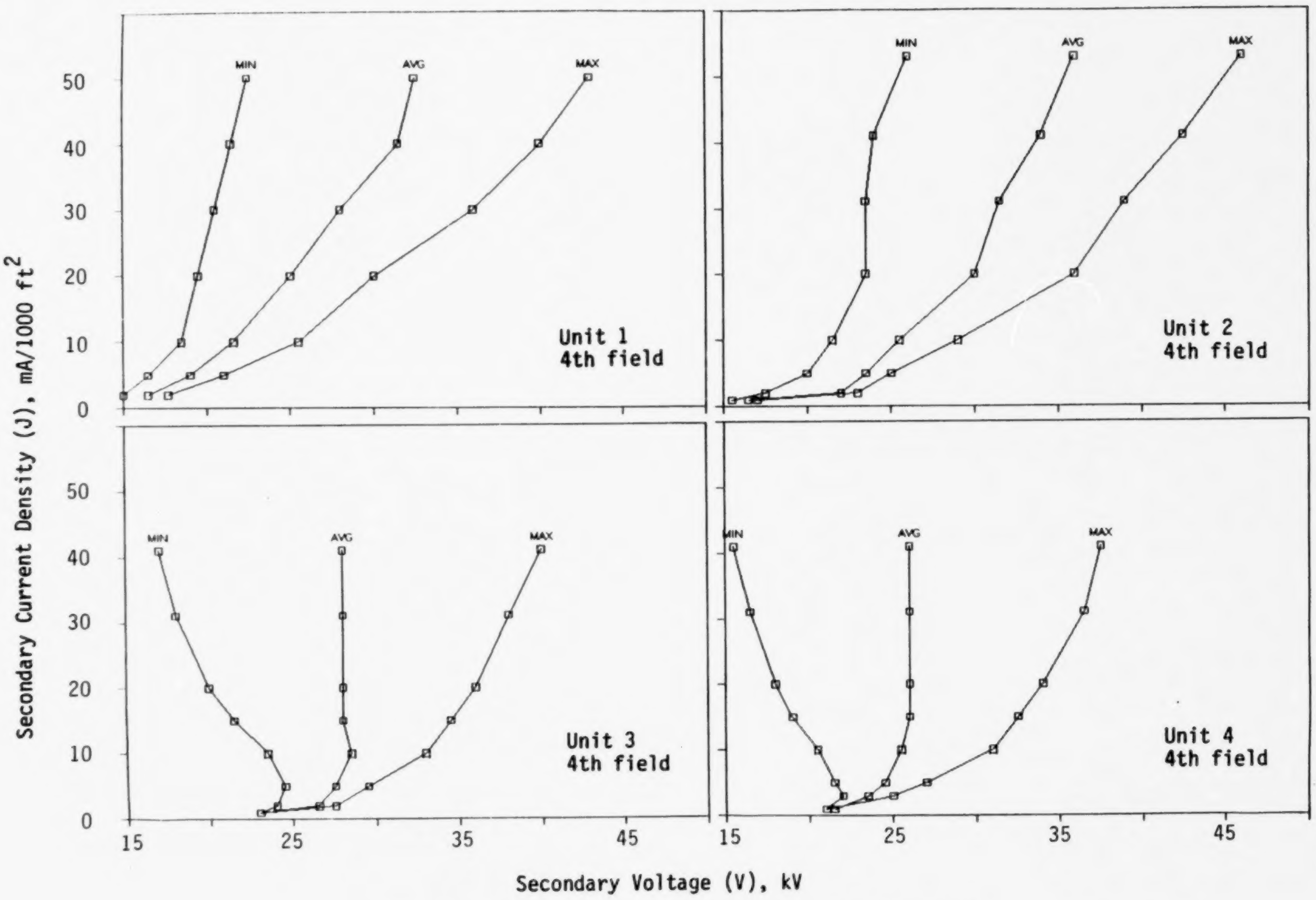

Figure 1. J-V plots of 4th field of Units 1, 2, 3 & 4

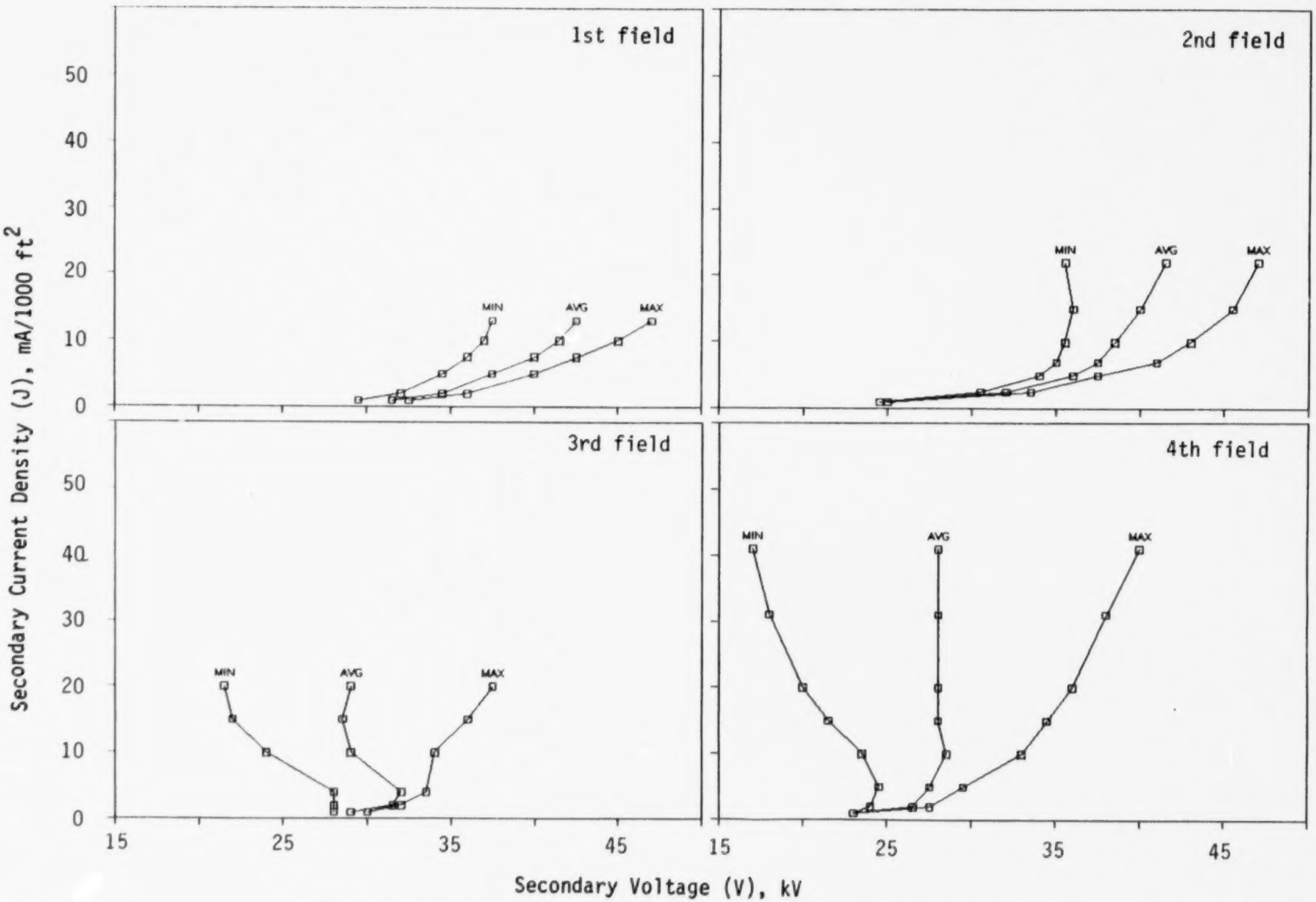

Figure 2. J-V plots of 1st, 2nd, 3rd, and 4th fields of Unit 3

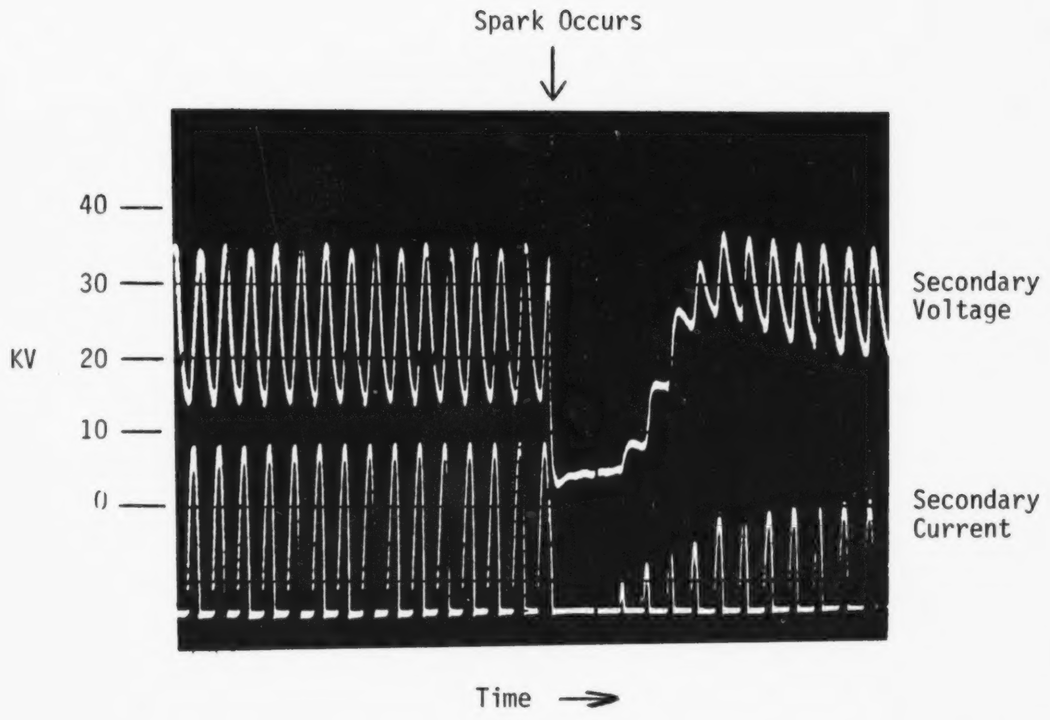

Figure 3. Voltage and current time traces when a spark occurs.

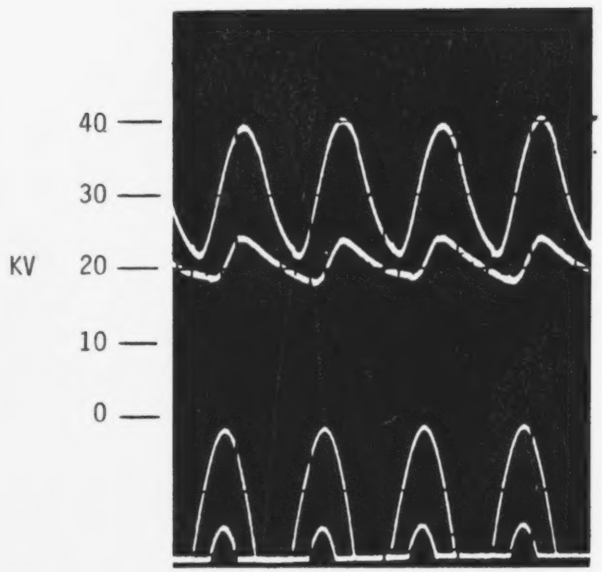

Figure 4. Voltage and current time traces without back corona. At 5 and 50 mA/1000 ft^2.

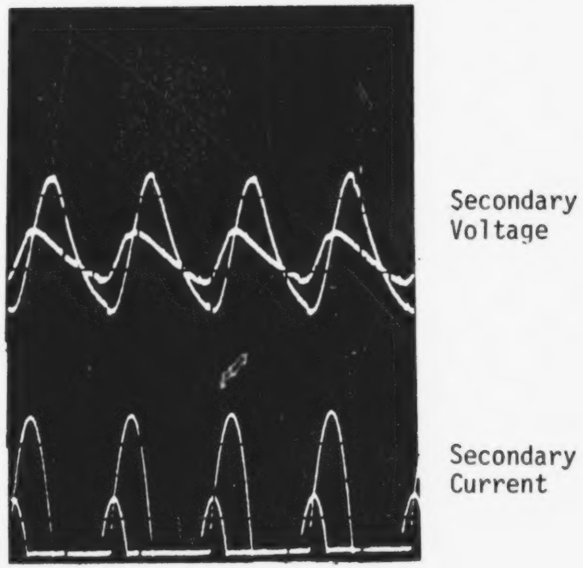

Figure 5. Voltage and current time traces with back corona. At 2 and 15 mA/1000ft^2.

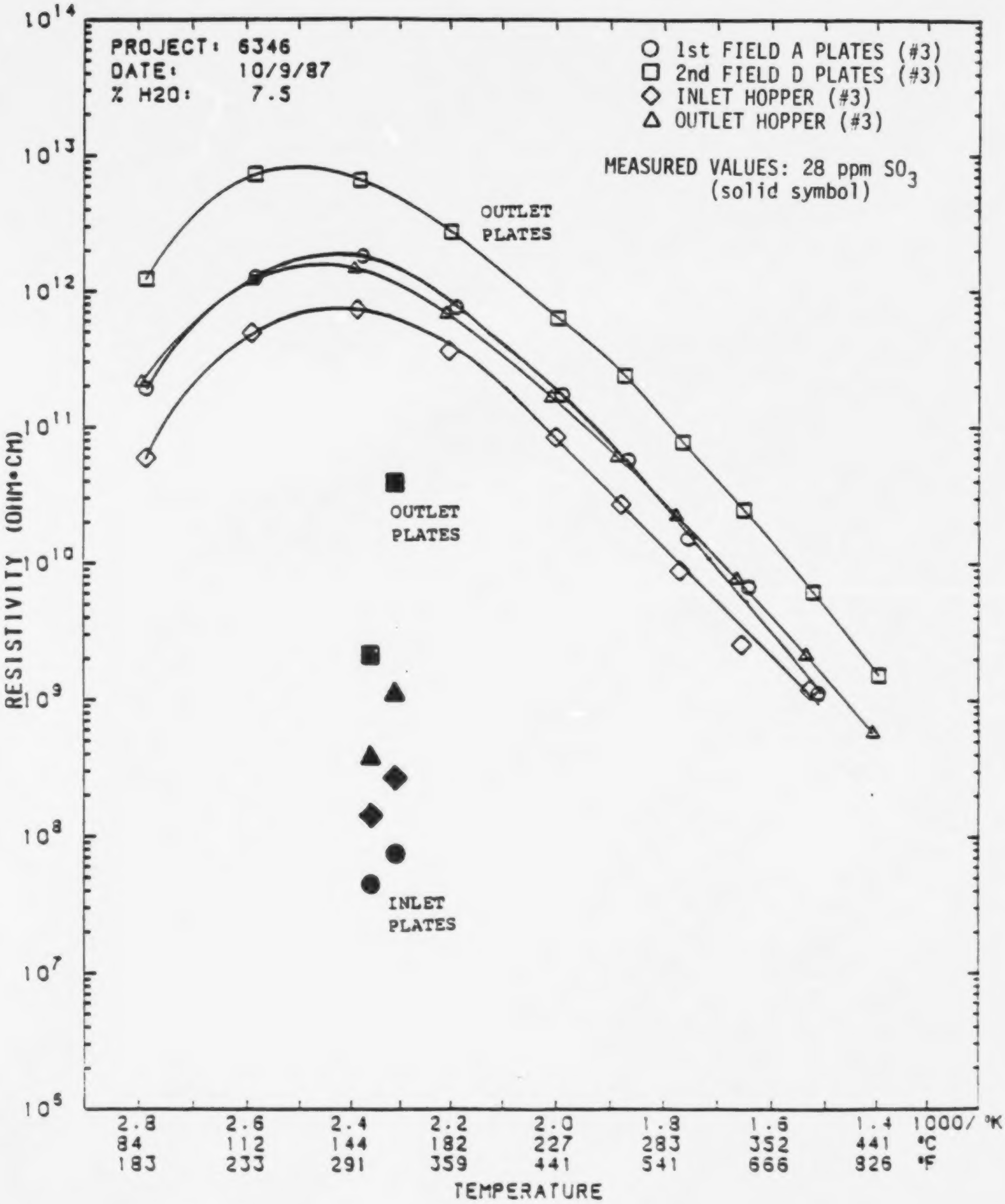

Figure 6. Lab measured resistivity vs. temperature of 1st and 4th field plates and inlet and outlet hopper samples of Unit 3.

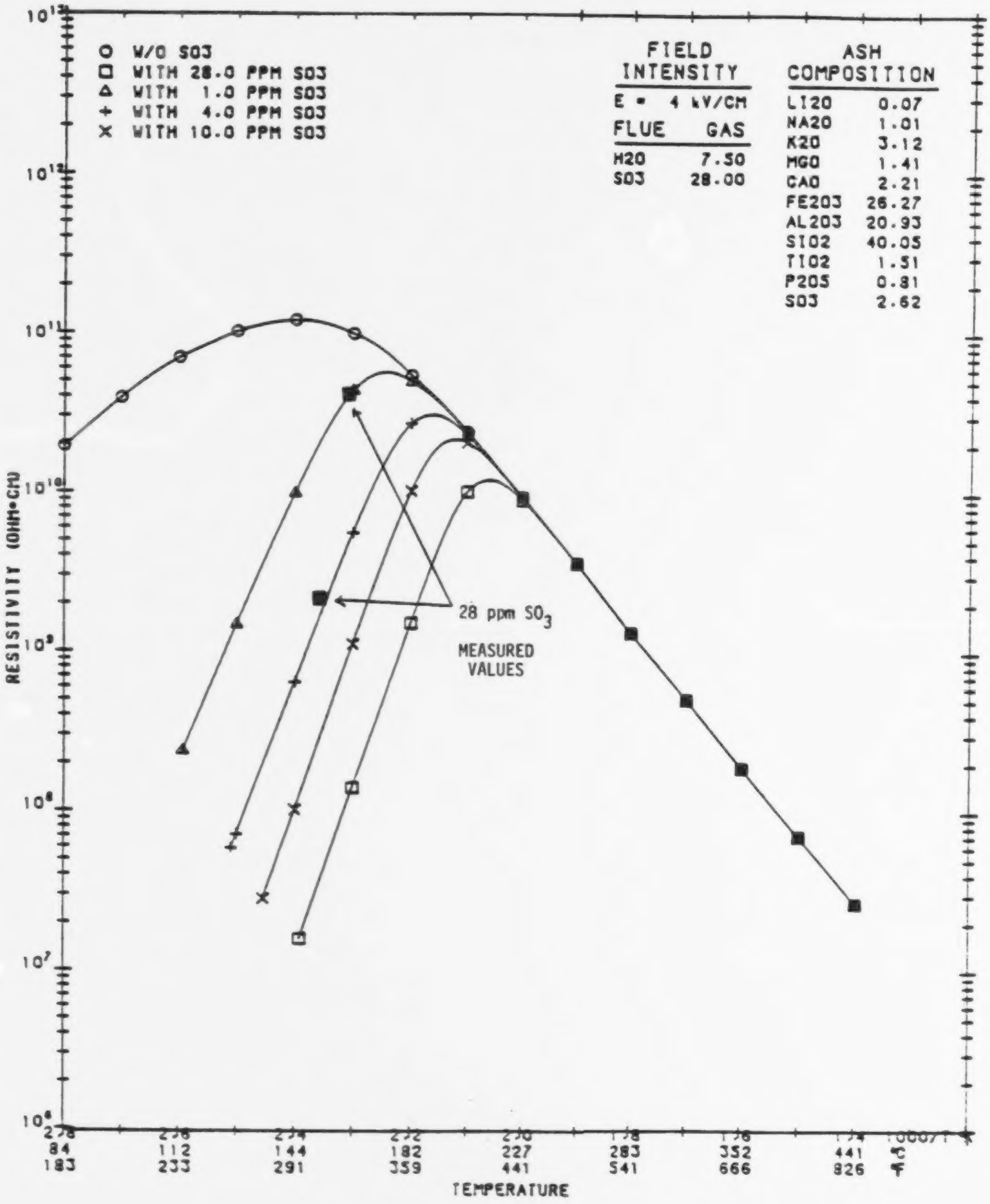

Figure 7. Predicted resistivity vs temperature of 4th field plate deposits for various SO_3 concentrations.

TABLE 1. PROXIMATE AND ULTIMATE COAL ANALYSIS

Proximate Analysis

	As Received	Dry Basis
% Moisture	2.10	xxxxx
% Ash	13.33	13.62
% Volatile	40.30	41.17
% Fixed Carbon	44.27	45.21
	100.00	100.00
Btu/lb	12132	12393
% Sulfur	5.27	5.38

Ultimate Analysis

	As Received	Dry Basis
% Moisture	2.10	xxxxx
% Carbon	66.30	67.72
% Hydrogen	4.64	4.74
% Nitrogen	1.00	1.02
% Chlorine	xxxxx	xxxxx
% Sulfur	5.27	5.38
% Ash	13.33	13.62
% Oxygen (diff.)	7.36	7.52
	100.00	100.00

TABLE 2. UNITS 1-4 PRECIPITATOR SPECIFICATIONS

	Units 1&2	Units 3&4
Gas Flow Rate (acfm)	900,000	930,000
Actual Efficiency	98.0%	95.5%
Gas Velocity (ft/sec)	5.95	6.15
Treatment Time (sec)	4.0	3.9
SCA (sq ft/1000 acfm)	179	173
	Units 1, 2, 3 & 4	
Number of Gas Passages	112	
Gas Passage Dimensions	30 ft. high, 24 ft. long, 9 in. wide	
Collection Surface	161,000 ft^2	
Aspect Ratio	.8	
Number of T/R Sets	8 (each 45 KV, 1200 mA)	
Available Corona Current	8000 mA	
Available Corona Power	240 KW (30 KV, 8000 mA)	
Available Current Density	50 mA/1000 ft^2	
Specific Corona Power	260 watts/1000 acfm	

TABLE 3. UNIT 3 FLY ASH ANALYSES

Field	1st	2nd	3rd	4th
% Soluble Sulfate	6.7	9.4	11.3	13.7
% Loss on Ignition	8.6	11.2	11.6	14.1
% Mineral Analysis				
Li	0.06	0.06	0.07	
Na	0.83	0.86	1.0	1.0
K	2.6	2.6	3.2	3.1
Mg	1.2	1.2	1.4	1.4
Ca	1.9	1.9	2.2	2.2
Fe	26.0	27.0	24.6	26.1
Al	21.6	21.0	21.4	20.8
Si	41.8	41.3	40.7	39.8
Ti	1.4	1.4	1.6	1.5
P	0.41	0.44	0.08	0.80
S	1.7	2.0	1.9	2.6

OVERVIEW OF KEYSTONE STATION'S OPACITY DEGRADATION AND SUBSEQUENT IMPROVEMENTS

David W. Read
Daniel L. Strein
Pennsylvania Electric Company
Johnstown, PA 15907

Alex Zarechnak
MPR Associates
Washington, D.C. 20036

ABSTRACT

Prior to the conversion to balanced draft and the installation of spiral finned, in-line economizers, both Keystone Units' precipitators performed considerably more efficiently than would have been predicted based on current analytical models and utility experience. Subsequent to these modifications, the precipitators' performance degraded to the point where substantial generation load reductions were required to comply with regulatory opacity limits on a consistent basis. Through a diligent operations and maintenance effort, extensive engineering testing and analysis, and relatively low cost conventional and creative capital projects, the performance of the precipitators was restored to previous above average performance with the essential elimination of all load reductions due to environmental limits.

BACKGROUND

Keystone Station Units 1 and 2 are 850 MW units which went into commercial operation in 1967 and 1968, respectively. These units, operated by the Pennsylvania Electric Company (Penelec), are mine mouth plants, burning the same coal. Each unit includes a Combustion Engineering designed pulverized coal, tangentially fired twin furnace boiler, which was originally designed for forced draft operation. The design of each unit also includes two cold side Research Cottrell precipitators for fly ash removal. The precipitators are divided into four chambers with each chamber divided into four electrical sections in the direction of flue gas flow. Figure 1 shows the precipitator arrangement and layout.

Based on operating experience and design data, the precipitators at Keystone Station appear to be marginal in size. Current design criteria would require a precipitator collector area of approximately 300 SCA for the coal typically burned at Keystone Station to achieve a 99.5% efficiency. The actual SCA provided by Keystone is only 208. Precipitator testing performed in 1982 on Unit 1 and 1981 on Unit 2 indicated marginal precipitator performance with total emissions near the regulatory limit. At that time, ash resistivity was reported to be low and precipitator velocities marginal to high.

Opacity monitoring was initiated at Keystone Station in December, 1982 in accordance with an agreement with the Pennsylvania Department of Environmental Resources (PaDER). The monitors were installed in each precipitator outlet duct, down one-third of the height from the top, immediately inside the concrete stack. Keystone Station operated with no loss of generation due to violation of the opacity regulatory operating limit (20%) for two years following this installation. Typical opacity was near 10% with little spiking.

Opacity violations and consequent loss of generation first occurred on Keystone Unit 2 following its Fall 1984 scheduled outage and then on Unit 1 following its 1985 scheduled outage. During these outages, the economizers were replaced and the boilers were converted to balanced draft operation. The replacement economizer was the third economizer installed in each unit. The original economizer was a staggered-flow, continuous-fin design with a heat transfer surface area of approximately 318,000ft^2. This design was replaced in the mid 1970's with a staggered-flow, spiral-fin design economizer whose heat transfer surface area of 638,000 ft^2, was significantly greater than the first economizer. The current replacement is a spiral-fin, in-line design with a heat transfer surface of 645,000 ft^2. An induced draft fan was added in each precipitator outlet duct, upstream of the opacity monitor location. This involved significant modifications to the exit ductwork and removal of the stack baffle. The locations of the opacity monitors were not changed.

Keystone Unit 2 was load limited following its outage in late December 1984 due to excessive opacity (exceeding the regulatory operating limit of 20%). The extent of the opacity load limitation was variable but initially averaged 150 MW and then decreased with time as corrective actions were implemented. The loss of generation resulting from the opacity problem at Keystone Units 1 and 2 throughout the period of problem investigation and solution is summarized in Figure 2. The losses attributable to the regulatory operatory limit reflect the load reduction necessary to maintain the unit opacity less than 20%. These losses are especially important for Keystone Station since it is normally base loaded and one of the largest and most economical units operated in the PJM grid.

THE CORRECTIVE ACTION PROCESS

The significant Unit 2 loss of generation following the December 1984 scheduled outage prompted immediate action by station personnel to correct the opacity. Precipitator inspections and initial testing were performed in early January, 1985. Plant efforts to reduce opacity by modifying boiler and precipitator operating parameters throughout January were not successful although short periods of operation at full load with acceptable opacity were achieved.

On January 31, 1985 Penelec formed an Opacity Task Force, including personnel from Keystone Station, Conemaugh Station, Penelec Generation Production Engineering and MPR Associates, to address the opacity problem in a systematic fashion. The objectives of the task force were to develop and execute a corrective action plan to restore the performance of the Keystone precipitators. The Opacity Task Force embarked on an aggressive approach along parallel paths to identify the cause of the opacity problem and identify a practical solution as soon as possible. To structure and control this parallel approach an "Opacity Factors Tree" was formulated, as shown in Figure 3. This logic chart provides a fundamental reference for the establishment of the most critical parameters affecting opacity and the associated factors which influence these parameters. Implicitly, this logic chart also suggests that there may be several simultaneous contributing causes of high opacity and that there may be more than one solution.

An initial analysis of the Keystone Unit 2 opacity problem was performed by the Opacity Task Force in an effort to identify the most likely contributors to the opacity problem. This analysis involved a review of the documented influence of each of the 36 parameters shown on Figure 3. Based on the available data from precipitators testing, emissions control literature and station operational changes, the parameters affecting opacity were ranked from 1 to 4 in order of their potential for causing the Keystone Unit 2 opacity problem. The parameters were investigated in order based on the highest potential impact. For each of the parameters, the impact on the opacity problem was quantified in terms of measurable boiler and precipitator properties as much as possible. The data available from Keystone Unit 2 and other comparative sources, such as Keystone Unit 1, were evaluated and preliminary conclusions identified where necessary. Additional analyses and testing efforts were performed as appropriate to evaluate each potential cause. The assistance of outside testing organizations and established precipitator experts was also used in these evaluations.

As shown in Figure 3, opacity measurement is dependent on a large number of factors. These factures interact in the boiler, precipitator, and opacity monitor to affect the reported opacity. The investigation of each of these factors was performed as a separate task, however, they were often interrelated in their impact on opacity. No single area of the investigation was found to control opacity at all times. The complexity of boiler and precipitator operation made it impractical to isolate the parameter of interest while holding all other factors constant to quantify its effect on opacity. In addition, the constraints of planned outage scheduling and the need for timely improvements often required implementation of several recommended modifications at once, impairing the ability to determine the effect of each modification separately. Thus, the investigations have not quantified the relative contribution of each of the factors to the opacity problem. However, the important contributors were defined and appropriate corrective actions were implemented as appropriate.

The three primary causes of the Keystone Station opacity problem were identified as follows:

- o increased fly ash resistivity (due to temperature and SO_3 effects)

- maldistribution of precipitator flue gas flow, and
- uneven temperature gradients across the face of the precipitator.

The results of the investigations are detailed in the following discussions, with emphasis on the three primary factors identified above.

RESISTIVITY CHANGES DUE TO TEMPERATURE AND SO_3

One of the unexpected results of the Unit 2 outage was the difference in precipitator current densities. In the first half of 1985, Unit 1 with its continued straight-line low opacity had current densities between 40 and 55 ma/1000 ft^2 while Unit 2 with its high and erratic opacity, had current densities as low as 12 ma/1000 ft^2 and was never higher than 38 ma/1000 ft^2. A typical difference in opacity levels between the two units was a factor of two or more. The strong relationship between current density and opacity for Unit 2 at this time was established during a controlled set of precipitator tests conducted in February, 1985; the results of which are presented in Figure 4.

The difference in current density between the two units was an indication of a difference in resistivity in the fly ash, even though both units were burning the same coal. Based on data in Reference 1, the measured change in current density was consistent with a change in resistivity of approximately an order of magnitude. Direct in-situ measurements of fly ash resistivity confirmed the higher resistivity for Unit 2 but the scatter in the measurements made accurate determination of resistivity differences difficult. The search for the source of this apparent change in resistivity focused on two issues: flue gas temperature and SO_3 concentration.

Part of the change in resistivity and thus current density could be attributed to the replacement of the economizer. Fly ash fouling of the new economizer resulted in increased flue gas temperatures. Inlet temperatures to the Unit 2 precipitator were typically 20°F higher than for Unit 1. The effect of temperature on resistivity was calculated using the model in Reference 1 with chemistry analysis of actual ash samples from Units 1 and 2. For typical temperature conditions near 300°F and at moderate SO_3 levels near 4.0 ppm a 20°F rise in temperature was calculated to result in an increase in resistivity by a factor of 2 to 3. Extensive gathering and analysis of operational data at Keystone allowed the construction of statistically significant correlations (2) between the measured flue gas temperature, the calculated resistivity and the measured precipitator current density. Based on this data the effect of a 20°F increase in temperature results in a decrease of approximately 5 ma/1000 ft^2 - significant, but not sufficient to explain the typical 20-25 ma/1000 ft^2 difference in current density between the two units. Examination of the daily variations in average temperature for the two units confirmed that the lower current densities and higher opacities on Unit 2 persisted even at equal average temperatures, and equal coal chemistry.

Nonetheless, efforts continued to improve the thermal performance of the economizer and reduce the average flue gas temperature. The addition of economizer sootblowers was identified and subsequently implemented as a practical solution to reduce the ash fouling and to reduce the average flue gas temperatures to expected values.

To determine whether the continuing differences in current densities were due to differences in SO_3 concentrations in the flue gas, three sets of SO_3 tests were conducted. In each set of tests, SO_3 was measured in both Unit 1 and Unit

2 at similar locations. The first two sets of SO_3 tests were conducted after the Unit 2 economizer replacement and balanced draft conversion but before the Unit #1 modification. The third set of tests was conducted after Unit 1 was converted to balanced draft and the economizer was replaced.

The first set of tests was conducted in May 1985 at the discharge of the air heaters. The results are summarized in Figure 5 and show that the available SO_3 in the flue gas on Unit 1 was nearly twice that of Unit 2. Calculations based on Reference 1 indicate that these differences in SO_3 levels correspond to a difference in resistivity of approximately an order of magnitude. It was concluded that most of the observed differences in current densities were attributed to unexplained differences in the available level of gaseous SO_3.

Measurements were also made of water-soluble sulfates in the fly ash collected both upstream and downstream of the air heater to provide an indirect measure of available SO_3. These measurements indicated consistently higher values for the Unit 1 ash than for the Unit 2 ash. This was consistent with the gaseous SO_3 measurements, indicating that not only was more SO_3 available at Unit 1 but more SO_3 was also deposited on the ash, as would be expected.

The measured SO_2 levels in both units were the same; the conversion rate of SO_2 to SO_3 in Unit 1 was thus nearly twice that of Unit 1. These measured Unit 1 conversion rates are substantially higher than values reported at other plants (3) for comparable conditions. A search for the root cause of the higher SO_3 conversion rate in Unit 1 was pursued with a literature search and a second set of tests. One candidate cause identified in the literature was contact with carbon steel surfaces where increased area and increased contact time were thought to increase the conversion of SO_2 to SO_3 (4,5). However, the literature search uncovered relatively sparse information regarding the catalytic effect of ferrous materials in the flue gas stream on the conversion of SO_2 to SO_3. Specifically, the extent of oxidation depends on the condition of the metallic surfaces in the boiler system and the amount of catalytic dust (e.g. Fe or V) in the boiler. The literature search did not provide sufficient information which could be used to quantify the potential effect of the economizer replacement at Keystone on SO_3 concentration.

The second set of SO_3 tests allowed simultaneous sampling of the flue gas stream upstream and downstream of the economizer. The results from these tests are summarized in Figure 6.

The following observations were made from a review of the test data:

- The measured SO_3 average concentrations entering the economizer were 2.8 ppm higher for Unit 2.
- The differences in SO_3 concentration downstream of the economizer were greater than above the economizer. The average SO_3 differential of 5.5 ppm downstream of the economizer was approximately twice the upstream differential.
- The differentials in the sulfur trioxide concentration between units measured in the first set of tests downstream of the air heater were near 5.5 ppm, the same as the differential upstream of the air heaters, measured in the second set of tests.
- Large differences in SO_3 concentrations were measured between ducts. The trend of these differences was consistent in both units (i.e., the SO_3 concentration in the C duct is higher

than in the A duct for both units).

The economizer SO_3 test was intended to determine whether the replacement Unit 2 economizer was a major contributor to the SO_3 deficiency. The test results did not conclusively attribute the deficiency to the economizer, although some impact was identified. The equal magnitude of the SO_3 deficiency upstream of the economizer to that generated in the economizer indicates that both the combustion zone and catalytic reduction of SO_2 may be deficient in Unit 2. However, the data also suggests that accelerated decay of SO_3 in Unit 2, perhaps as a result of the lower pressure, may be responsible for the measured deficiency. Further understanding of the chemical equilibrium of sulfur oxides in flue gas is required to distinquish between these several possible causes.

The third set of tests was conducted after Unit 1 underwent the same modifications as Unit 2, including economizer replacement and conversion to balanced draft. Although the same basic controlled condensation sampling and testing method was used as in the previous two sets of tests, the test equipment and testing contractor were different and the resulting data included greater scatter. The measurements showed that the SO_3 levels in both Units 1 and 2 were now the same and the previously high conversion rate of SO_2 to SO_3 in Unit 1 was reduced to a level more typical of industry experience. These test results are consistent with the conclusion that the replacement of the economizer, and/or the conversion to balanced draft operation in both Units 1 and 2 resulted in lower SO_3 levels.

In an effort to compensate for the SO_3 deficiency in Unit 2, a gaseous SO_3 injection system was tested. The SO_3 was injected into the hot side of the air heaters on all three ducts. The SO_3 flue gas conditioning system proved to be an effective resistivity modifier and did increase the precipitator's current density. However, it had a minimal positive affect on opacity during its test program. The flue gas conditioning (FGC) did reduce opacity during periods of high exit gas temperatures, but only by 2% or less. The original correlation of current density with opacity established by the tests in Figure 4 without SO_3 injection was no longer applicable under the conditions of SO_3 injection. The reasons for this different behavior were not confirmed and testing with SO_3 injection was not pursued further.

FLOW DISTRIBUTION

When the units were converted to balanced draft, induced draft fans were added in each precipitator outlet duct upstream of the opacity monitor location. This involved significant modifications to the exit ductwork and removal of the stack baffle. Detailed flow testing was performed at the precipitator inlet and a review of the flow distribution data both prior to and subsequent to the conversion outage indicated an increase in maldistribution in the vertical and horizontal directions. This maldistribution indicated that flue gas was passing above and below the precipitator collector plates. In addition, hopper sneakage flow during operation had been observed through observation ports in the precipitator access doors. The presence of hopper sneakage flow and a vertical flow maldistribution had also been identified by visual inspections of the precipitator internals. In order to reduce the hopper sneakage flow and to improve the inlet vertical velocity profile, modifications to the precipitator inlet nozzle flow baffles and/or inlet perforated plate were investigated by performing a single chamber model flow study at Boyle Labs.

The objective of the single chamber flow study was to identify flow baffle and/or inlet perforated plate modifications that would reduce collector plate bypassing and improve the vertical flow distribution. The modifications being considered were limited in scope to those considered practical for field installation during a unit forced outage. The flow baffle and inlet perforated plate modifications to be tested, listed in order of preference based on field installation considerations, were as follows:

- Existing Flow Baffle Modifications

  a. Remove flow baffles
  b. Change flow baffle angle (currently at 30°)
  c. Cut flow baffle trailing edge (reduce length of baffle)
  d. Modify flow baffle vertical spacing

- Inlet Perforated Plate

  a. Remove existing blocking strips at center
  b. Reduce ash gap at bottom of plate
     (Existing gap = 21 inches high)

The single chamber model tests demonstrated that removing the blockage strips covering the center region of the first perforated plate greatly reduced gas velocities in the lower collecting area of the first field and greatly improved the overall vertical profile across the precipitator opening as indicated in Figure 7. Additional testing of the various modifications of devices as stated above did not significantly reduce flow conditions at the bottom of the precipitator opening either singly or in combination with the recommendation.

The 21-inch ash gap at the bottom of the first perforated plate was normally blocked by collected fly ash. Model testing indicated that removing this blockage resulted in increased gas sneakage in the lower region of the collector plates. Since the ash is normally removed during precipitator cleaning, it was recommended that this gap be reduced to 4 inches.

The recommendations of the model study were implemented during a forced outage. Subsequent field testing verified that the vertical velocity profile had improved and that the overall flow distribution was better. The impact of these improvements on opacity was considered positive but it was not possible to quantify because of the inherent variability of other factors.

TEMPERATURE DISTRIBUTION ACROSS FACE OF PRECIPITATORS

The third major cause of the opacity problem investigated was the large temperature profile at the face of the precipitators. This investigation is described in detail in an associated paper titled "Flue Gas Temperature Mixing to Improve Electrostatic Precipitator Performance at Keystone Generating Station"(6).

A large temperature gradient of approximately 80°F at the precipitator face had always existed on both Keystone units. Temperature maldistribution is an inherent problem with the Ljungstrom regenerative air heaters. Prior to the reduction of SO_3 resulting from the balanced draft/economizer replacement outages, the temperature gradient did not result in an opacity problem. However, the temperature maldistribution did impair precipitator performance in the marginal resistivity condition following the outages. Large differences in current density were observed between the four chambers of each precipitator corresponding to the temperature variation between the chambers. Rappers-on rappers-off testing verified that significant fly ash reentrainment from the cold chambers was occurring when the average flue gas temperature was relatively low. Raising the average flue gas temperature at the air heater outlet alleviated the reentrainment from the cold chambers while driving the hot chambers into a high resistivity condition reducing their current density and collection ability. This range of resistivity condition also limited the effectiveness of SO_3 injection.

A model study was conducted to design a device that would reduce the temperature gradient to current design standards of approximately 20°F without degrading the flow distribution. Temperature mixing tunnels were shown to result in a more uniform temperature and were installed during the Unit 2 Summer 1986 scheduled outage. Field testing following the outage verified that the mixing tunnels significantly reduced the temperature maldistribution without degrading the flow distribution and pressure loss beyond accepted levels. Precipitator performance improved substantially and opacity was reduced with the correction of this long standing deficiency.

OTHER FACTORS

As previously stated, all the areas of the Opacity Task Force investigations have not been presented in this paper. However, in addition to the three primary factors impacting opacity, a number of other important effects were quantified in the investigations. The following is a brief summary of some of those other investigations:

o	Rapper Operation	Optimized rapper sequency is important to the control of opacity. Upgraded controls were installed. Power strategy was shown to be vital to achieving acceptable opacity. Extensive experimentation including rapper on/off testing established optimum strategy.
o	Comparison of Precipitator Efficiency to Industry Experience	Collection efficiency prior to outage was exceptionally good. Following the balanced draft/economizer replacement outage, the efficiency degraded to a level consistent with industry experience for this size precititator.
o	Coal Chemistry Variability	Multiple regression analysis of operational data described in Reference 2 identified the significant influence of natural variations of the sulfur and ferric oxide content of the coal. The results are summarized below:

EFFECT OF VARIATION IN FLUE GAS TEMPERATURE AND COAL CHEMISTRY ON PRECIPITATOR CURRENT DENSITY

Parameter	Range	Effect on Current Density
Flue gas temperature	260-325°F	15 milliamps/1000 sq. ft.
Sulfur content	1.5-2.0%	10 milliamps/1000 sq. ft.
Ferric oxide content	7-14%	10 milliamps/1000 sq. ft.
Sodium oxide content	0.2-1.0%	5 milliamps/1000 sq. ft.

o Precipitator Mechanical Conditions	No significant impact on opacity problem was found. Repairs were all normal maintenance.
o Precipitator Electrical Conditions	No significant impact on opacity problem was found. Modifications have improved reliability.

CONCLUSIONS

Based on the results of the Keystone Opacity Task Force investigations, the primary cause of the Keystone opacity compliance problem is thought to be the reduction in the SO_3 available in the flue gas following the balanced draft/economizer outage. The investigations were inconclusive in determining whether the economizer replacement, the balance draft conversion or both modifications were responsible for this reduction. The excellent opacity performance previously experienced at Keystone Station is attributed to the abundance of SO_3 in the flue gas which resulted in maximum electrical power input and compensated for the small precipitator size. The Keystone Station precipitator operation just prior to the conversion outages was exceptional compared to typical industry performance.

In addition to the reduction in SO_3, the changes implemented during the balanced draft/economizer outages also aggravated the marginal precipitator flue gas temperature and flow conditions. The economizer replacement resulted in increased flue gas inlet temperatures; thereby increasing the flyash resistivity. The addition of induced draft fans resulted in increased flow maldistribution and raised slightly the already high flue gas velocities. This resulted in regions in the precipitator with substantial reentrainment and ash hopper sweepage. Thus, both collection and retention of fly ash were adversely affected during the outage. The effects of the high resistivity and high velocity conditions on opacity were aggravated by the large temperature gradient across the precipitator face, even though the temperature gradient by itself had not resulted in a previous opacity problem.

The improvements in the Keystone Station opacity performance are attributable to unit modifications and careful operation of precipitator and boiler. The major improvements made include:

- o Operational changes to optimize precipitator rapping strategy, control furnace combustion conditions, and control exit flue gas temperature with the air heater bypass dampers.
- o Installation of ducts to improve temperature distribution.
- o Addition of economizer sootblowers to reduce the flue gas

temperature and increase economizer performance.

- Removal of inlet perforated plate blocking strips to improve the velocity distribution.

Since the implementation of all the above modifications, the opacity has returned to pre-conversion outage levels and the chargeable loss of generation has been essentially zero. The precipitators once again are operating exceptionally well compared to predictions using current utility and analytical models. Additional research into the mechanisms of SO_3 production is needed to further understand and characterize utility precipitator design and operation.

The aggressive parallel corrective action approach utilizing fundamental relationships of all the parameters affecting opacity was instrumental in correcting the opacity problem in a timely and practical manner.

The work described in this paper was not funded by the U.S. Environmental Protection Agency and therefore the contents do not necessarily reflect the views of the Agency and no official endorsement should be inferred.

ACKNOWLEDGEMENTS

E. B. Bird	-	MPR Associates
J. M. Dudeck	-	Pennsylvania Electric Company
C. A. Hainsey	-	Pennsylvania Electric Company
J. M. Russell	-	MPR Associates
F. D. Wood	-	Pennsylvania Electric Company

REFERENCES

(1) Gooch, J. P., Southern Research Institute. A Manual For the Use of Flue Gas Conditioning for ESP Performance Enhancement. EPRI CS-4145, August 1985.

(2) MPR Report 931. Keystone Generating Station, Effect of Coal and Ash Variability on Precipitator Performance, May, 1986.

(3) Southern Research Institute. A Study of Resistivity and Conditioning of Fly Ash EPA-R2-72-087, February, 1972.

(4) Kanowski, S. and Coughlin, R. W. Catalytic Conditioning of Fly Ash Without Addition of SO_3 From External Sources. Environmental Science and Technology, 11:1, January, 1977.

(5) Barrett, R. E. Hummell, J. D., and Reid, W. T. Formation of SO_3 in a Non Catalytic Combuster. Journal of Engineering for Power, April, 1986.

(6) Dudeck, J. M. and Bird, E. B. Flue Gas Temperature Mixing to Improve Electrostatic Precipitator Performance at Keystone Generating Station. Paper presented at 1988 EPRI/EPA Seventh Symposium on the Transfer and Utilization of Particulate Control Technology, Nashville Tennessee, March, 1988.

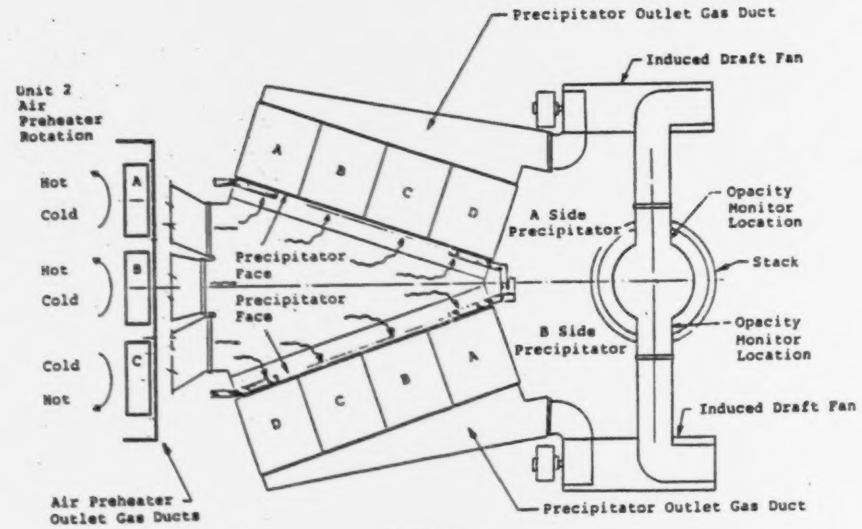

PLAN VIEW

Precipitator Design Data	
Gas Flow (each side)	1,350,000 cfm
Gas Temperature	270°F
Average Gas Velocity	6.41 fps
Inlet Loading	4.0 grains/cu. ft.
Guaranteed Exit Loading	0.02 grains/cu. ft.
Guaranteed Efficiency	99.5%

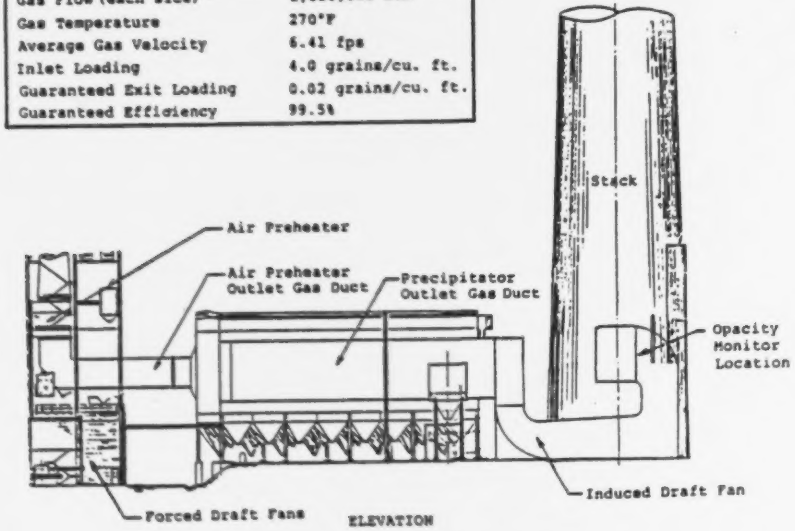

ELEVATION

KEYSTONE STATION
PRECIPITATOR ARRANGEMENT

FIGURE 1

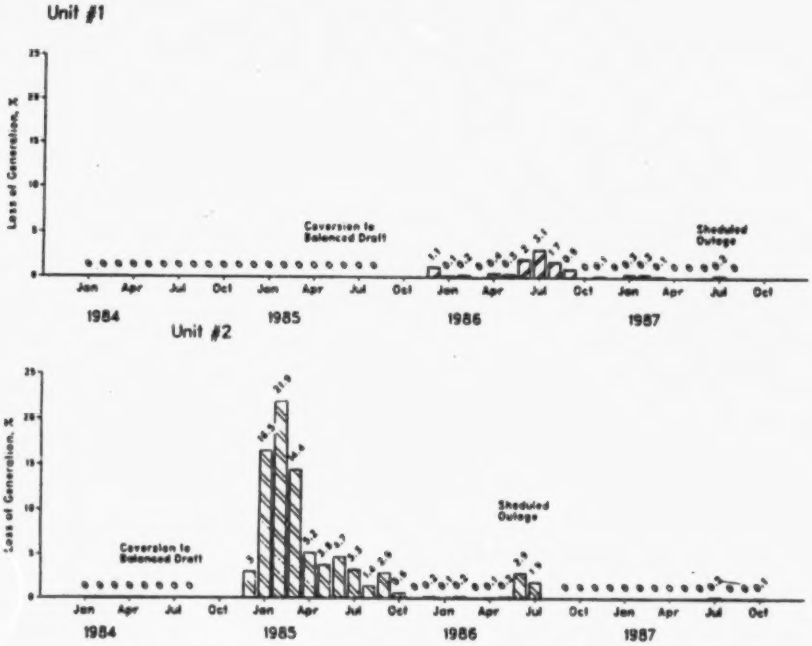

Keystone Station
Monthly Loss of Generation
Attributed to Opacity

FIGURE 2

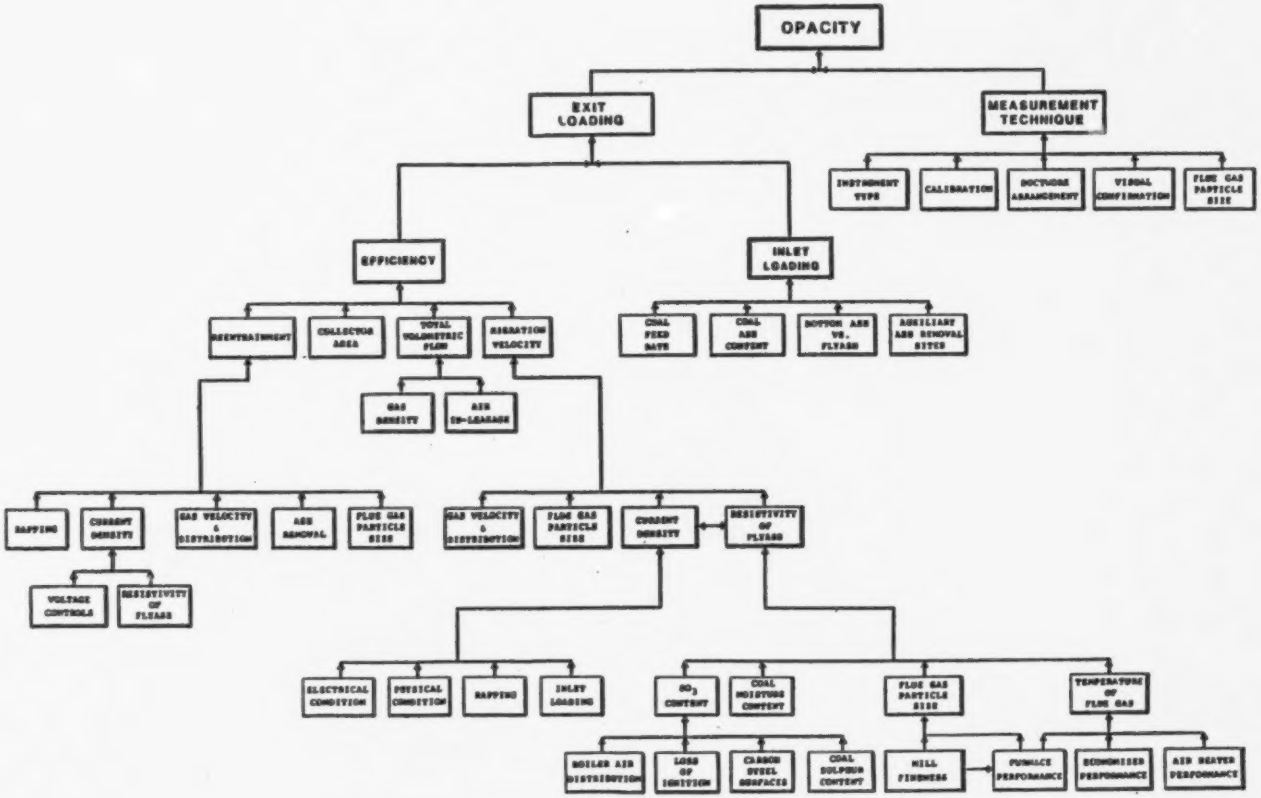

OPACITY FACTORS TREE
Figure 3

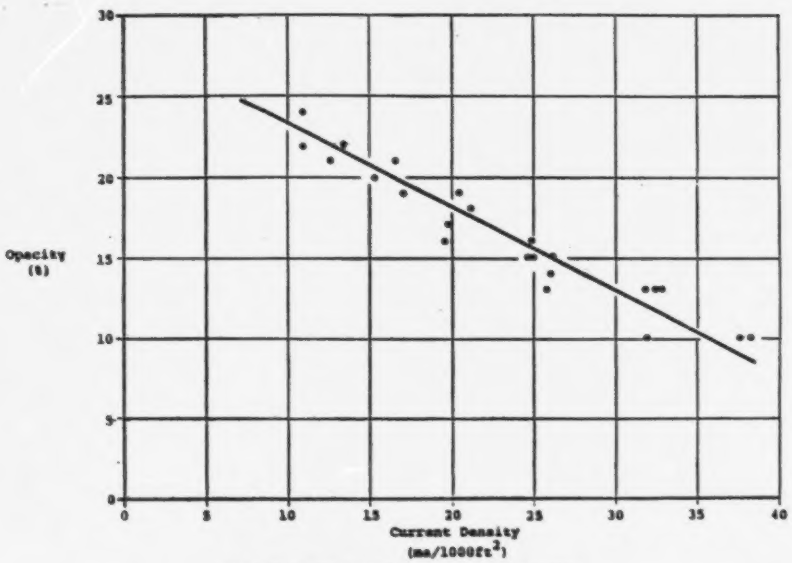

EFFECT OF CURRENT DENSITY ON OPACITY DURING FEBRUARY TESTING PERIOD

FIGURE 4

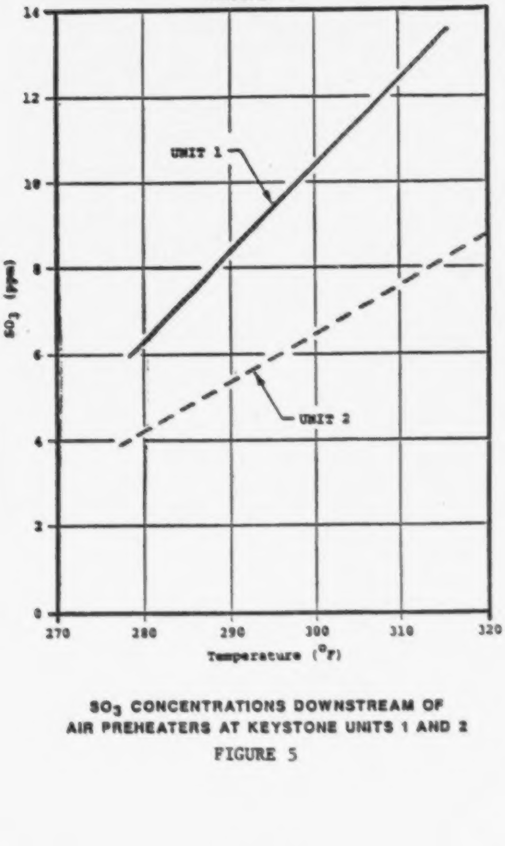

SO$_3$ CONCENTRATIONS DOWNSTREAM OF AIR PREHEATERS AT KEYSTONE UNITS 1 AND 2

FIGURE 5

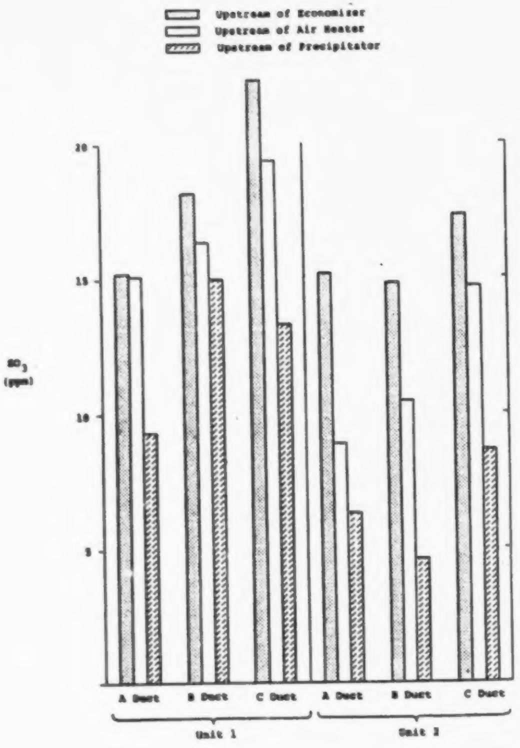

KEYSTONE STATION
ECONOMIZER SULFUR TRIOXIDE TEST
SULFUR TRIOXIDE BY DUCT
FIGURE 6

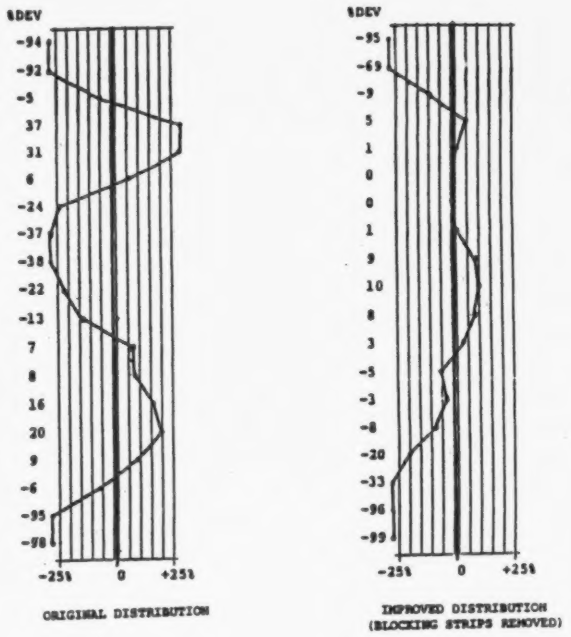

RESULTS

- PRINCIPLE IMPROVEMENT IS ACHIEVED FOR SWEEPAGE FLOW AT BOTTOM OF PRECIPITATOR
- OVERALL VERTICAL FLOW DISTRIBUTION IS ALSO IMPROVED

KEYSTONE UNIT 2
OPACITY PROBLEM
RESULTS OF SINGLE CHAMBER STUDY

FIGURE 7

FLUE GAS TEMPERATURE MIXING TO IMPROVE ELECTROSTATIC PRECIPITATOR PERFORMANCE AT KEYSTONE GENERATING STATION

John Dudeck
Pennsylvania Electric Company
Johnstown, PA 15907

Edward B. Bird
MPR Associates, Inc.
Washington, D.C. 20036

ABSTRACT

Following a balanced draft conversion and economizer replacement, Keystone Unit 2 experienced substantially higher stack gas opacity requiring periodic load reductions. A large (80°F) air heater outlet flue gas temperature differential contributed to this degraded performance. This paper describes the model testing, design, and field implementation of a flue gas temperature mixing device designed to reduce the flue gas temperature maldistribution and improve electrostatic precipitator performance. This temperature mixing device consists of two gas transfer ducts located below the rotating regenerative air heater immediately upstream of the precipitator. The gas transfer ducts reduced the flue gas outlet duct temperature differential to 20°F by mixing the hot and cold gas streams inherent in this air heater design. The investigation and installation of the temperature mixing device was a significant part of a comprehensive precipitator improvement program which reduced stack gas opacity and eliminated loss of generation due to the regulatory opacity limit.

BACKGROUND

The most effective solutions sometimes come from the least expected sources. As described in a companion paper (1) standard troubleshooting techniques (2) were applied to an opacity problem at the Keystone Generating Station. Although corrective actions based on these techniques improved opacity, they were insufficient to eliminate all loss of generation. Additional improvement in precipitator performance was obtained by reducing the temperature maldistribution across the face of the precipitator. Since the original flue gas temperature distribution at Keystone is typical of plants with rotating regenerative air heaters, Keystone's experience may be of benefit to other plants.

Keystone Units 1 and 2, rated at 850 MWe gross capacity, were placed in commercial operation in 1968 and 1969 respectively. The steam generators are Combustion Engineering split furnace, tangentially fired, supercritical, combined circulation units. Flue gas from each steam generator flows through three vertical shaft Ljungstrom air heaters into an eight chamber Research Cottrell electrostatic precipitator arranged in a chevron configuration. Precipitator arrangement and design data is shown in Figure 1.

During the Keystone Unit 2, Fall 1984 scheduled outage, the furnace was converted from forced draft to balanced draft operation and the staggered tube, spiral fin economizer was replaced with an in-line tube, spiral fin economizer. Following the outage, Unit 2 typically experienced continuous load losses of up to 150 MWe due to excessive opacity. Load reduction was necessary to comply with the station regulatory operating limit of 20% opacity. Loss of generation due to opacity reached as high as 22% per month.

After the outage, one minute average opacity was highly variable and was maintained just below 20% by the load reductions. This is in contrast to previous operation near a steady 8% opacity at full load. The instantaneous opacity trace was marked by extensive spiking and precipitator electrical power was much lower than previous Unit 2 experience. At this time, the Unit 1 precipitator continued to operate well and exhibit behavior similar to Unit 2 before the outage.

In the Spring of 1985, an aggressive program of precipitator testing at both Units 1 and 2 coupled with station operational modifications was initiated to limit the Unit 2 loss of generation (1). This program reduced the Unit 2 loss of generation attributable to opacity to less than 0.5% with typical opacity levels of 12% to 15%.

Following the Unit 1, Fall 1985 scheduled outage when similar economizer and balanced draft modifications were made, the same adverse impact of the outage modifications was observed. The operating practices developed for Unit 2 successfully reduced but did not eliminate the Unit 1 loss of generation. As part of a comprehensive precipitator improvement program to reduce stack gas opacity and eliminate all loss of generation due to the regulatory opacity limit, the possible adverse affect of temperature maldistribution on both Units 1 and 2 was investigated.

DISCUSSION

WHY TEMPERATURE DISTRIBUTION BECAME A SUSPECT

Ljungstrom regenerative air heaters are used at Keystone Station to transfer heat from the flue gas leaving the economizer to the combustion air. Unit 2 air heater rotation is shown on Figure 1; a cut-away view of the air heater is shown in Figure 2. Each air heater rotates at approximately 1 revolution per minute through the flue gas. This rotation introduces an 80°F flue gas temperature differential across each of the three air heater outlet ducts due to the decrease in the heat transfer rate as the air heater baskets heat up while traversing the duct. This duct temperature differential along with the duct geometry results in a temperature differential of up to 70°F across each precipitator face as shown in Figure 3.

At Keystone each precipitator chamber is electrically isolated. The large temperature range across the precipitator face results in different average temperatures and different operating conditions in each chamber. As shown in Figure 4, a change in flue gas temperature of 80°F results in a change in fly ash resistivity of 2 orders of magnitude. High resistivity fly ash, which is difficult to collect, occurs in the high temperature chambers. Low resistivity fly ash which is susceptible to reentrainment, occurs in the low temperature chambers. The hot chambers were characterized by low current densities of 10-20 mA/1000 ft^2, while cold chambers had current densities as high as 30-40 mA/1000 ft^2. Variations in current density due to mechanical or electrical problems were ruled out by several detailed internal inspections.

Average air heater temperature can be controlled to some extent by the operation of the combustion air heater bypass dampers or by biasing the forced draft fan air flow. Both of these methods were used by Keystone Station operators to change average flue gas temperature on specific air heaters. For example, chamber D of precipitator B in Figure 1 is relatively hot because of the clockwise rotation of air heater C. Chamber D could be cooled by increasing the combustion air flow through air heater C resulting in an increase in current density in that chamber. However, such tuning of the hot chamber would result in increased fly ash reentrainment from the coldest chambers (e.g. chambers A, B and C of precipitator B), whose temperature would simultaneously be reduced. Increased reentrainment could be detected through several observation ports installed in the precipitator side walls. Raising the temperature on the other hand could reduce reentrainment in the coldest chambers, but would also reduce current density in the hottest chambers. Because of the duct geometry, there seemed to be a narrow band of average temperatures that minimized opacity. However the limits of this band varied, perhaps due to periodic changes in coal properties (3). Successful tuning of all individual chambers by adjusting the bypass dampers was not possible.

The required efficiency of the Keystone precipitators is 99.5%. The design specific collection area (SCA) is 208 ft^2/1000 ACFM and the design velocity is 6.41 ft/sec. By today's standards, this is a marginal design. In particular, the relatively high velocity aggravated any reentrainment in the low temperature chambers.

MODEL TESTING

A model study was initiated in January, 1986 to identify a temperature mixing device that could substantially reduced the range of flue gas temperatures at the precipitator inlet and thereby result in more uniform fly ash resistivity. The specific goals were to achieve the following conditions at the air heater duct outlet. (Velocity RMS is the Root Mean Square of the velocity differences from the average and is a measure of the flow distribution.)

1. Horizontal temperature variation of 25°F or less;
2. Vertical temperature variation of 10°F or less;
3. Velocity RMS distribution of 7.4 or less;
4. Additional duct pressure drop of 3.0 in. w.g. or less.

The horizontal temperature limit of 25°F at the air heater duct outlet was selected in order to achieve a maximum temperature variation of 20°F or less at the precipitator inlet. The limit on the velocity RMS distribution was based on the baseline model test results (Table 1). The induced draft fans installed during the balanced draft conversion could accommodate an additional 3.0 inch water gage pressure drop.

Model Description

The model used in the study was a 1/12 scale acrylic plastic replica of the Keystone Unit 2 air heater (4). The model extended from just above the air heater hot end flange to the chevron inlet. The duct arrangement modeled was for the C air heater; an outboard arrangement. In the final model testing, the mixing device was also qualified on a model of the inboard duct arrangement of the B air heater.

The rotation of the air heater basket was not modeled; however, the basket itself was simulated with a stationary flow straightener. Upstream of the air heater, the model was divided into two separate temperature regions; half the air heater at ambient air temperature, the other half at heated air temperature. During preliminary testing the heated air was 40°F above the ambient temperature. For final qualification testing the heated air was 80°F above ambient temperature.

The model differed from field conditions in a number of respects. In the field, there is a continuous variation from low to high temperature across the air heater. This was modeled by two distinct temperature regions as described above. In the field, the actual temperature range is from approximately 260°F to 340°F; the model used ambient air for the cold side and ambient air heated by 40°F or 80°F for the hot side. Finally the field fluid medium is flue gas laden with particulate while the model fluid medium was air. These model limitations were recognized and it was concluded that the model could still provide the basis for developing a suitable design that would eventually be verified by field testing after installation.

Qualification Testing

To qualify the model study approach, baseline model test results were compared to measured field data. The baseline model is a reproduction of the existing Keystone geometry. The duct between the air heater outlet and the precipitator chevron inlet was modeled with the existing elbow turning vanes in the vertical leg and two rows of ladder turning vanes in the horizontal leg (Figure 5). The elbow turning vanes are installed to turn the flow horizontally, while the ladder vanes maintain the flow evenly distributed within the horizontal duct.

Field data and baseline model test results (Test 4) are summarized in Table 1 for the study objectives described above. The vertical and horizontal temperature differences for the field and model compare well. (No comparative pressure drop is available for the field data.) The velocity RMS is higher for the field than for the model data but both model and field geometries show a relatively uniform distribution. The differences between the baseline model and field data were considered acceptable.

Evaluation Testing

The evaluation testing was performed in two phases. Phase 1 involved testing devices in the horizontal leg of the duct immediately upstream of the chevron leading to the precipitator. Phase 2 involved testing in the vertical leg of the duct immediately downstream of the air heaters. During Phase 1, a variety of devices were tested with all existing turning vanes in place. The model test results from this phase of testing (Tests 1 through 25, not shown in Table 1) indicated that a mixing device in the horizontal leg of the air heater duct would not meet the goals of the study. Most of the devices from this phase were rejected because the exit gas temperatures were not sufficiently uniform. Those devices that did produce uniform temperatures resulted in extreme flow maldistribution or excessive pressure drop. It appears that attempts to mix in the horizontal duct were unsuccessful because the flow is too closely coupled in this region. The stratified hot and cold streams have insufficient opportunity to mix uniformly.

In Phase 2 of the study, five alternative temperature mixing devices were tested in the vertical leg of the air heater duct.

1. Two round ducts 4-1/2 foot in diameter, Test 34;
2. Two 4-1/2 foot square ducts, Test 35;
3. Two flat plates 7 foot wide, Test 41;
4. Four flat plates 7 foot wide, Test 43;
5. Four 7 foot wide flat plates on the cold side, a 4-1/2 foot square duct on the hot side, Test 44.

These tests were all conducted with the elbow turning vanes removed and both sets of ladder turning vanes retained (except for Test 43 which also retained the elbow vanes). A comparison of the vertical and horizontal temperature differences for these tests indicate that the two square duct design (No. 2 above, Test 35) most closely met the study goals of 10°F vertical and 25°F horizontal temperature difference. This device was selected for further testing to improve the velocity profile which still showed an RMS distribution greater than the design goal.

Tests 46 through 59 were conducted with the square ducts to determine if the velocity profile could be improved while maintaining adequate temperature mixing and without introducing excessive pressure drop. Variations tested included partial and complete removal of the ladder turning vanes and the addition of a uniform perforated plate. The results indicate that Test 59 most closely met the study goals. The temperature mixing ducts modeled in Test 59 are shown in Figure 6.

The two 4-1/2 foot square ducts were the largest that would fit in the 36 x 14 foot opening below the air heater and represent about 8% of the total flow area. The square ducts provide approximately 20% more area for gas transfer than the round ducts. The ducts transfer a portion of the hot gas stream to the cold side and a portion of the cold gas stream to the hot side as well as provide turbulent mixing.

FIELD RESULTS

The Keystone Station temperature mixing ducts were installed in Keystone Unit 2 in July, 1986 during a scheduled outage. The temperature profile across the precipitator face was measured following the outage. Figure 7 shows the dramatic improvement achieved compared to the original temperature distribution depicted in Figure 3. The temperature variation across the precipitator was reduced from 70°F to less than 20°F. In addition, velocity traverses taken after the outage showed that the velocity profile at the precipitator inlet had not been impaired by the temperature mixing ducts.

Precipitator operation following the outage was significantly better with the temperature mixing ducts installed. Average opacity was reduced to 8%, the level experienced before the economizer/balanced draft boiler modifications. Based on the favorable Unit 2 opacity behavior, the temperature mixing ducts were also installed in Unit 1 in November, 1987.

CONCLUSIONS

The temperature mixing ducts successfully reduced the precipitator inlet temperature maldistribution at Keystone Station. Following installation of the mixing ducts and implementation of other corrective actions (1), precipitator operation was improved and opacity was reduced to the levels experienced before the 1984 and 1985 boiler modifications. All loss of generation attributable to opacity was eliminated. The balanced draft conversion and economizer replacement did not cause the flue gas temperature maldistribution; this maldistribution was present before the modifications were made and is inherent in the rotating regenerative air heater design. Although the temperature maldistribution was not the root cause of the high opacity following the boiler modifications, reducing the maldistribution was a significant part of a comprehensive program to eliminate the loss of generation.

REFERENCES

1. Read, D.W., Strein, D.L., and Zarechnak, A. Keystone Generating Station opacity problem, overview of degradation and subsequent improvements. Paper presented at 1988 EPRI/EPA Seventh Symposium on the Transfer and Utilization of Particulate Control Technology, Nashville, Tennessee. March, 1988.

2. Gooch, J.P., Southern Research Institute. A manual on the use of flue gas conditioning for ESP performance enhancement. ERPI CS-4145, August, 1984.

3. MPR report 931. Keystone Generating Station, effect of coal and ash variability on precipitator performance. May, 1986.

4. Kilvinger, F.S., and Zemke, L.A., Boyle Engineering Laboratories Co. Inc. Project #1112, Report of temperature mixing tests conducted in three dimensional model of the air heater ducts of Pennsylvania Electric Company's Keystone Station - Unit #2. July 25, 1986.

The work described in this paper was not funded by the U.S. Environmental Protection Agency and therefore the contents do not necessarily reflect the views of the agency and no official endorsement should be inferred.

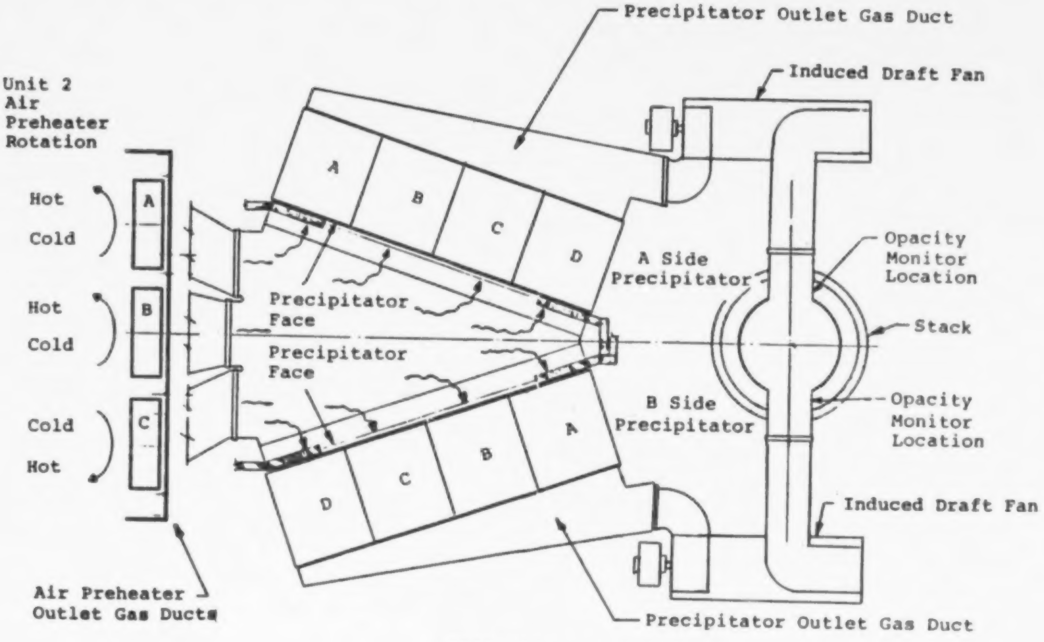

PLAN VIEW

Precipitator Design Data	
Gas Flow (each side)	1,350,000 cfm
Gas Temperature	270°F
Average Gas Velocity	6.41 fps
Inlet Loading	4.0 grains/cu. ft.
Guaranteed Exit Loading	0.02 grains/cu. ft.
Guaranteed Efficiency	99.5%

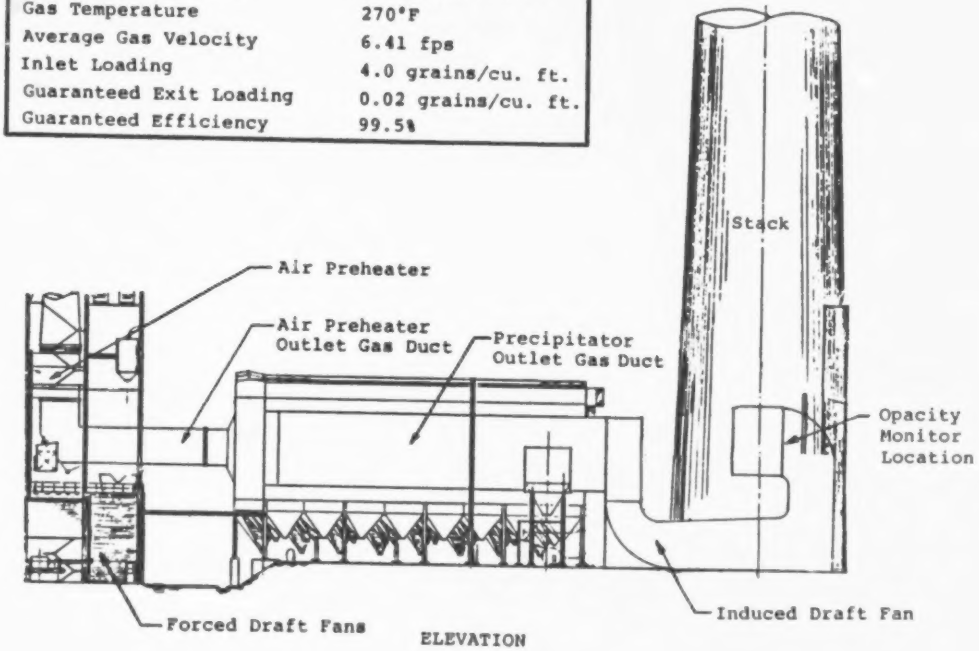

ELEVATION

KEYSTONE STATION
PRECIPITATOR ARRANGEMENT

FIGURE 1

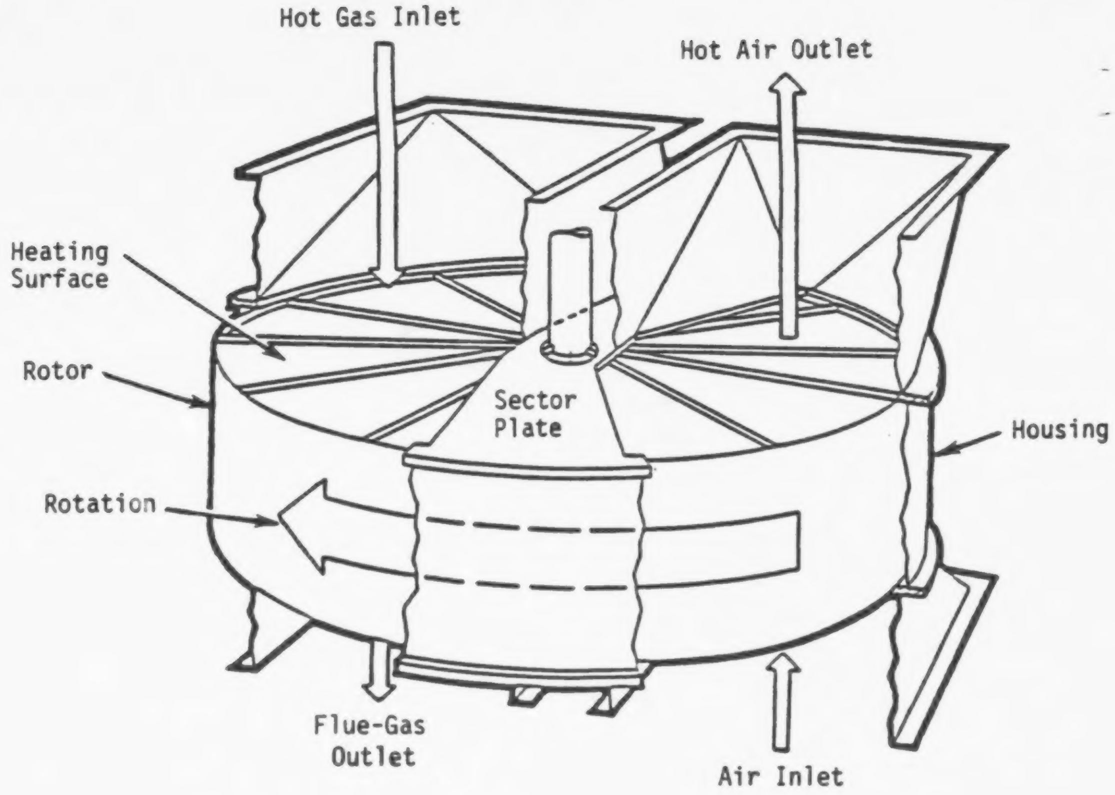

ROTATING REGENERATIVE AIR HEATER

FIGURE 2

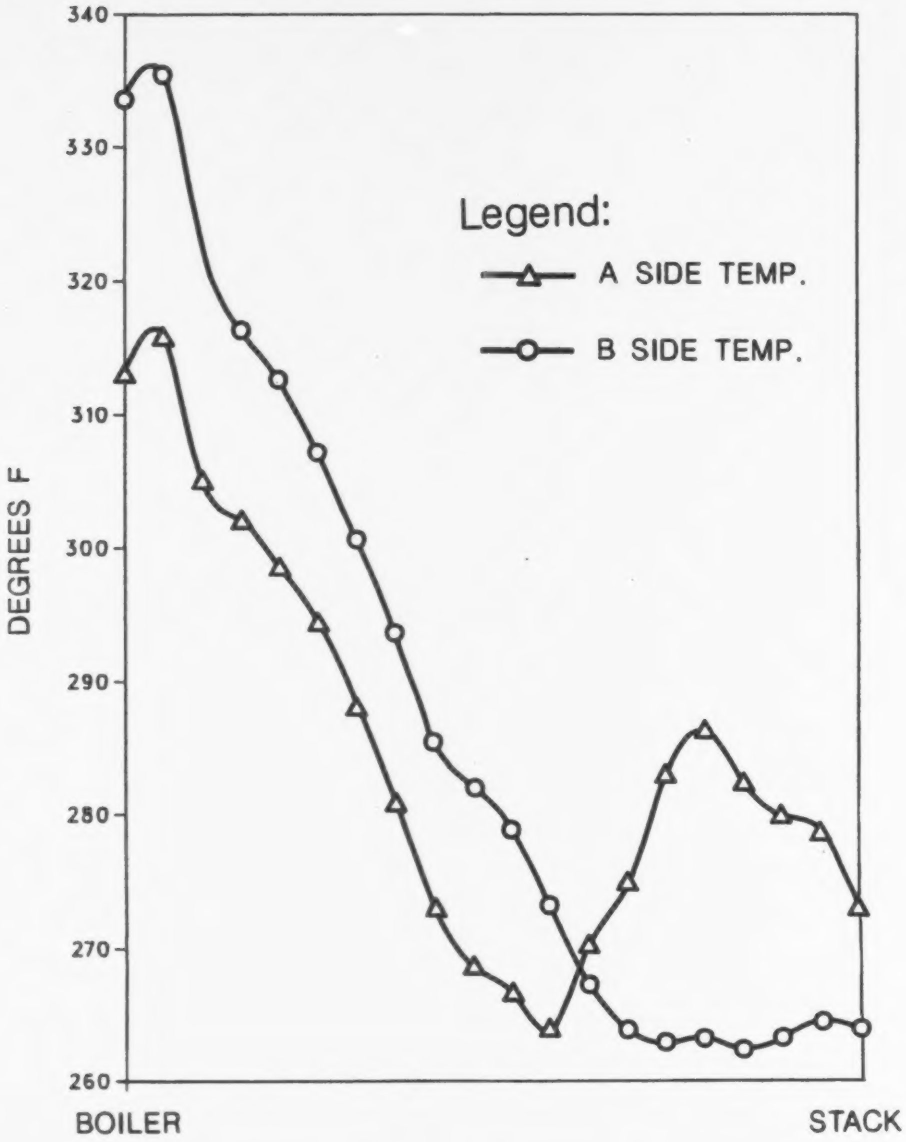

KEYSTONE UNIT 2
PRECIPITATOR TEMPERATURE DISTRIBUTION
WITHOUT TEMPERATURE MIXING DUCTS

FIGURE 3

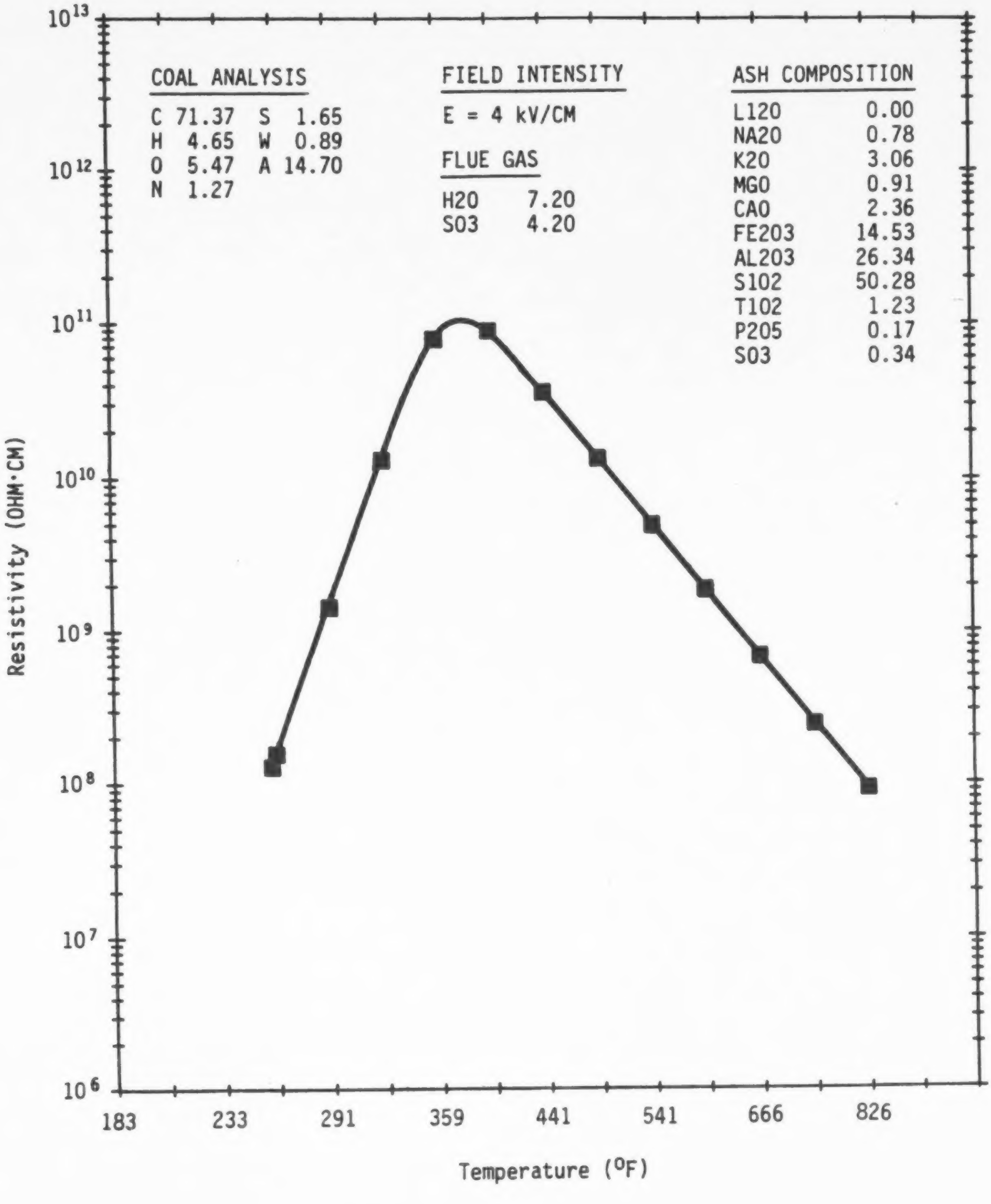

KEYSTONE UNIT 2
COMPUTER PREDICTION OF FLYASH RESISTIVITY

FIGURE 4

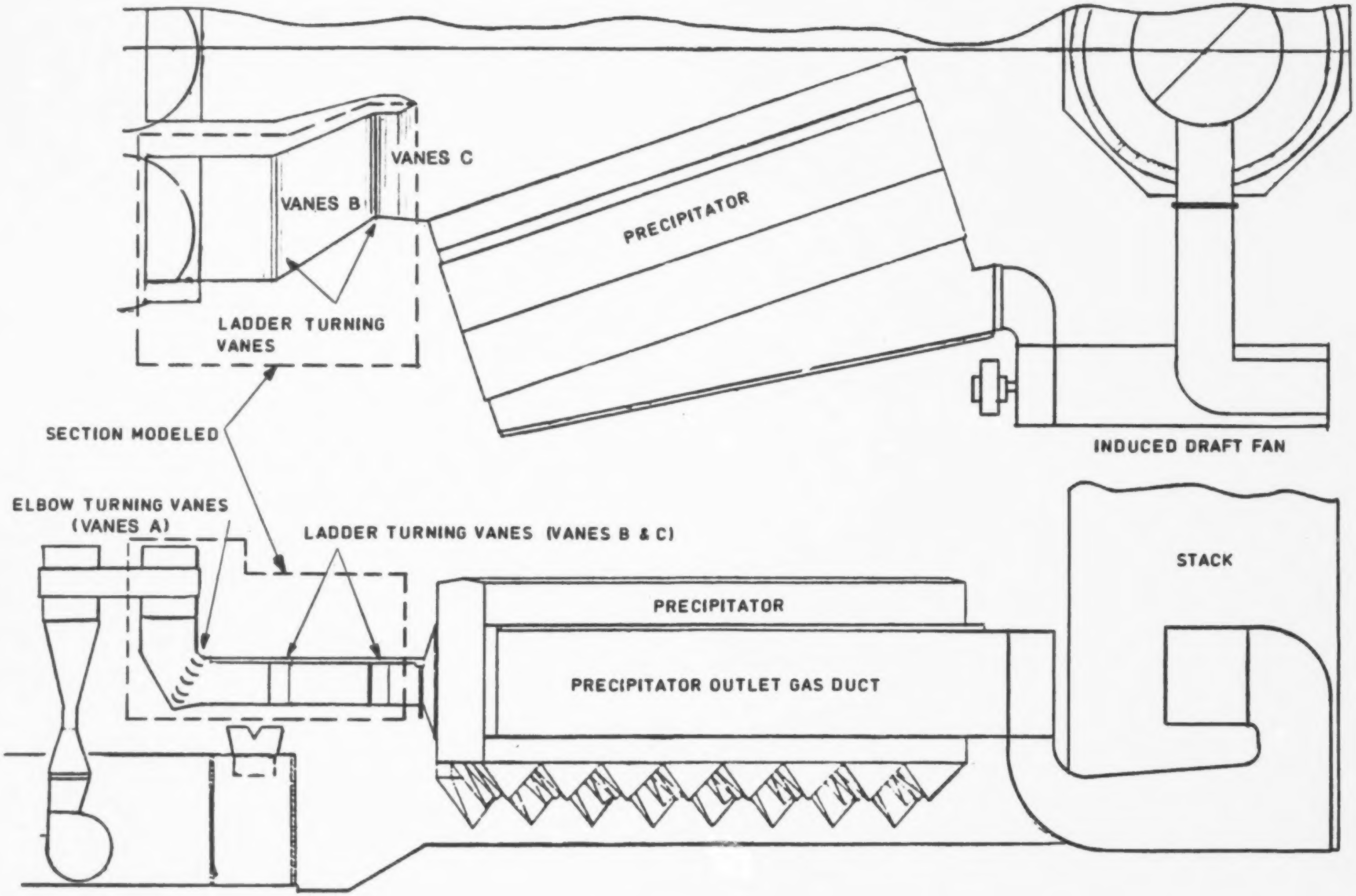

KEYSTONE STATION
AIR HEATER DUCT ARRANGEMENT

FIGURE 5

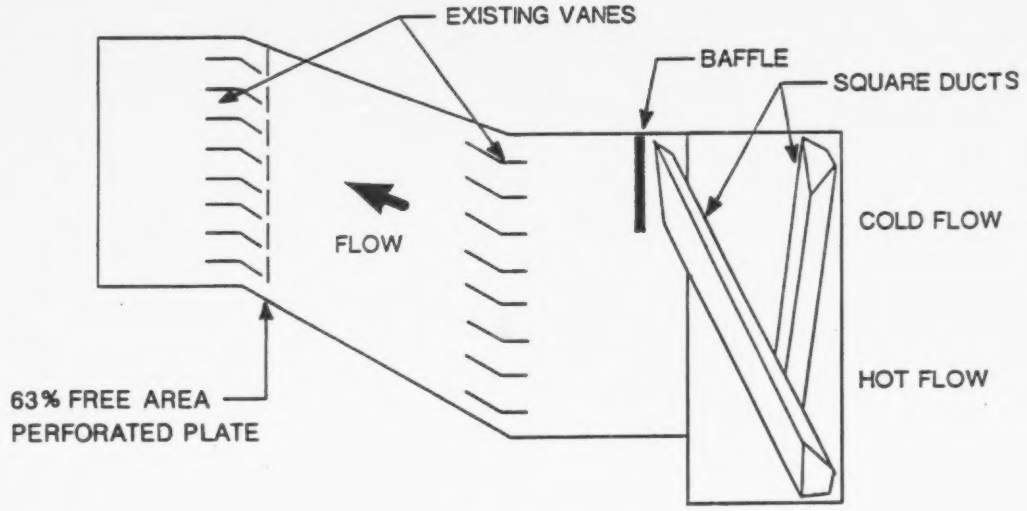

PLAN

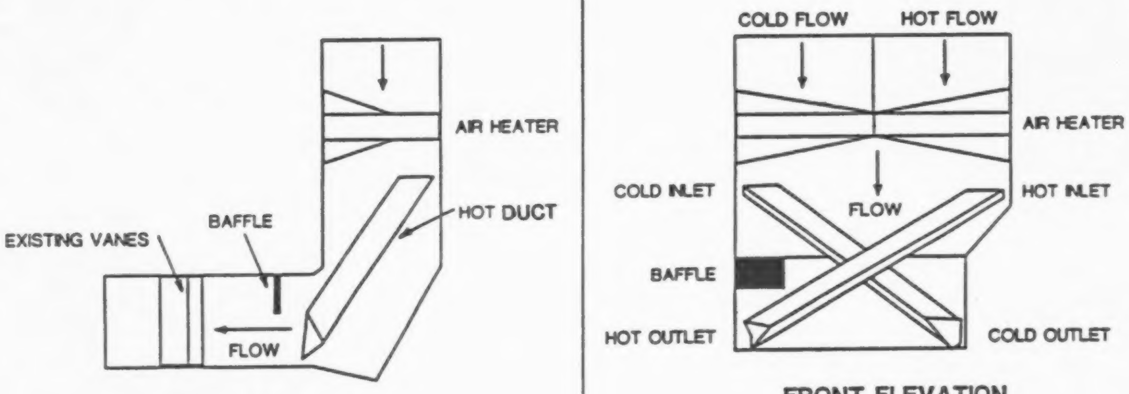

SIDE ELEVATION

FRONT ELEVATION
(VIEW FROM CHEVRON DUCT)

KEYSTONE STATION
TEMPERATURE MIXING DEVICE

FIGURE 6

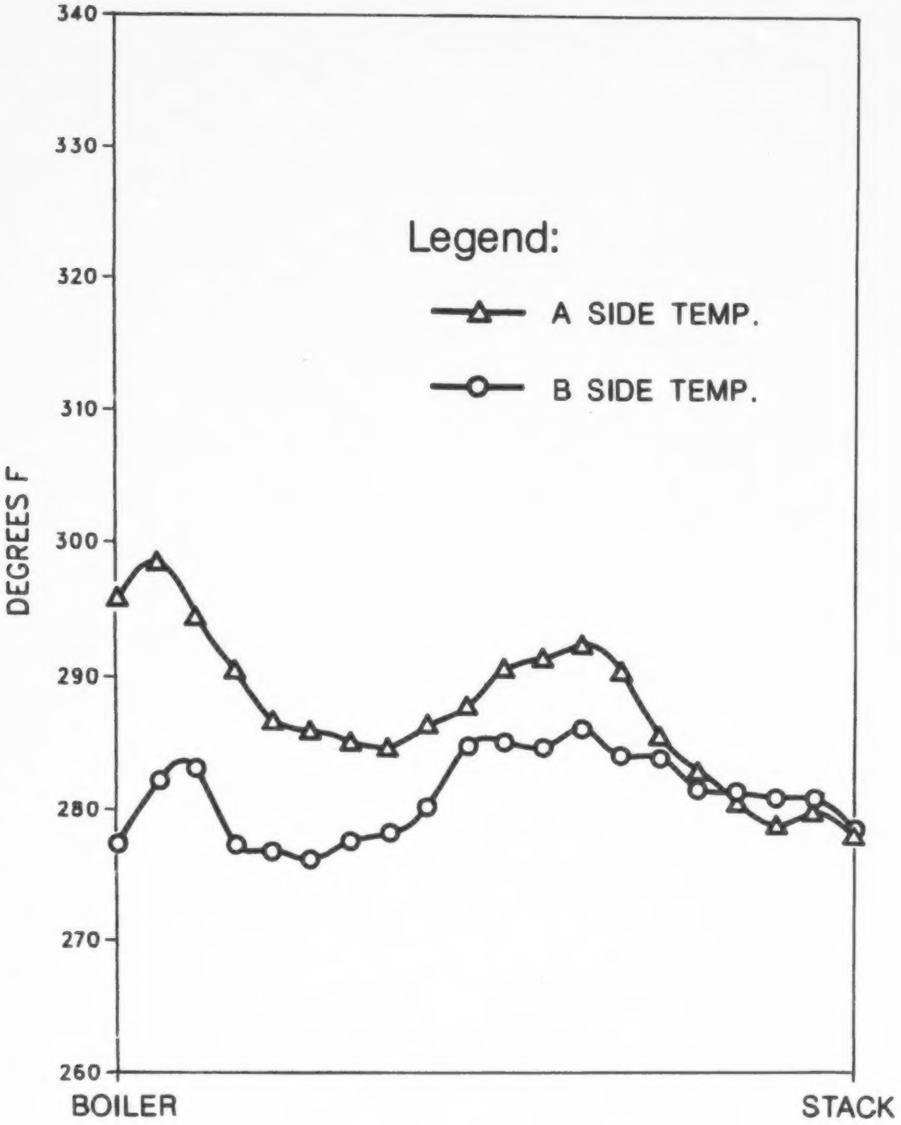

KEYSTONE UNIT 2
PRECIPITATOR TEMPERATURE DISTRIBUTION
WITH TEMPERATURE MIXING DUCTS

FIGURE 7

TABLE 1. KEYSTONE STATION AIR HEATER TEMPERATURE MIXING STUDY - TEST RESULTS

Test Number	Temperature Difference °F			Pressure Drop Inches W.G.		Velocity RMS %	Test Description
	Inlet Horizontal	Outlet Horizontal	Outlet Vertical	Model	Correct		
Field	--	86	1	--	--	11.2	Field data from February 7, 1985, Unit 2 emissions testing (Test 1, duct A)
4	81	77	2	0.35	0.29	7.39	Model baseline, no mixing devices, all vanes in
34	80	40	7	0.74	0.61	15.2	Two round ducts, 4-1/2 foot diameter, vanes A out, B and C in
35	81	21	11	1.21	1.05	15.3	Two square ducts, 4-1/2 foot on a side, vanes A out, B and C in
41	79	22	24	0.73	0.63	17.7	Two flat plates, 7 foot wide, vanes A out, B and C in
43	81	31	29	0.89	0.79	14.2	Four flat plates, 7 foot wide, vanes A, B and C in
44	81	31	11	1.03	0.82	18.6	Four flat plates, 7 foot wide, on cold side and square duct, 4-1/2 foot on a side, on hot side, vanes A out, B and C in
46	78	22	8	1.99	1.67	8.09	Two Square ducts, 4-1/2 foot on a side, vanes A out, B and C in, 63% free area perforated plate on the leading edge of vanes C
59	81	20	7	2.02	1.72	7.90	Two square ducts, 4-1/2 foot on a side, vanes A, B and C in, 63% free area perforated plate on the leading edge of vanes C 3 foot x 5 foot baffle added

Notes: 1. Vanes A, B, and C referenced in the test description refer to the elbow turning vanes, upstream ladder turning vanes, and downstream ladder turning vanes respectively (see Figure 5).

2. "Correct" pressure drop is corrected to field velocity (3502 fpm) and flue gas density (0.05 lb/ft3).

PERFORMANCE OF THE DALE STATION PRECIPITATORS WITH INCREASED PLATE SPACING

E. C. Landham, Jr.
Southern Research Institute
Birmingham, Alabama

James M. Shipp
James K. Neathery
East Kentucky Power Cooperative, Inc.
Winchester, Kentucky

Ralph F. Altman
Electric Power Research Institute
Chattanooga, Tennessee

ABSTRACT

The high level of maintenance required to maintain satisfactory performance of the electrostatic precipitators installed on Dale Station units 3 and 4 has prompted a complete internal rebuild. The new precipitator design includes wider collecting electrode spacing in the same casing along with rigid discharge electrodes. The lower specific collecting area due to wider spacing did not result in a loss of precipitator performance. This paper discusses the history of the ESP operating problems, previous upgrading efforts, and the rebuild process of the two units. The particulate collection performance and electrical operation of the precipitators before and after the rebuild are analyzed.

INTRODUCTION

In late 1987, the precipitators on units 3 and 4 at East Kentucky Power Cooperative's (EKPC) Dale Station were rebuilt because the level of maintenance required to maintain acceptable performance was becomming excessive. The original precipitators had a traditional weighted wire design with collector plates spaced at nine inches. SO_3 conditioning was used to improve the collection of the fly ash which, without conditioning, had a high electrical resistivity. EKPC management made the decision to rebuild the precipitators with a twelve-inch plate spacing to make use of rigid discharge electrodes possible even though this change would reduce the specific collection area (SCA) from 400 to 320 ft^2/kacfm. Experience abroad with precipitators using wide plate spacing indicated that increasing the spacing would not reduce performance and could potentially improve reliability. Further, comprehensive pilot-scale tests of the wide-plate-spacing concept sponsored by the Electric Power Research Institue (EPRI) indicated that increasing the plate spacing from nine to as much as eighteen inches would not decrease performance even though the SCA would be reduced by a factor of two.

In order to document the effect of an increase in plate spacing on the performance of a full-scale precipitator, EPRI, the National Rural Electric Cooperative Association, and EKPC agreed to jointly sponsor performance tests of the rebuilt precipitators. These results could be compared with results obtained by EKPC during a performance upgrading program completed several years before the precipitators were rebuilt. This comparison, a summary of the operating history of the precipitators, and a description of processes used to rebuild the precipitators are provided in this paper.

PLANT AND ELECTROSTATIC PRECIPITATOR DESCRIPTION

The Dale Station is located near Boonesboro, Kentucky, on the Kentucky River. The plant consists of units 1 and 2 (22 MW each) completed in 1954 and units 3 and 4 (66 MW each) completed in 1957 and 1960, respectively. Originally, particulate emissions from units 3 and 4 were controlled only by mechanical collectors. Precipitators were retrofitted to those two units in 1975 by American Standard, leaving the mechanical collectors in place. The original ESP design was a cold-side, weighted-wire configuration with 9-inch collector plate spacing. The design fly ash emission limit was 0.29 lb/E6-Btu, and the opacity limit was 40%. Since the original ESP casing was retained, these limits still apply to the units after the rebuild.

HISTORY OF ESP UPGRADING EFFORTS

ESP performance problems became evident only weeks after the units were commissioned. Fly ash buildup on the collector plates and emitting electrodes became so severe that the units had to be shut down almost every weekend to remove the deposits by water washing. Collecting plates warped due to structural deficiencies and the repeated thermal transients of frequent outages. The reduced electrical clearances resulting from the warped plates caused reduced ESP power levels and, subsequently, high particulate emissions.

Plant personnel devised standoffs and spacers to align the plates and maintain plate-to-wire spacing. These devices substantially improved alignment, but dampened the rapping forces. A more intense rapping system was installed to provide more energy to the plates. However, this change accelerated cracking and failure of the plate support system.

In 1975, the State of Kentucky lowered the Dale Station's SO_2 emission limit from 3.2 to 1.8 lb/E6-Btu. The lower emission limit was achieved by switching the coal supply from a 1.5% to a 0.7% sulfur coal. As a consequence of this change, fly ash resistivity became excessive, with values exceeding 10^{12} ohm-cm.

A Wahlco SO_3 conditioning system was installed in 1980. Adequate dispersion of the SO_3 was difficult to achieve because of uneven gas flow distribution across the ESP inlet duct. This difficulty notwithstanding, the conditioning system lowered the fly ash resistivity to levels consistently less than 10^{11} ohm-cm. With SO_3 conditioning, the ESP could be operated within particulate emission limits as long as a good mechanical condition was maintained. However, the mechanical and structural problems continued to limit availability despite intensive maintenance efforts. Consequently, the decision was made to rebuild the internals of both precipitators.

ESP REBUILD PROCESS

Based on ESP research funded by EPRI, EKPC decided to specify a wide plate spacing design with a rigid discharge electrode system. Increasing the plate spacing (from 9 to 12 inches) within the same ESP shell would require a decrease in specific collection area (SCA) from 400 to 320 ft^2/kacfm. However, a careful inspection of the ESP structure and casing indicated both were sound, and it was determined that it would be more cost effective and require a shorter outage if only the internals of the ESP were replaced.

The rebuild of the Dale 3 and 4 ESPs was competitively bid, and Research-Cottrell was awarded a contract to furnish all labor and material to complete the project. The method of construction/demolition was left open to the vendor. The following two options were considered: 1) remove the plates and electrodes through 2 or 3 incisions in the penthouse and weather enclosure area and 2) remove the ash hoppers for access through the bottom of the structure. After careful consideration of both options, the first option was chosen, and work to rebuild unit 4 was begun in late May 1987. The rebuild of this ESP was completed two weeks ahead of schedule in mid-July 1987. Rebuild of unit 3 was started in early July and finished in October.

FINAL ESP DESIGN

In addition to wider plate spacing and rigid discharge electrodes, a number of other changes in the ESP specifications were made during the rebuild. A comparison of the unit 3 and 4 ESPs prior to and after the rebuild is shown in Table 1.

The new ESP configuration consists of four fields in the direction of gas flow with two transformer-rectifier (T-R) sets per field. An electromagnetic impact rapping system provides rapping energy directly to the collecting plates and electrode frames, with each rapper serving a maximum of two plates. Each high voltage frame is suspended from two points and stabilized at the bottom by small standoff insulators. The decision to double the number of T-R sets on the new ESPs (from 4 to 8) was made because this change would increase sectionalization resulting in greater reliability and control efficiency. Because of the higher voltages required with wider plate spacing, all of the T-R sets were replaced.

State-of-the-art microprocessor systems were added to control electrode rapping and T-R operation. An energy management system (EMS) connected to both ESPs receives opacity feedback signals to automatically regulate T-R set power levels. The new control system also allows the option of reduced-power rapping. This option powers down a T-R set and initiates a rapid cycle of rapping (for one to five minutes per hour). Reduced-power rapping cycles are currently being used on the first fields of each ESP. Observations reported by plant personnel are that the use of reduced-power rapping in the first field and reduced-power operation of the entire ESP at low load (a result of EMS operation) has reduced opacity from 15% to less than 10% at high-load operation. In the near future, intermittent energization (IE) capability will be added to the T-R controls which may further reduce power consumption and improve performance.

ESP PERFORMANCE

Following the rebuilds of the unit 3 and 4 ESPs, Southern Research Institute (SRI) performed comprehensive tests of the performance of both units. The performance measurements were made during extended periods of continuous, full-load operation. Since EKPC did not wish to regularly use SO_3 conditioning after the rebuild, the majority of the test program was conducted without conditioning. However, limited data with conditioning in use were collected on unit 4 to evaluate its effects. In addition to the data obtained by SRI after the rebuild, previous data collected by SRI and by others were available for comparison.

The performance history of the Dale 3 and 4 ESPs is illustrated in Table 2. Both particle emissions and ESP efficiency data are shown for significant periods in the units' lives. The efficiency data were measured only across the ESPs and do not include the efficiency of the mechanical collectors. Data from the original acceptance tests in 1975 show acceptable performance, well within the emissions limit of 0.29 lb/E6-Btu. Shortly after this period, degradation of performance began to occur as described previously. Subsequent tests conducted in 1976 and 1978 indicate that both units were operating out of compliance, with ESP collection efficiencies of less than 90%. In 1980, several modifications were made to enhance ESP performance including installation of alignment spacers, addition of an SO_3 conditioning system, and adjustment of the gas flow distribution. With these enhancements, ESP efficiency was improved considerably (95-96%), although particle emissions were close to the compliance limit with little operating margin.

Since the rebuild, the performance of the ESPs has been quite good. Without SO_3 conditioning in use, ESP collection efficiency was measured at 98.69% for unit 3 and 97.40% for unit 4. This corresponds to emission rates of 0.062 and 0.030 lb/E6-Btu for units 3 and 4, respectively. Variations in ESP inlet mass loading account for the apparent discrepency between the efficiency and outlet emissions for the two units. Differences in coal composition, coal mill type, and mechanical collector efficiency are responsible for the higher inlet mass loading (and resulting higher efficiency) observed on unit 3.

Comparison of the 9-inch and 12-inch plate spacing data indicates the two spacings produce equivalent performance. During the 1975 tests, the ESPs were in relatively good mechanical condition and had been recently washed to eliminate excessive dust deposits. The 1975 data, therefore, represent the best possible performance of the original ESPs. (This level of performance could only be maintained for a short period of time.) The ESP efficiency and emissions after the rebuild (1987) are approximately the same as indicated by the 1975 tests. The main difference is that the rebuilt ESPs can maintain that level of performance indefinitely.

With 12 ppm of SO_3 addition, the unit 4 ESP performance improved considerably. Collection efficiency was measured at 99.65% with outlet emissions of 0.007 lb/E6-Btu. This result was achieved despite SO_3 distribution problems which produced a factor of two gradient in additive concentration across the ESP outlet duct.

As mentioned earlier, mechanical collectors with design efficiencies of 80% are installed ahead of both the unit 3 and 4 ESPs. The collection efficiency data noted above (and in Table 2) do not include the effect of these collectors. Most of the particles collected in these devices are large and would be easily collected in the first field of the ESP. Therefore, the measured total mass efficiency of the ESPs would be higher if the mechanicals did not exist. It is also unlikely that the outlet emissions would increase significantly without the mechanicals. Since most ESP installations do not include mechanical collectors, an estimate of the performance of the ESPs (after the rebuild) without the mechanicals may be useful. If the collection efficiency of the mechanical collectors is at least 70%, the system efficiency would be in excess of 99% without SO_3 conditioning and better than 99.9% with SO_3 addition.

The recently promulgated Federal PM_{10} standards are an attempt to limit the concentrations of small particles in the atmosphere. The PM_{10} standards currently refer only to ambient particulate levels and have not yet been applied to point-source emissions, although such application is anticipated. While no completely satisfactory method of measuring PM_{10} emissions exists as yet, an approximation can be derived from the outlet particle size distribution measured on unit 4. The emissions corresponding to PM_{10} sizes without SO_3 conditioning on this unit are estimated to be 0.020 lb/E6-Btu, while during SO_3 addition these emissions dropped to 0.002 lb/E6-Btu.

ESP PERFORMANCE ANALYSIS

The improved performance of the ESPs can be traced primarily to improved electrical operating conditions in the ESP fields. This is likely due to the improved alignment of the discharge and collecting electrodes and to reduced ash layer thickness. Although comparable ESP electrical characteristics and ash resistivity measurements were not obtained for most of the data of Table 2, a comparison can be developed between the latest test program and a limited ESP performance analysis conducted by SRI in 1981. Since the results for units 3 and 4 are similar, the discussion will be limited to unit 4 which has the more extensive data set.

In June 1981, The V-I curves shown in Figure 1 were measured on the unit 4 ESP during conditioning with 60 ppm of SO_3. In addition to one shorted field, these curves indicate generally poor electrical operating conditions existed in the ESP. (Operation with only three fields was a regular occurrence for both of the ESPs.) The average ESP current density was 2.5 nA/cm^2 at an ESP voltage of 27 kV. The in situ measured ash resistivity was 4E10 ohm-cm. Although this is a rather high resistivity for that level of SO_3 addition, the resistivity was low enough that we can conclude it was not responsible for the poor ESP electrical operation. Measurements of the ESP collection efficiency or outlet emissions were not made at this time, but performance was certainly poor. Computer model projections indicated collection efficiency was likely to be in the low to mid 90% range.

In 1987, after the rebuild, the ash composition appeared to be somewhat different than that encountered in 1981. The most important difference was that the sodium oxide content of the ash had increased by more than a factor of 3 (from 0.25% to 0.78%). The 1987 ash had somewhat lower natural resistivity and responded more readily to SO_3 conditioning than the 1981 ash. However, valid comparisons between these periods can still be developed.

Figure 2 shows the 1987 V-I curves measured on the unit 4 ESP when no SO_3 conditioning was in use. Current density was over 6 nA/cm^2 with average voltages of 44 kV while collecting ash with an in-situ measured resistivity of 1E11 ohm-cm. Although the power input to the ESP is limited by ash resistivity, these curves indicate much better electrical operation than in 1981 when the resistivity was one-half order of magnitude lower. Therefore, even though no conditioning was used and the resistivity was higher than in 1981, the electrical conditions in the ESP were improved by the rebuild.

During SO_3 conditioning of the unit 4 ESP the electrical operation improved even more dramatically. Figure 3 displays representative V-I curves for that test period. In general, there was no regular sparking, and the fields operated at either voltage or current limit. Average current density was 27 nA/cm^2, while average voltage exceeded 59 kV. Measurement of in-situ ash resistivity could not be conducted during these tests due to the location of the SO_3 injection probes. Flue gas analyses at the ESP outlet indicated that the SO_3 concentration in the flue gas varied from 9 ppm to 20 ppm across the duct during a nominal addition rate of 12 ppm. These conditions were simulated in a laboratory resistivity apparatus which indicated that this ash would respond well to this level of SO_3 addition. The ash collected in the ESP probably had bulk resistivity values in the low-E9 ohm-cm range.

MATHEMATICAL MODEL COMPARISON

Comparison of the measured performance of an ESP with the calculations performed by the SRI/EPA Mathematical Model of ESP Performance can provide insight to performance problems and limitations. Information concerning the operating conditions of the Dale 3 and 4 ESPs, measured during the 1987 test program, was used as model input. Three sets of operating conditions were modeled:

1. Dale unit 4 Without SO_3 Conditioning.
2. Dale unit 4 With SO_3 Conditioning.
3. Dale unit 3 Without SO_3 Conditioning.

Calculated ESP collection efficiencies are plotted against the actual measured efficiencies in Figure 4. Figure 4 was taken from EPRI report CS-5040 and demonstrates the ability of the model to simulate the performance of the population of ESPs contained in the EPRI data base. All calculated data in this figure assume gas sneakage of 5% per baffled section and gas velocity standard deviation of 15%. The good agreement between the calculated and measured values at Dale indicate that serious mechanical problems do not exist and that the units are performing as expected for the conditions of inlet ash and flue gas. The slightly larger disagreement for the Dale 3 test is probably due to the fact that the inlet particle size distribution of this unit was not measured. The Dale 4 distribution was used for the Dale 3 model input, but this is not entirely appropriate due to different coal mill types and slightly different coal composition for the two tests.

SUMMARY AND CONCLUSIONS

The Dale Station ESPs have been successfully rebuilt and tested. The following summary statements can be made about the performance and operation of the units:

- Increasing the collecting plate spacing from 9 inches to 12 inches did not produce a detrimental effect on ESP performance in spite of a 20% reduction in SCA. Emission rates are lower than at any other time in the units' history.
- The rebuild has eliminated the plate warping and other electrode problems experienced over the life of the ESPs. The limits on electrical operating conditions are now determined by the characteristics of the collected dust layer rather than the electrode alignment. Shorted fields are rare.
- The units are now capable of continuous operation while meeting both particle and SO_2 emissions limits.

- The total system collection efficiency (including mechanical collectors) is estimated to be in excess of 99% without SO_3 conditioning and over 99.9% with SO_3 in use.

- Excessive dust layer buildups on the ESP electrodes have largely been eliminated. This improvement is due the redesigned electrode and rapping system and is possibly enhanced by advanced control techniques.

- Use of SO_3 conditioning to meet particulate emission limitations is no longer required. However, the use of SO_3 conditioning can produce very low particle emission rates from these ESPs.

- The use of state-of-the-art control systems and control strategies, such as reduced power rapping and energy management, has resulted in an ESP installation which provides good performance at reduced operating cost.

The work described in this paper was not funded by the U. S. Environmental Protection Agency and therefore the contents do not necessarily reflect the views of the Agency and no official endorsement should be inferred.

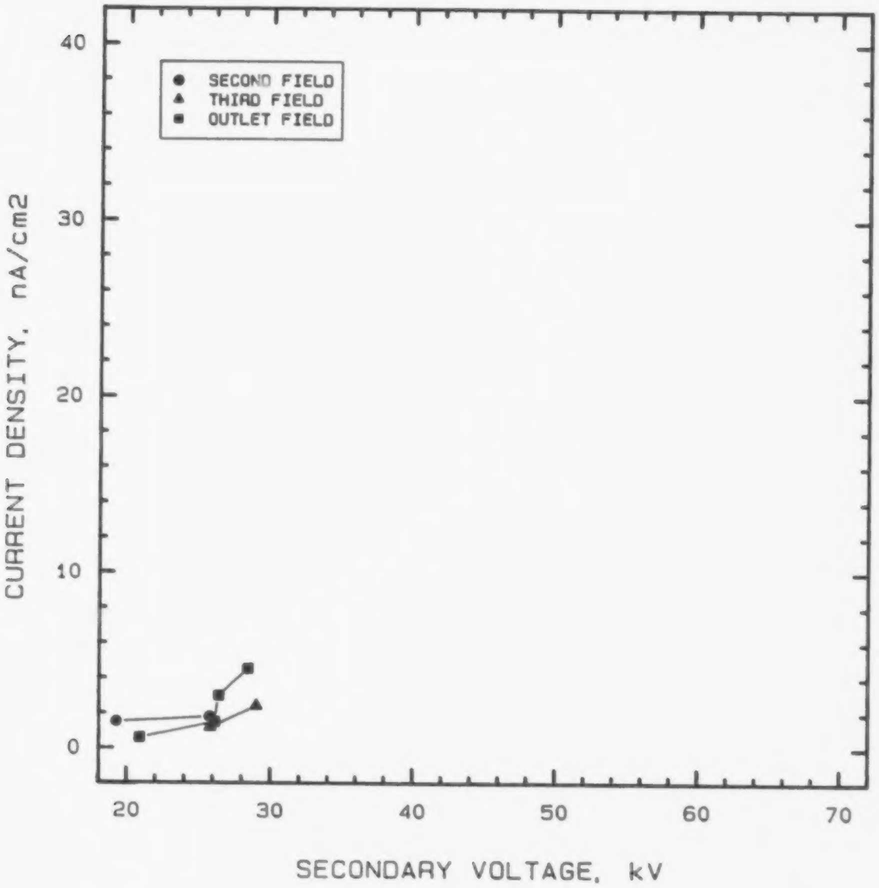

Figure 1. Voltage-Current Density Characteristics of the Dale Unit 4 ESP with SO_3 Conditioning Prior to the Rebuild.

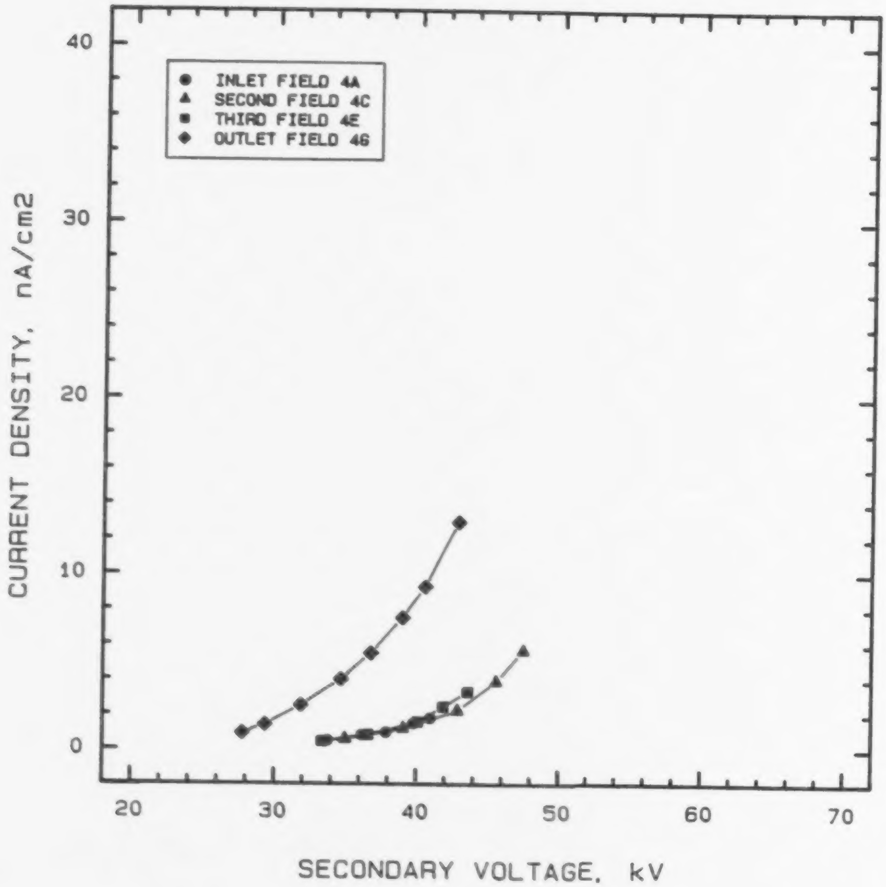

Figure 2. Voltage-Current Density Characteristics of the Dale Unit 4 ESP without SO_3 Conditioning After the Rebuild.

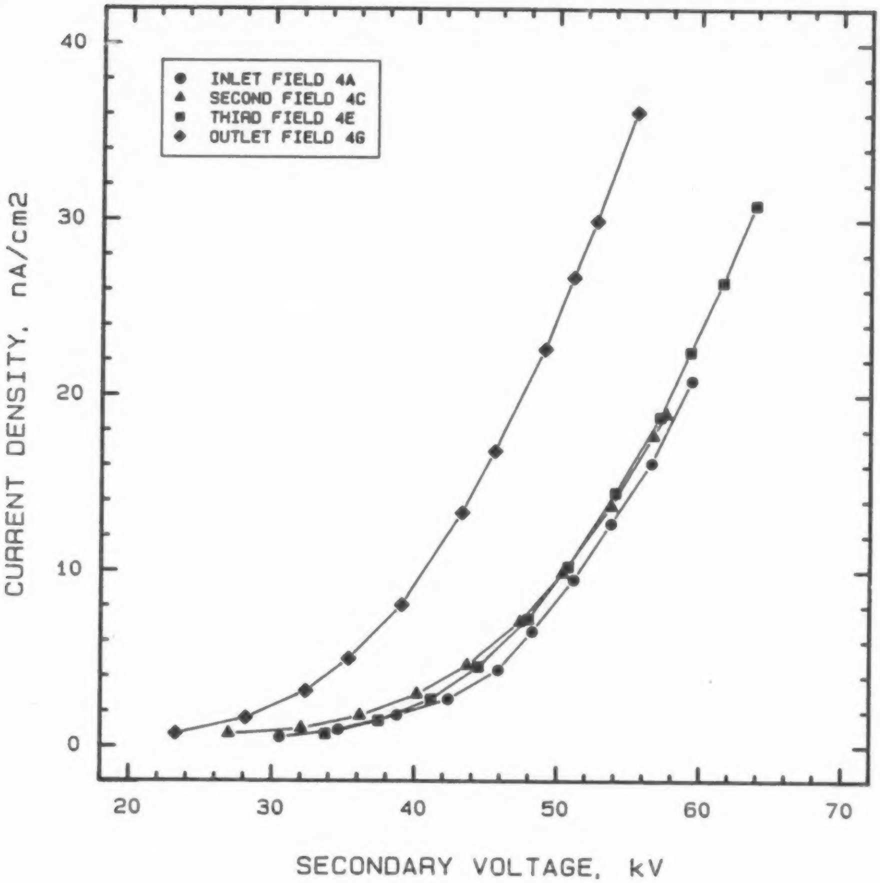

Figure 3. Voltage-Current Density Characteristics of the Dale Unit 4 ESP with SO_3 Conditioning After the Rebuild.

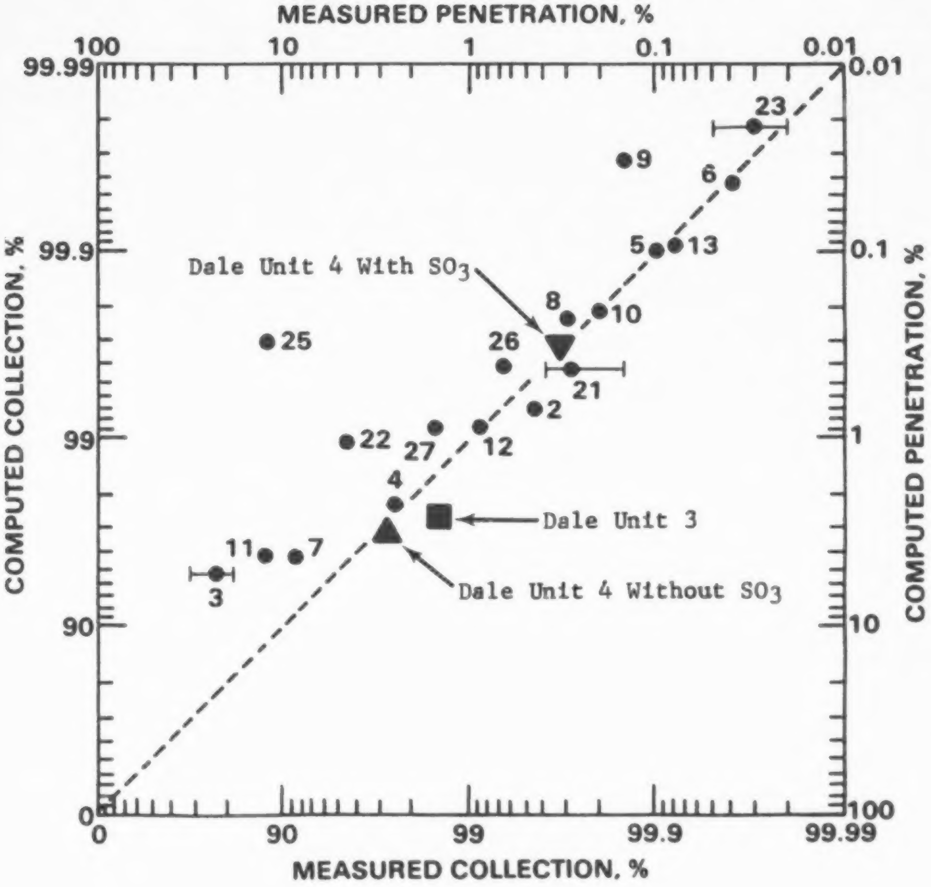

Figure 4. Measured ESP Collection Efficiencies Compared with ESP Model Computations for Dale Station and EPRI CS-5040 Data Base.

Table 1. Changes in the Dale 3 and 4 ESPs.

	Before Rebuild	After Rebuild
Design Collection Efficiency, %	96	98
Plate Spacing, inches	9	12
SCA, ft^2/kacfm	400	320
Total Collecting Area, ft^2	144,448	98,208
Number of Plates per Rapper	5	2
Discharge Electrode Type	Weighted Wire	Rigid
Number of T-R Sets per ESP	4	8
Number of Electrodes per ESP	2880	880
T-R Set Voltage Rating, kV	45	55
T-R Control Type	Analog	Micro
Flue Gas Conditioning	Yes	No

Table 2. Performance History of Dale ESPs

Year	SCA, ft^2/kacfm	Mass Emissions, lb/E6 Btu	Collection(1) Efficiency, %	SO_3 Addition, ppm	Comments
			Dale Unit 3		
1975	408	0.075	98.75	0	Original Startup
1978	396	1.290	69.95	0	Degraded Performance
1980	417	0.254	95.83	15	First Upgrades
1987	320	0.062	98.69	0	Rebuilt ESP w/o SO_3
			Dale Unit 4		
1975	395	0.054	---	0	Original Startup
1976	380	0.305	87.00	0	Degraded Performance
1980	393	0.239	96.08	16	First Upgrades
1987	317	0.030	97.40	0	Rebuilt ESP w/o SO_3
1987	340	0.007	99.65	12	Rebuilt ESP with SO_3

Notes: 1. Collection efficiency of ESP only. Data does not include removal by the mechanical collector.

EXPERIENCE WITH PULSED ENERGIZATION AND BACK-CORONA SUPPRESSION OF ELECTROSTATIC PRECIPITATORS

by: Kjell Porle
Fläkt Industri AB
Växjö, Sweden

Keith Bradburn
Flakt Inc
Knoxville, Tennessee

ABSTRACT

Today, pulsed energization is a well-known and reliable technique.

The authors have had the opportunity to obtain experience with millisecond pulsing[1] as well as microsecond pulsing[2] from hundreds of industrial installations, including new ESPs as well as upgraded old ones. These installations are located in more than twenty (20) countries around the world and represent a wide variety of processes. Therefore, the statistics are reliable.

Substantial advantages such as emission reductions up to 85% and/or 50 to 90% power saving, have been achieved for several applications.

One salient experience is that the pulsers installed must be tuned - amplitudes, pulse frequencies - to the local operating conditions in order to achieve the improvements reported. Retuning is not required, however, unless the operating conditions are drastically changed.

INTRODUCTION

The formation of back-corona during high-resistivity dust conditions is a factor that limits the utilization of Electrostatic Precipitators (ESPs). Until recently, the means to overcome this disadvantage has been to build larger ESPs and/or condition the flue gases. Neither of these methods is attractive to the end user of ESPs.

New energization methods developed during the past few years -- pulsating high voltage and current optimization -- have extended the resistivity range in which ESPs can operate efficiently.

---

1) Equipment used Semipulse^R
2) Equipment used Multipulse^{TM}

Because of the high capital risk involved the new methods have been investigated and introduced in three steps:

(1) Pilot scale testing

(2) Step by step introduction, first in retrofit situations, later in new plants.

(3) Using the accumulated data for costing of new plants and evaluation of risk exposure.

This paper presents a summary of the three steps.

PILOT SCALE TESTING

PLANT DESCRIPTION

The ideas behind the new energization methods have been thoroughly tested in pilot scale. Our pilot consists of two parallel casings, one containing standard equipment the other containing the new features. Simultaneous measurements on the two casings operating on identical flue gas yield very accurate relative data. The pilot is placed in a slip stream from the main inlet duct to a full size precipitator after a 630 MW$_e$ boiler at Ensted Power Station in Denmark. Thus comparison between pilot and full scale is also achieved. It is of great benefit that this station fires imported coals from many sources like USA, Australia, Poland with ashes both easy and difficult to collect.

The sampling and control equipment is automatic and computerized on both pilot and full scale precipitators. This reduces the cost of testing and/or increases the scope of test program.

PULSING EQUIPMENT

Two types of electric pulsing equipment are available on the market, differing in the way of producing the pulsed power.

The first type supplies very short (50 - 100 microsec) pulses of very high instantaneous voltage and current (typically 80 - 100 kV). This requires high-tech equipment at approximately 5 times the price of regular T/R-sets. Figure 1a shows the typical curve form for the units tested.

The second type is much simpler. It produces something similar to the "true" pulsing by blocking a suitable number of half-waves from the regular full-wave T/R-sets. The cost for this "semi-pulse" operation is only some extra software in the microprocessor controling the T/R-set. Figure 1b shows the typical curve form.

For further detail see ref (1), (2).

PILOT PLANT OBSERVATIONS

Windows installed on the roof directly above each section enabled observations of what happened inside the electrical system with the human eye, without disturbing the precipitation in the fields. The following description includes visual, as well as electrical, observations during the firing of Ulan coal (S = 0.55%) from Australia. Table 1 shows the typical ash mineral analysis of the coal. The resistivity, measured in the lab, was 4×10^{13} ohmcm at 120°C, the operating temperature of the pilot ESPs. The investigation in this particular case was made with a helical wire, or spiral, discharge electrode. Three spirals were used per 750 mm wide collecting plate.

Fig. 2 shows current/voltage characteristics for various semipulse charging ratios, CRs, in the second field. Voltages are shown as time average values. The conclusion from the shown curves would be that there is very little back-corona present, if any at all. The lower voltages for CRs of 1:7 and 1:15 were expected. It is now possible to further analyze the conditions.

Fig. 3 shows typical voltages during the operation of an ESP. The figure defines peak (p), average (av) and valley (v) voltages.

Fig. 4 shows the peak and valley voltages corresponding to the average values in Fig. 2. The peak values steadily rise with increased current density. The valley values -- especially for 1:1 -- decrease at the same time. This indicates that the ESP discharges faster, the higher the current is. The valley voltage increases with higher current for ESPs operating under no back-corona conditions. It may therefore be concluded that there is considerable back-corona for 1:1, according to Fig. 4, and less, or little, for the other CRs. The three curves were recorded within the same range of pulse currents. Thus, the highest average current for 1:1 was seven times higher than the average current for 1:7, etc. It is then obvious that the lower peak voltages for 1:1, compared to 1:7 and 1:15 for the same pulse current, indicate strong back-corona -- the peak is depressed as the back-corona continuously discharges the bus section. The time between the pulses -- less than 10 ms -- is too short for the back-corona to disappear. A CR of 1:15 produces higher peaks than 1:7, with about the same valley value. The interpretation for this must be that there is some back-corona still present for 1:7.

Visual observation through the ESP windows indicated clearly massive back-corona glow at a current density of 200 microA/m^2.

At 50 microA/m^2 and CR = 1:1 the distribution of visual corona between and along the discharge electrodes is very uneven. Large blotches of back-corona on the collecting electrodes follow the pattern of the glow on the discharge electrodes.

At the same average current density and CR = 1:15 the corona distribution is very even on the discharge electrodes - because of very high momentary current level - and the back-corona has disappeared.

This confirms that a large part of the advantage with pulsed operation is the improved current distribution in the ESP at low average current densities.

Experiments with different electrode geometries have been performed, naturally. We found that if the current distribution is uneven for geometrical reasons much less improvement with pulsed operation is obtained. See also fig 5 and 6.

The previous discussion of back-corona phenomena in combination with millisecond pulses is essentially valid for faster pulses, such as those used in the Multipulse^{TM} concept. Fig. 7 shows the peak and valley voltages in two different situations. The highest collecting efficiencies in the rear sections are mostly achieved at current densities where the valley voltage is maximum. In addition to current, optimization parameters include the pulse burst frequency and number of pulses per burst. The highest collecting efficiency in the front field energized with microsecond pulses is normally obtained for a current density close to the sparking level, regardless of any voltage peaks. In general the maximum improvement with Multipulse^{TM} is obtained in the rear sections.

FULL SCALE RESULTS

The scope of this paper does not warrant a detailed description of the installation and start-up procedures applied for the different plants. It should be noted, however, that the optimal adjustments of CR, current settings, pulse repetition frequency, amplitude do require a few days of judicious experimenting.

Figure 8 represents a normalized summary of the results from more than 2000 Semipulse^{R} units in operation (200+ in the USA).

Table 2 presents examples of actual results in a few full size plants. The data is "best available" information translated from the various types of instrumentation of the different sites. When the dust resistivity is low much power can be saved with only moderate or no loss in ESP efficiency. Where the resistivity is high both power and dust emission is reduced. The table shows examples of both.

The power consumption figures are either calculated from kV-mA-meter readings with manufacturer supplied T/R losses added or derived from the kWh-meters wherever installed.

The energy saving is based on full operation during an 8400 hour year. When all the T/Rs are controlled by an energy management system even less power is used during periods of low-load operation. Therefore the figures shown should be very conservative.

INVESTMENT EXAMPLES

Thorough pilot testing and checking of the results, in mostly retrofit installations, give solid background to predict the performance and economy of new plants. The following examples are abridged versions of actual cases.

Ashes from coal firing behave very differently in an ESP dependent of the source of the coal. The ESP size needed may vary in the range 1 - 4 correspondingly. In order to present an optimal combination of ESP size, pulsing equipment and power consumption the ESP supplier must be given realistic data on future coal supply and cost of power.

Table 3 is a summary of the following examples. A capitalized cost for power of 4000 US$/kW has been used in the table. This is a common figure applied in the US as well as in Europe although we have seen variations + - 50%.

EXAMPLE 1

This is an example for a power station where the coal is expected to yield high-resistivity ash. The evaluation is based on 100 MW and a dust emission of approximately 0.03 gr/ACF. Using standard T/R-sets one ESP cell with 6 fields is indicated. This is the base for comparison. For 200 MW we would use 2 cells, etc.

When Semipulse^{R} is used only 5 fields are needed, alt 1.

When a combination of Semipulse^{R} and Multipulse^{TM} is used only 4 fields are required, two of each type, alt 2.

Alternaive 2 is the best choice even when its lower space requirement is not considered.

EXAMPLE 2

If our 100 MW station will never fire coals with more than medium-resistivity ash the ESP can be selected smaller. Both the alternative solutions give similar cost.

EXAMPLE 3

This is a retrofit situation for a 200 MW boiler. The coal now being fired yields high-resistivity ash. The existing 4 field ESP must be extended to reduce its emission from 0.1 to 0.015 gr/ACF. Conventionally this requires extending the ESP with 3 more fields.

If Semipulse^{R} is used only one extra field is required, alt. 1.

The alt 2 with two Multipulse^{TM} units does not require any extension of the ESP at all. The extra bonus of very short down time for the plant is not evaluated here.

Note that the existing ESP must be in excellent repair. The electronic equipment cannot compensate for mechanical or design deficiencies. It can only remedy the performance deterioration caused by high resistivity.

EXAMPLE 4

A soda recovery boiler, 1550 tons dry pulp per day, requires an ESP for an outlet emission of 0.008 gr/ACF. The conventional ESP size, 100 %, requires a power input of 275 kW. The outlet emission is increased if the power is reduced by pulsing.

Let us increase the ESP size by 20% without adding bus sections. Then we can decrease the power with pulsing by 85% and still reach 0.008 gr/ACF. The capitalized cost of power more than outweighs the extra hardware investment.

A further advantage with this alternate solution is that the boiler capacity can be increased by 20% in the future (it normally happens) without need for ESP extension.

CONCLUSION

With SP energization the following advantages have been found:

- Emission reduction, up to 60%
- Power saving, up to 90%
- Reduced ESP size requirement up to 35% for some processes
- Almost no investment, as conventional transformer/rectifier is used for ESP.

With MP energization the following advantages have been found:

- Emission reduction up to 85%
- Power saving up to 90%
- Reduced ESP size requiremetn, up to 60% for some processes

The experiences gathered from hundreds of installations prove, that SP or MP is always more cost effective than conventional energization for high- and medium-resistivity dusts.

When the cost of energy is part of the investment evaluation, it has even been shown that for low resistivity dusts it can be profitable to build a slightly larger SP-energised ESP than a smaller, conventionally energized ESP.

REFERENCES

1. Porle, K. "One Back Corona in Precipitators and Supressing it Using Different Energization Methods"

2. Mauritzson, Ch. Porle, K. Kirsten, M. "Experience with pulsed energization of precipitators for a wide range of processes and operating conditions".

The work described in this paper was not funded by the U.S. Environmental Protection Agency. The contents do not necessarily reflect the views of the Agency and no official endorsement should be inferred.

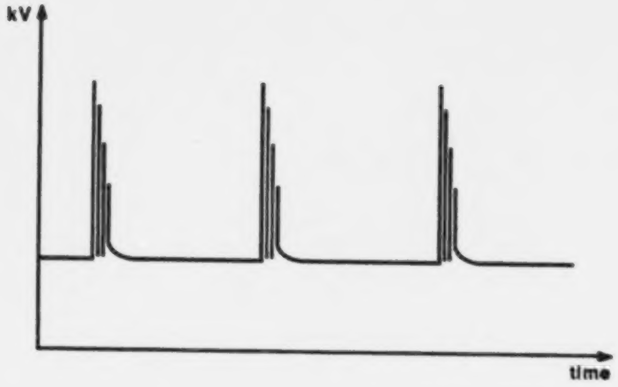

Fig 1a. Typical power bursts obtained from Multipulse^{TM} pulsing equipment.
Peak voltage 60 - 80 kV.
Timing 10 - 100 ms between bursts.

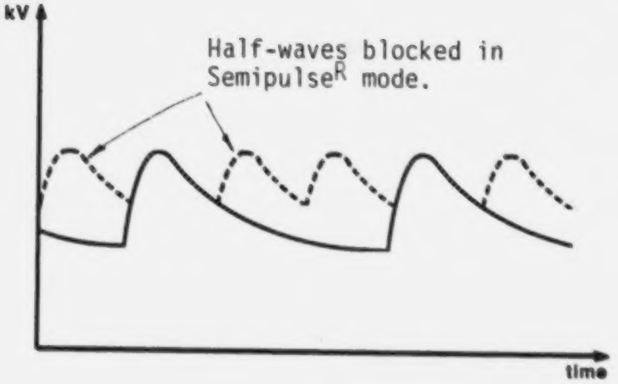

Fig 1b. Typical curves from standard T/R-set operating in full-wave or Semipulse^{R} mode.

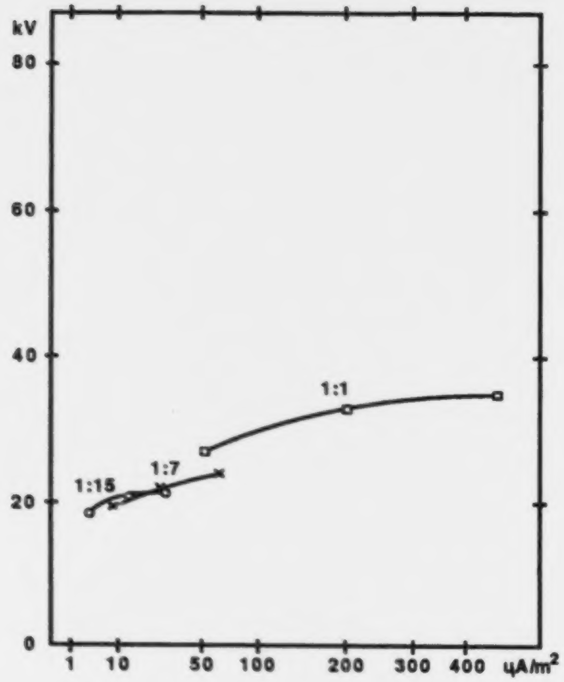

Fig 2. Measurement of average voltage alone is not sufficient for diagnostic purposes. (CR=1:7 interpret 1 of 7 half-waves passed, 6 blocked)

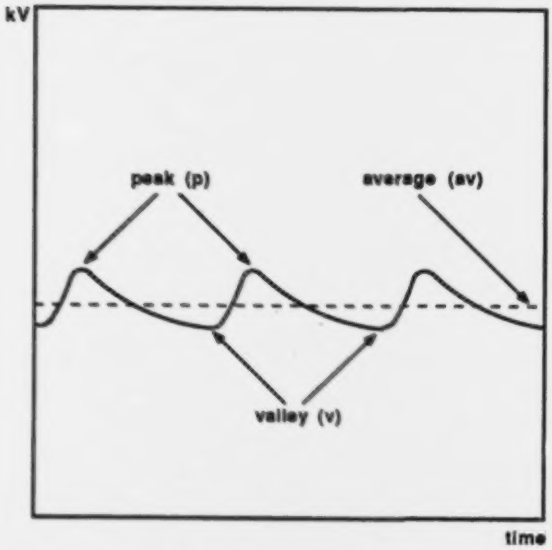

Fig 3. Peak and valley voltages should be measured.

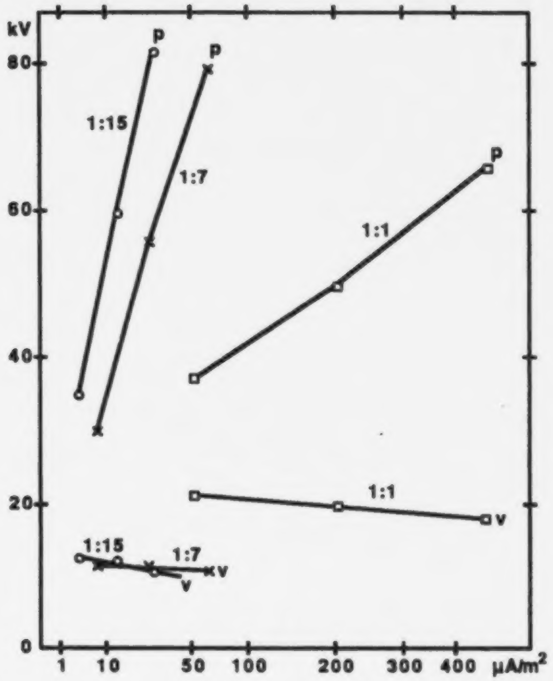

Fig 4. Peak and valley voltages measured for conditions of Fig 2.

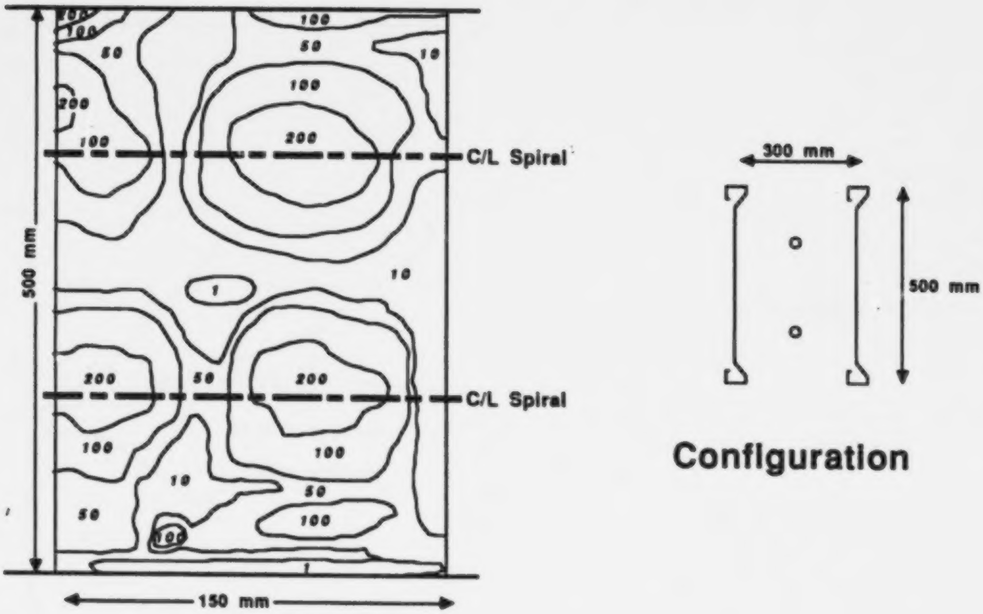

Fig 5. Current distribution on the collecting plate from spiralized wire discharge electrodes.
Average current = 280 microA/m^2
Coefficient of variation = 70%

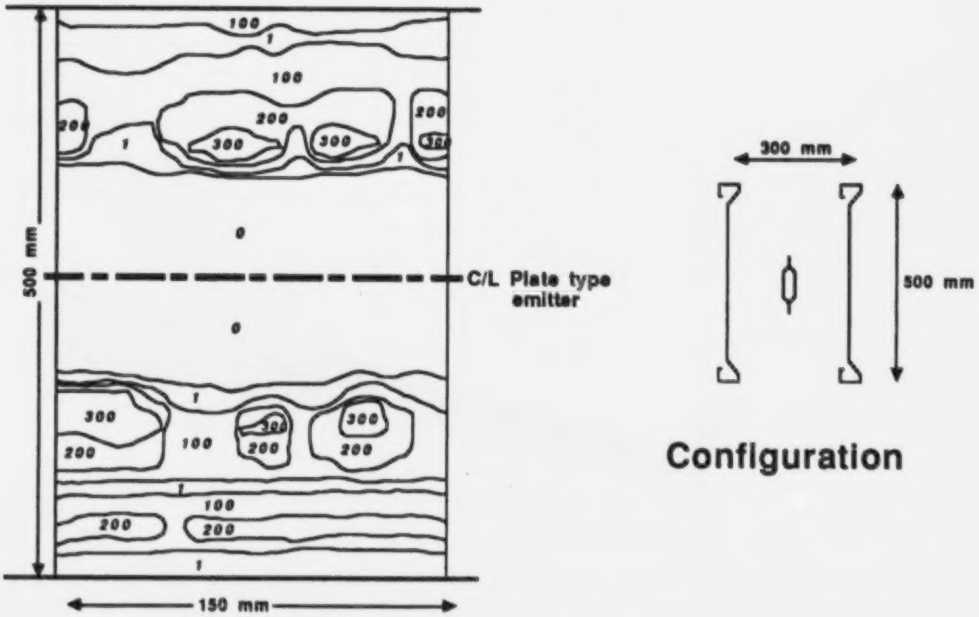

Fig 6. Current distribution on the collecting plate from plate-type discharge electrode.
Average current = 226 micro A/m^2
Coefficient of variation = 107%

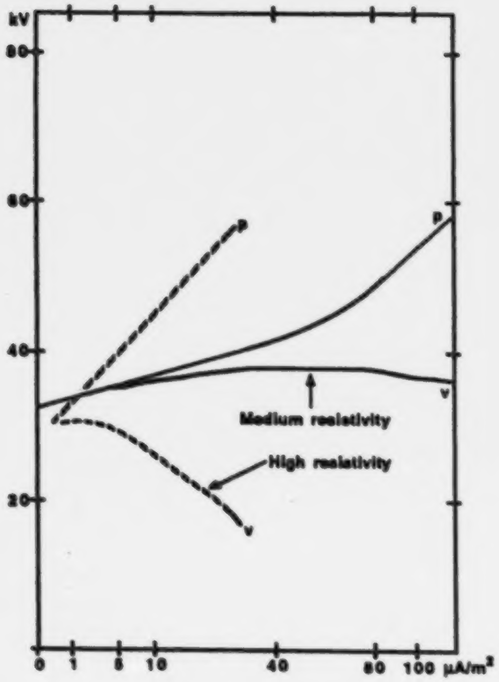

Fig 7. Peak and valley voltages for Multipulse^{TM} operation.

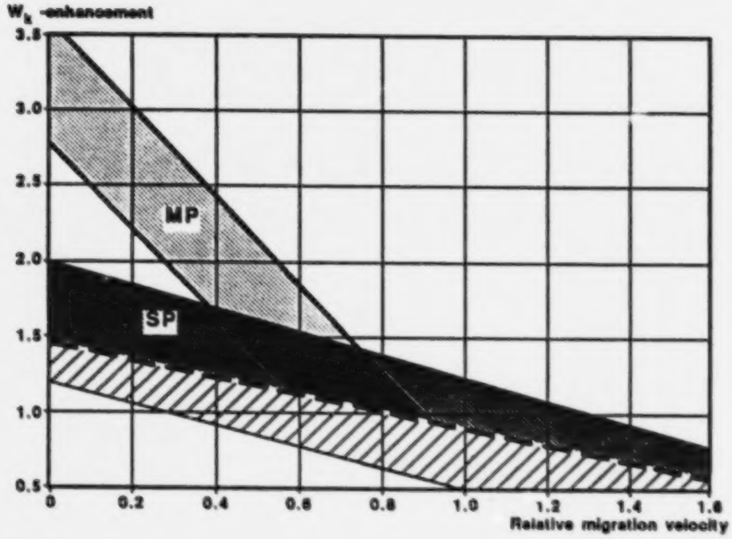

Fig 8. Performance enhancement in terms of modified migration velocity for Semipulse^{R} (SP) and Multipulse^{TM} (MP) operation. The left hand side represents high-resistivity dust, the right hand side low-resistivity. The shaded areas represent spiralized wire discharge electrodes. The hatched area contains tests run on several types of "rigid" discharge electrodes

TABLE 1. COAL ASH ANALYSIS - ULAN COAL

	%
SiO_2	81.40
Fe_2O_3	2.23
Al_2O_3	14.30
CaO	0.12
MgO	0.12
SO_3	0.07
K_2O	0.40
Na_2O	0.06
Li_2O	0.03

TABLE 2. LEGEND

Site	Country	Process, size
A	US	Utility, 400 MW, coal
B	US	Utility, 1150 MW, coal
C	US	Soda-Recovery, 320 000 ACFM
D	US	Industrial boiler, coal/biomass/sludge 355 000 ACFM
E	DK	Utility, 630 MW, coal
F	DK	Utility, 75 MW, coal
G	ES	Utility, 600 MW, coal
H	TW	Utility, 44 MW, coal
I	TW	Utility, 140 MW, coal
J	DK	Utility, 170 MW, coal
K	CA	Utility, 375 MW, coal
L	KR	Cement, clinker
M	KR	Cement, clinker
N	AU	Utility, 66 MW, coal
P	SA	Utility, 200 MW, coal
Q	JP	Sinterband, 353000 SCFM

TABLE 2 (cont'd). PERFORMANCE DATA

Site	T/R type$^+$	ESP Cells	ESP Fields	Outlet loading gr/ACF	Power consum. kW	Energy saving MWh/year
A	C	4	4	0.004	1530	
	S	4	1:3 1:3 1:5 1:5	0.004	336	10000
B	C	8	4	0-6*	2500	
	S	8	1:1 1:3 1:3 1:3	2-7*	720	15000
C	C	2	4	4-5*	225	
	S	2	1:5 1:5 1:3 1:1	4-5*	83	1200
D	C	2	3	2*	380	
	S	2	1:9 1:9 1:9	2*	80	2500
E	C	4	5	0.003-0.06	110	
	S	4	5	0.003-0.03	100	8400
F	C	2	2	0.08-0.23	80	
	S+M	2	1 + 1	0.04-0.08	18	520
	S	2	2	0.06-0.15	20	500
G	C	6	3	0.03-0.22	2130	
	S			0.03-0.12	125	16000
H	C	1	3	0.09	33	
	S	1	3	0.04	7	220
I	C	1	3	0.20	47	
	S	1	3	0.09	28	160
J	C	2	5	0.015	176	
	S	2	5	0.008	67	900
K	C	4	5	0.005-0.010	1230	
	S	4	5	0.005-0.010	100	9500
L	C	1	3	0.02	45	
	S	1	3	0.02	8	300
M	C	1	4	0.003-0.004	170	
	S	1	4	0.003-0.004	70	800
N	C	2	3	0.09-0.23	36	
	S	1	2 of 3	0.05-0.12	2(6+2x2)§	135
	M	1	2 of 3	0.03-0.045	2(2+2x2)§	135
P	C	4	3	0.26	95	
	M	2	1 of 3	0.11	2(28+3)§	275
Q	C	2	4	0.005	98	
	S	2	2 of 4	0.002	20	650

+ C = conventional T/R operation

S = Semipulse^{R} operation

M = Multipulse^{TM} operation

* Opacity %

§ Expected when fully equipped

TABLE 3. INVESTMENT EXAMPLES

	ESP coll area %	ESP fields	T/R type[+]	T/R power	ESP investm. USD M	Capit power USD M	Total eval. USD M
Example 1							
Base	100	6	6C	150	5.7	0.6	6.3
Alt 1	83	5	5S	40	4.7	0.16	4.9
Alt 2	75	4	2S+2M	32	4.2	0.13	4.4
Example 2							
Base	100	4	4C	145	3.8	0.58	4.4
Alt 1	88	3	3S	57	3.1	0.23	3.4
Alt 2	85	3	2S+1M	45	3.2	0.18	3.4
Example 3							
Extension	+75	+3	3C	145	1.2	0.58	1.8
Alt 1	+30	+1	5S	60	0.5	0.24	0.7
Alt 2	+0	+0	2S+2M	30	0.3	0.1	0.4
Example 4							
Base	100	3	3C	275	3.4	1.1	4.5
Alt	120	3	3S	40	3.7	0.2	3.9
Future	120	3	3C	330	-	-	-

[+] C = conventional T/R operation

S = Semipulse^{R} operation

M = Multipulse^{TM} operation

PROOF OF CONCEPT TESTING OF ESP RETROFIT TECHNOLOGIES FOR LOW AND HIGH RESISTIVITY FLY ASH

by: George Rinard
Senior Research Engineer
Department of Engineering
University of Denver
Denver, Colorado 80208

Marlin Anderson
Consultant
305 Marietta Drive
Hopkinsville, Kentucky 42240

Ralph Altman
Project Manager
Electric Power Research Institute
Chattanooga, Tennessee 37411

ABSTRACT

This paper describes the testing of a retrofit technology that has the potential of greatly improving collection efficiency of ESPs under certain operating conditions. The technology is a two-stage ESP with a cooled electrode precharger which has been under development at the University of Denver for the past seven years. Testing was performed on the EPA-University of Denver pilot scale ESP located at the Valmont Power Plant in Boulder, Colorado, at a scale of 6 MW equivalent. The pilot ESP has a conventional plate-to-plate spacing of 22.9 cm (9 in) and used 3.2 mm (1/8 in) diameter corona wires. Testing was done on moderately high and low resistivity flyashes, the resistivity being modified by SO_3 injection. To verify the results and provide a means of predicting performance at full-scale, empirical data were used to construct a mathematical model of the ESP for retrofit applications. Tests are now under way with the same pilot ESP with 6.35 mm (1/4 in) wires in the collector sections. The results of these tests will be reported later. The test equipment and procedures are described, the operational characteristics are discussed, and the test and modeling results are presented.

INTRODUCTION

For the past seven years, a two-stage precipitator using a cooled electrode precharger has been under investigation at the University of Denver. Promising results in the laboratory led to pilot scale tests at a scale of 5 MW equivalent on an ESP at the Valmont Power Plant in Boulder, Colorado. Early tests were done on a two-stage configuration using the precharger ahead of a plate-plate type of collector section (no corona wires). A collection efficiency of 99.5% (emission <0.03

lb/MBTU) was obtained with an SCA of 45 $m^2/m^3/s$ (230 ft^2/kacfm) while collecting flyash with a resistivity greater than 10^{12} ohm·cm and a gas velocity of 0.7 m/s (2.3 ft/s) (1). At a gas velocity of 1.4 m/s (4.6 ft/s) the efficiency dropped to 98.1% (emission <0.1 lb/MBTU). The lower efficiency was attributed to non-rapping reentrainment at the higher gas velocity.

These results are very good for ash resistivity this high and SCA this low. However, the significant reentrainment that occurs at high gas velocity is a potential problem for retrofit applications since high gas velocity is common in these situations. Retrofit applications are an area of great interest, and all these installations are conventional ESPs using wire-plate collectors. Consequently, following the plate-plate tests at Valmont, laboratory tests were performed at the EPA, Air and Energy Engineering Research Laboratory, Research Triangle Park, NC, with a pilot ESP with wire-plate collector sections (2). The results of these tests were very encouraging and limited pilot plant tests with wire-plate collectors were then performed at the Valmont Facility. These tests indicated an increase in efficiency from 93.7% to 97.3% with the addition of one cooled-precharger upstream of an ESP with SCA = 45.3 $m^2/m^3/s$ (250 ft^2/kacfm) (3). During these tests, the collector stages with conventional 3.2 mm (1/8 in) wire-plate geometries were operating in severe back corona collecting a very high resistivity flyash. The high resistivity was probably due to a reduced moisture level in the flue gas caused by excessive air leakage.

The results from all of these tests were encouraging enough to promote interest by potential users, and EPRI initiated a proof of concept test program at the Valmont Facility to evaluate the use of the cooled pipe precharger as well as large diameter wires as potential retrofit devices for use in conventional precipitators collecting high and medium resistivity flyash. This paper describes the test program, gives results to date, and discusses future tests.

PROOF OF CONCEPT TESTING

DESCRIPTION OF PRECHARGER AND TEST FACILITY

The precharger consists of a manifold of 6 cm (2.375 in) outside-diameter pipes and corona electrode as shown in Figure 1. In practice, a coolant is pumped through the pipes in order to lower the temperature and control the resistivity of the collected ash layer. Experience has demonstrated that resistivity can be reduced sufficiently to eliminate back corona without passing through the dew point of the flue gas. Therefore, the pipes remain dry and the collected ash layer can be removed by conventional rapping. Because back corona is eliminated in the precharger, the voltage and current in the precharger are higher than the collector sections and are more favorable for particle charging and collection. The geometry of the precharger also produces a higher electric field strength than flat collector plates would produce for the same voltage.

A description of the test ESP and operating conditions for the EPRI tests are given in Table 1. The ESP is on a slip stream of the Valmont Power Plant in Boulder, Colorado. The plant is a maximum 180 M Watts, nearly base loaded and burns low sulfur western coal. Typical analyses of the coal and flyash are given in Tables 2 and 3, respectively.

TEST PROGRAM

The current program is a proof of concept evaluation of the precharger as well as large diameter wires as retrofit technologies for a conventional wire-plate ESP collecting high and medium resistivity flyash. A parametric evaluation is being conducted with the number of prechargers, collector wire size, and ash resistivity as variables. Ash resistivity is varied by means of SO_3 injection. Before testing commenced in August of 1987, the ESP system was refurbished to eliminate problems that had occurred on earlier test programs.

The serious problem of air inleakage was determined to be due primarily to the gas-air heat exchanger used to control the temperature of the flue gas in the ESP. The heat exchanger was resealed to reduce leakage. This resulted in an increase in the flue gas moisture level from 4.7% to 8% by volume at standard conditions. Ash resistivity was reduced from over 10^{12} to the mid 10^{11} Ohm·cm range. These conditions are more typical of plants burning low sulfur coal than the conditions experienced when the air leakage was excessive.

Four additional T-R sets were installed so that each collector section and each precharger was a separate electrical section. In addition, automatic voltage controllers manufactured by Environex, were installed on each T-R set. Microprocessor controllers were used on the four ESP collector sections, and analog controllers were used on the four precharger sections. An SO_3 system built for EPRI at the Arapahoe Test Facility was installed at Valmont. The system uses a heated catalyst to convert SO_2 to SO_3. The SO_3 was injected up-stream of the ESP with approximately 3 seconds residence time before reaching the ESP.

The ESP was operated continuously 24 hours a day, 7 days a week. The temperature of the flue gas was controlled by an automatic, gas-air type heat exchanger. With this arrangement, the ESP reached steady state conditions in a reasonable period of time, and stable conditions could easily be maintained.

TEST RESULTS

Table 4 presents the chronology of the test program and the collection efficiency measured for each condition. Four sets of baseline tests were conducted as shown in Table 4. The conditions for these tests on the ESP without prechargers is given in Table 1. The efficiency for the first set of baseline tests was 97.9%. However, the baseline efficiency dropped to about 90% for the second and third sets of tests. These lower efficiencies are believed to be more representative of true baseline operation. It is likely that steady-state operation was not reached during the first series of tests.

During the first baseline tests, the voltage and current from first-to-last section were respectively 30 to 34 kV and 4 to 17 mA. The reduced current in the up-stream sections was apparently due to space charge effects. During the second baseline tests, the currents were about half that for the first baseline tests. However, the voltages were about the same for both tests.

The air in-leakage had gone up from the first to second baseline tests. Testing was stopped and the heat exchanger was resealed. After resealing, leakage was somewhat less than during the first baseline tests. However, the electrical conditions and collection efficiency were not materially improved, supporting the assessment that the precipitator had not reached steady-state operation during the first baseline tests.

A series of short duration tests were then performed, each a few days long. PC-4 with four prechargers, Baseline-3, PC-5 with prechargers 1 and 3, all gave about the same results as the earlier longer series of tests for the same conditions. A fourth baseline test, Baseline-4, gave 94.4% which was better than that obtained in the second and third baseline tests. However, the inlet loading for the fourth baseline tests was nearly twice that for any of the other baseline tests while the outlet loading was almost the same as for the other baseline tests.

The last two sets of tests were for SO_3 injection. In-situ resistivity measurements indicated that the SO_3 injection reduced the flyash resistivity from the mid 10^{11} to the low 10^{10} Ohm·cm. With SO_3 injection, the voltage was 35 to 40 kV and the current was 12 to 30 mA from the inlet to the outlet sections, respectively. SO_3-2 was a baseline SO_3 test with no prechargers, and PC-6 was a test with all four prechargers and SO_3 injection. The efficiency with the prechargers and SO_3 was only slightly higher than with SO_3 alone. As discussed later, there are reasons to believe that the efficiencies measured with SO_3 conditioning are lower than they should be.

The relatively low SO_3 collection efficiencies notwithstanding, the results indicate that the prechargers produce a substantial improvement in collection efficiency. Figure 2 shows the measured average penetrations as a function of the number of prechargers, both with and without SO_3 conditioning. The average penetration for the last three series of baseline tests was 0.086. The average penetration with all four prechargers in service was 0.009. These results indicate the prechargers reduced outlet emissions by a factor of 9.5. The results also indicate that it is not necessary to have prechargers in front of every collector stage to achieve a substantial improvement in collection efficiency. Two prechargers reduced emissions by a factor of 4.8, and three prechargers also reduced emissions by a factor of 4.8. The reason why the collection efficiency with three prechargers was not higher than with two was probably because in the case of two prechargers the first and third prechargers were energized, and for the case of three, the last three prechargers were used. Thus, in the case of two prechargers, there was more collection area downstream of the prechargers than was the case for three prechargers.

MATHEMATICAL MODELING OF VALMONT RESULTS

The value of pilot scale data is greatly enhanced if the data can be used to accurately predict full-scale performance. Mathematical and physical models of precipitators have been used successfully for this purpose. Modeling of the precharger/ESP was undertaken with one of the goals being the estimation of full-scale performance from pilot results. Before this goal could be realized, other questions had to be answered. First, would the model predict the observed performance of the ESP without precharger for realistic values of model input parameters? Since the model has proved to be an accurate predictive tool in the past (4), the converse of the above question was also relevant. Were the results from the pilot baseline tests in agreement with model predictions? Second, could the precharger performance be modeled with an existing model without significant modification?

The EPA/SoRI model, which has been well documented (5), was used in this effort. The model was developed for wire-duct geometries and employs empirical expressions to adjust the size dependent migration velocities for the nonideal effects of nonuniform velocity distribution, gas bypassage (sneakage) of collection zones, unmodeled effects, and reentrainment due to rapping. It was felt that, if the precharger could be simulated as a short wire-plate field, the model should give some indication of the efficiency enhancement produced by prechargers.

The approach taken was to use the ESP baseline data with and without SO_3 to determine the values for the nonideal parameters and to determine a realistic value for the reduced effective ion mobility. This parameter was adjusted in fitting the baseline data, and a value of 1.7 $cm^2/V{\cdot}s$ was chosen for modeling the baseline and precharger/ESP cases. Measurements of reduced effective mobility in simulated flue gases have been reported which range from 2.2 to 5.4 $cm^2/V{\cdot}s$ (6), while values from field data have been reported in the range of 1.5 to 2.1 $cm^2/V{\cdot}s$ (7). Thus the value used in this effort was felt to be realistic.

The inlet particle size distribution has a significant effect on the collection efficiency of a precipitator. Consequently, it is necessary that this parameter be specified as accurately as possible. For all of the model runs, the average of the log-normal distributions from all inlet impactor measurements made for the various test conditions was used. The average distribution had an MMD of 29.8 μm and a sigma of 5.21. This corresponds to a relatively fine distribution but it is courser (fewer particles in the smaller size fraction) than the average size distribution for flyash particles from 16 subbituminous coals found in an EPRI survey (8). That survey also found that there was more variability of the flyash size distribution from subbituminous coals than there was from ashes of bituminous coals. Figure 3 gives a comparison of the size distribution used for modeling to those found by the EPRI survey.

The electrical operating conditions for the model for each test condition were determined by averaging the readings from individual test series for each electrified section. The average secondary voltages were then reduced by the estimated voltage drops across the ash deposits on the collection plates. The voltage drop was determined from the product of the deposit thickness and the electric field strength by assuming a thickness of 3.2 mm (1/8 in) and computing the field strength from the resistivity times the average current density.

Model input parameters common to all of the test series are listed in Table 5. Average flue gas flow rates varied between test series by only 2 to 3%, and average temperatures by 5 to 6%. Variations of this magnitude for these parameters would have little effect on the model results. Therefore, the same values were used for all data sets.

The prechargers were simulated by representing them as an electrical section 15.2 cm (6 in) long with a single wire centered in each lane. The cold pipes are located on 22.9 cm (9 in) centers with the pipes having a diameter of 6 cm (2.375 in). Thus, the minimum distance between wire and pipe is approximately 8.8 cm (3.3 in). Decreasing the distance between the wire and plate would increase the average electric field strength in the inter electrode space while at the same time increasing the average gas velocity. The increased field strength would enhance both particulate charging and collection rates, but the increased gas velocity would decrease both rates. The spacing, 9.2 cm (3.62 in), which was used in the model was chosen by assuming a constant face velocity over the pipe.

The results of the model calculations are summarized in Table 6. The measured efficiencies are compared to calculated ones for three different combinations of percent sneakage and standard deviation, σ_g , in gas flow distribution. All of the values for sneakage and σ_g were in the range normally encountered in precipitators of modern design, and all yielded approximately the same results. The set for sneakage per baffled section = 0.05% and σ_g = 0.15% seemed to give the best overall fit, and only these numbers are shown in the table. For all the tests, the ESP configuration was the same with all four collecting sections energized. The conditions for the prechargers and SO_3 conditioning is given in the table for each test.

Agreement between measured and modeled results was poor for the first and fourth baseline tests, but it was very good for the other two baseline series. The first baseline data were taken just after the unit was put into service and, as stated earlier, the unit had probably not yet attained steady state conditions. To test this hypothesis, the model was run without reducing the voltages by the drop across the ash deposits and rapping was neglected. For these conditions, the computed efficiency was 97.17%. This is in better agreement with the measured value, but still under-predicts the collection efficiency by over half a percent. Drop-out in the inlet transition duct before steady state conditions were reached could have reduced the effective inlet loading and caused the ESP to appear to be more efficient than it was. The poor agreement for the 4th baseline series could have been due to a drastic change in particle size distribution. The fact that the inlet loading was almost twice that of earlier baseline tests indicates some change took place.

The model over-predicted performance for all tests with SO_3 conditioning. The precharger result that showed the largest percent difference (approximately 120% between measured and modeled values of penetration) was PC-6 for all four prechargers and SO_3 conditioning. If one assumes that the model predictions are accurate, the poorer than predicted performance with conditioning might have been due to increased reentrainment caused by changes in ash resistivity and/or changes in ash physical properties. Another possibility is that excessive SO_3 was being injected which caused an SO_3 aerosol to form downstream of the precipitator. The SO_3 aerosol would then contribute to the outlet loading. Also, the outlet filter substrates may have been reacting with the SO_3 laden flue gas. The filters were not saved, nor were sufficient outlet size distribution data taken to determine if any of these hypotheses are correct. Future SO_3 test plans include ash chemical analyses and outlet particle size data to test these hypotheses. In addition, tests will be conducted with the precharger pipes at a higher temperature which will result in a higher resistivity of the collected flyash.

A comparison of measured and calculated average collection efficiencies versus number of prechargers is given in Figure 4. The average for the baseline conditions does not include the first series of baseline tests, and the average for SO_3 conditioning does not include the first SO_3 series, since these were determined not to be representative of steady state conditions. The measured efficiency for zero prechargers is higher than that calculated primarily because of the high values obtained in the last series of baseline tests. Without the last series, the measured average efficiency would be essentially the same as that calculated. The calculated efficiency is given for the case of one precharger, but no measured values were obtained. The model predicts a four fold decrease in emissions as compared to the baseline for one precharger in front of the first collection field. The lower-than-predicted collection efficiency for the case of SO_3 conditioning is also apparent in this figure.

CONCLUDING REMARKS

The prechargers maintained good electrical operating conditions throughout testing. Conventional, modern, automatic voltage controls provided acceptable operation under all test conditions.

The collection efficiency with the prechargers was consistently higher than for the ESP alone and was somewhat higher than with SO_3 conditioning. The collection efficiency with the prechargers was much more stable and did not fluctuate as did the efficiency of the ESP alone. Emissions with four prechargers in service were typically a factor of 9.5 below baseline emissions. The model predicts that the emissions would be decreased by a factor of 4 with the installation of one precharger in front of the first field of the precipitator.

Simulation of the prechargers in the mathematical model by a short wire/plate section gave good fits of model predictions to measured performance. The model did not predict performance with SO_3, and the poorest predictions were for the case with both SO_3 and prechargers.

Additional testing is being performed using 6.3 mm (0.25 in) diameter wire in the collector section of the ESP to determine if further collection efficiency enhancement is possible. In addition, tests will be conducted to evaluate the unpredicted results with SO_3 conditioning and to see if the model continues to predict precharger performance.

The results obtained in the tests described above indicate that the Cooled Pipe Precharger can produce significant improvement in the performance of an ESP operating on high resistivity flyash. The scale of the Valmont Facility is large enough to provide reliable data. However, it will be important to carefully analyze these results and determine potential problems that may accompany scale-up to a full size unit. In addition, futher analysis is required to predict the effects of higher sulfur coals. With these precautions in mind, the results above and previous favorable cost analyses appear to more than justify full-scale tests.

ACKNOWLEDGMENTS

The work reported here was performed under EPRI contract No. RP-1835-9. Thanks is expressed to the Public Service Company of Colorado for their assistance in providing facilities and services to conduct the test program. Similarly, appreciation is expressed to the Environmental Protection Agency for cooperation in the use of the pilot scale ESP facilities at the Valmont Power Plant.

The work described in this paper was not funded by the U.S. Environmental Protection Agency and therefore the contents do not necessarily reflect the views of the Agency, and no official endorsement should be inferred.

REFERENCES

1. Durham, M. D., G. A. Rinard, D. E. Rugg, T. Carney, J. A. Armstrong, and L. E. Sparks, "Field Study of Multi-Stage Electrostatic Precipitators." The Fifth Symposium on the Transfer and Utilization of Particulate Control Technology, Kansas City, MO, August 27-30, 1984.

2. Rinard, G. A., M. D. Durham, D. E. Rugg, and L. E. Sparks, "Optimizing the Collector Sections of Multi-Stage Electrostatic Precipitators." The Fifth Symposium on the Transfer and Utilization of Particulate Control Technology, Kansas City, MO, August 27-30, 1984.

3. Rinard, G. A., M. D. Durham, and D. E. Rugg, "Pilot Plant Evaluation of the Cooled-Electrode Precharger as an ESP Retrofit Device." The Sixth Symposium on the Transfer and Utilization of Particulate Control Technology, New Orleans, LA, February 25-28, 1986.

4. McDonald, J. R., "Computer Simulation of the Electrostatic Precipitation Process." Proceedings: International Conference on Electrostatic Precipitation, October 1981, published by Air Pollution Control Association, P.O. Box 2861, Pittsburgh, PA, 1982.

5. McDonald, J. R., "A Mathematical Model of Electrostatic Precipitation (Revision 1): Volume 1. Modeling and Programming." EPA-600/7-78-11a, NTIS PB284-614, U.S. Environmental Protection Agency, Research Triangle Park, North Carolina, June, 1978.

6. Spencer, III, H. W., "Experimental Determination of the Effective Ion Mobility of Simulated Flue Gas." Proceedings: 1975 IEEE-IAS Conference, Atlanta, Georgia, September, 1975.

7. Mosley, R. B., J. R. McDonald, and L. E. Sparks, "Theoretical Methods for Predicting Electrical Conditions in Wire-Plate Electrostatic Precipitators." Third Symposium on the Transfer and Utilization of Particulate Control Technology, Orlando, Florida, March, 1981.

8. DuBard, J. L., and R. S. Dahlin, "Precipitator Performance Estimation Procedure." EPRI Report CS-5040, RP629-5. Electric Power Research Institute, Palo Alto, CA, 1987.

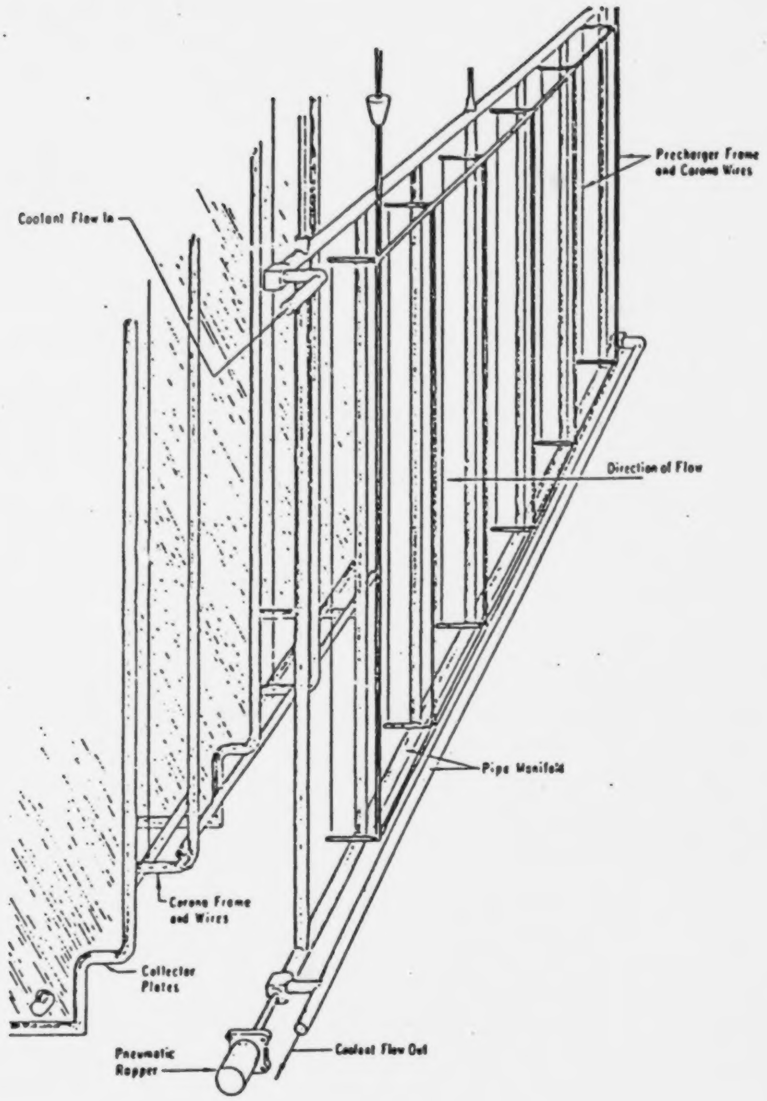

Figure 1. Cooled Pipe Precharger

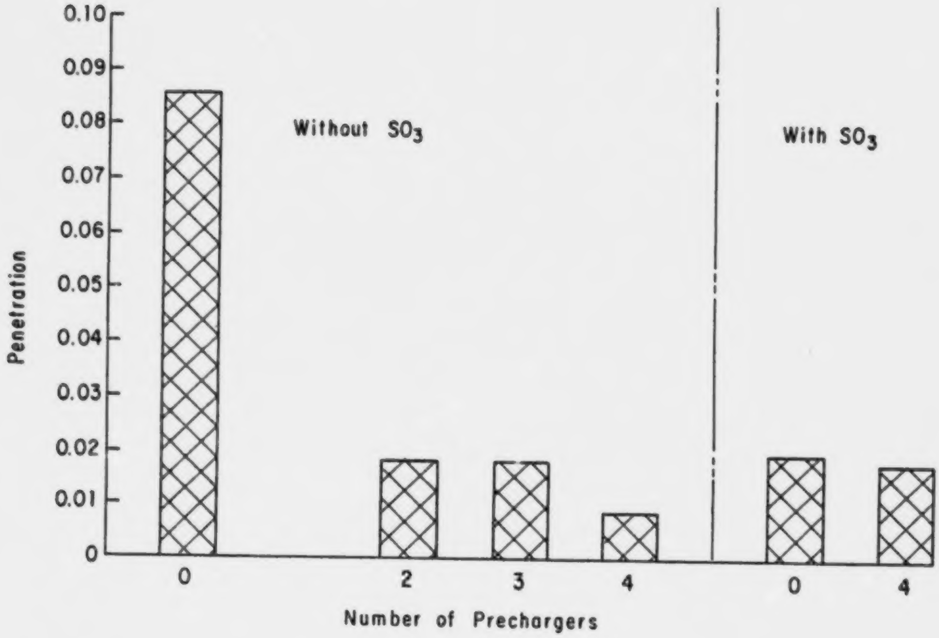

Figure 2. Penetration vrs. Number of Prechargers

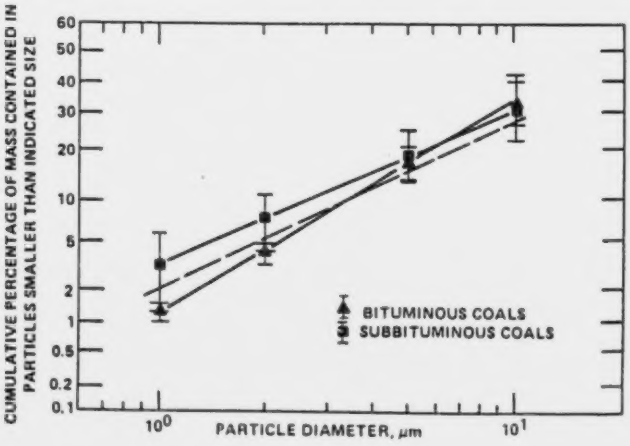

Figure 3. Comparison of Size Distribution Used to That Found by EPRI

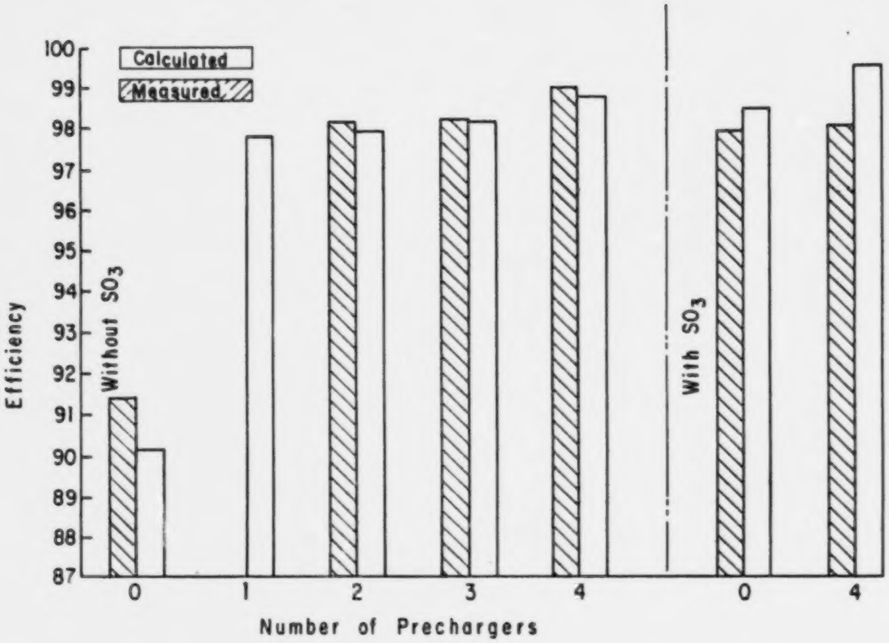

Figure 4. Measured and Calculated Collection Efficiency vrs. Number of Prechargers

TABLE 1

Description of the Valmont Test Facility

Flow Rate	8.5 m^3/s	(18000 acfm)
Gas Velocity	1.7 m/s	(5.6 ft/s)
SCA	37.8 $m^2/m^3/s$	(192 ft^2/kacfm)
Temperature	149°C	(300°F)
Collector Length	1.8 m	(6 ft)
Collector Spacing	23 cm	(9 in)
Gas Passages	6	
Number, Collector Sections	4	
Number, Precharger Sections	4	

TABLE 2

Ultimate Coal Analysis (%)

H_2O		9.77
C		67.49
H		4.49
N		1.56
S		0.26
Ash		5.02
O		11.14
	Total	100.00

TABLE 3

Elemental Ash Analysis (%)

SiO_2		59.54
Al_2O_3		23.79
TiO_2		0.78
Fe_2O_3		6.38
CaO		3.66
MgO		1.18
Na_2O		1.27
K_2O		1.92
P_2O_5		0.60
SO_3		0.51
	Total	99.63

TABLE 4

Test Program

1987

CONDITIONS	NO TESTS	EFF.	AUG.	SEP.	OCT.	NOV.
BASELINE - 1	11	97.9	▬			
SO_3 - 1	9	98.7	▬	▬		
PC-1, PRECHARGERS 1 to 4	40	99.1		▬	▬	
PC-2, PRECHARGERS 2,3,4	10	98.2			▬	
PC-3, PRECHARGERS 1 & 3	9	98.4			▬	
BASELINE - 2	7	90.4			▬	
PC-4, PRECHARGERS 1 & 4	4	98.9			▬	
BASELINE - 3	6	89.8			▬	
PC-5, PRECHARGERS 1 & 3	6	97.8				▬
BASELINE - 4	6	94.4				▬
SO_3 - 2	6	97.9				▬
PC-6, PRECHARGERS 1 to 4 & SO_3	9	98.2				▬

TABLE 5

ESP Data Used in Computer Model Simulation of Valmont Pilot

ESP Geometry		
Plate area per electrical section	80.3 m^2	(864 ft^2)
No. elect. sections in direction of gas flow	4	
Plate-to-plate spacing	22.9 cm	(9 in)
Wire-to-wire spacing	22.9 cm	(9 in)
No. of wires per passage per section	9	
Wire length per section	147 m	(483 ft)
Precharger Geometry		
Plate area per electrical section	6.7 m^2	(72 ft^2)
Plate-to-plate spacing	18.4 m	(7.23 in)
No. of wires per passage per section	1	
Wire length per section	21.9 m	(72 ft)
Electrical Operating Conditions		
Ratio of peak-to-average voltage	1.2	
Reduced ion mobility (cm^2/V-s)	1.7	
Gas Conditions		
Average volume flow rate	8.45 m^3/s	(17900 acfm)
ESP average gas velocity	1.66 m/s	(5.525 ft/s)
Precharger average gas velocity	2.1 m/s	(6.843 ft/s)
Average gas temperature	149°C	(300°F)
Average gas viscosity ($N \cdot S/m^2 \times 10^5$)	2.254	
Particulate Parameters		
Particle density (gm/cc)	2.27	
Particle dielectric constant	100	
Bulk resistivity (Ohm-cm)	5×10^{11}	
Bulk resistivity with SO_3 cond. (Ohm-cm)	1×10^{10}	
Inlet mass median diameter (μm)	29.8	
Inlet standard deviation, σ_p ,	2.51	

TABLE 6

Comparison of Efficiencies from Model Calculations with Measured Efficiencies of the Valmont Pilot

Test Series	Inlet Loading (gr/ACF)	Measured Efficiency (%)	Modeled Efficiency (%) S = .05 σ_g = .15
Baseline - 1 No Prechargers	1.086	97.85±.57	96.17
SO_3 - 1 No Prechargers	1.090	98.75±.58	99.06
PC - 1 Prechargers 1 to 4	0.912	99.08±.39	98.94
PC - 2 Prechargers 2, 3, 4	0.993	98.25±.46	98.21
PC - 3 Prechargers 1 and 3	0.763	98.42±.43	98.39
Baseline - 2 No Prechargers	1.063	90.37±2.44	90.59
PC - 4 Prechargers 1 to 4	1.469	98.86±.17	98.35
Baseline - 3 No Prechargers	1.156	89.75±1.56	89.77
PC - 5 Prechargers 1 and 3	1.698	97.83±.31	97.32
Baseline - 4 No Prechargers	1.833	94.42±.48	89.95
SO_3 - 2 No Prechargers	1.404	97.94±.58	98.53
PC - 6 Prechargers 1 to 4 and SO_3	1.343	98.17±.34	99.64

EXPERIMENTAL STUDY OF ASH LAYER DETACHMENT AND REENTRAINMENT UNDER NORMAL AND SHEAR RAPPING OF ELECTROSTATIC PRECIPITATOR COLLECTOR PLATES

by: D.H. Choi, S.A. Self, M. Mitchner, and R. Leach
Mechanical Engineering, Stanford University
Stanford, California 94305, U.S.A.

ABSTRACT

We have developed and tested a small electrostatic precipitator collector plate rapper. It is capable of delivering mechanical vibrations of controllable intensity and damping, in either normal or in-plane directions, under well-controlled conditions. Ash-rapping efficiencies were obtained, and novel methods to visualize the motion of the ash layer and to measure the rapping reentrainment were used. A simple analysis based on a theory of the electromechanics of an ash layer is performed, and some tentative criteria for rapping-system design are drawn.

1. INTRODUCTION

Understanding the plate-rapping process in electrostatic precipitators (ESP) has become an important issue because of the stringent requirements imposed on performance. Research and development efforts have concentrated mostly on studies of particle charging and transport, with little attention directed to the non-ideal effects resulting from rapping reentrainment and gas sneakage in the high-voltage clearance space above and the hopper space below the collecting plates. These non-ideal effects are known to reduce the overall collection efficiency of industrial ESPs, but insufficient quantitative knowledge has been available so far to make possible the design of precipitators which minimize such losses.

Rapping losses are reported in the literature [1] to account for up to 50% (by mass) of the uncollected particles, the loss from the last section being the most critical. Several sources [1,2] have commented on the negative effect arising from the increased stack emission during rapping cycles and different solutions have been implemented to control rapping reentrainment to acceptable levels. Unfortunately, in most cases, the solution has involved investing in larger precipitators, but the fundamental problem of optimizing the rapping process still persists. The goal of this study is to develop a sufficient understanding of the relevant physical phenomena to enable the rapping losses to become predictable and controllable by ESP designers.

Present rapping practice usually consists of periodic rapping blows to both the high-voltage and ground electrodes using either in-plane or out-of-plane hammer blows concentrated at discrete locations on the electrodes. The collector plates are made of thin-gauge steel sheets, reinforced by stiffening ribs running vertically. Typical heights range up to 15 m and widths range from 2 to 3 meters. Strong out-of-plane acceleration modes are excited in the plate when it is rapped [3], which cause the collected ash layer to detach from the collector surface and fall under gravity into the hoppers.

Under normal precipitating conditions, previous studies [4] have shown that the corona current flowing through the collected ash layer generates large internal cohesive stresses between the ash particles forming the layer as well as strong adhesive stresses between the particles adjacent to the metal surface and the surface itself. These stresses play an essential role in keeping the layer attached to the collector plates. As the layer grows thicker and less uniform in thickness, aerodynamic forces exerted by the air flow are able to reentrain particles from the outer surface of the layer. Studies performed by the Stanford group [4-6] show strikingly how the flow, the electrical conditions, and the ash layer thickness combine to generate deposition patterns, which reflect the surface distribution of ion current to the layer. Since continuous reentrainment caused by the air flow is also detrimental to ESP performance, plate rapping is usually scheduled to prevent the layer thickness from reaching values that are too large. To successfully detach the layer, the rapping blow must provide sufficient acceleration to overcome the cohesive stresses among ash particles or between the ash layer and the plate.

There is evidence that large out-of-plane accelerations of the plate produce massive ash reentrainment. The fact that any method of rapping very likely excites out-of-plane accelerations to some extent indicates that some reentrainment during rapping is almost unavoidable. Nevertheless, analyses of plate response [7-13] followed by experimental tests [3,14,15] have shown that these undesired out-of-plane modes can be minimized for a given geometry by applying certain criteria. In any event, the ultimate effectiveness of rapping optimization is still dependent on the ash layer response to the different excitation modes of the plate. Because this subject is still not well understood, we are conducting a systematic experimental study of the behavior of precipitated ash layers under varying flow and electric conditions when the plates are subjected to different modes of vibration.

2. PREVIOUS WORK

2.1. EXPERIMENTS

Some of the earliest rapping-efficiency measurements were conducted in the 1950s by Ruckelshausen [16] and by Sproull and Nakada [17]. More detailed studies of the rapping efficiency of a small-scale apparatus under a variety of electrical and ash conditions, using both in-plane and out-of-plane accelerations, were made in the 1960s by Sproull [2] and Hesselbrock [18]. Measurements were made of the efficiency of the rapping system (defined as the mass fraction of the dust initially precipitated on the rapped plate that is dislodged after one rap) while varying several conditions, including the rapping mode (in-plane or out-of-plane), the rapping intensity, the dust layer thickness, and the presence of corona current to the layer. The dust samples studied by these investigators included fly-ash from pulverized coal-fired power plants, copper ore reverberatory furnace dust, and rock dust from cement kilns. Since the electric resistivity of the dust is a function of temperature, several temperature values (21°, 93°, and 150°C) were used for each type of sample.

The principal conclusions from this work can be summarized as follows:

i) the rapping efficiency correlates generally with the maximum acceleration induced in the plate,

ii) in-plane rapping requires about twice as much maximum acceleration as out-of-plane rapping to dislodge the same fraction of the dust layer,

iii) the presence of corona current through the dust layer requires a greater maximum acceleration than without the corona current, in either rapping mode, to attain the same rapping efficiency,

iv) the rapping efficiency increases as the precipitated dust layer thickness increases,

v) for the same rapping efficiency (90%) and at a temperature of 150°C, cement dust requires a maximum acceleration five times higher than fly-ash (same layer thickness), even though the size distributions of these dusts are very similar,

vi) between the lower limit, when the temperature drops below the dew point, and the upper limit, when it is so high that some constituent of the dust begins to soften or melt, rapping becomes easier with increasing temperature,

vii) rapping with heavier hammers, keeping the impact energy constant, produces a greater maximum acceleration and, consequently, a higher rapping efficiency.

Among more recent experimental investigations concerning ash-rapping systems are those by Billington et al. [3], and Hieber and Jeselsohn [14], who analyzed the dynamic response of full-scale precipitator plates (with or without dust collected on them) to various in-plane and out-of-plane rapping blows. Their data show that, because of the impact, stress waves are generated in the plate, which travel at sonic velocities, causing complex in-plane and out-of-plane accelerations, and the presence of dust was found to dampen the plate's response. Another study by Enochson and McKeever [15] explored the vibration modes in a typical precipitator plate using real time digital Fourier analysis.

In addition, there was a study by Tassicker [19], where the rapping reentrainment losses of six full-scale precipitator installations were evaluated. According to this study, these losses represent about 30% of the total penetration for cold-side precipitators, and 60% for hot-side precipitators, being mainly in the 2-μm particle-diameter range and above. Also, Juricic and Herrmann [20] took some high-speed sideview photographs of dust layer dislodgement from a bench-scale precipitator plate, subjected to in-plane and out-of-plane vibrations. The low-frequency, out-of-plane component of the plate motion was seen to increase ash reentrainment.

2.2. THEORY

Theoretical work in the area of ash rapping systems can be divided into two major sub-areas: the study of the motion of collecting plates when subject to various types of initial mechanical excitations and the modeling of the dynamic response of collected ash layers subject to plate vibrations.

During the 1970s, Herrmann et al. [8-12], at Stanford, studied the dynamic response of rectangular plates, with initial imperfections, to in-plane and out-of-plane rapping, using both analytical and computational techniques. Numerical studies using finite-element methods to analyze the same problem were carried out by several researchers at Princeton University [3, 21-24]. There are strong indications in these numerical investigations that purely in-plane hammer blows can cause substantial out-of-plane buckling motion of the plate due to initial plate imperfections.

Juricic and Herrmann analyzed the dynamics of electrostatically precipitated fly-ash [13] and simulated the dust dislodgement process during rapping, by assuming that the layer behaves as a visco-elastic continuous material [7]. These simulations were compared with experimental data. Although the quantitative agreement was poor (a difference of two orders of magnitude), the simulations showed, qualitatively, the same trend of decreasing required maximum acceleration (for a constant rapping efficiency) with increasing bulk motion frequency, exhibited by the empirical data.

Computer simulations of full-scale electrostatic precipitators, which incorporate the rapping reentrainment characteristics via an empirical functional relation, were implemented in the work by Gooch and Marchant [25].

In the area of electromechanics of particulate layers, Moslehi [4] has given a comprehensive theory of the electromechanics of ash layers, in which the layer is modeled as a packed, three-dimensional array of uniform spheres. In particular, Figure 1 shows a cubic array, three particles thick, on a metal surface, with corona field and ion current lines terminating on the outer layer. To maintain continuity, current has to flow through (and over the surface of) the spheres, and passes between adjacent spheres through very small contact areas (resulting from elastic self-compression of the spheres). This causes very strong current concentrations to occur in the contact areas between spheres and between the lower spheres and the surface.

The problem was solved self-consistently using the Hertz formula [26] for the contact area, for all the regular packing modes for spheres. Basically, it is the Maxwell stress (i.e., the tension in the electric field lines) in and around contact areas which gives the layer its high cohesive and adhesive strengths. For typical conditions, internal cohesive stresses were calculated to be of the order of hundreds of g. It was found that, as the average current density increases, the contact areas increase so that the cohesive strength increases less than linearly with current. This theory was tested by electrical resistivity measurements of layers of glass beads (and of fly-ash) and good agreement was obtained.

From this theory, one expects the adhesive stresses to be larger than the cohesive stresses, because the compressive modulus of most metals is higher than for glass (the predominant material in fly-ash) and because of the different geometry. This is supported by our experimental observation that a very thin layer of ash always remains attached to the plate, even after very efficient raps, suggesting that the adhesive stresses are larger than the cohesive stresses.

3. APPARATUS AND TECHNIQUES

3.1. WIND TUNNEL TEST FACILITY

The Stanford laboratory precipitator consists of a relatively low-turbulence wind tunnel, of cross section 25 cm (10") wide by 75 cm (30") high, into which one or more precipitating test sections can be inserted in series. It is a versatile facility, in which realistic conditions of full-scale precipitators can be simulated, with the advantage of being able to isolate certain non-ideal loss mechanisms.

For the purpose of the present study, another branch was added to the existing wind tunnel, using the same induced draft fan and baghouse. It consists of an initial plenum where redispersed fly-ash is injected, followed by a test section consisting of a 1.8-m (6-ft) long wire-duct precipitator having seven wire electrodes 2.77-mm (0.109") diameter spaced every 25 cm (10") along the vertical midplane of the duct. This section has Lexan top and bottom walls that allow visual observations. It does not have any flow space above the collector plates for high-voltage clearance, nor any hoppers to collect the precipitated ash. Thus the loss mechanism associated with sneakage is effectively eliminated, allowing one to isolate and study the basic rapping process. Figure 2 shows a schematic of the wind tunnel facility. The flow velocity can be varied up to 8 m/s, corresponding to a throughput of 1.5 m^3/s (3,200 acfm). However, at a velocity of 2 m/s, more typical of modern precipitators, the throughput is 0.38 m^3/s (825 acfm) and the specific collector area (SCA) is 7.2 $m^2/m^3/s$ (36 ft^2/1000 cfm). The air stream is humidified with a swamp cooler to inhibit back-discharge.

On one of the collecting walls of the test section there is a rectangular opening, 30 cm (12") wide by 25 cm (10") high, 1.2 m (4 ft) downstream from the test section entrance with its lower edge 25 cm (10") above the tunnel floor, into which a test rapping plate can be inserted, with a gap of about 5 mm (1/5") on all sides. A rubber membrane is used to seal the gap. The collecting side of the rapping plate is flush with the inner surface of the precipitator section and the outer side is connected to a rigid concrete and steel structure through cantilevered steel beams. On the opposite wall, facing the rapping plate, there is a window into which either an aluminum or a Lexan plate can be fitted. It serves as a visual observation port through which video recordings of the falling ash layer can be made. Figure 3 shows a schematic of the test section in plan view.

Fly-ash is fed from a heated screw feeder into a sonic nozzle driven by compressed air, and injected through a tube counter to the main flow in the plenum section, well upstream of the precipitator section. This ash-laden air passes through a honeycomb that acts as a flow straightener and suppresses large-scale turbulence, producing a spatially uniform suspension. Usually a fine ash, of mean diameter by mass of 4-5 μm, from the Electric Power Research Institute's (EPRI) Arapahoe test facility is used and, with ambient air, no back-discharge is observed provided the relative humidity is greater than 50%.

For the rapping experiments described here we removed the first two wire electrodes and the last one to save precipitation time. The precipitator was energized to either polarity in the range 30 kV to 55 kV (pos) or 60 kV (neg), these being the corona onset and sparkover limits, respectively. At 50 kV, the linear current densities were ≈ 1.5 mA/m (neg) and ≈ 0.67 mA/m (pos). The corresponding average collector plate current densities are 1.68 mA/m^2 (neg) and 0.75 mA/m^2 (pos).

3.2. PLATE RAPPING MECHANISM

To study the dynamics of the ash layer during rapping of an electrostatic precipitator collector plate we built a rapping mechanism with the utmost simplicity. Highly in-plane or out-of-plane plate motion, with a minimum of other modes present, are produced by the present system. One can vary the maximum amplitude of the acceleration up to 500g (g = gravitational acceleration), with lowest mode frequencies up to 500 Hz. The rapped plate is made of 10-mm (3/16") thick aluminum sheet, stiffened by aluminum beams and aluminum honeycomb to minimize inter-mode coupling. It measures roughly 30 cm (12") wide by 25 cm (10") high and weighs only about 1.4 kg (3 lb).

In a recent paper by Self et al. [28] a rapping apparatus was described which delivered in-plane (shear) accelerations up to 300g maximum with bulk motion frequencies up to 500 Hz. The apparatus was used to make preliminary experimental studies of in-plane rapping efficiency, and is shown in Figure 4. It made use of the idea of cantilevered beams serving as springs to provide the restoring forces for the vibratory motion. Although that design produced the desired levels of acceleration in the in-plane mode, the associated out-of-plane motion of the rapped plate was quite high (an out-of-plane to in-plane accelerations ratio of 60%), making it difficult to interpret the experimental results for rapping efficiency. One of the main reasons for such a high ratio of out-of-plane to in-plane accelerations is the asymmetric motion of the rapped plate attached to the free end of the cantilever beams, as shown in Figure 5(a). Besides the effects of asymmetry, the plate motion also exhibited buckling modes because it was the bridging member linking the two cantilever beams and, therefore, subject to the high compressive and shear stresses resulting from the impulsive blow of the hammer rap on the anvil on the free end of the upper cantilever beam [see Figure 5(b)].

A natural extension of this design was found, which incorporated the symmetry lacking in the old one while keeping the high stresses away from the rapped plate. This new design utilizes the idea of leaf springs [see Figure 5(c)]. There are two aluminum beams, 5 cm (2") wide and 0.5 cm (3/16") thick, with both ends fixed to allow no translation or rotation. The position of these fixed ends can be varied, so as to vary the length (and therefore the spring constant) of the beams. An intermediate bridging member is connected at the center of the beams, to which the rapped plate can be attached either in the in-plane or out-of-plane direction. Figure 6 shows the normal rapping mechanism incorporating this design, used for the normal rapping experiments described in this article. We also damped the plate's motion using friction: two 1.25-cm (1/2") diameter bolts are symmetrically pressed on both sides of the bridging member, with a felt material in between. This system satisfied the initial design requirements of maximum displacements and accelerations of the rapped plate in the normal direction and produced in-plane (either vertical or sideways) accelerations smaller by at least a factor of three than the normal one.

Hammers with hard head materials, such as stainless steel, aluminum, or even Delrin, impacting a steel anvil produce very short impacts (on the order of tenths of milliseconds), where a larger part of the initial hammer impact energy is expended in exciting higher-order modes, instead of the lowest-order motion we are interested in. However, this impact time can be varied using anvils of different rubber materials and thicknesses. Matching the impact time to the period of the lowest frequency of oscillation in the normal direction, one minimizes the presence of higher modes, producing a more controlled motion of the plate. In our testing of the normal rapping rig, we have tried several rubber materials: butyl rubber, neoprene, pure gum rubber, cork material, etc. A pure gum rubber anvil, 5 mm (3/16") thick, produced the best combination of maximum acceleration and clean (with a minimum of high-frequency components) normal accelerations.

3.3. DIAGNOSTIC TECHNIQUES

The plate motion (displacement and accelerations) during rapping is measured using a Linear Variable Differential Transformers (LVDT) to determine the displacement in the direction of the hammer blow and piezoelectric accelerometers coupled to charge amplifiers to obtain accelerations in both the in-plane and out-of-plane directions. While the frequency response of the LVDT goes only to 3 kHz, the accelerometers have a much higher frequency response (up to the megahertz range). These differing bandwidths are acceptable since the acceleration signal contains many more high-frequency components, which are not evident in the displacement of the plate. The signals are digitized and stored on floppy disks in a minicomputer. The acceleration signals can also be processed with the computer to obtain the frequency spectrum of the plate motion during rapping. An analog-to-digital (A/D) board with 150 kHz sampling rate converts the analog electrical signals (from -10 to 10 volts) into 12-bit binary numbers which are then transformed into physical quantities using calibration factors. The 12-bit digitization limits the resolution of the readings. For typical charge amplifier gains, the mininum resolvable acceleration is about 0.5g, which is adequate for our purposes. All motion sensors have been calibrated to accuracies of at least one twentieth of their full scale, using either factory-supplied calibrators or calipers (in the case of the LVDTs) with 20 μm accuracy.

Visual observation of the behavior of the ash layer is made using a fast charge-coupled video camera (at up to 1000 frames per second). Direct frontal views are recorded as well as side-elevation views (using mirrors). For the fastest recording rate, two 300-watt tungsten-halogen lamps are used to illuminate the plate. We selected lamps of high output power in the red end of the visible spectrum because the camera is most sensitive in that wavelength range. A trigger system was built to sense the falling hammer and switch a high-power light-emitting diode, positioned within the field-of-view of the camera, to indicate the instant of hammer impact on the anvil of the rapping plate (to within the precision of the camera framing interval). The same signal is also used to trigger a storage oscilloscope (recording the in-plane and out-of-plane acceleration signals), as well as the data-acquisition computer system. The trigger system can be adjusted to trigger in advance of the impact, to ensure that the initial part of the signal is recorded. Figure 7 shows the distribution of the sensors on the plate, as well as the location of the LED-photodector triggering system.

From the camera record, overall qualitative observations of the ash dynamics can be made, as well as some quantitative measurements such as the sliding velocity of various portions of the ash layer and the velocity of dust puffs (resulting from reentrainment) being carried off by the air flow. The lateral views can also be correlated with the degree of reentrainment due to rapping since they show in some detail how the initially compacted ash layer is projected in the normal directtion by the out-of-plane components of the plate motion.

We also estimate the apparent density of the collected ash layer using a specially designed micrometer to measure the thickness distribution of the ash layer deposited on the aluminum plate opposite to the rapped plate. This was done only after having ensured that ash deposition during the collection stage takes place symmetrically. The layer thickness decreases from the upstream to the downstream side of the rapped plate due to the higher ash concentration on the upstream side and also from top to bottom due to gravitational settling. Maximum-to-minimum thickness ratios are about 4 in typical runs.

The rapping efficiency is obtained by measuring the mass of ash dislodged from the plate by the rap, which is collected in a tray resting on the bottom of the tunnel, and dividing it by the initial mass of ash layer present on the plate. The latter is measured a posteriori by brushing the remaining portion of the layer from the plate after the rapping run is completed. Since the breakdown of the layer into small pieces and their subsequent downward motion under gravity are not of a very deterministic character, several rapping runs are made under the same conditions to establish some reliable meaning to the rapping efficiency thus determined. One has to be mindful of the fact that the various portions of the rapping plate are subject to different levels of motion (acceleration levels and frequency spectrum) and that the layer thickness and the current density (and hence the cohesive and adhesive forces) vary with position on the plate. Therefore, the rapping efficiency represents the integrated result of how each of these factors are effective in causing particular areas of ash to detach from the plate. Normally, because the upstream portion of the plate collects a thicker layer of ash, it is more efficiently rapped off than the downstream portion.

We define rapping reentrainment as the fraction by mass of the ash layer collected on the plate, which detaches from the surface when rapping takes place, but fails to get collected in the hoppers, getting carried away by the air flow and escaping the precipitating section, representing a loss factor for that section. Since a practical precipitator comprises several collecting sections in series, a simple calculation shows that ash reentrained from the front sections is efficiently recollected in the following sections. However, the recollected fraction decreases towards the end of the precipitator and it is clear how critical is the reentrainment from the last section. For the purposes of our small-scale experiment, we will define rapping reentrainment as the fraction of the ash detached from the plate by the rap which is recollected in a given area of (clean) collector plate positioned just downstream from the end of the rapped plate. The geometry and location of this recollecting plate and its position will be optimized to relate such rapping reentrainment measurements as far as possible to quantities of interest in full-scale systems.

Another approach currently being explored is to use an optical particle size analyzer to sample the dust-laden air downstream of the rapped plate at regular time intervals, in order to monitor the ash flux in the gas stream during the rapping process. A preliminary run has registered a significant flux of particles, primarily in the diameter range of 5-10 μm immediately after the rapping of the plate. It seems likely that these particles are agglomerates released from the plate. Since this technique yields information about ash fluxes at discrete points in space, while the former approach of recollecting the reentrained ash by means of a secondary reprecipitating section gives integrated information (over space and time), the two methods should complement one another to provide a more thorough understanding of the reentrainment phenomenon.

3.4. EXPERIMENTAL PROCEDURE

A single rapping run consists of the following steps:

i) Turn on the wind tunnel and set the flow velocity. A Pitot tube placed at the exit of the test section is used to measure the flow speed. Precipitate fly-ash on the tunnel side walls (including the rapping plate) for a period ranging from 15 to 60 min.[1] Typically we use a flow speed of 1 to 2 m/s and the wires are energized to -50 kV.

ii) At the end of the precipitation period, stop the air flow and switch off the voltage.[2] Remove the aluminum plate fitted into the opening opposite to the rapping plate and measure the thickness distribution as well as the total mass of the layer collected on it. Clean the tunnel side wall below the plate to be rapped. Install tray at the bottom of the tunnel, adjacent to, and underneath the rapping plate, to collect the ash dislodged by the rap.[3]

iii) Place a clear Lexan window in the opening opposite to the rapping plate to allow visualization of the rapping process. Place the high-power LED (used to record the impact time in the video tape) so that it is visible at the top-downstream corner of the video camera field of view. Align and focus the video camera.

iv) Slowly turn up the voltage to the desired level and then turn on the air flow again,[4] but with no ash feed, so that a clear view of the rapping event may be obtained.

v) Now the system is ready for the rapping hammer blow.[5] Turn on and reset the LED trigger circuit: the LED in the video screen turns on and will only turn off 5 msec before the hammer hits the plate. Turn on the charge amplifiers and LVDT circuit, and start the data-acquisition computer program.[6]

vi) Turn on the halogen lamps, set the video recording speed (usually 1000 frames/sec) and start recording. Rap the plate by allowing the hammer to fall and hit the anvil on the plate.[7] Stop the video recording 1 or 2 sec after the rap.[8] Turn off the lamps to avoid excessive heating of the plastic window.

vii) Turn off the air flow and the high voltage in that order. Brush off into the tray ash reattached in the area below the rapping plate (this occurs frequently with current-on rapping runs). Remove the tray and weigh it.

---

[1] The layer thickness increases with collecting time, and can be increased by applying higher voltages (limited only by spark-over). In our experiments, collecting for 30 min typically produced an ash layer of average thickness of 1.5 mm (0.06").

[2] The order is important since, in reverse order, massive layer fall-off and reentrainment occurs.

[3] This tray is made of plexiglass (to avoid arcs from the high-voltage electrodes). Before installing the tray, the collector area surrounding the rapping plate was cleaned using a brush. (This step is necessary to avoid ash from those areas falling into the tray.)

[4] This is for the case when a current-on and flow-on rapping run is desired. One can choose to have either or both of these off during rapping.

[5] The hammer mass, head material, and initial height are chosen before the run.

[6] The connections to the computer are made prior to the run; the software program starts acquiring data following an external trigger signal, which is provided by the LED triggering system. Refer to Figure 7 for an overview of this triggering system.

[7] A latch mechanism prevents the hammer from hitting the plate twice if it bounces on first impact.

[8] The time it takes for the ash layer to slide down the plate is approximately 300 to 400 msecs.

viii) Reinsert the tray and brush off the rest of the ash remaining on the plate into it. Weigh it again. This determines the total mass of ash initially collected on the rapping plate.

ix) Turn off all remaining components and clean the wind tunnel for the next experiment.

At the end of the run, the acceleration and displacement signals are stored in the computer, and are saved on floppy disks for further analysis. The same signals are displayed on the storage scope and may be photographed.

Preliminary experiments using different rapping conditions and electrical and flow conditions have been made, to explore the parameter space and to test improvements in the apparatus and techniques. Some of the parameters varied in these runs are: voltage (and consequently current) levels, polarity, impact parameters, ash layer thickness, and flow velocity. The parameter ranges used in these runs encompass the usual range of operating conditions for industrial ESPs.

In the future, it is planned to run a matrix of rapping experiments for a wide range of conditions to pinpoint important parameters and to obtain a quantitative understanding of the physical mechanisms of ash layer dislodgement and reentrainment.

4. RESULTS

4.1 IN-PLANE (SHEAR) RAPPING EXPERIMENTS

The apparatus and experimental techniques used to obtain rapping efficiencies and study the detachment and further motion of the precipitated ash layer after an in-plane rap were described in a previous paper by Self et al. [28], with some preliminary results. We shall briefly summarize the main results for in-plane rapping in the paragraph below.

Figure 8 shows accelerations in the in-plane (vertical) and out-of-plane directions and the in-plane displacement obtained from doubly integrating the acceleration measurement. The two accelerometers were attached at the top-downstream corner of the back face of the rapped plate, and the LVDT at the bottom-upstream corner, as shown in Figure 4. A hammer, of total mass 1.5 kg (3.3 lb) with a Teflon head, falling from an initial height of 60 cm (2.0 ft) impacting on an aluminum anvil attached to the free end of the upper cantilever beam, produced the motion shown in Figure 6. Fast Fourier transforms (FFT) of the amplitude of both accelerations are also presented in the same figure. The in-plane acceleration shows a strong component around 90 Hz, which corresponds to the lowest frequency of the mass-spring system. Higher-order modes were also present, as seen in the spectral data. The out-of-plane acceleration had a maximum value of about 40% of the maximum in-plane acceleration, and was composed of much higher frequencies than the in-plane signal.

Table 1 summarizes the results of the exploratory rapping runs made up to that time. Negative polarity discharge was used in all runs and the linear current densities through the high-voltage wire electrodes are given. The out-of-plane accelerometer had not been installed at the time runs #1 through #6 were made. We did not measure the precipitated ash layer thickness in those runs, either.

Figure 9 shows the rapping efficiency versus current density from runs #1, #2, and #6, which had approximately the same amount of precipitated ash and acceleration levels. In the same figure we have also plotted results for out-of-plane rapping.

Video camera recordings were made in some of the runs and show some interesting features of the rapping process, such as how the presence of corona current strongly affects the ash layer detachment and subsequent motion, and how the out-of-plane components of the plate motion affects reentrainment. For the high accelerations used in these runs, the ash layer was successfully dislodged from the plate in all runs, breaking down into a number of smaller pieces which then fell down under gravity. The corona current affected the motion of the falling smaller pieces, being very effective in reattaching them onto the rapped plate. The measurement of the falling velocity in the absence of corona current indicated an effective vertical acceleration of about 0.5g, making it evident that there was a friction force acting on the smaller pieces sliding down the plate surface. The reattachment of some pieces in the presence of corona current suggests that the friction force varies as the piece travels down the plate surface, increasing with time until it is so strong as to stop its vertical motion, causing it to reattach onto the plate. The dynamics involved in this reattaching process and the microscopic state of the sliding layer close to the plate surface are not well understood at the moment. They need further study since they play an important role in the rapping process.

Very little rapping reentrainment was observed in the video recordings of runs #7 through #13, where the air flow speed was kept at 1.0 m/s. No quantitative measurement of the total mass of reentrained ash has been obtained so far.

4.2 OUT-OF-PLANE (NORMAL) RAPPING EXPERIMENTS

Figure 10 shows typical records from the two accelerometers attached to the rapped plate, that measure the in-plane and out-of-plane accelerations, and from an LVDT position transducer, placed to measure out-of-plane displacement. They show the plate response to a hammer, of total mass 3.0 kg (6.6 lb) with a stainless steel head, falling from an initial height of 30 cm (1 ft), impacting a pure gum rubber anvil attached to the bridging member of the plate, as shown in Figure 6. The sensors were placed on the backside of the plate after having checked that the accelerations (and consequently the displacements) are uniform over the plate surface within 15% variation.

Fast Fourier transforms of the amplitude of both acceleration signals are plotted in the same figure in the insets. One can see that the maximum in-plane vertical acceleration is about 30% of the corresponding out-of-plane value (290g). This is an acceptable ratio because we have seen in previous experiments with in-plane rapping that a 100g vertical acceleration is not enough to dislodge the ash layer in the thickness range less than 5 mm. The FFT of the out-of-plane acceleration shows two strong components: the lowest frequency, around 120 Hz, corresponds to the lowest frequency of the mass spring system, while the higher frequency around 800 Hz is presumably associated with the third-order frequency of the leaf spring beams (the second-order mode is not excited in our system because of the symmetry). The vertical acceleration trace shows evidence of coupling with the lowest mode in the later stages (20 msec after contact), but initially is seen to be composed of a large number of higher-order modes, which may be due to bending of the plate or to longitudinal waves. We can also see from the time trace of the displacement that the friction damping is effective in introducing rapid decay of the vibrations.

Table 2 summarizes the results of the exploratory rapping runs made so far. Negative polarity discharge was used in all runs.

In runs #1 through #6, we observed back corona discharge spots on the precipitated layer and attribute their appearance to the low humidity of the ambient air at the time of the experiments. The primary effect of this was to raise the current level due to the space charge neutralization effect caused by the back corona. Thus, the current density during precipitation as well as during rapping was unusually high (reaching sometimes values as high as 1.6 mA/m) when compared to corresponding in-plane rapping experiments made previously. Run #7 did not indicate occurrence of back discharge.

Figure 9 shows the rapping efficiency as a function of the current density applied during rapping for these normal rapping experiments as well as the corresponding data for in-plane rapping [28]. We observe the rapping efficiency to decrease with current density for both rapping modes, but the normal rapping generally has a lower efficiency than the in-plane rapping for approximately the same levels of current density, maximum acceleration, and layer thickness.

The ash layer remaining on the rapped plate after the normal rap had an aspect different from the one after an in-plane rap. For the in-plane rap, the remaining layer showed no signs of having been subjected to heavy stress, having essentially the same appearance as before the rap. For the out-of-plane rap, however, the outer surface of the layer was affected, where thin superficial layers were torn away from the underlying layer still attached to the plate. Figure 11 shows photographs of remaining layer portions (a) after an in-plane rap and (b) after an out-of-plane rap.

Recent recordings from out-of-plane rapping experiments contrast vividly with those of in-plane rapping ones in that the former show large amounts of ash layer being projected out into the air stream by the strong out-of-plane plate motion, forming a dense cloud which was carried away by the flow stream. They also show that, in the cases of rapping without any corona current, the ash layer breaks up into smaller pieces--similarly to what happens with in-plane raps--and falls under gravity. Unlike the in-plane cases, this detachment-breakup-fall cycle does not happen immediately following the rap but takes about 300 msec to start.

5. ANALYSIS

Rapping efficiency measurements made under different conditions generally agree with the observations of previous workers. In addition, the video recordings of the ash dislodgement and subsequent motion provide some new insight into the dynamic behavior of the ash layer under rapping conditions. A careful study of these recordings leads to the following tentative conclusions:

i) In high-efficiency in-plane rapping runs resulting in high rapping efficiency, the ash layer typically takes 300 to 350 msec to be completely removed from the plate.[1] This is the time taken for the top-downstream portion of the layer to slide to the bottom of the plate and corresponds to an average acceleration during the fall of ≈ 0.5g. It also implies that it takes about 25 to 35 in-plane lowest-frequency oscillations of the plate for the ash layer to completely fall.

ii) The corresponding characteristic falling time for high-efficiency out-of-plane rapping events is 800 msec on average.[2]

iii) In all in-plane rapping runs, the ash layer is fully dislodged immediately after the rap, breaking up into a number of large and small pieces that start to fall under gravity, maintaining their integrity. In most current-on cases, however, some of these falling pieces reattach to the surface, resulting in low rapping efficiencies. The important, but subtle, point here is that the rap itself is strictly not less efficient than in the current-off runs, but that the corona current induces an attractive force between between the layer and the surface throughout the whole process, and forces the layer to reattach even after falling some distance.

One may obtain a simple criterion for ash layer detachment by considering the equilibrium of a homogeneous layer, of uniform thickness, subjected to a slowly increasing acceleration in either in-plane or out-of-plane directions (refer to Figure 12). In the quasi-static limit, the stresses are given by:

---

[1] Maximum acceleration levels of 300 to 400g were used in these runs. The plate bulk motion had maximum amplitudes of 0.3 to 0.5 mm and natural frequencies around 90 Hz.

[2] Maximum accelerations around 290g, with corresponding displacements in the order of 0.3 mm and lowest frequency of 120 Hz, were applied in the out-of-plane rapping experiments.

$$\sigma_{\text{shear}} = \rho(\delta - x)a_{\text{shear}} \tag{1}$$

In both cases, the maximum stress in the layer occurs at the plate. The layer stays attached until:

$$\sigma_{\text{shear}_{\text{max}}} \equiv \rho\ \delta\ a_{\text{shear}} \geq \sigma^{\star}_{\text{shear}} \text{ or } \sigma^{\star\star}_{\text{shear}} \tag{2}$$

where $\sigma^{\star}_{\text{shear}}$ is the shear cohesive strength of the layer, and $\sigma^{\star\star}_{\text{shear}}$ is the shear strength of adhesion between the layer and the plate. If $\sigma^{\star}$ is smaller, we expect a monolayer of ash to be left on the plate, and, if $\sigma^{\star\star}$ is smaller, we expect a clean plate after the rap. In either case, Eq. 2 indicates that the minimum acceleration for detachment is inversely proportional to layer thickness. Also, because the cohesive and adhesive strengths increase with current density, the acceleration for dislodgement also increases with current, as observed.

iv) In contrast, out-of-plane raps (with same intensity as the in-plane ones) in the presence of corona current are unable to detach the ash layer from the plate surface. At most, some portions of ash from the outer surface of the layer were projected off, suggesting an entirely different dynamical picture. Although the layer detachment with in-plane rapping could be reasonably modeled by a quasi-static theory where wave propagation through the layer was ignored, the boundary condition for the out-of-plane compressional stress waves at the free surface of the layer plays an important role in out-of-plane rapping. When the compressive (out-of-plane) stress wavefront reaches the free surface, it is reflected as a rarefaction wave causing tension between the ash particles. Detachment then occurs when the tensile stress is larger than the cohesive stress between two adjacent ash particles. Because the current distribution over the surface of the rapped plate is very irregular and patchy during precipitation (specially when negative polarity discharges are applied), the cohesive stress distribution in the layer is far from being uniform, leaving the layer with an irregular appearance [like that shown in Figure 11(b)] after an out-of-plane rap.

The detached piece carries much of the energy contained in the rarefaction wave front. It will be projected deep into the flow stream representing a serious reentrainment effect for out-of-plane rapping, an effect that is absent for the in-plane rapping.

v) The precipitation of an ash layer is a dynamic effect, involving how each particle packs into available depressions in the existing ash surface. Experiments by Fisher et al. [5,27] showed that, with (polydisperse) fly-ash, the layers are tightly packed when deposited where there is current, and loosely packed where there is no current. When the current is switched off the dense layer (precipitated with current) remains densely packed, and it retains a relatively high internal strength due to Van der Waals forces--but not as high as when current is flowing. One the other hand, a loosely packed layer deposited without current has much lower internal strength and, thus, is likely to be easily rapped and reentrained. Because the ion current density distribution on the collector is quite inhomogeneous, especially for negative corona on smooth wires and at low currents, the rapping efficiency and the degree of reentrainment may be expected to be sensitive to the electrical conditions, especially for out-of-plane raps.

6. CONCLUSIONS

A rapping system has been built to excite a small collector plate in a laboratory precipitator with well-controlled vibration modes. The apparatus and techniques used to describe the ash dislodgement efficiency of this rapping system are reported. Novel methods for ash motion visualization, as well as for measuring rapping reentrainment, are described. Some preliminary experimental measurements of rapping efficiency, made under different conditions, are in general agreement with previous investigations and have provided new insights into the physical process of ash dislodgement.

ACKNOWLEDGMENTS

This work was supported by the Electric Power Research Institute under Contract No. RP 533-1. The support and encouragement of Dr. J. Maulbetsch and Mr. R. Altman is gratefully acknowledged.

The work described in this paper was not funded by the U.S. Environmental Protection Agency and therefore the contents do not necessarily reflect the views of the Agency and no official endorsement should be inferred.

REFERENCES

1. Sproull, W.T. Minimizing rapping loss in precipitators at a 2000-megawatt coal-fired power station, J. Air Poll. Control Assoc. 22: 181-186 (1972).
2. Sproull, W.T. Fundamentals of electrode rapping in industrial electrical precipitators, J. Air Poll. Control Assoc. 15: 50-55 (1965).
3. Billington, D.P., Hieber, G., and Rummel, S. Full-scale, experimental study of rapped electrostatic precipitator plates, Research Report Number 77-SM-2, Dept. of Civil Engineering, Princeton University, 1977.
4. Moslehi, G.B. Electromechanics and electrical breakdown of particulate layers, Ph.D. Thesis and HTGL Report T-236, Stanford University, 1983.
5. Self, S.A., Mitchner, M., Fisher, M.F., Gere, D.S., and R.N. Leach. Corona discharge structure and its influence on precipitation and reentrainment, IEEE-IAS Conference Record, pp. 1128-1135, Philadelphia, PA (October 1981).
6. Self, S.A., Moslehi, G.B., Mitchner, M., and Leach, R. Electromechanics and reentrainment of precipitated ash, Proceedings of the International Conference on Electrostatic Precipitation, pp. 388-440, Monterey, CA (October 1981).
7. Juricic, D., and Herrmann, G. Modeling and simulation of dust dislodgement on collecting plates in electrostatic precipitators, 9th Annual Pittsburgh Conference on Modeling and Simulation, 1978.
8. Juricic, D., and Herrmann, G. The effect of traveling waves on the response of collecting plates in electrostatic precipitators, Pflüger-Festschrift, Hannover, 1977.
9. Pasic, H., and Herrmann, G. On rapping of plates of electrostatic precipitators, 2nd Conference on Mechanical Design & Production, Cairo, Dec. 1982.
10. Juricic, D., and Herrmann, G. Lateral response spectra of longitudinally rapped thin elements, 5th World Congress on Theory of Machines and Mechanisms, 1979.
11. Pasic, H., and Herrmann, G. Dynamic shear response of rectangular plates with initial imperfections, J. Mech. Design 102: 769-775, 1980.
12. Juricic, D., and Herrmann, G. Response of collecting plates in electrostatic precipitators due to shear rapping, J. Mech. Design 100: 105-112, 1978.
13. Juricic, D., and Herrmann, G. On the dynamics of electrostatically precipitated fly ash, Trans. ASME 101: 584-591, 1979.

14. Hieber, G.M., and Jeselsohn, F.S. Electrostatic precipitator plate rapping and reliability, EPRI Report FP-1006, Vol. 3, Part 2, Research Project 1180-10, October, 1980.
15. Enochson, L., and McKeever, B. Preliminary experimental determination of precipitator plate vibration modes by real time digital Fourier analysis, EPRI Report FP-1006, Vol. 3, Part 2, Research Project 1180-10, October, 1980.
16. Ruckelshausen, K. Über die Beseitigung von Staubansatzer auf technisch glatten Oberflächen durch Klopfen oder Vibrieren, Doctor's Thesis, Technischen Hochschule, Stuttgart, No. DK-68511, Giese-Druck Kg. Offenbach/M, 1957.
17. Sproull, W.T., and Nakada, Y. Operation of Cottrell precipitators, Ind. Eng. Chem. 43: 1350-1358 (1951).
18. Hesselbrock, H. Problems of electrical dust removal and requirements for further technical development, Staub 25: 32-42 (1965).
19. Tassicker, O.J. Rapping reentrainment losses in full-scale electrostatic precipitators, EPRI Report FP-1006, Vol. 3, Part 2, Research Project 1180-10, October, 1980.
20. Juricic, D., and Herrmann, G. High speed photography of dust layer dislodgement, EPRI Select Workshop for Electrical Precipitator and Fabric Filter Manufacturers, Denver, Colorado, November, 1977.
21. Dumitrescu, J.A., and Billington, D.P. Finite-element analysis of rapped electrostatic precipitator plates, Research Report SM-10-75, Dept. of Civil Engineering, Princeton University, December, 1975.
22. Chang, N., Lee, P.C.Y., Billington, D.P., and Mark, R. Simplified analytical study of rapped electrostatic precipitator plates, Research Report SM-11-76, Dept. of Civil Engineering, Princeton University, August, 1976.
23. Nagy, D.A., Chang, N., Billington, D.P., and Glennie, W. Finite element numerical studies of electrostatic precipitator plates, Research Report SM-9-77, Dept. of Civil Engineering, Princeton University, December, 1977.
24. Nagy, D.A., Billington, D.P., and Asher, N. Linear dynamic finite element studies of imperfections and eccentricities in electrostatic precipitator plate systems, Research Report SM-11-78, Dept. of Civil Engineering, Princeton University, July, 1978.
25. Gooch, J.P., and Marchant, G. Jr. Electrostatic precipitator rapping reentrainment and computer model studies, Research Project 413-1, Vol. 3, FP-792, Southern Research Institute, 1978.
26. Love, A.E.H. A Treatise on the Mathematical Theory of Elasticity, 4th edition, Dover Publications, 1927.
27. Fisher, M.J., Gere, D.S., Leach, R.N., Mitchner, M., and Self, S.A. Surface reentrainment of collected fly ash in electrostatic precipitators, Third Symposium on Transfer and Utilization of Particulate Control Technology, Orlando, Florida, March, 1981.

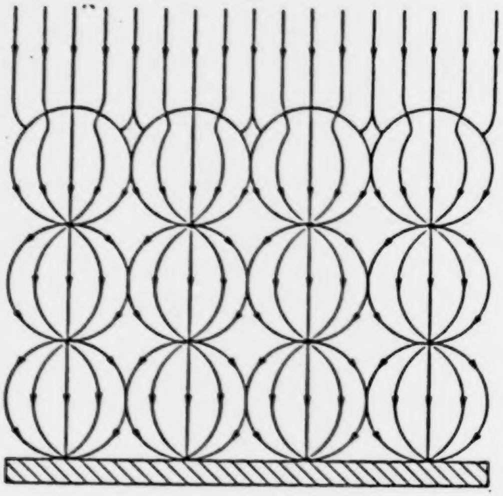

Figure 1. Model for current flow through a cubic array of resistive spheres.

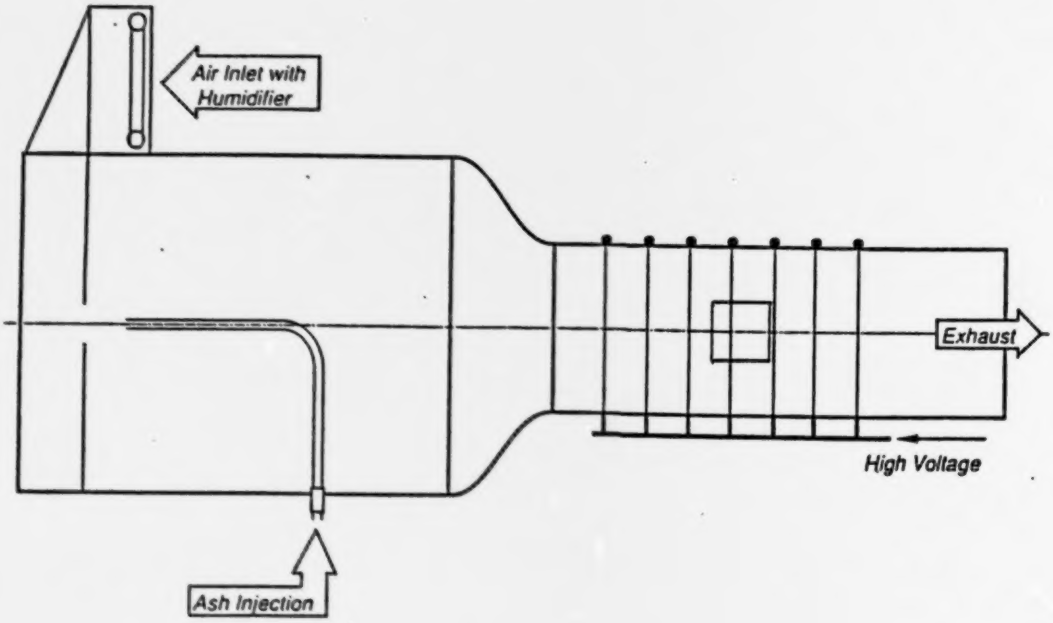

Figure 2. Wind tunnel facility: schematic.

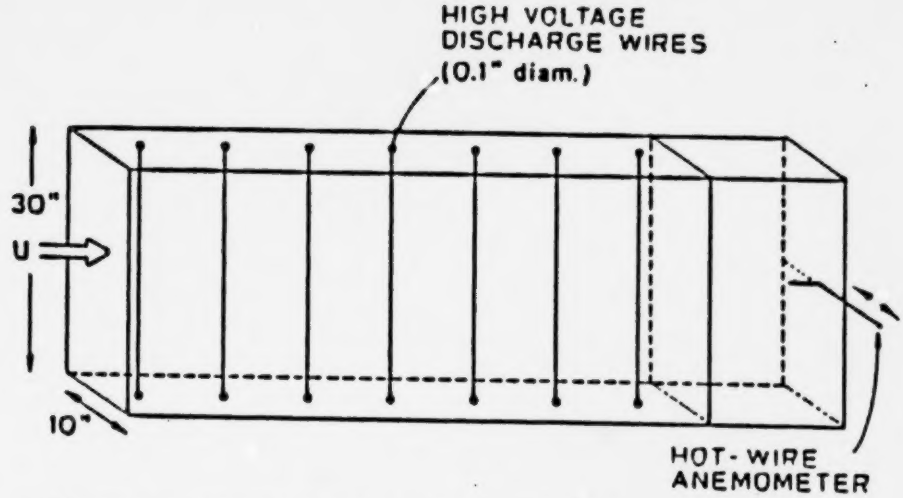

Figure 3. Stanford laboratory precipitator: schematic.

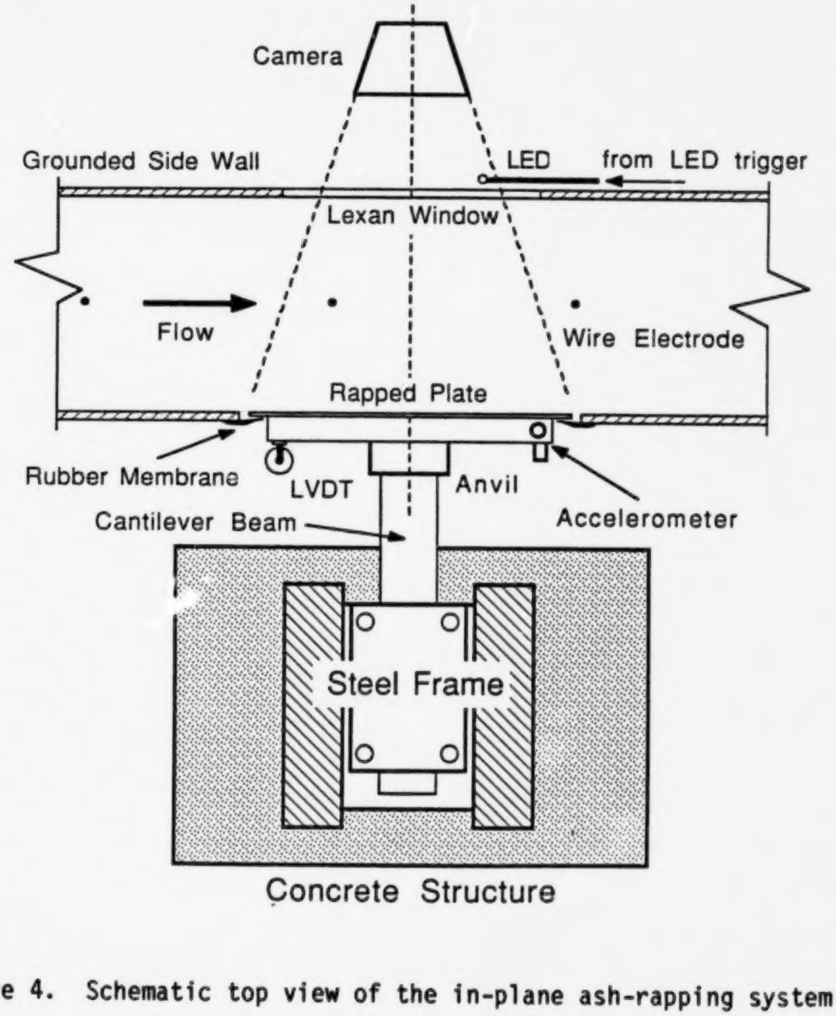

Figure 4. Schematic top view of the in-plane ash-rapping system.

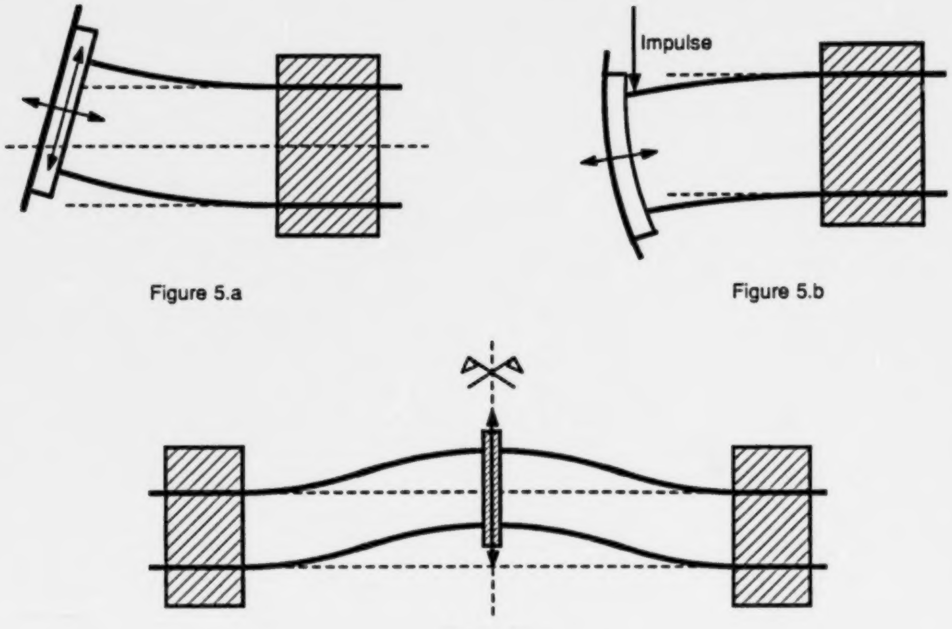

Figure 5.a

Figure 5.b

Figure 5.c

Figure 5. Schematic of two spring concepts: (a) in-plane rapping system showing the out-of-plane motion due to the angular displacement of the free ends of the cantilever beams; (b) in-plane rapping system showing the out-of-plane motion due to the buckling of the rapped plate; (c) new design--symmetry eliminated out-of-plane motion.

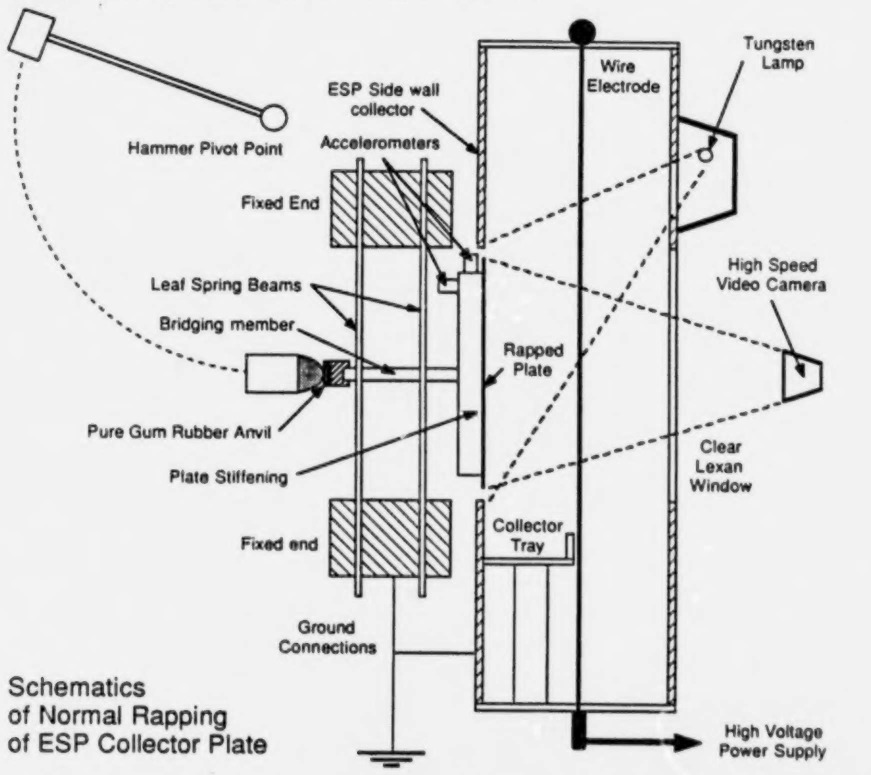

Figure 6. Schematic side-elevation view of the out-of-plane rapping system.

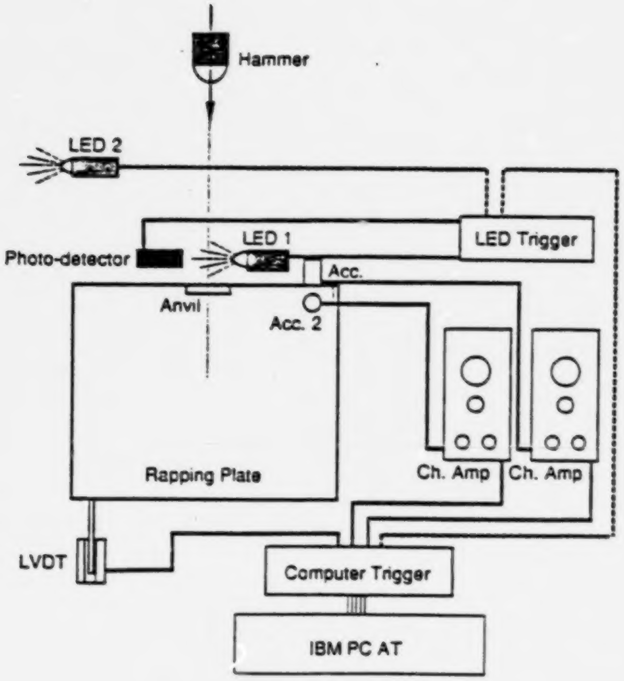

Figure 7. Data-acquisition instruments: schematic.

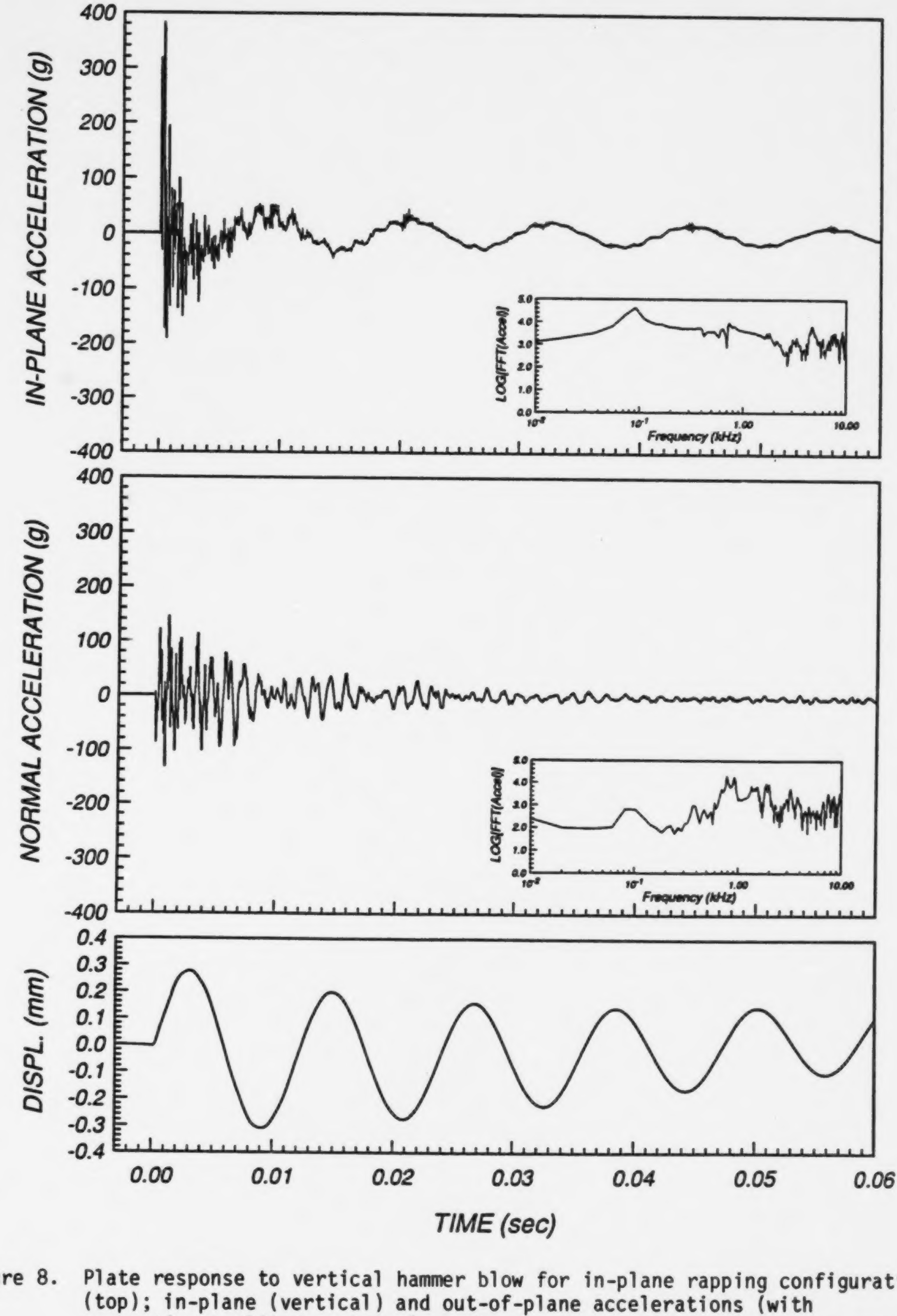

Figure 8. Plate response to vertical hammer blow for in-plane rapping configuration (top); in-plane (vertical) and out-of-plane accelerations (with respective amplitude spectra) at the top-downstream corner of the rapped plate (middle); in-plane displacement of the top-upstream corner (bottom).

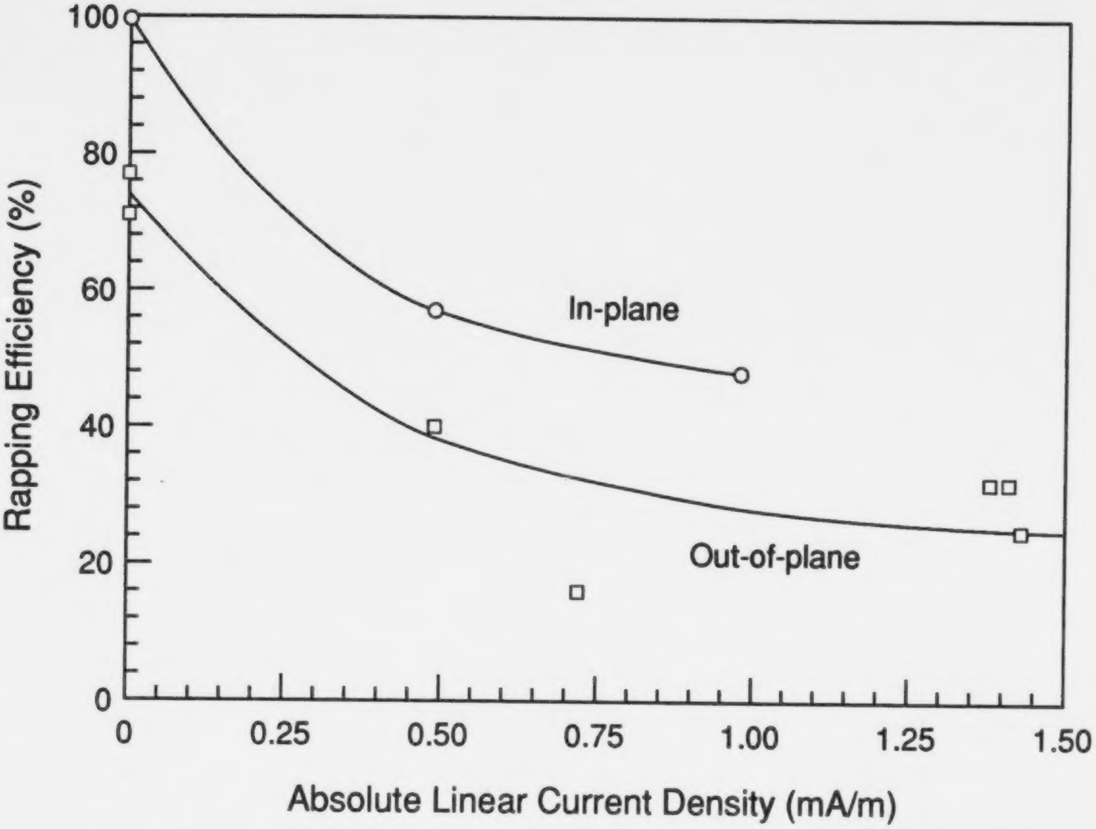

Figure 9. Plot of rapping efficiency versus current density applied during rapping; maximum in-plane acceleration ≈ 300g ~ 330g (in-plane rapping runs); maximum out-of-plane acceleration ≈ 290g (out-of-plane rapping runs).

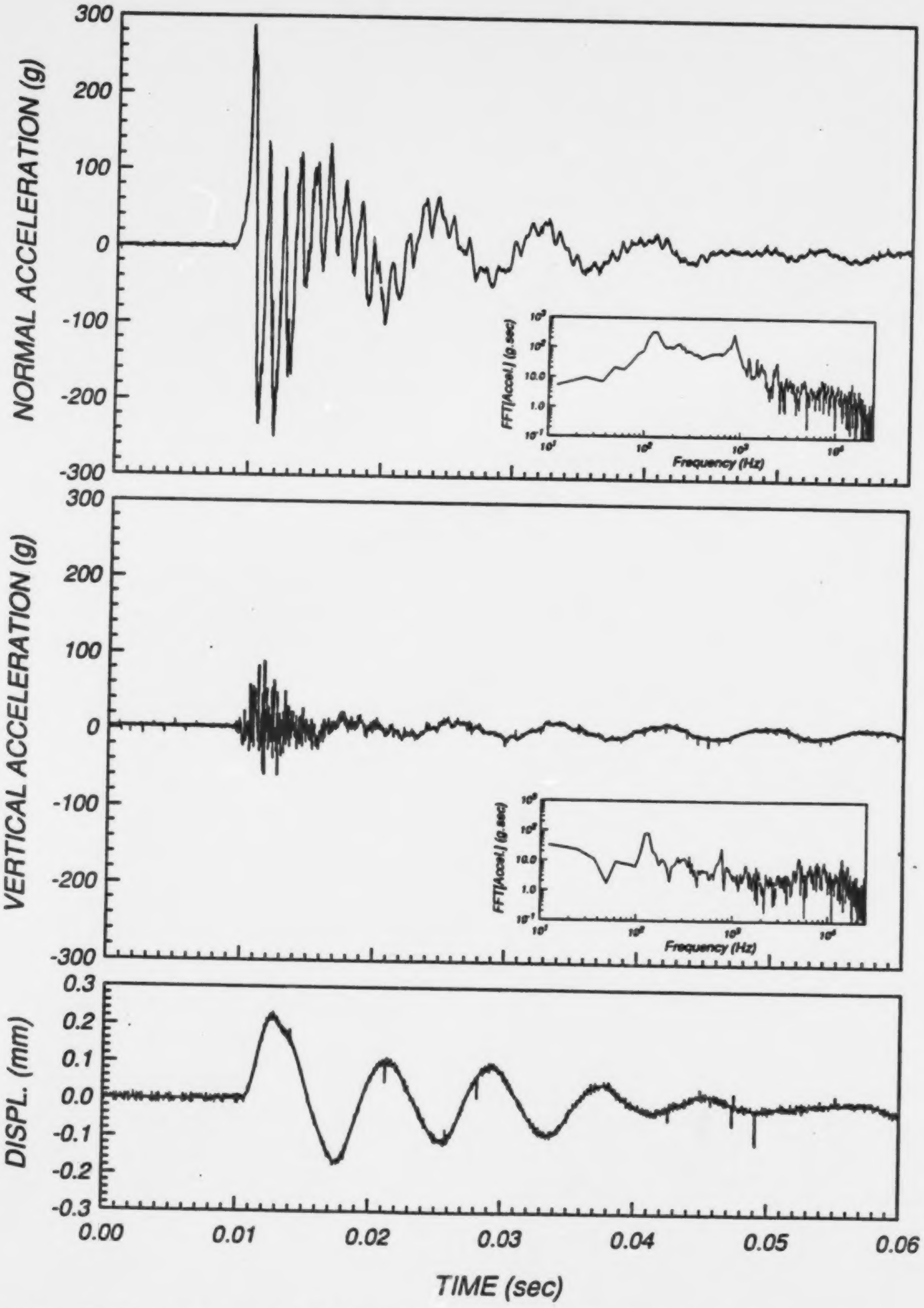

Figure 10. Plate response to horizontal hammer blow for out-of-plane rapping configuration (top); in-plane (vertical) and out-of-plane (horizontal) accelerations (with respective amplitude spectra) at the top-downstream corner of the rapped plate (middle); out-of-plane displacement of the top-upstream corner (bottom).

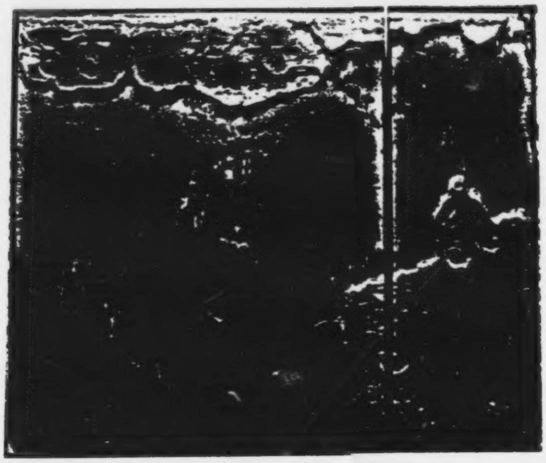

(a) an in-plane rap

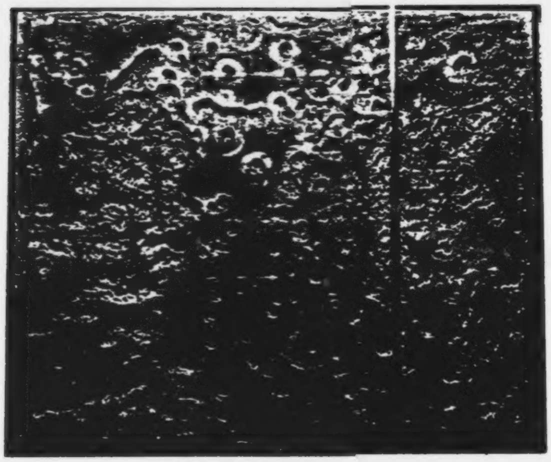

(b) out-of-plane rap

Figure 11. Photographs (top view) of the ash layer remaining on the rapped plate after one rapping blow.

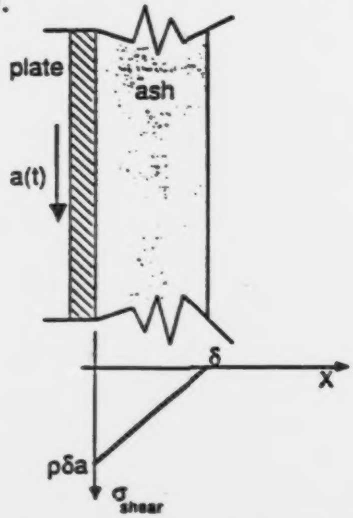

Figure 12. Model for current flow through a more densely packed array of resistive spheres.

TABLE 1

Run #	Precipitated Mass (grams)	In-Plane Acceleration (g)	Out-of-Plane Acceleration (g)	Applied Voltage (kV)	Current Density (mA/m)	Flow Speed (m/s)	Rapping Efficiency (%)
1	122.6	300	-	0	0	0	99.6
2	127.1	300	-	-50	0.49	0	57
3	140.7	360	-	-50	0.49	0	98
4	99.9	430	-	-50	0.49	0	67
5	131.7	80	-	0	0	0	69
6	113.5	330	-	-55	0.98	0	48
7	52.9	320	120	-50	0.53	1.0	99.1
8	34.6	280	110	-50	0.53	1.0	14
9	71.1	290	120	-50	0.53	1.0	38
10	64.9	310	180	-50	0.53	1.0	26
11	73.8	320	120	-50	0.53	1.0	41
12	176.5	300	120	-50	0.53	1.0	96.6
13	171.1	300	120	-50	0.53	1.0	95.1

TABLE 2

Run #	Total Collected Mass (grams)	Average Layer Thickness (mm)	Average Layer Density (kg/m)	Velocity (m/sec)	Current Density (mA/m)	Rapping Efficiency (%)
1	145.07	1.61	0.90×10^5	0	0	70
2	156.61	1.65	0.82×10^3	0	1.41	32
3	144.57	1.60	0.89×10^3	0	1.43	25
4	103.27	1.75	0.78×10^3	1.8	1.38	32
5	133.22	2.59	0.74×10^3	1.8	0.72	16
6	144.07	3.25	0.71×10^3	1.8	0	77
7	179.35	4.24	0.66×10^3	1.8	0.49	40

Analysis of the Performance of Multi-Stage Electrostatic Precipitators with Cooled Pipe Precharger

by

Leslie E. Sparks
United States Environmental Protection Agency
Air and Energy Engineering Research Laboratory
Research Triangle Park, NC 27711

Introduction

A major objective of the EPA electrostatic precipitator (ESP) program was to develop a high efficiency ESP for dusts with high electrical resistivity. Experimental and theoretical studies to meet this objective were conducted in cooperation with Denver Research Institute, Research Triangle Institute, and Southern Research Institute. These efforts were primarily devoted to developing a multi-stage ESP where particle charging and particle collection are carried out in physically separate stages of the ESP. Various charger and collector stage concepts were evaluated. This paper describes the work done with a cooled pipe charger developed in cooperation with Denver Research Institute. Most of the experiments described in the paper were carried out in the EPA in-house ESP pilot plant located at Research Triangle Park.

The cooled pipe charger

In the cooled pipe charger the normal collector plates are replaced by round pipes with high voltage electrodes suspended between them. A liquid, usually water, is circulated through the pipes to cool the surface of the collected dust layer. The cooling reduces the electrical resistivity of the collected dust layer sufficiently to avoid problems of back corona and sparking associated with high resistivity dusts. Since only the collected dust layer is cooled, the gas flowing through the ESP is maintained at normal flue gas temperature (about 150°C for coal fired fly ash).

The reduction in resistivity of the collected dust layer allows the charger to be operated at the high current densities necessary to produce high electrical charges on the dust passing through the charger. The pipe geometry also produces high electrical fields that increase the charging effectiveness of the charger.

The collector stage

The collector stage is required to provide high electrical fields to collect the particles charged in the charger. The collector stage operates at normal flue gas temperatures. This means that the collected dust layer in the collector stage can cause all the operating problems associated with high resistivity dusts. Collector stage concepts were thus designed to provide high electrical fields and low current densities.

The collector stage concepts evaluated were:

1. Flat plates.
2. Normal diameter wires with dc energization.
3. Normal diameter wires with pulse energization.
4. Large diameter wires with dc energization.
5. Large diameter wires with pulse energization.

Experimental studies

General

The experimental studies were carried out in the EPA pilot plant ESP. The pilot plant ESP is a single lane ESP with four independent electrical sections. The gas for the ESP is outside air that can be heated and humidified. Heating is provided by gas burners and humidification is provided by water injection. The dust for most of the experiments was redispersed fly ash fed through sand blast guns located after the gas burners. A few experiments were conducted with dust provided by injection of a lime slurry. The droplets in the slurry evaporated leaving behind lime particles.

ESP performance was determined by measuring the inlet and outlet particle size distribution and mass concentration. Particle size distribution measurements were made with cascade impactors calibrated by EPA personnel. Mass concentration measurements were made with in-duct filters and the cascade impactors.

The performance of the ESP as a conventional single stage ESP was carefully characterized for the range of dust resistivities and dust loading encountered in the multi-stage tests. This allows direct comparison of multi-stage and conventional ESP performance.

Results

Flat plates

The first collector stage configuration investigated was flat plates for the high voltage electrode. This collector configuration provided high electrical fields for particle collection and zero current. Initial tests of the multi-stage ESP in the charger flat plate collector configuration were impressive. However, long term performance of the flat plate collectors was little better than the base case ESP performance.

Additional experiments were conducted to determine the reasons for the poor long term performance of the flat plate collectors. These studies showed that the performance of the flat plate collectors was dominated by dust reentrainment from the collectors. The reentrainment could be minimized by operation at very low gas velocities.

This series of experiments showed that some current was necessary in the collector stage to provide a force to hold the dust layer to the plate and to provide some recharging of reentrained dust.

Normal wires dc energization

A series of experiments was conducted to determine the benefits of fitting the cooled pipe charger into a normal ESP. In these experiments the wire diameter was 0.32 cm and the ESP was operated with normal dc energization. The dust resistivity ranged from 5 x 10^{11} to 2 x 10^{12} ohm-cm.

Because of the high electrical resistivity of the collected dust layer, the current density in the collector stage was limited to 1 nA/cm^2. Even at this low current density, back corona was still a problem.

The performance of the multi-stage ESP with the cooled pipe charger and the normal wire collector was considerably better than that of the base case ESP for the high resistivity dusts studied. Base case ESP efficiency was 80% and multi-stage ESP efficiency was 95%. The performance improvement of the multi-stage ESP was evident over the entire particle size distribution.

Normal wires pulse energization

Pulse energization was applied to the collector stages to overcome the problems of back corona found with dc energization of the normal diameter wires. The pulse system was designed and constructed for EPA by Denver Research Institute. The pulse system provided a pulse width of about 100 μs.

The electrical conditions with pulse energization were more stable than those with dc energization. The collectors could be operated without back corona. The pulse energization provided some improvement compared to the dc energization. The efficiency of the pulse energized system was 97% compared to the 95% efficiency provided with the dc energization system.

While pulse energization allowed operation without back corona, it did not allow operation at high electrical fields.

Large diameter wires dc energization

The diameter of the discharge electrodes in the collector stage was increased from 0.32 to 0.95 cm in an effort to increase the electrical fields in the collector. The use of 0.95 cm diameter electrodes allowed operation of the collector stages at 8 to 10 kV higher than was possible with 0.32 cm diameter electrodes when collecting high resistivity dusts. The electrical operation of the 0.95 cm diameter wires was stabler than that of the 0.32 cm diameter wires.

The performance of the multi-stage ESP with 0.95 cm diameter wires was much better than that with 0.32 cm diameter wires. The mass collection efficiency was 99%.

Large diameter wires pulse energization

An attempt was made to operate the large diameter wire collectors with pulse energization. It was impossible to operate the 0.95 cm diameter wires with pulse energization without the ESP going into heavy back corona.

Conclusions

The experimental program showed that a multi-stage ESP based on the cooled pipe charger and large diameter wire electrodes in the collector stage provide order of magnitude performance improvements when compared with normal single stage ESPs. Order of magnitude economic analysis of the multi-stage ESP showed clear economic benefits to using multi-stage ESPs for applications where the electrical resistivity of the dust being collected is high.

The experiments also showed that multi-stage ESP technology can be considered for retrofit applications. The cooled pipe charger is physically small enough to fit between sections in many industrial ESPs. The performance of a multi-stage ESP with cooled pipe charger and normal wires in the collector was considerably higher than that of a conventional ESP.

Additional experimental research at larger scale is planned in cooperation with EPRI at the Valmont Power Plant operated by Public Service of Colorado.

ACOUSTIC SOOTBLOWER APPLICATIONS IN ELECTROSTATIC PRECIPITATORS

by: Jeff L. Shelton
The Drayton Corporation
P. O. Box 820
Jacksonville, AL 36265

ABSTRACT

Acoustic Sootblowers have been used very successfully in Electrostatic Precipitators. Applications include cleaning turning vanes, distribution plates, upper frames, collection plates and discharge electrodes. Justification for the purchase of the acoustic sootblowers have included: increased collection efficiency, reduced maintenance and increased precipitator up-time.

This paper will describe the installation of acoustic sootblowers in electrostatic precipitators at Northern States Power in Burnsville, Minnesota, Dundee Cement in Clarksville, Missouri, a chemical plant in the southeast, and City of Peru in Peru, Indiana.

INTRODUCTION

Acoustic sootblowers are low frequency, high energy cleaning devices which are driven by compressed air. The principle of operation is simple. Compressed air forces a diaphragm to flex which produces a pressure pulse. The pressure pulse is then amplified by the bell. The resulting sound pressure wave then causes the deposit to resonate and dislodge from the surfaces to which it clings. Once dislodged, it is then removed by gravity.

Northern States Power in Burnsville, Minnesota operates four (4) coal-fired boilers producing 440 MW of electric power. The flue gases from these boilers are treated by a total of eight (8) electrostatic precipitators. Each boiler has a primary and secondary precipitator.

The primary electrostatic precipitator on the #4 1.2 million pounds/hour boiler is a Research Cottrell unit. This precipitator experienced fly ash build-up on the upper frame, collection plates and discharge electrodes. This unit was equipped with MIGI electric plate rappers; the discharge electrodes were not rapped. The build-up created excessive sparking which decreased precipitator efficiency and life. In addition, the precipitator required water washing during planned outages to correct the problem.

Water washing was time consuming, expensive and only temporarily effective. In an effort to eliminate water washing and increase precipitator performance, it was decided that additional cleaning was required. In July of 1984, two (2) acoustic sootblowers were installed to supplement the existing rapping system. The acoustic sootblowers were installed in the inlet plenum looking across the gas passages. (See Figure 1) At this time, old deposits were not removed by water washing. (See Figure 2) The intent was to limit further fly ash accumulation. However, at the next scheduled outage, it was found that the internals were clean including the upper frame, plates, wires and walls were clean. (See Figures 3 & 4) Water washing was not required.

Initially, reintrainment was a problem for two (2) reasons. One was the operational cycle; this was eliminated by reducing the on-time of the acoustic sootblowers. The second was the location of the acoustic sootblowers. It was found that one (1) acoustic sootblower was cleaning the first two (2) fields of the electrostatic precipitator. The reintrainment problem was minimized by a secondary precipitator located down stream. This problem can be eliminated by installing the acoustic sootblowers in the top of the precipitator; thus limiting the cleaning to one (1) field at a time.

Dundee Cement in Clarksville, Missouri operates the largest wet process cement kiln in the world. (See Figure 5) The exhaust gas is treated by four (4) electrostatic precipitators in parallel. Corrosion forced Dundee Cement to rebuild two (2) of the precipitators in 1986. Due to frequent wire breakage, they decided to replace the weighted wire design with the state-of-the-art rigid electrode design.

After placing the re-built precipitators in service, it became apparent that the tumbling hammer rapping system was not keeping the rigid electrodes and collection plates clean. (See Figures 6 & 7) The dust build-up reduced collection efficiency to the point that to maintain acceptable opacity levels, the precipitator had to be taken off line to be cleaned every seven (7) to ten (10) days.

In an effort to solve the problem, Dundee Cement installed three (3) acoustic sootblowers in the outlet field. (See Figure 8). The outlet field was chosen because it experienced the greatest build-up problem. After the installation of the three (3) acoustic sootblowers, large amounts of dust were visually observed being dislodged while the acoustic sootblowers were in service. This observation was made through a sliding glass door equipped with lights which had been installed in the back wall of the precipitator. However, significant improvements in the opacity levels were not experienced.

After several weeks of monitoring the performance of the acoustic sootblowers, Dundee Cement decided to expand the installation. A total of six (6) additional acoustic sootblowers were installed. Three (3) were installed in both the second and third fields. The additional acoustic sootblowers were able to reduce opacity levels by 50% and eliminate the requirement to bypass the precipitator for manual cleaning.

To help measure the effects of dust build-up on the electrostatic precipitator's performance, Dundee Cement installed a recorder to track the current levels in the fields equipped with the acoustic sootblowers. The current levels were first recorded with the acoustic sootblowers in service. Once a trend was established, the acoustic sootblowers were taken out of service, resulting in a decrease of current levels within the first 24 hours. After 48 hours, there was an additional decrease in the current levels and a large increase in opacity readings. The acoustic sootblowers were then placed back into service and within 48 hours, the current increased to earlier levels with the opacity readings decreasing to acceptable levels.

The installation of acoustic sootblowers at Dundee Cement has reduced opacity levels by 50% and eliminated the requirement to take the precipitator off line to be cleaned every seven (7) to ten (10) days. In addition, they have kept the upper frame, walls and hoppers remarkably cleaner.

A chemical plant in the southeast which operates five (5) coal-fired boilers was experiencing hopper pluggage and high rapper maintenance on their electrostatic precipitators. These precipitators were also equipped with out-dated rapper controls.

The chemical plant solved these problems in their two (2) field Research Cottrell Electrostatic Precipitator by installing four (4) acoustic sootblowers. The acoustic sootblowers have successfully replaced 16 MIGI electric plate rappers and four (4) wire vibrators. The acoustic sootblowers have also been virtually maintenance free.

Before the installation of the acoustic sootblowers, they experienced numerous rapper spikes of approximately 10%. Now only one (1) of the acoustic sootblowers produces a spike. This acoustic sootblower is mounted in the outlet field next to the perforated plate and has an instantaneous spike of 20%. While the spike produced by this acoustic sootblower is higher than the rapper spikes, it is for a much shorter duration and does not occur as often. This results in lower intergrated six (6) minute opacity levels. Under normal operating conditions, opacity levels normally ran at 4% with the rapping system. Presently with the acoustic sootblowers, opacity levels have been reduced to 2%, a reduction of 50%.

Since the installation of the acoustic sootblowers, hopper pluggage has been eliminated and opacity levels have also decreased because of less reintrainment. The chemical plant had planned to spend up to $100,000.00 for new rapper controllers. However, since a small number of acoustic sootblowers has replaced a large number of rappers and vibrators, the new rapper controls will not be required.

The City of Peru operates one (1) 220,000 pound/hour Springfield Boiler. The flue gas is treated by a UOP Electrostatic Precipitator. This precipitator was erected in 1975 to replace a Western Mechanical Cylcone and was designed to be 97% efficient. The precipitator was equipped with twelve (12) wires and 24 plate MIGI electric rappers. Money was approved in 1987 to replace this rapping system due to high maintenance and poor performance. Pneumatic rappers were considered the best solution. Proposals were obtained from three (3) different vendors to retrofit this precipitator with pneumatic rappers. Prices varied from $20,000.00 to $30,000.00.

The City of Peru elected to install acoustic sootblowers in this precipitator instead of pnuematic rappers for two (2) reasons. The equipment cost was 75% lower for the acoustic sootblowers and operational costs were also much lower.

Since the installation of the acoustic sootblowers, several advantages have been realized. One, maintenance requirements have been virtually eliminated. The only maintenance that has been needed since the installation of the acoustic sootblowers has been the changing of an automatic timer. Previously rapper maintenance had required that two (2) people spend two (2) hours a day to keep the system operational.

The reduction of maintenance experienced with acoustic sootblowers has represented an annual savings of $10,800.00 based on $12.00 an hour per man working a 45 week year. Two, before the acoustic sootblowers were installed, hopper pluggage was a problem. This has been eliminated with the installations of the acoustic sootblowers.

While the City of Peru has not turned off their old electric rapping system, they have not performed any maintenance on the system. The acoustic sootblowers are responsible for cleaning more of the precipitator as more of the rappers fail.

CONCLUSION

The use of acoustic sootblowers in electrostatic precipitators can improve collection efficiency, reduce rapper maintenance and increase up-time. Collection efficiency can be improved by increasing the precipitator power, and reducing reintrainment in gas sneakage.

The acoustic sootblowers can improve the precipitator power when there is a dust build-up problem on the plates and wires. A good example is Dundee Cement where the precipitator performance deterioated over time as the dust caused current levels to decrease. (See Figures 9, 10 & 11) In this case, the electrostatic precipitator performance increased because of improved cleaning.

In many precipitators, improved power alone will not increase collection efficiency significantly because reintrainment and gas sneakage constitutes the largest source of opacity emmissions. In high efficiency electrostatic precipitators reintrainment may account for 50% to 70% of total emmissions. Acoustic sootblowers have proven that they can reduce reintrainment. Typically, opacity monitors today use intergrated six (6) minute averages to report emmissions. Since the acoustic sootblowers replace multiple rappers with a single unit, there are fewer spikes to be averaged into the reading. In addition, the spikes are for a shorter duration. This results in lower opacity levels.

There are several reasons why an electrostatic precipitator can experience gas sneakage. One of these reasons is poor gas distribution. Electrostatic precipitators have been designed with gas distribution devices such as perforated plates, turning vanes and good ductwork design to obtain proper distribution. When the gas distribution devices become plugged, the resistance to gas flow increases which causes gas flow to be shifted to cleaner areas. This effectively reduces the size of your precipitator, resulting in increased velocity, reduced treatment time and efficiency. (See Figure 12)

One good indication of poor gas distribution is build-up on the upper frame. This type of build-up is common especially in the inlet fields where you have upward gas vectors. Build-up on the upper frame adds mass to the wire frame and plate system which tends to dampen rapping energy thus reducing rapping efficiency. Acoustic sootblowers have proven to be very effective in removing this type of build-up.

The five (5) general types of rappers are 1- pneumatic-impact, 2-magnetic-impulse, 3-gravity-impact (MIGI), 4-electric or pneumatic vibrators, and 5-falling hammers. Acoustic sootblowers have proven to be effective in replacing all of these types of rappers. There are several cases where the acoustic sootblowers have not only replaced the existing rapping systems but have improved the performance of the precipitator.

Electrostatic precipitator down-time can be caused for several reasons. These reasons include build-up problems due to poor cleaning, and wire and plate failures due to over rapping. In many cases, poor cleaning leads to increased opacity levels so that manual cleaning is required to maintain acceptable emmission levels. Improved cleaning by acoustic sootblowers can completely eliminate this requirement.

One of the major causes of wire failure is heavy rapping. In fact, wires have been developed with spring shrouds to dampen the rap to increase wire life. The acoustic sootblowers operate at a frequency that vibrates the dust instead of the wire and elminates mechanical damage.

The work described in this paper was not funded by the U.S. Environmental Protection Agency and therefore the contents do not necessarily reflect the views of the Agency and no official endorsement should be inferred.

ACKNOWLEDGMENTS

The operational information on which this paper is primarily based was provided by the individuals listed below. Their input is much appreciated.

NAME	AFFILIATION
Mr. Bryce Eckelbarger	Peru Utilities Peru, IN
Mr. Andy Knox	Northern States Power Burnsville, MN
Mr. Bob Rucker	Dundee Cement Company Clarksville, MO

REFERENCES

1. U. S. Environmental Protection Agency. Operation and Maintenance Manual for Electrostatic Precipitators. EPA/625/1-85/017

Figure 1. Northern States Power Acoustic Sootblower installation.

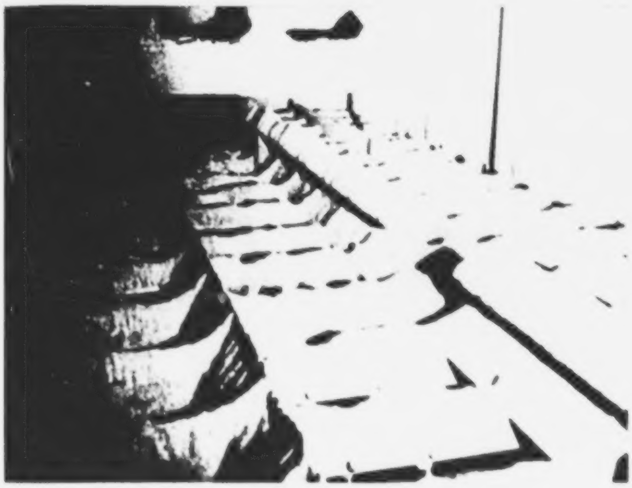

Figure 2. Northern States Power before Acoustic Sootblower installation.

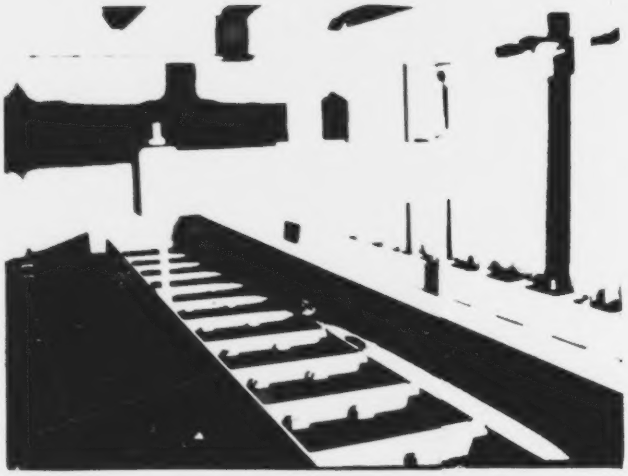

Figure 3. Northern States Power. Same view as Figure 2 after Acoustic Sootblower installation.

Figure 4. Northern States Power. Top view of plates and wires after installation of Acoustic Sootblower.

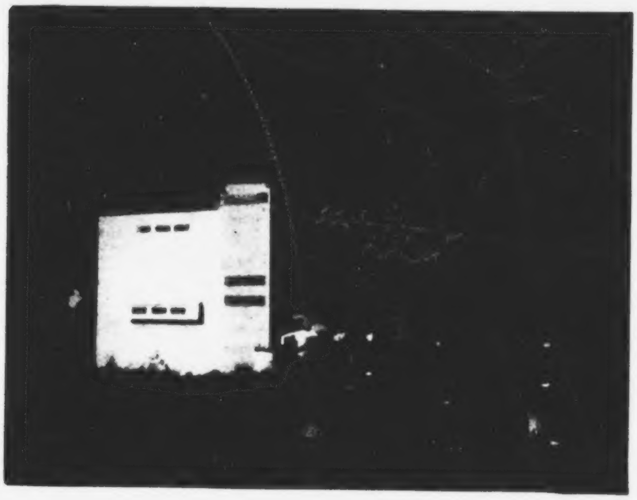

Figure 5. Dundee Cement Company

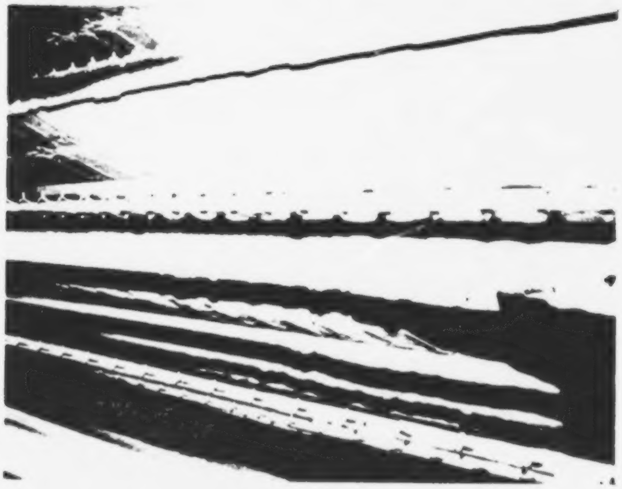

Figure 6. Dundee Cement. Buildup on rigid electrodes before Acoustic Sootblower installation.

Figure 7. Dundee Cement. Same view as Figure 6 after installation of Acoustic Sootblower.

Figure 8. Dundee Cement. Two of three Acoustic Sootblowers on outlet field.

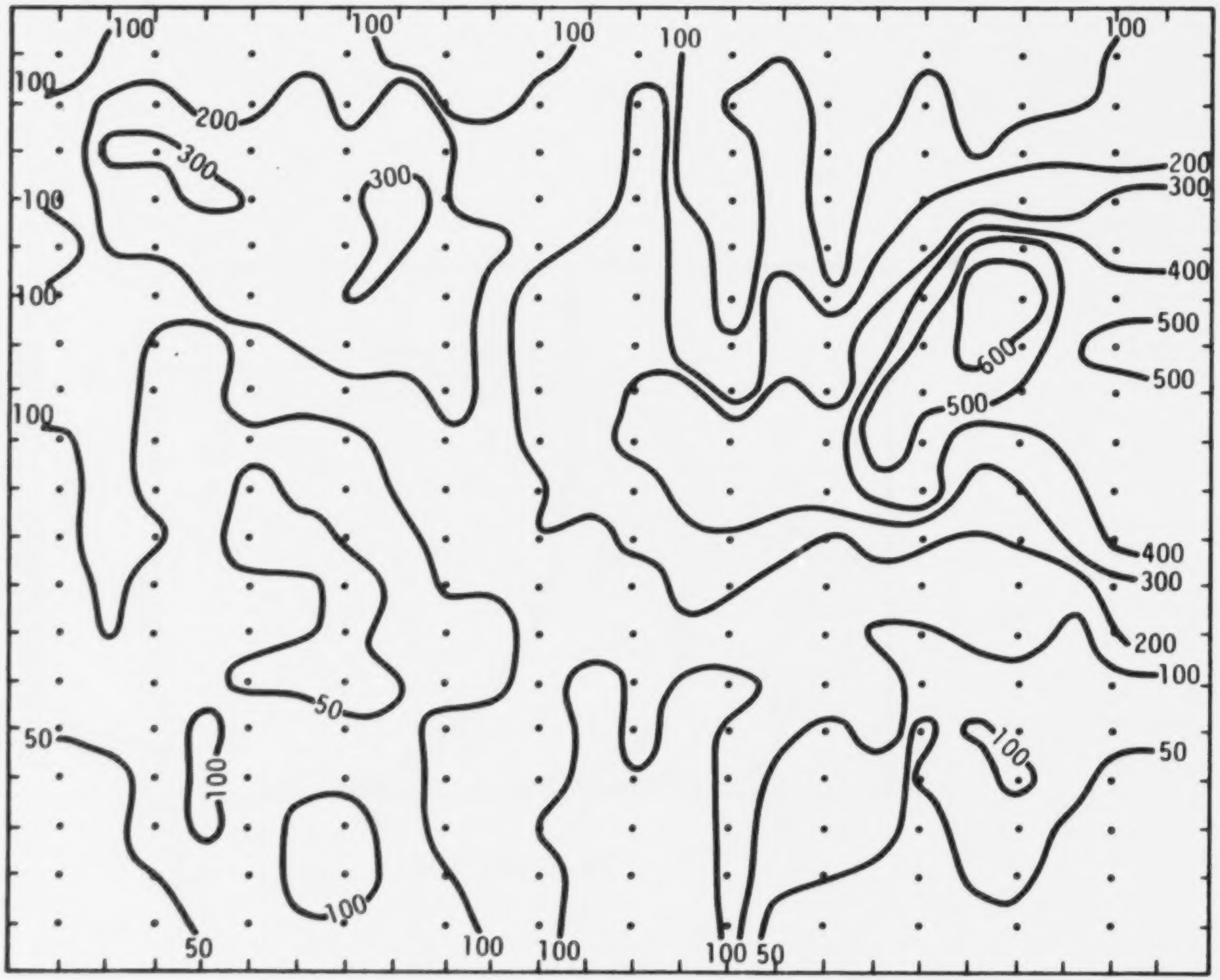

Figure 12. Velocity distribution patterns resulting from improper gas distribution. (Numbers are actual values in various portions of the ESP inlet. The average velocity through the unit is 166 ft/min.)[1]

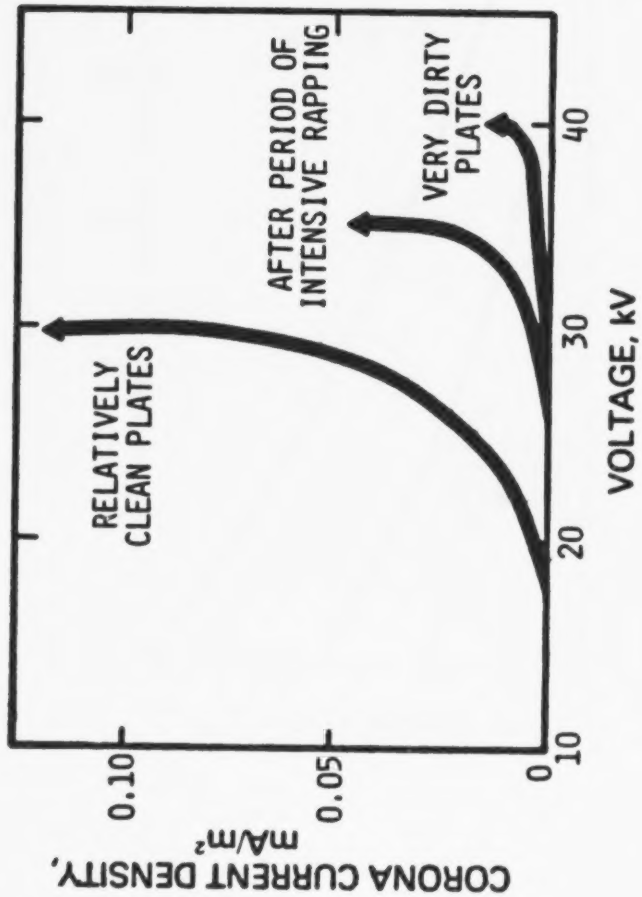

Figure 9. Variation of voltage current characteristics with collecting plate contamination.[1]

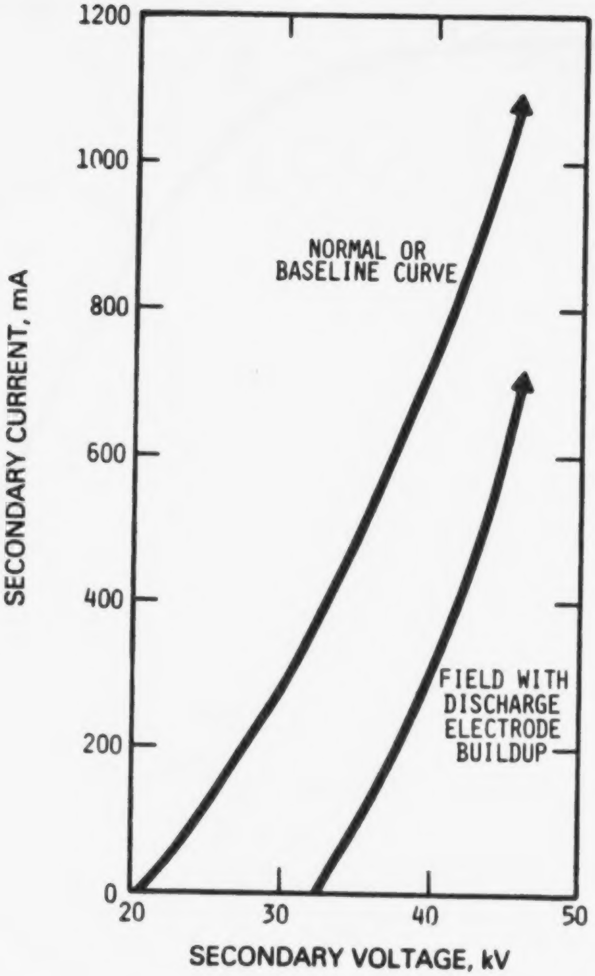

Figure 10. V-I curve for a field with excessive wire buildup.[1]

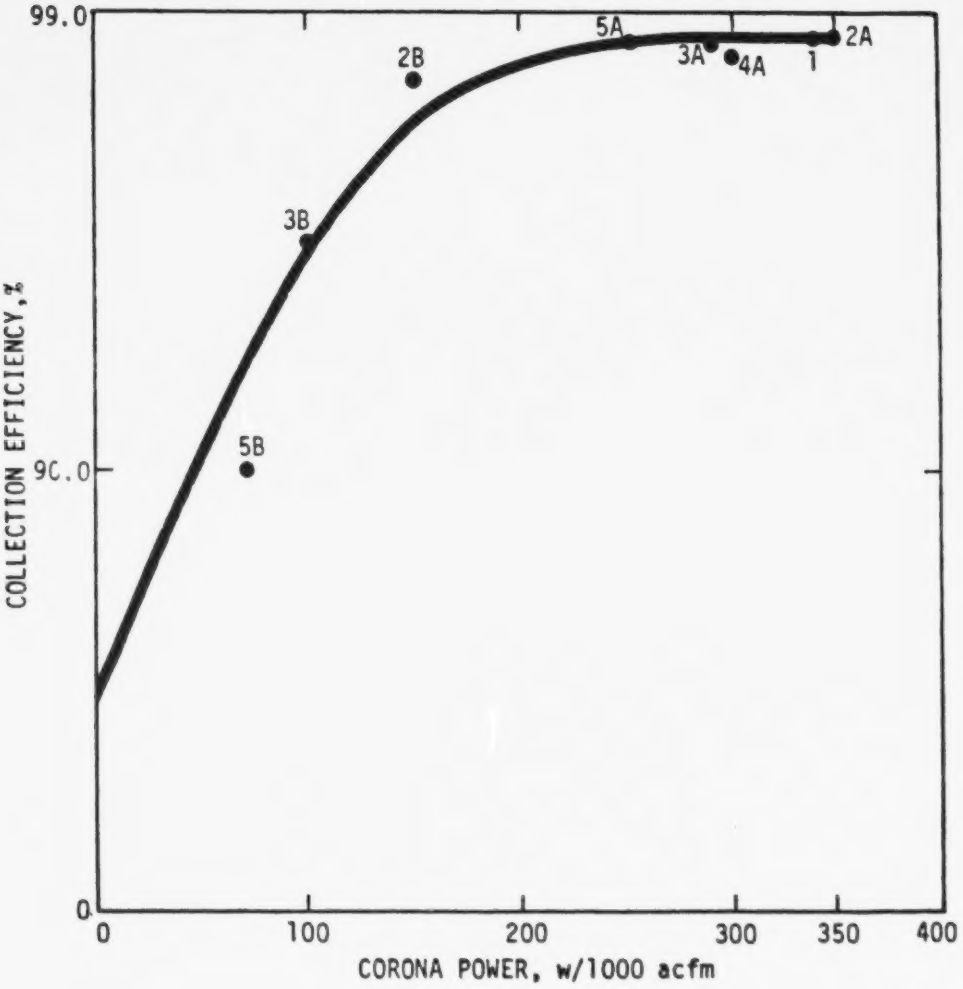

Figure 11. Corona power versus collection efficiency for a coal-fired utility boiler.[1]

A NEW CHEMICAL CONDITIONER TOGETHER WITH A SPECIAL FEED SYSTEM KEEPS PLANTS ON EMISSION COMPLIANCE AT LOW TREATMENT COSTS

by: R. K. Sinha, Ph.D.
Calgon Corporation
Pittsburgh, PA 15230

ABSTRACT

Chemical conditioning of fly ash continues to remain a viable and economical solution. Currently, two approaches of chemical conditioning are utilized. In one approach, water based proprietary liquid chemicals are applied, whereas sulfur trioxide in the vapor phase is utilized in the other approach. The first approach has traditionally been chemical thus operating cost intense, whereas the vapor phase approach has been capital intense. Treatment utilizing Calgon's combination technology of special chemicals and a unique feed system keep the treatment rate well below the industry standard.

For example, the Calgon FACT formulations when fed through the special feed system can lower the treatment level from the normal 1 to 2 pounds of chemical/ton of coal to less than 0.5 lb./ton.

This paper presents data on several industry and utility operations where Calgon's combination approach has kept the treatment rate to a minimal level.

The work described in this paper was not funded by the U.S. Environmental Protection Agency. The contents do not necessarily reflect the views of the Agency and no official endorsement should be inferred.

BACKGROUND

In the sixth symposium we presented data which showed that treatment with Calgon chemical conditioner helped several industrial operations meet particulate and opacity compliance on coal fired boilers. Our experience to date have shown that the treatment has been effective under widely varying situations. For example, in one case the operation involved burning less than 1% sulfur coal in pulverized equipment where the fly ash contained more than 15% unburned carbon and the ESP operated at temperatures around 450°F. While in another case, more than 2% sulfur coal is burned in stokers, but the ash contained more than 30% unburned carbon and the ESP operated at temperatures between 380 and 510°F. And yet in another case, a stoker operation burns less than 1% sulfur coal but the ESP operates around 350°F. In all these cases and the one specifically discussed in the present discussion, the ESPs were designed originally for burning 2 to 3% sulfur coal.

SYSTEM DESCRIPTION

This paper presents data on a 750 MW unit. The boiler is dry bottom, firing a pulverized, cleaned steam coal containing around 1% sulfur and 10-15% ash. The typical properties of the normally fired coal are given in Table 1. Like most utility operations, the load on this unit varies according to the demand rate. The unit operates between the ranges of 450 to 760 MW and under normal operation consumes about 5,000 tons of coal per day. At full load, the coal consumption rate reaches 300 tons/hour or 7200 tons/day.

The ESP is a Chevron design having twelve fields and 36 TR sets on each side. The units operate at 300 ± 20°F., depending on the load. Figure 1 shows the general arrangement. The ESP appears to be properly designed for coals containing more than 2% sulfur as the opacity from each side when burning design coal can be maintained below 20% under full load conditions. However, rapid deterioration in performance is observed when the coal is switched to low sulfur coal. The non-availability of 2% sulfur coal to the station presented us with the opportunity to evaluate the effectiveness of one of our flue gas conditioning products.

LABORATORY EVALUATION

Calgon has developed a water based product consisting of a mixture of organic and inorganic materials. The organic portion of the product is a conductive polymer whereas the inorganic portion is selected based on whether only a synergism to the conductive organic polymer is required or whether a synergism together with changes in the chemistry of the fly ash is also needed. The function of the conductive polymer is to help maintain the conductive layer on the fly ash particles by inducing the condensation of moisture and sulfuric acid. The increase in the electrical conductivity of the ash can be evaluated in the lab by resistivity measurements. The impact of the synergism by the inorganic components on the other hand, is seen from induced cohesion in the treated ash and is evaluated in the laboratory by changes in the angle of repose of the treated ash. Fly ash chemical analyses, resistivity and cohesion from the angle of repose are therefore the routine laboratory techniques employed by Calgon to select a treatment program.

The fly ash was collected from the several inlet and outlet hoppers of the North and South units of the ESP. These ash samples were analyzed for their crystalline compounds, elemental composition, unburned carbon content, and the pH of a 1% slurry in water. Special attention to their sodium content was paid, where in addition to the total sodium, their water and acid soluble fractions were also determined. Some of the analyses on typical inlet and outlet ash samples from this unit are shown in Tables 2 and 3.

Two things are worth noting from these analyses. The ash composition is basically similar irrespective of whether it came from the North side or the South side of the Chevron unit. This probably indicates no gross stratification in the ash as it traveled through the boiler unit nor that their is any gross change in the coal burner operation. The pH of the ash as well as the levels of the combustibles as indicated from the LOI values (Table 3, before treatment) differ substantially between the inlet and the outlet hoppers -- the pH decreases whereas the LOI increases. The decrease in the pH from the inlet to the outlet hoppers is probably typical of cold side ESPs. We have noted this in every case. One should expect it as there is a decreasing amount of ash left in the outlet fields to neutralize the acid condensing on the ash particles in these fields.

The trend of increasing LOI on the other hand is rather interesting. It indicates a preferential loss of carbon from the inlet fields followed by its redeposition in the outlet fields. This trend of carbon enrichment is believed to contribute significantly to plume opacity.

The data on the sodium profile of the ash (presented in Table 10) suggests to us that addition of sodium should be helpful from the standpoint of resistivity modification. The effects of the treatment on the cohesion of the ash, electrical resistivity and the angle of repose were determined next. Three types of treatment at a single level of dosage were evaluated and compared with the blank. The three treatments were: FACT-3000, FACT-5000, and sulfuric acid.

The effect of treatment on cohesion is shown in Table 4. Since this is a qualitative test, the ranking is presented as the final conclusion. The important thing to note from this table is that sulfuric acid does not improve cohesion whereas both of the FACT products are highly effective; FACT-5000 being as good as FACT-3000 treatment.

The impact of treatment on the resistivity at various selected temperatures is presented in Tables 5 and 6. Table 5 presents the data obtained from the descending profile whereas Table 6 shows the data for the ascending portion. The resistivity for the descending profile for all treatments together with the blank are consolidated in Figure 2.

Although the significance of the data from the ascending profile may be questioned by many on account of the existence of a moisture film on the ash particles, note some important differences among the treatments. The sample treated with sulfuric acid must not retain this film as it shows the highest resistivity and this appears true even at as low a temperature as 200°F. Treatment with FACT-3000 on the other hand must retain this conductive layer even at 400°F as the resistivity remains very low. FACT-5000 shows a similar but somewhat less pronounced effect. The blank or no treatment sample on the other hand appears to lose this conductive layer around 350°F. The data on the ascending profile, therefore, clearly shows that Calgon treatment with FACT products help maintain the conductive moisture film at high temperatures.

The descending profiles on the other hand are believed to show the true effects of the treatments on both the volume and the surface resistivities. Figure 2 as well as the data presented in Table 5 show that treatment with either FACT-3000 or FACT-5000 is superior to sulfuric acid whereas the treatment with FACT-5000 is apparently the most effective one. To illustrate, under descending conditions at 200°F, the resistivity of the ash treated with FACT-5000 is 2×10^9 ohm-cm as opposed to the blank at 1×10^{11}. Further, this fifty fold reduction in the resistivity over the blank by FACT-5000 treatment is at least ten fold lower than FACT-3000 and thirty-five fold lower than the sulfuric acid treatment.

Based on the results discussed above and the analysis (Table 1) of the coal, etc., a treatment with FACT-5000 was recommended and was accepted by plant personnel.

FEED SYSTEM AND TREATMENT STRATEGY

The feed system consisted of a bulk tank for product storage, a control center shed and the feed lances. The control center shed contained the metering pumps, dilution water and the atomizing air rotometer panels. A total of 24 lances, 12 on each duct work, placed at three foot intervals were utilized. The lance was a Calgon design in which special considerations were given to producing a consistent but uniform atomizing pattern from each of the six atomizing holes. The diameter and the angle of the holes with respect to each other were developed and finalized based on the quality of the 'fog' produced.

The product feed to each duct side was serviced with one metering pump. The metering pump was a Neptune diaphragm pump of duplex design rated at 18 gph per side. Under the full boiler load operation the two pumps together, at maximum settings, were capable of feeding at the rate of 4.8 lb. of product per ton of coal. The minimum treatment could be maintained at a level as low as 0.24 lb./ton by shutting one side of the pump off on each pump set-up. This provided a product volumetric feed rate range of 0.0025 to 0.05 gallons per minute per lance. Dilution water and a special flow control valve on each individual lance were utilized to ensure uniform and consistent product feed and to maintain a good atomization pattern. The feed pumps were capable of following the boiler load by accepting either a pneumatic or an electrical signal, but these controls were not utilized here. The sketches for the feed system and the lance are shown in Figures 3 and 4.

The lances were placed into the duct work coming immediately out of the air preheaters. At this point, the duct work had at least ten feet of straight run before it made an upward turn. The ESP box is located at lease 100 feet downstream of the feed point. The duct work at the point of feed is 9 feet deep. Calgon-developed special atomizing caps of narrow angle design were utilized for feeding the product. Based on the angle and the depth of spray, this 12 lance arrangement per duct side covered about 80% of the cross sectional area of the duct.

appears to lose this conductive layer around 350°F. The data on the ascending profile, therefore, clearly shows that Calgon treatment with FACT products help maintain the conductive moisture film at high temperatures.

The descending profiles on the other hand are believed to show the true effects of the treatments on both the volume and the surface resistivities. Figure 2 as well as the data presented in Table 5 show that treatment with either FACT-3000 or FACT-5000 is superior to sulfuric acid whereas the treatment with FACT-5000 is apparently the most effective one. To illustrate, under descending conditions at 200°F, the resistivity of the ash treated with FACT-5000 is 2×10^9 ohm-cm as opposed to the blank at 1×10^{11}. Further, this fifty fold reduction in the resistivity over the blank by FACT-5000 treatment is at least ten fold lower than FACT-3000 and thirty-five fold lower than the sulfuric acid treatment.

Based on the results discussed above and the analysis (Table 1) of the coal, etc., a treatment with FACT-5000 was recommended and was accepted by plant personnel.

FEED SYSTEM AND TREATMENT STRATEGY

The feed system consisted of a bulk tank for product storage, a control center shed and the feed lances. The control center shed contained the metering pumps, dilution water and the atomizing air rotometer panels. A total of 24 lances, 12 on each duct work, placed at three foot intervals were utilized. The lance was a Calgon design in which special considerations were given to producing a consistent but uniform atomizing pattern from each of the six atomizing holes. The diameter and the angle of the holes with respect to each other were developed and finalized based on the quality of the 'fog' produced.

The product feed to each duct side was serviced with one metering pump. The metering pump was a Neptune diaphragm pump of duplex design rated at 18 gph per side. Under the full boiler load operation the two pumps together, at maximum settings, were capable of feeding at the rate of 4.8 lb. of product per ton of coal. The minimum treatment could be maintained at a level as low as 0.24 lb./ton by shutting one side of the pump off on each pump set-up. This provided a product volumetric feed rate range of 0.0025 to 0.05 gallons per minute per lance. Dilution water and a special flow control valve on each individual lance were utilized to ensure uniform and consistent product feed and to maintain a good atomization pattern. The feed pumps were capable of following the boiler load by accepting either a pneumatic or an electrical signal, but these controls were not utilized here. The sketches for the feed system and the lance are shown in Figures 3 and 4.

The lances were placed into the duct work coming immediately out of the air preheaters. At this point, the duct work had at least ten feet of straight run before it made an upward turn. The ESP box is located at lease 100 feet downstream of the feed point. The duct work at the point of feed is 9 feet deep. Calgon-developed special atomizing caps of narrow angle design were utilized for feeding the product. Based on the angle and the depth of spray, this 12 lance arrangement per duct side covered about 80% of the cross sectional area of the duct.

The treatment strategy consisted of initially feeding the product at a high rate (1.4 to 2 lb./ton) to condition the system and then follow it by a gradual reduction and optimization of the treatment. The power levels (current and power densities) and the meter opacity (instantaneous and 24 hour average) were utilized as reactive means for monitoring the effectiveness of the treatment. These parameters were also monitored and data collected for the periods before and after the completion of the treatment programs. In addition to these parameters, the fly ash characteristics were also tracked and compared with the no treatment period.

RESULTS AND DISCUSSION

Before we discuss the treatment effects let me first describe the condition and the performance of the ESP units. The units were water washed in June 1987, in an attempt to improve their performance. This water wash, as expected, brought the daily average opacity below 20% from the 30% level. The effect of this water wash, again as expected, was short lived. Within a period of one month (by July), performance had degraded to the period before the water wash. In addition to this water wash and prior to initiating the Calgon conditioning program, the unit had an unscheduled outage for a couple of days. Boiler outages are also known to temporarily improve the ESP performance. Further, it was discovered on August 3, a day before the treatment program was initiated, that three of the thirty-six electrical sections on the South side unit had stopped functioning.

The program of conditioning with FACT-5000 was initiated at 4:00 PM on August 4 at a treatment rate of 1.4 to 2 lb./ton of coal. The lower rate of the treatment corresponded to boiler operation at full load whereas the higher rate corresponded to a daily average of coal usage.

The instantaneous meter opacity from both the North and the South units for the periods before, during, and after the termination of the conditioning program are shown in Figures 5 through 9. The ESP current density and the power density for cases with and without the treatment are compared in Table 7. The effect of the treatment on the daily average opacity and the frequency of Level 2 emission are compared in Tables 8 and 9, respectively.

It is interesting to note that even though the feed was initiated under full load condition and at a rate of only 1.4 lb./ton, the ESP power levels increased by 20% and the instantaneous opacity started to show a downward trend within six hours of starting the program. The power levels continued to increase and reached a two fold level within twenty-four hours of the treatment. As chemical conditioning is concerned, this is regarded as a very rapid response, particularly from a limping unit of this size. The daily average opacity showed the downward trends in proportion to the attendant increase in the power levels: in about twenty-four hours, the daily average opacity had dropped from the 30's to the mid-teens.

The next step in the program was to evaluate the effectiveness of reducing the treatment level. Table 8 and Figures 7 and 8 show these effects. The data shows that the opacity as well as the power levels and the Level 2 emissions could be maintained well within the goal even at as low a feed rate as 0.34 lb./ton coal.

Since the power levels (Table 8) in the ESP box could be maintained close to the ideal values even at treatment levels of 0.34 lb./ton coal, the next logical step was to lower the treatment dosage even further. Unfortunately, the feed pumps could not consistently feed the product at rates lower than 0.34 lb./ton. Therefore, the next thing attempted was to selectively take some of the TR sets (or sections) out of service. Six sections from each side of the ESP control box or a total of 12 sections out of 72 sections were therefore removed. Since three sections out of 72 were already not functioning, the removal of these sections made the unit actually operate with only 57 sections or at 79% of the original design.

Tests under these conditions (0.75 lb./ton feed rate and 59 sections in operation) showed that the opacity begins to climb. But even under these conditions, the daily average opacity could still be maintained below 20%. However, Table 9 shows that the frequency of Level 2 emissions climbed to six on the North side and thirteen on the South side. Increasing the dosage helped to bring the Level 2 emissions back to zero but optimization studies were not conducted.

The sodium profiles on the ash collected before and during the treatment are shown in Table 10. This table shows a complete profile on the sodium levels in the ash. The ash collected during the treatment shows an increase in the total as well as other types of sodium. This is expected since the treatment contained sodium as one of its components. But it is believed by us that the water and acid soluble sodium have more bearing on ash resistivity than the industry's practice of utilizing the total sodium. More data on this will be presented elsewhere.

CONCLUSION

The following conclusions are drawn from this study:

1) A treatment program selected by Calgon on the basis of its laboratory investigations is a valid approach.

2) Careful design considerations have helped Calgon put together a reliable but effective, simple and low cost feed system.

3) The chemistry based on a combination of organic and inorganic materials, as provided in Calgon FACT products, is unique. The effectiveness of these products have been proven on systems where either re-entrainment (of unburned carbon or fly ash) or poor collection due to underdesign or poor flue gas and coal chemistry are responsible for unsatisfactory performance.

4) The ESP responds very rapidly to FACT-5000 treatment and maintains its effectiveness at as low a dosage as 0.34 lb. product per ton of coal. At this rate, the cost is less than $0.20/ton of coal. The cost of treatment can be lowered further by feeding when operating only at high loads or by taking some of the TR sets out of service, or by a combination.

REFERENCES

1. Sinha, Rabi K., Sixth Symposium on Particulate Control Technology, Feb. 25, 1986, New Orleans, LA.

2. Bickelhaupt, R.E., Symposium On Electrostatic Precipitators For The Control Of Fine Particulates, 1975.

3. Bickelhaupt, R.E., Bickelhaupt Associated, Inc. - Private Communications, 1984-1987.

4. A Study of Resistivity and Conditioning of Fly Ash - Prepared by Southern Research Institute for EPA, Contract CPA 70-149, Feb., 1972.

FIGURE-1

CHEVRON DESIGN

ESP UNIT #10

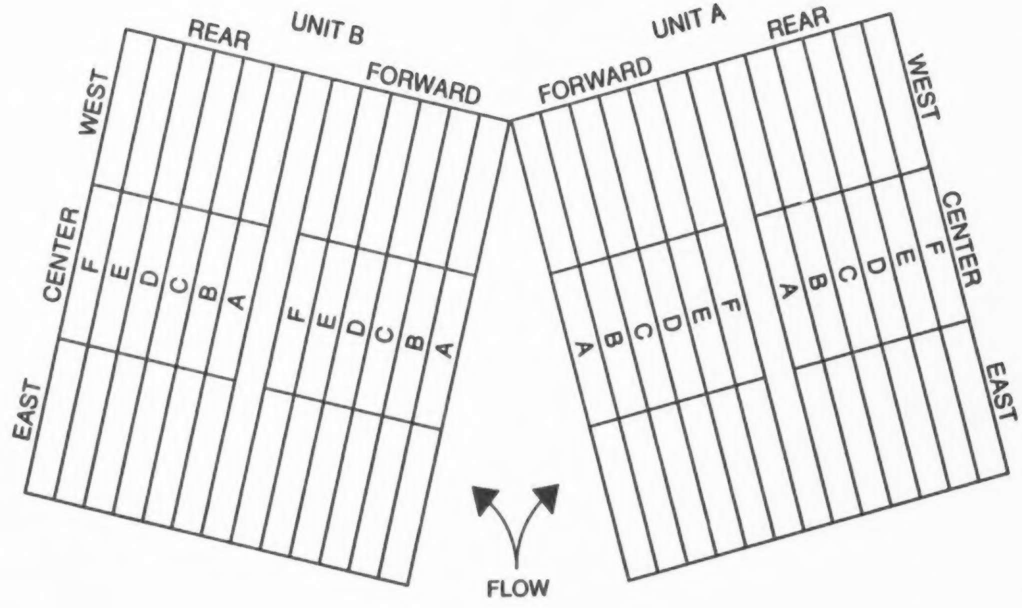

Figure 2. Resistivity in Accordance with IEEE Standard 548-1984

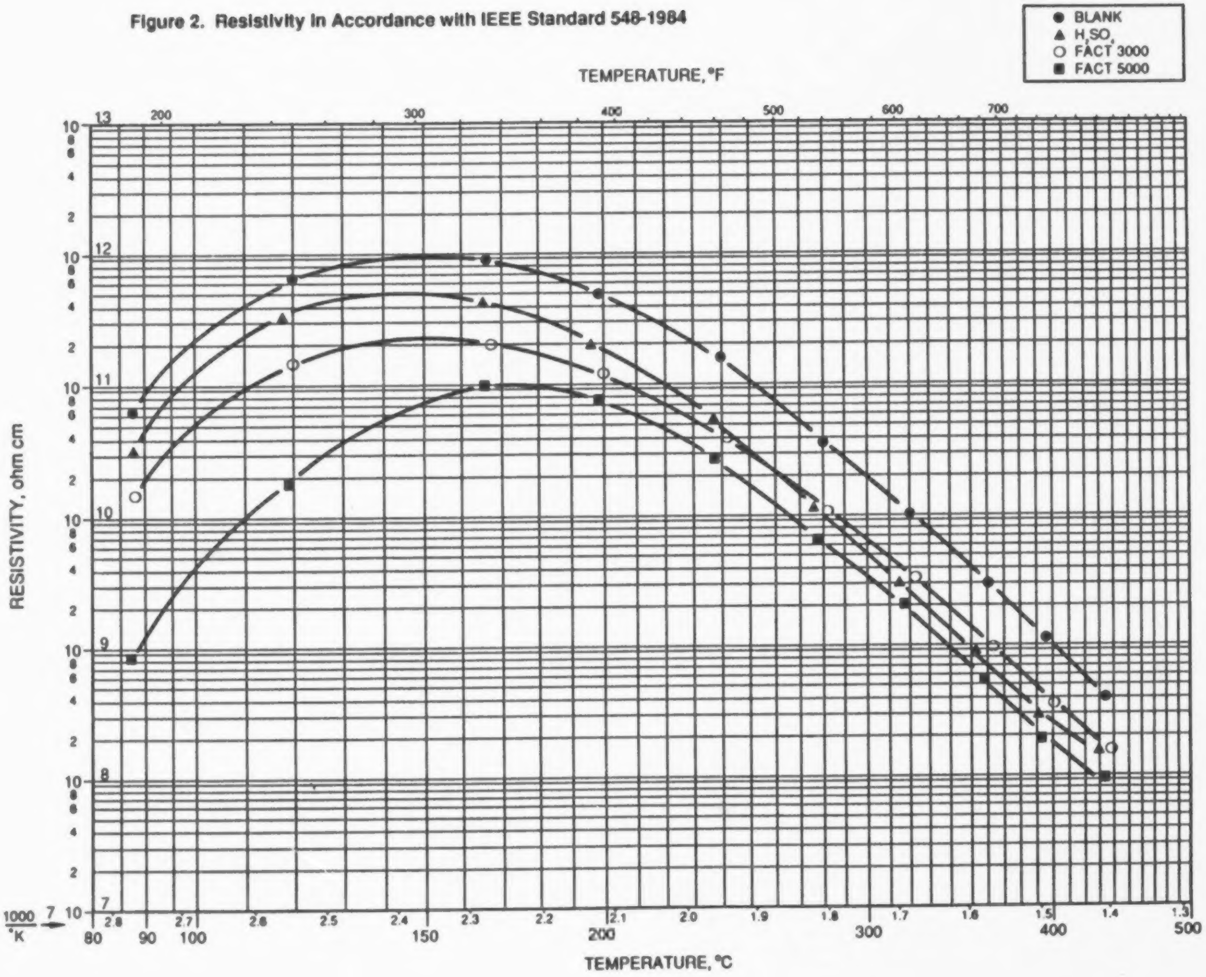

FACT FEED SET-UP

Figure 3

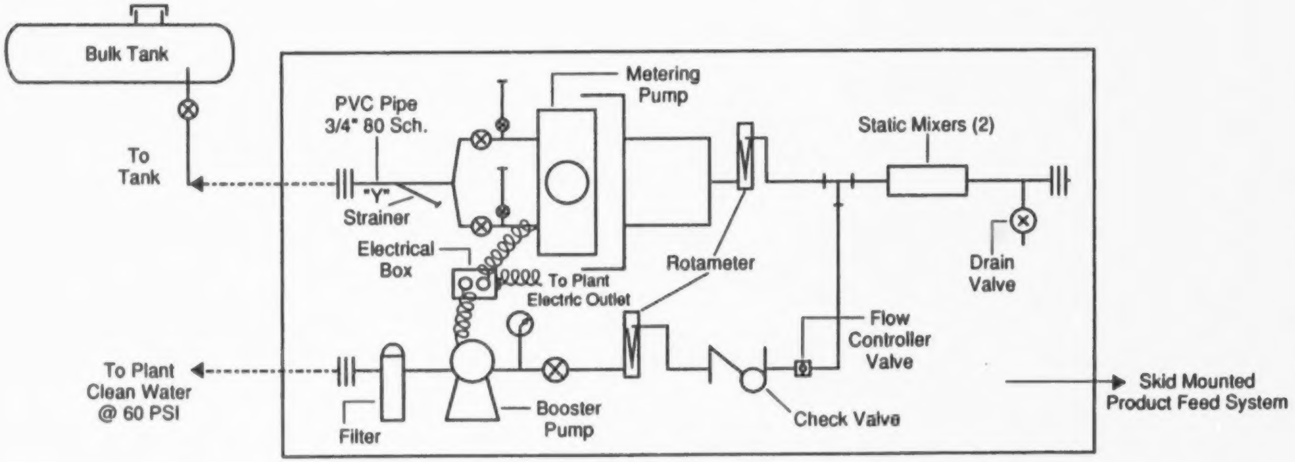

FACT FEED SET-UP

Figure 4

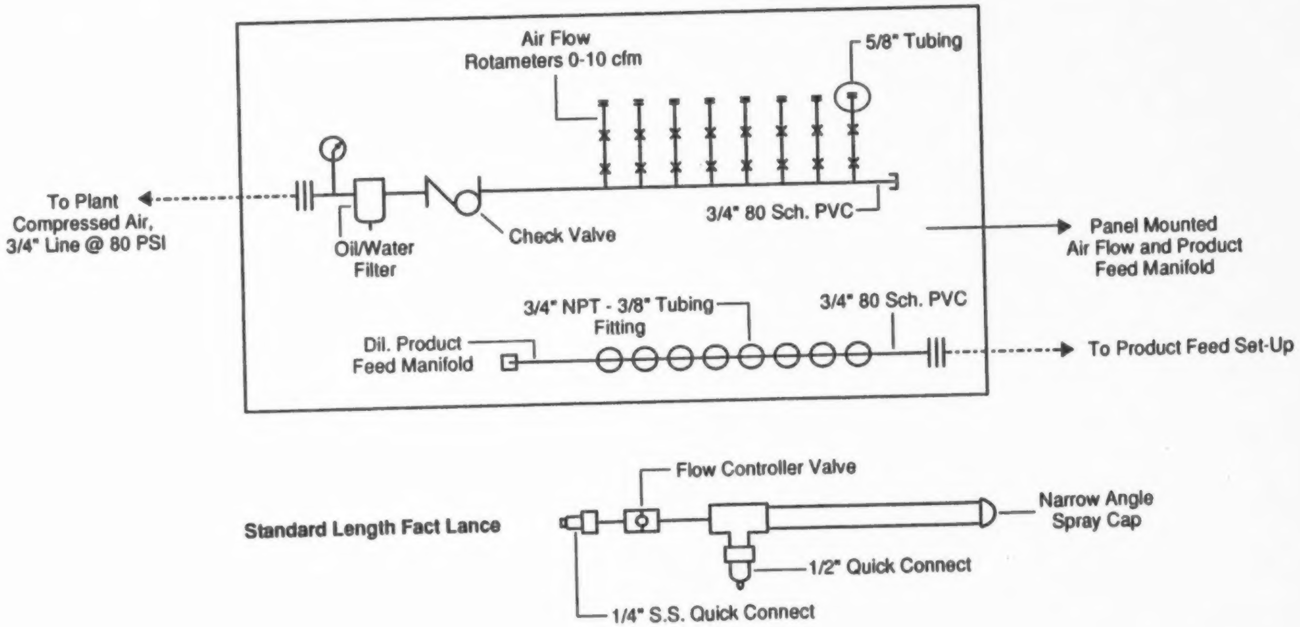

FIGURE-5

OPACITY TRACE (750 MW UNIT)

Before Treatment

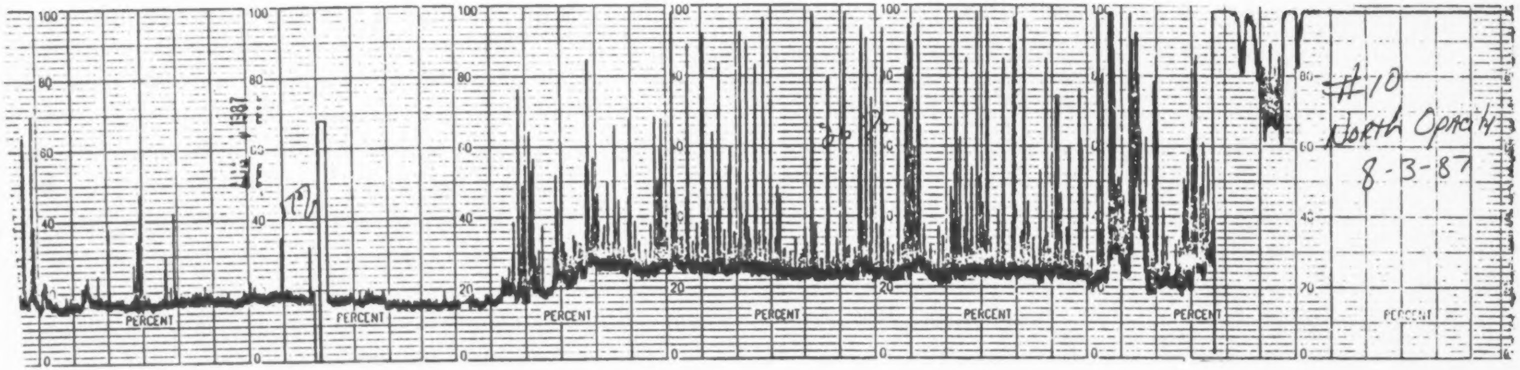

North Side

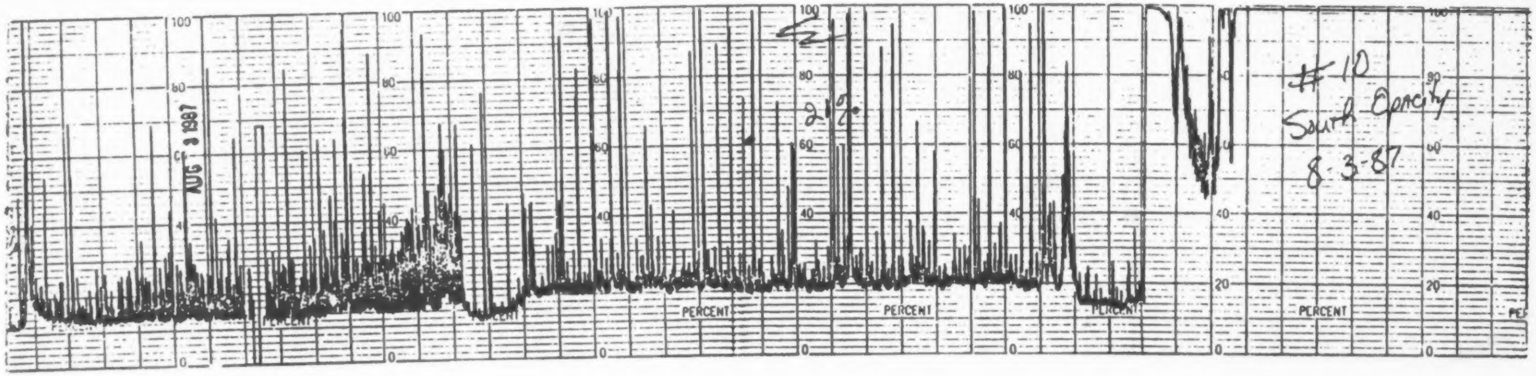

South Side

FIGURE-6

OPACITY TRACE (750 MW UNIT)

One Day After Fact-5000 Feed Initiation

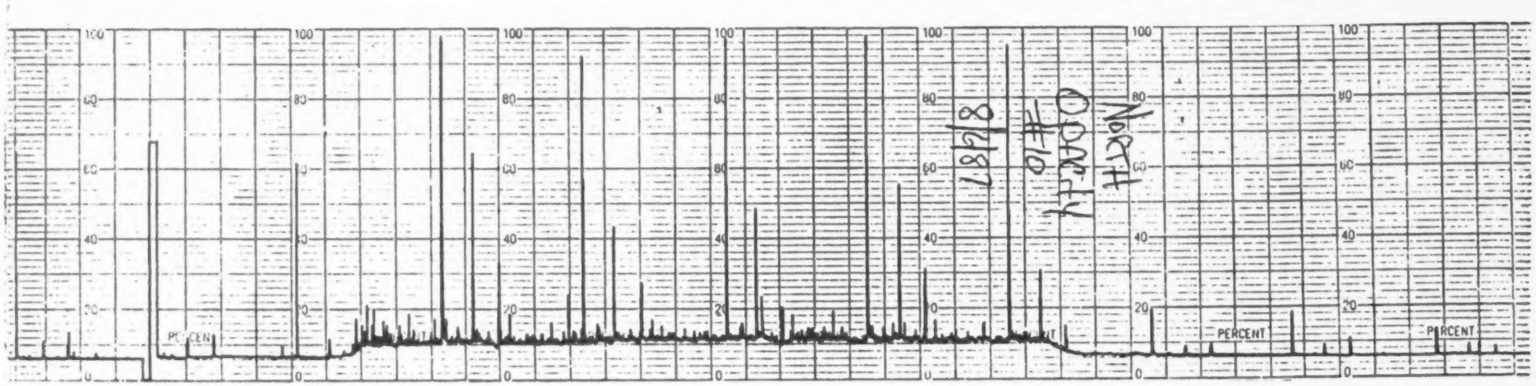

North Side

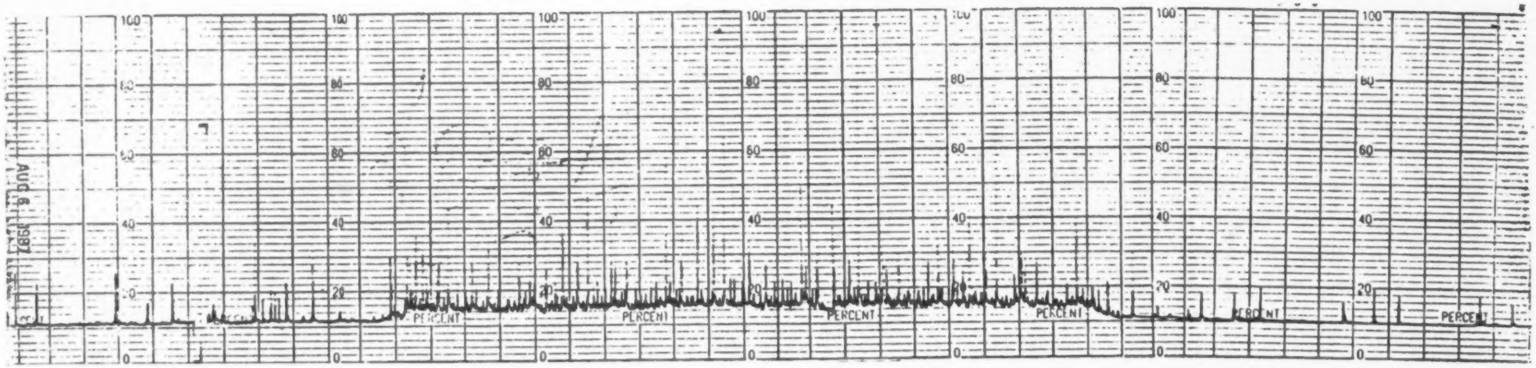

South Side

FIGURE-7

OPACITY TRACE (750 MW UNIT)

Several Days After Fact-5000 Feed Initiation

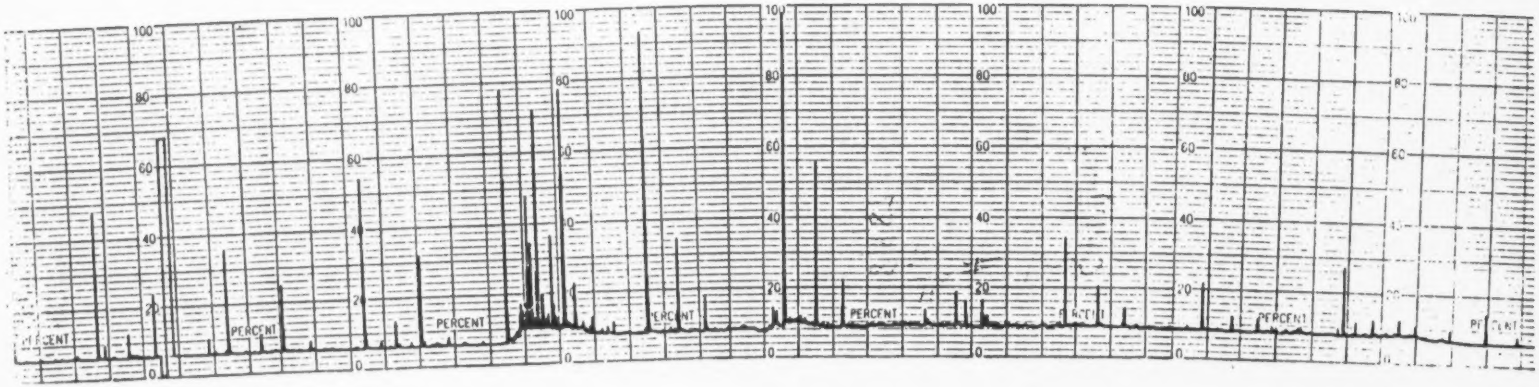

North Side

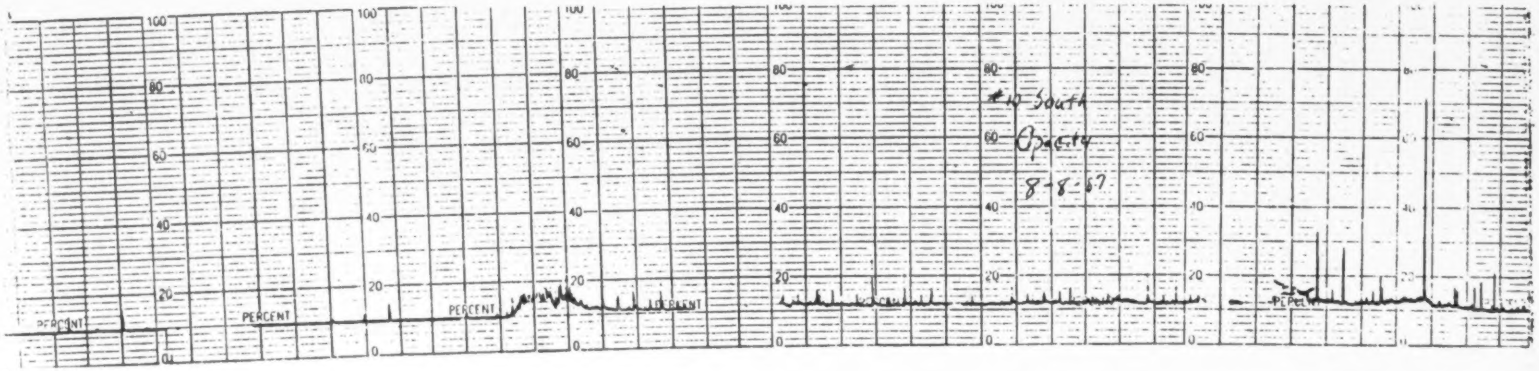

South Side

Figure 8. Opacity Trace (750 MW Unit) Feed Rate 0.34 lb/ton

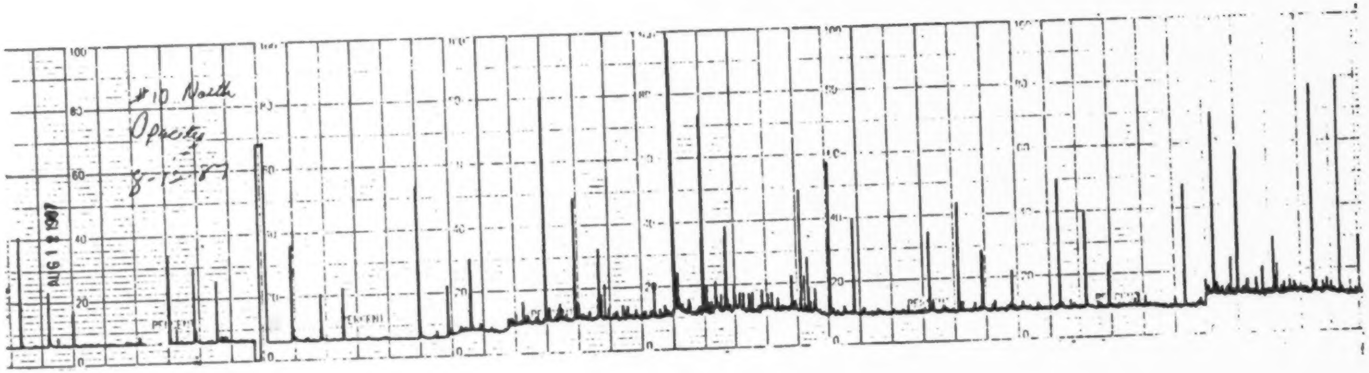

North Side

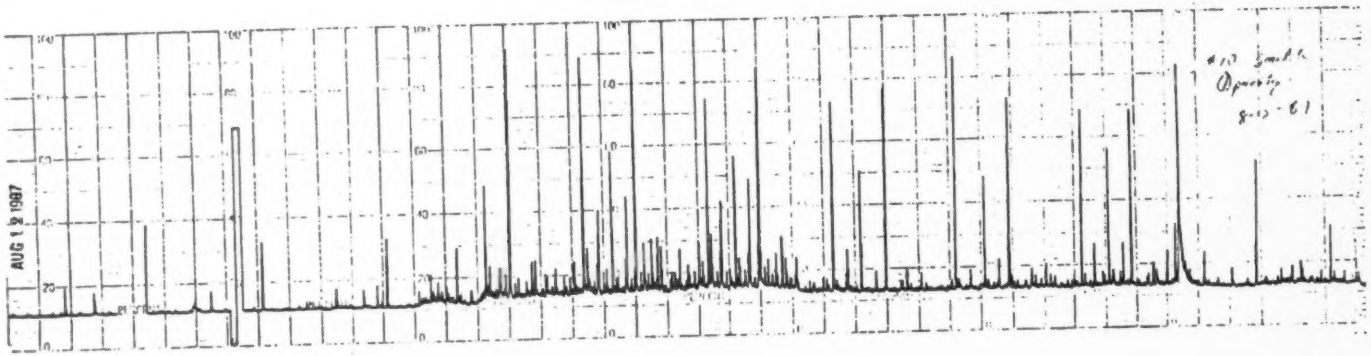

South Side

FIGURE-9

OPACITY TRACE

Two Days After Termination Of Fact-5000 Feed

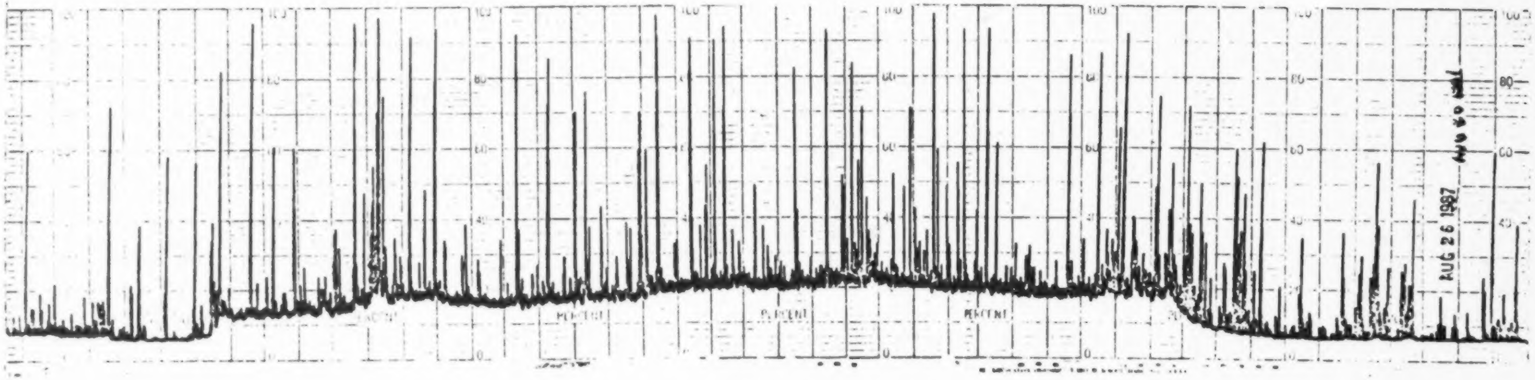

North Side

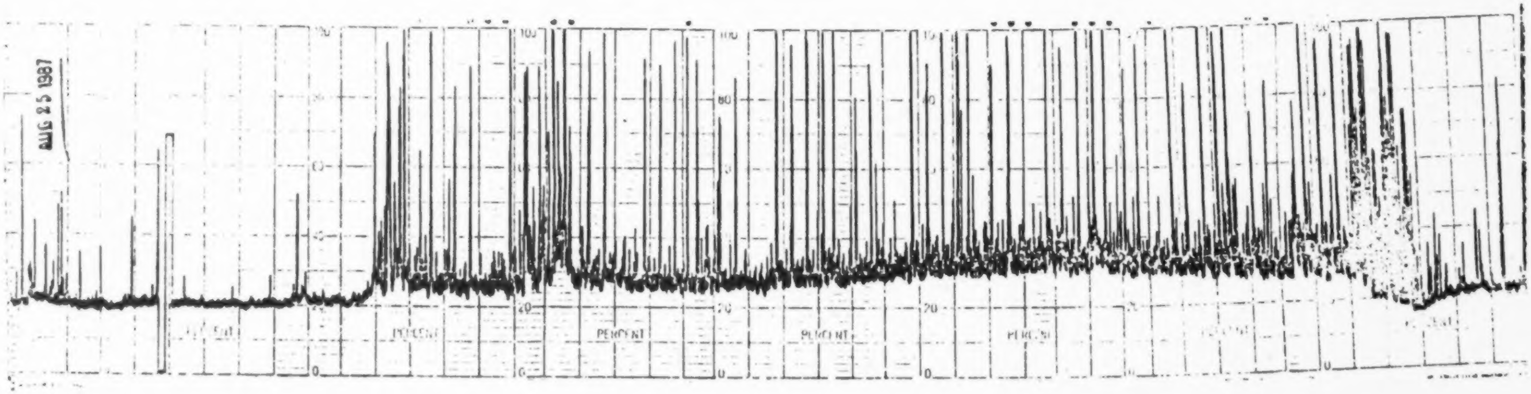

South Side

TABLE 1. TYPICAL ANALYSIS OF COAL

On As Received Basis	
Moisture:	7%
Ash:	11.5%
Sulfur:	2.8% (1.0%, this study)
BTU/lb:	12,400
SO_2/MM BTU:	4.6 lb.

TABLE 2. CHARACTERISTICS OF FLY ASH COLLECTED FROM ESP HOPPERS

	North Side		South Side	
	Inlet	Outlet	Inlet	Outlet
Crystalline Components				
Mullite:	20-30%	20-30%	20-30%	20-30%
Magnetite:	4-8%	---	4-8%	4-8%
Quartz:	4-8%	1-4%	4-8%	4-8%
Elemental Analysis				
Al_2O_3	25%	21%	25%	19%
CaO	1%	1%	2%	1%
CuO	<1%	<1%	---	<1%
Fe_2O_3	11%	10%	12%	9%
MgO	---	---	---	4%
P_2O_5	2%	2%	2%	2%
K_2O	3%	2%	3%	2%
SiO_2	50%	41%	49%	38%
SO_3	---	2%	---	2%
TiO_2	2%	2%	2%	1%

TABLE 3. FLY ASH PROPERTIES - EFFECTS OF TREATMENT ON FLY ASH ACIDITY AND COMBUSTIBLES

	Before Treatment		With Treatment	
	pH	LOI,%	pH	LOI,%
NORTH SIDE				
Inlet	9.4	4.0	5.4	4.0
Middle	7.4	6.0	4.5	10.0
Outlet	5.4	17.0	4.9	12.0
SOUTH SIDE				
Inlet	9.0	5.0	5.5	3.0
Middle	5.0	22.0	4.3	8.0
Outlet	4.9	22.0	3.9	11.0

TABLE 4. EFFECTS OF TREATMENT ON COHESION*

Treatment	Conclusion
Blank	Poorly Cohesive
Sulfuric Acid	Poorly Cohesive
FACT-3000	Most Cohesive
FACT-5000	Similar to FACT-3000

*Lab study from angle of repose determinations

TABLE 5. EFFECTS OF TREATMENTS ON ASH RESISTIVITY*
COMPOSITED ASH, LABORATORY IMPREGNATED

Descending Temp. °F	Blank	FACT-3000	FACT-5000	H_2SO_4
400	$4x10^{11}$	$1x10^{11}$	$6x10^{10}$	$1x10^{11}$
350	$8x10^{11}$	$2x10^{11}$	$1x10^{11}$	$4x10^{11}$
300	$1x10^{12}$	$2x10^{11}$	$7x10^{10}$	$5x10^{11}$
250	$5x10^{11}$	$1x10^{11}$	$2x10^{10}$	$3x10^{11}$
200	$1x10^{11}$	$2x10^{10}$	$2x10^{9}$	$7x10^{10}$

*Resistivity in ohm-cm

TABLE 6. EFFECTS OF TREATMENTS ON ASH RESISTIVITY
COMPOSITED ASH, LABORATORY IMPREGNATED

Ascending Temp. °F	Ash Resistivity, ohm-cm Blank	FACT-3000	FACT-5000	H_2SO_4
200	---	---	---	$7x10^{10}$
250	---	---	---	$1x10^{11}$
300	---	---	$1x10^{9}$	$1x10^{11}$
350	$3x10^{9}$	---	$1x10^{9}$	$1x10^{11}$
400	$1x10^{11}$	---	$8x10^{9}$	$7x10^{10}$

--- Denotes values less than 10^6 ohm-cm

TABLE 7. TREATMENT EFFECTS ON POWER LEVELS

FACT-5000 (750 MW UNIT)

Feed Rate (lb/ton)	Current Density (Ma/1000 ft^2)	Power Density (W/ft^2)
None	19-23	0.35-0.45*
None	8-10	0.2-0.3
1.4 (After 6 hr.)	19-23	0.36-0.5
1.4 (After 24 hr.)	29-32	0.56-0.63
1.1 (After days)	35-38	0.7-0.8
0.37 (After days)	22-28	0.4-0.6
None (2 days after)	12-16	0.2-0.3

*Unit after water washing

TABLE 8. EFFECTS OF TREATMENT ON OPACITY

Date	Daily Average, Opacity,% North	South	Feed Rate (lb/ton)
7/31/87	26	26	None
8/3/87	49	46	None (3 sections failed)
8/4/87	31	34	1.4 @ 4:00 PM
8/5/87	12	16	1.4
8/6/87	9	13	1.1
8/11/87	10	15	0.75
8/12/87	10	13	0.75
8/13/87	11	14	0.37
8/14/87	11	16	0.75(12 more sections removed)
8/15/87	9	15	0.37 (sections put back on)
8/17/87	11	17	0.34
8/20/87	9	13	0.34
8/22/87	FEED TERMINATED		
8/24/87	15	24	None
8/25/87	16	29	None

TABLE 9. TREATMENT EFFECTS ON LEVEL 2 EMISSIONS

Feed Rate (lb/ton)	Incidence/Day North	Incidence/Day South
None	100-160	100-150
1.4 (24 hours)	0	0
1.1 (Days)	0	0
0.95 (Days)	0	0
0.75 (Days, 12 sections cut out)	0-6	1-13
0.34 (Days)	0-4	4-18

TABLE 10. FLY ASH PROPERTIES - LEVELS OF VARIOUS TYPES OF SODIUM (PPM) IN ASH

SOUTH SIDE

	Before Treatment			With Treatment		
	Water Soluble	Acid Soluble	Total	Water Soluble	Acid Soluble	Total
Inlet Ash	70(NA)	220 (NA)	4450(NA)	80(60)	300(250)	4500(NA)
Outlet Ash	80(110)	260(290)	5190(NA)	220(140)	580(430)	5200(NA)

Notes: a. Values in parentheses are for North Side
b. NA means not available

EFFECTS OF TURBULENCE IN WIRE-PLATE PRECIPITATORS

by: S. A. Self, M. Mitchner, and K. D. Kihm
High Temperature Gasdynamics Laboratory
Department of Mechanical Engineering
Stanford University
Stanford, California 94305

ABSTRACT

The present work extends a previous study of the role of turbulence in particle transport under idealized conditions, to examine the effects of nonideal mechanisms that include nonuniform electric fields and diffusivity, nonzero space charge, and the nonuniform particle charge in single-stage precipitators (even with monodisperse particles) that results from a finite charging rate and finite particle diffusivity. The approach to achieving an improved understanding of actual electrostatic precipitators has been to start with a system where only the essential mechanisms are active, and then to add the effects of additional mechanisms one at-a-time, performing experiments and making theoretical calculations corresponding to the conditions of each stage, to the extent possible, to test our understanding. Several important simplifications have been found that will aid in the development of models of electrostatic precipitators. This work has also shown that despite these nonideal effects, precipitator performance exceeding that predicted by the so-called Deutsch model, is still possible.

1.0 INTRODUCTION

Despite their widespread and longstanding use, and not withstanding an increased research effort in recent years, the practical design of electrostatic precipitators remains essentially an art based on a highly oversimplified model (yielding the so-called Deutsch equation) supplemented by extensive empirical data compiled over the years from the performance of existing installations. When a new precipitator is constructed that is to operate under conditions that differ significantly from those in existing installations, the initial performance is often unacceptable, and very expensive procedures are required to rectify the situation. The objective of the work at Stanford has been to develop an improved understanding of the dominant processes that determine precipitator performance, with the goal of transforming precipitator design from an art form into an engineering science.

The work to be described in the present paper is concerned with one of the most important fundamental aspects of the precipitation process, viz. the transport of charged particles by the Coulomb force of the electric field through the turbulent flow of the carrier gas. This work can be summarized with reference to Table 1.

The transport of a dilute concentration of monodisperse particles is governed by the convective-diffusion equation, which describes how the ensemble-averaged particle number density $n(\vec{x},t)$ depends on position and time. This equation represents a statement of conservation of particles. Because the flow in any practical precipitator is necessarily turbulent, the particle number density, as well as other flow quantities, fluctuate in a random fashion on time and distance scales that are too small to be of practical interest. The particle conservation equation for a particular realization of the flow must therefore be ensemble-averaged to obtain an equation that involves just ensemble-averaged quantities. This procedure leads to the main assumption underlying the convective-diffusion equation, that the ensemble-averaged particle flux associated with the turbulent fluctuations can be described by Fick's law, i.e., by the expression $-D\nabla n$, where D is referred to as the particle turbulent diffusivity or diffusion coefficient. (Another assumption, justified for dilute dispersions, is that there exists no agglomeration or de-agglomeration of particles belonging to the size class of interest.)

Shown in Table 1 are the individual terms that constitute the steady-state convective-diffusion equation [1], and their physical interpretation. The term $\vec{u}\cdot\nabla n$ describes the effect of convection of particles by the mean gas velocity $\vec{u}$. The term $\mu\vec{E}\cdot\nabla n$ describes the effect of the convection of particles by the electric field $\vec{E}$, where

$$\mu = \frac{q\,C}{6\pi a \eta_g} \tag{1}$$

denotes the particle mobility and where

$$\vec{w} = \mu\vec{E} \tag{2}$$

is the particle velocity relative to the gas velocity--i.e., the so-called particle electric migration velocity. Here q and a denote the particle charge and radius, respectively, η_g ($\approx 1.8\times10^{-5}$ kg/ms^2, at room temperature) is the gas dynamic viscosity, and C is the Cunningham slip factor [2]. (For the particle sizes of interest in this report, $C = 1$.)

Because of Poisson's equation for the electrostatic field, $\nabla\cdot\vec{E} = \rho_c/\varepsilon_g$, the third term reflects the effect of the existence of a space-charge density ρ_c. (Here ε_g is the permittivity of free space.) If the distribution of particle charge is nonuniform, $\nabla\mu$ is nonzero, and the fourth term $n\vec{E}\cdot\nabla\mu$ accounts for this effect. The fifth term $\nabla\cdot(D\nabla n)$ accounts for the effect of either a uniform or nonuniform particle diffusivity.

Our approach to achieving an improved understanding of actual electrostatic precipitators (wherein all of the above mechanisms participate jointly) has been to start with a system where only the essential mechanisms were active, and to then add the effects of additional mechanisms one at-a-time, performing experiments and making theoretical calculations corresponding to the conditions of each step, to the extent possible. These steps are indicated in the remainder of Table 1. (Here the coordinates x and y refer to the streamwise and to the transverse plate-to-plate directions, respectively; the gas speed $u = |\vec{u}|$ is assumed uniform.) In the spirit of this approach, our initial efforts were directed toward studies of particle transport under conditions where both the electric field and the particle diffusivity were uniform.

A low-speed flow facility, shown schematically in Figure 1, was constructed to provide a uniform low-turbulence level ($\lesssim 0.3\%$) flow at the inlet of a test-section where various electrostatic precipitator configurations could be inserted. A novel method was developed to provide a monodisperse aerosol and to pre-charge the individual particles to the same value. Particle mobilities were determined directly by using a laser anemometer to measure the transverse velocity of single particles as they passed through a known transverse electric field applied between two 0.75-inch-diameter disks, spread 0.25 inches apart, that could be inserted into the laminar flow field just downstream of the nozzle exit, and then removed. To obtain a uniform electric precipitation field, a high voltage was applied between opposed parallel plates located at the test-section. Because the particle concentration was low and because there were no ions in the flow, the charge density was very small and its effects could be neglected. To obtain a uniform particle diffusivity in the core of the flow, grid-generated turbulence (which has been studied extensively) was produced upstream of the test-section. With these idealized conditions realized, it is possible to obtain an analytical solution of the convective-diffusion equation to compare with the experimental data. Because these results provide a base-case, they are summarized briefly in Sec. 2.0.

The grid-generated turbulence employed in our initial experiments resulted in relatively low values of the particle diffusivity ($D \lesssim 1.0$ cm^2/s). Because the turbulence levels in actual precipitators are much larger, we wished to extend our initial work to consider such conditions. For this purpose, we employed several baffle configurations in place of the grids, obtaining values of D up to about 20 cm^2/s at the location of the plates. To understand these data, it was found necessary to account for a nonuniform distribution of diffusivity. These results are summarized in Sec. 3.0.

The wire-plate configuration employed in actual one-stage precipitators results in a nonuniform distribution of $\vec{E}$. By employing relatively large-diameter wires and sufficiently low voltages, we were able to study these effects in the absence of a corona discharge. These results are described in Sec. 4.0.

The presence of a corona-discharge produces two new mechanisms--a nonzero ionic space charge and a nonuniform particle charge distribution. To separate the effects of these mechanisms, we employed uniformly pre-charged particles, charged to a value that was significantly larger than the charge a particle could acquire in the corona current. The results showing primarily the effects of space charge are described in Sec. 5.0. In Sec. 6.0, we present results obtained without pre-charging the particles and with both mechanisms active, as they would be in a single-stage precipitator.

2.0 UNIFORM PARTICLE DIFFUSIVITY AND UNIFORM ELECTRIC FIELD

The earliest theoretical model of precipitator performance was developed by Deutsch [3] in 1922, and this model is still widely used to design and evaluate electrostatic precipitators. In addition to the assumptions of uniform flow speed u, particle diffusivity, and electric field, the Deutsch model assumes that transverse turbulent mixing is sufficiently intense to maintain a uniform particle concentration distribution across the duct width at every axial location. This model leads to the result that the particle concentration decays exponentially in the x-direction according to the relation

$$n/n_0 = \exp(-wx/ud) \tag{3}$$

and that the collection efficiency for a precipitator of length x = L is given by the equation

$$\eta = 1 - \exp(-De) \tag{4}$$

where the "Deutsch number"

$$De = \frac{wL}{ud} \tag{5}$$

may be viewed as a dimensionless length. Here n_0 denotes the particle number density at the precipitator inlet and d is half the plate-to-plate spacing for a wire-plate precipitator. (For a plate-plate collector, d will denote the full plate-to-plate spacing.)

The measured efficiencies of commercial precipitators are commonly found to be less than that predicted by the Deutsch equation, and sometimes considerably less. This experience has led to a widespread belief in the industry, that the Deutsch efficiency represents a theoretical optimal level of performance.

It is known for a uniform laminar flow without mixing that the efficiency for $De \leq 1$ is given by

$$\eta = (1 - De) \tag{6}$$

and that for $De \geq 1$ the efficiency is 100%. This observation suggests for finite, but nonzero, values of the particle diffusivity that the efficiency should fall between the laminar and Deutsch limits. With the assumptions of this section and assuming a plate-plate collector, the appropriate form of the convective-diffusion equation is shown in Table 1. (For precipitator conditions, the axial diffusion term $D(\partial^2 n/\partial x^2)$ may often be neglected.)

Strictly speaking, the particle diffusivity cannot be uniform over the entire flow region since at the duct walls, it must approach the Brownian diffusivity D_B which, for 4-μm diameter particles, has the value 6.0×10^{-7} cm²/s. The diffusivity must decrease from a core value on the order of 1 cm²/s to D_B in a region close to the plate that one may refer to as a "diffusivity layer." Near the plate $(\partial n/\partial y)$ is expected to be much larger than $(\partial n/\partial x)$, which suggests that the term $u(\partial n/\partial x)$ may be neglected in comparison with $w(\partial n/\partial y)$. If this condition is satisfied in the diffusivity layer and if this layer is thin, then one may show [4,5] that the boundary conditions for the noncollecting plate and the collecting plate, respectively, are

$$D \frac{\partial n}{\partial y} - wn = 0 \quad \text{(zero flux condition)} \tag{7}$$

$$\frac{\partial n}{\partial y} = 0 \quad \text{(zero slope condition)} \tag{8}$$

Here D denotes the core-value of the diffusivity.

A rigorous analysis of the process of precipitation for flow with arbitrary values of D based on the preceding assumptions is presented in references [4] and [5]. In addition to the dimensionless Deutsch number, a second dimensionless number

$$Pe = wd/D \tag{9}$$

appears, that we refer to as the electric Peclet number. Physically Pe provides a measure of the ratio of transverse particle transport resulting from the electric field to that resulting from diffusion. Thus $Pe \to \infty$ $(D \to 0)$ corresponds to laminar flow, while $Pe \to 0$ $(D \to \infty)$ corresponds to the Deutsch model.

For a uniform particle number density profile at the entrance, the analysis leads to a normal mode expansion. The profile evolves with axial distance until the dominant mode remains as a self-similar solution. Calculated profiles for the dominant mode for different Peclet numbers are shown in Figure 2. For large Pe (small D) the particles are "heaped up" towards the collecting wall $(y = d)$, while for low Pe (large D) the profile is flatter and tends to a uniform profile in the Deutsch limit $Pe \to 0$. The efficiency as a function of De and Pe, obtained by integrating the concentration profiles, is shown in Figure 3.

In the entrance region, where the profile evolves from the uniform profile assumed by Deutsch to that of the dominant mode, the efficiency increases from an initial Deutsch value to the higher value of the dominant mode, as shown in Figure 3. In the limit, as the Peclet number becomes very large, the curves approach the result for laminar flow. It should be noted that typical modern high-efficiency precipitators employ a value of the Deutsch number of about 5 or 6 to achieve efficiencies of ~99.5%. Figure 3 clearly indicates that such efficiencies should be attainable with values of the Deutsch number a factor 3 or 4 smaller if turbulent diffusion could be controlled to give Peclet numbers in the range Pe = 20 to 30.

A comprehensive experimental check, using the apparatus previously described, of the validity of the theoretical predictions of the analysis based on the convective-diffusion equation has been carried out, as reported in references [4], [6], and [7]. The theory was tested by measuring the concentration profiles n(y) (by a non-intrusive light-scattering technique) which constitutes a more rigorous test than just an efficiency measurement. Typical concentration profiles at different stations along the flow direction are shown in Figure 4. The solid curves are calculations for an assumed turbulent diffusivity of $D = 1.2\ cm^2/s$, which value is close to that to be expected for the large grid used here, and corresponds to a Peclet number of Pe = 125. Similar measurements were made over a range of (measured) migration velocities, stations (i.e., x-positions), and diffusivities (different grids) spanning the range of Deutsch parameter 0.05-1.0 and Peclet number 30-350. All these profile measurements can be compared with theory in a normalized plot as shown in Figure 5. The fact that the data fall close to the theoretical curve for a wide range of the parameters is strong evidence of the essential correctness of the theory. The efficiencies corresponding to the three conditions of Figure 4 are shown plotted as points in Figure 3. Since for Pe = 125 the efficiency curve is very close to the laminar limit, we see that the agreement between experiment and theory is also very good when examined in these terms.

For the low levels of grid-generated turbulence used in these experiments, corresponding to De in the range $0.6\text{-}1.2\ cm^2/s$, the Peclet numbers are large (Pe > 30). On the other hand, commercial precipitators almost certainly have much larger values of diffusivity, and lower values of Pe, because they are designed with little regard for flow quality, principally because there has been little recognition of its importance. Even for relatively moderate values of Pe, we see that there exists the potential for significant improvement in precipitator efficiency and size over that predicted by the Deutsch equation.

3.0 NONUNIFORM DIFFUSIVITY AND UNIFORM ELECTRIC FIELD

Because existing commercial electrostatic precipitators almost certainly have much smaller values of Pe than those obtained in the work described in the previous section, experiments were undertaken in which the turbulent diffusivity was much larger than that which could be obtained with grids. It is known for isotropic homogeneous turbulence that

$$D \propto V^* L^* \tag{10}$$

Here V^* and L^* are characteristic values of the turbulent velocity and length scale (of the energy-containing eddies), respectively. Using this relationship as a guide, experiments were undertaken using the three turbulence-generating configurations shown schematically in Figure 6.

Shown in Figure 7 are hot-wire anemometer measurements of the mean streamwise gas velocity and the r.m.s. intensity of the streamwise turbulence fluctuations made at several downstream locations for the case of the 2-cm single baffles. Similar measurements were made for the other two baffle configurations. The flow separation and reattachment caused by the baffles result in the formation of large eddies that interact and then tend to dissipate as the gas proceeds downstream. As a result, asymmetric and unstable three-dimensional flows are observed initially within a certain distance from the baffles. The upstream edge of the plate-plate collector, used to produce a uniform electric field, was therefore placed 40 cm downstream of the last baffle, where the flows exhibited reasonably uniform core conditions but where the turbulence intensity was still quite large.

Particle concentration measurements for the 2-cm single baffles are shown in Figure 8(a) for a migration velocity w = 7.5 cm/s and in Figure 8(b) for w = 20 cm/s.

In each figure, data are shown for measurements made 20 cm and 40 cm from the collector inlet. All measurements shown in these figures were made for an average gas speed of 200 cm/s. Similar concentration profile measurements were made for the other baffle configurations and for other values of the average gas speeds, for a total of six conditions in all.

The dashed curves shown in Figure 8 were calculated using the uniform diffusivity theory dicussed in the previous section. (For these calculations the value used for the particle diffusivity, $D = 17.5\ \text{cm}^2/\text{s}$, was obtained by the method described below. The theoretical profiles are relatively insensitive to variations in the value of the diffusivity within a factor of about two.) We see that the theoretial curves agree reasonably well with the data near the collecting wall, but that there is a marked discrepancy near the noncollecting walls. Similar behavior was exhibited for all six measurement conditions.

The discrepancy at the noncollecting wall appears to stem from the assumption in the theory that the particle diffusivity is uniform, whereas in fact, D must become very small at the noncollecting wall. This too-large value of D causes the predicted turbulent diffusion flux of particles from the core region toward the noncollecting wall to be too large, and therefore the predicted particle concentration in the near-wall region will also be too large. The reason that the uniform diffusivity theory agreed well with the data for the grid-generated turbulence described in the previous section was that the thickness of the region of rapidly varying diffusivity (that we called the diffusivity layer) was small.

In order to seek better agreement with the concentration profile data for the baffle-generated turbulence, the nonuniform diffusivity model shown in Figure 9 was assumed. The value of the particle diffusivity at the wall is taken to be the value actually at the edge of the viscous sublayer, $D_w \approx 0.019\ \text{cm}^2/\text{s}$, and the boundary conditions at this location can be shown to be the same as those employed for the uniform diffusivity model, viz. zero flux at the noncollecting wall and zero gradient at the collecting wall.

To apply this model, it is necessary to specify the values of two parameters, the diffusivity layer thickness ξ and the core diffusivity D. On the basis of flow measurements, such as those shown in Figure 7, and as a result of some exploratory calculations, it was determined that a reasonable value for the diffusivity layer thickness for all the experimental conditions examined was $\xi = 0.3d$. The core diffusivity was determined for each baffle-configuration, mean gas speed, and axial location, by fitting the calculated concentration profile to the data for the lower value of migration velocity w. Comparison of the data with a calculation performed for the higher value of w (but with the same value of D previously determined) then provided an independent measure of the success of the assumed nonuniform diffusivity model.

The solid curves in Figure 8 show the results of the calculations for one set of conditions, and are representative of the results obtained for all six cases examined. We see that the nonuniform and uniform diffusivity calculations agree approximately with each other and with the data near the collecting wall, but that the nonuniformity model provides much better agreement with the data near the noncollecting wall. Values of the core diffusivity determined by the fitting procedure described above for $w = 7.5$ cm/s are seen to do a good job of predicting the profiles for $w = 20$ cm/s.

By integrating the experimental concentration profiles one can obtain the corresponding experimental efficiencies. These values measured at $x = 40$ cm for two different values of w are shown plotted in Figure 10 vs. the Deutsch number (with x corrected for the upstream fringing electric field) for the three different baffle configurations. Even for these highly turbulent flows the measured efficiencies are seen to be significantly larger than those predicted by the Deutsch model.

It is also of interest to compare the measured efficiencies with the uniform diffusivity model. This comparison is provided by the lines in Figure 10 labeled by different values of the electric Schmidt number Sc. The results presented in terms of the Peclet number in Figure 3 are presented here in terms of an alternative dimensionless parameter

$$Sc \equiv \frac{Pe}{De} = \frac{ud^2}{DL} \tag{11}$$

in order to be able to extract the value of the uniform diffusivity D that best approximates the data. We see that the experimental points fall approximately on lines of constant Sc having values that are roughly a factor of half of those calculated using the core values of diffusivity obtained by fitting the measured concentration profiles with the nonuniform diffusivity model (and hence values of diffusivity that are roughly twice the previous values).

4.0 NONUNIFORM ELECTRIC FIELD AND UNIFORM PARTICLE DIFFUSIVITY

The preceding sections have dealt with cases for which the electric field is uniform, as indicated schematically in Figure 11(a), and can be approximated in the laboratory by applying a voltage between opposed parallel plates. Such a configuration would correspond to a plate-plate collector in a 2-stage precipitator.

For large single-stage electrostatic precipitators, the electric field distribution is more like that shown schematically in Figure 11(b), and is clearly nonuniform. In such precipitators the voltage applied between the wires and plates is sufficiently high to produce a corona current, so that the particles are both charged and transported to the plates in the same device. (The regular field lines depicted in Figure 10(a) would actually correspond only to the case of a positive corona.) To study first just the effects of the nonuniform electric field, the simplified case has been considered where the voltage, in effect, is below the threshold for corona onset and the particles are pre-charged.

For the electric field we may use the known closed-form expression [8] for an infinite array of wires of radius a and wire-to-wire spacing 2h placed along the centerplane between infinite parallel plates separated by a distance 2d, where $(a/d) \ll 1$. (Since the plates in our case are idealized as semi-infinite, this expression approximates the electric field in the vicinity of the inlet.) The case being considered here would therefore correspond to a wire-plate collector in a 2-stage precipitator. As an aid to our understanding, it is useful first to consider laminar flow ($D = 0$) and then to describe the turbulent flow work ($D \neq 0$).

LAMINAR FLOW

The particle trajectories for the two types of collector are shown in Figure 12. For the plate-plate collector the trajectories, shown as oblique straight lines in Figure 12(a), result from the superposition of a uniform transverse particle migration velocity w (which is proportional to the electric field vector $\vec{E}$) and a uniform axial particle velocity u in the flow direction. The normalized particle flux profile $\Gamma(y)/\Gamma_0$ equals unity in the region where particles are present, and is zero elsewhere. The collection is completed in a normalized length $\bar{x}_1$ $(= x_1/d) = 1/\varepsilon$, corresponding to a value of the Deutsch number $(De)_1 \equiv \bar{x}_1\varepsilon = 1$. Here $\varepsilon \equiv w/u$ is the ratio of the particle migration velocity to the inlet streamwise velocity.

For the wire-plate collector in the case of laminar flow, the particle continuity equation for the particle number density $n(x,y)$ reduces to the form

$$\frac{\partial n}{\partial x} + F(x,y)\,\frac{\partial n}{\partial y} = 0$$

where $F(x,y) = \varepsilon_o G_y/(1 + \varepsilon_o G_x)$. Here $\varepsilon_o = w_o/u$ is the ratio of the particle electric migration velocity w_o to the mean inlet gas speed u. The particle velocity w_o corresponds to the value of electric field $E_o = V_o/d$, where V_o is the applied potential between the wires and the plates. The vector $\vec{G} = (G_x,G_y)$ is the nondimensional wire-plate electric field distribution $\vec{E}/E_o$, which depends on the three geometric parameters h, a, and d. If all the lengths are nondimensionalized by d, then $\vec{G} = \vec{G}(\bar{x},\bar{y},\bar{h},\bar{a})$, where $\bar{x} = x/d$, $\bar{y} = y/d$, $\bar{h} = h/d$, and $\bar{a} = a/d$.

The method of characteristics applied to this equation yields the result that the particle number density $n(x,y)$ is constant along characteristic lines given by the differential equation $(dy/dx) = F(x,y)$. The characteristics are identical with the particle trajectories. Thus along a trajectory, n remains constant with the value n_o set by the inlet boundary, which we shall take to be a constant, independent of the coordinate y.

As shown in Figure 12(b), the particle trajectories for the wire-plate collector, corresponding to the geometry of Figure 11(b), are no longer straight lines, but exhibit a "wavy" character [9,10]. (The trajectories are shown only for one-half of the space between the plates. Because of symmetry, the trajectories reflected in the plane of the wires are the same.) As the particles approach a wire, they experience a larger electric field and therefore a greater force. The spatial variation in the transverse electric field component E_y and the resulting transverse repulsive force causes the trajectories to be wavy, as shown, with the particles nearest the wires showing the largest effects.

The streamwise component of the electric field E_x (absent for a plate-plate collector) causes the particles, on the average, to be slowed, thereby reducing the average particle streamwise velocity $u(x,y)$ and causing the normalized particle flux profile $\Gamma(y)/\Gamma_o$ at an x-position to exhibit the shape indicated. Since in the region where particles are located, the particle concentration retains its inlet value, the spatial variation of $\Gamma(x,y) = n_o\, u(x,y)$ results directly from the variation in the average particle streamwise velocity.

The particle penetration is obtained by performing the integration $P = \int_0^1 (\Gamma(\bar{y})/\Gamma_o)d\bar{y}$. The precipitation efficiency must then be of the form $\eta \equiv 1 - P = \eta(\bar{x},\varepsilon_o,\bar{h},\bar{a})$. Replacing $\bar{x}$ by $De_c = \bar{x}\varepsilon_c$, where $\varepsilon_c = w_c/u$ and where w_c is the migration velocity for some characteristic electric field E_c, we would have for the functional form of the efficiency $\eta = \eta(De_c,\varepsilon_o,\varepsilon_c,\bar{h},\bar{a})$.

The simplest choice for ε_c would appear to be $\varepsilon_c = \varepsilon_o$. Shown in Figure 13(a) are the results of calculation [9,10] for η as a function of $De_o = \bar{x}\varepsilon_o$, for representative values of ε_o and $\bar{h}$, and for the case $\bar{a} = 0.01$. As $\bar{h} \rightarrow \bar{a}$, corresponding to very close-spaced wires, the efficiency curve tends to that of a plate-plate collector. As the wire spacing h increases, the Deutsch number De_o for 100% efficiency increases. This behavior occurs because for a fixed $E_o \equiv (V_o/d)$, the surface-averaged values of the precipitating field $E_y(x,y=d)$ on the collector decreases as the wire spacing increases. The dependence on the parameter $\varepsilon_o \equiv (w_o/u)$ is weak when the results are plotted in this fashion so that to a good approximation, the number of independent dimensionless variables are reduced to three, and we may write $\eta \equiv \eta(De_o,\bar{h},\bar{a})$.

The foregoing results suggest that instead of the selection $E_c = E_o$, a more appropriate choice would be $E_c = E_{av} \equiv \langle E_y(x,y=d)\rangle$, where E_{av} denotes the surface-averaged precipitating field on the collector. When the results of Figure 13(a) are replotted against the Deutsch number $De_{av} \equiv (w_{av}\bar{x}/u)$, based on $w_{av} = \mu E_{av}$ (here μ is the particle mobility), the efficiency curves for all values of $\bar{h}$ collapse onto the curve for the plate-plate case, as shown in Figure 13(b). Moreover, the solutions for other values of $\bar{a}$ of interest exhibit approximately this same behavior. Thus the number of independent dimensionless variables is reduced from an original four to one, and we may write $\eta \simeq \eta(De_{av})$. We see that with this choice of variables, a very significant simplification is achieved.

TURBULENT FLOW

Theory

To explain the particle number density profiles measured in a plate-plate collector with highly turbulent flows (see Sec. 3.0) required that a nonuniform model be employed only near the noncollecting plate--that the description of particle transport in terms of a uniform diffusivity was quite acceptable near the collecting plate. In a wire-plate collector the noncollecting surface consists of the relatively very small surface of the wires, and additionally, there will be very few particles near the wires (except, possibly, the first one or two wires near the precipitator inlet). Therefore the uniform diffusivity model should provide a good approximation for charged particle transport in a wire-plate collector.

The form of the convective-diffusion equation that applies in this case is shown in Table 1. In addition to the new terms accounting for a nonzero component of the electric field in the x-direction E_x, the term $\partial^2 n/\partial x^2$ must be retained in the diffusion term for at least two reasons. First, it is not evident that this term is small in the vicinity of a wire. Second, the wires exert a repulsive Coulomb force on incoming particles: In order to account for this "upwind" effect, the convective-diffusion equation must be of elliptic type.

This equation has been solved numerically [9,11] in conjunction with the appropriate boundary conditions, for a collector with 20 wires (modeled as strips) and with an effective normalized wire diameter (2a/d) = 0.027. Figure 14 shows the particle concentration as a function of $\bar{x}$ in four planes, $\bar{y}$ = 0, 0.15, 0.5, and 1.0, for the typical parameter values ε_0 = 0.1 and Pe_0 = 2.5. It is seen that, as expected, the particle concentration generally decreases along the flow direction ($\bar{x}$) for all $\bar{y}$ planes, and increases towards the collector ($\bar{y}$ = 1). However, the concentration profile in the x-direction shows marked periodic behavior near the centerplane (small $\bar{y}$) while near the collector ($\bar{y}$ = 1) it decreases monotonically. Along the centerline ($\bar{y}$ = 0) the concentration decreases suddenly near the upstream edge of the strip where there is a strong repulsive force on the particles. Downstream of an electrode the concentration increases again due to turbulent diffusion into the region of low field midway between electrodes, until the upstream edge of the next strip is approached. This is the origin of the successively decreasing peaks in $\bar{n}(\bar{x})$. Far downstream of the last electrode the concentration tends to a constant value, independent of $\bar{y}$, since there is negligible electric field and turbulent diffusion causes the profile to be flat.

Shown in Figure 15(a) is the efficiency as a function of the Deutsch number De_0 (based on $E_0 = V_0/d$), for the typical values h = 1, $\bar{a}$ = 0.02, $\varepsilon_0 = (w_0/u) = 0.1$, and for several values of the Peclet number $Pe_0 \equiv (w_0 d/D)$. (The break in the curves at De_0 = 4, beyond which the efficiency remains constant, corresponds to the x-coordinate of the last wire.) The general trend of the efficiency curves with De_0 and Pe_0 is similar to that for a plate-plate collector, but the efficiency, for the same values of De and Pe is significantly lower. This behavior reflects the fact that for equal applied voltages, the wire-plate geometry has a significantly lower surface-averaged electric field at the collector surface than the uniform field E_0 of the plate-plate collector.

As for the laminar flow case, one may replot the results with De and Pe based on the surface-averaged field on the collector E_{av}, instead of E_0. When this replotting is done the results, as shown in Figure 15(b), agree closely with those calculated for a plate-plate collector (that has a uniform field). Thus, for calculating the efficiency it is a good approximation to use the simpler uniform electric field theory provided this field is identified with the surface-averaged field $E_{av} = \langle E_y(x,y=d) \rangle$.

Experiment

The plate-plate collector apparatus previously described was converted to a wire-plate collector by installing ten wire (of diameter equal to 0.89 mm) electrodes along the midplane of the plate-plate configuration. Experiments were performed with applied voltages V_0 less than the corona threshold voltage of 14.0 kV, and mono-charged monodisperse pre-charged particles were employed. Particle concentration profiles were measured at the transverse midplane between the eighth and ninth wires, where the mean particle velocity equals the mean gas velocity (since the axial electric field component E_x is ideally equal to zero at this location). Measurements were made both for low turbulence levels, by accepting whatever free-stream turbulence conditions were produced by the wind tunnel itself, and for high turbulence levels by employing the 2-cm baffle upstream-turbulence-generating configuration previously discussed.

Shown in Figure 16 are the particle concentration profiles measured with low and with high turbulence levels, for different values of the applied voltage expressed in terms of the dimensionless parameter $\varepsilon_0 = w_0/u$. Here u is the mean gas speed and $w_0 = \mu V_0/d$ is the particle migration velocity for a reference electric field equal to V_0/d. The quantity d denotes the wire-to-plate distance. The diffusivity values D, shown in the captions, were determined by fitting the experimental efficiencies to those predicted by the uniform diffusivity and uniform electric field theory discussed in Sec. 2.0. The value of the effective uniform field was chosen to equal the surface-averaged electric field of the actual nonuniform field distribution, as supported by theory.

For the low-turbulence case, shown in Figure 16(a), the steep gradients in the particle concentration profiles indicate that the effect of the higher turbulence level existing in the wire wakes is small. The large electric field existing near the wires quickly depletes these regions of particles so that after passing the first one or two upstream wires, most of the particles are located outside the wake region where the free-stream turbulence level is relatively low, and uniform. For the high-turbulence case, shown in Figure 16(b), the baffle-generated turbulence level dominates the wake turbulence so that the diffusivity is again relatively uniform. The larger diffusivity causes the particle concentration profiles to be smoothed out in comparison to the results shown in Figure 16(a).

The efficiencies for the two cases discussed above, and for a second high-turbulence case at a different mean gas velocity (u = 100 cm/s), are shown plotted in Figure 17 as a function of the Deutsch number based on w_{av}, i.e., the particle migration velocity for the surface-averaged electric field. Also shown are the lines of constant electric Schmidt number ($Sc = ud^2/DL$) given by the uniform properties theory for a plate-plate collector discussed in Sec. 2.0. We can see first that the efficiencies, even for the large-turbulence-level cases, significantly exceed the Deutsch limit. Second, all the experimental points corresponding to the same flow conditions fall approximately on a single Schmidt number line. This behavior supports the applicability of the idealized plate-plate collector theory to the description of a wire-plate collector based on the concept of the equivalence of space-averaged fields.

Since the Sc number depends on the single fluid property D, these results can be used to back out the effective values of diffusivity shown in the caption of Figure 16. If we regard the wire-plate collector as two plate-plate collectors, with a common noncollecting plate occupying the symmetry plane passing through the wires, then we can use these values of D to obtain the theoretical particle concentration profiles shown in Figure 16. The theory and data are seen to agree very well, except possibly near the centerline. The cusps in the theory curves are artificial and result from the zero flux boundary condition imposed separately on either side of the centerline.

The theory described at the beginning of this section with a zero-slope boundary condition imposed at the symmetry plane would represent more closely the actual experimental configuration, but such calculations are lengthy and were not performed in this study. The uniform diffusivity plate-plate model with the electric field set equal to the surface-averaged field at the collecting wall is seen to provide a good approximation for predicting not only the global efficiencies for wire-plate collectors, but also the detailed particle concentration profiles.

Before moving to the next topic, it will be useful to describe here an alternative method of presentation of the theoretical efficiencies η (or penetrations P) predicted by the uniform diffusivity and uniform electric field model. The results of this theory, as shown graphically in Fig. 18, are of the form $P \equiv (1 - \eta) = P(De,Sc)$. Instead of expressing precipitator performance in terms of P (or η), one can introduce the concept of the effective electric migration velocity, w_{eff}. This quantity is defined as the value the migration velocity would need to be in order that the predicted (or measured) P (or η) be given by the Deutsch theory, i.e., $P = \exp(-w_{eff}L/ud)$. Equating these two expressions for P, one can write

$$\left(\frac{w_{eff}}{w}\right) = -\frac{\ln P(De,Sc)}{De} \qquad (12)$$

This form of presentation therefore removes the exponential-like dependence of P on De. Since $P = n/n_o$, $(-dn)/n = (w_{eff}/ud)dL$: We may therefore interpret the fractional collection per unit length as proportional to w_{eff}.

The relation (12) is shown plotted in Figure 18, together with the experimental points taken from Figure 17. The line Sc = 0, for which $(w_{eff}/w) = 1$, corresponds to the Deutsch model ($D \rightarrow \infty$). With increasing Sc (decreasing D), the curves (w_{eff}/w) rise increasingly above $(w_{eff}/w) = 1$ with increasing De (i.e., increasing length or migration velocity).

5.0 EFFECT OF SPACE CHARGE

In the experiments described to this point, conditions were selected so as to prevent the onset of corona discharges within the collector volume. The only source of space charge would have been the pre-charged particles, but the particle number density was so small that the effects of the associated space charge were negligible. However, for experiments that correspond to a single-stage precipitator, with particles being charged in corona discharges and being collected in a single device, the ionic space charge is usually sufficiently large that its effects need to be examined. However, the problem is complicated by the fact that the two effects of space charge and of nonuniform particle charge are simutaneously present, making it difficult to sort out the separate effects of each mechanism acting alone.

To overcome this difficulty, experiments were performed using corona discharges to produce a space charge, but employing particles that were pre-charged to a value larger than could be achieved by the corona discharge acting alone (except for possibly a relatively small fraction of particles). A uniform, spatial distribution of particle charge was therefore maintained and the only new feature was the presence of the space charge mechanism.

The saturated value of charge acquired by a particle in an electric field E_c by ionic bombardment is given by the expression [2]

$$q_{sat} = 12\pi\,\varepsilon_g\left(\frac{\kappa}{\kappa + 2}\right)E_c\,a^2 \qquad (13)$$

Here $\varepsilon_o = 8.85\times10^{-12}$ F/m is the permittivity of free space, a is the particle radius (2 μm for this work), and κ is the relative dielectric constant of the particle ($\kappa = 2.46$ for oleic acid, used in this work). To keep the value of q_{sat} low, it was necessary to keep the value of E_c low. The wires employed in the wire-plate precipitator apparatus described in Sec. 4.0 were therefore replaced by wires having a diameter of 0.10 mm. The threshold corona onset voltage for this geometry was measured to be 5.0 kV (in contrast to 14.0 kV for the 0.089-cm diameter wires used in previous experiments).

The amount of pre-charge was set to a value three times the approximate maximum value of q_{sat} calculated by using for the charging field the value V_0/d. For these conditions the particles were collected so rapidly that very few remained in the gas at the measurement location used previously--i.e., between the eighth and ninth wires. For these experiments the measurements of particle concentration were therefore made at the midplane between the second and third wires, corresponding to $x = 12.7$ cm.

The measured particle concentration profiles for both positive and negative coronas are shown in Figure 19. These data are for low turbulence conditions, without upstream turbulence-generating obstacles, and should be compared to the profiles shown in Figure 16(a) that were obtained for similar conditions, but with no space charge effects. We may note first that the profiles for positive and negative coronas are quite similar, with the increased scatter shown for the negative corona attributable to the nonuniform tuft-like discharge structure associated with the negative corona.

Comparing Figure 16(a) and Figure 19, it appears that the presence of space charge does not affect the particle concentration profiles in a major way, although there are significant differences. The absence of particles from the vicinity of the midplane passing through the wires is much more pronounced with space charge present, and the transition to the particle-containing regions much more abrupt.

The behavior in the near-wall region is also different. We may note first that although the profiles shown in Figure 16(a) and Figure 19 were obtained at fixed locations for increasing values of the applied potential, the profiles obtained for a fixed potential and increasing values of x would be very similar. It is somewhat simpler to describe the difference between these figures in terms of the latter picture. At $x = x_0$, $n/n_0 = 1$, and as x increases, in the absence of space charge, the value of n/n_0 initially remains unity within near-wall plateau regions that gradually shrink to zero when the transition transverse concentration gradients move sufficiently close to the collecting walls that they begin to reduce the value of n at the walls. By contrast, in the presence of space charge, the constant n/n_0 plateau region is replaced by a region where n/n_0 decreases in the transverse direction with a small value of $|\partial n/\partial y|$ away from the walls, and at the same time the wall-value of n/n_0 decreases in the streamwise direction.

A numerical analysis of the particle continuity equation for the conditions of these experiments, as given in Table 1, was not undertaken. The effort to develop a numerical method for solving this equation coupled to Poisson's equation would have exceeded the scope of the present study. However, it is relatively simple to show that the decrease of the near-wall value of n with increasing x is consistent with nonzero values for the space charge and for the transverse gradient in n. (It should be pointed out that with corona discharges present, it is possible to generate corona winds that affect the distribution of gas velocity. However, the corona discharge in these experiments were relatively weak [4,7], and no effects attributable to corona winds were evident in the data.)

6.0 EXPERIMENTS FOR SINGLE-STAGE PRECIPITATOR CONDITIONS

For bombardment charging in a corona discharge (which is the dominant charging process for the 4.0-μm diameter particles employed here), the saturation charge is proportional to the charging field, as shown by Eq. (13). The charge is acquired as a function of time according to the relation

$$q(t) = \frac{q_{sat}}{1 + (\tau/t)} \qquad (14a)$$

where the characteristic time for charging (i.e., the time for the particle to acquire half its saturated value) is

$$\tau = \frac{4\varepsilon_g E_c}{J} \tag{14b}$$

Here J is the ion current density. The values of both E_c and J are large near the wire and are much smaller near the collector plates. These nonuniformities in E_c and J result in a nonuniform distribution of particle charge and, hence, of particle mobility, which is accounted for by the term $n\vec{E}\ \nabla\mu$ in the equation governing particle transport shown in Table 1.

Particles entering near the centerline will tend to quickly get charged to the saturation level, whereas particles entering near the plates will tend to be charged more slowly and to a lower level. The charging process is clearly quite complicated, and no attempt has been made in the present work to undertake any modeling studies. However, exploratory experiments were performed for both positive and negative corona discharge, and for both low and high levels of turbulence. The measurements point out some of the dominant physical features resulting from charging in a precipitator environment and shed new light on the importance of gaining a more complete understanding of the role of charging on precipitator performance.

The major new feature of the experiments to be described in this section was the use of a radioactive source of Kr 85 to neutralize any charge the particles may have acquired prior to their passage into the precipitator. Thus the entire charging occurred as the particle passed through regions of space occupied by corona discharge. The precipitator consisted of ten 0.1-mm diameter wires, and measurements were made in the midplane between the eighth and ninth wires.

The particle concentration profiles measured with a positive corona for increasing values of the current per unit length (i/ℓ) are shown in Figure 20(a). These profiles are seen to exhibit extremely sharp and well-defined peaks on either side of the centerline, with maximum values of n/n_0 as large as 1.8--i.e., a higher density than the inlet value. These peaks, which were not observed in any measurements with pre-charged particles, including those with space charge present, must occur as a result of a nonuniform particle charge (and, hence, mobility) distribution.

In the presence of the strong and highly nonuniform electric field and ion current near the wire electrodes, particles closest to the wire are most highly charged, thereby leading to a rapidly decreasing distribution in particle mobility towards the grounded walls. The more highly charged particles are forced to move rapidly away from the wires by the stronger electric field. Particles further away from the wires, which have a lower mobility and are exposed to a relatively lower electric field, are not forced to move as quickly. As a result, the particle number density forms a peak at a certain location where particles are piling up. The distance of the peak formation from the centerline increases with increasing linear current density.

The heights of the peaks decrease and the widths increase with increasing discharge current, and the peaks eventually disappear when the linear current density is very large. This transition occurs when most particles have been collected (owing to the high current density) and insufficient numbers of particles remain for the piling-up process to take place. Since the data are steady and highly reproducible, it can be inferred that the core flow must have remained non-turbulent in the positive corona discharge. This conclusion is consistent with the laser Doppler measurements of turbulence intensity presented in Figure 21(a), which show that the positive corona does not increase the turbulence level (except near the walls, where an instability exists [4,7]).

Measurements of the concentration profiles for the negative corona discharge are presented in Figure 20(b). The inlet conditions are identical to those for the case of the positive corona results shown in Figure 20(a). The concentration peaks, which were observed with the positive corona, have now been broadened by the particle mixing that results from turbulence induced by the corona tufts, as shown in Figure 21(b), and vestiges of the peaks are barely discernible. It is not possible to obtain good reproducibility as demonstrated by a comparison of the two sets of measurements for $i/\ell = 0.04$ mA/m.

Another factor which may also contribute to the loss of well-defined concentration peaks is the nonuniform particle charging that occurs as a result of the spatially inhomogeneous structure of the negative corona discharge tufts: Particles, which are exposed to the locally intensified ion current from a corona tuft, will attain a higher charge, compared with particles which are traveling in the regions between the tufts. It should also be noted that the method of measurement (counting laser-scattering events) used in these experiments is actually proportional to the mean particle flux--i.e., the product of the mean velocity and the particle number density. Hence the ordinates in Figure 20 are more precisely equal to $(un)_{\text{corona on}}/(un)_{\text{corona off}}$, which equals n/n_0 only if the mean velocity remains unchanged with the wires energized or unenergized. Since the tufts are observed to change positions on a time scale on the order of a few seconds, quasi-steady corona winds could be set up by the tufts that would cause this condition to be violated.

Measurements of the turbulence induced by negative corona discharge tufts are plotted in Figure 21(b). As expected [4], the negative corona increases the flow and the particle turbulence level significantly beyond that measured without the corona discharge. The measurements are not well reproducible and the velocity fluctuation level increases as the grounded collector walls are approached. Since the characteristic time scale for the velocity fluctuations is very much smaller than that for movement of the discharge tufts (on the order of seconds), it appears that the increased turbulence in the core results from flow instabilities associated with the interaction of the main gas flow and corona-winds induced by the discharge tufts. The increased fluctuation levels near the walls could result from the impingement on the walls of jets of the corona-wind induced by the tufts.

To examine the effect of highly turbulent flow entering the precipitator, two opposed 2-cm-wide baffles [see Figure 6(b)] located approximately 40 cm upstream of the precipitator were employed to generate the turbulence. Particle concentration profiles measured between the eighth and ninth wires (as before) are shown in Figure 22 for several different values of the linear current density i/ℓ. The results for the positive corona in Figure 22(a) show, first, that the turbulence eliminates the concentration peaks observed for low-turbulence flow, as presented in Figure 20(a). We may note also the similarity between these profiles and those obtained for the same turbulence-generating conditions, but with pre-charged particles, as shown in Figure 16(b). Since highly charged particles retain their charge even when moved to the near-wall region, this similarity may be interpreted as showing that the mixing action of the turbulence tends to homogenize the spatial distribution of particle charge, thereby producing approximately the uniform charge distribution of the pre-charged particles.

Concentration profiles for the negative corona discharge are shown in Figure 22(b). Except for the change in polarity, the conditions for Figures 22(b) and 22(a) are identical. Unlike the results for the corresponding negative corona low-turbulence flow presented in Figure 20(b), the measurements are now quite reproducible and show little scatter in the data. The particle concentration profiles now for positive and negative corona are in fact very similar, although there is a marked difference in the nature of these two kinds of corona discharge. This behavior occurs because the turbulence induced by the negative corona discharge is dominated by the baffle-generated turbulence. As shown in Figure 21(b) the induced turbulence intensity was about 5% over much of the core, whereas the baffle-generated turbulence level at the precipitator inlet was measured to be about 12%.

The precipitation efficiencies determined from the foregoing concentration profiles are given in Table 2. The fact that the applied voltage for a given linear current density is larger for positive corona than for negative corona probably is the main reason for the generally higher efficiencies obtained with positive corona. Another factor may be that with positive corona, particles are almost always passing through regions of ion current, whereas with negative corona, particles may spend an appreciable fraction of their transit times in regions between discharge tufts where they would temporarily cease being charged. (On the other hand, while within a discharge tuft the current density would be larger and therefore the charging rate would also be larger.)

Perhaps the most striking feature of these data is that for otherwise identical conditions, the efficiencies are higher for high turbulence conditions than for low turbulence. This aspect of the data is completely reversed from the large body of theory and experiments obtained with pre-charged particles that shows high turbulence levels to be detrimental to precipitator performance. There is not a contradiction here, because the latter experiments were focused on the question of particle transport, and all the particles were specifically prepared so as to carry the same value of charge. In fact, the mixing property of turbulence, as referred to earlier, may be advantageous during the charging process that occurs primarily within some inlet region of a precipitator. The extent of this charging region can be estimated using Eq. (14). Thus, for example, for $i/\ell = 0.04$ mA/m, the particle must travel about 3.4 wire spacings to reach 80% of the saturation charge; for $i/\ell = 0.6$ mA/m, the particle must travel about half a wire-wire spacing to become 80% charged.

To describe the charging process that takes place in the entrance region of a precipitator, we may employ a highly simplified model that is based on the Deutsch model, but accounts for increasing particle charge by assuming that the electric migration velocity w is an increasing function of the axial distance x. The model does not account for variations of w in the transverse direction y, and assumes that field charging occurs under conditions of uniform electric field and current density. The assumption of an approximately flat particle number density profile near the precipitator inlet is not unreasonable.

Since a particle located at position x has been charging for a time $t = x/u$, we may write in accord with Eq. (14), that

$$w(x) = \frac{w}{1 + \tau/t} = w\left[\frac{x}{x + u\tau}\right] \tag{15}$$

Here w is the migration velocity of a particle [see Eqs. (1) and (2)] carrying the saturated charge q_{sat} given by Eq. (13).

On the basis of the Deutsch number model expressed in differential form, we can write

$$\frac{dn}{n} = -\frac{w(x)dx}{ud} = -\frac{w}{ud}\,\frac{x\;dx}{x + u\tau} \tag{16}$$

Integrating both sides of this equation from x = 0 to x = x, we have

$$\ell n\left[\frac{n(x)}{n_0}\right] = -\left(\frac{w}{ud}\right)\left[x - u\tau\cdot\ell n\left(\frac{x + u\tau}{u\tau}\right)\right] \equiv -\frac{w_{eff}x}{ud}$$

Thus the finite charging rate effect can be expressed in terms of an effective migration velocity given by the relation

$$\frac{w_{eff}}{w} = 1 - \frac{\ell n[1 + (x/u\tau)]}{(x/u\tau)} \tag{17}$$

The finite charging rate effect introduces a new dimensionless parameter $x' = x/u\tau$ which represents the axial distance into the precipitator in units of the characteristic charging distance $u\tau$ (i.e., the distance the particle travels at the gas velocity in the time required for the particle to acquire half its saturation charge).

The relationship (17), expressing the effect of finite charging rate is shown plotted in Figure 23. The quantity (w_{eff}/w) starts at zero when $(x/u\tau) = 0$, increases rapidly, and then slowly approaches the asymptotic value of unity. It would be useful to compare this behavior with experimentally derived values, $(w_{eff}/w)_{exp}$. We were able to follow this approach for the experiments using precharged particles because the value of the electric migration velocity w was measured directly. In the present experiments the particles have different migration velocities, and we have no experimental measurements for w. However, we can proceed in an approximate manner using theory as a guide.

If we take for the charge q in Eq. (1) the value of the saturation charge q_{sat} given by Eq. (13), we can write (in SI units)

$$w_{th} \simeq \left\{\frac{12\pi\ \varepsilon_g[\kappa/(\kappa + 2)]}{6\pi\ \eta_g}\right\} a\ E_c E_p \simeq 1.13\times10^{-12}\ E_p E_c \text{ m/s} \qquad (18)$$

The subscript (th) is used to indicate that this value of the migration velocity is based on theoretical considerations. The quantity E_p denotes the precipitation electric field, and is interpreted as the surface-averaged field at the collecting wall. It is known that this field in the presence of space charge (as described by Poisson's equation) is significantly larger than the field that exists in the absence of space charge (as described by Laplace's equation). The value of the charging field E_c will also be affected by space charge. The detailed numerical calculation of these fields for the conditions of the experiments reported here was beyond the scope of present work. However, we can use the reference field $E_o = V_o/d$ as a rough estimate of E_p and E_c, to obtain the value (in SI units)

$$w_{th} \simeq 1.13\times10^{-12}\ E_o{}^2 \qquad (19)$$

Similarly, the characteristic charging time can be estimated (in SI units) as shown below:

$$\tau = \frac{4\varepsilon_o E_c}{J} \approx 4\varepsilon_o E_c \frac{4h}{I/\ell} = 16\times8.85\times10^{-12}\times.0254\times \frac{E_c}{I/\ell} = 3.60\times10^{-12}\times \frac{E_o}{I/\ell} \qquad (20)$$

(Here the wire-to-wire spacing 2h is taken equal to the plate-to-plate spacing 2d.) The values calculated in this manner for (w_{eff}/w_{th}) and for $(x/u\tau)$ (with x = .406 m) are shown in Table 3 and are plotted in Figure 23.

For lower values of the charging parameter $(x/u\tau)$, the data appear to conform approximately in shape to the theory curve,[1] but for larger values of $(x/u\tau)$, the "experimental" (w_{eff}/w_{th}) values increase more rapidly than theory and, in fact, exceed the value one, which is the asymptotic maximum value of the finite charging rate theory. Although the number of data points for large $(x/u\tau)$ are fewer than desirable, there is a clear indication that the behavior in this range represents the effect of finite diffusivity in particle transport, which we know leads to values of (w_{eff}/w) greater than one.

To obtain a "theory" that combines the effects of both finite charging rate and finite diffusivity, we may employ the ad hoc procedure of simply multiplying the values of (w_{eff}/w) based on finite diffusivity by the finite charging rate factor given in Eq. (17). Although not rigorous, this procedure should give a result which is approximately correct. Since the results of the finite diffusivity theory are expressed as a function of the Deutsch number De (and the dimensionless number $Sc = ud^2/xD$, where D is the particle diffusivity--as in Figure 18), the finite charging rate effect needs to be expressed in terms of De instead of $(x/u\tau)$. For the conditions of these experiments, the transformation between $(x/u\tau)$ and De is defined by the values for these quantities shown in Table 3. The theory for the combined effects of finite charging rate and finite diffusivity, obtained in this manner, are shown by the solid curves in Figure 24. Also shown, for comparison, are the corresponding (dotted) curves for finite diffusivity acting alone, and the experimental points for (w_{eff}/w_{th}) replotted as a function of De.

---

[1] Given the major simplifications necessary to adjust the data so as to permit a comparison with the theory, good agreement with respect to magnitude would not be expected, but a comparison with general trends is justified.

The similarity in the shapes of the theory and data curves supports the assertion previously made that data for low values of De reflect primarily the effects of finite charging, and for higher values of De one sees that the effects of finite diffusivity dominate. It is of interest to note from the theory curves that a full recovery from the poor performance near the entrance of the precipitator owing to the finite charging rate is not made, even for relatively large values of De (because of the slow variation in the log function that governs the approach of the particle charge to its saturation value).

For both positive and negative corona, and irrespective of turbulence level, (w_{eff}/w_{th}) starts from zero at about the corona onset voltage V_{crit} corresponding to De = 0.37. Then (w_{eff}/w_{th}) increases quite rapidly with increasing $V_o > V_{crit}$. The fact that (w_{eff}/w_{th}) increases more rapidly for negative than positive corona (irrespective of the turbulence level) may be due, at least in part, to the fact that the current density is higher for negative corona at the same V_o.

It is also quite evident (except at the highest values of De) that (w_{eff}/w_{th}) is larger for high turbulence than for low turbulence. This behavior supports the hypothesis that turbulence, by its enhanced mixing action, promotes more effective charging for both polarities. It should also be noted that in the range where De is not too large, the beneficial effect of low turbulence on particle transport (see Figure 18) is relatively small. This beneficial effect becomes relatively stronger for larger value of De.

Although the number of experimental points is few, nevertheless there is reasonably clear evidence for both positive and negative corona that at the largest De values obtained experimentally, there is a cross-over in the values of (w_{eff}/w_{th}) for the low and high turbulence cases. Clearly, at the largest De values, the beneficial effect of low turbulence on transport more than compensates for the detrimental effect of low turbulence on particle charging. Moreover, the low turbulence curves are increasing with a significantly greater slope than the high-turbulence curves, as one would expect fom the effect of turbulence on particle transport (see Figure 18).

In the experiments, the maximum value of De was set by the onset of sparking when $V_o \sim 2\ V_{crit}$ (corresponding to $De_{max} \sim 4\ De_{min}$), so that unfortunately the data are not as complete as desirable to establish firmly that for larger De values the beneficial effect of *low* turbulence on particle *transport* increasingly overrides the beneficial effect of *high* turbulence on particle *charging*. This situation stems from the fact that *only a* relatively short precipitator, L = 40.6 cm (8 wires), was used. To obtain data at larger (and more realistic) values of De measurements should be made for larger L. However, under these conditions, the efficiency is very high and it is not easy to obtain accurate measurements of penetration (and w_{eff}) by measuring the concentration (or flux) profile by the laser-scattering technique.

In conclusion, it should be noted that the beneficial effect of high turbulence on particle charging is mainly operative near the precipitator entrance, whereas the beneficial effect of low turbulence on particle transport is operative throughout the precipitator. Thus, an effective strategy may well be to exploit both beneficial effects simultaneously, by deliberately designing for a reasonably high turbulence level near the entrance in a duct which is otherwise designed for low turbulence. The foregoing analysis points out the need for a more systematic study of the effect of turbulence on particle charging in single-stage precipitators.

ACKNOWLEDGMENTS

This work was supported by the National Science Foundation under grants No. CPE-7926290 and No. CBT-8217719, and in part by the Electric Power Research Institute under contract No. RP-533-1. We wish to acknowledge also the valuable laboratory support provided by Rodman Leach.

The work described in this paper was not funded by the U.S. Environmental Protection Agency and therefore the contents do not necessarily reflect the views of the Agency and no official endorsement should be inferred.

REFERENCES

1. Friedlander, S.K. Smoke, Dust and Haze, John Wiley & Sons, New York, 1977. pp. 162-164.

2. White, H.J. Industrial Electrostatic Precipitators, Addison-Wesley, New York, 1963.

3. Deutsch, W. Bewegung und Ladung der Electricitatstrager in Zylinder Kondensator. Ann. Physik 68: 335-344, 1922.

4. Leonard, G.L. Effect of turbulence on electrostatic precipitator performance. HTGL Topical Report 196, Stanford University, April 1982.

5. Leonard, G.L., Mitchner, M., and Self, S.A. Particle transport in electrostatic precipitators. Atmos. Envir. 14(11): 1289-1299, 1980.

6. Leonard, G.L., Mitchner, M., and Self, S.A. Experimental study of the effect of turbulent diffusion on precipitator efficiency. J. Aerosol Science 13: 271-284, 1982.

7. Leonard, G.L., Mitchner, M., and Self, S.A. An experimental study of the electrohydrodynamics flow in electrostatic precipitators. J. Fluid Mech. 127: 123-140, 1983.

8. Spiegel, M.R. Complex Variables (Schaum Series). McGraw-Hill, New York, 1974. pp. 252-253.

9. Kihm, K.D. Effects of Nonuniformities on Particle Transport in Electrostatic Precipitators. Ph.D. Thesis, Stanford University, March 1987.

10. Kihm, K.D., Mitchner, M., and Self, S.A. Comparison of wire-plate and plate-plate electrostatic precipitators in laminar flow. Jour. Electrostatics 17: 193-208, 1985.

11. Kihm, K.D., Mitchner, M., and Self, S.A. Comparison of wire-plate and plate-plate electrostatic precipitators in turbulent flow. Jour. Electrostatics 19: 21-32, 1987.

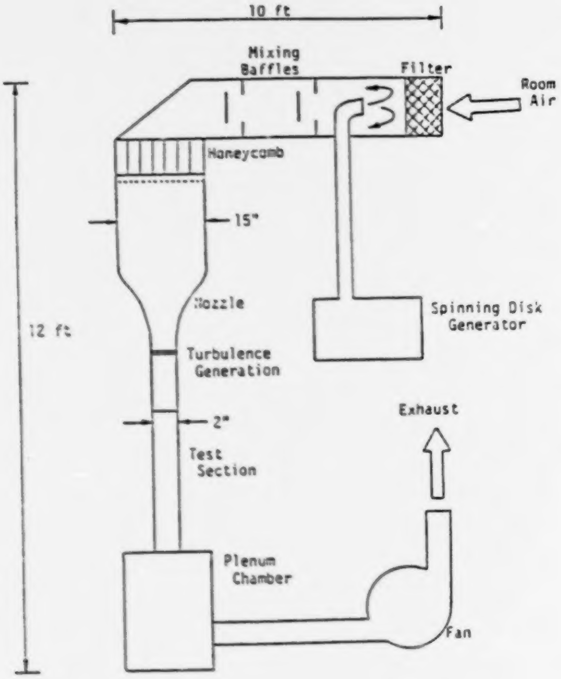

Figure 1. A schematic drawing of the experimental facility.

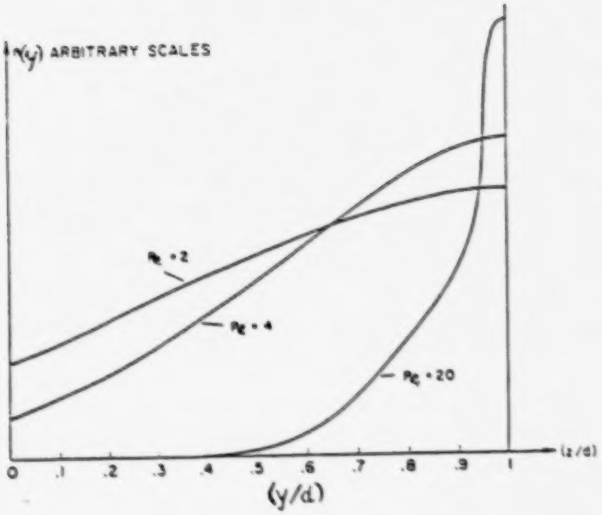

Figure 2. Concentration profiles for various values of Pe.

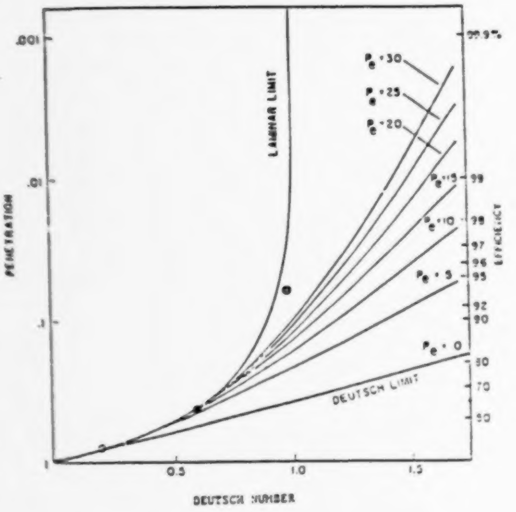

Figure 3. Collector efficiency as a function of the Deutsch number for different values of the Peclet number.

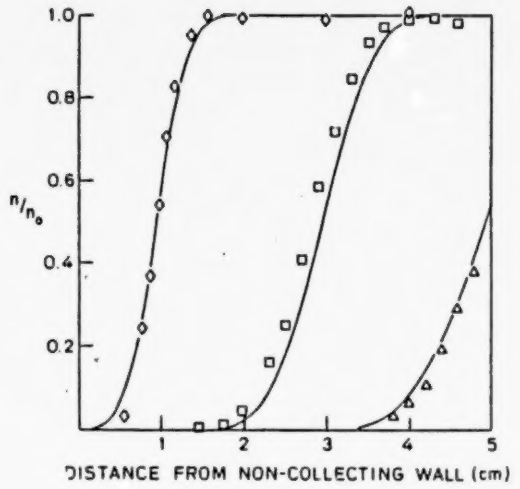

Figure 4. Particle concentration profiles: u = 300 cm/s, w = 30 cm/s; x = 5 cm ◇; x = 25 cm □; x = 45 cm Δ. Large mesh grid, D = 1.2 cm²/s.

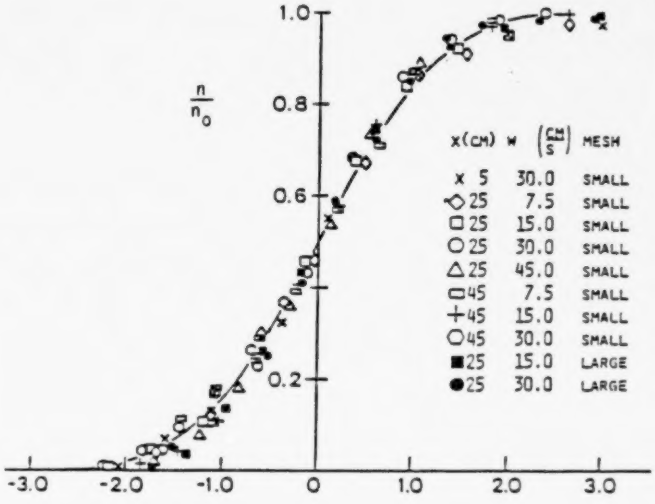

Figure 5. Particle concentration profiles plotted in self-similar form.

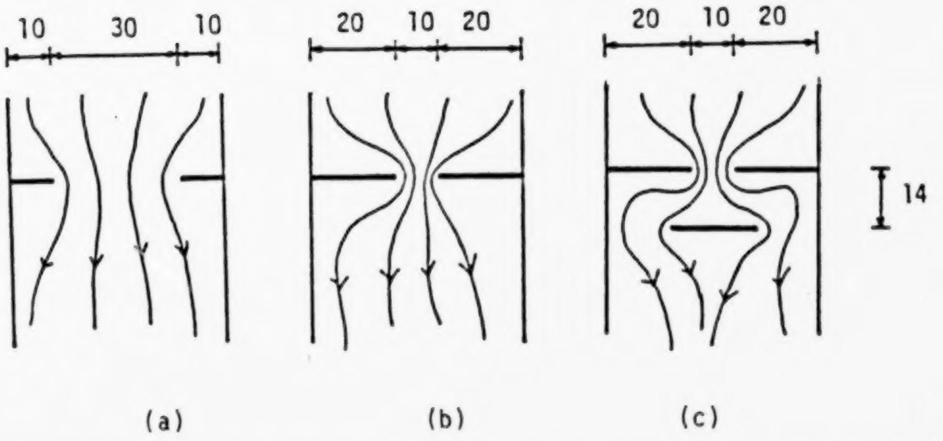

Figure 6. The turbulence-producing baffle configurations: (a) 1-cm baffles; (b) 2-cm baffles; and (c) 2-cm double baffles.

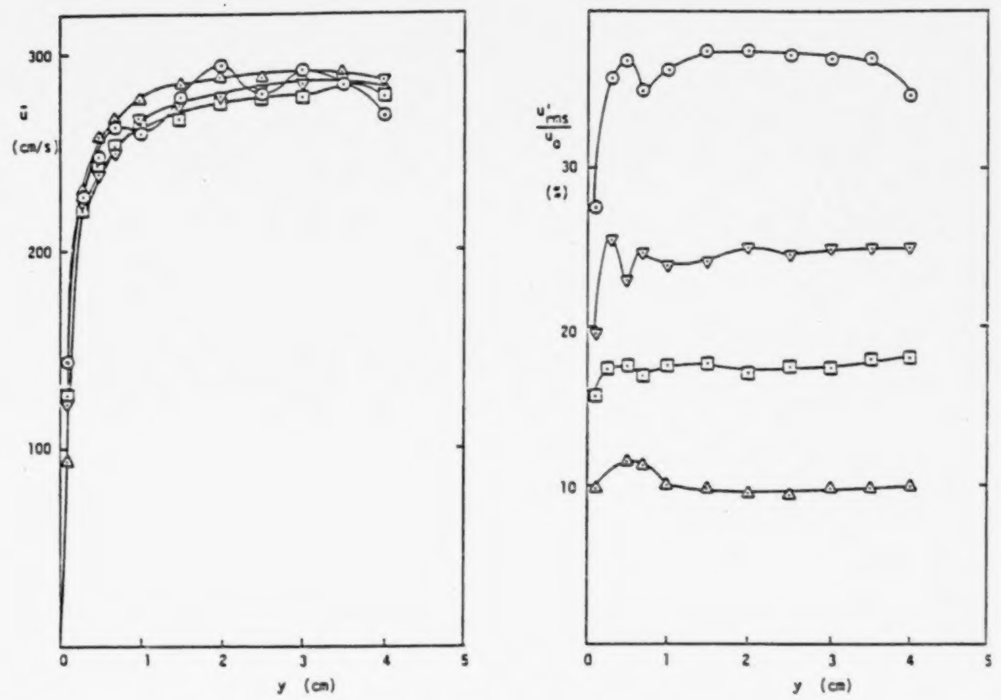

(a) (b)

Figure 7. Hot-wire anemometer results for the flow generated by 2-cm baffles: u = 280 cm/s; x = 30 cm ⊙; x = 40 cm ▽; x = 50 cm ◻; x = 90 cm △; (a) mean gas velocity; and (b) turbulence intensity.

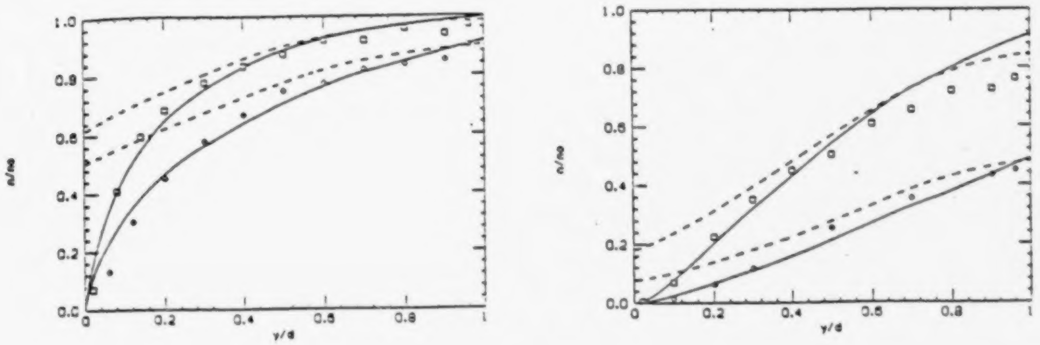

(a) (b)

Figure 8. Particle concentration profiles for 2-cm baffles: u = 200 cm/s; D = 17.5 cm^2/s, $\xi/d = 0.3$; x = 20 cm ◻; x = 40 cm ◇; (a) w = 7.5 cm/s; and (b) w = 20 cm/s. Theory: uniform diffusivity -----; nonuniform diffusivity ——.

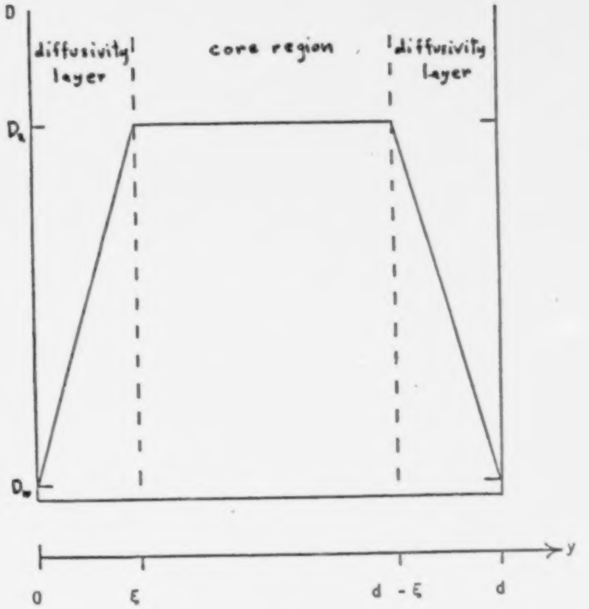

Figure 9. A schematic distribution of the nonuniform particle diffusivity in the plate-plate collector geometry.

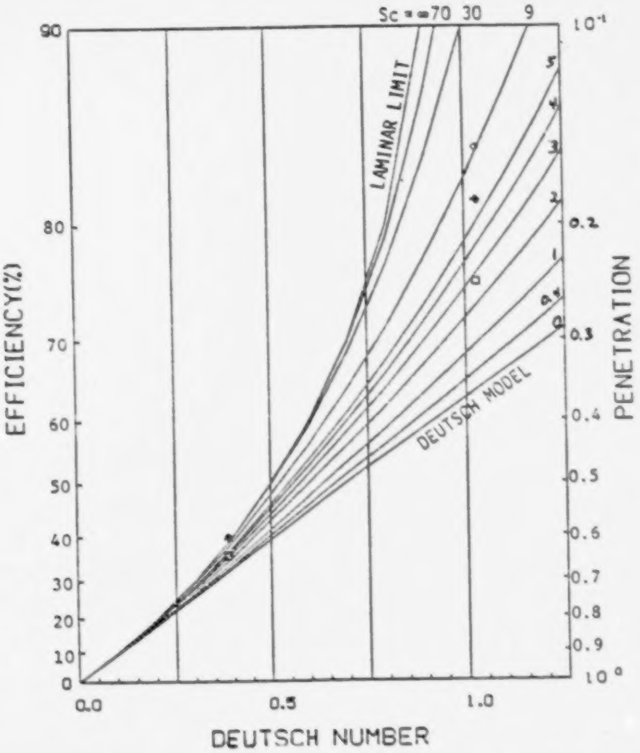

Figure 10. The plate-plate collector efficiency as a function of the Deutsch number for three different incoming turbulence conditions generated by three different baffle configurations: x = 40 cm from the inlet; 1-cm baffles ◇ (Sc = 14.8); 2-cm double baffles ⊕ (Sc = 11.1); 2-cm baffles □ (Sc = 6.35) (Schmidt numbers listed here are obtained from the estimated values of the core diffusivity by use of the nonuniform diffusivity model calculations.)

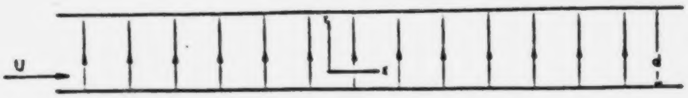

(a) Plate-plate collector

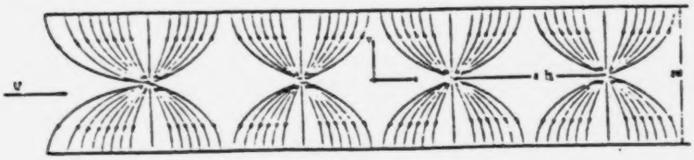

(b) Wire-plate collector (h = d)

Figure 11. Comparison of electric field lines for plate-plate and wire-plate laminar-flow collectors (h = d).

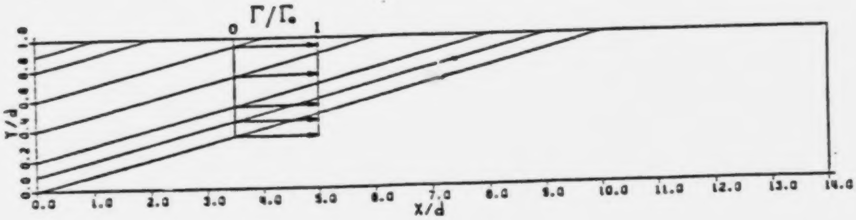

(a) Plate-plate collector

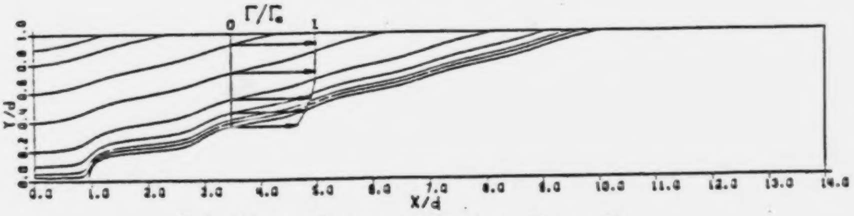

(b) Wire-plate collector (h = d)

Figure 12. Comparison of particle trajectories and fluxes for plate-plate and wire-plate laminar flow collectors.

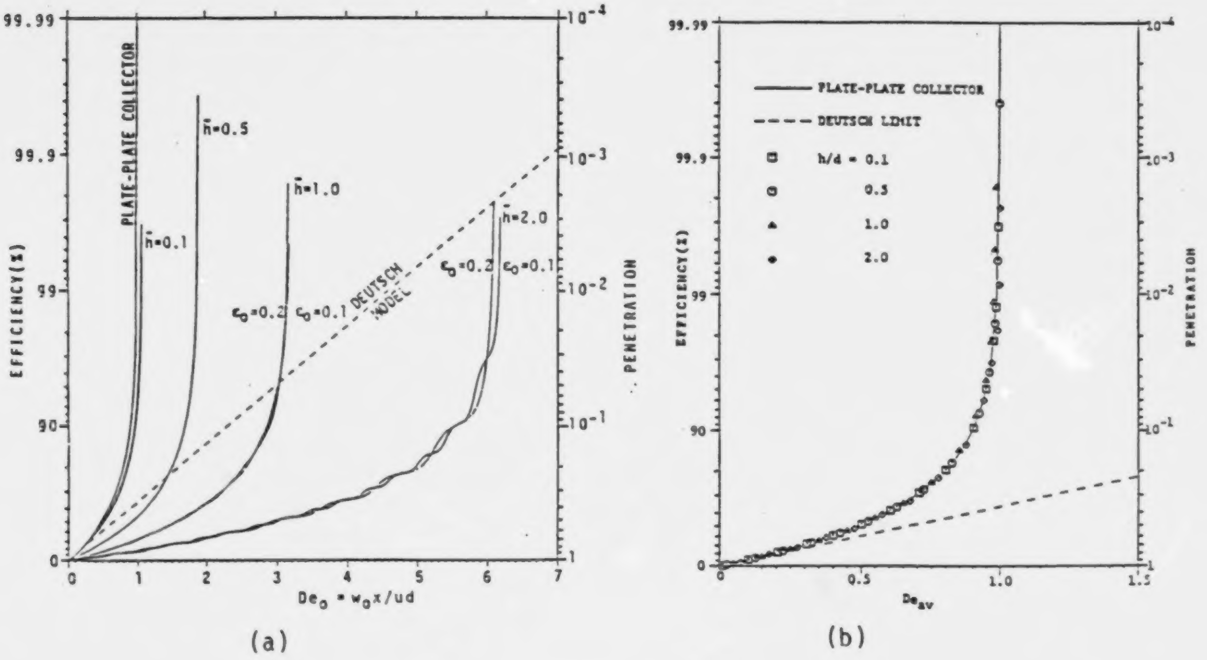

Deutsch number based on $E_0 \equiv (V_0/d)$ Deutsch number based on E_{av}

Figure 13. Dependence of collection efficiency on Deutsch number for laminar flow wire-plate precipitators ($\bar{a}$ = 0.01). Also shown are the plate-plate and Deutsch model (very large transverse turbulent diffusivity) cases.

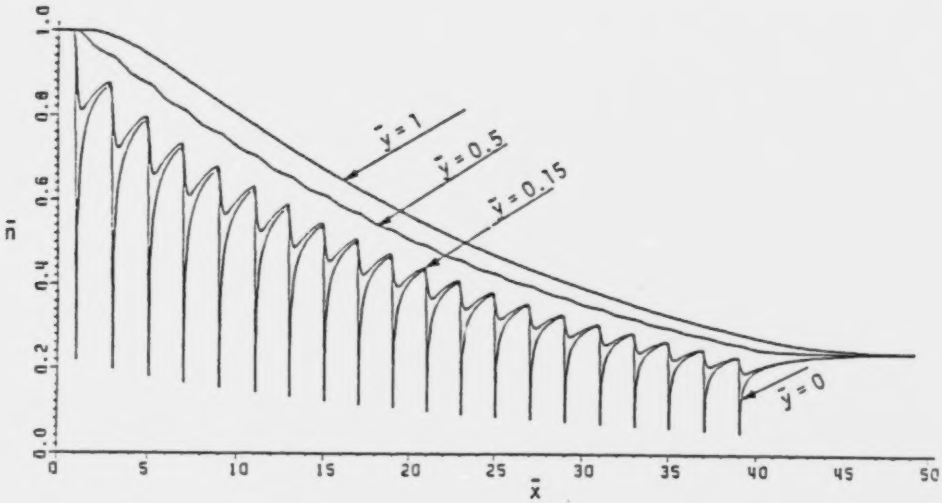

Figure 14. Distribution of the particle concentration profiles for the strip-plate collector as a function of x/d at y/d = 0, 0.15, 0.5, and 1.0, b/d = 0.02, $\varepsilon_0 = (w_0/u) = 0.1$ and $Pe_0 = 2.5$.

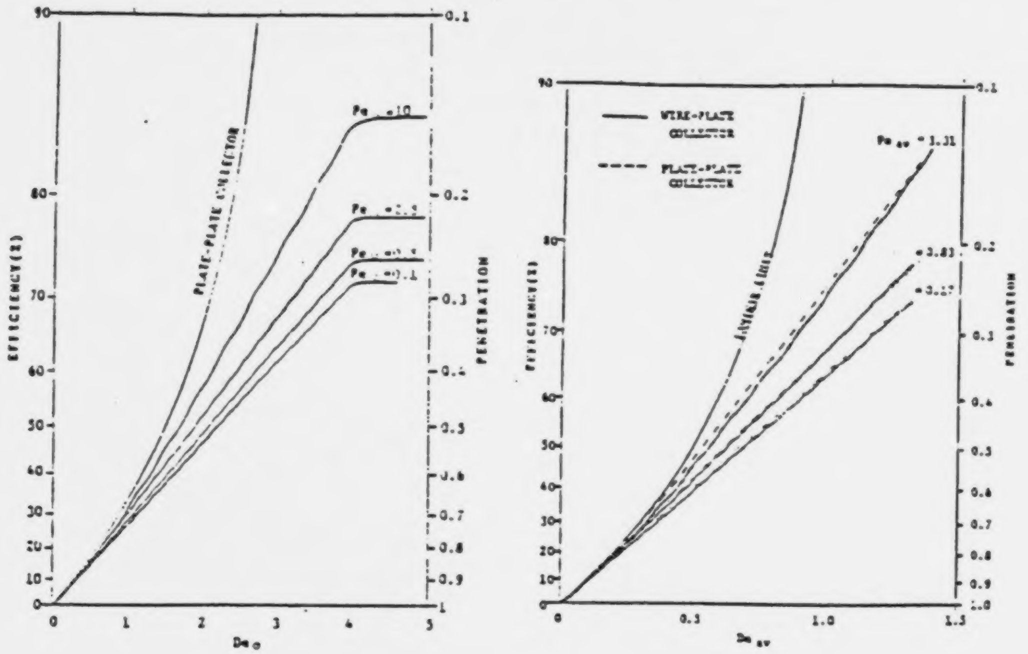

(a)

Deutsch and Peclet numbers based on E_0

(b)

Deutsch and Peclet numbers based on E_{av}

Figure 15. Dependence of collection efficiency on Deutsch number and Peclet number for turbulent flow wire-plate precipitators ($\bar{a} \simeq 0.02$), assuming a uniform value of diffusivity.

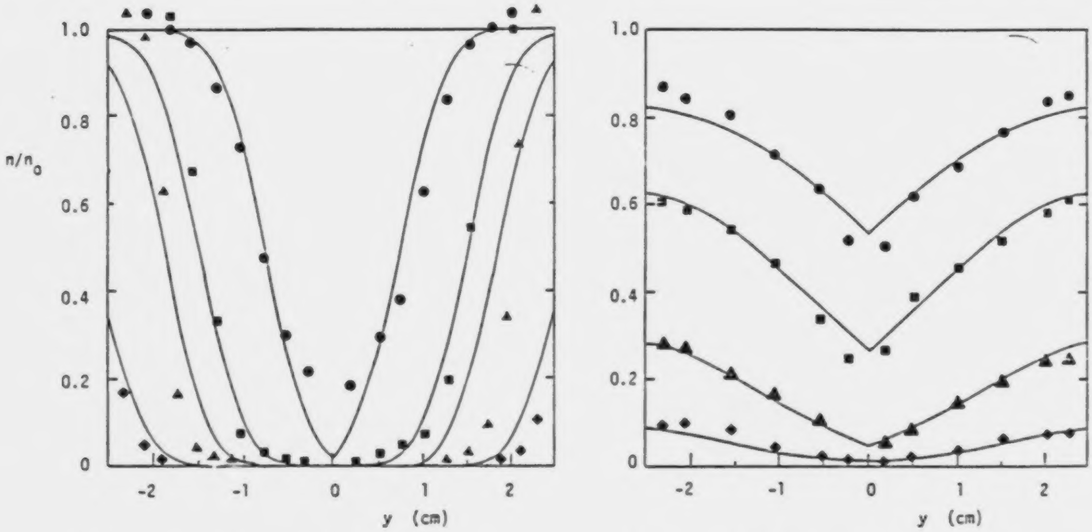

(a) Low inlet turbulence:

(b) High inlet turbulence generated by the 2-cm baffle configuration:

D = 0.4 cm²/s; ε_0 = 0.05 ●; ε_0 = 0.10 ■; ε_0 = 0.125 ▲; and ε_0 = 0.175 ◆

D = 10.0 cm²/s; ε_0 = 0.05 ●; ε_0 = 0.10 ■; ε_0 = 0.20 ▲; and ε_0 = 0.30 ◆

Figure 16. Particle concentration profiles in the wire-plate collector: u = 200 cm/s, x = 43.2 cm. Theory ———.

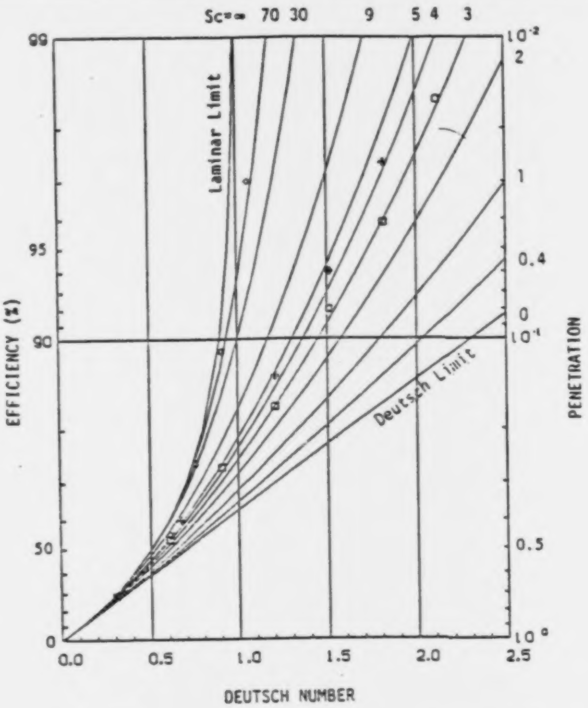

Figure 17. The collector efficiency as a function of the Deutsch number for different values of the Schmidt number: low turbulent flow (u = 200 cm/s) ◇; highly turbulent flow (u = 100 cm/s) ⊕; and highly turbulent flow (u = 200 cm/s) □. The flow turbulence is generated by 2-cm baffles.

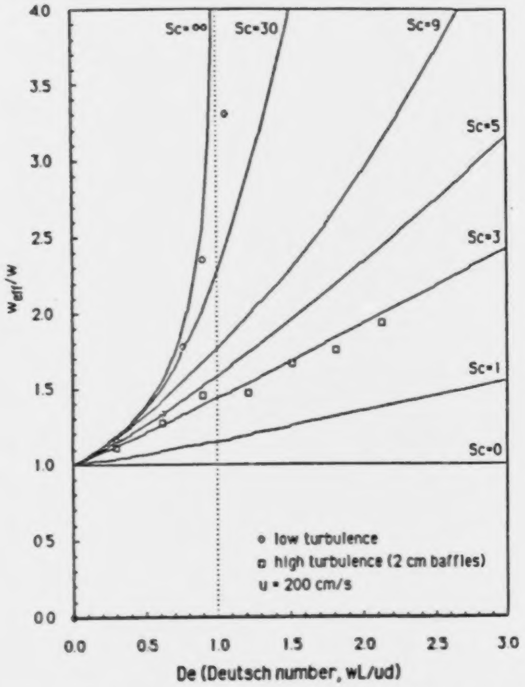

Figure 18. Precipitator performance expressed in terms of the effective migration velocity w_{eff}, given by the theoretical model that assumes uniform diffusivity and uniform electric field. Here w denotes the actual particle migration velocity, De is the Deutsch number, and Sc is the electric Schmidt number. The points represent experimentally determined values of the ordinate and abscissa, as discussed in this section.

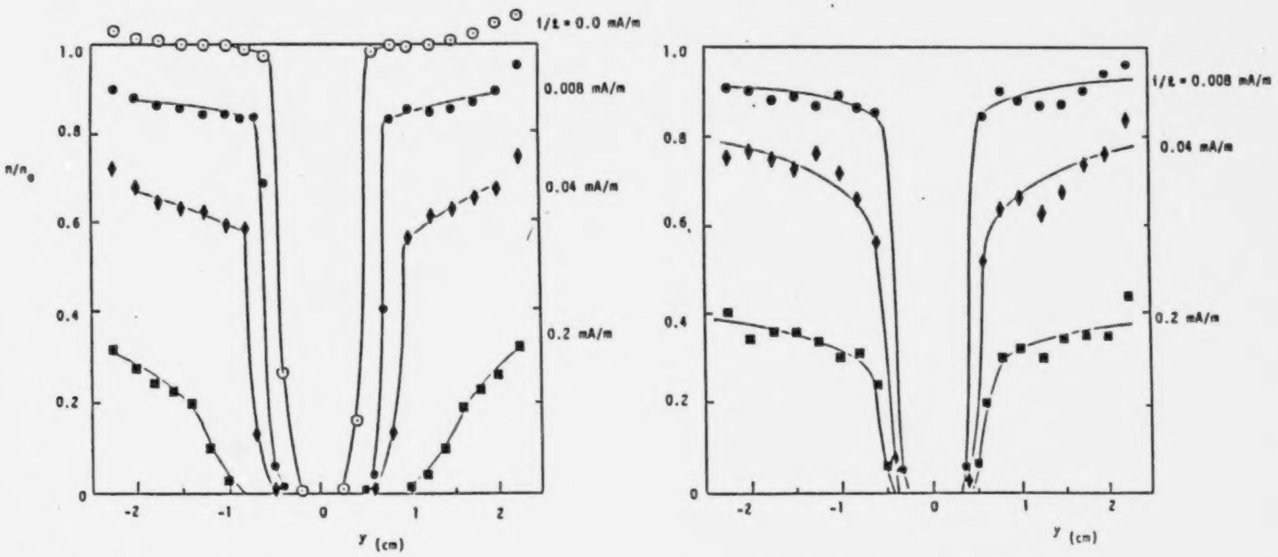

(a) positive corona

(b) negative corona

Figure 19. Particle concentration profiles in the wire-plate precipitator with precharged particles: u = 200 cm/s, x = 12.7 cm, wire diameter = 0.1 mm; i/ℓ = 0 ⊙; i/ℓ = 0.008 mA/m ●; i/ℓ = 0.04 mA/m ◆, and i/ℓ = 0.2 mA/m ■.

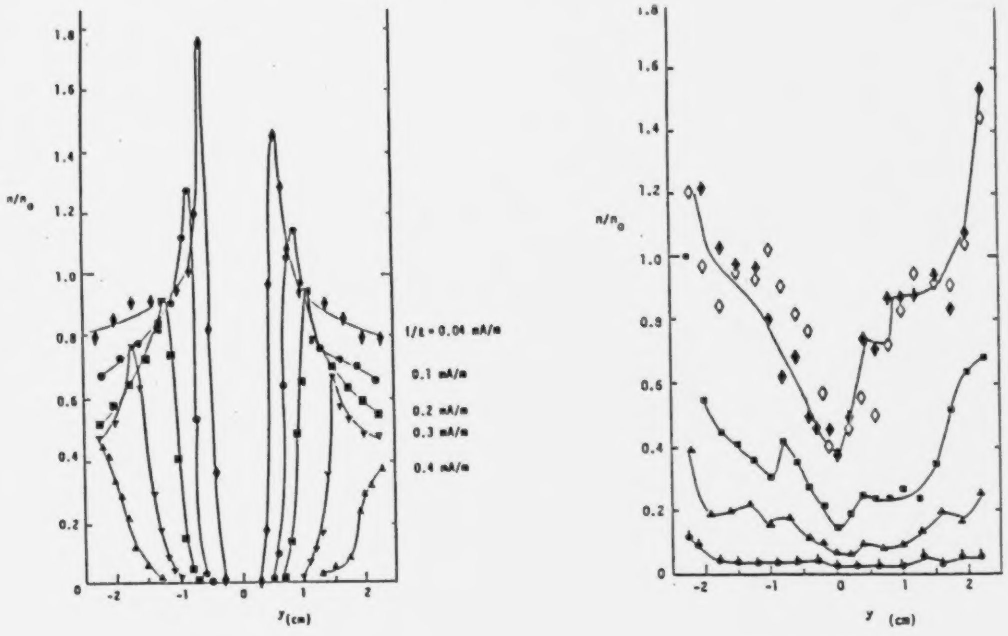

(a) positive corona

(b) negative corona

Figure 20. Particle concentration profiles in the wire-plate precipitator with initially neutralized particles: u = 200 cm/s, x = 43.2 cm, wire diameter = 0.1 mm; i/ℓ = 0.04 mA/m ◆, ◇; i/ℓ = 0.1 mA/m ●; i/ℓ = 0.2 mA/m ■; i/ℓ = 0.3 mA/m ▼; i/ℓ = 0.4 mA/m ▲; and i/ℓ = 0.6 mA/m ◐.

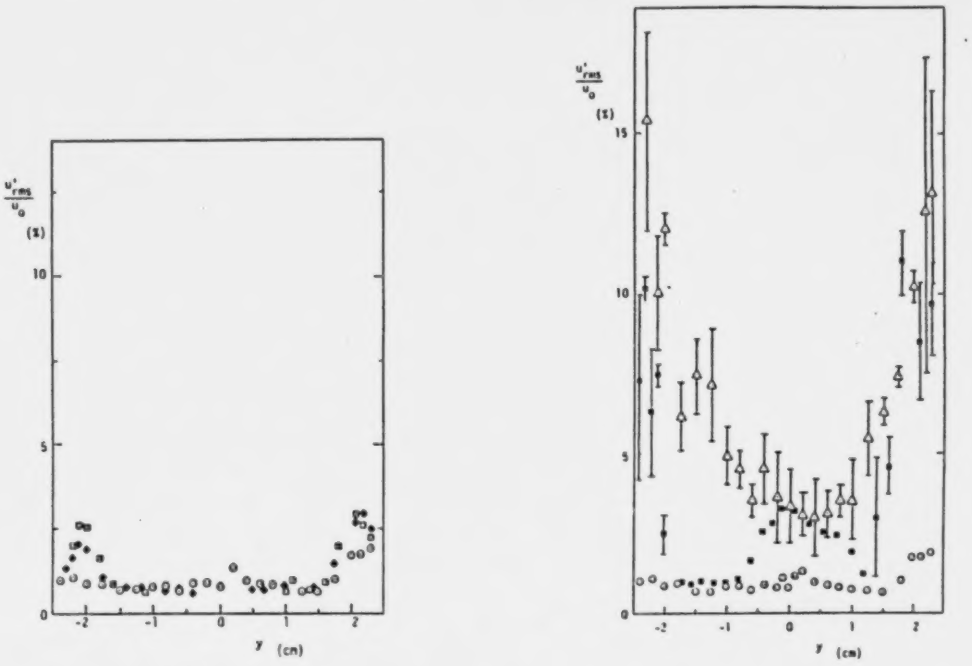

(a) positive corona

$i/\ell = 0$ ⊙; $i/\ell = 0.04$ mA/m ◆; $i/\ell = 0.1$ mA/m ⊡.

(b) negative corona

$i/\ell = 0$ ⊙; $i/\ell = 0.04$ mA/m ■; $i/\ell = 0.2$ ▲, ◆. (Extended bars represent the data fluctuations of repeated measurements.)

Figure 21. Laser Doppler measurements of turbulence intensity for initially neutralized particles in the wire-plate precipitator: u = 200 cm/s.

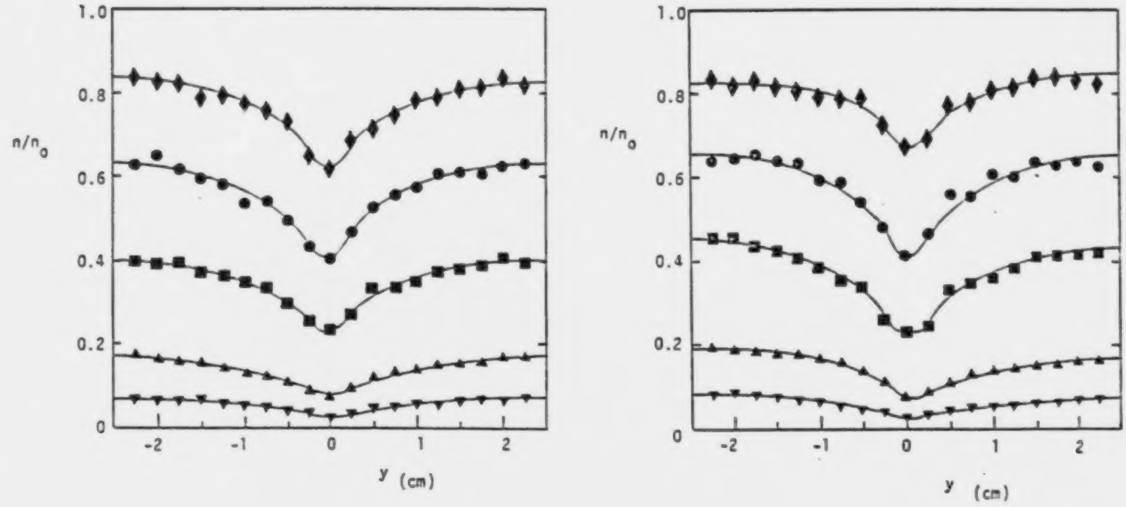

(a) positive corona

(b) negative corona

Figure 22. Particle concentration profiles in the wire-plate precipitator with turbulent flow generated by the 2-cm baffles: u = 200 cm/s, x = 43.2 cm, wire diameter = 0.1 mm; $i/\ell = 0.04$ mA/m ◆; $i/\ell = 0.1$ mA/m ●; $i/\ell = 0.2$ mA/m ■; $i/\ell = 0.4$ mA/m ▲; $i/\ell = 0.6$ mA/m ▼.

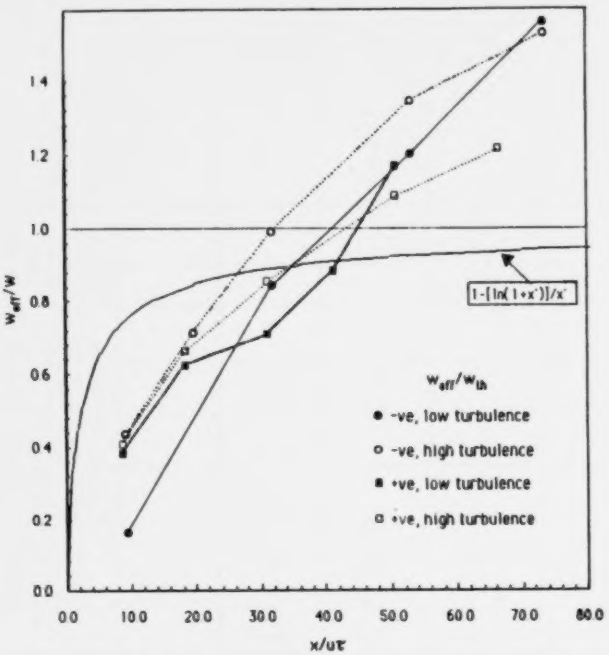

Figure 23. Reduction in precipitator efficiency, expressed in terms of w_{eff}/w, resulting from the finite particle charging rate. Theory is based on an extension of the Deutsch model. Experimental points are the values of w_{eff}/w_{th} determined from measurements with 0.1-mm wires (made between the 8th and 9th wires) for increasing values of corona current.

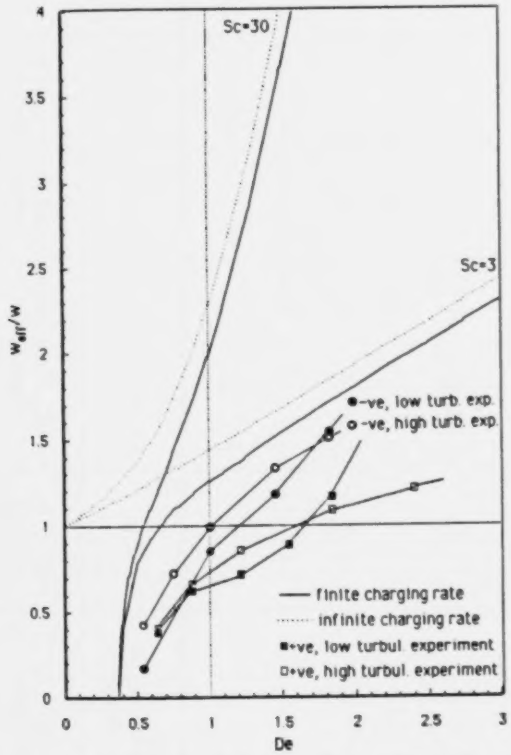

Figure 24. Precipitator performance showing the combined effects of both finite charging rate and finite diffusivity for the conditions of the experiments described in this section (x constant, and increasing corona current).

TABLE 1. TERM-BY-TERM ANALYSIS OF MECHANISMS GOVERNING PARTICLE TRANSPORT IN ELECTROSTATIC PRECIPITATORS

Main Focus of Interest	Mechanism					Experimental Conditions							Section
	Particle Convection by Mean Gas Flow	Particle Convection by Electric Field	Effect of Space Charge	Effect of Non-uniform Particle Charge	Turbulent Particle Diffusion	Experi-mental Configu-ration Used	Exper. Turbu-lence Level		Pre-Charged Par-ticles		Corona Dis-charge		
							low	high	yes	no	yes	no	
general steady-state convective-diffusion eqn.	$\vec{u}\cdot\nabla n$	$+\mu E\cdot\nabla n$	$+n\mu\nabla\cdot\vec{E}$	$+n\vec{E}\cdot\nabla\mu$	$= \nabla\cdot(D\nabla n)$	-							
uniform E uniform D	$u\,\frac{\partial n}{\partial x}$	$+\mu E_y\,\frac{\partial n}{\partial y}$			$= D\,\frac{\partial^2 n}{\partial y^2}$	plate-plate collector	✓		✓			✓	2.0
uniform E nonuniform D	$u\,\frac{\partial n}{\partial x}$	$+\mu E_y\,\frac{\partial n}{\partial y}$			$= D\,\frac{\partial^2 n}{\partial y^2} + \frac{\partial D}{\partial y}\,\frac{\partial n}{\partial y}$	plate-plate collector	✓	✓	✓			✓	3.0
nonuniform E uniform D	$u\,\frac{\partial n}{\partial x}$	$+\mu E_y\,\frac{\partial n}{\partial y} + \mu E_x\,\frac{\partial n}{\partial x}$			$= D(\frac{\partial^2 n}{\partial y^2} + \frac{\partial^2 n}{\partial x^2})$	wire-plate collector	✓	✓	✓			✓	4.0
space-charge ≠ 0 uniform particle charge	$u\,\frac{\partial n}{\partial x}$	$+\mu E_y\,\frac{\partial n}{\partial y} + \mu E_x\,\frac{\partial n}{\partial n}$	$+n\mu\,\frac{\rho_c}{\epsilon_v}$		$= D\,\frac{\partial^2 n}{\partial y^2}$	wire-plate charger/ collector	✓		✓		✓		5.0
space-charge ≠ 0 nonuniform particle charge	$u\,\frac{\partial n}{\partial x}$	$+\mu E_y\,\frac{\partial n}{\partial y} + \mu E_x\,\frac{\partial n}{\partial x}$	$+n\mu\,\frac{\rho_c}{\epsilon_v}$	$+n\vec{E}\cdot\nabla\mu$	$= D\,\frac{\partial^2 n}{\partial y^2}$	wire-plate charger/ collector	✓	✓		✓	✓		6.0

TABLE 2. EFFICIENCIES (%) DETERMINED FOR SINGLE-STAGE WIRE-PLATE EXPERIMENTS

i/ℓ (mA/m)	Positive Corona			Negative Corona		
	V_0 (kV)	low turb.	high turb.	V_0 (kV)	low turb.	high turb.
0.04	6.57	21.9	23.1	6.11	8.7	20.7
0.1	7.71	41.9	43.7	7.14	-	41.4
0.2	9.10	58.0	64.8	8.22	57.0	62.5
0.3	10.24	74.4	-	-	-	-
0.4	11.18	88.3	86.5	9.89	81.9	85.4
0.6	12.78	-	94.6	11.15	94.2	93.9

Wire diameter, $2a = 0.1$ mm; precipitator length, $L \simeq 40.6$ cm; precipitator breadth (height), $b = 25.4$ cm; plate-plate spacing, $2d = 5$ cm; wire-to-wire spacing, $2h = 5.08$ cm; gas velocity, $u = 200$ cm/s.

TABLE 3. CALCULATED VALUES OF w_{th}, De ($=w_{th}x/ud$), AND $x/u\tau$, BASED ON MEASURED ELECTRICAL CONDITIONS AND EFFICIENCIES (TABLE 2)
The values of w_{eff} are obtained using Eq. (12)

Electrical Conditions		Charging Time	Charging Parameter	Migr. Velocity	Deutsch Number	w_{eff}, cm/s		w_{eff}/w_{th}	
i/ℓ, mA/m	V_0, kV	τ, ms	$x/u\tau$	w_{th}, cm/s	De	lo trb	hi trb	lo trb	hi trb
0.00	+5.00	∞	0.00	4.5	0.37	--	--	--	--
0.04	+6.57	23.63	8.60	7.8	0.63	3.0	3.2	0.38	0.41
0.10	+7.71	11.09	18.32	10.7	0.87	6.7	7.1	0.62	0.66
0.20	+9.10	6.55	31.04	15.0	1.22	10.7	12.8	0.71	0.85
0.30	+10.24	4.91	41.38	19.0	1.54	16.8	--	0.89	--
0.40	+11.18	4.02	50.53	22.6	1.84	26.4	24.6	1.17	1.09
0.60	+12.78	3.06	66.31	29.5	2.40	--	35.9	--	1.22
0.04	-6.11	21.98	9.25	6.7	0.55	1.1	2.9	0.16	0.43
0.10	-7.14	10.27	19.78	9.2	0.75	--	6.6	--	0.72
0.20	-8.22	5.91	34.37	12.2	0.99	10.4	12.1	0.85	0.99
0.30	--	--	--	--	--	--	--	--	--
0.40	-9.89	3.56	57.13	17.7	1.44	21.0	23.7	1.19	1.34
0.60	-11.15	2.67	76.01	22.5	1.83	35.0	34.4	1.56	1.53

A NEW CONCEPT IN ELECTROSTATIC PRECIPITATOR GAS DISTRIBUTION

by: Arthur G. Hein
Hipp Engineering Ltd.
200 - 520 West 6th Avenue
Vancouver, B.C. V5Z 4J5
Canada

ABSTRACT

Field observations indicating that uniform gas flow at the precipitator outlet may not result in best performance led to a study of how re-entrainment and changes in gas distribution within a precipitator affect performance. A computer model developed in the study predicted that an improvement over uniform flow performance is possible by using controlled non-uniform gas distributions at both the inlet and the outlet faces of the precipitator. The model was used to study how changes in precipitator side view geometry affect performance and offers explanations for the reduction in precipitation constants experienced with larger installations.

The work described in this paper was not funded by the U.S. Environmental Protection Agency. The contents do not necessarily reflect the views of the Agency and no official endorsement should be inferred.

1. INTRODUCTION

Dust re-entrainment and gas flow distribution are important mechanical factors that affect the performance of electrostatic precipitators. This paper summarizes a study utilizing a computer model to simulate the changing conditions within a precipitator caused by re-entrainment and by variations in gas distribution.

Initial work on the model involved developing correlations that would explain

- field observations and published test data that show most of the dust emission occurs from the lower part of the precipitator outlet face; and
- field observations that indicate precipitators with outlet nozzles that lift the gas generally perform better than those with outlet nozzles that draw the gas downward.

The computer model was used to demonstrate that with a uniform inlet gas distribution, the precipitator outlet nozzle configuration affected the performance as suggested by the field observations. Further work with the model involved varying the inlet gas distribution as well as the outlet. This resulted in a prediction that controlled non-uniform gas distributions at both the inlet and the outlet are better than a uniform gas distribution.

The model was also used to study how the side view geometry of a precipitator affected performance. The common relationships used to determine the precipitator collecting surface area for a particular application do not specify how the surface should be arranged. Side view geometry influences performance as confirmed by the following observations.

- The length/height aspect ratio is recognized as an important design parameter. Precipitators with low aspect ratios do not perform well.
- Pilot size precipitators generally operate with higher precipitation constants than full sized precipitators.
- The trend to higher efficiencies and larger gas volumes has produced precipitators with increased curtain height. It also has resulted in reduced values of precipitation constants and modified equations to fit the measured performance data.

Re-entrainment of dust as it falls from the point of collection to the bottom of the precipitator is believed to be responsible for these observations and the simulations used in the computer model provide mathematical explanations for them.

The purpose of this paper is to describe the computer model and to illustrate the qualitative trends predicted by the model. The paper begins with a review of observations relating to re-entrainment and gas flow distribution that are basic to understanding the model. This is followed by a description of the model and some results from testing the model.

2. RE-ENTRAINMENT

Re-entrainment is the loss back into the gas stream of dust that had been deposited on precipitator electrodes. Mechanical shaking, called rapping, is required to dislodge the dust which then falls due to gravity toward the bottom of the precipitator. The rapping cycle is usually controlled at intervals to allow a layer of dust with some mass to accumulate on the collecting surfaces between raps. Considerable re-entrainment takes place upon rapping and the affected gas passages become heavily filled with dust. Direct visual observation of re-entrainment is difficult, however, other observations may be used to reconstruct what takes place.

A loosely packed dust layer accellerating downward through the gas stream produces viscous forces that cause erosion and re-entrainment of some of the dust. Abrasion between the dust layer and the electrodes also causes the falling dust layer to break up and disperse. These actions result in a short duration of high dust concentration toward the bottom of the gas passages in which electrodes have been rapped. Rapping is often accompanied by a "puff" as indicated by continuous monitoring equipment or seen visually from the stack. Rapping puffs do not occur just from outlet field rapping. They have been observed from rapping the inlet fields in a three-field pecipitator.

Re-entrainment of dust as it falls from the electrodes and gravity settling of uncollected dust both increase the dust loading in the lower zone as the gas flows through the precipitator. The resulting non-uniform dust load at the outlet has been reported by the Southern Research Institute for tests on a nearly full-scale pilot precipitator (1) and has also been observed visually in full-scale installations.

Not all dust falling from the collecting surfaces is dislodged during rapping. Some is dislodged between rapping cycles. This has been observed through windows on the top of operating precipitators and is confirmed by the Southern Research Institute tests. If dust was dislodged only during rapping, then the top-to-bottom dust loss between rapping cycles would tend to be uniform, however the loss reported between raps is still much higher at the bottom than at the top. Thus the actions causing re-entrainment occur not only during rapping cycles but at all times.

3. GAS DISTRIBUTION

Uniform gas flow throughout the precipitator is generally accepted as giving the best performance. This is based in part on mathematical analyses that assume a constant dust distribution over a cross-section perpendicular to the gas flow. This dust distribution would occur only if no dust was re-entrained during the fall toward the bottom. Re-entraiment increases the dust loading at the bottom of the precipitator relative to the top. Uniform gas flow, although best for a uniform top-to-bottom dust loading, may not be best for a non-uniform loading.

The treatment zone of a precipitator operates at low velocity and offers little resistance to gas flow, therefore very little influence is required to change the flow distribution from top to bottom.

Inlet gas distribution has been considered more critical to performance than outlet gas distribution. Many precipitators have been installed with corrective devices at the inlet but with none at the outlet. If the outlet ductwork has a tendency to draw the gas flow upward or downward, there will be large scale vertical movement of the gas as it flows from the inlet to the outlet. For those installations in which the gas flow is drawn downward, higher than average gas velocity occurs in the treatment zone where the dust concentration is higher than average. Poor overall performance and heavy rapping losses have been observed in some of these. On the other hand, ductwork that favors a higher flow toward the top of the outlet results in lower than average flow in the more heavily loaded zone. Installations with this configuration usually perform without heavy rapping losses.

4. MODEL DESCRIPTION

4.1 OVERVIEW

A side view precipitator analysis is required to study these observations relating performance to gas flow distribution and to re-entrainment. The investigation must consider changes from the top to the bottom as the flow travels from inlet to outlet.

A two-dimensional computer model was developed. The model divides the side view of the precipitator treatment zone into elements using a grid as shown by Figure 1. The model treats each grid element as a miniature precipitator and applies the classic Deutch-Anderson equation (see paragraph 5.3) using the gas velocity at the center of the element and dust loading at the inlet of the element, to compute the dust collected by the element and the dust load leaving the element.

4.2 SKEW FACTOR

A skew factor ranging between the limits of -1 and +1 was defined to study variations in gas distribution from the top to the bottom of the precipitator. This is shown by Figure 2.

The model applies the skew factor value assigned at the inlet face to determine the flow velocity for the elements across the inlet face. It then adjusts the velocity skew in a linear fashion from the inlet to the outlet while maintaining a constant total flow across each vertical increment to arrive at the skew factor value assigned at the outlet face.

4.3 RE-ENTRAINMENT FUNCTION

The dust collected by an element is eventually dislodged and must fall through all the elements below it to be removed by the precipitator. Some of it will be re-entrained as it falls downward. A function is required to express the quantity of dust re-entrained into each element below the element in which it was collected as it falls to the bottom of the precipitator. Figure 3 illustrates the re-entrainment model.

The re-entrainment function has the form $r = f(s)$ where

r is the fraction of dust entering the top of an element that leaves the outlet end rather than the bottom of an element.

s is the number of elements below the element in which the dust was collected.

A simple function $r = A \times s^B$ was used to demonstrate the effects of re-entrainment. For a value of $B = 2$, re-entrainment varies with the square of the distance the dust has fallen, and for $A = .005$, most of the dust falling from the top element will be dispersed before reaching the bottom of a 10 element grid. The model applies the re-entrainment function to the dust collected in each element as it falls through the elements below it. Dust collected in the top element falls through 9 elements, and for the assumed constants only 18.8% reaches the bottom. Dust collected in the fourth element above the bottom falls through only 3 elements, and 93.1% reaches the bottom. These results are illustrated by Figure 4.

4.4 GRID DIMENSIONS

The number of grid elements in each direction is variable. Choosing the number of vertical elements is related to expressing the re-entrainment function in sufficient detail. Choosing the best number of horizontal elements is not as clear. For a given overall efficiency and given re-entrainment constants, increasing the number of horizontal elements decreases the difference between the dust loading at the top and the bottom leaving the precipitator and decreases the proportion of the total loss due to re-entrainment.

4.5 PERFORMANCE COMPUTATION

The model uses a numerical procedure to compute performance column by column, beginning with the element at the top of the inlet face.

Except for the elements along the top row and at the inlet face, the inlet load to each element has two components; the outlet load from the element immediately upstream, and the re-entrainment losses from dust falling through the element immediately upstream. The dust entering each element per unit of time and the velocity at the center of the element are used to compute the collection by the element.

The re-entrainment function is applied to the dust collected in each element and the re-entrained dust becomes part of the inlet dust loading for the elements in the next column. This procedure is applied to each successive column to arrive at the outlet face losses. If the outet skew factor is different than the inlet, adjustments are applied to account for discontinuity in flow between elements in adjacent columns to ensure all the dust leaving one column is accounted for in the inlet loading to the next column.

Except for the bottom row of elements, the dust collected by each element is subject to re-entrainment and only the dust falling below a bottom element is truly collected.

5. MODEL TEST RUNS

The relationships presented in this section were developed by first choosing a reference condition with a specified overall efficiency and running the model to establish the precipitation constant. This constant was then used in further runs to calculate new efficiencies for changes in gas distribution (pp 5.1 and 5.2) or geometry (pp 5.3). The model was tested with a set of conditons as follows.

- A precipitator operating at an overall efficiency of 99.0% with uniform gas flow distribution was used as a reference point for all runs.
- The test runs with re-entrainment use the function and constants as described in pp 4.3.
- A grid with dimensions of 10 vertical by 6 horizontal elements was used for the fixed geometry runs and as the basis for comparing changes in geometry.

With non-uniform gas flow it is necessary to distinguish between the dust load per unit time and dust concentration. In the shaded figures, dust load per unit time is displayed graphically.

5.1 FIXED GEOMETRY, NO RE-ENTRAINMENT, VARY THE GAS DISTRIBUTION

5.1.1 Uniform Inlet and Uniform Outlet Gas Distribution

For this condition, the model produced the uniform top-to-bottom dust loadings shown by Figure 5.

5.1.2 Uniform Inlet Distribution, Vary the Outlet

A series of runs produced the charactaristic shown by Figure 6. The best performance was with uniform flow. Performance fell off equally with either a negative or a positive skew as the increased losses in the high velocity zone outweighed gains in the low velocity zone. Holding the outlet distribution uniform and varying the inlet produced a similar characteristic and showed that performance was slightly more sensitive to the inlet than to the outlet gas flow distribution.

5.1.3 Skewed Inlet Distribution, Vary the Outlet

Figure 7 illustrates that with an inlet skew in one direction and an outlet skew of equal magnitude but opposite direction, the performance is almost as good as with uniform gas flow distribution. This result is important when considering performance with re-entrainment. Figure 8 shows the dust loading with this gas distribution.

The conditions with the skewed gas distribution at the inlet face of Figure 8 illustrate the difference between dust concentration which is uniform top-to-bottom, and dust loading per unit time which is non-uniform.

5.2 FIXED GEOMETRY, WITH RE-ENTRAINMENT, VARY THE GAS DISTRIBUTION

5.2.1 Uniform Gas Distribution

With uniform gas flow and a re-entrainment function, the dust distribution is not uniform leaving the precipitator. The loading at the bottom becomes progressively higher than at the top as the flow travels from inlet to outlet as seen in Figure 9.

Notice that the elements across the top row of the model are not affected by re-entrainment losses as defined by the model, and the performance across the top is therefore as predicted by the Deutch-Anderson equation. This information can readily be used to determine the contribution of re-entrained dust to the total emission. For this example, the contribution due to re-entrainment is 80 percent.

The outlet dust distribution shown in Figure 9 suggests moving away from uniform gas distribution at the outlet of the precipitator. Raising the flow would result in less treatment time at the top where the gas is clean and more treatment time at the bottom in the more heavily loaded zone. The model was tested to demonstrate this.

5.2.2 Uniform Inlet Distribution, Vary the Outlet

The initial objective of the study was to display the characteristic shown by Figure 10. Note there is only a little improvement available as the outlet skew is increased above 0.0, but that for a skew up to +0.4 the performance is better than for uniform flow. The performance falls off very quickly with a negative inlet skew.

5.2.3 Skewed Inlet, Vary the Outlet

A series of runs was conducted with a fixed negative skew at the inlet while varying the outlet. These runs produced the surprising results shown by Figure 11.

The model predicts that a substantial improvement in performance is available for a negatively skewed inlet combined with a positively skewed outlet of similar magnitude. Figure 12 shows the dust loading with this gas distribution.

The improved performance may be explained by considering the dust loss in two fractions.

The first fraction is dust which has not previously been collected. This fraction is not affected by re-entrainment and would therefore be little affected by the skewed gas distribution as was shown by Figure 7.

The second fraction is dust which was collected and then re-entrained. This fraction is affected by the skewed distribution. Since the skewed distribution introduces more of the dust closer to the bottom, the average distance for collected dust to fall to the botttom is less and re-entrainment losses are reduced.

5.3 UNIFORM GAS DISTRIBUTION, WITH RE-ENTRAINMENT, VARY THE GEOMETRY

The model was tested with changes in geometry in order to compare predictions of performance with other predictions and with field experience.

The Deutch-Anderson equation

$$Q = e^{-(A/V)w}$$

where Q is fractional loss

A is effective collecting surface area

V is the gas flow rate

w is the overall migration velocity

relates specific collecting surface area A/V to performance with a single parameter w, regardless of the length/height aspect ratio. Introducing a re-entrainment function results in performance being dependent on how the surface is arranged. Figure 13, based on uniform gas flow, illustrates the trends predicted by the model.

If the collecting surface height is held constant and the collecting surface area is increased by extending the length in the direction of gas flow, then performance increases at a rate slightly better than predicted by the Deutch-Anderson equation. If the collecting surface length is held constant, and the collecting surface area is increased by extending the curtain height, then performance increases at a rate much less than predicted by the Deutch-Anderson equation and more like the performance predicted by the Matts-Ohnfeldt modified Deutch-Anderson equation

$$Q = e^{-(A/V)w^k}$$

with the commonly assigned exponent k = 0.5. An increase in re-entrainment losses is responsible for the reduced performance. If the collecting surface area is increased by keeping the aspect ratio constant, then performance falls between lines 3 and 4.

Figure 14 shows the trends predicted by the model with various collecting surface heights. Better performance with shorter surfaces is consistent with pilot precipitator experience. Reduced performance with taller surfaces is consistent with recent experience with large precipitators where performance has generally fallen below the prediction by Deutch-Anderson and resulted in performance equations with more than one constant.

6. ASSUMPTIONS

6.1 The model assumes time averaged conditions and applies the same precipitation constant to previously uncollected dust as to re-entrained dust. In practise, previously uncollected dust is well dispersed, whereas the dust load contribution due to rapping re-entrainment is heavily concentrated during short time intervals. The constants may be much different.

6.2 The model does not account for gravity settling of uncollected dust.

6.3 Linear gas distribution skews have been used to show trends. Nonlinear skews at the inlet and outlet may give better performance.

6.4 The model assumes a linear change in the gas distribution profile from the inlet skew to the outlet skew. In practise, the gas distributions may be controlled at the precipitator inlet and outlet faces, and the change in the skew from the inlet to the outlet may not take place in a linear fashion.

7. CONCLUSIONS

7.1 A two-dimensional side view model of a precipitator can be used to study the effects of re-entrainment and of changing gas distribution within a precipitator.

7.2 The model shows effect on performance of the gas flow distribution at the outlet face is about the same as at the inlet face.

7.3 Measurement of dust emission at the top of the precipitator outlet face can be used to determine the Deutch-Anderson precipitation constant without re-entrainment.

7.4 Re-entrainment causes changes in the overall precipitation constant with changes in side view geometry. Re-entrainment as defined in this paper can be used in conjunction with the Deutch-Anderson equation to explain the higher precipitation constants experienced with the small pilot precipitators and the lower precipitation constants experienced with the larger precipitators utilizing increased collecting surface height.

7.5 The model predicts that controlled non-uniform gas distributions at the inlet and the outlet faces can be used to improve the performance of a precipitator.

8. RECOMMENDATIONS

8.1 A statistical review of precipitator performance related to ductwork configuration should be conducted. This would help confirm the model predictions of improved performance with skewed gas distributions.

8.2 The top-to-bottom dust distribution profile at the outlet face of full scale precipitators with reasonably uniform gas flow distribution should be measured to establish re-entrainment functions.

8.3 The model predictions of improved performance with skewed distributions should be tested on a full scale installation, preferrably where the tests described in recommendation 2 have been conducted.

9. PATENTS

United States Patent 4,695,297 has been issued to the author. This patent describes supplying more than one-half the total gas flow into the lower half of the treatment zone and exhausting more than one-half of the gas flow from the upper half of the treatment zone. A Canadian patent is pending.

10. REFERENCE

1. Spencer, H.W., Southern Research Institute, 1976, "Rapping Re-entrainment in a Nearly Full-Scale Pilot Electrostatic Precipitator", EPA-600/2-76-140

11. ILLUSTRATIONS

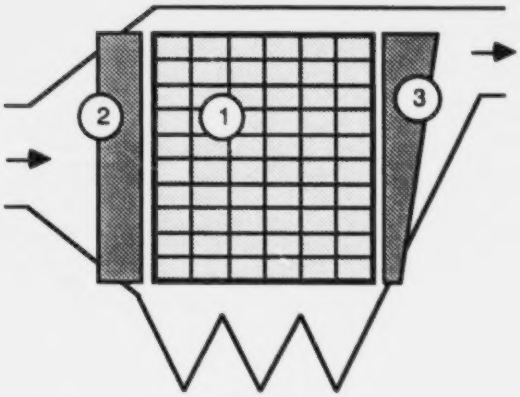

Figure 1 Precipitator side view. 1 is the model treatment zone grid. 2 and 3 are graphic indications of the gas flow distributions with ductwork favouring uniform inlet and raised outlet flow.

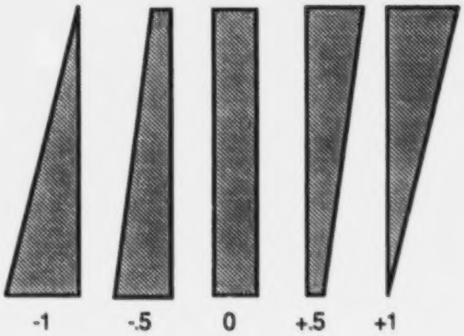

Figure 2 Skew factor definition. A negative skew favours flow toward the bottom and a positive skew favours the top. The skew factor for uniform flow is zero.

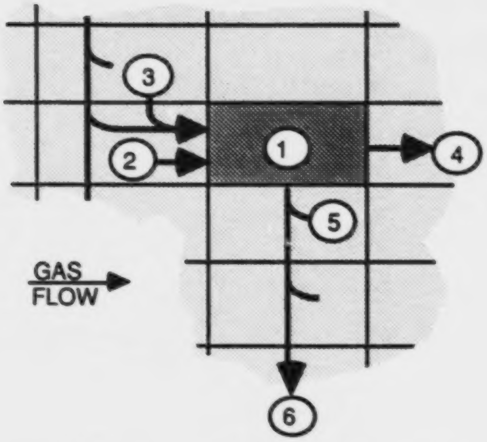

Figure 3 Re-entrainment model.
1 element under consideration
2 inlet load from upstream element
3 inlet load due to re-entrainment from higher upstream elements
4 loss from element 1
5 re-entrainment loss of dust collected in element 1
6 remainder from element 1

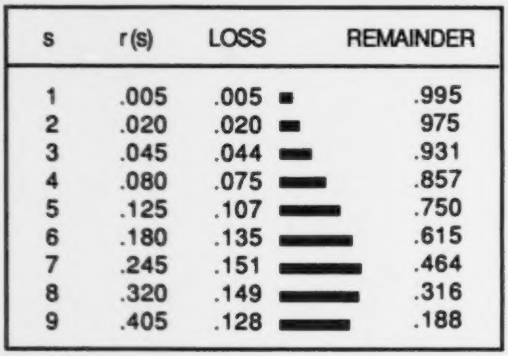

s	r(s)	LOSS	REMAINDER
1	.005	.005	.995
2	.020	.020	975
3	.045	.044	.931
4	.080	.075	.857
5	.125	.107	.750
6	.180	.135	.615
7	.245	.151	.464
8	.320	.149	.316
9	.405	.128	.188

Figure 4 LOSS is the fraction of the initial collection dispersed into element s. REMAINDER is the fraction of the initial collection still falling downward after passing through element s.

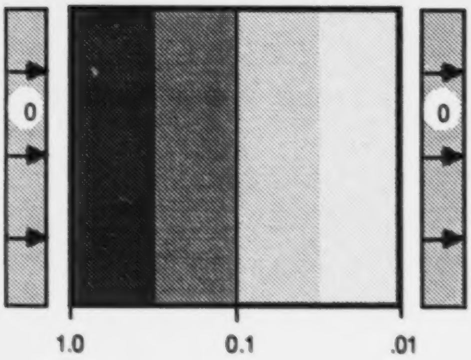

Figure 5 Dust loading with uniform inlet and outlet gas flow and no re-entrainment as given by the Deutch-Anderson equation.

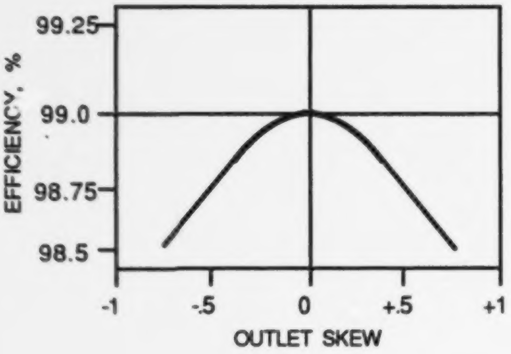

Figure 6 With no re-entrainment and zero inlet skew, performance falls off equally with either a positive or negative outlet skew.

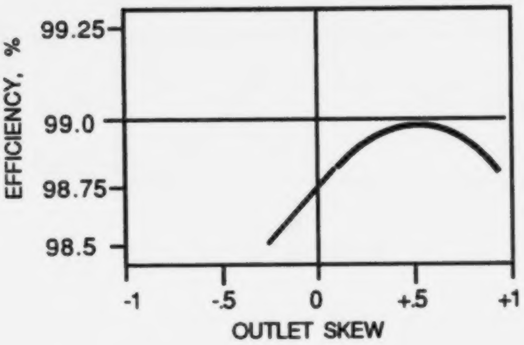

Figure 7 With no re-entrainment and a -0.5 inlet skew, performance increases with a positive outlet skew to near that of uniform flow.

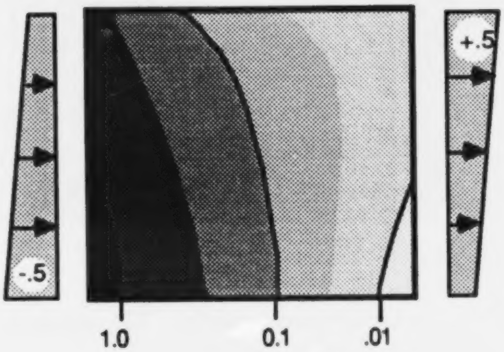

Figure 8 Dust loading with the -0.5 inlet and +0.5 outlet skews shown at the maximum point of the Figure 7 curve.

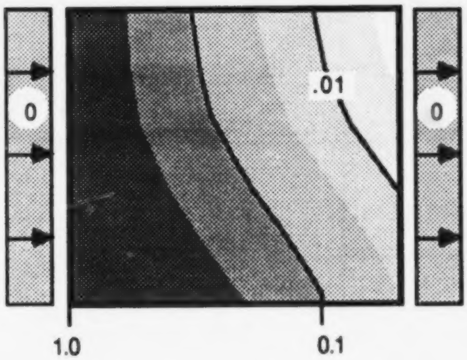

Figure 9 Dust loading with re-entrainment and uniform inlet an d outlet flows as shown at the 0 skew 99% efficiency reference point of the Figure 10 curve.

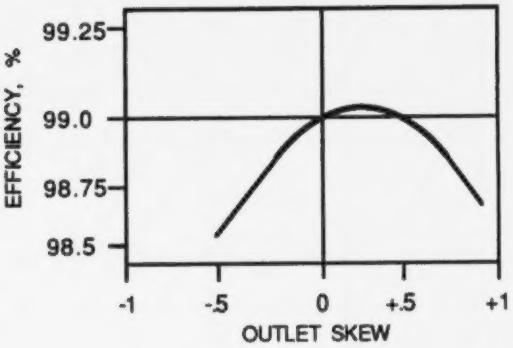

Figure 10 With re-entrainment and uniform inlet gas flow distribution, performance falls off quickly with a downflow(-) outlet but improves a little with an upflow(+) outlet.

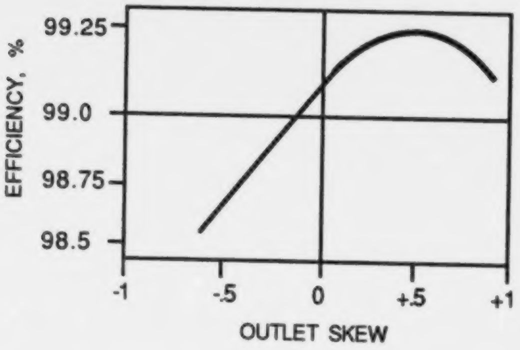

Figure 11 Performance with an inlet skew of -0.5 and with re-entrainment. A positive outlet skew to about +0.5 improves performance well above the 99.0% achieved with uniform flow.

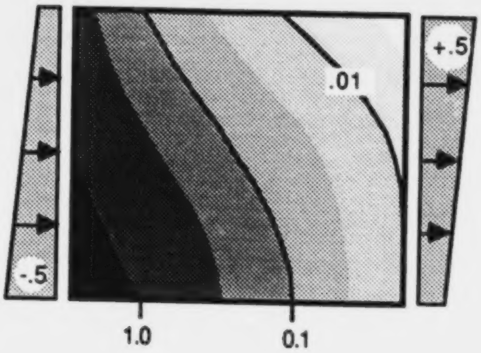

Figure 12 Dust loading with a -0.5 inlet skew and a +0.5 outlet skew as shown at the point of best performance by the Figure 11 curve.

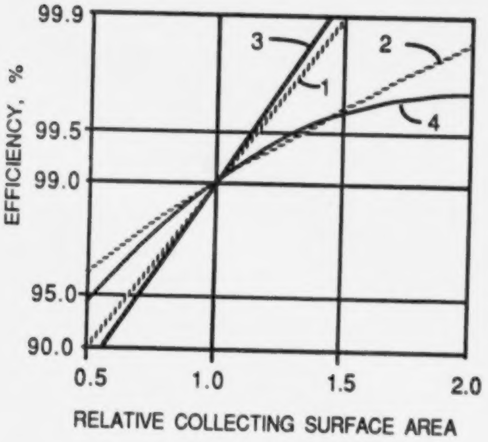

1 Deutch-Anderson
2 Modified Deutch-Anderson, k =.5
3 Vary the collecting surface length
4 Vary the collecting surface height

Figure 13 Uniform gas flow and re-entrainment. Lines 3 and 4 show that performance depends on how the collecting surface is arranged.

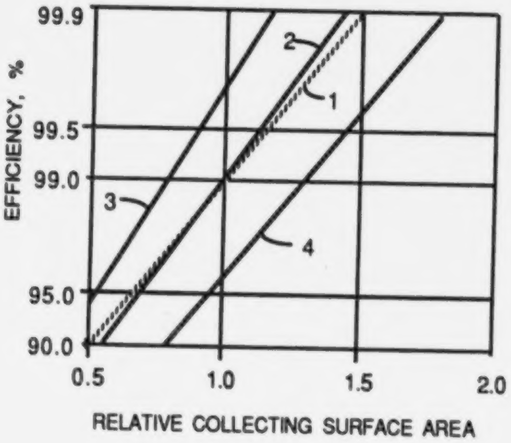

1 Deutch-Anderson
2 Base collecting surface height,h
3 Collecting surface height = 0.5h
4 Collecting surface height = 1.5h

Figure 14 Uniform gas flow and re-entrainment. For a given surface area, performance decreases with increased collecting surface height.

STRUCTURAL REPAIR OF LARGE HOT-SIDE ELECTROSTATIC PRECIPITATORS - AN UPDATE

By: Charles A. Altin
Project Manager
Raymond A. Schmidt
Senior Structural Design Engineer
Kiran K. Fatehpuria
Senior Structural Design Engineer
Ebasco Services Incorporated
Norcross, Georgia 30092

ABSTRACT

Recently, the electric utility industry has been faced with environmental regulations which encouraged and even demanded the use of lower sulfur coals. In some instances, low sulfur coals caused performance problems in existing precipitators and created concern about new installations. In the early- to mid-1970s, hot-side precipitators appeared to offer a solution to the cold-side performance problems. Initially, hot-side precipitators were installed on relatively small generating units and met with a good deal of success. This success coupled with the need for large increases in generating capacity prompted the industry to consider using hot-side precipitators on larger units. Over the past ten years, great attention has been given to the performance problems of hot-side precipitators as a function of fuel quality. However, little has been reported on the structural implications of operating larger structures at sustained high temperatures.

This paper discusses the results of structural investigations on large hot-side electrostatic precipitators conducted over the past nine years. These investigations resulted in the development of a unified theory of the dynamics of structural distress experienced by hot-side precipitators. Once the theory of distress was formulated, an analytical computer model was developed. This computer model can simulate the progressive and irreversible damage experienced by precipitators and then produce a repair strategy. In addition to the inclusion of conventional loading criteria such as wind, snow, and seismic excitation, the model incorporates loadings due to thermal gradients within the structures; effectiveness of sliding bearings; fly ash buildups in ductwork; redistribution of loads due to uplifted columns; and asymmetrical expansion due to the time dependency of heat transfer.

STRUCTURAL REPAIR OF LARGE HOT-SIDE ELECTROSTATIC PRECIPITATORS - AN UPDATE

For more than 60 years, the electric utility industry has been using electrostatic precipitators for the control of fly ash emissions. As the size of coal-fired electric generating units increased and environmental regulations became more stringent, precipitator suppliers had to design larger, more efficient precipitators. When these precipitators were placed into service, precipitator suppliers gained valuable experience which led to better sizing procedures, expanded data bases, improvement of internal components, and the engineering and design of larger more complex structures - in essence, a self-generated learning curve.

As electric utilities sought to control emissions of sulfur oxides, the use of lower sulfur coals became more widespread. However, in many cases the use of low-sulfur coal resulted in poor performance for traditional cold-side precipitators. Cold-side precipitators located downstream of the air heaters, whose flue gas temperatures normally range between 260° and 300°F, encountered high-resistivity conditions. In an attempt to overcome high-resistivity conditions, some suppliers found that in their initial characterizations of eastern low-sulfur coals, fly ash resistivity levels significantly and dramatically decreased when flue gas temperatures exceeded 600°F. This reduction in resistivity indicated that it would then be possible to collect the fly ash if a precipitator was located upstream of the air heater. Flue gas temperatures leaving the economizer would normally be in the range of 550° to 850°F. Thus, the term "hot-side precipitator" was developed.

From a performance standpoint, initial installations of hot-side precipitators were generally on relatively small units firing eastern low-sulfur coals. These units performed very well with little variation in the effective migration velocity. This, then, seemed to be the answer to the variability in performance experienced by cold-side precipitators in terms of reduced effective migration velocities, wire and plate fly ash buildups, and back ionization conditions. Initially, the reduction in the variability of effective migration velocities associated with hot-side precipitators led to expedient simplifications in sizing hot-side precipitators with migration velocities on the order of 10 cm/sec. This hot-side sizing factor, when compared to cold-side sizing factors, resulted in precipitator casings which offered a competitive advantage over cold-side precipitators. The trend of applying hot-side precipitators to low-sulfur coals expanded into the western coal marketplace. As more experience was gained with hot-side precipitators on a greater variety of coals, the popular notion or hope of universal sizing factors eroded. In the early to mid-1970s, hot-side migration velocities dropped to approximately 6 cm/sec for western coals. During this time, some suppliers maintained that cold-side precipitators could be designed and successfully operated on these same western coals; however, cold-side precipitators still tended to be slightly larger and more expensive than comparable hot-side units. As the economic advantages of hot-side precipitators diminished, both hot- and cold-side units were applied to low-sulfur coal units during the 1970s. However, toward the end of the 1970s and into the early 1980s, many hot-side precipitators operating on low-sulfur western coals, especially those from the Powder River Basin, experienced moderate to severe back ionization conditions which dramatically reduced collection efficiencies. At first there was disbelief that hot-side precipitators could be that sensitive to coal characteristics. It was then thought that performance problems were site specific, but finally there was the realization that it was generic in nature. As such, alteration of fly ash resistivity, i.e., fly ash chemistry, by the addition of sodium-based compounds was then considered and instituted by many utilities in order to improve precipitator performance levels. It was found that higher sodium content fly ashes caused many units to experience long-term performance degradation due to wire and plate buildups. These buildups frequently required water washing, sand blasting, or mechanical cleanings of the precipitators to restore performance levels on a routine basis.

As with the case of the performance problems, the structural design of hot-side precipitators underwent a learning experience. The structural design of hot-side precipitators basically evolved from experience with a few small industrial and utility units. These small precipitators tended to have minimal structural problems and exhibited small degrees of thermally induced movement. These precipitators were relatively simple structures with a minimal number of integral gas paths. In addition, these structures experienced flue gas conditions which produced relatively uniform temperature conditions across the face of the precipitators. Success, from both structural and performance standpoints, with these small precipitators provided the suppliers with the confidence to design larger utility installations.

Concurrent with the success of these early installations, the utility industry found itself building significantly larger generating units for which hot-side precipitators would have to be designed. There were wide variations in unit sizes which in turn translated into varying degrees of structural design experience and expertise amongst the precipitator suppliers. In recognition of this diversity of experience, each supplier had to endeavor to keep abreast of developing technology through literature in the public domain, its own research and development programs, and a continuing analysis of recent and current projects to identify and cope with problem areas. It would reasonably take up to two years after a unit went into operation for field experience to be translated into design modifications for new units.

At that time, scheduling and commercial pressures were such that hot-side precipitator design assumptions regarding flow distribution patterns, thermal gradients and their time dependence, asymmetrical casing expansion, thermal insulation effectiveness, thermal creep, insulating effects of fly ash, load transference and rotational forces within the supporting structural systems, and heat transfer may not have been fully analyzed or appreciated. As such, some hot-side precipitators experienced deformation of structural components, cracking of structural elements, the tearing of welds, uplifted support columns, and nonfunctional or destroyed sliding bearings, all of which affect the precipitator's structural integrity and may affect performance.

In 1976, specific information regarding the design of hot-side precipitators was available to all precipitator suppliers. Joy/Western Precipitation authored two publicly available technical papers entitled, "Hot-side Electrostatic Precipitator Design & Experience" and "Structural Behavior in Hot Precipitator Systems," presented in January 1976 and March 1976, respectively. These papers presented specific design information and concepts regarding the nature, magnitude and effects of thermal gradients, expansion and creep in hot-side precipitators. These papers addressed topics such as beams subjected to thermal gradients; temperature gradients and the effects on internal bracing members in terms of tension/compression forces; temperature distribution within structural members based on actual test data; stresses associated with uninsulated sections of ductwork; yield and tensile strength comparisons as a function of temperature between carbon steel (ASTM A36) and Corten steel (ASTM A242); thermal creep as it affects discharge electrode material based on specific testing performed by Joy; impact of fatigue and thermal cycling on selected materials of construction; influence of temperature on the linear coefficient of thermal expansion for ferritic and austenitic steels; expansion joint stress/cycling design impacts; effects of temperature on the modulus of elasticity and tensile strength for ferritic and austenitic steels; allowable stress levels for carbon steel, Corten, and 304 stainless steel as a function of temperature and structural member type; and a methodology for selecting stub column length. In addition, these papers pointed out that failure to consider the consequences of the foregoing topics would result in distortions within the precipitator structure producing buckled members, failed connections, and misalignment of internals which will all have cascading affects on precipitator performance. It appears that in spite of this information, many hot-side precipitators have suffered from structural distress.

STRUCTURAL EVALUATION PROGRAM

In order to properly assess the level of structural distress experienced by these hot-side precipitators and to establish appropriate remedial action plans, we embarked on developing an evaluation program aimed at producing an in-depth understanding of the structure's dynamics. This program resulted in the development of a computer model to perform detailed structural analyses of the casing, inlet and outlet nozzles, and supporting structures. The evaluation program contains the following elements:

- Visual inspection of precipitator casing and internal structural members, supporting columns and their sliding bearings, ductwork and expansion joints, and the precipitator system supporting substructures.
- Measurement of thermally induced movements of the precipitator casing, internal casing members, sliding bearing supports, and associated nozzles and ductwork.
- Temperature profile measurements of flue gases, structural members in and out of the gas stream, and at the sliding bearing interface.
- Computer analysis to determine stress levels in structural members along with stress reversal conditions.
- Development of feasible repair or replacement scenarios using the computer model.

The starting point for the evaluation is a thorough visual inspection conducted by a team of structural engineers and precipitator specialists usually accompanied with plant personnel. This inspection must be very detailed in terms of not only observing a bowed beam or cracked platework, but noting exact locations, dimensions, and characterizations where appropriate. Of course, inspection of casing internal wind bracing will be limited by the degree of access. Usually, interfield walkways permit this type of inspection although examination of uppermost wind bracing may require the use of ladders. Structural members must be examined to determine if bows exist, whether contact has been made with the collecting plates, and if end connections are intact. Further, columns should be inspected for cracks in the webs and flanges. Hopper connections to bottom ring support beams must also be examined for cracking or tearing of welds or platework. Supporting stub columns and sliding bearings must be examined to determine if the column is bent, rotated or uplifted, and if the bearings are intact with their teflon fabrics in place and functional. Bearing movements are relatively easy to determine in terms of magnitude and direction by using the "polished" area of the stainless steel sliding surface as a reference point. It should be noted that access to these bearings may be limited and almost always requires the use of a ladder. In inspecting the ductwork, floor cracks and torn corner connections can be readily located as depressions in fly ash deposits if the deposits are not too deep. Ripples or buckling in vertical ductwork plating usually can be seen by sighting along the ductwork wall. Internal ductwork bracing must also be inspected for buckling and/or torn connections. Roof cracks may only be evident when ladders or special rigging are utilized. Roof cracks can be suspected if significant rusting of structural members can be observed. This rusting would be indicative of water infiltration. Expansion joints should be inspected for cemented ash deposits which may restrict movement and for tears in the fabric which would be an air infiltration site. The supporting substructures must be inspected to determine if bowed members exist which may be indicative of an insufficient design or load transference and/or differential foundation settlement.

The next phase of the evaluation involves using a surveying crew to make measurements of the thermally induced movements of the precipitator and its associated ductwork. Siting targets, as typified by Figure 1, are welded to the casing at three elevations on each casing corner and at certain critical locations on the ductwork. Figure 2 depicts a typical arrangement for the placement of these targets. Of course, target placement will be a function of visibility from benchmark locations. The measurements are taken when the precipitator is in a "cold" position and then again in a "hot" condition after several days of operation. These measurements will indicate the degree of thermally induced movement experienced by the precipitator along with the asymmetrical or nonparallel movements of end panels. Further, these measurements establish the rotational effects on casing columns and vertical growth in both casing and ductwork. Moreover, these measurements serve as boundary conditions in the computer model since displacements are calculated and are compared to field measurements as part of the model verification process. In addition, when these measurements are repeatedly performed over several unit start-up/shutdown cycles, the extent and rate of progression of plastic deformation of the precipitator system can then be quantified. Intermediate exterior stub column movements can also be measured using this surveying technique. Interior stub column movements are extremely difficult to obtain due to equipment blocking the line of sight. Physical measurement of these column movements under hot conditions may not be practical due to high temperature zones around the column, which would be hazardous to personnel.

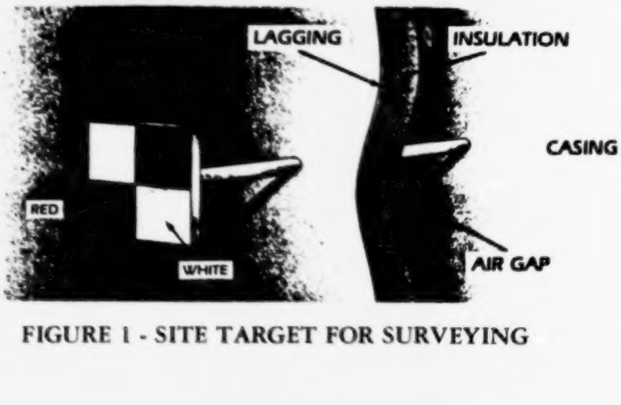

FIGURE 1 - SITE TARGET FOR SURVEYING

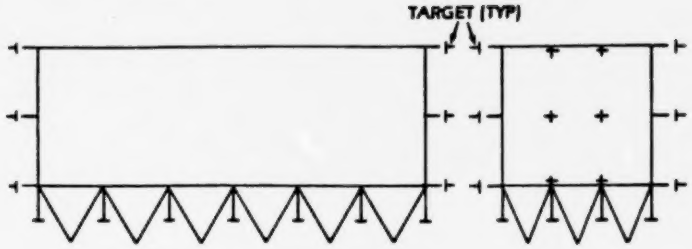

FIGURE 2 - SITE TARGET LOCATION

Although measurement of the horizontal movements of these interior stub columns is of significance, it is most important to be able to determine whether or not these columns are subjected to uplift conditions. Therefore, we developed a device, as depicted by Figure 3, which can accurately measure vertical column uplift as well as indicate horizontal movement in one direction. The device was designed to cope with high temperature conditions while using materials with small coefficients of thermal expansion in order to significantly reduce measurement errors. The device is located as close as practical to the sliding bearing assembly at the bottom of the stub column. This location provides for easier installation and clearances during operation. Further, steel and ambient air temperatures will be lower at this location as opposed to those higher up in the hopper crotch area. The pyrex rod pointer would be set at a benchmark location in the cold position. Once the precipitator has been operational for several days, a measurement is obtained by the location of the pointer relative to the benchmark. This measurement then indicates the degree of uplift experienced by the column. Of course, not every column should be fitted with such a device. The device should only be used when it is indicated by visual inspection and/or computer model analysis that an uplift condition could exist.

Where casing internal wind bracing is bowed and there may be the possibility of contact with the collecting plates, a "feeler gauge," as depicted by Figure 4, is used. This gauge is located in the middle of the structural member directly opposite the edge of the collecting plate. When the gauge is installed, the sliding solid rod is extended to a point where it makes contact with the plate. The fit between the solid rod and the sleeve should be tight in order to avoid movement due to vibration. After the unit is operated, the precipitator would be removed from service and the location of the solid rod is observed and measured. Should the face of the rod be flush with the edge of the structural member, then it can be reasonably inferred that at some point in time contact was established. Most probably the contact would have occurred under start-up conditions and may not be observed as lower power levels for that section of the precipitator during normal operation.

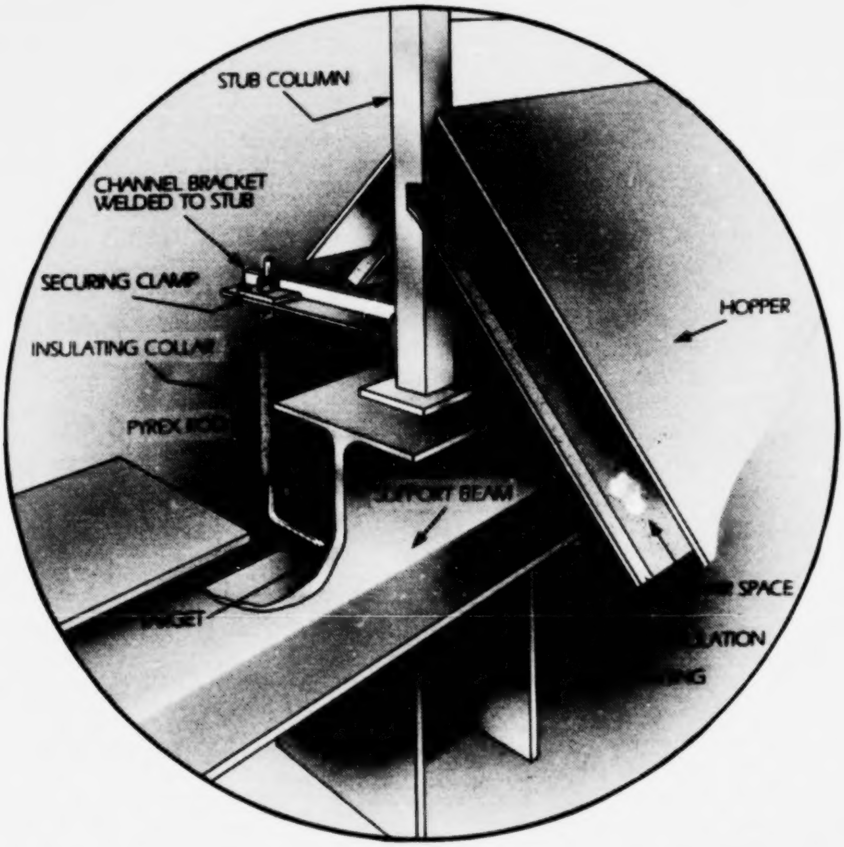

FIGURE 3 - MONITORING DEVICE FOR MEASURING COLUMN UPLIFT

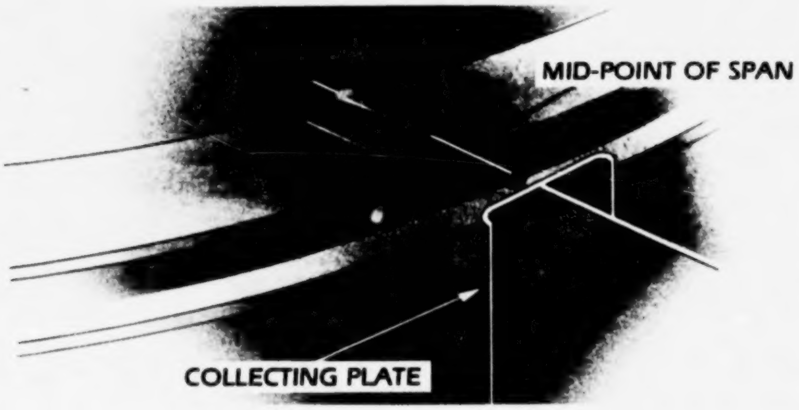

FIGURE 4 - WIND BRACING FEELER GAUGE

The evaluation continues into an investigation of thermal gradients and system response times of flue gases and structural members. In general, there is little organized data available relating to flue gas temperature profiles at the economizer exit, within the precipitator, and at the entrance to the air heater, especially under start-up and shutdown conditions. Hence, the first step in this portion of the investigation is to use existing plant computer equipment to record specific data. In most cases, the average temperatures at the economizer exit and air heater inlet are readily available from plant data logs. In terms of establishing the average precipitator internal gas temperature, a good approximation would be to average the temperatures of the economizer outlet and air heater inlet. Since there are at least two precipitator casings on large units, individual gas path temperatures should be used. In addition to taking the data under start-up conditions, shutdown or cooldown conditions are also important to the structure. This data will give operators a better understanding of the precipitator process conditions and be helpful in determining when to energize or deenergize the precipitators. Further, in combination with data gathered regarding thermal gradients experienced by structural members within the precipitator system, these flue gas temperature profiles can establish, through the use of the computer model, a practical limit on minimum and maximum unit ramp rates in order to avoid structural damage.

In addition to obtaining overall flue gas temperature profiles, it is necessary to obtain specific gas and structural steel temperature profiles within the precipitator system. In order to obtain this data, an array of thermocouples is installed in selected gas paths of the precipitator. These arrays are located at the inlet, midsection, and outlet of each of the gas paths to be studied. It should be noted that extreme care must be used in the selection of gas paths to be studied to assure that the data is representative of the thermal gradients within the structure. Figure 5 depicts a typical structural arrangement for an individual gas path. Large precipitator casings can typically have up to eight of these structural gas paths. Figure 5 indicates the location of thermocouples for the measurement of flue gas and steel temperatures. Gas temperature probes are located, as a minimum, at the wind bracing levels which are usually at the one-third points. In some instances, it may be helpful to locate additional gas temperature probes just above the bottom ring beam. Figure 6 depicts a typical design for such a gas temperature probe. Structural steel thermocouples are placed on the bottom and top ring beams and on the wind bracing members. Figure 7 depicts the arrangement of two thermocouples on the bottom ring beam. One thermocouple is located on the top flange of the beam, and the other is positioned at the base of the beam's web. These two thermocouples will provide data relative to the average temperature of the ring beam which determines the amount of thermal growth which will occur. The bottom ring beam also is the main controlling element in determining restraining forces within the structure. In addition, since bottom ring beams can vary in depth from two to five feet, thermal gradients within the beam can be significant. Should significant gradients occur, then the beam will bow due to differential thermal growth across the web. Figure 8 depicts the placement of the thermocouple on the upper and lower wind bracing members. Since the member is relatively small in size in comparison to other members and located directly in the path of the gas, the thermocouple is placed in the center of web. Figure 9 depicts the location of the thermocouple on the upper ring beam. This thermocouple is usually placed on the bottom flange due to accessibility. Wherever possible, it is advisable to place an additional thermocouple at the top of the web or on the top flange, similar in arrangement to the bottom ring beam.

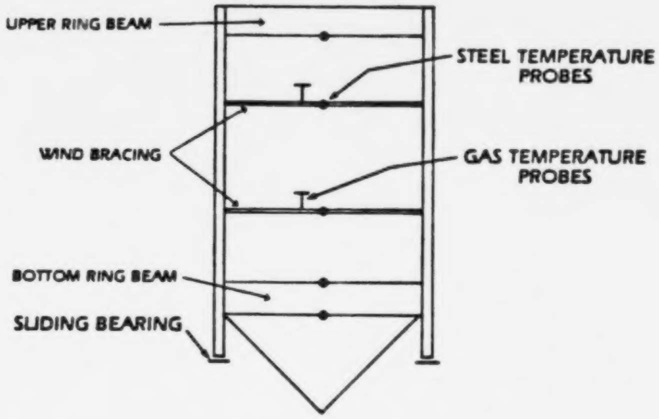

FIGURE 5 - TYPICAL GAS PATH STRUCTURAL ARRANGEMENT

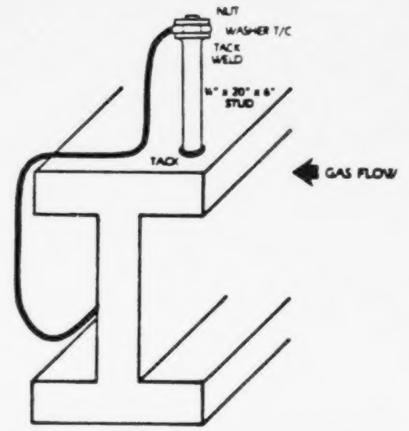

FIGURE 6 - GAS PATH TEMPERATURE PROBES

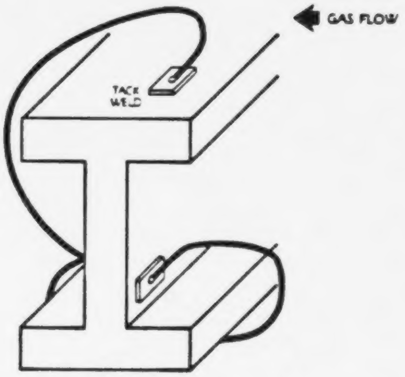

FIGURE 7 - BOTTOM RING BEAM TEMPERATURE PROBES

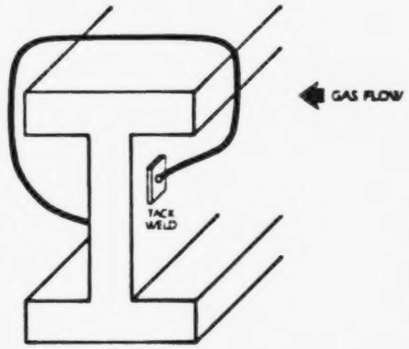

FIGURE 8 - UPPER AND LOWER WIND BRACING TEMPERATURE PROBES

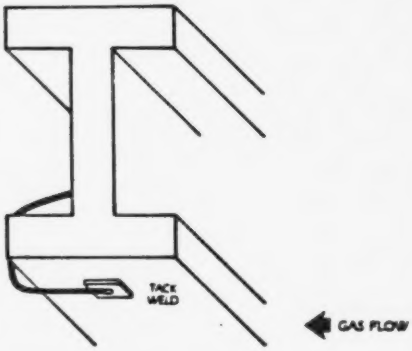

FIGURE 9 - UPPER RING BEAM TEMPERATURE PROBES

Thermocouple data collection can be accomplished via an automated system with storage on magnetic disks or tape. This approach allows for easy retrieval and analysis. A more cumbersome approach to data collection would be to employ miltipen strip chart recorders. As such, data analysis becomes much more labor intensive. Depending upon the extensiveness of the testing program, budget and scheduling constraints, the data collection approach must be addressed on a site-specific basis.

PROGRAM RESULTS

The implementation of these structural evaluation programs has resulted in a greatly expanded understanding of the structural dynamics of hot-side precipitators. In many instances, these insights may seem simplistic and logical but either have been overlooked or ignored in hot-side precipitator design. However, if hot-side precipitators are to maintain their structural integrity, it is paramount that structural evaluations be performed and structures so modified using these insights.

In terms of the measurement of thermal expansion, it has been found that in every case the precipitator casing expands in an asymmetrical manner. This actual expansion is at odds with the symmetrical expansion concepts used in the original design. Figure 10 illustrates the degree to which asymmetrical expansion can exist. Data was obtained after units had stabilized at load and with relatively consistent flue gas temperatures for several days prior to obtaining hot measurements. Opposite casing walls do not move in a manner parallel to one another. In essence, the top front grows more than the bottom and the front can move more than the rear. These movements produce rotational effects on the casing support columns while introducing some additional degree of misalignment of collecting plates. These movements must also be considered when aligning certain types of high voltage rappers. These measurements make it apparent and contrary to many original design concepts, that the precipitator casing does not reach an overall equilibrium steel temperature. The failure to reach an overall equilibrium temperature is due to flue gas temperature gradients; differential thermal response times of various structural components; nonuniform effectiveness of thermal insulation; and the insulating effects of fly ash deposits. In addition to the precipitator casings experiencing asymmetrical expansion, the inlet and outlet nozzles are also subject to such expansion. As depicted by Figure 11, vertical movement of the precipitator casing can lift the nozzle off its supports. Unloading the nozzle support system causes the nozzle to rotate toward the support. This rotation can result in tension tears at the nozzle top and compression buckling at the nozzle base. In addition, nozzle rotation also transfers additional load to the front row of precipitator columns.

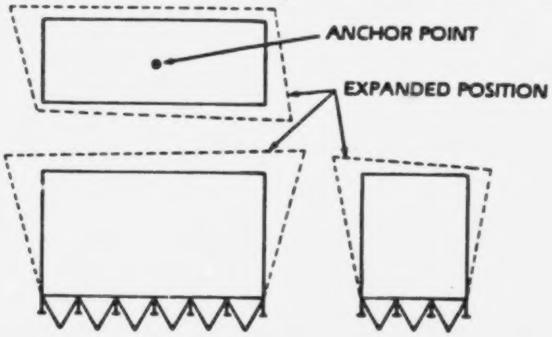

FIGURE 10 - ASYMMETRICAL CASING EXPANSION

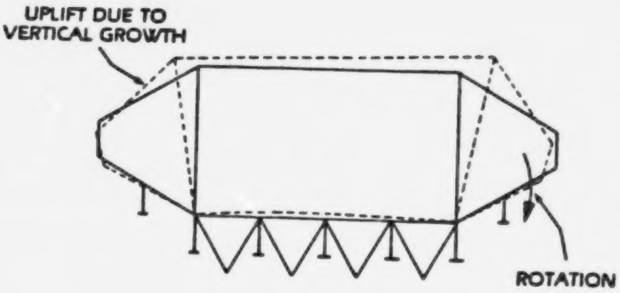

FIGURE 11 - NOZZLE MOVEMENTS

In understanding the thermal response times of the equipment in the hot-side precipitator system, i.e., precipitator, economizer and air heater, to start-up and shutdown conditions, it is necessary to develop time temperature profiles. These profiles can generically be depicted for large units by Figures 12, 13 and 14. Figure 12 illustrates the magnitude of the delay in average gas temperatures under cold start-up conditions. In the space of two hours, the economizer exit gas can experience up to a 300°F increase. During that same period of time, the air heater inlet temperature can exhibit a 200°F increase. It is interesting to note that during this period of time, the flue gas temperature drop through the precipitator and its associated ductwork can amount to 250°F. The flue gas temperature drop does reach a steady-state condition for approximately 24 hours. At such time, a 50°F temperature drop may not be uncommon. It should be noted that generally when conceptual studies were performed in evaluating hot- and cold-side precipitator options, anticipated flue gas temperature drops would have been on the order of 25°F or less. There is the possibility that if these higher gas temperature drops were factored into the economic evaluation, the hot-side option may not have been considered viable.

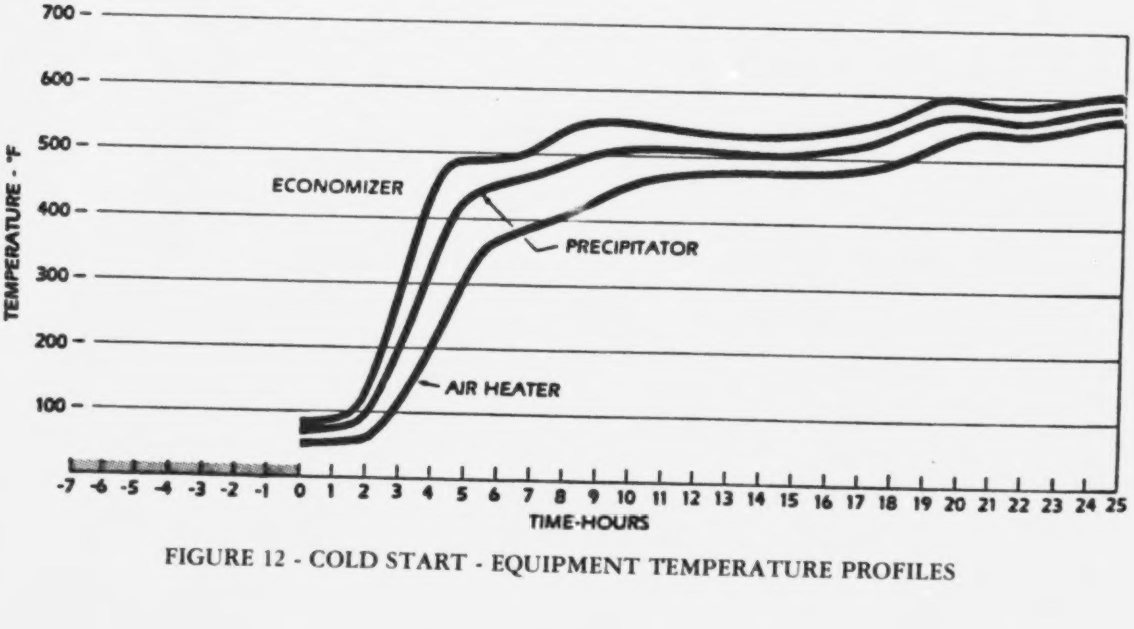

FIGURE 12 - COLD START - EQUIPMENT TEMPERATURE PROFILES

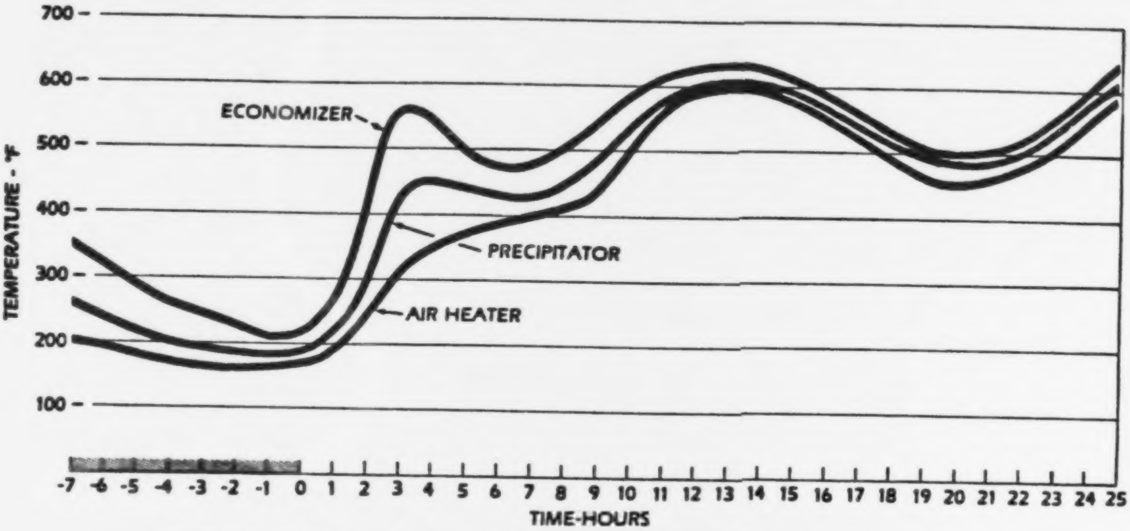

FIGURE 13 - HOT START - EQUIPMENT TEMPERATURE PROFILES

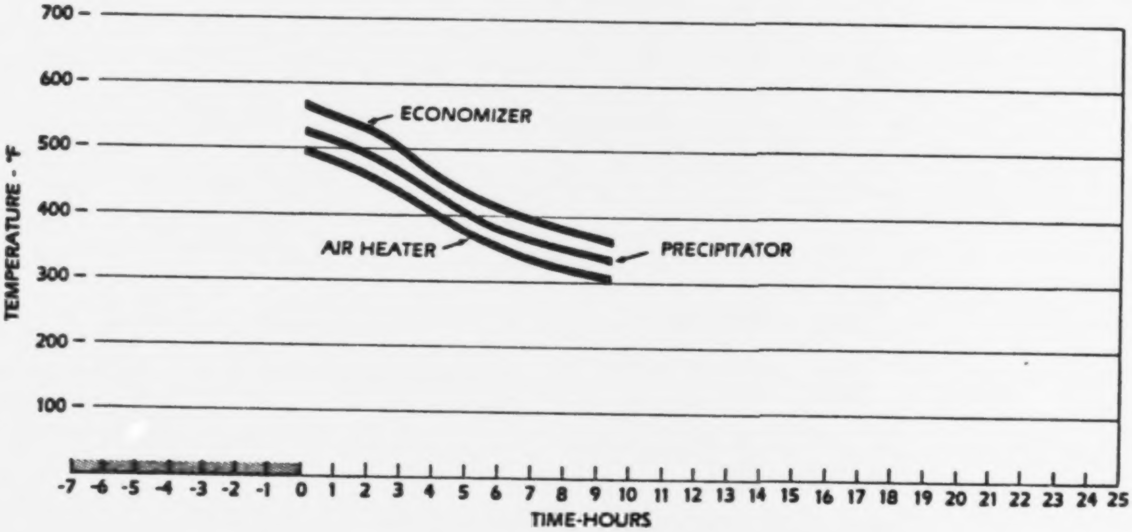

FIGURE 14 - EQUIPMENT COOLDOWN PROFILE RATES AFTER UNIT SHUTDOWN

Under a hot restart condition as depicted by Figure 13, the same pattern exhibited by Figure 12 is repeated; however, the time frame is compressed. Whereas under the cold-start condition, it took up to eight hours for the economizer exit to reach the peak temperature; under the hot restart condition, this peak can be reached in three hours. Again, the flue gas temperature drop through the precipitator is on the order of 250°F, with a steady-state drop of 50°F. Hot restarts or even major load swings can thermally stress the precipitator system almost as much as a cold start.

Precipitator cooldown profiles as typified by Figure 14, indicate that flue gas temperatures will drop to approximately one-half of peak operating temperatures over a nine-hour period without the benefit of forced cooling. This cooldown period is important because in terms of forced cooled units, ambient temperatures are usually reached within the precipitator in twelve hours. Thus, the precipitator can be thermally stressed again in terms of gradient reversals by forced cooling. Wherever practical, hot-side precipitators should be naturally cooled.

When investigating the effects of thermal gradients on the precipitator system, one must quantify the degree to which temperature stratifications occur within the flue gases. As an example, Figure 15 represents the gas temperature profile at the inlet and outlet of a single structural bay within a precipitator. It must be noted that large units may have up to 16 such structural bays. Gas temperatures obtained at the vertical one-third points, as shown by Figure 5, during a cold start, indicate that the lower portion of the inlet experienced temperatures up to 350°F hotter than the upper portion of the inlet. This differential temperature can be attributed to not only temperature stratifications within the gas stream, but also channeling of the flue gases through selected portions of the precipitator. It required more than twenty-two hours of operation for these gas temperatures to approach uniformity, i.e., within 25°F of one another. Due to the heat transfer moderating effects of the collecting plates, the upper and lower outlet gas temperatures are virtually identical as would be expected.

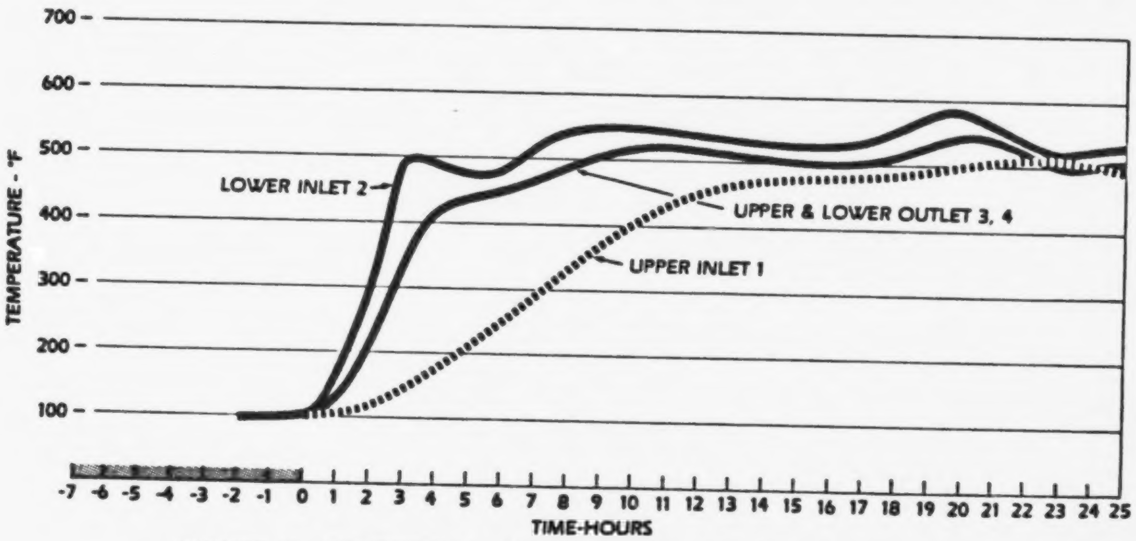

FIGURE 15 - INDIVIDUAL GAS PATH, COLD START CONDITION
GAS TEMPERATURE - TIME DIAGRAM

These patterns are repeated during hot restarts, as depicted by Figure 16, with peak differential temperatures approximately 200°F lower than under cold-start conditions. In addition, under hot restart conditions, there is a very steep gradient right after start-up which can produce 200°F differentials in a matter of minutes as opposed to hours.

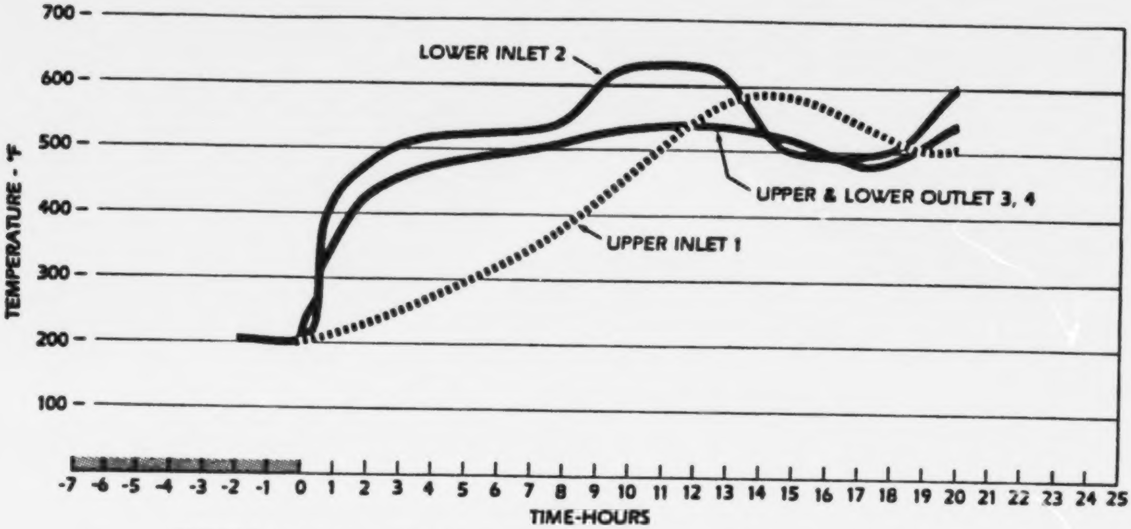

FIGURE 16 - INDIVIDUAL GAS PATH HOT RESTART CONDITION
GAS TEMPERATURE - TIME DIAGRAM

Once the degree of temperature stratification within the flue gases is determined across the face of the precipitators, the data regarding the temperature gradients to which the structural members are subjected can then be examined. Figure 17 depicts the temperature time relationship for major structural components at the inlet of a typical structural bay. Under a cold-start condition, the upper and lower wind bracing along with the upper ring beam temperature profiles tend to follow one another with a maximum differential of approximately 75°F occurring some four hours after start-up. The upper and lower wind bracing respond very quickly to changes in flue gas temperatures since they are emersed within the gas stream. On the other hand, the bottom ring temperature profile lags behind that of the wind bracing by at least six hours. As such, there is a 250° to 300°F peak temperature differential between the wind bracing and the bottom ring beam. After approximately ten hours of operation, these differentials are reduced to about 50°F under near steady-state conditions. In analyzing the restraining forces within the precipitator structure, it is found that the bottom ring beam controls the major movements of the structural system.

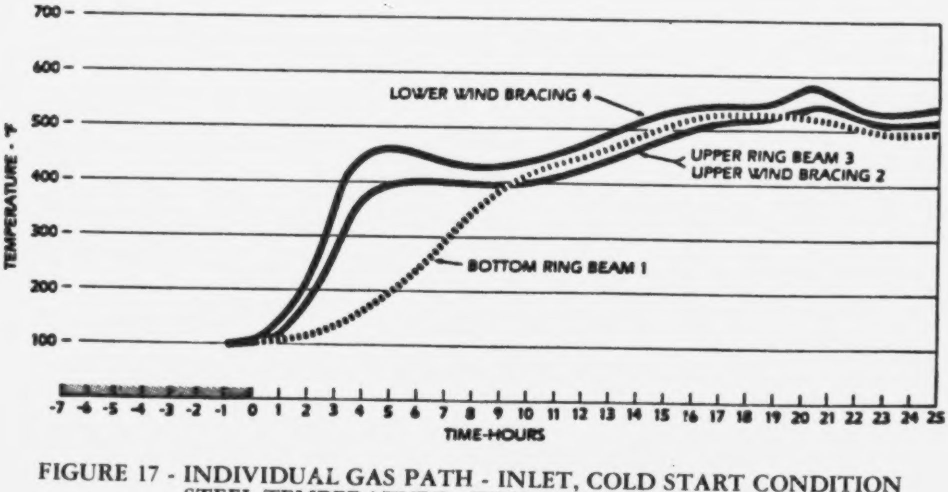

FIGURE 17 - INDIVIDUAL GAS PATH - INLET, COLD START CONDITION
STEEL TEMPERATURE - TIME DIAGRAM

In terms of a hot restart condition as depicted by Figure 18, the same basic pattern occurs in terms of temperature profiles of the major structural elements. However, the peak temperature differential between the wind bracing and the bottom ring beam is on the order of 225°F; but it occurs within the first two hours of operation with a much steeper slope to the curve than under a cold-start condition. Even under a hot restart condition, it still takes approximately ten hours for these differentials to reach the 50°F level.

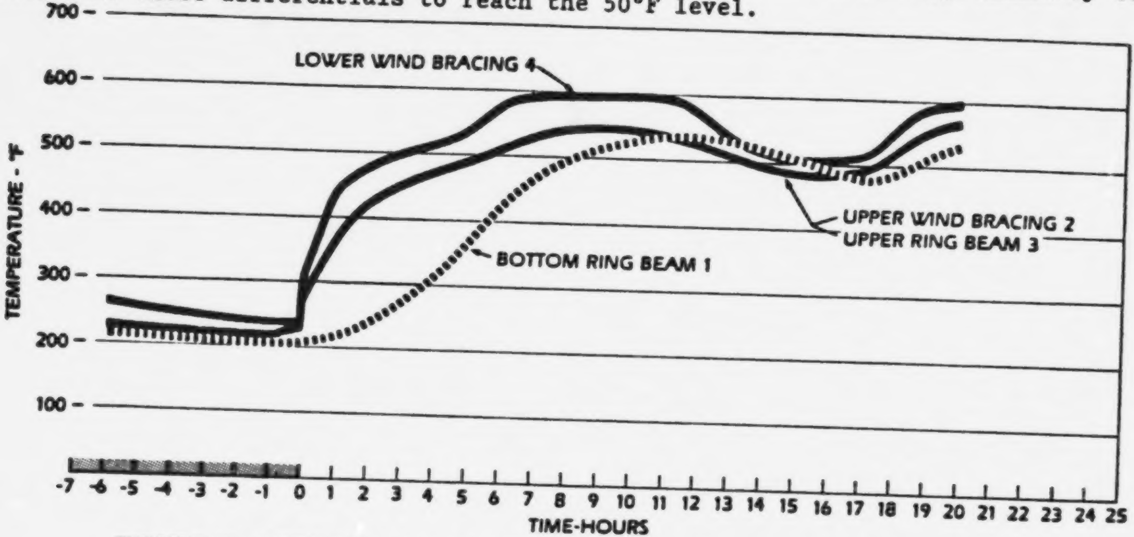

FIGURE 18 - INDIVIDUAL GAS PATH - INLET, HOT RESTART CONDITION STEEL TEMPERATURE - TIME DIAGRAM

In terms of the outlet of the precipitator, the temperature profiles of the structural members as depicted by Figure 19 under cold-start conditions produce a 250°F differential between the wind bracing and bottom ring beam. Further, as would be expected, the upper and lower wind bracing have essentially the same temperature profile. It is also interesting to note that whereas at the precipitator inlet differential temperatures between the wind bracing and bottom ring beam reach the 50°F level after ten hours of operation, it requires more than twenty-four hours for these members in the outlet to reach a 100°F level. This time lag between the inlet and outlet bottom ring beam is a major factor in the asymmetrical growth of precipitator casings and must be accounted for in any structural analysis of the precipitator system.

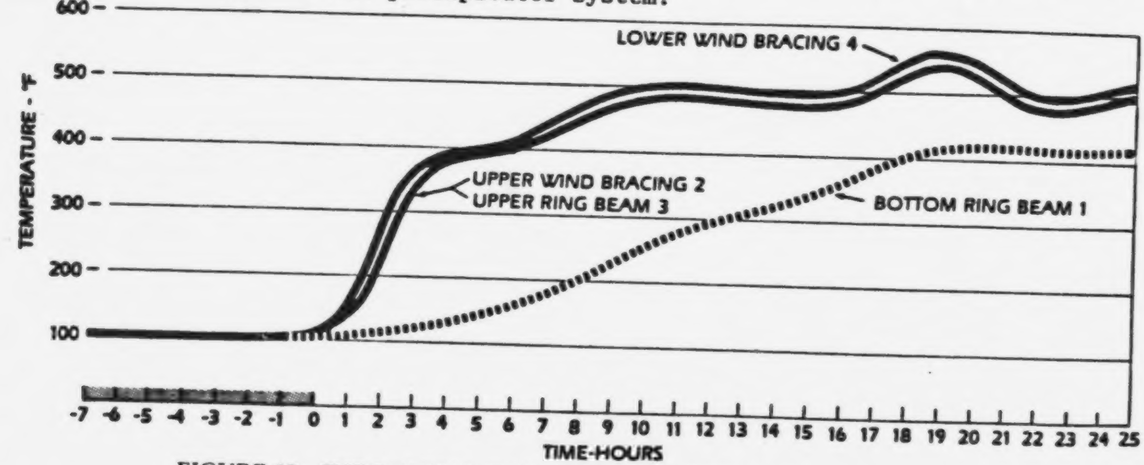

FIGURE 19 - INDIVIDUAL GAS PATH - OUTLET, COLD START CONDITION STEEL TEMPERATURE - TIME DIAGRAM

Again, under hot restart conditions, the precipitator outlet as depicted by Figure 20, experiences temperature differentials of approximately 225°F between the wind bracing and bottom ring beam. Essentially the same temperature profile patterns exist under cold and hot restart conditions. However, under the hot restart condition, the 50°F differential level between the wind bracing and bottom ring beam can be reached after approximately twelve hours of operation.

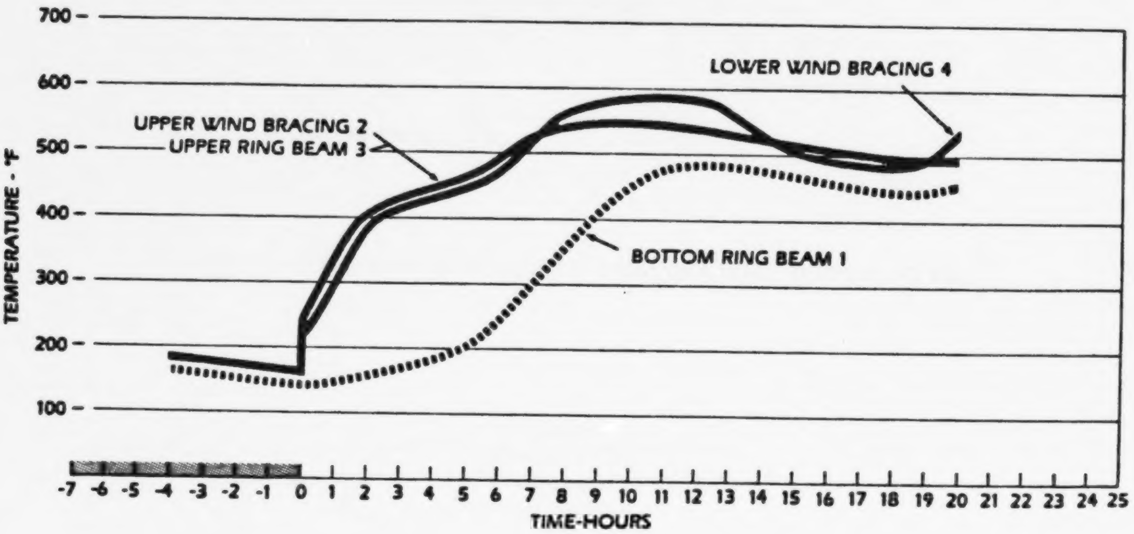

FIGURE 20 - INDIVIDUAL GAS PATH - OUTLET, HOT RESTART CONDITION STEEL TEMPERATURE - TIME DIAGRAM

UNIFIED THEORY OF THE DYNAMICS OF STRUCTURAL DISTRESS

This data has lead to a more complete understanding of the precipitator's structural dynamics. The structural dynamics can be pictorially represented by Figures 21 and 22. With reference to Figure 21, attention must first be directed toward the affect of the bottom ring beam. As depicted by the time-temperature profiles, the bottom ring beam heats up and consequently expands more slowly than any other major structural component. As such, the bottom ring beam becomes the principal restraining force within the structure. It must be noted that when the bottom ring beam expands, it can produce horizontal thrusting forces in excess of one million pounds under fully restrained conditions, i.e., bolted or welded connections. These forces are of such a magnitude that it would be impractical and undesirable to design such a rigid structure. Consequently, sliding bearings are utilized to permit the casing to expand in essentially an unrestrained manner. Individual sliding bearings, if properly functioning, usually impose restraining forces upon the structure of 15,000 pounds or less. These sliding bearing frictional forces are relatively small when compared to other forces acting upon the structural system. However, should the sliding bearing fail and have metal-to-metal contact occur, then the resulting restraining forces would be on the order of 150,000 pounds, which is significant and can result in deformation of structural members.

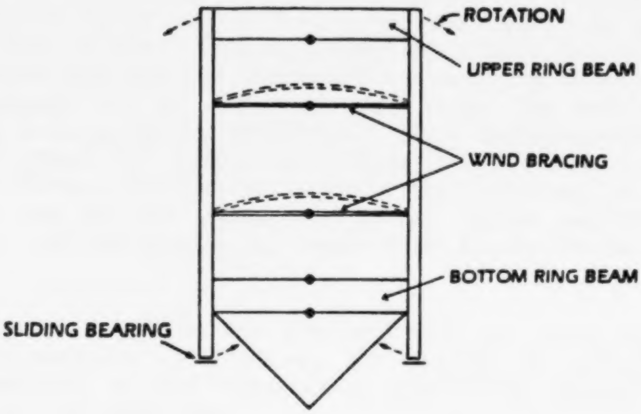

FIGURE 21 - DEFORMATION DUE TO TEMPERATURE DIFFERENTIALS

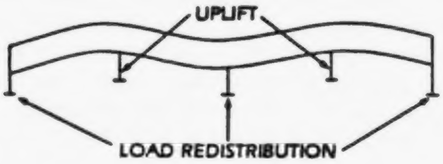

FIGURE 22 - TYPICAL BOTTOM RING BEAM DEFORMATION DUE TO THERMAL GRADIENTS

The upper ring beam is relatively free to expand except as restrained by the stiffness of the columns and their end connections to the ring beam. In observing and comparing the time-temperature profiles for both the upper and bottom ring beams, it is apparent that the upper ring beam heats up much faster than the bottom ring beam. As such, the columns are moved outward thus inducing a rotational movement. The column then pivots about the connection to the bottom ring beam. This action in turn is translated into a rotation of the precipitator stub columns. Hence, the sliding bearings are subjected to rotational forces which require the use of a spherical bearing design. It should be noted that many hot-side precipitators have "flat-type" bearings which will be subjected to failure by load concentrations due to reduced bearing areas or by "squeezing" out the teflon bearing material.

The wind bracing is located directly in the flue gas path and heats up the most rapidly of any of the other major structural components. These wind bracing members will thermally expand but the columns will prevent or limit such movement. As such, the member will bow along its weak axis. Depending upon the orientation of the weak axis, the bowed members may contact the collecting plates causing misalignment and possible plate damage. Some wind bracing members may have a cross section configuration which resists bowing but the thermally developed forces are then transmitted into the end connections. These end connections will deform or tear apart thus making the wind bracing member totally ineffective. In some cases, the wind bracing/end connection combination have punched holes in the main support columns. These deformations and failures will have a significant affect on the structural integrity of the precipitator.

With reference to Figure 22, the thermal gradients within the bottom ring beam, which may be on the order of 100°F or more, may cause the beam to grow more at its top than at the bottom. This differential growth produces bowing of the ring beam. The columns are rigidly connected to the ring beam, thus effectively making the beam segments act as one very long beam. As such, the bowing on a localized basis will produce column uplifting. This column uplifting causes load redistributions throughout the structure. These load redistributions may result in deformation of critical structural members and overloading of some of the sliding bearings to the failure point, which may induce additional deformation within the structure. Column uplift may range from barely being perceptible to 2 inches.

The thermal gradients within the precipitator can cause significant deformation of structural members. Of course, the degree of deformation will be a function of the magnitude of the temperature gradients, number of occurrences, and the flexibility of the structure.

COMPUTERIZED STRUCTURAL ANALYSIS MODEL

With this understanding of hot-side precipitator structural dynamics, the next phase of the evaluation program was to determine specific loading and stress levels within the precipitator system. As one evaluates the structural characteristics of precipitator systems, it becomes apparent that the system can not be considered as a rigid structure. More appropriately, the structure must be viewed as a series of interconnected space frames. Further, the arrangement of hoppers, platework and truss members create a situation were the precipitator has characteristics of both rigid and flexible structures at the same time. As such, the precipitator system must be viewed as a completely indeterminate structure. Compounding the problems associated with analyzing an indeterminate structure, the varying nature and time-dependency of thermal gradients adds to the complexity of the analysis.

In assessing the structural complexity of the precipitator system, it was determined that the most cost-effective and in reality the only practical method of performing a complete structural analysis, would be to develop a computer model. The model would use the results of inspections and field measurements as input and would be analyzed using nonlinear, three dimensional finite element techniques. All structural components are modeled in accordance with their originally designated function such as tension or compression bracing members and compression only sliding bearings. Platework and hoppers are represented by equivalent bracing systems. Typically, an average sized precipitator will have between 1200 to 1500 structural elements represented in the model by approximately 500 node points. The system is analyzed for loadings attributable to gravity, internal gas pressure, fly ash deposition, wind, snow, seismic excitations and thermal gradients. Material properties are also inputted to the model reflecting their dependency on temperature and the effects of thermal creep, by lowering allowable yield points. Further, in the model these loads reflect their time-dependency during start-up, normal operation, and shutdown conditions.

The initial phase of the structural analysis involves the calibration of the computer model to accurately reflect the actual condition of the precipitator system. With data generated through field measurements and observations, the model is run and adjusted where needed to account for every instance of structural distress or failure and deflection, especially those associated with construction errors. It should be recognized that construction errors such as failure to remove temporary erection bolts, welding of slotted connections and poor welding practices, can produce structural distress or failures over and above that created by normal loading conditions. This calibration and verification step in the application of the model is most critical in producing reliable results. The second phase of analysis involves iterative investigations into whether the structural system is stable in its current configuration or will it be subject to additional failures as a result of progressive deterioration. Should a progressive failure mode exist, then the model identifies those critical repairs which must be made in order to reestablish system structural integrity. Should progressive failures not exist, but overstressing of principal structural components does, the model develops modifications to relieve such overstress conditions. Once the model has developed the appropriate repair and/or modification requirements, the model is further utilized to formulate detailed construction plans so as to prevent any damage to the structure during the implementation of repair/modification scenarios.

This model has been successfully utilized on two major hot-side precipitator installations as part of an overall structural evaluation program.

CONCLUSION

In summary, many hot-side precipitators are experiencing some degree of structural distress. The degree of distress can range from minor cracks in platework to situations where some portion of the precipitator system is subject to sudden, catastrophic failure. One electric utility has had to abandon 2100 MWs of hot-side precipitators in favor of fabric filters at one station. This may be an extreme case, but utilities must keep this case in mind and plan a formalized inspection program for their hot-side precipitators. The program should include a thorough inspection on an annual basis, conducted by qualified structural engineers. Further, a detailed record of the inspection findings must be evaluated and retained in order to determine the degree of permanent deformation experienced by the precipitators. Should it be discovered that the precipitators are in some form of structural distress, then an evaluation program should be implemented on an individual unit basis. This evaluation program would normally include physical measurements (i.e., temperature gradients), reevaluation of the original design assumptions, and the use of computer model analysis of the precipitator system to determine the extent to which repairs are needed in order to maintain or attain system structural integrity.

The work described in this paper was not funded by the U.S. Environmental Protection Agency and therefore the contents do not necessarily reflect the views of the Agency and no official endorsement should be inferred.

A SELF-CONSISTENT DEUTSCHIAN ESP MODEL

by: M. G. Faulkner
J. L. DuBard
Southern Research Institute
Birmingham, AL 35255-5305

L. S. Hovis
Air and Energy Engineering Research Laboratory
U. S. Environmental Protection Agency
Research Triangle Park, NC 27711

ABSTRACT

The electrostatic precipitator (ESP) model developed by Southern Research Institute (SRI) for EPA does a good job of simulating the performance of cold-side utility fly ash ESPs with typical values of inlet mass loading. To increase the accuracy of model predictions in unusual situations, such as high inlet mass loading or abnormally low current, a revised version of the model has been developed. Both versions of the model apply the Deutsch equation to narrow particle size bands over short ESP length increments to determine particle collection efficiency. In the standard ESP model, the particle charge and the collecting electric field are calculated independently and are based on a rough estimate of space charge effects. In the revised model, the particulate space charge is rigorously calculated. The particle charge and the collecting electric field are interrelated through the space charge, and all calculations are iterated to self-consistency in each length increment throughout the entire ESP. The revised model has been used on several plants from the SRI ESP data base. The results of this modeling as well as a description of the structure of the model will be presented.

This paper has been reviewed in accordance with the U.S. Environmental Protection Agency's peer and administrative review policies and approved for presentation and publication.

INTRODUCTION

A more general and more powerful mathematical model of electrostatic precipitation (ESP) has been developed at Southern Research Institute (SRI). The standard version of the ESP model developed by SRI for EPA, now in its third revision (1), does a good job of simulating the performance of cold-side utility fly ash ESPs with typical values of inlet mass loading. To increase the responsiveness of the ESP model to situations having high inlet mass loading and/or abnormally low corona current, a revised version of the model has been prepared. Both versions of the model apply the Deutsch equation to narrow particle size bands over short ESP length increments to determine particle collection efficiency. In the standard version, the effects of particulate space charge are estimated by a formula which predicts an effective mobility for combined ions and particles and a reduced ion density for particle charging. These estimated values are then used to calculate separately the electric field at the plate and the particle charge which are required for the Deutsch equation.

The revised model is a more rigorously Deutschian model than the standard ESP model. Care was taken in setting up the algorithm to ensure that all equations conform to the premises on which the Deutsch particle collection equation was based. The calculations of particle charge and collecting electric field are interrelated and made fully self-consistent throughout the ESP. This paper describes the structure of the revised ESP model and compares the standard and revised versions of the model using data from full-sized utility ESPs.

MATHEMATICAL STRUCTURE

Summary diagrams of the logic used in the standard and revised versions of the ESP model are shown in Figures 1 and 2. Both versions of the model use iteration to achieve self-consistency in the calculation. In the standard model, an estimated value of the overall collection efficiency must be furnished as part of the input data. This efficiency value is used to estimate the space charge effects, as shown in Figure 1. The particle charge and collecting electric field are then calculated independently of each other in each incremental length. The test of convergence is made when the overall collection efficiency is compared to the estimated value. If the two do not agree, the calculated value is taken as the new estimate and the entire process is repeated until the efficiency values do agree or the maximum number of iterations is reached. After this point, the calculated efficiency is corrected for the effects of gas bypassing the electrified zone of the ESP (sneakage), non-uniform gas velocity distribution, and rapping reentrainment. All of these corrections reduce the overall efficiency of the ESP.

As previously mentioned, the standard ESP model works well for utility fly ash precipitators under typical operating conditions, as previously documented (2). Recently, SRI has been involved in research on dry sorbent addition to flue gas. This results in very high dust loads in the ESP and requires an ESP performance model which is more accurate than the standard model in high dust load conditions. In addition, examination of the standard model has disclosed three areas of deficiency in the model:

1. The space charge effects are not explicitly calculated but are estimated based on an effective mobility which accounts for fast moving ions and slow moving particles. The effective mobility is not a composite of mobilities but is given by an equation that applies only to small particles near the collection plate.

2. The electric field and particle charge calculations are not mathematically connected.

3. An empirical correction factor must be applied to the average migration velocities of small particles to make their calculated efficiencies match measured data.

To correct these shortcomings and to obtain an ESP model that is more responsive to changes in dust load, a revised ESP model has been developed.

The underlying assumptions for the revised version of the model are:

1. The interelectrode space charge due to charged particles is uniformly distributed in the gas stream. The assumption of uniformity is particularly good for fine particles in a turbulent gas flow. The fine particles are especially important in ESP modeling because they are the most difficult for an ESP to collect.

This allows the development of a rigorously Deutschian model, as these were the conditions for which the Deutsch equation was derived.

2. The space charge due to ions is not uniformly distributed because the ions follow the electric field lines which are non-uniform in the interelectrode space.

3. The total space charge density is the sum of the particulate and ionic space charge densities. These two components are treated separately and explicitly, in contrast to the approximate treatment of a combined ionic and particulate space charge in the standard version of the model.

4. The current is ionic except in the laminar boundary layer at the collection plate. This simplification results from the assumption that the particles are stationary in a given length increment. This is a good approximation since the particulate mobility is several orders of magnitude less than the mobility of the ions. Since the particles are stationary, only the ionic current density appears in the current continuity equation.

5. The ionic mobility is used only in the calculation of the ionic current density on the plate. The mobility drops out of the equations in the remainder of the interelectrode space.

6. The particulate current density is included when determining the total current density on the collecting plate. The particulate current density is computed from the calculated particle charges and Deutsch migration velocities of the different size particles.

7. Overall convergence of the iterative calculations of the interelectrode electric field and space charge density is tested using the measured average plate current density as a mathematical boundary condition.

Based on these assumptions, the revised model was constructed as shown in Figure 2. Rather than test for self-consistency after the efficiency for the entire ESP has been calculated, as in the standard model, the revised model makes the calculation in each length increment fully self-consistent before proceeding to the next length increment. Self-consistency is obtained by alternating the calculations of the electric field and the particle charge, which are connected through the space charge, until the change in the average electric field calculated in successive field/charge iterations becomes sufficiently small. At this point the calculation is assumed to have converged. Following convergence, the collection efficiency is calculated for each particle size using the Deutsch equation. The number of particles in each size band remaining in the gas stream is determined, and the efficiency calculation proceeds to the next length increment of the ESP.

The algorithm in the revised ESP model includes corrections for the non-ideal effects of gas sneakage, non-uniform gas flow, and rapping reentrainment. Gas sneakage occurs when a portion of the particle-laden gas passes through the ESP in a non-electrified path, such as along the roof or dust hopper. These particles are not subjected to charging and collection. The effects of gas sneakage have been incorporated into the revised model in the following way. At the beginning of each section, a specified fraction of the particles in each size band are set aside while the remaining particles are subjected to the precipitation process. At the end of each section, the set-aside particles are remixed with the other particles. To account for the reduction in charging due to sneakage, the particle charge is averaged downward at the end of each section.

The effect of a non-uniform gas velocity in an ESP is to reduce the collection efficiency. In the standard version of the ESP model, this is done by applying a correction factor to the exponent of the Deutsch equation for each size band. The correction factor is obtained from an equation which describes a family of curves that were generated by calculating the efficiency of a pilot ESP for a range of gas velocities and then summing the efficiencies according to the distribution of the gas velocities measured in the ESP. For correctness, such a study should be made for each ESP being studied. However, this is not practical and the correction factor based on the pilot study has been used with good results for a wide range of ESPs. Since no better method for performing this correction is available, the correction is made in the same way in the revised ESP model.

To correct the efficiency calculation for the effects of rapping reentrainment, the rapping routine from the standard ESP model has been adapted to the revised model. This routine was based on a study of utility fly-ash ESPs. The algorithm adds mass to the ESP outlet emissions, in an amount proportional to the mass collected in the final ESP section. This additional mass is distributed among the particle size bands according to a 6 μm mmd log-normal distribution.

COMPARISON OF RESULTS

The revised version of the ESP model has been compared to the standard version on the basis of computed changes along the length of the ESP in values of the following parameters:

- accumulated particle charge,
- average and collecting electric field,
- total, ionic, and particulate space charge density,
- ionic and particulate plate current density, and
- total particulate mass penetration.

The results of the comparison for a pulverized-coal-fired power plant ESP are shown in Figures 3 through 9. The ESP chosen for this comparison features a 25 cm (10 in.) plate spacing, good electrical power input, and a moderate dust loading of 3.7 g/m^3 (1.6 gr/acf). The ash has a moderate resistivity (2 x 10^{10} ohm-cm) and a particle size distribution that is typical for fly ashes from eastern bituminous coal. The first three fields, divided into 0.3 m (1 ft) length increments, are shown in the data comparisons.

Figure 3 shows the rate of charge accumulation for three particle sizes. The reduction in the charge on the particles can be attributed to the reduced average electric field used in the charging calculation (shown in Figure 4). The reason for the reduction in the revised model is that the average field is calculated by actually averaging the electric fields over the interelectrode space in each length increment. In the standard version, the value of the average field is obtained by dividing the applied voltage in each field by the wire-to-plate distance, a calculation which is valid only on the wire-to-plate line. The steps in the curve for the standard version are due to changes in the applied voltage between fields.

Figure 4 also shows the enhancement of the collecting electric field (the field at the plate) due to the presence of charged particles. This effect is observable because the revised version of the model calculates the effects of space charge on the electric field explicitly. The standard version, which does not directly relate the field calculation to particle charge, does not show this phenomenon. This is an important effect because the Deutsch migration velocity is directly proportional to the field at the plate.

Figure 5 compares the total space charge density at the plate (directly opposite the wire) for the standard and revised versions of the model. In the standard model, no specific requirements are made on the space charge density regarding the number of charged particles present in the gas stream. The calculation is made as if only ions were present, except that an effective mobility for combined motions of ions and particles is used instead of the ionic mobility. In the revised model, where the particulate and ionic space charge are treated explicitly, the total space charge density at every point in the interelectrode space is constrained to be equal to or greater than the minimum charge density provided by a uniformly distributed, stationary cloud of charged particles. As shown in Figure 5 the space charge density starts at a high value due to the rapid charging of entrained particles and then decreases as particle collection takes place.

In Figure 6, the total space charge density for the revised model shown in Figure 5 has been broken down into its ionic and particulate components. Comparison of the figures shows that, in the first half of the ESP, the particulate space charge density is the major component of the total space charge density. Only in the last few increments of this example does the ionic space charge exceed the particulate space charge. These data are not available in the combined ions and particles treatment used in the standard version of the model, but may be easily obtained from the revised model which keeps track of ions and charged particles separately.

In contrast to the dominance of the particulate space charge density, the current density on the plate is overwhelmingly ionic in nature. Figure 7 shows this for both the standard and revised versions of the model. Note that the particulate and ionic current densities are plotted on the same scale, demonstrating the difference in magnitude between the two components. The minimum difference is a factor of 10, with the average difference exceeding 2 orders of magnitude.

Figure 8 shows the incremental mass penetration calculated for the standard and revised versions of the model. The greater collecting electric field in the revised model produces a greater efficiency (lower penetration) even though the ultimate particle charge is less than in the standard version. These curves represent the ideal efficiency only and do not contain any non-ideal effects.

Figure 9 shows the effects of 5% gas sneakage. The remixing of the gas which had bypassed the electrified portion of the ESP causes a sudden increase in the number of particles present at the end of each ESP section. This is clearly shown in Figure 9 by the vertical lines at increments 10, 20, 30, and 40.

EVALUATION

The primary reason for the development of the revised ESP model was to provide an ESP performance model which is responsive to changes in dust loading. This goal has been met. As shown by the preceding data comparisons, the revised model clearly demonstrates the effects of its explicit space charge calculation. The sensitivity of the revised model to changes in dust load is shown in Figure 10, where the calculated particle charge for a 1.2 μm diameter particle is plotted as a function of distance down the ESP. The plant which provided the model input data has an abnormally high inlet dust load of 22 g/m^3 (9.4 gr/acf). In Figure 10, the dust load has been arbitrarily reduced for comparison purposes. The lowest dust load, a value typical of many ESPs, shows high initial charging followed by a slow increase due to diffusion charging. The middle value shows a decreased charging rate for the first two length increments, followed by slow charge increase at about the same level as the curve for low dust load. For the highest dust load (the actual dust load for this ESP) the charging rate is greatly reduced in the first three length increments. In the next five increments, the charging is totally suppressed until the space charge is reduced by particle collection, after which charging resumes. Note that these are not real data, because the dust load cannot be changed without changing the electrical operating conditions of the ESP. However, these hypothetical data show that the revised ESP model reacts to changes in dust load. The standard ESP model gave the same charge for all dust loads, yielding a curve which closely resembles the curve for the lowest dust load in Figure 10.

The second reason for revising the ESP model was to eliminate the three deficiencies in the standard model: estimated space charge, separate electric field and particle charge calculations, and empirical correction of small particle migration velocities. The first two deficiencies were eliminated by the structure of the revised model. It was hoped that making the revised model rigorously Deutschian would remove the need for correcting small particle migration velocities (the third deficiency). That this was not the case can be seen in Figure 11, which shows the ratios of measured migration velocity to migration velocity calculated by the revised model without the correction factor, for 10 cold-side utility ESPs. These plants were chosen from the SRI ESP data base (2). The measured migration velocities were determined from the fractional penetration data using the Deutsch equation. The calculated data were generated using the values for gas sneakage and non-uniform gas velocity standard deviation which have proven to be most typical of the power plants in the data base (0.05 and 0.15, respectively) and include the effects of rapping reentrainment. The line in Figure 11 represents a second-order least-squares fit to the data. This curve is very similar to the curve produced by the same data using the standard ESP model. By including an empirical correction factor similar to the one in the standard model, the performance projections can be corrected, as shown in Figure 12.

SUMMARY

The revised ESP model represents an improvement over the standard model in that the calculations of particle charge and collecting electric field required for the Deutsch equation are not separate but are interrelated such that the charging and field calculations are made self-consistent in each length increment of the ESP. This is done by treating the particulate space charge explicitly and by alternating the calculations of particle charge and field until both become constant. The algorithms used in the revised model are conceptually rigorous, except for the continued use of an average interelectrode electric field in the charging calculation. However, this field is not the voltage divided by wire-to-plate distance, as in the standard version of the model, but rather the spatial average of the field values obtained in the interelectrode space. Considering the random motion of fine particles through regions of different field strength and the computational problem of keeping track of particle charge accumulation, this may be the best way to calculate the charge. The revised algorithm contains no estimated effects such as the space charge adjustment or combined mobility of ions and particles which are found in the standard model. These features result in a model which is responsive to changes in dust load as well as electrical conditions. Since there are no estimates based on full-sized ESPs used in the calculation, the revised model can be used to calculate efficiencies for unusual cases such as pilot ESPs with very low currents.

Following the theoretical efficiency calculation, two non-rigorous corrections are applied to model predictions: the calculation of rapping reentrainment and the correction of small particle migration velocities. The rapping correction must be empirical in nature because no applicable theory exists. That a correction factor is necessary for a rigorously Deutschian model to match the small particle migration velocities in full-size ESPs indicates a shortcoming in the Deutsch theory, possibly due to an oversimplification in the underlying assumptions of the theory. At this time, however, there are no competing theories of ESP particle collection which do not also require empirically derived constants.

REFERENCES

1. Faulkner, M. G., and DuBard, J. L. A Mathematical Model of Electrostatic Precipitation (Revision 3). EPA-600/7-84-069a,b,c. (Volume I, Modeling and Programming: NTIS PB84-212-679; Volume II, User's Manual: NTIS PB84-212-687; FORTRAN Source Code Tape: NTIS PB84-232-990). U. S. Environmental Protection Agency, Research Triangle Park, North Carolina. 1984.

2. DuBard, J. L. and Dahlin, R. S. Precipitator Performance Estimation Procedure. EPRI CS-5040. Electric Power Research Institute, Palo Alto, California, 1987.

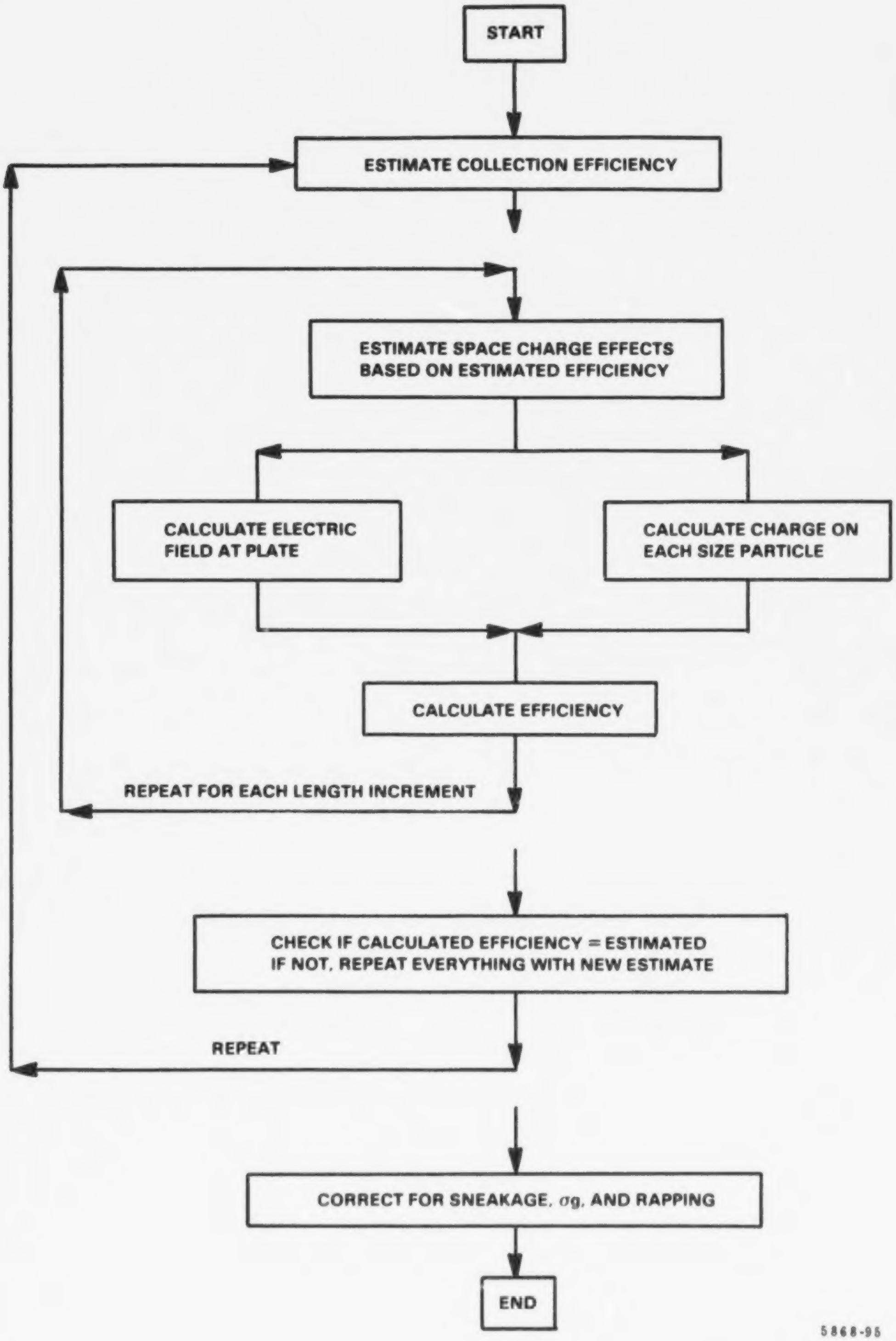
START
ESTIMATE COLLECTION EFFICIENCY
ESTIMATE SPACE CHARGE EFFECTS BASED ON ESTIMATED EFFICIENCY
CALCULATE ELECTRIC FIELD AT PLATE
CALCULATE CHARGE ON EACH SIZE PARTICLE
CALCULATE EFFICIENCY
REPEAT FOR EACH LENGTH INCREMENT
CHECK IF CALCULATED EFFICIENCY = ESTIMATED IF NOT, REPEAT EVERYTHING WITH NEW ESTIMATE
REPEAT
CORRECT FOR SNEAKAGE, σg, AND RAPPING
END
5868-95

Figure 1. Logic diagram for the standard version of the ESP model (Revision 3).

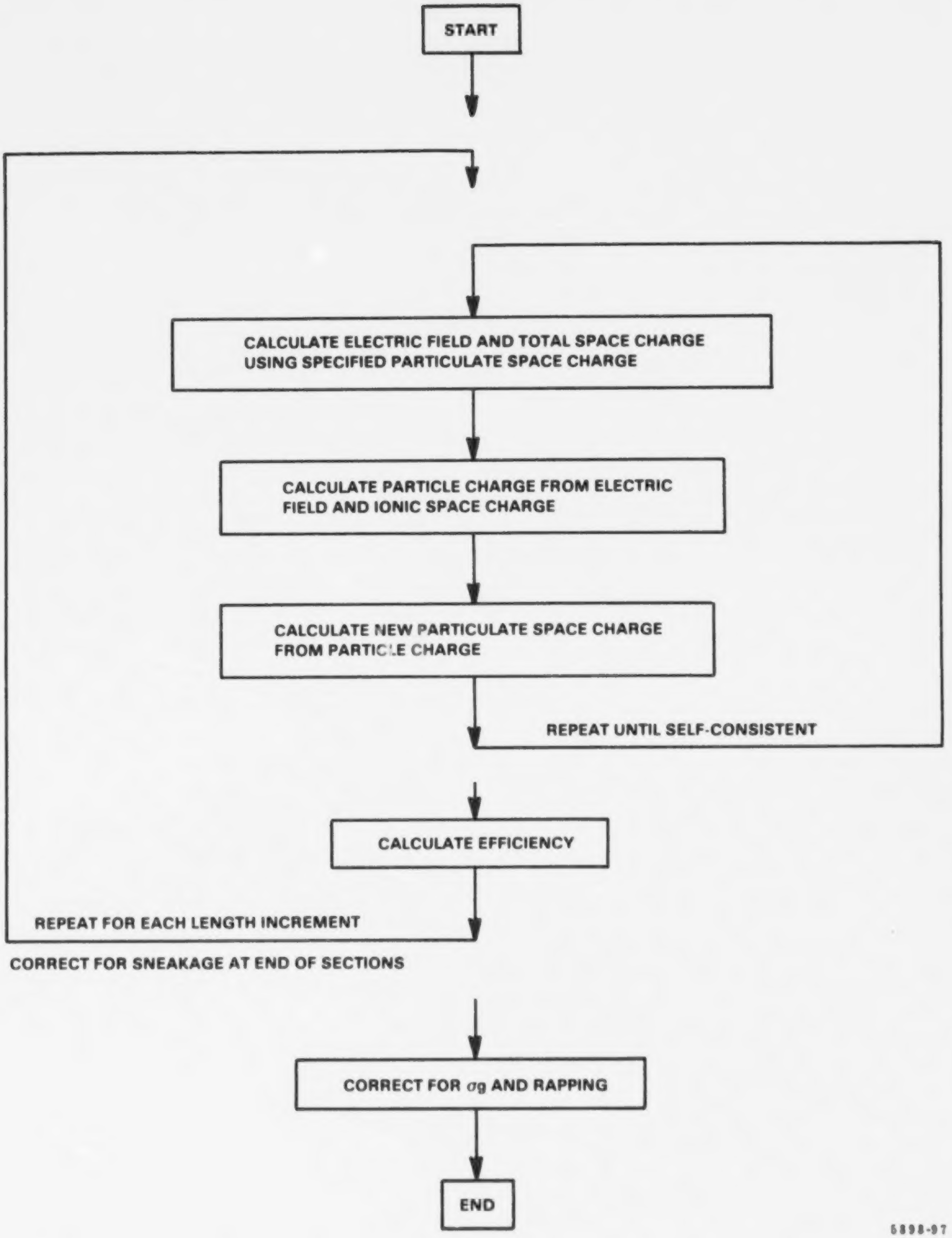
START
CALCULATE ELECTRIC FIELD AND TOTAL SPACE CHARGE USING SPECIFIED PARTICULATE SPACE CHARGE
CALCULATE PARTICLE CHARGE FROM ELECTRIC FIELD AND IONIC SPACE CHARGE
CALCULATE NEW PARTICULATE SPACE CHARGE FROM PARTICLE CHARGE
REPEAT UNTIL SELF-CONSISTENT
CALCULATE EFFICIENCY
REPEAT FOR EACH LENGTH INCREMENT
CORRECT FOR SNEAKAGE AT END OF SECTIONS
CORRECT FOR σg AND RAPPING
END
5898-97

Figure 2. Logic diagram for the revised version of the ESP model.

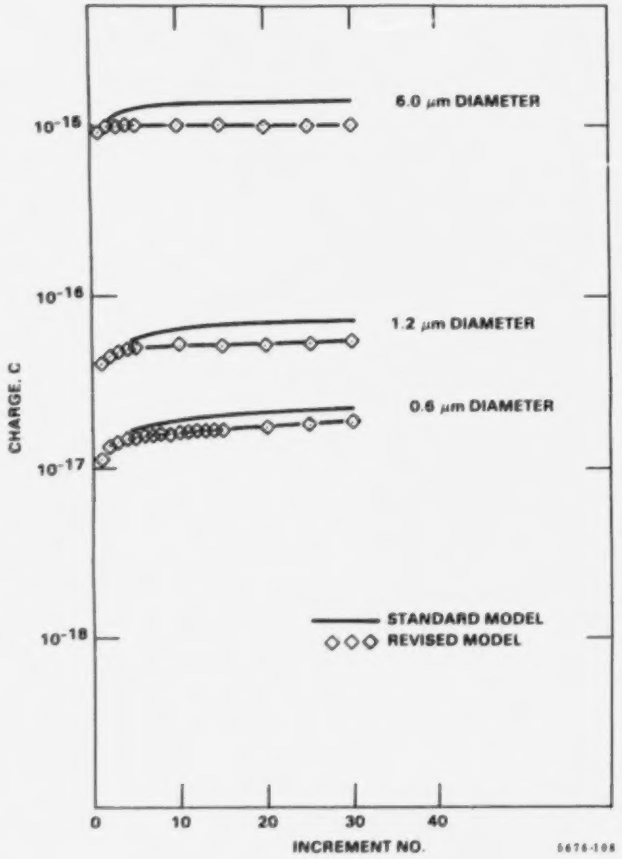

Figure 3. Particulate charge calculated by the standard and revised versions of the ESP model.

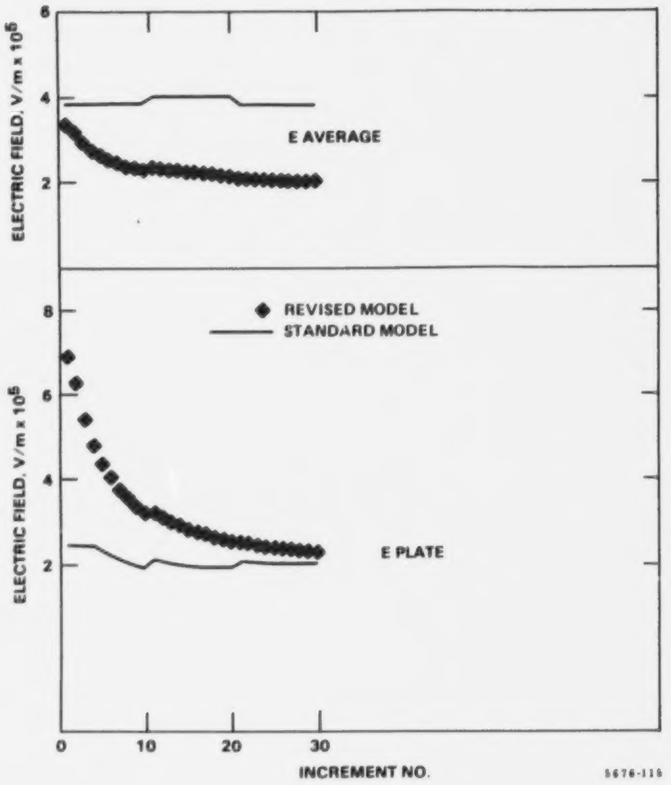

Figure 4. Calculated electric fields for the standard and revised versions of the ESP model.

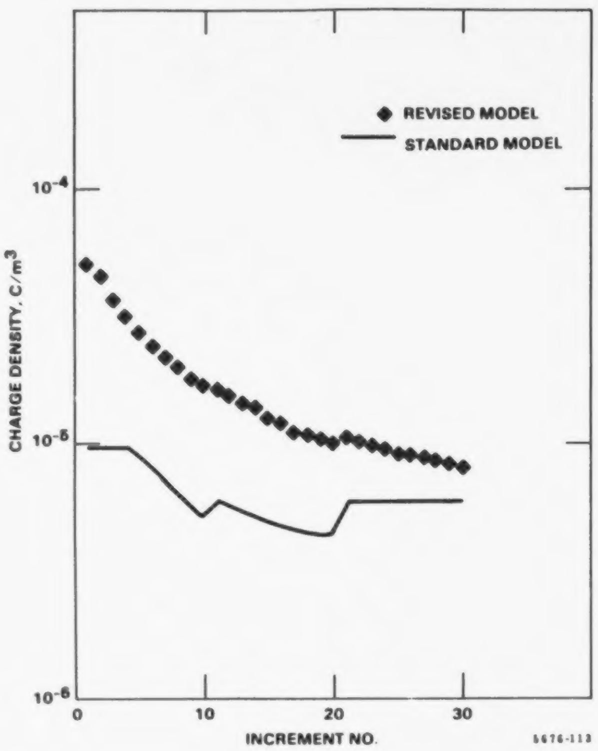

Figure 5. Total space charge density calculated by the standard and revised versions of the ESP model. The calculation point is at the plate directly opposite the wire.

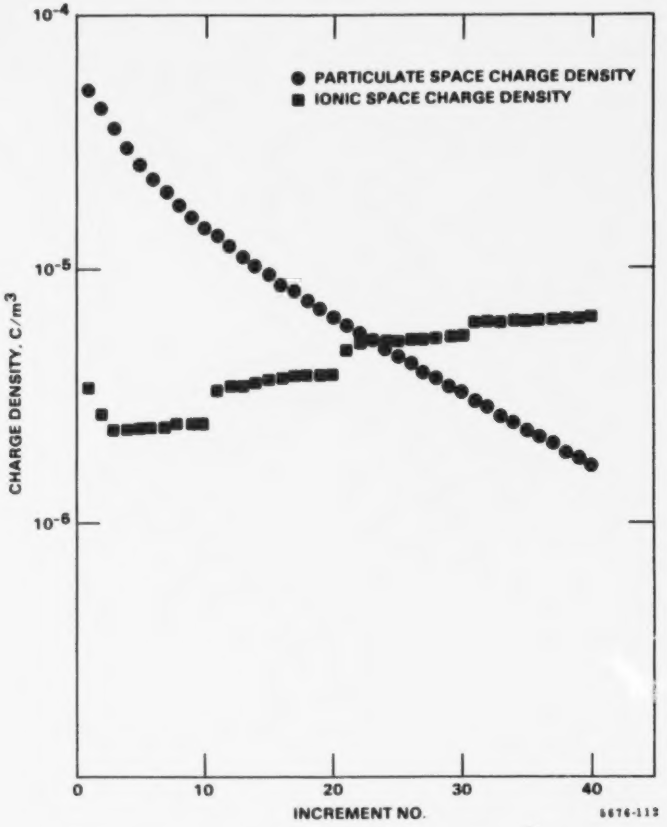

Figure 6. Particulate and ionic components of the space charge calculated by the revised version of the ESP model. The calculation point is at the plate directly opposite the wire.

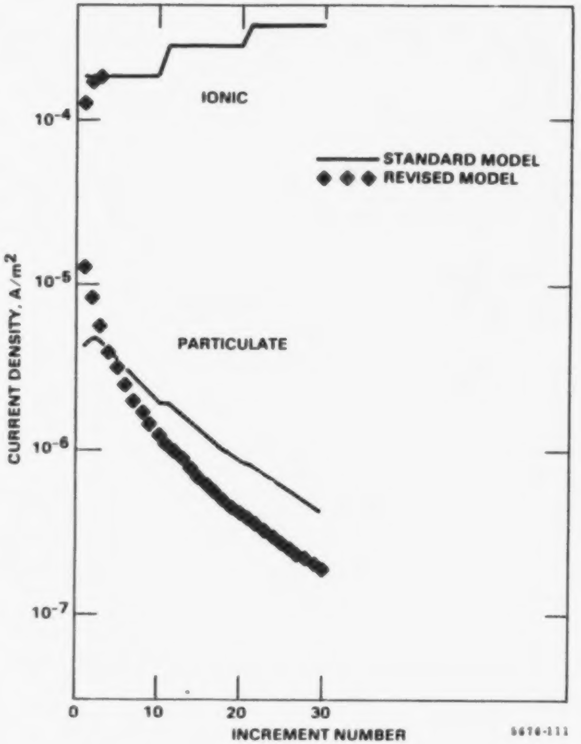

Figure 7. Ionic and particulate current densities predicted by the standard and revised versions of the ESP model.

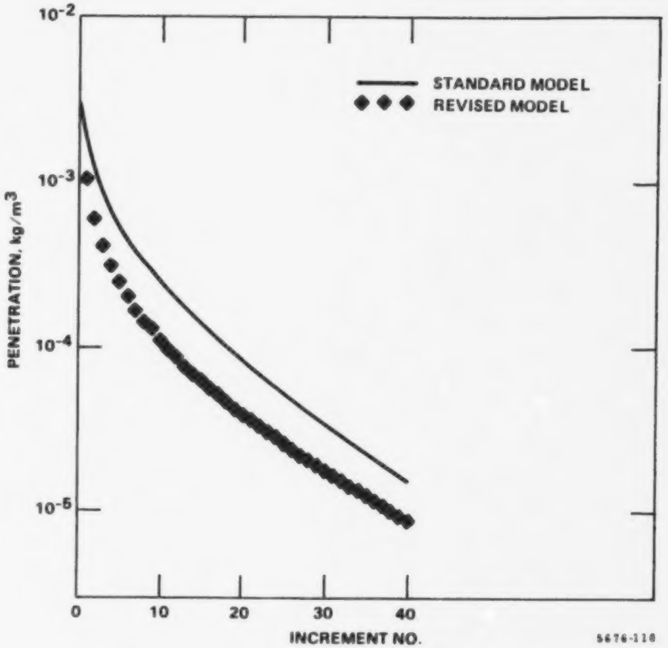

Figure 8. Mass penetration calculated by the standard and revised versions of the ESP model.

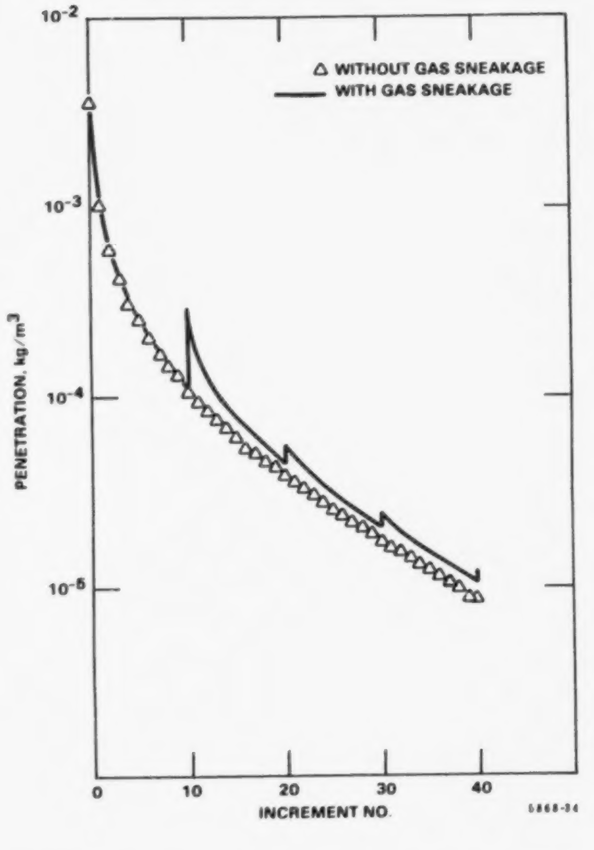

Figure 9. Mass penetration calculated by the revised version of the ESP model with 5% gas sneakage.

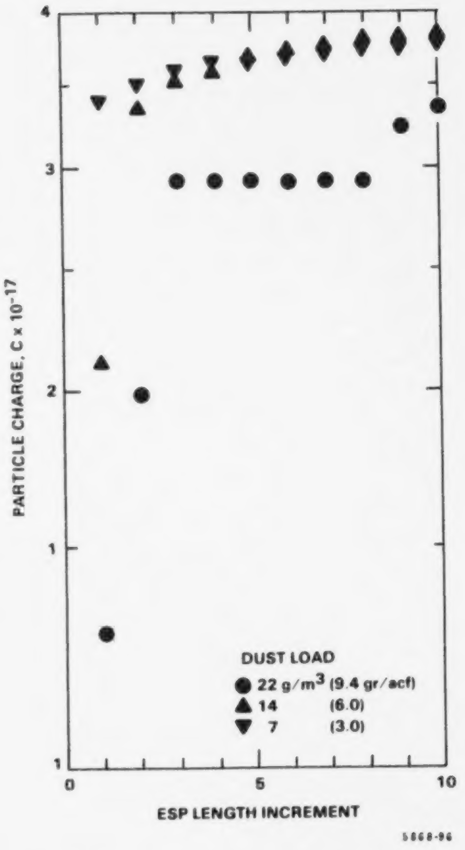

Figure 10. Particle charging rate for three dust loads using the revised version of the ESP model.

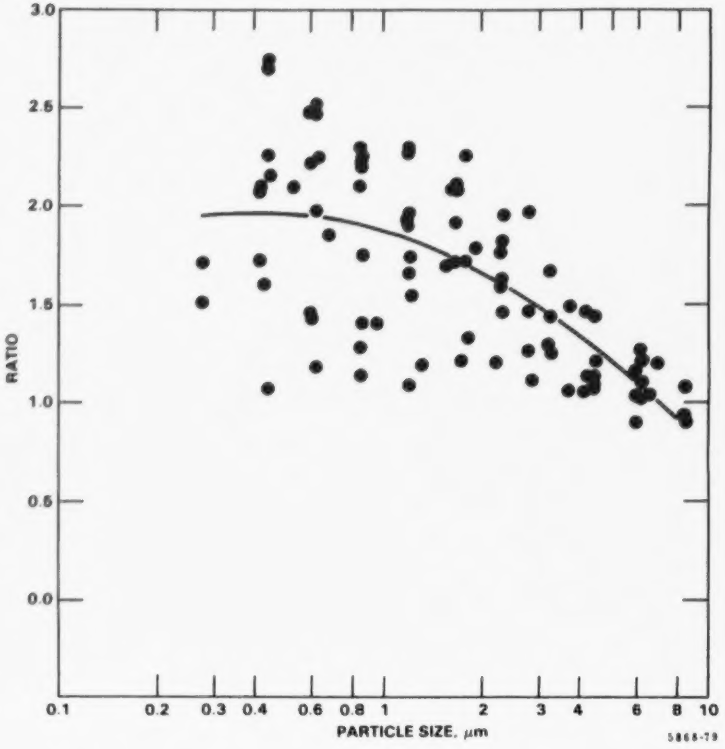

Figure 11. Ratio of measured migration velocity to computed migration velocity for 10 plants (revised model without the correction factor). The line is a second-order least-squares fit to the data.

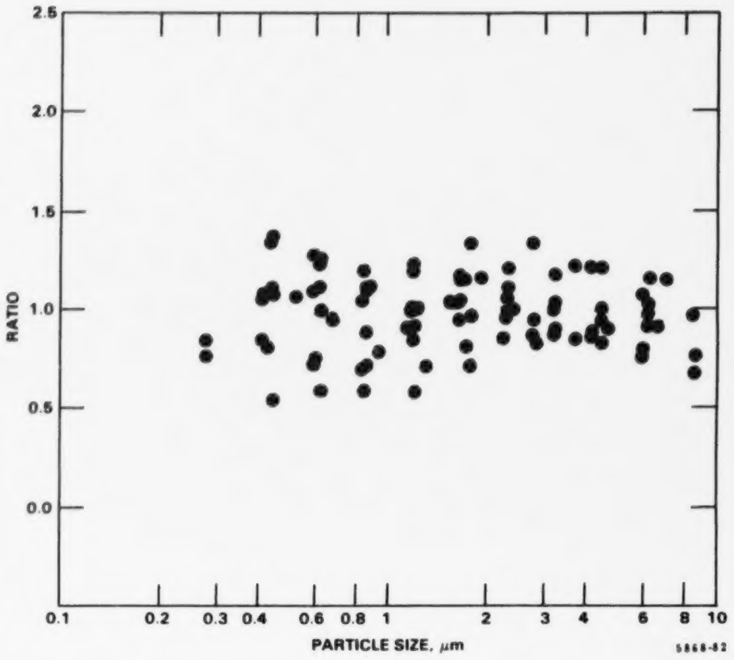

Figure 12. Ratio of measured migration velocity to computed migration velocity for 10 plants (revised model with revised correction factor).

A PILOT SCALE STUDY OF WIDE PLATE SPACING FOR PRECIPITATORS

J.K. Horrocks, R.G. Corbin and D.E. Towell
Central Electricity Research Laboratories,
Kelvin Avenue, Leatherhead, Surrey, England

The work was carried out at the Leatherhead Laboratories of the Technology Planning and Research Division and the paper is published with permission of the Central Electricity Generating Board.

The work described in this paper was not funded by the U.S. Environmental Protection Agency. The contents do not necessarily reflect the views of the Agency and no official endorsement should be inferred.

ABSTRACT

Measurements of e.m.v. and collection efficiency in a 3 zone pilot scale precipitator operating on flyash in a flue gas containing water vapour and both with and without sulphuric acid were made at differing plate spacings and wire pitches with gas velocities up to 2.4 m/s and inlet dust concentration up to 20 g/m^3. Collection efficiencies were substantially independent of plate spacing at current densities exceeding 100 μA/m^2. In the absence of significant contributions from particulate space charge e.m.v's increased less rapidly with spacing at current densities below 50 μA/m^2 in line with collector plate fields calculated by a finite difference scheme. Similar overall trends of e.m.v. with spacing and current density were observed with acid conditioned and unconditioned ash. However with acid conditioned ash the hoppers make a more significant continuous contribution to the net efficiency.

PREAMBLE

There is a body of evidence which suggests that plate type electrostatic precipitators built to the mechanical standards of the 1980s and with the sophisticated energisation now available do not deteriorate in performance as the distance between the collector plates is increased above the 250-300 mm spacing which is typical of existing plant operating in the United Kingdom. Although theories have been advanced to explain the effect there is at present no full explanation of the phenomenon nor is there agreement concerning its applicability in all situations. Using the experimental facility at CERL over a period of time observations have been made of the effects of plate-spacing on precipitation performance in a variety of situations i.e. in the upstream or downstream zones of a precipitator and over a range of parameters relevant to power station ESPs in the UK. This statement contains some fruits of that investigation. It covers experiments on a fairly high resistivity fly-ash material not untypical of conditions encountered with UK coals and on the same material conditioned with sulphuric acid vapour.

The studies cover place-spacings of 200, 300 and 400 mm and with discharge electrodes at pitches of 150 and 300 mm. For each geometry performance measurements were made over a range of energisation, at duct velocities between 1.6 and 2.4 m/s, and with inlet concentrations of 10 and 20 g/m^3. For each operating condition and geometry the electrical characteristics and a breakdown of each zone of the precipitator were recorded.

The discussion which follows concentrates on the simplicities rather than the complexities which have emerged.

EXPERIMENTAL DETAILS

Details of the precipitator are available elsewhere (1). A direct contact natural gas burner preheats air which is modified by the injection of water and fly-ash to resemble a flue gas. The test sections comprise a single gas lane of three separately energised fields between which an interzone permits access by diagnostic probes (Figure 1).

Certain important quantities remained fixed throughout the experiments. Fly-ash was of two batches obtained from a power station and stored under dried air at ambient temperatures. The size distribution of this material measured both as a liquid dispersion and as pneumatically conveyed into the test duct remained remarkably consistent with a mass median diameter of 10-12 micron. The water vapour content of the gas was maintained at about 4% by weight. Under these conditions the untreated fly-ash has an in-situ resistivity approaching 10^{12} Ωcm. With acid injection fly-ash resistivity was reduced by an order of magnitude. The feed rate of fly-ash, the gas temperature, and the flow of gas were closely controlled at levels indicated in the summary table (Table 1). A fixed rapping schedule obtained: inlet zones were rapped at 15 minute intervals, zone 2 and zone 3 at 30 minutes and 60 minutes respectively. No attempt was made to optimise the rapping intervals dependent upon the operating conditions of the precipitator or the collector spacing.

Performance information was derived from the weight gain of collector plates, discharge wires, and hoppers in each zone of the precipitator in relation to the weight decrement of the inlet feed hopper.

The majority of performance measurements were made at different though fixed zonal currents within a range of plate current density typical of large precipitation plant. A few performance measurements were made close to the maximum level of current and voltage achievable.

ELECTRICAL BEHAVIOUR OF DIFFERENT WIRE PLATE CONFIGURATIONS

In the debate about precipitator performance with different electrode geometries the electrical conditions which define operation occupy a central role. The performance tests in this series of investigations were conducted each under controlled current conditions within a range of current densities at the collector plates embracing those encountered on plant precipitators. Limiting electrical conditions were separately determined.

Electrical Breakdown

The spark limit associated with each geometry, dust burden and dust condition were established in a separate series of measurements: the results are summarised in Figure 2. Spark limits are characterised by the mean breakdown field V_b/D and the current input I_b immediately preceeding breakdown. The mean breakdown field increases with dust burden and the mean current flux at breakdown decreases with dust burden. Figure 2 distinguishes unconditioned fly-ash and fly-ash conditioned by the indicated level of sulphuric acid vapour.[1] There is a marked consistency in the data for unconditioned fly-ash. Sulphuric acid vapour causes a change in the appearance of the curves. The upward trend of breakdown current density as dust burden reduces is still apparent but less marked: the mean breakdown fields are higher for all dust burdens. (N.B. The extremely high breakdown field for one geometry at 10 vpm and the unusual lack of dependence of current on dust burden remain to be explained[2].)

Voltage/Current Characteristics

The effects of spacing and wire pitch on the electrical characteristics of the zones can best be seen as the field (V/D) plotted against plate current density in Figure 3 with the plates and wires cleaned of fly-ash. By plotting these same data as the square of the electric field versus current density it is possible to project back the linear asymptote to zero current density and arrive at values for the corona threshold field. When this is done for the clean system the values so obtained agree well with the predictive method of Sekar and Stomberg (1981) if in Peeks law for the breakdown field a value of 0.001 m is used for the effective radius of the twisted square wires.

Thus we find:

$$E_t = E_{peek} \frac{\ln(\sinh \pi D/P)}{\pi D/P}$$

Above threshold the characteristics of the different configurations are well described by an expression of the form given by P. Cooperman (3)

---

[1] The quoted concentrations in vpm refer to the concentration before absorption by the ash. No vapour can be detected in the ash laden gas.

[2] Fouling of the discharge electrode may have occurred under prolonged exposure to acid conditions.

$$j = \frac{24K\varepsilon_o V(V-V_t)}{PD^2 \ln(d/a)}$$

again with the effective wire radius a = 0.001 m, and the radius of the equivalent cylinder, d = 4D/π.

The differences in the electrical characteristics of the different wire-plate geometries tend to disappear when there are high concentrations of dust in the gas stream as is amply demonstrated in Figure 4. Dust burden suppresses the current flux for a given mean field - an effect which is discernible at all dust concentrations over 2 g/m^3 and even at the narrowest plate spacing used during these experiments.

The effect of acid conditioning is scarcely distinguishable from that of burden in its effect on the electrical characteristics. In Figure 5 the characteristics are separated by both burden and acid treatment. A substantial increase in mean electric field follows the introduction of acid at all current densities in excess of about 50 $\mu A/m^2$.

We may summarize as follows: Acid and dust increase the applied field both at breakdown conditions and at current densities which are typical of plant operation. When in the following discussion, we compare performance at the same current densities this is only approximately at the same applied field; when dust burdens were low higher applied fields were experienced at reduced spacing for the same current densities.

COLLECTION CHARACTERISTICS

Over a period of time observations of performance relating to individual precipitator components (collector plates, discharge electrodes, hoppers) as well as those of whole fields were collected and stored in a database for subsequent statistical analysis. These measurements relate to four electrode geometries described electrically in Figures 2-4. They cover a range of inlet dust concentrations, acid treatments, gas velocities and collector current densities.

The levels of the independent variables and their combinations in the database will be found listed in Table 1. Not all velocities and inlet concentrations are represented for every geometry, current density level and dust condition. Despite these concessions to time and effort the database contains information on more than 80 experiments.

For the whole three-field precipitator the primary correlating variable is found to be current density. Although for any set of operating conditions (dust burden, acid injection rate etc.) the applied field V/D and the current density are equally good correlating variables, when the conditions change the collection efficiency is better correlated with current density than with the applied field. This should not be taken to imply that the same applies in each zone. To establish the role of current density in the final zone independently of the others separate tests were conducted with a common upstream condition and several levels of current density in the final zone. These tests showed that high values of current density are not productive of improved performance in the final zone if the previous zones are performing at high efficiency.

The overall performance of the precipitator on unconditioned fly-ash at different plate spacings is summarized in Figures 6-8. Figure 6 collects together normalised effective migration velocities for all experimental runs with unconditioned ash. It includes the collection of the plates only in the intervals between rapping events. The material continuously collected by the hoppers is however included in the emv plotted in Figure 7 which represents the total collect of the precipitator. A comparison of Figures 6 and 7 reveals the importance which attaches to continuous collection of the hoppers. They contribute between 2 and 3 cm/s to the effective migration velocity.

The proportionality of emv and plate spacing is clearly apparent in both Figures 6 and 7 at current densities in excess of 100 $\mu A/m^2$. However there is a marked decline in emv at low current densities which more significantly affects the data for wider collector spacing. This impression is reinforced by Figure 8 which plots overall efficiency. Efficiencies for all burdens and velocities coalesce at higher current densities but at the low current density of 50 $\mu A/m^2$ the narrower spacing has an efficiency advantage.

The data for acid conditioned ash tell a similar story (Figure 9). At higher current densities the wider spaced collectors exhibit a proportionally greater effective migration velocity but there are indications that this is not maintained at current densities below 70 $\mu A/m^2$.

The emvs for high inlet concentrations and for the wire pitch/spacing ratio (0.15:0.3) are marginally but consistently higher than for the lower concentrations and higher ratio of pitch to spacing.

DISCUSSION

It has been widely reported that the efficiency of a wire-plate electrostatic precipitator is either independent or occasionally improves as the separation of the collector plates increases. This implies that as the plate spacing increases there is a corresponding increase in the Deutschian effective migration velocity. It will be noted that the results reported in the previous section also support this view for the range of geometries studied, and for the higher and lower resistivity dusts provided that the comparison is made at similar levels of collector plate current flux[1]. We have examined the simplest and most popular explanation of this effect, that space charge induced fields at the collector surface which increase with the plate separation cause the observed proportionality of emv and invariance of efficiency with spacing.

---

[1] At only approximately similar values of applied field, V/D.

The space charge hypothesis is not immediately self evident but under certain assumptions we expect it to be true. The following simple example illustrates the general character of the hypothesis. Take the Deutschian description of precipitator performance,

$$\eta = 1 - \exp\left(-\frac{\omega \ell}{2uD}\right)$$

in which ℓ is the length of the collecting plate, u is the gas velocity, and D is the plate to wire separation, i.e. half the plate spacing. ω is the effective migration velocity which we expect to depend upon particle size, particle charge and the electric field. Thus assuming that whatever else is occurring within the precipitator the basic driving force for migration involves a balance of the electric forces upon the charged particle and the viscous drag we write,

$$\omega \propto E_c E_d = ab \left(\frac{V}{D}\right)^2 = ab\, E_o^2$$

where E_c is the effective electric field charging the particles, E_d is the effective electric field causing their collection. V is the applied voltage and a and b are factors of proportionality. 'a' includes the constants for particle charging and migration, and 'b' is a parameter which relates the effective charging and collecting electric fields to the value of the applied field, $E_o = (V/D)$. If precipitator efficiency is to be constant the exponent in the Deutsch equation must also be constant.

Since we have experimentally observed that the proportionality of e.m.v. and spacing is associated with roughly similar applied fields E_o the parameter b must vary as the spacing to explain the observed behaviour.

By way of illustration consider the one-dimensional solution of Poisson's equation for the electric field between parallel plate electrodes in the presence of a uniformly distributed space charge. For this system we have the electric field at the collector surface, E:

$$E_w = \frac{\rho D}{2\xi_o} + E_o$$

where ρ is the space charge density. If we make the classical Deutsch assumption that it is the electric field at the collecting surface which determines the rate of deposition and supplement this with the further assumption that the pertinent charging field is similarly related to the mean field E_o we have the following relationship

$$E_c E_d = E_w E_o = \left(E_o + \frac{\rho D}{2\xi_o}\right) E_o$$

whence:

$$b = 1 + \frac{\rho D}{2\xi_o E_o}$$

showing that the parameter b could indeed increase with plate spacing in a manner which for certain choices of space charge density and electric field approximates proportionality. Note that $\rho D/2\xi_o E_o$ must exceed unity for this condition to apply. For a typical E_o (~.3 MV/m) this implies that ρ ~5 $\mu C/m^3$.

The wire plate system is more complicated. Castle et al. (13) have drawn similar conclusions concerning the enhancement of the electric field at the wall from a consideration of the wire-plate model of G. Cooperman correctly observing that in the wire plate geometry the Laplace field at the wall is often dominated by ionic space charge fields. In view of the complex geometry of the Laplace field and ionic space charge distribution resort was made in this study to a finite difference calculation scheme (see Appendix) to evaluate the wall fields correctly.

Computations were undertaken for each experimental electrode configuration at various voltages and current densities. The particulates were represented by a space charge uniformly distributed. Figure 10 illustrates the behaviour of E_W/E_o for these configurations under two values of particulate space charge. It will be seen that E_W/E_o increases quite rapidly over the range of separations of interest and falls below unity for the narrower spacings because the Laplace field at the wall in these geometries is less than the mean field V/D.

At the higher current flux of 140 $\mu A/m^2$ and with a particulate space charge of 10 $\mu C/m^3$ the normalised collecting field E_W/E_o increases by 3:1 as spacing increases by a factor of 2. Without any contribution from particulates the ratio is about 2:1. At the low current flux of 50 $\mu A/m^2$ the above ratios are 2:1 and 1.6:1 for conditions with and without particulate space charge.

It may be noted that the measured level of particulate space charge (10 $\mu C/m^3$) makes a substantial difference to these predictions. The value assumed may be too high and in any case does not apply throughout all fields. The observed effect on e.m.v. of high inlet dust burden (Figure 7) does suggest some effect of particulate space charge but not of the order which the wall field calculations might suggest. Measurements of particle charge are in hand using a laminar sampling probe in the interzones. Indications are that for particles of more than a few microns there is a pronounced charge deficit (based on an estimate of saturation charge in the upstream field). It is yet too early to say whether this charge deficit is dependent upon geometry.

We may say that in the absence of a significant contribution from particle space charge (which must apply to the later fields in the precipitator) the e.m.v. relationship with spacing follows with the predicted field at the collector.

Both experimentally measured e.m.v.'s and computed collector plate fields rise less rapidly with spacing at lower current densities i.e. below ~70 $\mu A/m^2$.

It is possible that this latter observation may be relevant to ESPs which are forced by the nature of the fly-ash to operate at low levels of current density. In such cases the lack of ionic space charge would militate against wider spacings unless discharge electrode geometry were modified to enhance the Laplace fields at the collector surfaces.

APPENDIX 1. CALCULATION PROCEDURE FOR THE ELECTRIC FIELD

The electric field, E, in the wire-plate geometry is found by solving Poisson's equation for the potential, ϕ, together with current continuity in the region and including a contribution to the space charge from particles, which gives rise to the following non-linear coupled set of equations:

$$\nabla^2\phi = -\frac{q_i + q_p}{\xi_0} \qquad \text{... (A1.1)}$$

$$\nabla q \cdot \nabla\phi = \frac{(q_i^2 + q_i q_p)}{\xi_0} \qquad \text{... (A1.2)}$$

where ξ_o is the dielectric constant,
q_i is the ion space charge density,
q_p is the particulate space charge density,

The equations are solved subject to the following boundary conditions:

$\phi = 0$ on the collector (clean plate condition)
$\phi = V$ fixed on the discharge electrode (operating voltage)
$\nabla\phi = 0$ on at the inlet and exit, sufficiently far away from the electrodes
$q_i = q_{io}$ fixed on emitting portions of the discharge electrode

The ionic space charge density at the discharge electrode is determined by the detailed physics of the corona generating process: it is too complicated to be included within our model framework. Instead, the boundary q is arbitrarily fixed in the calculation procedure, and values which produce an average current in the observed range at the collector plate are deemed physically valid.

The particle space charge is assumed to be distributed evenly throughout the volume. The real distributions were not known, but high levels of turbulence are observed in precipitators with corona generation (14,16), it is therefore reasonable to assume strong mixing and near uniform concentration gradients. Concentration measurements made recently in the interzones of this precipitator have revealed concentrations differing by less than a factor 2 between the wall plane and the discharge wire plane.

Computational Method

Following the method of Leutert and Bohlen a finite difference scheme was employed in which the region between wire and collector was divided into a rectangular mesh with one corner node representing the wire. With such a representation, the solution is grid dependent, but the best solution will occur when the grid spacing is a fixed fraction of the actual wire size modelled. In this series the optimum grid spacing was found by comparing the Laplace solution with another derived from a finite element computation (17) in which the discharge electrode dimension and shape were modelled in detail.

After the grid has been determined, particulate space charge was added to the solution region, and ionic space charge set at the discharge electrode. The solution was determined by iteration between the potential field from equation (A1.1) with a given space charge distribution from the previous iteration, and finding the ionic space charge distribution from equation (A1.2) using the newly updated values of potential, until the changes in either parameter were within a set tolerance (1.0%). When convergence was attained, the average current density, and electric field at the collecting plate, and the average field from the wire to the plate were calculated and output.

The more accurate finite element scheme was not used for the full study because of the greater computing overheads and much extended computing time.

REFERENCES

1. Horrocks, J.K. and Moore, M.J., The Precipitator Test Facility at CERL and the Use of Continuous Weighing in the Diagnosis of Precipitator Processes and Re-entrainment Phenomena, Third International Conference on Electrostatic Precipitation, Abano, October 1987.

2. Sekar, S. and Stomberg, H., On the Prediction of Current-voltage Characteristics for Wireplace Precipitators. Jn. of Electrostatics, 10, 1981.

3. Cooperman, P., A Theory for Space Charge Limited Currents with Application to Electrostatic Precipitation, AIEE Trans., Pt. 1, 1960.

4. Masuda, S., Present Status of Wide-spacing Type Precipitator in Japan, EPA Symposium, Denver, 483-501, 1979.

5. Heinrich, D.O., Electrostatic Precipitator Collector Spacings Above 300 mm (12")? Atmospheric Environment, Vol. 13, 1707-1711, 1974.

6. Weber, V.E. and Wiggers, H., Untersuchungen an einem Laborelektrofilter uber die Einflusse der Gassenbreite und der Gasgeschwindigkeit auf das Abscheideverhalten und die Staubkonzentrationsverteilung. Staub-Reinhalt Luft, Vol. 40, No. 11, 469-473, 1980.

7. Kawamura, T., One Duct Model Study of Extremely Wide Spacing Electrostatic Precipitation for Iron Ore Sintering Exhaust Gas. Second Int. Conf. on Electrostatic Precipitation, Kyoto, Japan, 858-863, 1984.

8. Chen, G.J. and Wang, L.Q., The Research and Application of Electrostatic Precipitator with Wide Spacing and Cross-positioned Channel Collecting Plates in Power Plant. Second Int. Conf. on Electrostatic Precipitation, Kyoto, Japan, 362-365, 1984.

9. Darby, K., Plate Spacing Effect on Precipitator Performance. Second Int. Conf. on Electrostatic Precipitation, Kyoto, Japan, 376-383, 1984.

10. Altman, R.F., Driggers, G.W., Gray, R.W., DuBard, J.L. and Landham, Jr., E.C., Technical Evaluation of Plate Spacing Effects on Fly-ash Collection in Precipitators. Proc: Fifth Symp. on the Transfer and Utilization of Particulate Control Technology, EPRI CS-4404, Vol. 2, Paper 22, 1986.

11. W. Diener, Operating Results of Commercial Precipitators with 400 mm Plat Spacing, Proceedings of the Second International Conference on Electrostatic Precipitation, Kyoto, Japan, 12-15 November, 384-386, 1984.

12. Misaka, T., Sugimoto, K. and Yamada, H, Electrical Field Stength and Collection Efficiency of Electrostatic Precipitator Having Wide Collecting Plate Pitches, CSIRO Conference on Electrostatic Precipitation, Leura, 23-24 August 1978.

13. Castle, G.S.P., Bracha, W.S. and Elmoursi, A.A., Electric Field Conditions in Conventional and Wide Duct Precipitators, Third International Conference on Electrostatic Precipitation, Abano, October 1987.

14. Self, S.A., Kihm, K.D. and Mitchener, M., Precipitator Performance Improvement Through Turbulence Control, Third International Conference on Electrostatic Precipitation, Abano, October 1987.

15. Leutert, G. and Bohlen, B., The spatial trend of electric field strength and space charge density in plate type electrostatic precipitators, Staub-Reinhalt Luft, Vol. 32, 27, 1972.

16. Corbin, R.G., Some interesting features of corona induced secondary flows in electrostatic precipitators. Eighth Int. Conf. on gas discharges and their applications (GD85), Oxford, 16-20 Sept., pp 187-190, 1985.

17. Hutton, A.G., Smith, R.M. and Hickmott, S., The computation of turbulent flows of industrial complexity by the finite element method - Progress and prospects. Int. J. for numerical methods in fluids, Vol. 7, pp 1277-1298, 1987.

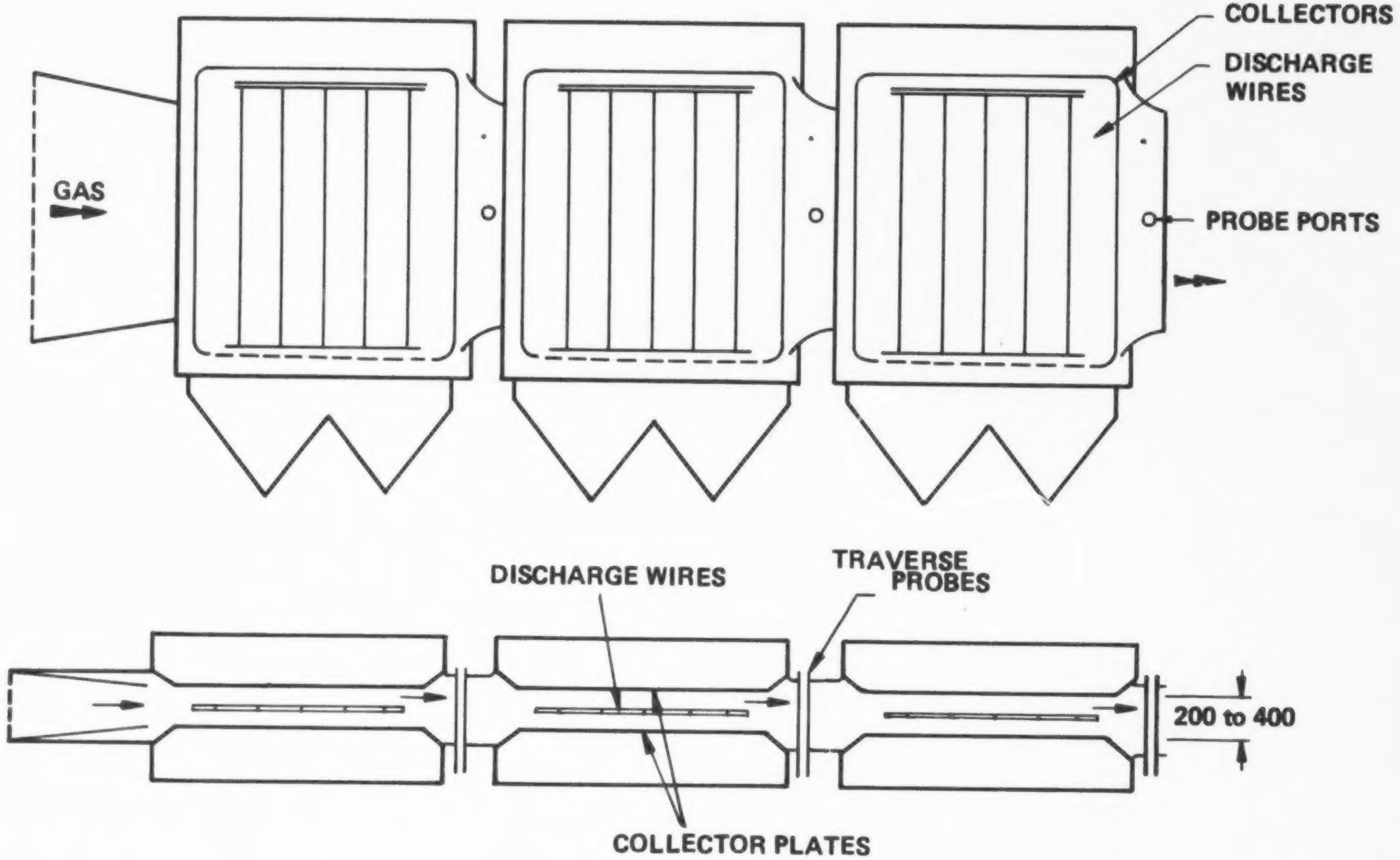

FIG. 1 TEST PRECIPITATOR: IN-LINE FIELDS WITH VARIABLE SPACING

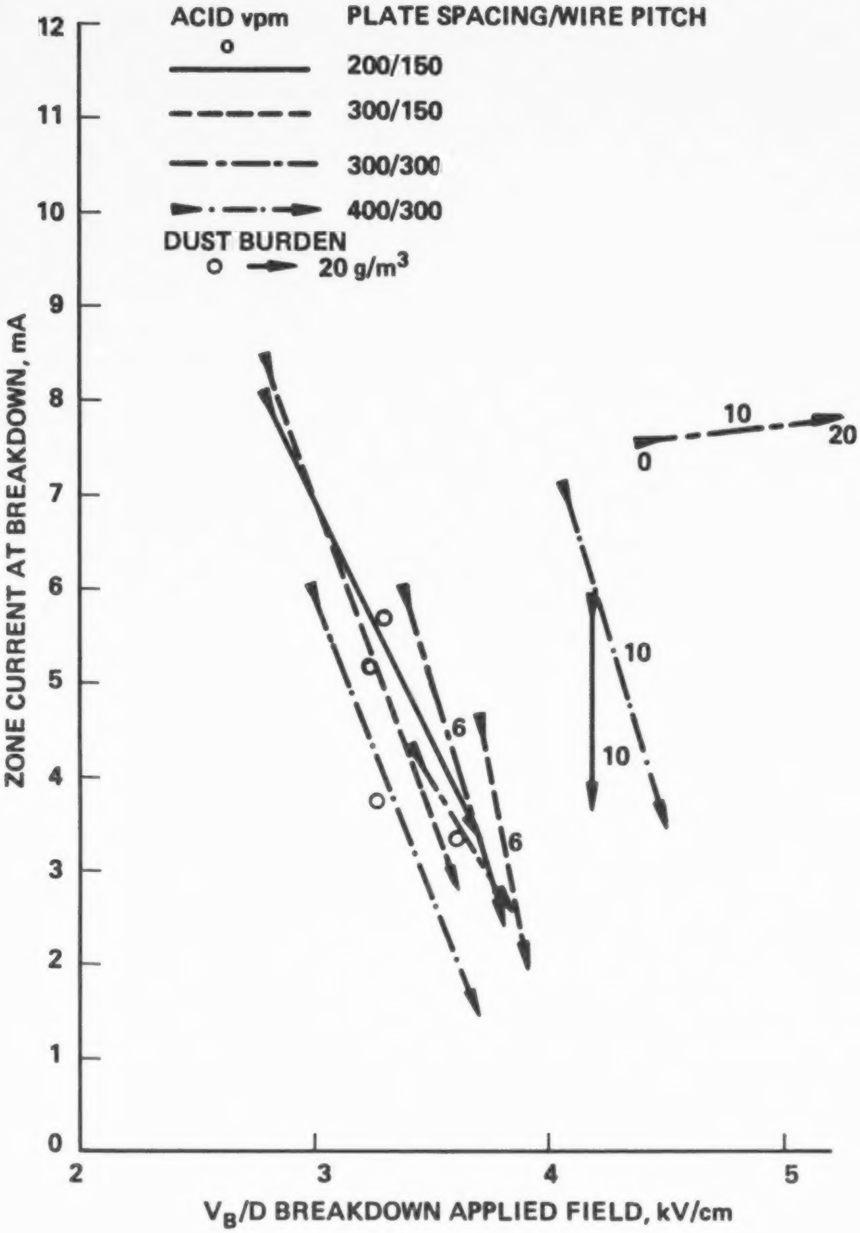

FIG. 2 ELECTRICAL BREAKDOWN CHARACTERISTICS: ZONE 1

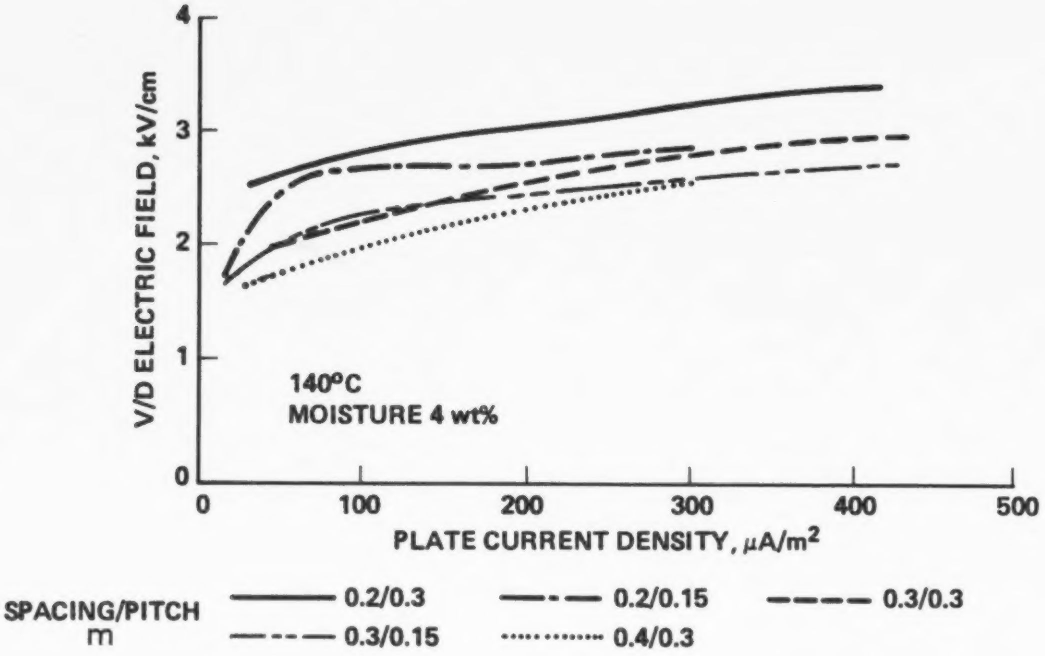

FIG. 3 ELECTRICAL CHARACTERISTICS OF THE CLEAN ELECTRODES

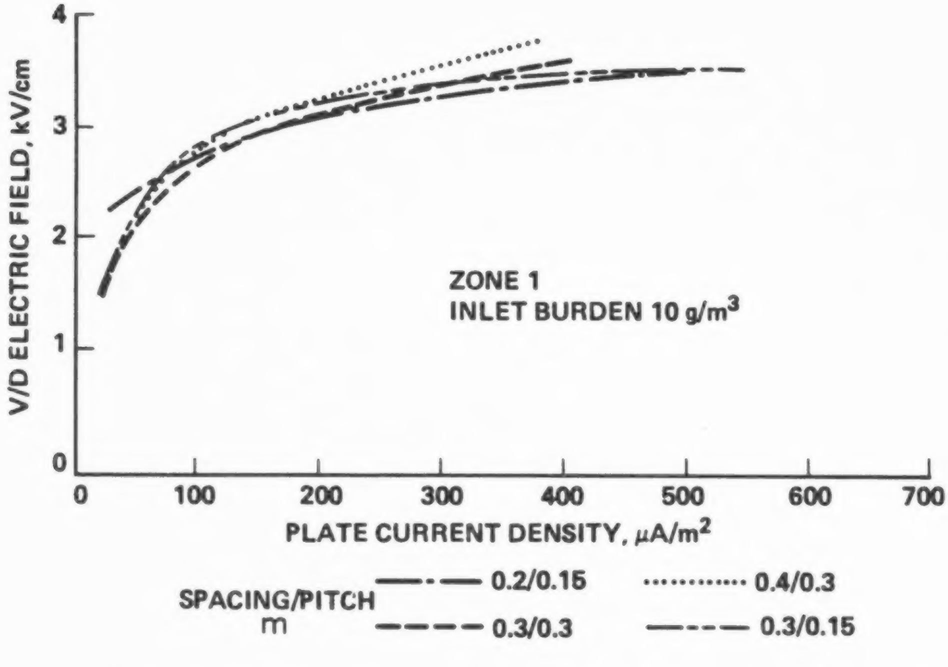

FIG. 4 ESP ELECTRICAL PERFORMANCE AT HIGH DUST BURDENS

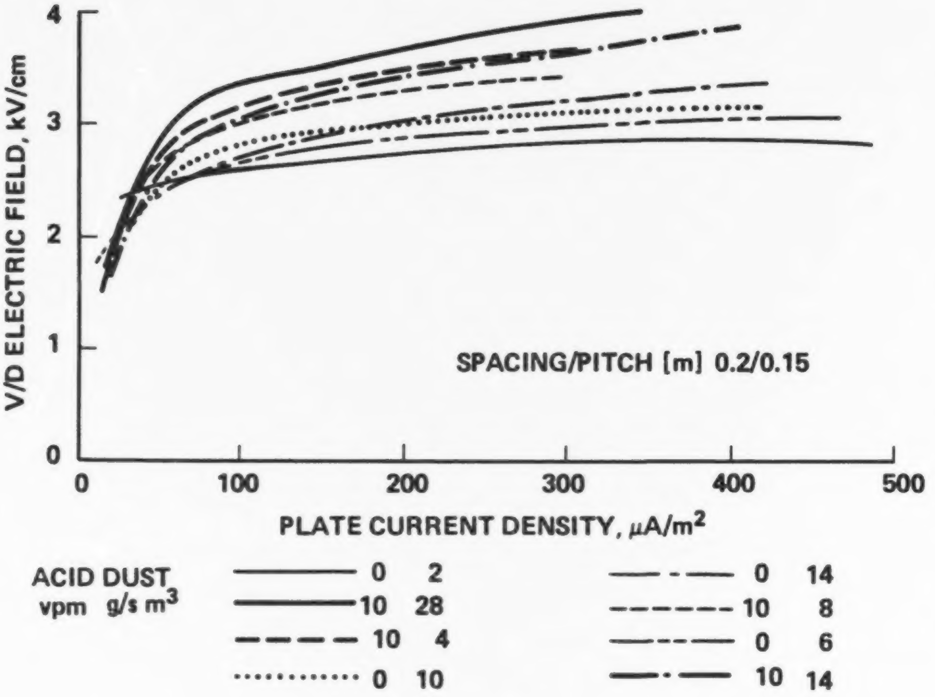

FIG. 5 DEPENDENCE OF FIELD ON CURRENT, ACID AND DUST

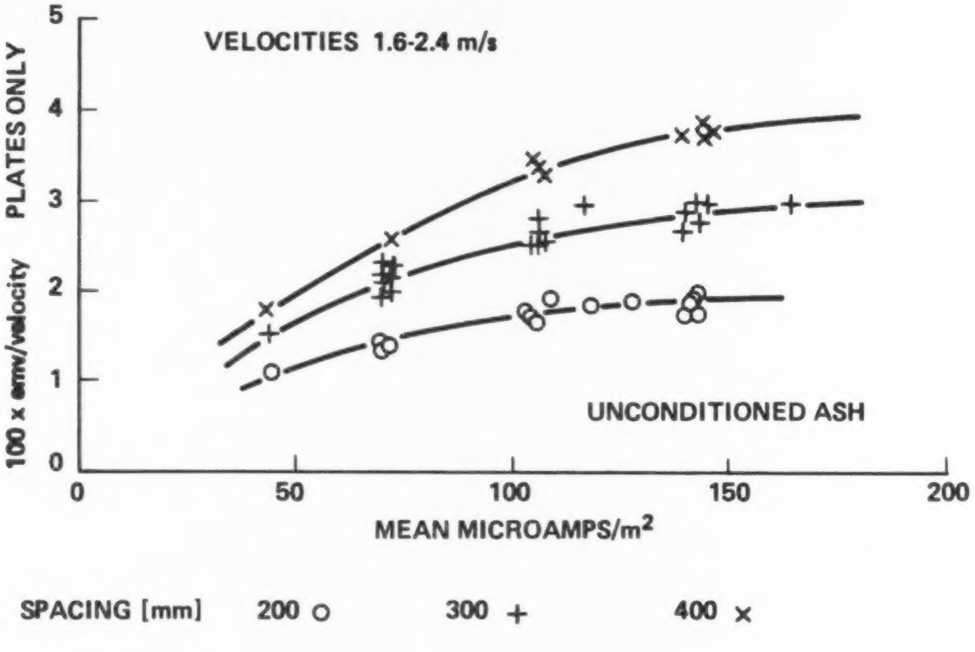

FIG. 6 ESP ALL PLATES PERFORMANCE WITH CURRENT AND SPACING

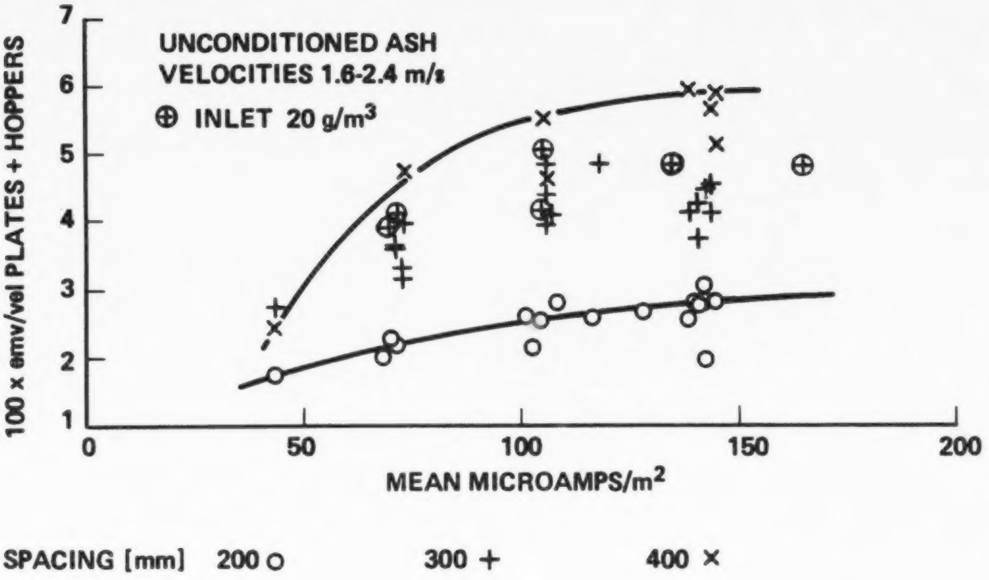

FIG. 7 ESP ALL ZONES PERFORMANCE WITH CURRENT AND SPACING

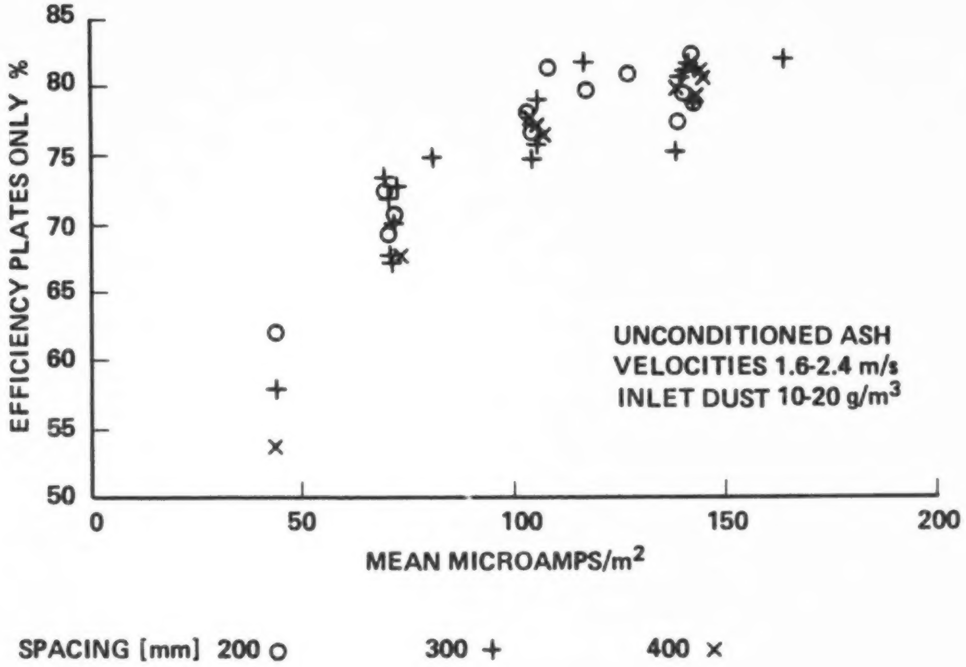

FIG. 8 ESP ALL PLATE PERFORMANCE WITH CURRENT AND SPACING

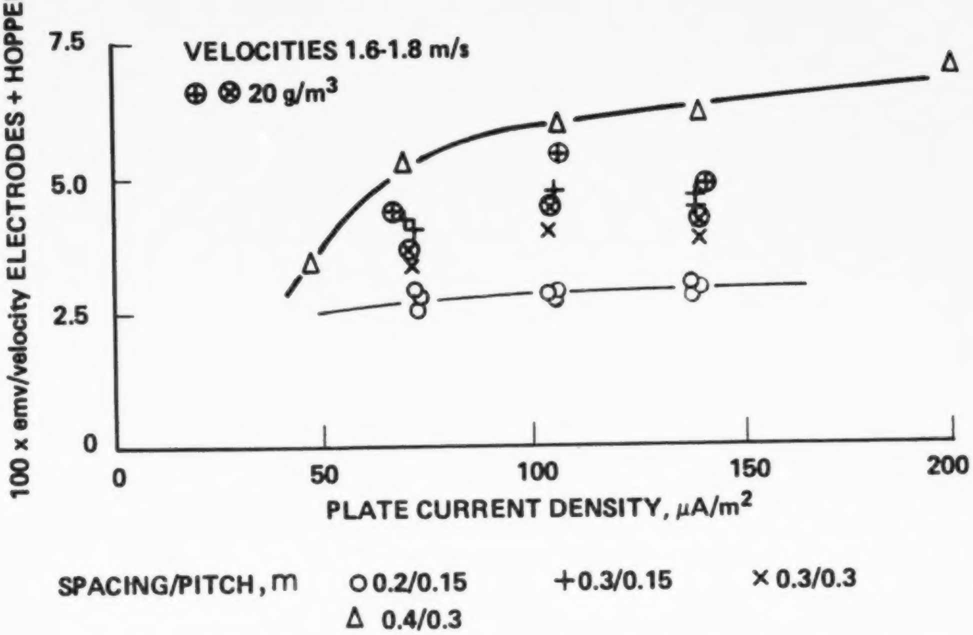

FIG. 9 ESP ALL ZONES PERFORMANCE WITH CURRENT AND GEOMETRY. ACID CONDITIONED ASH

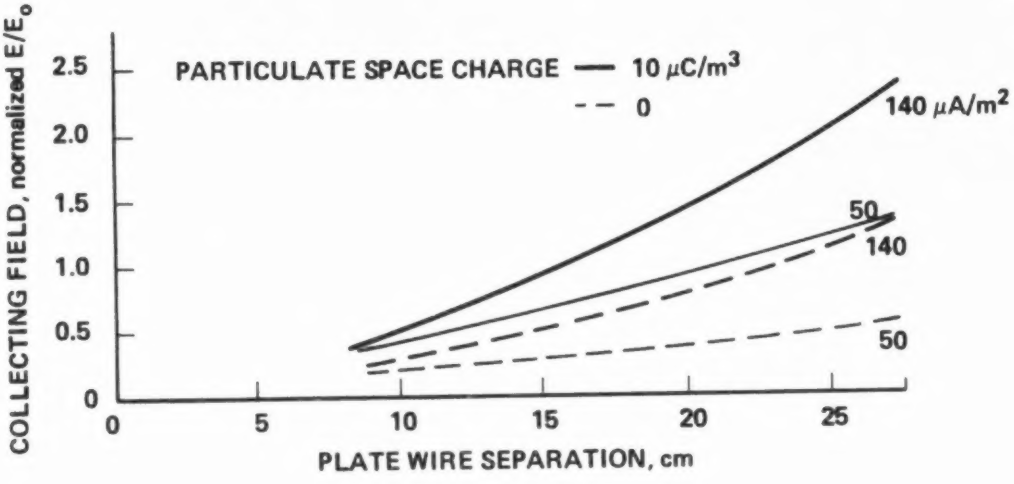

FIG. 10 COMPUTED AVERAGE COLLECTING FIELD: EFFECT OF SPACING

TABLE 1. PERFORMANCE DATABASE

Plate Spacing m	Wire Pitch m	Inlet Duct gl m^3	Gas Velocity m/s	Acid vpm	Current $\mu A/m^2$
0.2	0.15	2.0	1.8	0.0	44,71,105,109,117,128,140,143,(483)
0.2	0.15	10.0	1.8	10.0	72,106,140,(325)
0.2	0.15	10.0	2.4	0.0	71,105,141
0.2	0.15	10.0	2.4	10.0	72,106,140
0.2	0.15	20.0	1.8	0.0	70,103,143
0.2	0.15	20.0	1.8	10.0	72,105,141
0.2	0.15	10.0	1.6	0.0	43,70,73,105,116,139,142,164,(648)
0.3	0.15	10.0	1.6	6.7	70,139
0.3	0.15	10.0	1.6	10.0	139
0.3	0.15	10.0	2.4	0.0	71,105,139,(380)
0.3	0.15	10.0	2.4	0.0	71,106,140
0.3	0.15	10.0	2.4	6.7	72,106,141
0.3	0.15	20	1.6	0	70,104,139
0.3	0.15	20	1.6	10	69,107,140
0.3	0.30	10	1.6	0	71,105,143,(488)
0.3	0.30	10	1.6	10	71,103,141
0.3	0.30	10	2.4	0	72,105,142
0.3	0.30	20	1.6	0	71,105,142
0.3	0.30	20	1.6	10	70,103,138
0.4	0.30	10	1.6	0	42,105,144
0.4	0.30	10	1.6	10	46,69,106,138,210
0.4	0.30	10	2.0	0	73,107,145
0.4	0.30	10	2.4	0	139
0.4	0.30	20	1.6	0	105,143,(413)

( ) Zone 3 values. Maximum level run.

PARTICLE CHARGING AND COLLECTION EFFICIENCY IN A LABORATORY SCALE ELECTRON BEAM PRECIPITATOR

W.C. Finney, J.S. Clements, and R.H. Davis

Department of Physics
Florida State University
Tallahassee, FL 32306

ABSTRACT

Earlier studies have shown that a bench scale electron beam precharger can charge aerosol particles to levels of up to five times those predicted by the classical Pauthenier field charging equation. This result is principally due to space charge enhanced electric field and free electron charging. Electron beam precharging of resuspended particles simulating fly ash has now been successfully demonstrated in the laboratory scale FSU Electron Beam Precipitator (EBP) test system. The EBP is a fully instrumented, two-stage, 2000 ACFM wind tunnel housing a precharger employing a 100 keV electrostatic accelerator. A new Mk. II version of the E-beam precharger was tested upstream from a conventional wire-plate electrostatic precipitator operating as a low current collector. Using 1 μm diameter particles, system collection efficiencies of 99.9+ percent have been achieved. The particle penetration reduction parameter "α" ($\alpha = P_2/P_1$), showed that E-beam precharging decreased the overall system penetration by a factor of over 100. The effective particle migration velocity (w) was found for experiments operating the collector alone as a conventional ESP (w_1) and with both the precharger and collector activated (w_2). Calculated performance enhancement parameters "H" ($H = w_2/w_1$), produced migration velocity increase factors of up to 5 in many cases. The results of optimization studies now underway using the Mk. II E-beam precharger in the EBP wind tunnel will be reported.

INTRODUCTION

Two-stage electrostatic precipitators (ESPs) have been the focus of extensive investigation during the past decade. These studies have shown that two stage operation can offer advantages over conventional electrostatic precipitation by separating the functions of charging and collection while optimizing both. The Aerosol Physics Group at the Florida State University has concentrated its effort on the advancement of particle emission control technology by using an electron beam (E-beam) precharger as the first stage in an integrated system. The subject of this work is to develop a laboratory-scale Electron Beam Precipitator (EBP) which will remove fine, respirable particles at very high collection efficiencies.

An electron beam precharger is an ion current separation and collection device for charging particles to very high levels in an electric field (1). The very large ion current densities and elevated electron energies found in electron beam prechargers (2) are expected to decrease the time necessary for field charging of large particles and increase diffusion charging of small particles, respectively. Also, high ion current densities will cause a localized space charge enhancement of the electric field, which will increase the level of field charging of the larger particles.

In addition to high ion current densities, another characteristic of electron beam prechargers is the presence of large numbers of free electrons. Small radius particles will be charged to high levels by free electron diffusion charging in an E-beam precharger (3). This gives E-beam precharging an advantage over conventional electrostatic precipitators which generally collect fine, high resistivity particles with greatly reduced efficiency.

Two preliminary precharging investigators preceded the current one. In the first, prechargers using high electron beam energy (1 MeV) were tested both in and outside the EBP wind tunnel (4). These Mk. I precharger experiments showed that the electron beam energy must be closely matched to the precharger electrode geometry in order to avoid spurious ionization of opposite sign to the copious working ions. The presence of a small number of ions opposite in sign to the working ions severely limited the charge on the particles, even when the working ions outnumbered the spurious ions by a factor of 100 or more.

The E-beam energy/electrode geometry matching condition necessitated the development of a low energy (100 keV) electron beam precharger. In the second investigation, bench scale tests of the low energy bi-electrode precharger configuration produced very good particle charging results for 1 and 3 μm diameter polystyrene latex (PSL) particles (5). Particle charging was as much as a factor of 3 larger than that predicted by the Pauthenier ionic field charging theory and the importance of delineating the ionization and charging zones was confirmed.

The results of these bench scale experiments were incorporated into the design of the latest precharging configuration, the Mk. II. Upon installation of the Mk. II precharger in the EBP wind tunnel, a program of tests was begun and the early results were very promising (6). The results of the latest Mk. II E-beam precharging experiments focusing on several important variables are the subject of this work.

ELECTRON BEAM PRECIPITATOR WIND TUNNEL

A unique device combining a fully functional electrostatic precipitator with electron beam accelerator technology has been constructed at Florida State University. The laboratory scale Electron Beam Precipitator (EBP) which was used to test the Mk. II E-beam precharger is shown in Fig. 1. The EBP is basically an instrumented, closed circuit wind tunnel composed of a number of specialized modules separated by ductwork sections. Specifications of the wind tunnel are as follows: Outside dimensions = 20 ft long by 8 ft wide; Single Pass Length = 45 ft; Ductwork Size = 12 in by 12 in (1 ft^2); Construction = #304 12 gauge stainless steel; Gas Velocity Range = 1 to 35 ft/sec; Maximum Gas Flow Rate = 2000 ACFM. Specialized modules of the EBP include the circulation fan, an aerosol entrainment module, two monitoring modules, the precharger and collector comprising the precipitator, and an absolute filter. EBP subsystems which are associated with the wind tunnel are several high voltage power supplies for the precipitator; gas condition sensors; particle number, size, and charge monitors; a microcomputer with a data conditioning system; three aerosol generators; a closed-circuit TV system; and a humidity control device.

For the present experiments, a Collison nebulizer fluid atomization aerosol generator (FLAG) produced a monodisperse test aerosol of 1.3 μm diameter polystyrene latex spheres (PSL) at relatively low loadings. Hot wire anemometers and electronic temperature and humidity sensors measure these parameters at several locations in the wind tunnel. Climet optical particle counters wired to a multichannel analyzer provided a real time indication of the continuously sampled gas stream. A microprocessor-based data acquisition and analysis system (Fig. 2) was used to accumulate, condition, process, and store all signals from the precharger, collector, and electronic monitors. In addition, all monitors and power supplies have remote controls and readouts to isolate the operator from the electron beam precharger.

Gas velocity changes within the wind tunnel must be carefully documented since the critical regions are of different sizes. Cross sectional areas for the various modules are as follows: precharger sub-duct = 0.25 ft^2; wind tunnel ductwork monitoring, and aerosol entrainment modules = 1 ft^2, collector = 4 ft^2. Therefore, gas passing through the system from precharger to wind tunnel to collector experiences a 16:4:1 velocity reduction.

PRECHARGING AND COLLECTION

A low energy electron beam accelerator was designed and constructed for use with the Mk. II precharger (Fig. 3). The accelerator consists of a hot filament cathode and accelerating electrodes at high voltage which are all contained within a 5 cm diameter PVC tube that is under high vacuum. In operation, electrons emitted by the hot filament are accelerated by the potential difference to the final ground electrode where they pass through a 25 μm thick aluminum foil window into air. The energy of the electron beam can be set between 0 and 100 keV and the current can be varied between 0 and 10 μA. The range of the beam in air at a working energy of 90 keV is on the order of 7 cm.

A sub-duct or prosthesis has been installed in the EBP racetrack to accept the Mk. II bi-electrode precharger. The cross section of the sub-duct was calculated to be 36 in^2 in order to satisfy the energy/geometry matching requirement for an E-beam energy of about 100 keV. As shown in Fig. 4, the E-beam enters the sub-duct perpendicular to the gas flow. Three rack and one plate electrodes are arranged in a semicircular pattern approximately 17.5 cm from the beam window and grounded cathode electrode. The rack electrode assemblies are each composed of three 0.6 cm thick, 12.5 cm high stainless steel rods The racks are designed to allow gas and particles into the charging zone while providing a high electric field. The 20 cm x 30 cm aluminum backing electrode is positioned parallel to the flow. All of the rack and plate electrodes are electrically interconnected and are served by a high voltage power supply.

Operating principles of the Mk. II bi-electrode E-beam precharger are as follows. The electron beam is delivered into the ionization region just in front of the end of the beam tube. Electron beam ionization forms a plasma of positive and negative ions and free electrons in this zone. The charge density is separated by an electric field which is imposed by the precharger electrodes. The grounded beam tube electrode (cathode, -) attracts positive ions while the positively biased rack and plate electrodes (anode, +) attract negative ions and electrons. As each electrode is approached from the center, the average charge becomes increasingly monopolar. Particles in the gas stream traversing the charging zone pass through a predominantly negative charge flux, are charged to a high level, and then flow through the downstream anode racks to the collector. Charged particles pass through the anode racks because their mobility is at least several orders of magnitude lower than that of ions and electrons, which migrate rapidly to electrodes of opposite polarity. Ions and electrons not attached to particles ("waste" ions) are attracted to the racks and are removed from the flow going to the collector.

The collecting section downstream from the precharger is the other component of the two-stage E-beam precipitator. The collector was designed to model a downsized conventional wire-plate electrostatic precipitator. The reason for using a wire-plate design is two-fold: 1. to compare a high current collector operated as a single-stage ESP to a low current collector used as the second stage for a precharger, and 2. to realistically assess the performance of the E-beam precharger in a retrofit circumstance, i.e. upstream from a conventional wire-plate collector.

The specifications of the collector module and its internal components are as follows: Configuration - 2 channels, 3 sections each channel (6 total fields); Module Dimensions - 7.5 ft long x 4.5 ft high x 1.25 ft wide; Corona Wire Length - 48 in (122 cm); Corona Wire Diameter - 0.109 in (2.8 mm); Wire-to-Plate Spacing - 3 in (7.72 cm); Plate Dimensions - 4 ft high by 2.5 ft wide (12 plates - 120 ft^2 total); SCA (ft^2 per 1000 ACFM Gas Flow) - 200 at a Gas Velocity - 2.5 ft/sec.

EXPERIMENTAL CONDITIONS AND PROCEDURES

The procedure for completing an experimental "run" is normally a five step process. These steps are listed in tabular form below.

1. Fan on, PSL injected.
2. Fan on, PSL injected, Collector energized.
3. Fan on, PSL injected, Collector energized, E-beam on, Precharger energized.
4. Fan on, PSL injected, Collector energized, (E-beam and Precharger turned off).
5. Fan on, PSL injected, (Collector turned off).

An optical particle counter located downstream from both the precharger and collector continuously monitors the concentration of 1.3 μm diameter PSL particles. For each of the five experimental steps above, a count total for Channel 12 (1-2 μm diameter) from the multichannel analyzer is obtained every 84 seconds. The independent variables which affect particle charging and collection efficiency of the two stage system are: 1. gas velocity through the precharging and collecting modules; 2. electric field in the precharger and collector; 3. current density in the precharger and collector; and 4. electron beam energy and current in the precharger. In the group of experimental runs reported here, certain experimental parameters were varied while others remained constant. Each parameter is listed below with either its unchanging value or an indication of its variability.

Constants:

1. Gas Temperature and Humidity: 25°C, 40% RH.
2. Test Particles: 1.3 μm diameter PSL.
3. Collector Polarity: Negative.
4. Precharger Polarity: Negative ions and free electrons.

Variables:

1. Precharger Gas Velocity: 4, 8, 28 ft/s
2. Collector Electric Field: 3.0 - 4.5 kV/cm
3. Collector Ion Current Density: 0.05 - 0.5 mA/m^2
4. Precharger Electric Field: 0 - 6.4 kV/cm
5. Precharger Ion Current Density: 0.1 - 0.5 mA/m^2
6. E-beam Energy (Initial): 60 - 90 keV
7. E-beam Current: 0 - 10 μA

Data in the form of particle counts at discrete intervals in the 1 to 2 μm diameter range were used to calculate the collection efficiency of the collector alone (η_1) and the collector with the precharger (η_2). Averaging the two sets of collector data taken before and after the precharging data offset any small changes over time in input particle concentration. The particle penetration through the precipitator ($p = 1 -$ efficiency) was used for comparison purposes since the fraction of particles remaining after collection (penetration) is of greater importance than the fraction collected (efficiency).

Comparing penetrations quantitatively requires the use of several parameters which can be calculated from the data. The parameter "α" is found by dividing the collector-only penetration by the precharger-collector penetration. This gives a dimensionless figure for the improvement in penetration due to the contribution of the precharger. Another important indicator of precipitator (and precharger) performance is the empirical migration velocity (w), also known as the precipitator rate parameter. It is calculated using the Deutsch-Anderson collection efficiency equation (7), which uses the measured efficiency, the precipitator plate area, and the gas flow volume to find the effective w. Dividing the precharger collector migration velocity (w_2) by the collector-only migration velocity (w_1) gives $w_2/w_1 =$ "H", which is the precharger performance enhancement parameter (8).

If precharging improves the performance of the precipitator through a higher collection efficiency, then both the calculated α and H values will be greater than 1. The actual efficiency improvement will be indicated by α while the increase in effective migration velocity of the charged particles will be given by H. Even small increments of increase in H above 1 represent a significant increase in particle charge from precharging because of the exponential nature of the collection process. The greatest improvement should be found at the lowest initial efficiency because it is more difficult for a precharger to improve upon an already highly efficient precipitator.

EXPERIMENTAL RESULTS

The results of the first set of experiments are summarized in 21 representative runs and are shown in Table 1 at the end of the paper. Gas velocity through the precharger, as expected, greatly affects system performance (Runs 1-4). At electric field values of either 3 or 3.5 kV/cm, raising the wind tunnel velocity substantially decreases both the initial (collector only) and precharger efficiencies. The α values show a drop from 107 to 5.4 when gas velocity is doubled and a reduction from 6.3 to 1.5 when the velocity is increased seven-fold. Migration velocity changes are not as pronounced, however. Increasing the flow from 4 to 8 ft/sec results in a slightly higher migration velocity improvement factor, while an increase from 4 to 28 ft/sec produces a slight decrease in H.

Four electric field values (Runs 5-8) were used in the collector in these experiments. Collector voltage and thus electric field was varied during the runs from 23 kV (3 kV/cm) to 35 kV (4.5 kV/cm), while measured ion current increased from 0.5 to 5.2 mA. Corona onset occurs at approximately 15 kV, and from this point the current vs. field curve rises exponentially, similar to the classic clean plate curve (Fig. 5). The reason for selecting these four collector voltages was to ascertain the efficiency improvement contributed by the precharger at both low and high initial collector efficiencies.

System particle collection efficiencies range from 85.3% up to 99.9% as collector electric field is raised from 3.0 to 4.5 kV/cm (Fig. 6). This represents a factor of 150 increase in efficiency for the higher collector voltage. The improvement in efficiency due to precharging decreased, however, with increasing collector electric field ($\alpha = 3.5$ and 1.4 for $E = 3.0$ and 4.5 kV/cm, respectively). Migration velocity improvement factors also decreased continuously with increasing collector field, from a high of 2.9 at an electric field of 3.0 kV/cm to a low of slightly more than 1 at 4.5 kV/cm.

Two precharging parameters can be directly controlled, electron beam energy (60, 70, 80, 90 keV) and precharger electric field (0-6.4 kV/cm). As E-beam energy is reduced from the standard level of 90 keV (Runs 13-16), the precharger-collector particle removal efficiency decreases although there seems to be little effect until the energy drops below 80 keV. Very high α values, in excess of 100, were found at both 90 and 80 keV energies. Also uniformly high were the H factors; migration velocity increases of up to a factor of 5 (Runs 13 and 14) were found when operating the E-beam precharger upstream from the collector.

The level to which aerosol particles can be precharged is determined by the charging electric field, and thus by the electrode voltage. Runs 13-17 and Runs 18-21 are for two different sequences of applied precharger electric field. In both sequences, collection efficiencies increase with precharger voltage up to a maximum at 4.6 kV/cm (50 kV). At higher electrode voltages, collection efficiency drops off somewhat. Alpha (α) values reach a pronounced maximum at the 50 kV voltage level, while the corresponding H factors follow a similar but more gradual trend.

The highest collection efficiency obtained during this first set of experiments was 98.99% for the collector alone and 99.97% for the E-beam precharger-collector combination. Reasons for such high efficiency levels include: 1. low precipitator sneakage, 2. low particle concentration, 3. slow gas velocity, 4. high SCA, and 5. well controlled laboratory conditions.

DISCUSSION AND ANALYSIS

1. E-Beam Energy and Range Calculation

Determining the range (stopping distance) of an electron beam having an initial accelerated energy of 90 keV requires several corrections to account for energy losses. Before the E-beam enters the precharger, it must pass through a thin aluminum foil window (25 μm) separating the accelerator (which is at high vacuum) from atmospheric pressure. Upon entering the air column, the beam will lose the remainder of its energy in the ionization process by collision with air molecules. The energy loss and E-beam range using NASA tables (11) are as follows:

Energy loss to foil window = (stopping power) x (density, Al) x (thickness) (1)

Loss of E-beam in precharger = (Initial Beam Energy) — (Loss to Window) — (Loss to Air Column). (2)

$$\text{Range (cm) of beam in air column} = \frac{\text{Range (per g/cm}^2\text{)}}{\text{Density of air (g/cm}^3\text{)}} \quad (3)$$

As an example, for an E-beam of 90 keV initial energy and a 25 μm thick aluminum foil window, the beam loses 23 keV down to 67 keV delivered energy, and the range of the 67 keV delivered energy beam in the precharger (air column) is 6.6 cm. For the other tested E-beam energies, the following values apply:

Table 2. Electron Beam Energy vs. Range in Air

Initial Energy (keV)	Loss to Window (keV)	Delivered Energy (keV)	Range in Air (cm)
90	23	67	6.6
80	25	55	4.7
70	27	43	3.0
60	30	30	1.6

In the present configuration, the E-beam window to precharger anode distance is about 17.5 cm. Therefore, at the maximum beam energy of 90 keV initial (67 keV delivered), the beam range is less than half of the precharger width. At lower energies, the ionization zone occupies a progressively smaller fraction of the precharger.

2. Gas Velocity.

The residence time of particles in the precharger, and specifically in the charging zone, is of major importance to EBP system performance. For a given path length, as gas speed is increased, residence time decreases which allows less time for particles to acquire maximum charge. According to field charging theory (10, 11), the particle charge at time t is related to the saturation charge by the following equation:

$$q(t) = q(\infty) \frac{t/\tau}{1 + t/\tau} \quad (4)$$

$q(t)$ = charge at time t
$q(\infty)$ = saturation charge
t = residence time
τ = charging time constant

If t is a low multiple of τ, then the particle will not reach saturation charge and therefore will not be collected with maximum efficiency. To raise particle charge, then, the residence time t should be increased to $t \geq 5\tau$.

Residence times corresponding to the three tested gas velocities can be calculated using the path length of the charging zone, which is approximately 30.5 cm (12 in). Using the particle diameter and dielectric constant, and the precharger electric field and ion current density, the particle charge due to ionic particle field charging can be found for various residence times. The results of these calculations are shown in Table 3. The electric field value in Table 3 assumes a 50 kV voltage applied across the 10.9 cm wide charging zone (17.5 cm - 6.6 cm) from the end of the E-beam range (virtual cathode) to the rack electrodes (anode). The virtual cathode is used because the bipolar plasma created by the E-beam is very conductive and acts as an extension of the cathode.

Table 3. Theoretical Particle Charge vs. Precharger Residence Time

Experimental Conditions	Residence Time (msec)	E = 4.6 kV/cm Charge (C)	Electronic Charges
Saturation	-------	3.60×10^{-17}	225 e
4 ft/sec	167	3.03×10^{-17}	189 e
8 ft/sec	83	2.61×10^{-17}	163 e
28 ft/sec	24	1.56×10^{-17}	97 e

Calculated values of charge show that at the lowest gas velocity, the final theoretical particle charge approaches but does not equal the saturation charge. At higher gas velocities (shorter residence times) the theoretical particle charge falls off considerably to levels much lower than saturation. This helps to explain the dramatically lower collection efficiencies, α values, and H factors which all depend upon the migration velocity, and ultimately, the particle charge.

3. Collector Electric Field.

The operation of a conventional electrostatic precipitator is affected by a number of physical and electrical parameters. Precipitation is most commonly described in terms of the Deutsch-Anderson particle collection efficiency equation (7):

$$\eta = 1 - \exp\left(-\frac{A}{V}w\right) \qquad (5)$$

η = particle collection efficiency
A = collector plate area
V = gas flow volume through precipitator
w = empirical particle migration velocity.

Given a constant specific collection area, the parameter which ultimately determines the collection efficiency is the migration velocity of the particles to be removed. If migration velocity can be increased in the collector, efficiency should improve. The theoretical migration velocity equation for field dependent charging (12) is given as:

$$w = \frac{2\epsilon_o E_o E_p a}{\eta_g} \qquad (6)$$

w = theoretical migration velocity
ϵ = permittivity of free space
E_o = charging electric field
E_p = collecting electric field
a = particle radius
η_g = gas viscosity

From the above equations, as collector electric field is raised, the migration velocity and thus the collection efficiency should increase.

As shown in Fig. 6, initial (collector-only) particle collection efficiencies increase considerably with electric field. It follows that in each case, when the precharger is also operating, collection efficiencies will be higher at larger electric field values. However, it is difficult to gain incremental improvements in collection efficiency with precharging when the efficiency of the collector is already very high. Precharging always produces efficiency increases (α always > 1), but the effect is similar at high initial efficiencies.

The values of both w_1 and w_2 increase as collector voltage is raised because migration velocity is proportional to the electric field. Even at the maximum field value of 6.4 kV/cm, the migration velocity is somewhat low at 1.7 cm/sec. This is compared to the theoretical value of 4 cm/sec for 1.3 μm diameter particles. Experimental w values are typically smaller than the theoretical w in full size electrostatic precipitators. This is usually attributed to a number of non-ideal gas flow and electrical conditions which may also be affecting the laboratory-scale EBP.

4. E-Beam Energy

As initial electron beam energy is reduced from the maximum value of 90 keV, the level of particle precharging and the collection efficiency decreases. Since both ion current and electron range decrease with lower beam energy, several related effects are at work here. The particle charging rate depends upon, among other parameters, the ion current density (J) in the precharger. The equation for the charging rate (12) shows that as J is reduced, the charging time constant will increase:

$$\tau = \frac{4\epsilon_0 E}{J} \qquad (7)$$

τ = charging time constant
ϵ_0 = permittivity of free space
E = charging electric field
J = ion current density

Conversely, higher ion current density in the charging zone will result in a faster particle charging rate.

One source of higher ion current density is greater E-beam energy. As beam energy is increased, more ion pairs are formed, creating greater ion current and current density. A reduction in the charging time constant and an increase in collection efficiency should be expected, therefore, at a delivered beam energy of 67 keV compared to 30 keV. The number of ion pairs formed by an electron beam is proportional to the beam energy by the following equation:

$$n = \frac{\Delta E\ (\text{eV})}{32.4\ (\text{eV/ion pair})} \qquad (8)$$

n = number of ion pairs created per 1 beam electron
ΔE = energy loss of the E-beam in the gas
32.4 eV = specific ionization in air.

As an example, for $\Delta E = 67$ keV, $n = 2068$ ion pairs. Ion pair production, which in turn determines the current density in the precharger, is as follows for the other tested beam energies:

Table 4. Delivered E-Beam Energy vs. Ion Pair Production

Delivered E-Beam Energy (keV)	Ion Pair Production per Electron
67	2070
55	1700
43	1330
30	930

From the above calculations, an E-beam of 67 keV delivered to the ionization zone produces about 2070 ion pairs per electron while a 30 keV delivered beam produces only 930 ion pairs per electron. It follows that fewer ion pairs in the ionization zone reduces the current density in the charging zone which lowers the charging rate.

The data confirm the projected increase in ion current as shown in Fig. 7. Precharger ion current plotted against E-beam energy shows that current and current density increase with beam energy, but at an ever increasing rate. As evidenced by the previous calculations, initial electron beam energies of 90 or even 80 keV are sufficient to meet the requirements of a beam energy/electrode geometry matched precharger. However, in this particular precharging configuration, any E-beam energy lower than 80 keV has too short a range with insufficient ion current to be effective at charging particles to the maximum possible level.

5. Precharger Electric Field.

Precipitator collection efficiency depends upon particle migration velocity, which in turn depends upon the charging and collecting electric fields. In a two stage system such as the Mk. II precharger-collector arrangement, the charging electric field is measured in the precharger. Pauthenier's ionic field charging equation (10) describes the saturation charge on a spherical particle in an electric field as follows:

$$q(\infty) = \frac{12\pi\epsilon_o\epsilon_s a^2 E}{(\epsilon_s + 2)} \qquad (9)$$

$q(\infty)$ - saturation charge of particle
ϵ_o - permittivity of free space
ϵ_s - specific dielectric permittivity
a - radius of particle
E - charging of electric field

For a given particle radius and dielectric constant, the level of saturation charge varies with the charging electric field. Restated, a higher voltage on the precharger electrodes will result in a greater particle charge and, ultimately, increased collection efficiency.

As shown in Fig. 8, the data follow the field charging equation. Both the collection efficiency improvement due to the precharger (α value) and the migration velocity parameter (H value) increase with electric field from 0 through 4.6 kV/cm (50 kV applied voltage). Alpha values peak at this electric field and then fall as field is increased to 6.4 kV/cm (70 kV).

Above about 4.6 kV/cm, the electric field may influence the dimensions of the ionization zone. The primary electron beam is attracted toward the anode beyond its normal range of 6.6 cm at 90 keV (67 keV delivered). This could extend the leading edge of the bipolar ionization zone, causing a reduction in size of the charging zone. A fraction of the test gas flowing through the precharger may be exposed to the bi-polar charge region, resulting in the discharging of particles which pass through this region.

Another occurrence detrimental to particle charging at electric fields above 4.6 kV/cm is that of secondary ionization. Secondary electrons formed in the zone of primary ionization can be re-energized by sufficiently high electric field strengths to create new bipolar ion pairs in the originally monopolar charging zone, which will squelch ionic particle charging. The fact that secondary ionization may occur in the Mk. II precharger at high electric field strengths is graphically supported in Fig. 9. As applied electric field is increased, ion current increases exponentially which is the characteristic benchmark for secondary ionization. A balance should be struck between an electric field value too low to promote saturation charging and a value so high that secondary effects ultimately eliminate the monopolar charging zone. For the present precharger geometry, the optimum field value has been empirically determined to be 4.6 kV/cm.

The reduced system performance above 4.6 kV/cm may also be due to the use of high anode voltages to produce the charging electric field. Positive corona may be occurring along the anode electrodes at voltages above 50 kV. This would generate positive ions in the previously monopolar (negative) charging region which would partially discharge some of the particles. Maximum particle charging requires a proper combination of precharger electric field, ion current density, and electron beam energy.

CONCLUSIONS

Electron beam precharging and its effect on particle collection efficiency has been studied extensively in a fully instrumented laboratory-scale electron beam precipitator (EBP). Precharging was tested here in a retrofit configuration upstream from a collecting section similar to a conventional electrostatic precipitator. A wide variety of physical and electrical parameters were varied to determine an optimum set of conditions which gave the best system performance.

The electron beam precharging configuration developed for these experiments was the Mk. II model. Particle collection efficiencies of as high as 99% using the collector-only and 99.97% for the precharger-collector combination represent the best system performance to date. Both the penetration reduction value ($\alpha = P_2/P_1$) and the migration velocity improvement factor ($H = w_2/w_1$) are good measures of the effect that precharging has on the system collection efficiency. Values of α exceeding 100 and H factors of more than 5 occur at low gas velocity (4 ft/sec), low collector electric field (3.0 kV/cm), matched E-beam energy (90 keV), and optimized precharger electric field (4.6 kV/cm).

Proper matching of the electron beam energy and the precharger electrode geometry and field are critical to successful particle precharging. Directing the particle flow through the charging zone and increasing the residence time in the precharger both maximize particle charge and collection efficiency. Balancing the electron beam energy (range) and the applied electric field delineates the charging zone near the electrodes, while providing an adequately high field to approach the saturation limit for ionic field charging. Optimizing all experimental parameters has provided a data base for further study of electron beam precipitation at a larger scale. Future work should include achieving higher particle charging by utilizing the free electron diffusion charging process occurring in the E-beam precharger.

> The work described in this paper was not funded by the U.S. Environmental Protection Agency and therefore the contents do not necessarily reflect the views of the Agency and no official endorsement should be inferred.

REFERENCES

1. Davis, R.H., W.C. Finney, and L.C. Thanh. Electron Beam Ionization for Coal Fly Ash Precipitators. In: Processings of the American Nuclear Society Topical Conference on Atomic and Nuclear Methods in Fossil Energy Research. Mayaguez, Puerto Rico, December 1-4, 1980.

2. Finney, W.C., L.C. Thanh, J.S. Clements, and R.H. Davis. Primary and Secondary Ionization in an Electron Beam Precipitator System. In: Proc. of the 3rd Symposium on the Transfer and Utilization of Particulate Control Technology, Volume II, Electrostatic Precipitators. EPA 600/9-82-0056, pp. 358-369, 1982.

3. O'Hara, D.B., J.S. Clements, W.C. Finney, and R.H. Davis. Aerosol Particle Charging by Free Electrons. Accepted by the Journal of Aerosol Science, 1988.

4. Clements, J.S., A.Q. Mizuno, and R.H. Davis. Particle Charging with an Electron Beam Precharger. In: Proc. of the 5th Symposium on the Transfer and Utilization of Particulate Control Technology, Volume 1. EPRI CS-4404, p. 15-1, 1986.

5. A.Q. Mizuno, J.S. Clements and R.H. Davis. Use of an Electron Beam for Particle Charging. In: Conf. Record of the IEEE-Industry Applications Society Annual Meeting, pp. 1215-1219. Chicago, IL, October, 1984.

6. Finney, W.C., J.S. Clements, and R.H. Davis. Electron Beam Precharging of Particles in a Laboratory Scale Electrostatic Precipitator. In: Conf. Record of the IEEE-Industry Applications Society Annual Meeting, pp. 1124-1134. Denver, CO, October, 1986.

7. Oglesby, S., and G.B. Nichols. Electrostatic Precipitation. Marcel Dekker, Inc., New York, N.Y. 1978.

8. Masuda, S. State of the Art in Precharging. In: Proc. of the 2nd International Conference on Electrostatic Precipitation, Senichi Masuda, Ed. Sponsored by the International ESP Steering Committee and the Institute of Electrostatics, Japan. Published by the Air Pollution Control Association, U.S.A. Paper 4-1, p. 177, 1985.

9. Berger, M.J. and S.M. Seltzer. Tables of Energy Losses and Ranges of Electrons and Positrons. NASA Circular SP 3012, p. 124, 1964.

10. Pauthenier, M.M., and M. Moreau-Hanot. La Charge des Particules Spheriques dans un Champ Ionise. Journal de Physique et le Radium 3: 590, 1932.

11. White, H.J. Particle Charging in Electrostatic Precipitation. AIEE Trans. 70: 1189, 1951.

12. Mizuno, A.Q. Review of Particle Charging Research. In: Proc. of the 1st International Conference on Electrostatic Precipitation, Harry J. White, Ed. Sponsored by EPRI, IGCI, and APCA. Pub. by the Air Pollution Control Association, U.S.A. p. 304, 1982.

*Supported in part by the U.S. DOE Contract No. DE-AC22-83PC60266.

Table 1. Mk. II Electron Beam Precharging Data.

Run No.	Precharger Gas Velocity (ft/sec)	Collector Electric Field (kV/cm)	Electron Beam Energy (keV)	Precharger Electric Field (kV/cm)	Coll. Only (η_1)	Prech. and Coll. (η_2)	$\alpha = \frac{P_1}{P_2}$	Coll. Only (w_1)	Prech. and Coll. (w_2)	$H = \frac{w_2}{w_1}$
1	4	3.0	90	4.6	68.64	99.71	107.0	0.29	1.48	5.10
2	8	3.0	90	4.6	30.29	87.03	5.4	0.18	1.04	5.78
3	4	3.5	90	4.6	97.72	99.96	63.0	0.96	1.99	2.07
4	28	3.5	90	4.6	34.89	56.09	1.5	0.76	1.46	1.92
5	16	3.0	90	4.6	48.40	85.30	3.5	0.67	1.94	2.90
6	16	3.5	90	4.6	83.70	95.08	3.3	1.83	3.04	1.66
7	16	4.0	90	4.6	98.74	99.27	1.7	4.42	4.96	1.12
8	16	4.5	90	4.6	99.86	99.90	1.4	6.63	6.97	1.05
9	4	3.0	90	4.6	68.64	99.71	107.0	0.29	1.48	5.10
10	4	3.0	80	4.6	68.64	99.71	104.0	0.29	1.47	5.07
11	4	3.0	70	4.6	70.73	98.78	23.8	0.31	1.12	3.61
12	4	3.0	60	4.6	70.73	92.36	3.8	0.31	0.65	2.10
13	4	3.0	90	0	98.99	98.66	1.0	1.17	1.20	<1
14	4	3.5	90	0.9	98.99	99.26	1.4	1.17	1.25	1.07
15	4	3.5	90	2.8	98.99	99.79	4.7	1.17	1.57	1.34
16	4	3.5	90	4.6	98.99	99.88	8.3	1.17	1.71	1.46
17	4	3.5	90	6.4	98.99	99.76	4.1	1.17	1.53	1.31
18	4	3.5	90	3.7	98.55	99.91	16.1	1.08	1.78	1.65
19	4	3.5	90	4.6	98.55	99.96	36.6	1.08	1.98	1.83
20	4	3.5	90	5.5	98.55	99.94	26.1	1.08	1.88	1.74
21	4	3.5	90	6.4	98.55	99.86	10.9	1.08	1.67	1.55

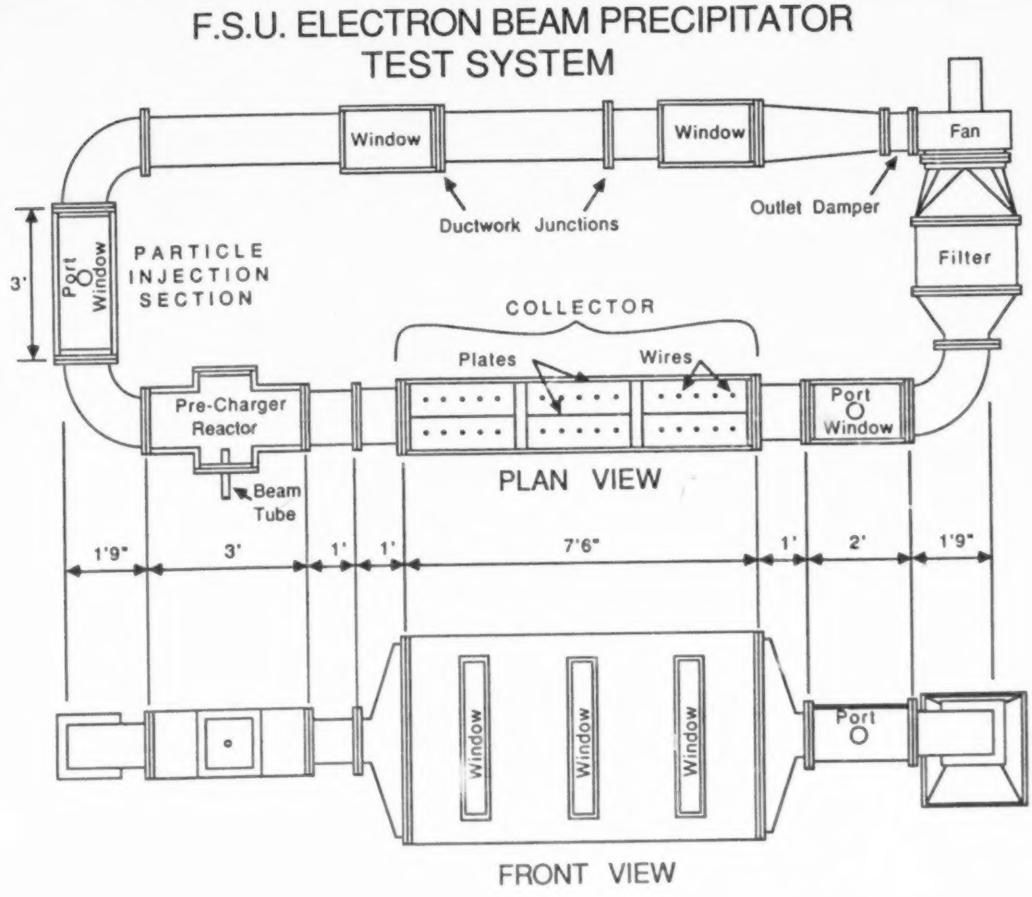

Figure 1. The Two-Stage FSU Electron Beam Precipitator (EBP) Wind Tunnel.

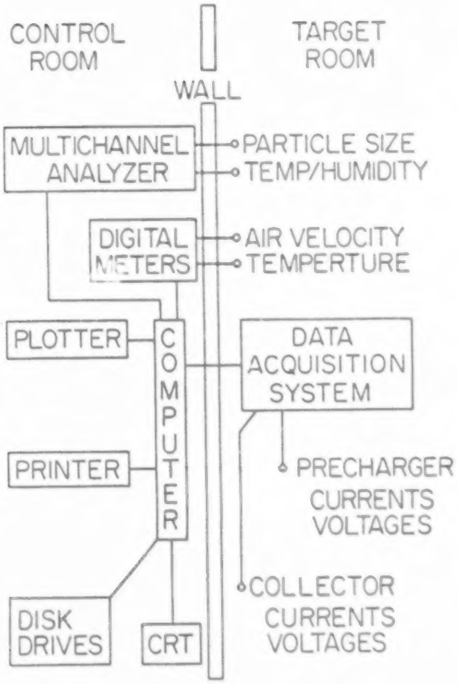

Figure 2. The EBP Data Acquisition and Analysis System.

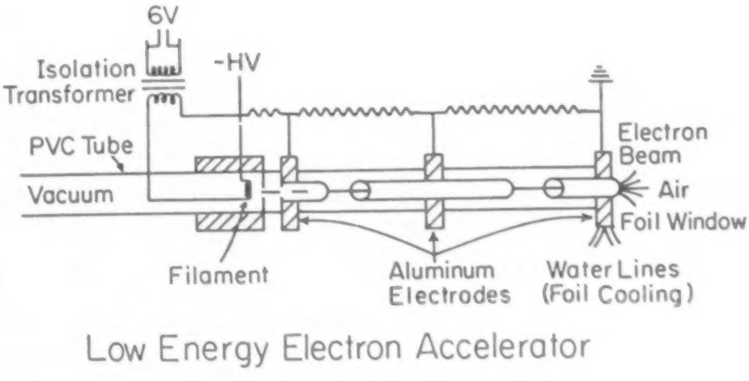

Figure 3. Schematic Diagram of the 100 keV Electron Beam Accelerator.

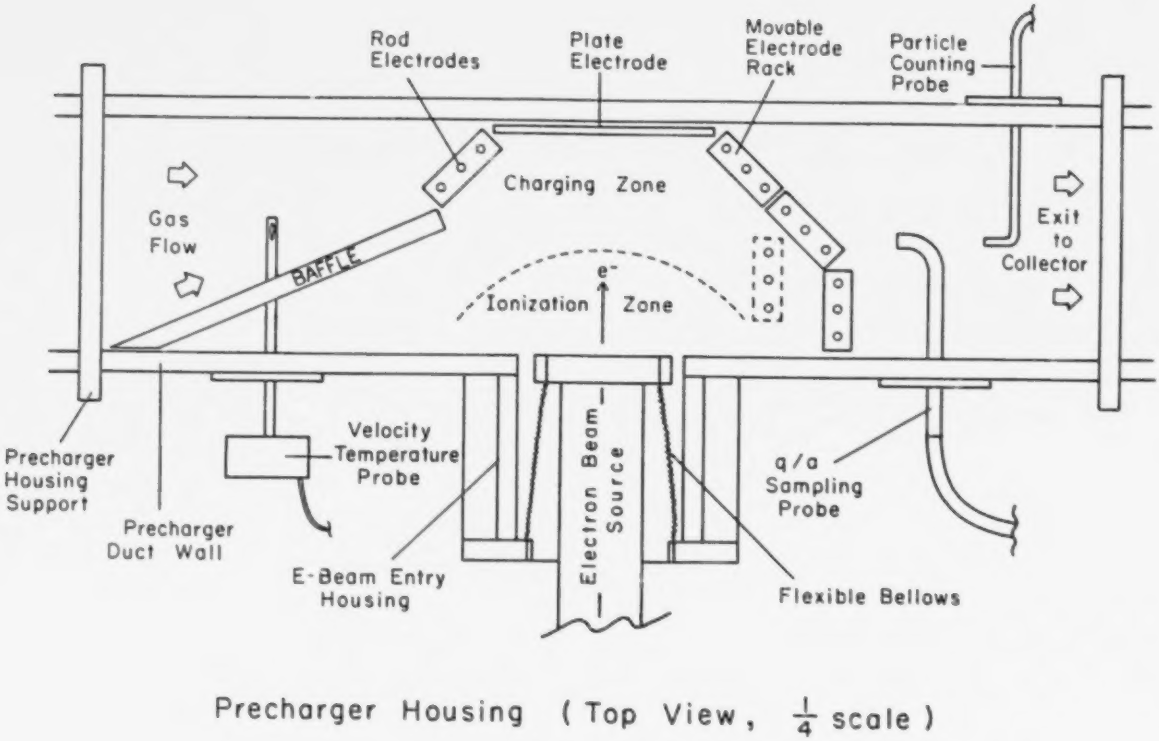

Figure 4. Top View of the Mk. II Electron Beam Precharging Module and Electrode Arrangement.

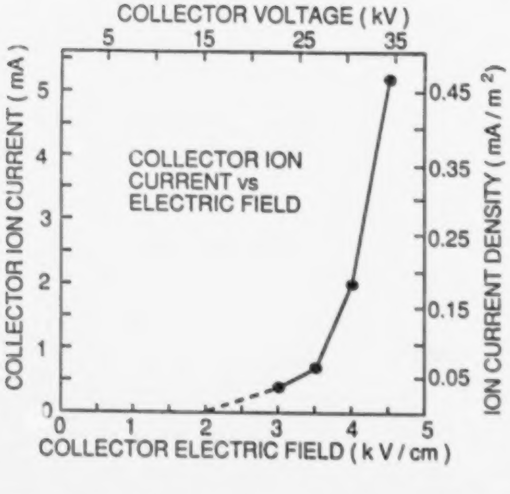

Figure 5. Collector Ion Current and Density vs. Electric Field.

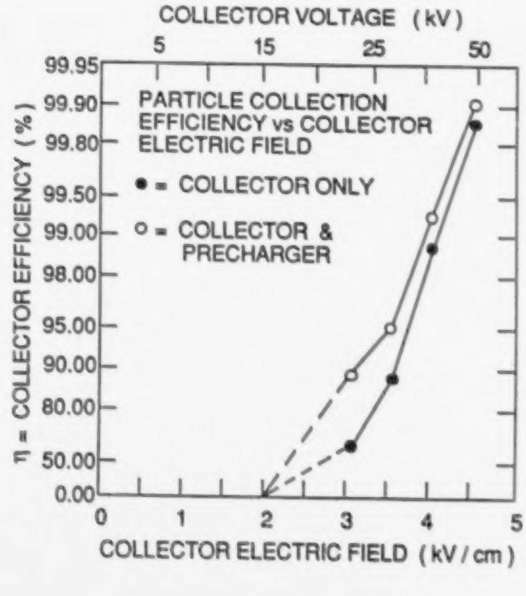

Figure 6. Particle Collection Efficiency vs. Collector Electric Field.

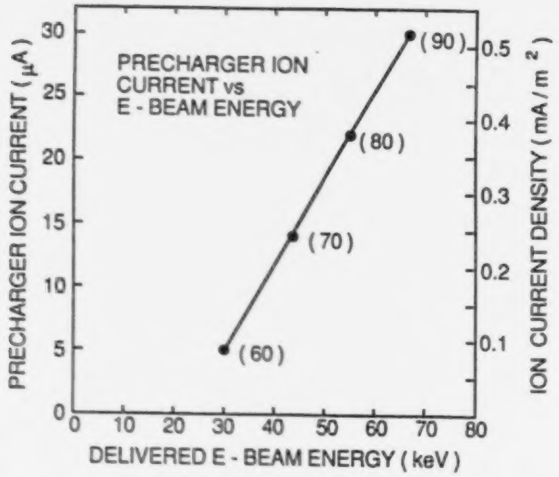

Figure 7. Precharger Ion Current and Density vs. E-Beam Energy.

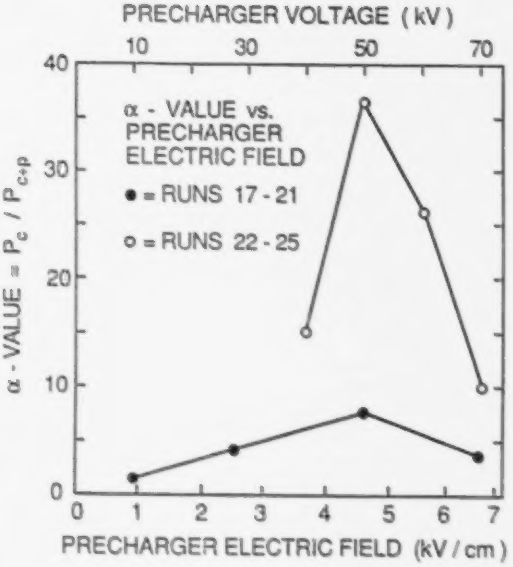

Figure 8. Penetration Reduction (α) vs. Precharger Electric Field.

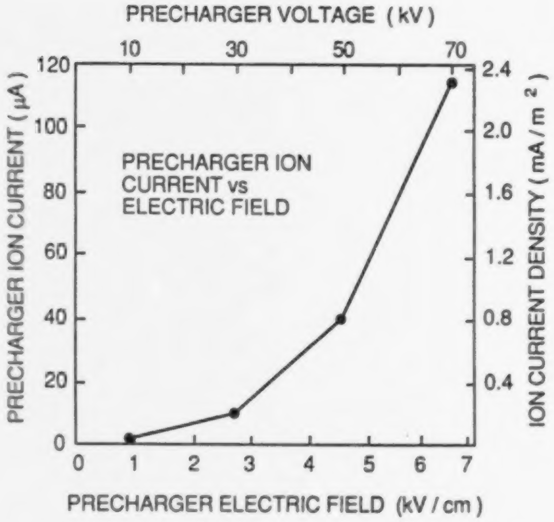

Figure 9. Precharger Ion Current and Density vs. Electric Field.

CALCULATION OF ELECTRIC FIELD AND CURRENT DISTRIBUTIONS ALONG PROFILED COLLECTING ELECTRODES IN A WIRE-PLATE ELECTROSTATIC PRECIPITATOR.

C.E. ÅKERLUND
FLÄKT INDUSTRI AB, Växjö, Sweden

ABSTRACT

Most numerical calculations of the electric field and current distribution inside a wire-plate electrostatic precipitator are simplified by the assumption that the plates are flat. In industrial precipitators the plates always have protrusions to make them stiff. For an application of this design with ion space charge, but negligible dust space charge, the author has used a combined finite element-computer aided design method for calculating the field strength and current density distribution at some interesting areas on a profiled collecting electrode.

The calculations show that the field strength may rise significantly at the top of a protruding part, despite its well-rounded shape. The field magnification factor is about 1.7, based on the field strength at the flat part of the electrode. The results confirm that the collecting plate must be carefully designed to avoid sparking when the voltage is too low. The protrusion attracts the flow of current, but the current densities at the protrusion, and at the area nearest to the discharge electrode, are almost the same.

INTRODUCTION

Changes in the interior design of wire-plate electrostatic precipitators are contemplated from time to time by manufacturers to improve performance. The effect of the changes can be determined by tests, but if the theory is understood, much test work can be avoided. Among electrical properties, the electric field and current distribution in the interelectrode space, and on the collecting electrode, are the key properties to investigate.

Over the past 30 years a number of authors have published their findings on field and current distribution based on evaluations of experimental measurements, or the use of different mathematical methods. Sigmond has recently reviewed some of these methods [1] . To master the numerical calculation all models have been referred to a configuration of one or more discharge wire electrodes midway between two grounded flat plates.

In full-scale precipitators the collecting electrodes are never flat but are designed with bends or other stiffening elements to withstand mechanical forces. It is well known that the field strength at protrusions is higher than at flat surfaces. An elevated field strength entails a serious risk of spark-over when the voltage is too low [2].

Several finite element programs exist for calculating field strength distribution at complicated geometries. One such program has been developed by ASEA, Sweden. To calculate Poissonian fields, the program requires the space charge distribution in the interelectrode space as input. In the first zones of an electrostatic precipitator the dust space charge dominates over the ion space charge. The dust space charge is considered to be equally distributed and the ion space charge neglected. In this case ASEA's program is quite a useful tool [3] .

For application with unequally distributed ion space charge and negligible dust space charge the author has used a combined finite element computer aided design method to establish a base for numerical calculation of the electric field and current distribution at some interesting areas of a profiled collecting electrode.

THEORETICAL CONSIDERATION

Consider the tube of flux shown in Figure 1

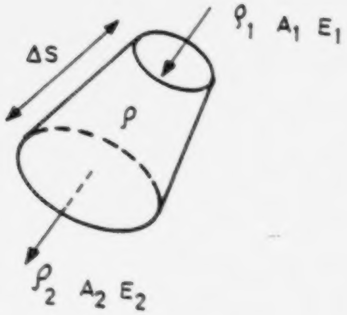

Figure 1. Tube of flux

From Gauss' law

$$E_2 A_2 - E_1 A_1 = \frac{\rho}{\varepsilon_0} \frac{A_1 + A_2}{2} \Delta s \qquad \text{(approximatively)}$$

Hence

$$\Delta(E\ A) = \frac{\rho\ A}{\varepsilon_0} \Delta s$$

and consequently

$$\Delta E = -E \frac{\Delta A}{A} + \frac{\rho}{\varepsilon_0} \Delta s \tag{1}$$

Further, since current out = current in

$$\mu \rho_2 E_2 A_2 = \mu \rho_1 E_1 A_1 \quad \text{or}$$

$$\rho_2 \left(E_1 A_1 + \frac{\rho}{\varepsilon_0} A\ \Delta s\right) = \rho_1 E_1 A_1$$

It follows that

$$(\rho_2 - \rho_1) E_1 A_1 = - \frac{\rho_2 \rho}{\varepsilon_0} A\ \Delta s$$

and, finally

$$\Delta\rho = - \frac{\rho_2 \rho}{\varepsilon_0} \frac{A}{A_1} \frac{\Delta s}{E} \tag{2}$$

By numerical integration from a discharge point on the wire along a flux line, the field strength, the charge and the current densities at a specified surface can be calculated using equations (1) and (2).

APPLICATION

To verify the calculation method let us consider a configuration with two concentric cylinders. The cylinder radii may be compared with a frequently used discharge wire radius (r_0 = 0.00135 m) and a wire to plate spacing ($r_{0.15}$ = 0.15 m), respectively.

The onset field strength for concentric cylinders is calculated with Peek's formula [4] , which gives

$E_0 = 57.7$ kV/cm and

$V_0 = 36\,700$ V for zero current

For I = 450 μA/m we get

$\rho = 51.1\ \mu C/m^3$

With step sizes from 0.1 mm at the wire to 9.0 mm at the outer cylinder, a stepwise integration of (1) and (2) gives

$E_{0.15} = 2.2$ kV/cm at the outer cylinder

and

$V_{tot} = 54\,800$ V

Calculation of $E_{0.15}$ according to Oglesby and Nichols [5] gives

$E_{0.15} = 2.2$ kV/cm

and V_{tot} according to Lawless and Sparks [6]

$V_{tot} = 54\,200$ V

The difference between this voltage, and that calculated by the author, is explained by the limited accuracy of the numerical procedure.

For a wire-plate configuration investigated earlier by the author [3, 7] an investigation is made under the assumption that a diverging unipolar ion flow will not distort the electric field lines away from the zero-space-charge (Laplacian) pattern, but may change the voltage distribution along the field lines (Deutsch's assumption). Flux tubes from the discharge to the collecting electrodes are designed with high accuracy in a computer-aided design system using coordinates of static field lines calculated with a finite element program. The flow of current through the flux tube is followed and the charge density and electric field strength defined along the line by stepwise calculation.

Along each flow line

$$\int_{0}^{s} E\,ds = \text{constant}$$

The corona is assumed to start simultaneously over the whole electrode surface as soon as the corona voltage is reached, regardless of the onset surface field distribution. By increasing corona current, the starting field strength is supposed to stay unchanged.

Figure 2 shows the equipotentials with field lines at corona onset and zero current.

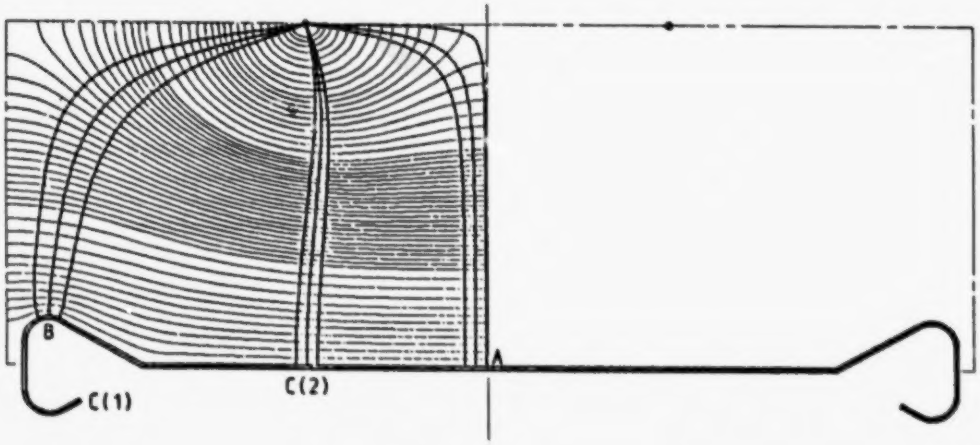

Figure 2. Tubes of flux

Deutsch's assumption is an approximation that preferably should be used at low current densities only.

When the current is gradually increased the curvature of the equipotentials will assume a different shape. This is illustrated in Figure 3 which shows the equipotentials in a zero space charge field (solid lines) and an equally distributed charge field (dashed lines). In the vicinity of the emitting and the collecting electrodes the lines coincide, while there is a marked difference in shape in the intermediate area. The difference in shape means that the ion flow lines to areas A and B on the plate will not fully coincide with the Laplacian field lines shown. The lines to A and B in the space charge field will be shorter, while the lines to C (2) in the space charge and space charge free fields can be considered equally long.

At constant onset field strength, and with the same starting and end point of the field line, it can be assumed that the field strength at the collecting electrode increases when the length of the field line decreases. Thus, with a flow of current, the field strenght at A and B, calculated with Deutsch's assumption, will be at the lower side, while the field strength at C (2) will not be influenced by the assumption.

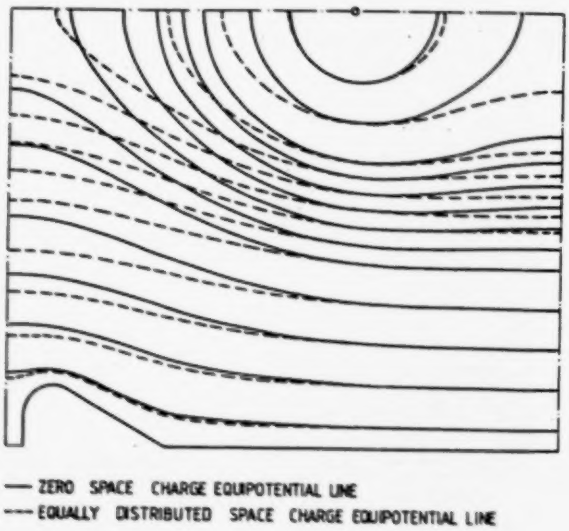
— ZERO SPACE CHARGE EQUIPOTENTIAL LINE
--- EQUALLY DISTRIBUTED SPACE CHARGE EQUIPOTENTIAL LINE

Figure 3. Equipotential lines

The current distribution along a profiled grounded plate can be measured in the laboratory. One method is to glue a thin film on the plate with squares of conductive material isolated from one another. The current to each square is measured. One frequently used square size is 9x9 mm, with 1 mm spacing between squares. Flux tubes were drawn in the CAD system to allow comparison between the numerical analysis and laboratory measurements. The width of the tubes was 9 mm at the plate. The tubes were divided lengthwise in square sections, about 100 in each tube. A stepwise calculation of charge density and field strength was made starting from the wire surface. A measured value [8] was selected as the corona starting voltage. Space charge values at the wire were assigned to give a total voltage drop from wire to plate equal to the measured value.

RESULTS

Figure 4 shows the variation in electric field strength along the flux lines. Figure 5 shows the variation in charge density. The perpendicular distance between the flux line (dashed) and the spline is proportional to the local value of the electric field strength and the charge density, respectively. It is clearly visible in Figure 4 that the field strength drops drastically when the flux line leaves the area close to the discharge wire and reaches a minimum in the area around F,G and H. From there the field strength increases gradually along the flux lines to areas A and C. Close to area B the field strength increases rapidly, illustrating the field magnification at protruding parts. The charge density distribution in Figure 5 does not have the same tendency. The results of the calculation are shown in Table I.

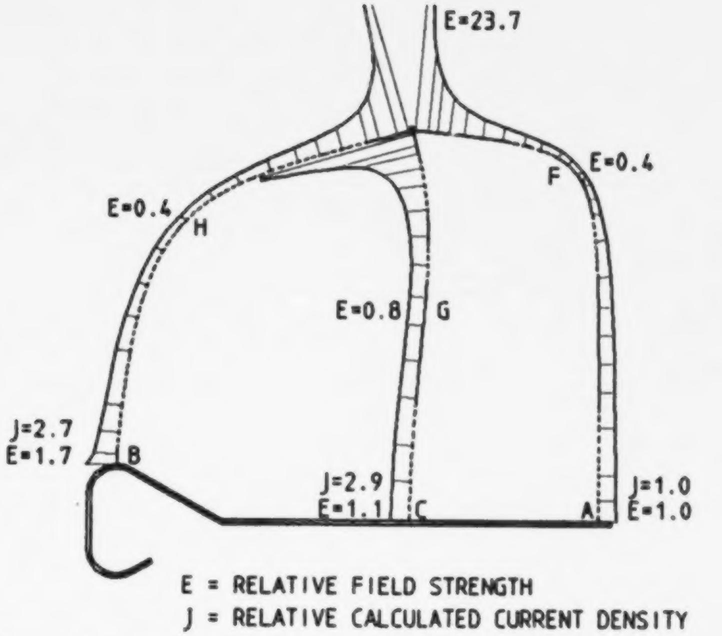
E=23.7
E=0.4
F
E=0.4
H
E=0.8
G
J=2.7
E=1.7
B
J=2.9
E=1.1
C
A
J=1.0
E=1.0
E = RELATIVE FIELD STRENGTH
J = RELATIVE CALCULATED CURRENT DENSITY

Figure 4. Electric field strength along field lines

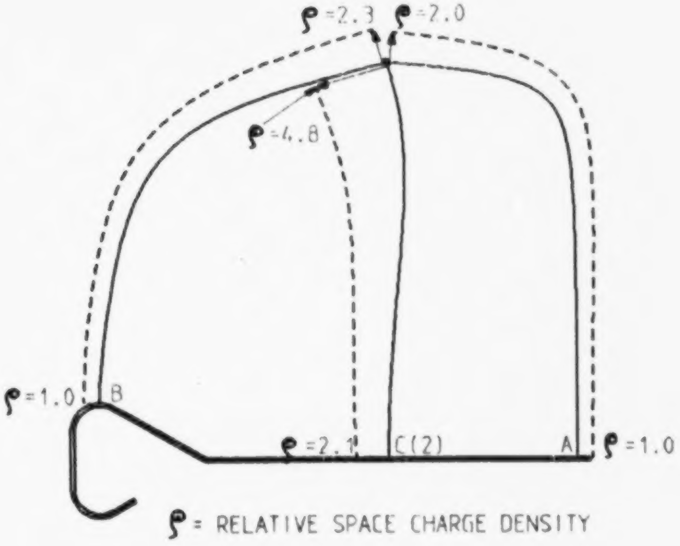

Figure 5. Space charge along field lines

TABLE 1.

Electric field strength, voltage and current density at areas A, B and C in Figure 2.

Calculated		Flux tube		
		A	B	C
V stat	kV	37.4	37.4	37.4
E plate stat	kV/cm	1.1	1.7	1.1
ρ wire	$\mu C/m^3$	5.8	10.4	17.9
V tot	kV	48.0	48.0	48.0
E plate tot	kV/cm	2.2	3.8	2.4
ρ plate	$\mu C/m^3$	3.0	4.7	8.0
j plate	mA/m^2	0.12	0.32	0.35
I wire	$\mu A/m$	0.52	1.43	1.56
I plate	$\mu A/m$	0.52	1.44	1.57
Measured				
j plate	mA/m^2	0.12	0.35	0.21

It can be seen from Table 1 that the flow of current in each tube is next to constant. The minor increase from wire to plate can be explained by the stepwise calculation.

Calculated and measured values of current density at areas A and B are in agreement. At C the measured value is lower than the calculated. The measurements further show that the area on the left-hand side of area C (towards the profile) has a higher density than area C. This verifies a well-known established fact. Two adjacent emitters interfere with each other and deflect the current in the transverse direction.

In a configuration with two flat plates and a row of discharge electrodes the calculated current density on the plate is maximum in the area nearest to the discharge electrode. With profiled plates, this area and the protrusion have a current density of the same magnitude. In the area in between, at the tuck where the protrusion starts, the field strength and current density are low. Thus, at a profiled plate, the current distribution will also be markedly affected by a smooth protrusion.

From Figure 4 it can be seen that the field magnification factor is about 1.7, calculated on the fields at the top of the profile and the flat plate. Even a well rounded protrusion on a collecting electrode has a field strength magnification which can not be ignored.

CONCLUSION

The calculation method used by the author requires only uncomplicated software programs and a computer-aided design system. These tools are normally available within research organizations and manufacturing companies, which is not the case with computer programs solving Poisson's equation and the current continuity equation in parallell. Results are obtained which are well in line with measurements. The flow of current from wire to plate is examined and the space charge, field strength and current densities calculated. Thus, the effect of changes in precipitator geometry on these electric properties can be fully understood.

LIST OF SYMBOLS

A	cross section of flux tube element	(m^2)
E	field strength	(V/m)
I	current	(A/m)
j	current density	(A/m^2)
r	cylinder radius	(m)
s	length of flux tube	(m)
Δs	length of element in flux tube	(m)
V	potential	(V)
ρ	charge density	(C/m^3)
μ	mobility (1.8 x 10^{-4})	(m^2/Vs)

REFERENCES

1. R.S. Sigmond, The unipolar corona space charge flow problem, Journal of Electrostatics, 18, 1986, 249-272.

2. S. Sekar, H. Stomberg, On the prediction of current - voltage characteristics for wire plate precipitators, Journal of Electrostatics, 10, 1981, 35-43.

3. H. Stomberg, C-E Åkerlund, On the influence of field strength in wire-plate electrostatic presipitators with regard to the electrode configuration and dust space charge, Journal of Electrostatics, 17, 1985, 85-94.

4. F.W Peek Jr, Dielectric phenomena in high-voltage engineering, McGraw-Hill, 1929 73.

5. S. Oglesby Jr, G.B. Nichols, Electrostatic Precipitation, Marcel Dekker Inc, 1978, 32.

6. P.A. Lawless, L.E. Sparks, Prediction of voltage-current curves for novel electrodes arbitrary wire electrodes on axis, EPRI CS - 4404, Volume 2, Project 1835 - 6, Proceedings February 1986, 4-1 --- 4-14.

7. C.E. Åkerlund, Determination by experimental method of the static field strength in wire-plate electrostatic precipitators with profiled collecting electrodes., Journal of Electrostatics, 17, 1985, 137-144.

8. Fläkt Industri AB, Test report TM V-79.006, Private communication.

The work described in this paper was not funded by the U.S. Environmental Protection Agency. The contents do not necessarily reflect the views of the Agency and no official endorsement should be inferred.

THREE-DIMENSIONAL SECONDARY FLOW AND ELECTROHYDRODYNAMICS FOR VARIOUS ELECTROSTATIC PRECIPITATOR CONFIGURATIONS

by: Toshiaki Yamamoto, Phil A. Lawless
Research Triangle Institute
Research Triangle Park, NC 27709

and

Norm Plaks, Leslie E. Sparks
Air and Energy Engineering Research Laboratory
U.S. Environmental Protection Agency, MD-61,
Research Triangle Park, NC 27709

ABSTRACT

The two-dimensional secondary flow and electrohydrodynamics (EHD) in the wire-to-plate electrostatic precipitator (ESP) have been the subject of several studies. However, the research has not yet been done on the three-dimensional configuration due to its complexity. In this presentation, the state-of-the-art two-dimensional secondary flows and EHD flow interactions are reviewed for commonly used electrode arrangements, and the three-dimensional structures of secondary flows and EHD are investigated. These investigations should provide insight into the particle motion in the charging zones. Moreover, electrical sneakage in relation to the particle transport is evaluated.

This paper has been reviewed in accordance with the U.S. Environmental Protection Agency's peer and administrative review policies and approved for presentation and publication.

INTRODUCTION

In the process of particle collection in an electrostatic precipitator (ESP), the charged particles are transported to the collector wall by the combined influences of Coulomb force due to the electric field and flow interaction. An understanding of flow characteristics is particularly important because the nature of the flow perturbations produced by the secondary flow is very sensitive to the ESP geometry and corona polarity. Flow characteristics that are especially needed to be understood include secondary flow (sometimes referred to as electric wind, corona wind, or ionic wind) and electrohydrodynamic (EHD) flow interaction. For instance, it is much easier to characterize the positive corona on the smooth corona wire that produces a uniform corona along the wire as opposed to a negative corona that produces a local tuft corona.

In this presentation, the state-of-the-art two-dimensional secondary flows and EHD field are reviewed for various electrode geometries. Then the three-dimensional structures of secondary flows and EHD flow interaction are explored. Also, particle motion in the charging zone and electrical sneakage in relation to the particle transport are investigated for commonly used ESP electrode arrangements. Where secondary flows are shown on the various figures, there is no simultaneous primary flow implied.

TWO-DIMENSIONAL SECONDARY FLOWS AND EHD FIELDS

Much work has been done for one-dimensional secondary flow over the last decade, but the present discussion is limited to two-dimensional studies. A schematic diagram of electrode arrangements that have been commonly used is shown in Figures 1(a) to 1(f). A wire-to-plate in the open channel is shown in Figure 1(a); a point-to-plate in the open channel in Figure 1(b); a wire-to-plate in duct geometry representing a Cottrell ESP in Figure 1(c); a needle electrode parallel to the collection plate in duct geometry representing a United McGill ESP in Figure 1(d); an equally spaced barbed wire or point electrode facing upstream and downstream of the gas flow direction in Figure 1(e); and a wire-to-pipe geometry, known as the cold pipe precharger, in Figure 1(f). Figures 1(a) to 1(f) thus are the typical electrode configurations. Table 1 summarizes the overall review of the two-dimensional secondary flows and EHD flow interactions.

Yabe et al. (1) have carried out a theoretical calculation of the secondary flows for a single wire-to-plate geometry in the open channel, as shown in Figure 1(a). The numerical solutions obtained showed a circulatory motion in the vicinity of the corona wire, as shown in Figure 2. Adachi (2) and Yamamoto (3) used a Schlieren technique to visualize the secondary flows for the wire-to-plate in the open channel geometry. Figures 3(a) and 3(b) show the side view and frontal view, respectively, of the secondary flow for the negative corona when the applied voltage (V_0) is 12.5 kV and the wire-to-plate distance (d) is 3.0 cm. A bell-shaped and jetlike streaming flow from each tuft is observed, but qualitative analysis was not available.

Adachi et al. (4) carried out the numerical simulation of a secondary flow of negative corona for a needle-to-plate in the open channel configuration, as shown in Figure 1(b) both experimentally and theoretically. Yamamoto (5) also measured the secondary flow using the Schlieren system. To obtain the strength of the secondary flow, the needle electrode was placed perpendicular to the plate because this is one of the few possible arrangements that allow measurement of the secondary flow velocity. The three needles were 2 cm apart, and the needle-to-plate distance (d) was maintained at 1.6 cm. Flow visualizations are shown in Figure 4. The magnitude of the secondary flow velocity was determined by measuring the distortion of the thermal gradient shadows arising from the electrode for a known primary flow velocity. The maximum velocity obtained for V_0 = 12 kV was as high as 10 m/s in the vicinity of the corona point, which agreed well with Adachi et al.'s measurements (4).

Many studies have been done on the secondary flows for the wire-to-plate in the duct geometry (a typical ESP geometry). Ramadan and Soo (6) first presented the secondary flow distributions. However, the analytical solution was limited to the model space-charge case. Robinson (7) studied the secondary flow distribution using a diffusion model, and the results were compared with experimentally obtained helium-concentration profiles. Circulatory cells along the wire (as depicted in Figure 5) were presented.

Yamamoto and Velkoff (8) carried out numerical simulations in which ionic space charge was included to solve the Poisson equation for the electrostatic field. This result was incorporated into the Navier Stokes equations to solve the EHD field. Positive corona was used because only secondary flows and EHD flow interactions could be made visible for positive corona with Schlieren techniques. Negative corona creates an additional dimension along the wire, and experimental results showed excellent agreement with numerical simulations for one- and two-wire configurations. The typical results for secondary flow and EHD for the two-wire plate configuration are shown in Figures 6 and 7, respectively. The direct overlay between the experimental and numerical streamlines for the one-wire configuration is shown in Figure 8(a), and flow visualization for the two-wire configuration is shown in Figure 8(b). Note that the maximum secondary flow velocity obtained was 1.15 m/s for the average field (E_0) of 5.0 kV/cm and d = 3.0 cm and that it was always located between two electrodes. Leonard et al. (9) also conducted an experiment for both positive and negative corona and confirmed the results.

Ushimaru et al. (10) computed the EHD flow interaction using a turbulence model for the wire-to-plate ESP with baffle plates. The results are shown in Figure 9. Mazumder et al. (11) and Shimoda et al. (12) used laser doppler anemometry to measure the EHD velocity plot for laboratory-scale ESP. Watanabe (13) and Okubo et al. (14) also carried out the numerical simulation of EHD for the wire-to-plate configuration. Okubo's results are very similar to the results obtained by Yamamoto and Velkoff (8). Recently, Koopsman (15) demonstrated the secondary flow distribution using a turbulence model, and laser doppler measurements were performed to support the results.

Yamamoto (3) presented the flow visualization of secondary flow and EHD for the needle or plate in the duct geometry, as shown in Figure 1(d). Figure 10(a) shows the secondary flow pattern for V_0 = 12.5 kV and d = 3.0 cm. Whenever the jetlike flow exists, the surrounding fluid is entrained across the mixing layer because of the effect of velocity gradient and viscosity, resulting in the counterclockwise circulatory cell under the needle electrode. Figure 10(b) shows the secondary flow for the same electrode arrangement, except the electrodes are perpendicular to the plate. A pair of flow circulations were observed. As the needle-to-needle spacing becomes narrower with respect to needle-to-plate distance, the circulatory cells generated become smaller and eventually lead to small eddies or turbulence. Figure 11 shows the EHD flow interaction when the primary flow velocity (U_0) is 0.6 m/s and V_0 = 14 kV. The momentum transfer between the primary and secondary flows at the mixing layer causes the circulatory cell to reverse, resulting in the clockwise circulation. As the primary flow further increases, the EHD flow interaction is gradually reduced and becomes insignificant when the primary flow velocity exceeds 1.8 m/s.

Larsen and Sorrensen (16) and Sorrensen et al. (17) measured root mean square values of EHD velocity distributions using laser doppler anemometry. Particle motion reveals complex three-dimensional flow patterns with rolls of axial velocity. A secondary flow and EHD field for an axially aligned barbed wire electrode, as shown in Figure 1(e), is shown in Figure 12.

Yamamoto (18) carried out preliminary numerical simulations for the wire-to-pipe configuration, as shown in Figure 1(f). Figure 13 shows the secondary flow distribution. Two flow fields (both with d = 11 cm and U_0 = 1.0 m/s) are illustrated in Figure 14; V_0 = 0 kV for Figure 14(a) and V_0 = -61.5 kV for Figure 14(b).

EFFECT OF SECONDARY FLOW ON TURBULENCE

It is known that the secondary flow interacts with the primary flow and increases the turbulence. It is more significant for the negative corona because of three-dimensionality. Figure 15 shows the characteristics of EHD for the case of positive polarity with a one-wire configuration (5). The flow is initially well controlled and very uniform at the ESP inlet; e.g., a laminar flow for this arrangement. The flow interaction is first observed when the primary flow velocity is 0.3 m/s and the applied voltage exceeds 8.0 kV, which is only 1.2 kV above the corona onset voltage. At 9.0 kV, the flow is reflected toward the corona wire. The deflection reverses near the wire, and the stream moves toward the plate as it passes the corona wire, as shown in Figure 7. When the voltage is above 13.0 kV, it becomes very difficult to visualize the flow patterns because the flow is perturbed by the secondary flow, resulting in a turbulent regime. Region (I) indicates no flow interactions, and line (I) is the corona onset voltage. Region (II) is the flow interaction region that is visible when the Schlieren method is used. A circulatory cell is formed in region (III). Region (IV) is a turbulent regime that is difficult to visualize. Line (V) indicates the field breakdown (sparking). The turbulence level depends on corona polarity, current density, and mean flow velocity. Turbulence level and frequency response in the channel flow (5) were measured as the primary flow; as the applied voltage increases, both the turbulent intensity and frequency response also increase. The general dependence of the turbulence intensity on the current density, corona polarity, and mean gas flow velocity is well summarized in Self et al. (19).

Shaughnessy et al.'s (20) interpretation was that the ion current density is a vector whose curl determines the generation of vorticity. For wire-plate ESP, the current density always has a rotational component (i.e., curl J is not zero); therefore, the secondary flow and turbulence are produced.

THREE-DIMENSIONAL SECONDARY FLOW AND EHD FIELD

Based on an awarenesss of the two-dimensional studies of secondary flows, EHD, and the current density distribution, one could estimate three-dimensional structures of secondary flows and EHD flow interactions for various electrode configurations. Electrical sneakage in relation to the particle transport could also be investigated.

For positive corona in the wire-duct geometry, uniform corona is generated along the wire where no three-dimensional secondary flow and EHD are formed. However, negative corona generates a local tuft discharge along the wire, resulting in three-dimensionality. Figure 16 shows the computed current density distributions for the negative tuft corona or micropoint on the wire (21). Figure 17 illustrates the predicted three-dimensional secondary flow from individual tufts or micropoints on the wire. It forms a skewed vortex ring that is elongated normal to the wire and compressed in the wire direction due to the electric field from the wire. Because individual tufts are different in strength and not stationary, the vortices generated are less organized and more unstable between the tufts. Therefore, the zone of circulatory cells formed (III) in Figure 15 becomes much narrower, and the EHD field has a greater tendency to become turbulent as compared to the positive corona. As the tuft or micropoint spacing becomes narrower with increasing current, these rings merge and lead to the two-dimensional circulatory cells, as shown in Figure 6. At the same time, the turbulence level increases, which tends to destroy the circulatory cells.

Figure 18 shows the predicted three-dimensional EHD field for various tuft spacings. The flow starting at position "a" moves upward because of the induced elliptic circulatory cell and is reflected down to the plate as it passes through the cell (a-a'-a). The flow starting at position "b" moves upward as well as sideways because the cell size is reduced in this direction (b-b'-b). However, as the tuft spacing decreases, the upward motion increases everywhere, resulting in a two-dimensional EHD, as shown in Figure 7.

It is known that fine particles tend to follow closely the EHD streamlines. The fluid passes shown in the figures mentioned above translate into the motion of fine particles, some fraction of which escape through the charging zone; this action is especially significant for wide tuft spacing. This phenomenon is known as electrical sneakage and causes the reductions of charge on the particles and particle migration, resulting in deleterious effects on the performance of the ESP.

Based on the current density distribution measured for the multipoint electrode in the duct geometry (3), shown in Figure 1(d), the ellipsoidal secondary flow is expected to occur below the electrodes, as shown in Figure 19. The size of the secondary flow is characterized by the half-distance between points and the electrode-to-plate distance.

Figure 20 shows the predicted three-dimensional EHD field, which could be described as the flow over an ellipsoidal moving body. Similarly, the flows starting at positions "a," "b," "c," "d," and "e" follow passes (a-a'-a), (b-b'-b), (c-c'-c), (d-d'-d), and (e-e), respectively. However, as the point spacing decreases, the adjacent ellipsoidal cells merge, and upward motion again increases everywhere. The EHD field becomes similar to the tuft corona EHD field, as shown in Figure 18.

The current density distribution for staggered point electrodes becomes the combination of distributions of Figure 18. Mitchner et al. (22) showed the dust deposition distribution for this geometry, and Figure 21 shows the predicted EHD field. Electrical sneakage will be minimized for this geometry although turbulent intensity will be increased because of a zigzag motion in the EHD field.

CONCLUSIONS

Two-dimensional secondary flows and EHD flow interaction are further extended to the three-dimensional case. The structure and role of secondary flow and EHD for any electrode geometry can be estimated based on the current density distribution. These investigations should provide insight into the particle transport in the charging zone and illustrate the deleterious effects of electrical sneakage.

REFERENCES

1. Yabe, A., Mori, Y., and Hijikata, K. EHD study of the corona wind between wire and plate electrode. A.I.A.A.J. 16(4): 340-345, 1978.

2. Adachi, T. Ionic wind in the electrostatic precipitator--experimental treatment by the Schlieren method. Trans. I.E.E.J. 93-B(7):273-280, 1973.

3. Yamamoto, T. Investigation of three-dimensional secondary flow and the effects on particle transport. Paper presented at the International Symposium on Particulate and Multi-Phase Processes and Annual Meeting of the Fine Particle Society, Miami Beach, Florida. April 1985.

4. Adachi, T., Masuda, S., and Akutsu, K. Velocity distribution of negative ionic wind in the corona discharging space with needle to plate electrodes. *JIEE Japan*. 51-A(5):259-266, 1977.

5. Yamamoto, T. Electrohydrodynamic secondary flow interaction in an electrostatic precipitator. Ph.D. Thesis. Department of Mechanical Engineering, Ohio State University, Columbus, Ohio. 1979.

6. Ramadan, D.E., and Soo, S.L. Electrohydrodynamic secondary flow. *Phys. Fluids*. 12:1943-1945, 1969.

7. Robinson, M. Effects of corona discharge on electric wind convection and eddy diffusion in an electrostatic precipitator. ERDA, Health and Safety Lab. Rep. HASL-301. 1976.

8. Yamamoto, T., and Velkoff, H.R. Electrohydrodynamics in an electrostatic precipitator. *J. Fluid Mechanics*. 108:1-18, 1981.

9. Leonard, G.L., Mitchner, M., and Self, S.A. An experimental study of the electrohydrodynamic flow in electrostatic precipitators. *J. Fluid Mechanics*. 127:123-140, 1983.

10. Ushimaru, K., Butler, G.W., and Milovsoroff, P. An experimental and theoretical investigation of electrostatic precipitators. Flow Research Report No. 219. Flow Research Company. 1982.

11. Mazumder, M., Clark, W., Ware, R., McLeod, P., Hood, W., Straub, J., and Wanchoo, S. Application of laser doppler instrumentation to particle transport measurements in an electrostatic precipitator. *In*: Third Symposium on the Transfer and Utilization of Particulate Control Technology, Volume II. EPA-600/9-82-005b (NTIS No. PB83-149 591). 1982. pp. 169-178.

12. Shimoda, M., Yukitake, T., and Ohtsuka, K. Measurements of charged particles in electostatic precipitators. *In*: Proceedings of the Second International Conference on Electrostatic Precipitation, Kyoto, Japan, 1984. pp. 972-978.

13. Watanabe, T. Computer simulation of flyash trajectory in an ESP. Paper presented at the Third International Conference on Electrostatic Precipitation, Abano, Italy. October 1987.

14. Okubo, T., Yano, H., Nomoto, K., and Adachi, T. Analysis of flow for the wire-plate electrode geometry. *In*: Proceedings of the Ninth Annual Meeting of the Institute of Electrostatics Japan, October 1985. pp. 17-20.

15. Koopmans, G. Corona wind in plate-wire ESP's. Paper presented at the Third International Conference on Electrostatic Precipitation, Abano, Italy. October 1987.

16. Larsen, P.S., and Sorrensen, S.K. Effect of secondary flows and turbulence on electrostatic precipitator efficiency. *Atmospheric Environment*. 14:1289-1299, 1984.

17. Sorrensen, L.S., Larsen, P.S., Christensen, E.M., and Christiansen, V.J. Secondary flow and turbulence in negative-corona precipitator with large diameter. Paper presented at the Third International Conference on Electrostatic Precipitation, Abano, Italy. October 1987.

18. Yamamoto, T. Particle migration for the wire-pipe precharger. *In*: Proceedings of the Seventh Annual Meeting of Institute of Electrostatics Japan, Tokyo, Japan, October 1983. pp. 162-165.

19. Self, S.A., Mitchner, M., Khim, D.H., and Leach, R. Effect of turbulence of precipitator performance. *In*: Proceedings of the Second International Conference on Electrostatic Precipitation, Kyoto, Japan, 1984. pp. 249-264.

20. Shaughnessy, E.J., Davidson, J.H., and Hay, J.C. The fluid mechanics of electrostatic precipitators. *Aerosol Science and Technology*. 4:471-476, 1985.

21. Yamamoto, T., and Sparks, L.E. Numerical simulation for three-dimensional tuft corona and electrohydrodynamics. *IEEE Trans. on Industry Applications*. IA-22(5):880-885, Sept./Oct. 1986.

22. Mitchner, M., Fisher, M.J., Gere, D.S., Leach, R.N., and Self, S.A. Surface reentrainment of collected fly ash in electrostatic precipitators. *In*: Third Symposium on the Transfer and Utilization of Particulate Control Technology, Volume II. EPA-600/9-82-005b (NTIS No. PB83-149 591). 1982. pp. 97-108.

TABLE 1. TWO-DIMENSIONAL SECONDARY FLOW AND EHD FIELD

Electrode configuration	Secondary flow		EHD	
	Theory	Experiment	Theory	Experiment
Figure 1(a)	Yabe (1)	Adachi (2)		
		Yamamoto (3)		
Figure 1(b)	Adachi (4)	Adachi (4)		
		Yamamoto (5)		
Figure 1(c)	Ramadan (6)			
	Robinson (7)	Robinson (7)	Robinson (7)	Robinson (7)
	Yamamoto (8)	Yamamoto (8)	Yamamoto (8)	Yamamoto (8)
				Leonard (9)
			Ushimaru (10)	Ushimaru (10)
				Mazumder (11)
				Shimoda (12)
			Watanabe (13)	
			Okubo (14)	Okubo (14)
	Koopmans (15)	Koopmans (15)		
Figure 1(d)		Yamamoto (3)		Yamamoto (3)
Figure 1(e)		Larsen (16)		Larsen (16)
		Sorrensen (17)		Sorrensen (17)
Figure 1(f)	Yamamoto (18)		Yamamoto (18)	

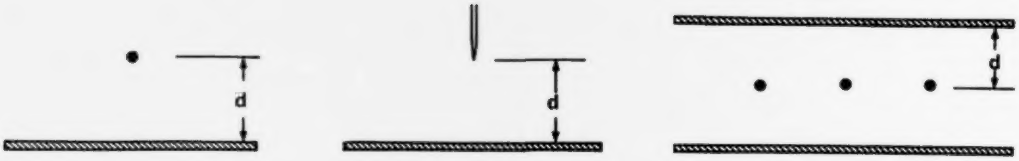

(a) Wire-to-plate in open channel

(b) Needle-to-plate in open channel

(c) Wire-to-plate in duct geometry

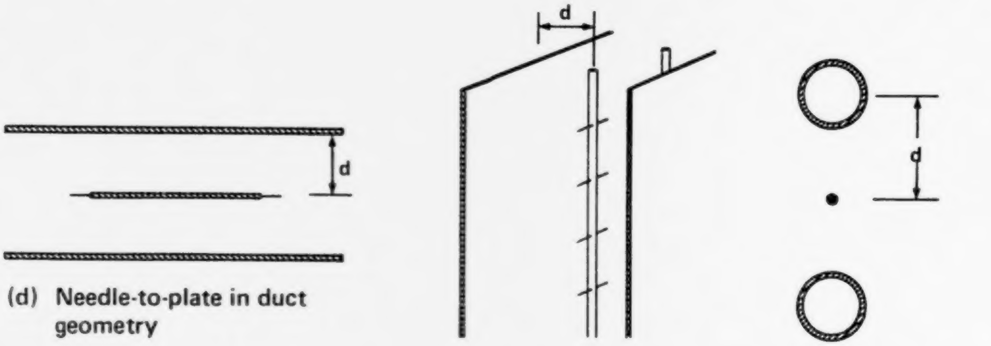

(d) Needle-to-plate in duct geometry

(e) Barbed wire in duct geometry

(f) Wire-to-pipe configuration

Figure 1. Schematic diagram of various electrode arrangements.

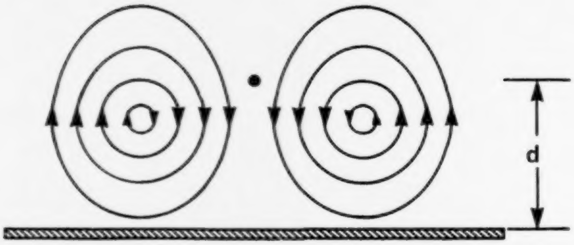

Source: Yabe et al. (1).

Figure 2. Schematic diagram of secondary flow for wire-to-plate in open channel ($d = 2.0$ cm, $V_o = 8.3$ kV, $V_{max} = 1.8$ m/s).

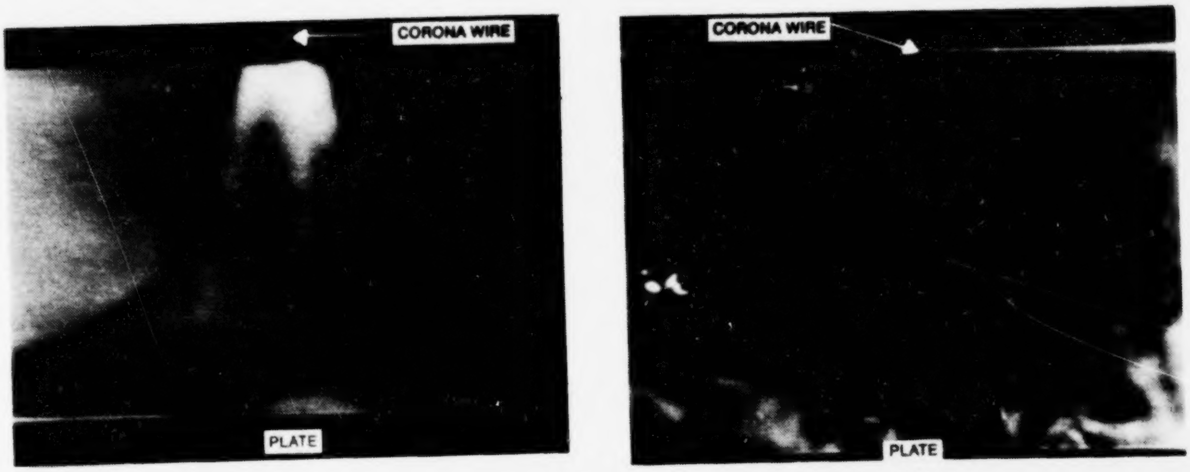

(a) (b)

Source: Yamamoto (5).

Figure 3. Secondary flow for negative corona in wire-to-plate open channel: (a) side view, (b) frontal view (d = 3.0 cm; $V_o = -12.5$ kV).

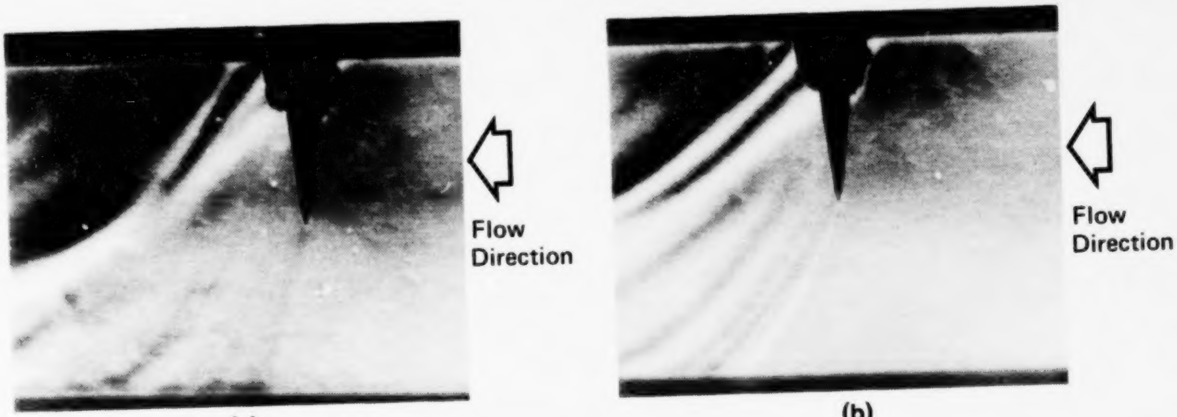

(a) (b)

Source: Yamamoto (5).

Figure 4. Secondary flow for needle-to-plate configuration (a) $U_o = 0.91$ m/s, $V_o = -7.5$ kV; (b) $U_o = 1.83$ m/s, $V_o = -7.5$ kV.

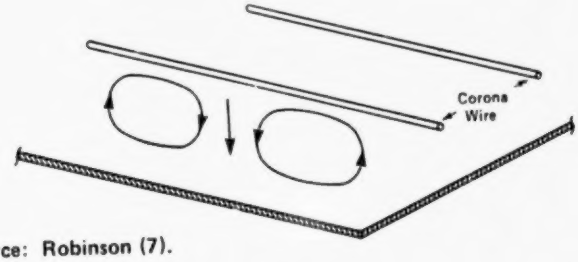

Source: Robinson (7).

Figure 5. Schematic diagram of Robinson's secondary flow distribution for the wire-to-plate in the duct geometry.

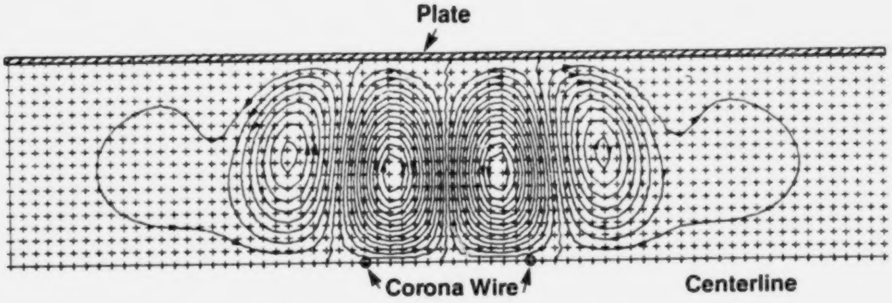

Note: Actual scale for wire-to-plate distance is one-half.
Source: Yamamoto (5).

Figure 6. Secondary flow distribution for the two-wire configuration (E_o = 5.0 kV/cm).

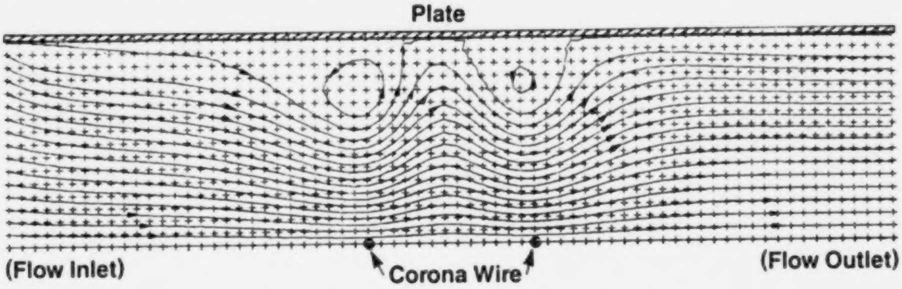

Source: Yamamoto (5).

Figure 7. EHD flow interaction for the two-wire configuration (U_o = 0.61 m/s, E_o = 5.0 kV/cm).

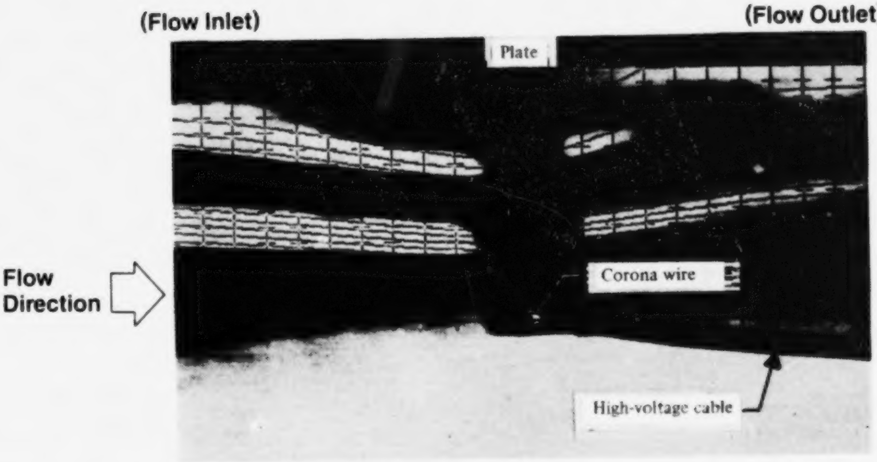

Source: Yamamoto (5, 8).

Figure 8a. Direct overlay between experimental and numerical streamlines for one-wire configuration (U_o = 0.91 m/s, E_o = 5.0 kV/cm).

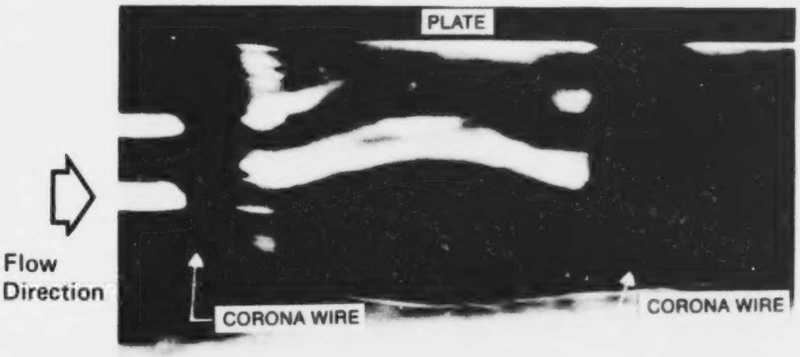

Source: Yamamoto (5).

Figure 8(b). Flow visualization for two-wire configurations (U_o = 0.91 m/s, E_o = 5.0 kV/cm).

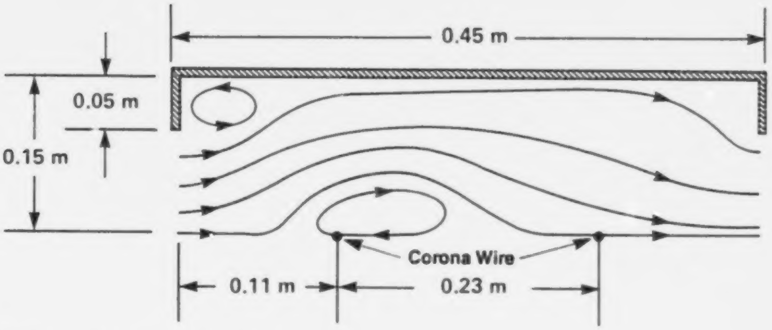

Source: Ushimaru et al. (10).

Figure 9. EHD flow interaction for the two wires with baffle plate in the duct geometry (d = 0.15 m, U_o = 0.6 m/s, E_o = 4.0 kV/cm).

Source: Yamamoto (3).

Figure 10a. Secondary flow for a multipoint electrode in the duct geometry (d = 3.0 cm, V_o = +12.5 kV).

Source: Yamamoto (3).

Figure 10(b). Secondary flow for a multipoint electrode with electrodes perpendicular to the plate.

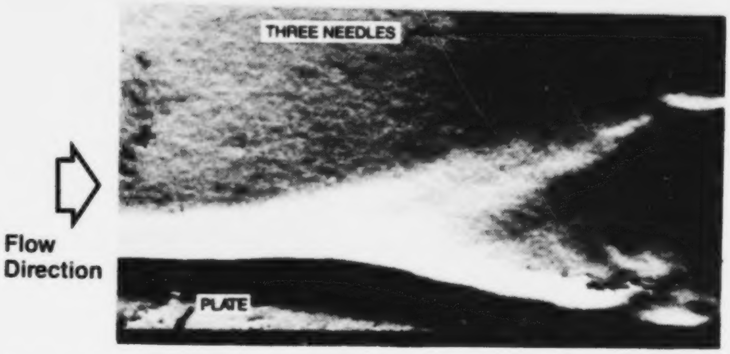

Source: Yamamoto (3).

Figure 11. EHD flow interaction for the point-to-plane in the duct geometry (d = 3.0 cm, V_o = +14 kV).

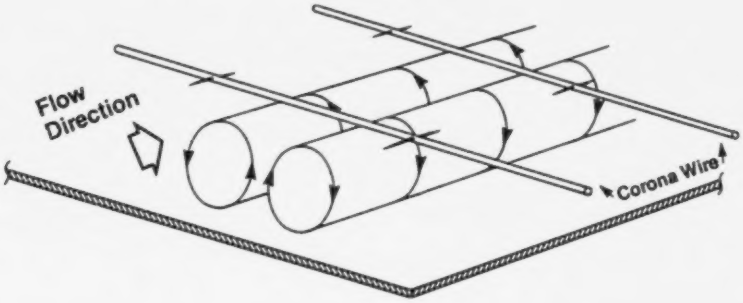

Source: Larsen and Sorrensen (16).

Figure 12. Schematic diagram of secondary flow and EHD for the barbed wire in the duct geometry (d = 10 cm).

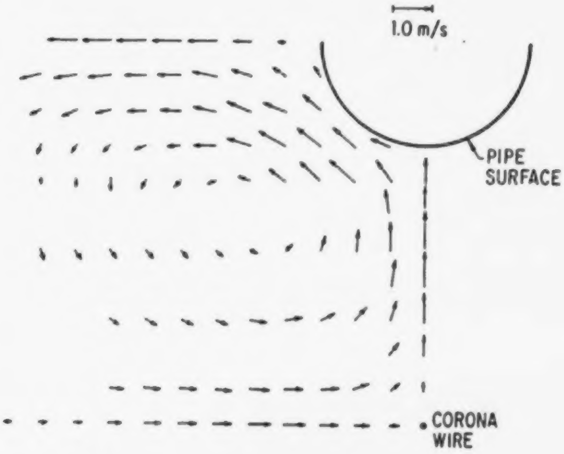

Source: Yamamoto (18).

Figure 13. Secondary flow fixed for wire-to-pipe geometry (d = 11 cm, V_o = −61.5 kV).

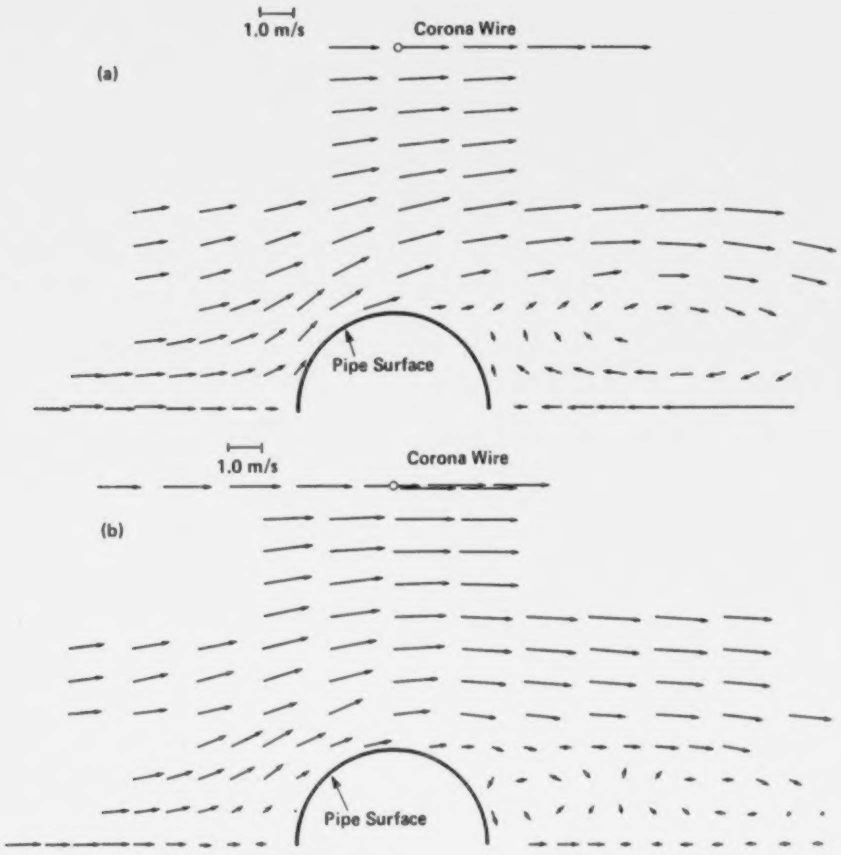

Source: Yamamoto (18).

Figure 14. EHD field for the wire-to-pipe geometry.
(a) $U_o = 1.0$ m/s, $V_o = 0$ kV,
(b) $U_o = 1.0$ m/s, $V_o = -61.5$ kV

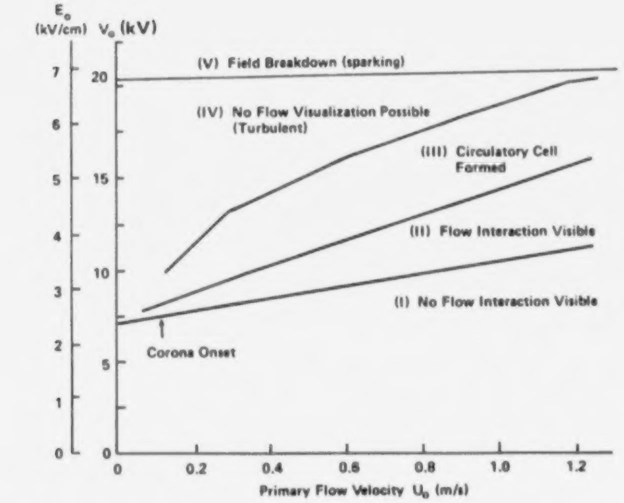

Source: Yamamoto (5).

Figure 15. Flow interaction for various electrical potentials and cross flow velocities for the one-wire configuration (d = 3.0 cm).

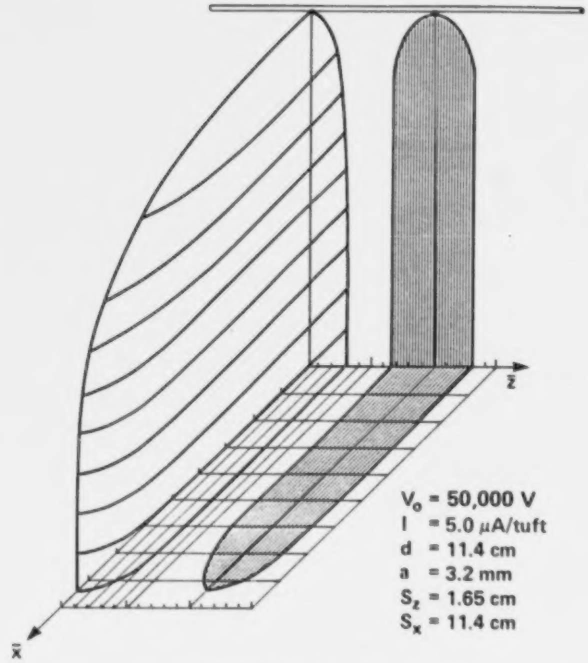

Source: Yamamoto and Sparks (21).

Figure 16. Three-dimensional current density distributions for tuft corona or micropoint on the wire.

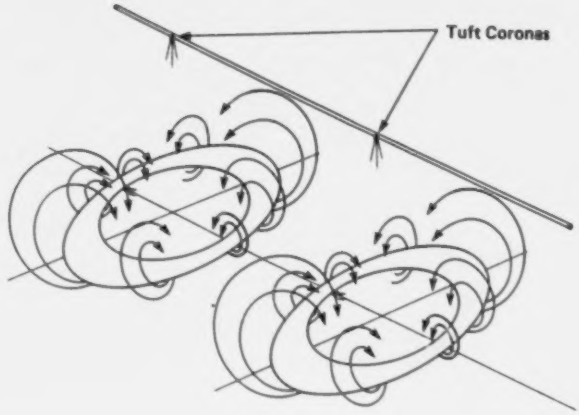

Source: Yamamoto and Sparks (21).

Figure 17. Predicted three-dimensional secondary flow for tuft corona or micropoint point on the wire.

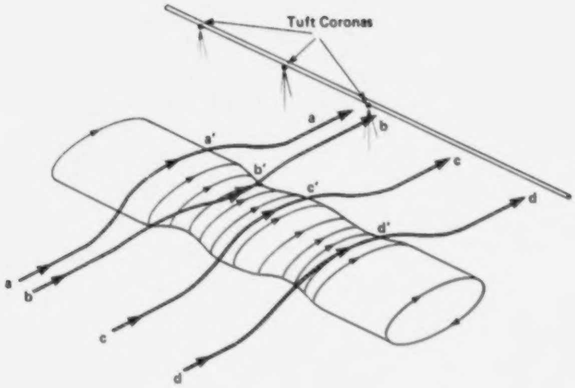

Source: Yamamoto and Sparks (21).

Figure 18. Three-dimensional EHD field for tuft corona or micropoint on the wire.

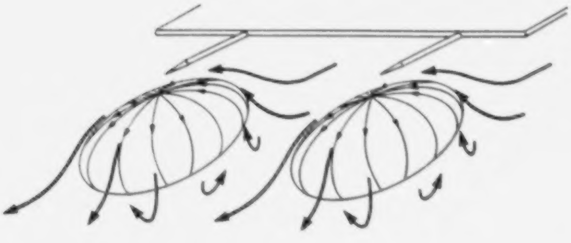

Source: Yamamoto (3).

Figure 19. Three-dimensional secondary flow for needle on plate-to-plate electrode.

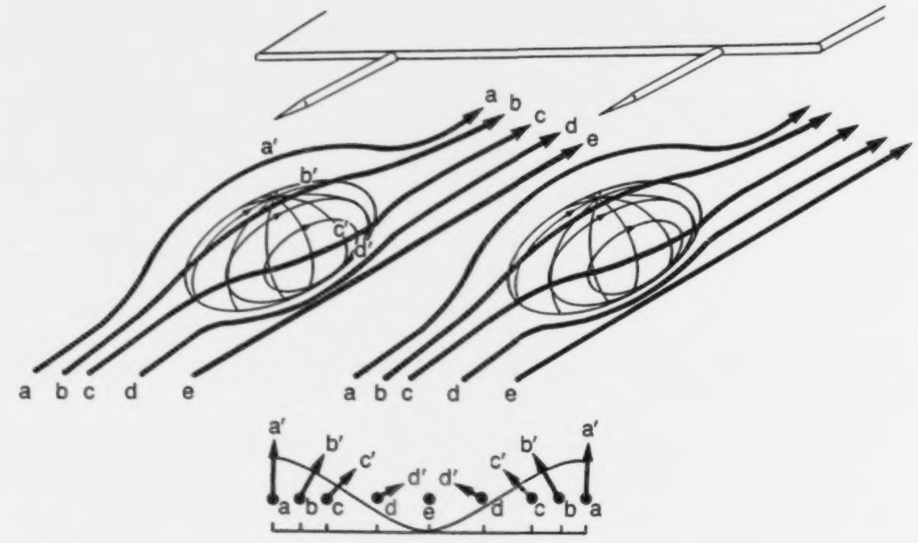

Source: Yamamoto (3).

Figure 20. Three-dimensional EHD field for needle on plate-to-plate electrode.

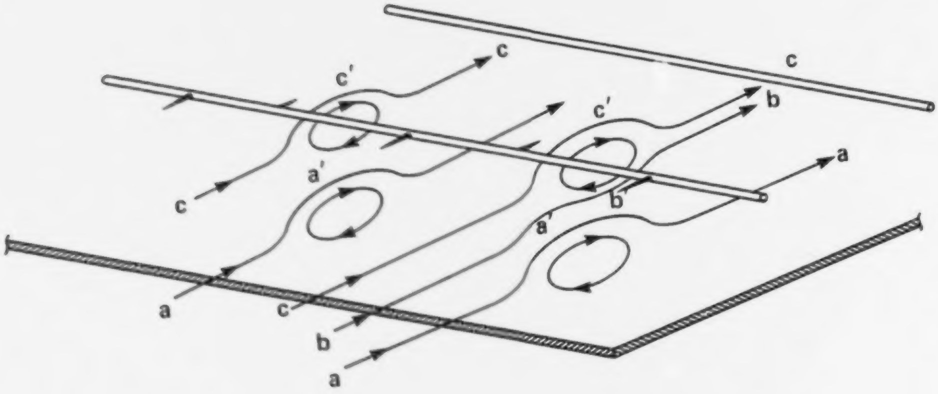

Figure 21. Three-dimensional EHD field for staggered point electrodes.

AN INTERACTIVE MODEL FOR ANALYSIS OF ELECTRICAL CONDITIONS IN ELECTROSTATIC PRECIPITATORS

Phil A. Lawless
Research Triangle Institute
Research Triangle Park, NC 27709

Norman Plaks and Leslie E. Sparks
U. S. Environmental Protection Agency
Air and Energy Engineering Research Laboratory
Research Triangle Park, NC 27711

ABSTRACT

Modeling of electrostatic precipitator (ESP) performance hinges on knowing or predicting the electrical conditions. An earlier version, Version 1.0, of the interactive models described here produced excellent predictions of laboratory ESP voltage/current curves with positive and negative glow corona. Further research was able to establish a working knowledge of the difference between negative glow and tuft corona, and that knowledge has been translated into Version 2.0 of the interactive model.

At the same time, important effects of particulate space charge, dust layer resistivity, and dust layer breakdown have also been incorporated. Because the particulate space charge dominates much of the electrical operation of the ESP, it is important to provide a strong coupling between the collection of particles and the electrical operating points. This has been accomplished to a large extent in Version 2.0, and to an even greater extent in the Version 3.0, which is under development.

This paper summarizes the essential features of the interactive models, and develops important relationships that have guided and contributed to their success.

This paper has been reviewed in accordance with the U. S. Environmental Protection Agency's peer and administrative review policies and approved for presentation and publication.

INTRODUCTION

The original impetus for an interactive V-I model was to allow the user to program electrode configurations that mimic electrodes other than round wires and predict their characteristics. Version 1.0 (1) of the model was successful in allowing arrays of round wires to be accurately characterized, as long as smooth wires were used, to maintain negative or positive glow corona.

Since real electrodes operate in the tuft corona mode (2,3), it was necessary to redesign the model to accommodate tuft corona, for more accurate predictions of real ESP electrodes. In the course of that redesign, several important considerations were uncovered that relate to electrodes of all possible designs. These factors were incorporated into Version 2.0 in an empirical way, which was, nevertheless, a major improvement over Version 1.0.

Additional work (4) showed the importance of coupling the particulate space charge and its removal with the effects of space charge on the electrical operating point. Although the process should ideally be carried out on a wire-by-wire basis, it is possible to get good model results on a section-by-section basis. Version 3.0 carries this program out in greater detail.

The factors that are so important to the operation of a corona electrode are: the saturation current density, the space charge effect of ions, the particulate space charge, the limitation of charging by a finite supply of ions, the universal spread of current, and resistive layer effects. When these effects are understood, then the operation of almost any corona electrode can be understood in terms of these quantities. The advantage of this approach is that analytical methods can be applied to make mathematical predictions, and the time-consuming numerical methods might have to be employed only for more accurate refinements of the analytical solutions.

For a model that is expected to give a user rapid interaction, the analytical approach is very important, because it makes choices of electrode design or investigation of effects much easier. Under those conditions, some sacrifice of accuracy is permissible.

FUNDAMENTAL RELATIONS

The electrical corona is a finely balanced process in which free electrons gain energy from the electric field, continuously ionize gas molecules, and provide a source of ions for charging particles. The electrons must be replenished, or the corona will die out. The electron growth must also be bounded, or the ionization will become intense enough to develop a spark. Fortunately, the ions produced are the solution to both problems. Positive ions can combine with electrons to produce photons that replenish the source of free electrons, or they can release free electrons from the electrode surface. The buildup of ions in the space between electrodes creates an electric field which opposes the free-electron ionization, and stabilizes the corona. The movement of those ions from the corona source to the collector is the area on which the V-I model concentrates.

SATURATION CURRENT DENSITY

Consider two electrodes, separated in space by a distance L. If there is an unlimited source of ions at one electrode, what is the maximum current density that can arrive at the other electrode? This has been addressed by Sigmond (5), who derives the following relation:

$$j_s = k\mu\epsilon V^2/L^3 \qquad (1)$$

where j_s is the saturation current density, k is a constant depending on the electrode geometry, μ is the ion mobility, ϵ is the permittivity of space, V is the voltage applied between the electrodes, and L is their separation. In the wire-cylinder geometry, k = 1, and in the wire-plate geometry it is approximately 1.

No greater current density than this can flow under the assumptions of a single ion polarity and mobility. If a greater current density is observed experimentally, it points to the presence of additional ion carriers.

If the current density is saturated, then two corollary conditions also apply: the electric field is uniform along the path L, and the electric field is zero at the source electrode. Both corollaries follow from the concept that, at saturation, as many ions as possible fill the electrode gap. If the electric field were non-uniform, ions would leave the higher field regions faster than they would the lower field regions, leaving room for more ions. Similarly, if the electric field at the source electrode were not zero, the electrode could supply ions to the electrode gap faster than they were being removed.

These corollaries seem counter to the usual understanding of electrical corona wires, with a high field near the wire, falling to a lower value at the plate. Those conditions, however, apply for low values of current density, and not for the conditions near saturation. As any corona source, tuft or glow, delivers increasing amounts of current, the maximum current density will approach the saturation limit, as given by Eqn. 1.

This is shown in Figure 1, taken from (2), with the addition of a glow corona current density line. If all curves were followed to higher voltages, the differences between them would become a small fraction of the total current density.

GLOW AND TUFT CORONAS

The first interactive model stimulated an interest in the distinction between glow corona (for which Version 1.0 predicted the corona onset voltages with great accuracy) and tuft corona (for which the predictions were in considerable error, but which is the most common form of corona in ESPs). There are distinctions between the two forms of corona in both the current density directly under the wire and in the spread of current transverse to the wire.

For the purposes of distinguishing these two areas of interest, the current density under the wire and its voltage dependence will be called a V-j curve. The whole current, including the transverse spread, and its voltage dependence will be called a V-I curve.

Glow Corona Current Density. The important feature of glow corona is that it is sustained by photon feedback in the electron avalanche process; therefore, it covers the whole surface of the corona wire. The corona onset field is given by an empirical relation for round wires, Peek's law (6), and the onset voltage is a function of the electrode geometry. The glow corona can be controlled to have very low current densities near the onset voltage, and for a wide range of voltages above that. The maximum current density is reasonably close to the saturation value only for voltages much greater than the corona onset voltage.

In cylindrical geometry and with no particulate space charge, the differential equations for the whole V-j curve can be solved analytically. See Reference (7), for example. If this solution is evaluated at high current densities, the saturation relation results, and the electric field becomes uniform over most of the electrode gap. The electric field does not approach zero at the electrode, because the corona process is not modeled in detail, but only assumed to require Peek's field at the corona wire.

In the wire-plate geometry, the empirical results from Version 1.0 were that the current density at the plate directly under the wire follows the same relationship that the wire-cylinder corona device does, with a minor correction for the value of electric field at the plate at corona onset. Version 1.0 can model clean plate glow corona curves with excellent agreement (8). We also find that, when the computed glow corona curves are calculated to high current densities, they approach the saturation curve.

If a spatially constant immobile space charge is added to either electrode system, the differential equations can no longer be solved analytically (at least, not easily). The effect of the space charge on the corona onset voltage can be calculated, in either geometry, by integrating the electric field due to space charge from the wire to the outer electrode. That voltage must be added to the normal corona starting voltage to obtain the new starting voltage in the presence of the space charge. At voltages above the corona onset, the effect of space charge can be estimated, but not derived rigorously.

For voltages above the corona onset, the current density must converge slowly toward both the zero space charge value and the saturation current density. That is because the ionic space charge will eventually dominate the effects of the particulate space charge as it becomes larger. Unfortunately, the algorithm used in Version 1.0 did not have these characteristics. Although it behaved satisfactorily for normal 1/8-in. (0.32 cm) corona wires, for much smaller wire diameters, the calculated current densities crossed the saturation current density line. In Versions 2.0 and 3.0, another algorithm is used, and it does give the correct behavior.

Although the algorithm is expressed in complicated code, the concept is quite simple. Every point along a V-j curve has associated with it an average ionic space charge that is unique. At low current densities, the average space charge is low, and it grows nonlinearly, but monotonically, with current density. The effect of the average space charge is to raise the operating voltage for the corona. That is, the difference in voltage between that corresponding to the current density and the corona onset voltage is due to the presence of the average space charge, almost wholly. The corona region itself is very little affected by the presence of the ionic space charge cloud. Therefore, the presence of a particulate space charge will have the same effect on the V-j curve as an equivalent amount of ionic space charge, except for the associated current density.

Figure 2 shows this effect schematically. The solid line below the voltage axis corresponds to the current density axis shifted to the corona onset voltage. The V-j curve corresponding to operation with different amounts of space charge is that part of the zero space charge V-j curve that has been translated vertically downward until it crosses the zero current density line at a voltage corresponding to the space charge offset voltage. From this figure, it can be seen that one V-j curve is all that is needed to calculate the V-j curve in the presence of any amount of space charge.

Tuft Corona Current Density. The current density for tuft corona is quite simple: it is the saturation current density curve offset by from a few hundred to a few thousand volts for nearly all voltages above the corona onset. This is seen in Figure 1 and has been reported in Reference 3. The important feature of tuft corona is that it is sustained by positive ion feedback, which confines the ionization to a very small region and makes it more efficient. Assuming that each positive ion created in the corona eventually releases a new free electron, it can be shown that the electric field at the surface of the wire required to sustain continuous corona is just 0.6 times Peek's value (2,6).

When tuft corona first occurs as the voltage on a wire is raised, it usually will be at a voltage above that corresponding to 0.6 times the Peek onset, but continued operation will bring the value down. The positive ions that accumulate at the tuft are responsible for the lowered threshold, and the corona runs itself at the steady state condition produced when each ion is used effectively. Under normal conditions, an individual tuft may be unsteady near its onset voltage, but stabilizes within a few hundred volts above onset. The unsteady nature of the tuft is believed to be due to small variations in feedback efficiency with time.

The positive space charge in the corona zone can be calculated to be quite large, and it is likely that the electric field near the positive part of the corona column is almost zero, as is required for the saturation condition. The voltage drop along the positive column is enough to account for the voltage offset between the actual tuft curve and the saturation curve in Figure 1. In Versions 2.0 and 3.0, the voltage offset is assumed to be 50 percent of the corona onset field times the wire radius, a characteristic voltage of the order of a few thousand volts for normal wires.

When particulate space charge is added to the system, the corona onset voltage must shift upward. However, in this case, the current density quickly increases, within a few hundred volts, to the same saturation curve as before, except that it corresponds to the higher voltage. This is shown in Figure 3. When a corona tuft is activated, it is totally activated.

Nonetheless, a whole corona wire activates tufts relatively slowly as the voltage is raised. The reasons for this are not clear, but presumably an active tuft collects all the stray positive ions in the near vicinity and reduces the likelihood that a new tuft can form nearby. The number of tufts varies roughly linearly with voltage from the tuft corona onset voltage up to the glow corona onset voltage (2). A linear rise is assumed in Versions 2.0 and 3.0 of the model.

The model also allows for a mixed corona mode, where the tuft onset voltage is between 0.6 and 1.0 times Peek's value. In this mode, tufts are activated linearly in voltage until the glow onset voltage is reached; whereupon, the remaining fraction of the wire exhibits the glow V-j curve behavior. This situation has been observed in laboratory experiments, but is not expected to be a realistic mode in operating cold side ESPs. In applying the model to hot side ESPs, corona factors of 0.9 to 1.0 gave the best fits of the measured V-I curves.

CURRENT DENSITY DISTRIBUTIONS

In beginning with the saturation relation and proceeding through the tuft and glow V-j relations, we have assumed that the current density value under the wire will be easy to relate to the current density at other locations on the collecting plate surface. It is. In fact, the universality of the relation is the factor that attracted attention when Version 1.0 was being developed.

The relation is that the current density at any point off the wire-plate axis is equal to the current density on that axis, j_0, multiplied by the cosine of the angle, θ, between the point and the axis raised to a power, n:

$$j_\theta = j_0 \cdot \cos^n(\theta). \tag{2}$$

The relation of these quantities is shown in Figure 4. Note that the relationship holds for the component of current density normal to the collecting plate. The same angular relation holds in the interelectrode gap, as long as the angle is reevaluated and the component of current density normal to a plane parallel to the collecting plate is considered. The value of the exponent may change somewhat with position in the gap.

The exponent in this relationship varies between 2 and 4, for the most part. It is approximately equal to 2 in the vicinity of the wire for glow corona at low current densities. In this case, the ions follow electric field lines without seriously distorting them. It is adequate to observe that the electric field component normal to the plate follow a $\cos^2(\theta)$ dependence near the wire, and $1/\cosh(\theta)$ at the plate, which is within a few percent of $\cos^2(\theta)$ for a wide range of angles.

At high current densities, where j_0 approaches the saturation value, the value of n approaches 4. The $\cos^4(\theta)$ law is a well-known optical law for the intensity of a beam of light projected at an angle with respect to a surface normal. The same considerations hold for a saturated current source (that is, the ions are projected on straight-line paths). The $\cos^4(\theta)$ law is considered to be the saturation current density distribution law.

Glow corona, therefore, has an exponent that varies from 2 to 4, depending on the current density level and position in the gap. The models assume a form for the variation that takes into account the relative contributions of the electrostatic and the ionic space charge parts of the field.

The tuft corona is slightly more complex. It has been shown (2) that the current density distribution from an isolated tuft approximates a $\cos^5(\theta)$ distribution. This is due to the extra degree of freedom the ions have to reach the plate at different azimuthal angles around the wire-plate axis. When arrays of tufts on a wire are considered, however, the average distribution of current becomes much closer to the $\cos^4(\theta)$ law, particularly at voltages well above corona onset. That is, the current density distribution for a single tuft at corona onset may be approximately $\cos^5(\theta)$, but by the time several more tufts are activated at higher voltages, the dependence is close enough to $\cos^4(\theta)$ to no longer make any difference.

Limits of the Distribution. The cosine power law distributions can be thought to apply to single corona wires for all angles up to ± π/2 radians. The contribution to the total current for angles greater than about π/3 radians is negligible. For small angles, the cosine exponent does not even need to be known with high accuracy, because the current density does not change much with angle.

When several corona wires are placed close together, approximately the same distance apart as the wire to plate distance, then the current density distributions would overlap to a significant degree if all angles were included. The experimental evidence is that the current density patterns do not overlap, but are simply truncated at their common boundary, which lies halfway between the wires. Even if one wire is in corona and the adjacent one is not, the models all assume that truncation occurs halfway between the electrodes. The error associated with this process is small because most of the current is accounted for in the regions immediately under the wires.

SPARKING

Sparking is the electrical breakdown of the gap caused by the simultaneous presence of large quantities of positive and negative ions. Sparking is initiated by repeated traversals of the gap by positive streamers, which heat the gap and supply the ions need for the spark. Therefore, the models assume that streamer propagation conditions are the threshold for spark formation.

Streamers require a minimum field to propagate, and an empirical relation has been given in Reference 9. In Versions 1.0 and 2.0, this sparking threshold was approximated by a temperature and pressure dependent relation with values adjusted to give typical voltages at sparking. In Version 3.0, the full relation has been used, which includes a major effect of water vapor. For most of the normal cold-side ESP operating range, these three versions are in good agreement.

The streamers must be able to propagate all the way from wire to plate (with positive corona) or from plate to wire (with negative corona). Therefore, the position of the electric field minimum must be calculated and evaluated. For glow corona, there is a pronounced minimum field along the axis from wire to plate. This minimum is enhanced by the presence of particulate space charge. For tuft corona, assuming that the electric field is uniform, there is no unique location for the minimum field, and the value at the plate can be taken.

Sparking will occur when the minimum propagation condition occurs for any of the wires in a given electrical section. The models all evaluate the position and current density for each wire for which sparking would occur, and then pick the lowest voltage from that set as the sparking potential of the section. In practice, small mechanical and environmental differences may significantly affect the onset of sparking, but the model calculations are the first attempts to produce a sparking limit on the operation of ESPs.

BACK CORONA

Back corona and sparking are related, because both are manifestations of bipolar ions in the electrode gap. If the electric field conditions in the gap are not conducive to sparking, then stable back corona can occur, in which the ions of opposite polarity add to the flow of current and reduce the charge on particles.

Back corona occurs when the electric field in the accumulated dust becomes large enough to sustain a corona-like discharge in the layer. The electric field in the layer is maintained by the normal flow of ions from the electrode gap onto the surface of the dust, with current carriers in the dust continuing the flow to the plate. Although the flow of current in the dust layer has been shown to be highly nonlinear and, therefore, not ohmic in nature, it is still useful to describe the characteristics in terms of Ohm's law, with the understanding that the effective resistivity of the layer may depend on the internal field and the current carriers.

Because back corona occurs in the gas in the pores of a layer, it would be assumed to obey Paschen's law, or at least depend on the gas temperature. However, limited experiments on back corona formation over a range of temperatures have shown that the breakdown field, evaluated as the product of local current density and resistivity just prior to breakdown, is approximately constant, with a value of 10^6 V/m. The models incorporate this value as the limit for formation of back corona. Any smaller field will not produce breakdown, and any larger field will be immediately reduced to this value by the additional ions of the opposite polarity.

This apparent deviation from Paschen's law may be the result of strong local heating in the gas, making the influence of environmental temperatures small in comparison. Or, it may come from microscopic effects in the dust pores, such as field enhancement. The use of a constant breakdown field will not be much in error as long as resistivities are measured or calculated at fields near this breakdown value.

When back corona occurs, the injection of ions of the wrong polarity makes all the model calculations invalid, because the glow and saturation relations all assume unipolar ions. Nonetheless, Versions 2.0 and 3.0 will continue to calculate V-j curves, with an effective ion mobility that approaches twice the unipolar mobility as the total current density grows above the back corona threshold. The effect on the V-I curves is similar to experimental measurements, but no accuracy is claimed for the calculation. The only merit claimed for the technique is that the operating voltage of a section does not exceed the back corona onset by very much under these assumptions, as seems to occur with real ESPs.

LIMITED ION SUPPLY

One problem that has confronted all ESP models is the limited supply of ions available for charging at any point in space. Normal charging theories predict the charging rate for a single particle immersed in a field of ions, with a concentration appropriate for the current density. The theories are derived for the dilute particle limit. In the ESP, however, the number of particles may exceed the number of ions available, particularly at the inlet where the particle concentration is greatest or during rapping, when large numbers of particles are reentrained. Defining the charge on the particles under these conditions of limited supply is difficult, and no charging theories have addressed the problem.

The law of charge conservation can be used to limit the total amount of charge that can be transferred to the particles; that is, considering a volume of gas containing particles, only as much charge can leave that volume per unit time as enters it in the same time. If all the ionic current were deposited on the particles without reaching the plate, then the particulate current leaving the volume could not exceed the particulate current entering the volume plus the ionic current. To phrase it in another way, the space charge increase cannot exceed the integrated current into the volume divided by the velocity flux out of the volume, neglecting collection. Figure 5 shows the relationship between these quantities. An uncharged particulate cloud enters the control volume at velocity, v. An average ionic current, I_{in} (the product of the average current density and length of the volume), also enters from the corona wire. The total current out of the volume, I_{out} (the product of particulate space charge, gas velocity, and height of volume), is carried by the particles.

If the individual charges on particles calculated by dilute charging theories produce a space charge increase that exceeds the current into the volume, then the charge increase must be corrected to meet that limit. In Version 3.0, this correction is applied equally to all particle sizes and equally to the contributions due to field charging and diffusion charging. This correction allows the particulate space charge to remain within the limits defined by the conservation law, but may not represent adequately the state of charge on the individual particles. Until further theoretical and experimental work is done, however, this approach remains the best approximation to the actual charging conditions.

INTERACTIONS

Reference 4 proposed a diagram-based method for self-consistently calculating the electrical operating point of a wire electrode, based upon the relations between particle charging, particulate space charge, particle removal, and space-charge-induced shifts in the V-j curve. That method has been implemented in the coupled V-I and performance programs, but on a section-by-section basis. Given enough computer memory, it would be possible to do the calculations on a wire-by-wire basis, but the additional information that would have to be entered into the program would make it clumsy to use.

This section discusses the interactions of various fundamental aspects of the V-j models and their approximate implementations in the programs.

SPACE CHARGE EFFECTS

The effect of particulate space charge on the current density under the wire has already been included in the discussions of the V-j curves for tuft and glow corona. Space charge also has the effect of modifying the current density distribution. When the particulate space charge contribution is much larger than the ionic contribution, the current density is more sharply peaked under the wire than in its absence. Effectively, the exponent in the cosine power law is larger than normal. When the ionic space charge is larger than the particulate space charge, then the current density distribution exponent approaches its normal value.

This effect holds whether current source is a glow or a tuft. The models correct for the space charge effect differently for the glow or tuft cases, but the general effect remains the same. The tuft current density is assumed to be quite narrow, with a current density exponent value as high as 100 - 300 for voltages very near the onset voltage. The rationale for this extreme case is that the tuft near corona onset does not saturate the electrode gap, and the ions move directly to the plate without spreading. This assumption has not been tested experimentally, but is consistent with numerical solutions of the geometry that have a point source injection of ions at the wire electrode.

DUST LAYER RESISTIVITY

The dust layer, under the Ohm's law assumption, has two principal effects and one minor effect, as long as the electric field in the layer remains below the breakdown value. The minor effect is that the thickness of the dust layer reduces the electrode gap and thereby alters the corona onset voltage. It is difficult to imagine ESPs operating with dust layers several inches thick, but the models can accommodate them.

The first principal effect of the resistive layer is to modify the apparent V-j curve. It does this because the voltage drop across the layer is added to the voltage drop across the gap for a given current density:

$$V_t(j) = V_g(j) + V_d(j) \tag{3}$$

where, for a given current density, j, V_t is the total (or terminal) voltage, V_g is the voltage across the interelectrode gap (given by either the tuft or glow equation), and V_d is the dust layer voltage. The layer voltage is the product of the electric field in the layer and the layer thickness, and the electric field is the product of the layer resistivity and the local current density:

$$V_d(j) = j\rho d \tag{4}$$

where j is the current density, ρ is the resistivity, and d is the thickness. Note that, for best accuracy, ρ must be determined at the current density for which the calculation is being done. High resistivity dusts with realistic layer thicknesses can modify the shape of the V-j curve significantly.

The second effect of the resistive layer is to broaden the current density distribution. The reason for this is apparent in Eqn. 4, where the voltage drop through the layer depends on the current density at that point. If the current density is lower at one point than at another, the voltage drop through the dust layer is less at that point. Therefore, the gap voltage drop from that point to the corona wire will be higher, and the corresponding current density will also be higher than it would be if compared to the other point for the same gap voltage there. The greater the fraction of the total voltage that the dust layer assumes, the greater will be the spreading effect.

The equations governing this behavior can be solved in principle, but are quite complex. The resulting distribution does not appear to have a simple cosine law behavior, but rather exhibits a range of exponents over angles of interest. The models account for this broadening and variation of exponents by evaluating and averaging the exponent at discrete angles over the range that the current flows from a given wire. For reasonable layer thicknesses, the changes in exponent are not large. Usually, back corona breakdown occurs before the dust layer seriously affects the current distribution.

SPACE CHARGE VARIATION

Although the particulate space charge is a continuously varying function in space, the V-j models for glow and tuft corona have been solved only by assuming a constant space charge value in the zone of influence of a corona wire. Within the framework of the interactive models, assuming a stepwise continuous space charge is not seriously inaccurate.

However, variations of space charge through a corona zone can be detected in the charging region of the first wire of the ESP. There, the space charge is expected to build up so rapidly that there should be a difference between the corona current measured upstream of the wire and downstream. The upstream current will be relatively little affected by the particulate space charge because it is in the process of accumulating, while the downstream current will be almost entirely suppressed by the space charge. Evidence for this behavior has been shown in laboratory experiments using segmented collection plates (10).

The variation of space charge in the models has been accounted for in simpler terms, as described in the following section.

IMPLEMENTATION IN MODELS

A performance model must be used with the V-I model because of the strong effect of particulate space charge. The performance model allows different particle size distributions to be tested, the charging conditions from the V-I model to be applied, and the space charge to be removed at a calculable rate.

Version 1.0 allowed for an adjustable space charge, with a certain fraction removed at each wire. From this model, the effects of space charge on the corona onset were first observed in detail, and section V-I curves which were composites of the individual wire V-I curves were calculated. One of the main effects detected was that several wires might not even have usable corona current at the sparking voltage of other wires in the same section, because of the variation of space charge from wire to wire.

In Version 2.0, this simplified approach was changed to allow for a uniform space charge removal rate, based upon the length of section traversed. Since the performance model could be used to calculate the space charge entering and leaving a section, a realistic removal rate could be ensured. These values of entering and exiting space charge provided the main coupling between the V-I and performance models. A voltage and current could be provided from the V-I model to the performance model. In the performance model, the particulate matter is charged and part of it collected. The values of space charge at the inlet and outlet of each section are calculated for recording, as are the removal rates. The V-I model is then rerun with the new space charge values, providing new voltages and currents for a second iteration. Convergence of the process usually occurs within two to three iterations, particularly for low particle loadings where the dilute charging theories are adequate.

Version 3.0 continues this general algorithm, but with more direct coupling between the V-I and performance models. Version 3.0 also includes the limitation on ion current addressed in section 2.6.

The performance model in Version 3.0 has also been significantly modified from Versions 1.0 and 2.0, which were derivatives of the EPA/Southern Research Institute performance model. The performance model in Version 3.0 now accounts for sneakage, rapping reentrainment, turbulent-diffusive collection, and several other important effects in more realistic ways than the previous versions do. The user has freedom to adjust more parameters, but most of the features of the older performance models can be reproduced by appropriate choices of values.

However, the performance model now makes very clear the impact that rapping reentrainment has on ESP performance. It also shows that some measured ESP efficiencies cannot be obtained assuming intense turbulence in the gas, but must be collected from a gas stream of relatively low turbulence. Version 3.0 also includes an opacity calculation for relating the mass emissions of the ESP to a stack opacity value.

SUMMARY

The relationships that have been described in this paper are the foundation for the interactive V-I models that have been and are being developed. The fundamental importance of the saturation current density has been emphasized because it has guided the development of these models and because it should be used in other models as a check on the validity of their conclusions.

These relationships have helped produce computer models that allow accurate calculations of V-I curves and of back corona onset or sparking onset, and provide the coupling between the V-I models and the performance models necessary for accurate prediction of ESP operation.

These models now make possible calculations of ESP performance from design data, and can be used to evaluate the performance of ESPs under conditions to which they have never been subjected.

REFERENCES

1. Lawless, P.A., and Sparks, L.E. An Interactive Computer Model for Calculating V-I Curves in ESPs. Version 1.0. EPA-600/8-86-030. (NTIS PB87-100046/AS) September 1986. Version 2.0 is under EPA review at this time, and Version 3.0 is under development.

2. Lawless, P.A., McLean, K.J., Sparks, L.E., and Ramsey, G.H. Negative Corona in Wire-Plate Electrostatic Precipitators. Part I: Characteristics of Individual Tuft-Corona Discharges. J. Electrostatics 18, pp. 199-217 (1986).

3. McLean, K.J., Lawless, P.A., Sparks, L.E., and Ramsey, G.H. Negative Corona in Wire-Plate Electrostatic Precipitators. Part II: Calculation of Electrical Characteristics of Contaminated Discharge Electrodes. J. Electrostatics 18, pp. 219-231 (1986).

4. Lawless, P.A., and Sparks, L.E. Modeling Particulate Charging in ESPs. Proceedings IEEE-IAS-1985 Annual Meeting, Toronto, CA (Lib. Cong. 80- 640527). pp. 1407-1411.

5. Sigmond, R.S. Simple Approximate Treatment of Unipolar Space-charge- dominated Coronas: The Warburg Law and the Saturation Current. J. Appl. Physics 53(2), 891-898 (1982).

6. Peek, F.W. "Cielectric Phenomena in High-Voltage Engineering," McGraw-Hill, New York (1929).

7. Oglesby S. Jr., and Nichols G.B. "Electrostatic Precipitation." Marcel Dekker, New York (1978).

8. Lawless, P.A., and Sparks, L.E. Prediction of Voltage-Current Curves for Novel Electrodes -- Arbitrary Wire Electrodes on Axis. In: Proceedings: Fifth Symposium on the Transfer and Utilization of Particulate Control Technology, 2, pp. 4-1 - 4-14. EPA-600/9-86-008b (NTIS PB86-167160), February 1986.

9. Phelps, C.T., and Griffiths, R.F. Dependence of Positive Streamer Propagation on Air Pressure and Water Vapor Content. J. Appl. Physics 47, 2929-2934 (1976).

10. Faulkner, M.G., DuBard, J.L., and Sparks, L.E. The Effect of High Mass Loading on Fly Ash Precipitators. In: Proceedings: Sixth Symposium on the Transfer and Utilization of Particulate Control Technology, 2, pp. 19-1 - 19-16. EPA-600/9-86-031b (NTIS PB87-147625), December 1986.

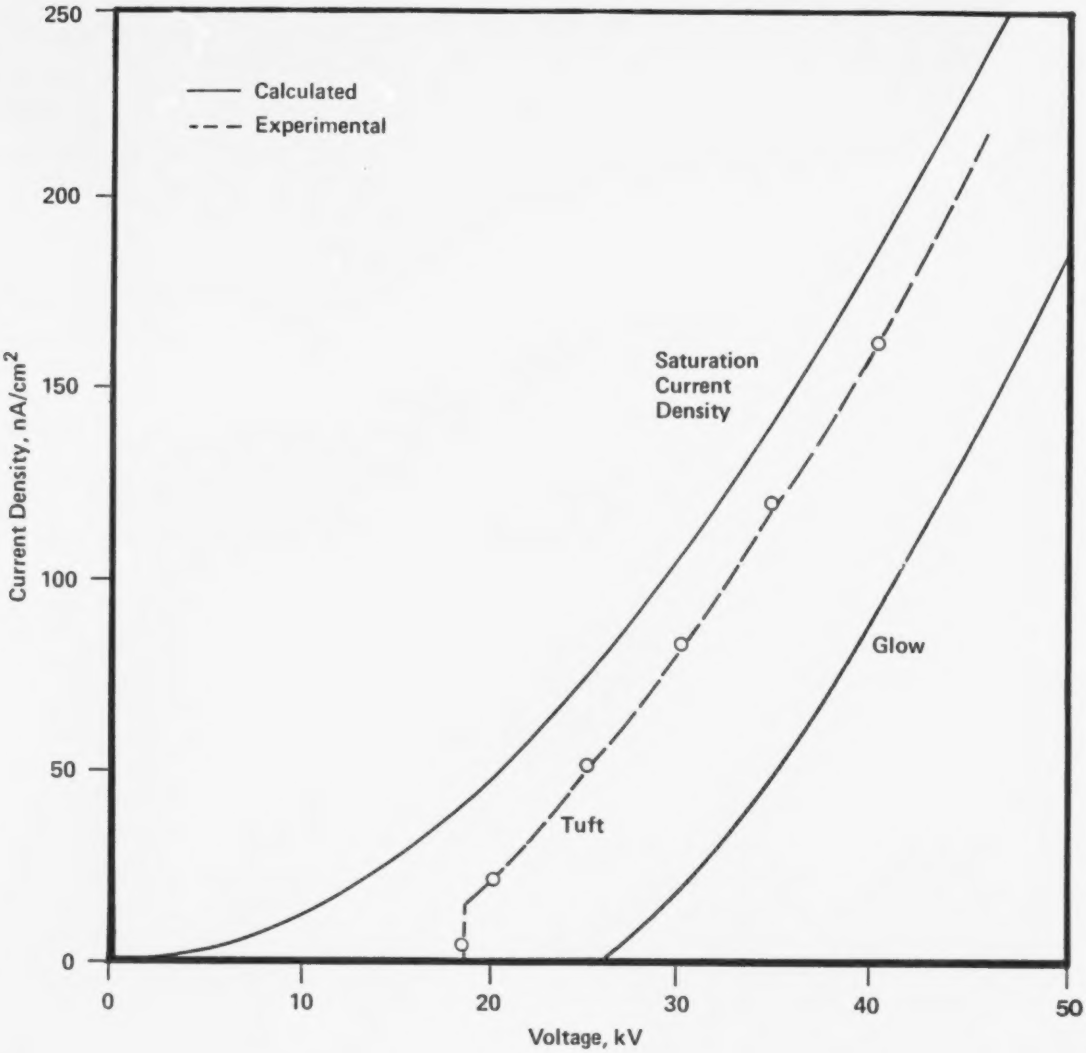

Figure 1. Convergence of tuft and glow corona curves to the saturation current density curve.

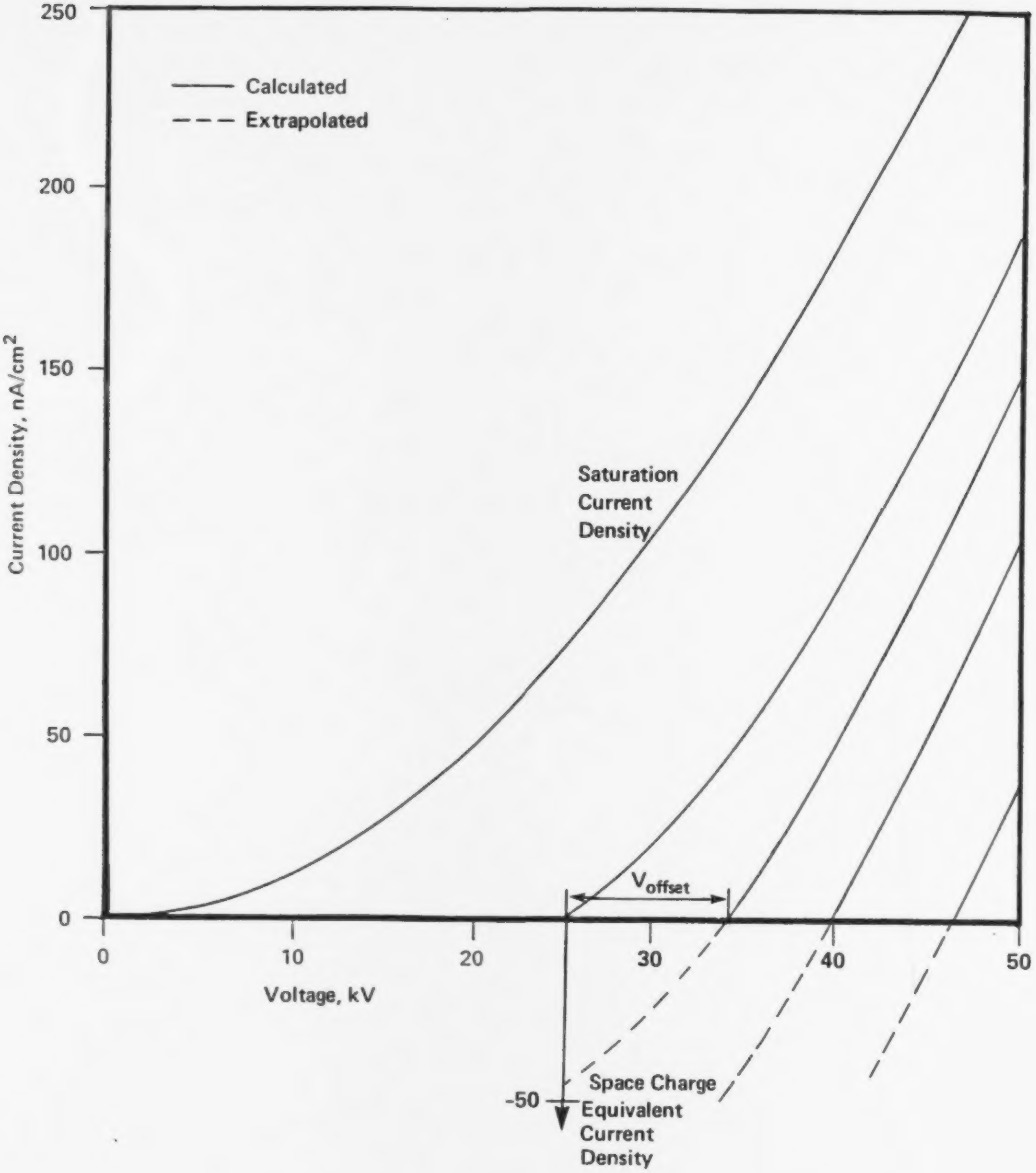

Figure 2. Shift of the glow corona V-j curve to account for increasing particulate space charge.

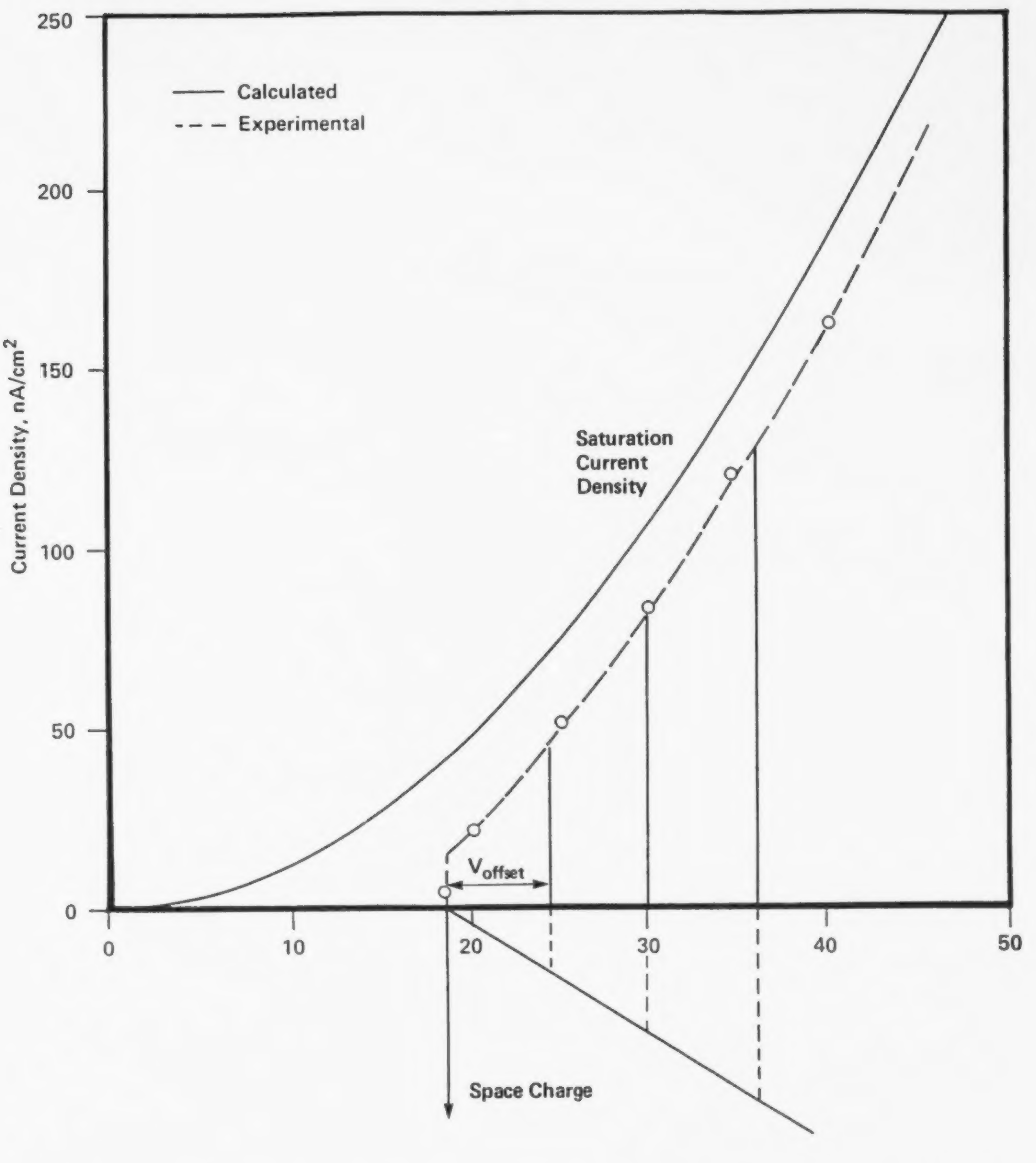

Figure 3. Shift of the tuft corona V-j curve due to increasing particulate space charge. The solid line below the x-axis shows the voltage offset due to space charge; its slope is a function of the electrode geometry.

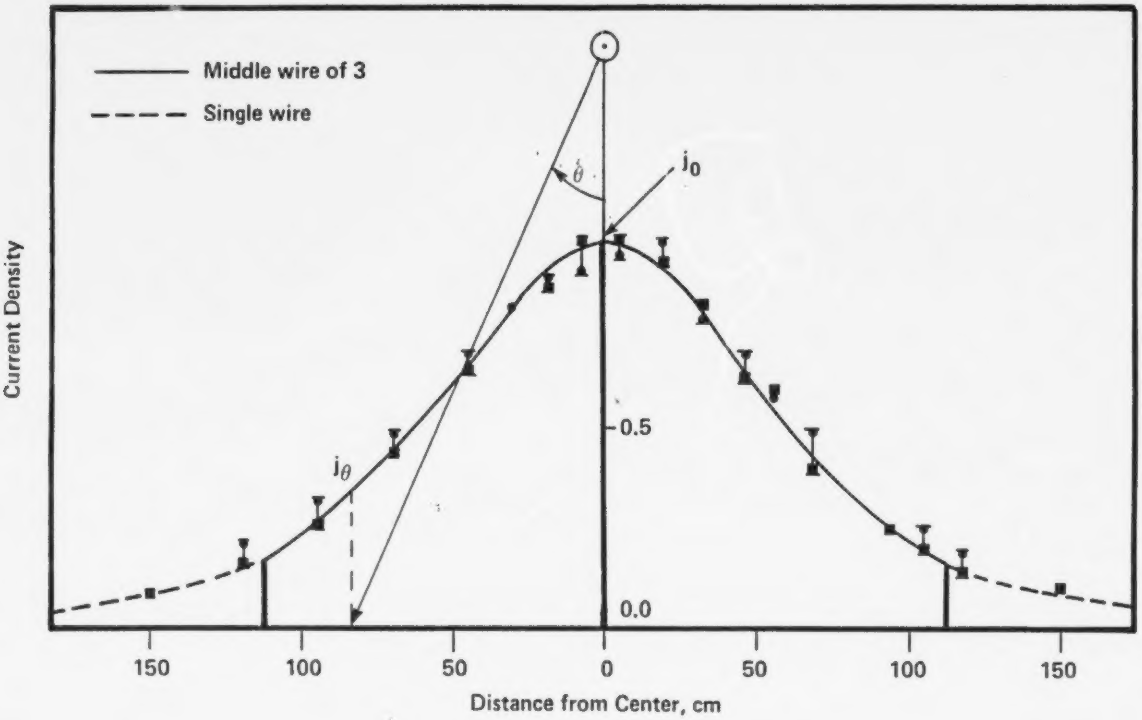

Figure 4. Current density as a function of angle from the wire-plate axis. The symbols represent measured current density values, normalized to the value at angle 0.

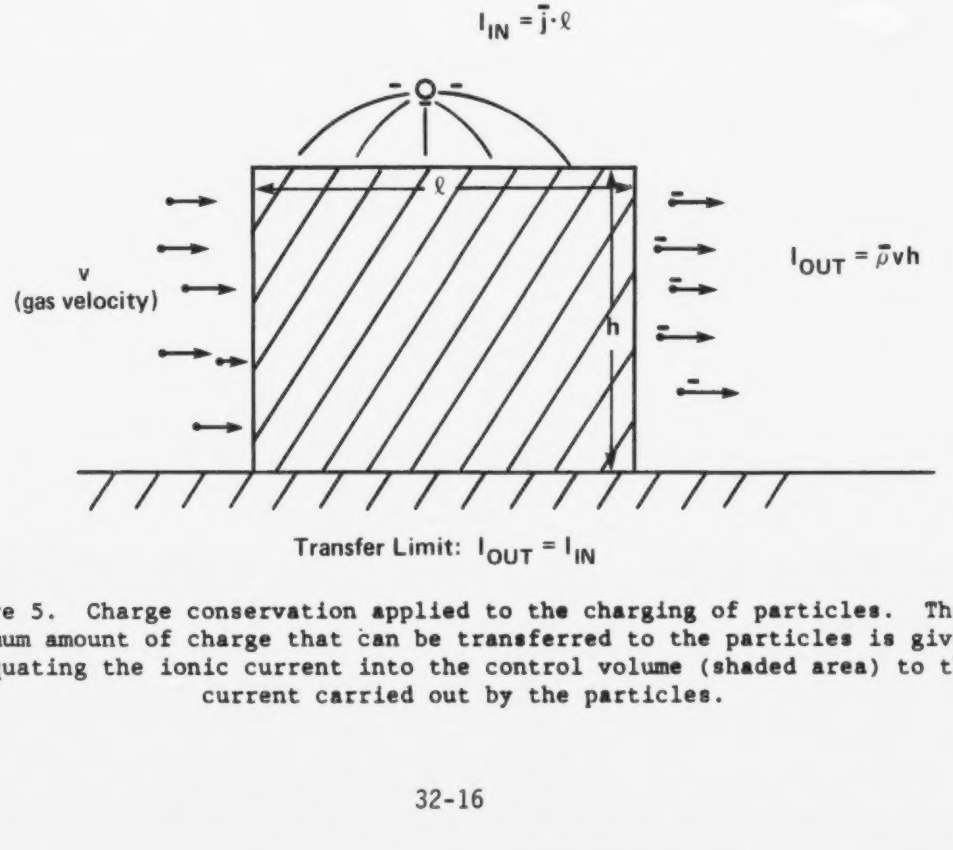
$I_{IN} = \bar{j} \cdot \ell$
ℓ
v
(gas velocity)
h
$I_{OUT} = \bar{\rho} v h$
Transfer Limit: $I_{OUT} = I_{IN}$

Figure 5. Charge conservation applied to the charging of particles. The maximum amount of charge that can be transferred to the particles is given by equating the ionic current into the control volume (shaded area) to the current carried out by the particles.

IMPROVING ESP PERFORMANCE BY REDUCING LOSSES

Phil A. Lawless and Toshiaki Yamamoto
Research Triangle Institute
Research Triangle Park, NC 27709

Leslie E. Sparks
U. S. Environmental Protection Agency
Air and Energy Engineering Research Laboratory
Research Triangle Park, NC 27711

ABSTRACT

This work is the outgrowth of a long series of computer models aimed at understanding ESP operation. The sectional performance model referred to here has been shown to describe the mass efficiencies of operating ESPs better than all other models it was compared with. The model provides insight into the operation of ESPs that stress the importance of controlling ESP losses, principally sneakage and rapping reentrainment. The accuracy of this particular model is not a question at this point, because all model comparisons are made in a relative sense, with predictions compared under the normal conditions and under reduced loss conditions. The improvement of ESP operation with reduced losses is often dramatic. We present methods of achieving lower sneakage and rapping losses, and evaluate their potential with the sectional model.

This paper has been reviewed in accordance with the U. S. Environmental Protection Agency's peer and administrative review policies and approved for presentation and publication.

INTRODUCTION

"Sectionalization" in an ESP is taken to mean that each section of an ESP should be treated as an independent, small ESP on its own, in series with others of like construction. In our discussion, we assume that sections (which are usually separated by walkways) are equivalent to electrical "fields," electrodes served by a common bus. The distinction between sections and fields can be important in some designs. Figure 1 shows the efficiency and penetration relations for the overall ESP performance as expressed in terms of the performances of the individual sections. The penetration expression is the simpler of the two representations and is the one that is used throughout the remainder of the discussion.

If we define the average penetration of a section as:

$$P = P_T^{(1/N)} \tag{1}$$

where P_T is the total penetration and N is the number of sections, then average penetration of a section is a way to put all ESP performances on a common basis. Naturally, we would expect an ESP with a large number of sections to be more efficient than one with a small number, even if they have the same SCA (specific collector area). By using the average section penetration, we can get a measure of the performance of each part of the ESP. To obtain the average penetration, we need to know only the overall penetration or efficiency and the number of sections.

Figure 2 shows a large number of operating ESP performance points, from the authors' files, plotted against their SCA. The SCA scale covers from small pilot units to the largest industrial ESPs. This plot shows the well-known trend that penetration declines very slowly with SCA, and there is little in this figure to distinguish the quality of operation of these ESPs. A group of wet ESPs, mostly Japanese in manufacture (1), are included in the figure as shaded squares. In this figure, there is little to distinguish the wet ESPs, with no rapping losses, from the better-performing dry ESPs that do have rapping losses.

Some of the better operating ESPs have average section penetrations below 0.2. This means that a three-section ESP would have an efficiency better than 99.2 percent. It is much more common, as we will see, for section penetrations to be in the range of 0.2 to 0.4.

Figure 3 shows these same operating ESPs plotted in terms of their average section penetration, with a separate curve for units with different numbers of sections. The solid lines in Figure 3 are theoretical curves of total ESP penetration based on the section penetration and the number of sections. We see that, for a given section penetration, increasing the number of sections makes the total penetration drop rapidly. Also, there are multiple ways of combining the number of sections and section penetrations to give the same total penetration.

The ESPs whose average section penetrations fall on the left end of the plot are the outstanding performers. Those that fall in the middle, the majority, perform well, but not outstandingly. Those that are on the extreme right perform poorly, usually because of a resistivity problem. The number of ESPs having section penetrations less that 0.2 is quite small. We take this to mean that an average section penetration of 0.2 is about the best that can be expected unless great care is taken. If we were to plot the section penetration as a function of SCA, we would find that both large and small SCA units can have section penetrations near 0.2.

The ESPs with the shaded squares are the wet ESPs from Japan. Wet ESPs should have no rapping losses, only sneakage losses. By eliminating the rapping losses, these ESPs are capable of much better performance on a section basis than dry ESPs. This advantage is enhanced by their avoidance of back corona as well, so that the wet ESPs collect particles quite well, and exhibit the lowest average section penetrations.

From this plot, we can estimate the least amount of sneakage that might be expected in ESPs. Most of the wet ESPs can achieve sneakage levels of 0.07 to 0.08. The best one achieves a sneakage of 0.045. These levels are consistent with the RTI sectional model fits (SN = 0.07) and with the Southern Research fits to modern ESPs (SN = 0.075) (2). Some of the dry ESPs, which include rapping losses, also have average section penetrations well below 0.2, including a few of about 0.1. These units can be interpreted as having low rapping losses, as well as low sneakage.

SECTION PENETRATION MODEL

The sectional model has been described in Reference 2 in detail. The section penetration that is calculated in the model takes the form:

$$P_s = Lf + (1 - Lf)xP_c \qquad (2)$$

where P_s is the penetration through the section from all causes, Lf is the loss factor defined below, and P_c is the penetration due to collection inefficiency. The loss factor includes the effects of sneakage and reentrainment due to rapping and other effects, and is given by:

$$Lf = SN + RR - (SN \times RR) \tag{3}$$

where SN is the fraction of the total gas flow that bypasses the collection zone and RR is the fraction of collected material that is reentrained. Any material that sneaks by the section cannot be captured and adds directly to the emission from that section. Only material that is captured can be reentrained by rapping, and that also adds directly to the emission. These two equations form the foundation of the sectional model.

Notice that if P_c, the penetration due to inefficient collection, is reduced to zero, the section penetration is equal to the loss factor. If the collection penetration is much smaller than the loss factor, the section penetration will not be very different from the loss factor. Only when the collection penetration is comparable to the loss factor does the overall penetration begin to grow. This implies two important conclusions:

1) Losses determine the best performance that can be obtained.

2) Reducing losses will not affect a poorly operating ESP very much. Reduced losses will only be apparent in units that have average section penetrations of 0.3 - 0.4 or less.

With the potential of achieving losses of about 0.05 for sneakage and 0.10 for combined losses, it is useful to see how lowered losses would impact ESP operation. The sectional model can be used to fit the SN and RR factors of a subset of the operating ESPs shown in Figure 2 for which enough additional information is available to calculate the collection penetration. With 26 cases in the subset, the average sneakage factor, SN, is 0.07 and the average reentrainment factor, RR, is 0.12.

With the model, we cut these factors in half: SN = 0.035 and RR = 0.06. This represents a goal that is close to being achieved in practice for a few ESPs. These reduced losses naturally lead to reduced total penetrations. The averaged reduction ratio of penetration, new penetration divided by old penetration, was 0.24 times the original values. If, instead, the SCAs of individual units were adjusted to hold original penetration levels, the new SCAs averaged 0.52 times the original SCAs.

Some units were considerable higher or lower than these values: the units with loss factors comparable to or lower than the average 0.19 value showed the greatest improvements from the hypothetical lower losses. The prospect of greatly reduced penetrations or reduced SCAs has stimulated work on means of reducing sneakage and rapping reentrainment. some of the results of this work are shown in the following sections.

REDUCTIONS OF SNEAKAGE

Figure 4 shows the approach we have taken toward examining the causes of sneakage and finding ways to reduce it. To put it simply, the driving force that moves gas out of the collection zone is the difference in pressure between the interior of the zone and the hopper/bus bar areas. This pressure difference arises because there is a pressure gradient along the length of the section. By relating the volume of flow leaving the collecting zone into these areas with the volume of flow entering the section, we can obtain a quantitative prediction of the sneakage fraction.

Reference 3 gives details of the calculations of the pressure gradient and the sneakage flows were given. For the purposes of this paper, the technique is important because it gives values of sneakage within a factor of 2 of the accepted values and because it tells us the parameters to vary to reduce sneakage.

The major factors affecting the pressure drop are the length of the section and obstructions to the flow. Obstructions are the baffles or stiffeners that intrude into the lane. The farther they intrude, and the more of them that there are, the greater will be the pressure drop along the length, and the greater will be the sneakage. The sneakage fraction can be reduced by making the plates higher, because the sneakage flows are primarily confined to the top and bottom of the lanes.

One major consequence of this concept is that we have here a partial explanation for the wide-plate spacing effect. If all other factors are equal, wider plate spacings would have a smaller fraction of lane obstructed, leading to reduced pressure drop and reduced sneakage. In ESPs where losses dominate section performance, the additional reduction of sneakage could more than make up for the reduced SCA of the wider plate spacing.

WAYS OF REDUCING SNEAKAGE

This brief description and the more detailed calculations in (3) suggest several ways in which sneakage can be reduced, without radical changes in ESP designs. The first is to reduce the protrusion of the stiffeners into the gas stream and their number. Every protrusion causes a drag on the gas flowing by it, and raises the local pressure. Reducing the drag is critical to reducing the pressure.

The second method is to increase the plate spacing. This has the effect of making the gas passage more open and the relative height of the stiffeners less important. It also reduces the SCA, but the reduction has not been found to be serious in high-performance ESPs.

Shortening the sections is a third way to reduce the total pressure drop and the sneakage flow. This conclusion assumes a fixed number of stiffeners or other drag-causing mechanisms per unit length. It also assumes that the sneakage flow is remixed with the main gas stream in the gap between sections.

Using anti-sneakage baffles is important, because such baffles place obstructions in the path of the sneakage flow downstream. The obstruction of the sneakage flow raises a back pressure which opposes the sneakage flow.

Another mechanical way to reduce sneakage is to increase the plate height. This might be difficult in some situations, but the sneakage reduction would be an added benefit in retrofit applications where the additional height is already needed for increased SCA or reduced gas velocity. The sneakage fraction will generally decrease in the same ratio as the height is increased.

A final proposed method for providing beneficial back pressure is to use a gas purge of the hopper and busbar areas, with gas taken from the outlet of the ESP. This would increase the total gas burden, but the reduction in sneakage would more than make up for the difference. The sectional model easily allows this kind of comparison.

MODEL ANALYSIS

We take four ESP cases from the accumulated database. These ESPs have been studied in some detail and represent a range of lossy operation, from fair to very good. The ESPs have different degrees of sectionalization, and this would be expected to affect the sneakage improvement possible through purging.

An ideal purge gas flow would deliver no additional gas to the mainstream, but would be a pressure "curtain" in the hopper and busbar areas. Such flows are not easily implemented. For the model analysis, we will assume that the purge gas confines the particle-laden gas to the collection zones, giving a sneakage factor of zero, but that it also adds to the gas volume of the following section by a fraction equal to half the original sneakage. That is, the gas volume flow will increase by the factor 1.035 for each successive section after the first.

This assumption will decrease the effectiveness of the purge technique for multi-section ESPs, because of the compounded increase of gas volume. We also assume that the only effect of the increased gas flow is a reduction in the SCA of each section, recognizing that the increased flows may scour the plates and increase rapping losses.

Case 1. Eight-section ESP

This case is the ESP at the Pleasant Prairie station, sized as a hot-side unit, but operated as a cold-side unit with SO_3 conditioning. The ESP has eight sections in series. Its normal operating penetration is 6.06×10^{-4}. When purging flows are added and the sneakage reduced to zero, the penetration rises to 9.0×10^{-4}, a slightly negative result.

Even if the purge flow could be held to zero, the sectional model predicts that the penetration would only drop to 5×10^{-4}. This result indicates that the section model, as implemented, relies heavily on the presence of some sneakage and rapping to calculate an average particle size distribution.

Case 2. Six-section ESP

This case is the hot-side ESP at the Navajo station, based on the EPRI-sponsored tests of many years ago (4). The ESP tested has six sections in series. Its normal operating penetration is 0.0106. It also shows a negative response to the effect of purging, with its penetration rising to 0.0143 at zero sneakage with no purging.

Case 3. Four-section ESP

This is Allen Unit 3, a hot-side ESP (4). It has four sections in series, and its normal operating penetration is 0.0062. With zero purge flow and zero sneakage, its penetration rises to 0.0216.

Case 4. Four-section ESP

This is the Johnsonville station ESP, an efficient cold-side unit (4). The ESP has four sections in series, and its normal operating penetration is 0.0013. This unit has low overall losses, based on its performance. with 0.035 purge flow, and zero sneakage, its penetration drops to 0.0008; with zero purge flow and zero sneakage, its penetration is 0.0007.

Discussion

These model results for reduced sneakage show more of the defects in the sectional model than a poor concept for the purge gas. By using a more complex model (5), we have verified that the penetration drops steadily with declining sneakage, under the assumption of no additional purge gas flow. The present sectional model blends the normal particle size distribution with the rapping particle size distribution, giving a composite size distribution that resembles those in actual practice. When the sneakage fraction is reduced to zero, the rapping component of the mixture is caught effectively in the succeeding section, and does not pass on to the later sections.

The model still shows that purge reduction of sneakage can produce favorable results, as in Case 4, where the ESP performance is strongly loss-limited, even in this simple model. However, the results of using this model for sneakage effects are mixed, and models which are more accurate than the sectional model should be used for evaluating the advantages of sneakage reduction.

REDUCING RAPPING LOSSES

According to our model, rapping losses are about twice as important for mass emission as sneakage losses. There is a strong connection between the two loss mechanisms, because the rapping puff tends to be composed of large, easily collected particles. If there were no sneakage paths from the early sections to the outlet, the rapping puffs of the inlet sections would be totally collected and not appear as opacity spikes.

Unfortunately, our understanding of rapping is less complete than for sneakage. Areas in which understanding could be improved are: agglomeration effects (how thick should the dust layer be before it is rapped?); the effects of gas velocity (is there a critical velocity where reentrainment becomes severe?); and the clamping of dust to the plates by the current passing through it (is uniform current density important?).

There are two areas related to rapping in which the models can shed some light: rapping frequency and the charge state of the reentrained dust.

RAPPING PERIOD

Within a given section, the dust is allowed to collect for a period of time before it is rapped. Over a number of rapping cycles, the layer thickness will alternate between a minimum value (ideally zero) and a maximum value.

The sectional model allows the quantity of material collected to be calculated as a function of time, if the particle loading at the inlet of the ESP is known. For the inlet section, the amount collected is given by

$$M_c = (1 - SN - P_c) x M_i \qquad (4)$$

where M_c is the mass collected per unit time, SN and P_c are as before, and M_i is the mass entering the section per unit time. No matter how long the material is allowed to collect, the sectional model assumes that RR times that amount is released to the gas stream when the plates are rapped.

If the material collects for too long a time, then Section 2 will see a momentary dust load higher than the inlet dust load. It is unlikely that Section 2 can handle a higher dust load than Section 1, and so there is a strong possibility of an overload, with consequently poor collection performance. A broad limit on acceptable loading for good collection in the Section 2 will occur when the mass of material reentrained divided by the gas volume contained between the plates of the ESP is equal to the mass per unit volume in the inlet stream.

A more stringent limit can be obtained by recognizing that the outlet concentration is proportional to the inlet concentration over a wide range of particle concentrations. Therefore, a concentration at the inlet of the Section 2 equal to the ESP inlet concentration will produce an outlet concentration, momentarily, $1/P_s$ times higher than normal. Therefore, the rapping period should be approximately P_s times shorter than the period that would overload Section 2.

Similar analyses can be applied to later sections of the ESP, with the knowledge that the mass collected on successive sections includes the normal inlet contributions plus fractions of the rapping puffs from the upstream stages. Because of the size-dependent collection efficiencies of ESPs, these fractions should be determined with a more detailed model.

CHARGE STATE

The second area in which models can make a contribution to the understanding of rapping losses is in recharging of the reentrained material. The particles lose their charge when they are collected on the plates, within a few milliseconds for normal resistivities. However, the layer itself retains a charge on its surface under most conditions.

The surface charge is required wherever the electric field in the gas is different from the electric field in the layer, and the magnitude of the surface charge is proportional to the difference between the two fields. The electric field in the layer is set by the current density flowing through the layer and the resistivity of the material. Low resistivity materials in normal ESPs will exhibit a positive surface charge, and high resistivity materials will exhibit a negative surface charge.

When the dust layer is rapped from the plates, the surface charge is carried into the gas stream. There is no way to know how the charge is distributed among all the particles, but it is likely that the charge per particle is fairly uniform, because of multiple contacts between particles. This surface charge then becomes a particulate space charge that is fed into the next section.

If the particulate space charge is positive (low resistivity dust layer), then it will increase the electric field in the following section and is likely to induce sparking. Even if sparking does not occur, the positive charge must be neutralized by negative ions before normal charging can take place. The model concepts can aid in evaluating the amount of space charge (from the amount of material reentrained) and its charge state. In this case, the thickness of the layer is not important, as long as the same fraction is reentrained into the gas stream, because the same fraction of the surface charge would also be entrained.

Standard charging theories can then be used to estimate the amount of time the particulate cloud remains below normal charge levels. This low-charge time effectively reduces the SCA of the section and the subsequent collection of the particles. These effects predict that the contributions of rapping to the total emissions would be greater for low resistivity dusts (for which the surface charge is high) and for high resistivity dusts (for which the recharging conditions are poor) than for moderate resistivity dusts.

RAPPING ELIMINATION

There are two ways in which the rapping problem can be completely eliminated from consideration. The first way is by using wet ESPs. We have already seen that the average section penetration of wet ESPs can be outstanding. In addition, back corona or resistivity problems disappear and the volume of gas treated is lower than with other types of ESPs. The second way to eliminate rapping reentrainment is to take parts of the ESP offline before rapping them, much as is done with fabric filters.

Figure 5 shows the concept of offline rapping. When the time comes for a chamber to be rapped, its gate valve or damper is closed and all sections are rapped simultaneously and vigorously. There is no danger of rapping reentrainment, so the plates can be well cleaned. The chamber can be deenergized during rapping for better cleaning. Then, the power can be restored, the damper opened, and the ESP resumes normal operation, until the next chamber needs to be rapped.

The offline rapping concept does require frequent operation of the dampers for the separate chambers, although the frequency of rapping would probably not have to be as large as in conventional rapping. A modified offline rapping strategy would be to allow normal rapping for all sections but the outlet, which would be taken offline for rapping. In this way, the offline operation might occur only once a day.

The sectional model is well-suited for evaluating these strategies with some simple assumptions. During normal operation, we assume rapping reentrainment is about half the normal value and set RR = 0.06. This is to help account for non-rapping reentrainment and for the change of particle size through the ESP. Without some reentrainment (in this model), the collection is superb, but unrealistic. In a more complex model, the RR factor could be reduced to zero, or some small value to account for non-rapping reentrainment. During rapping, the chamber being rapped is assumed to have zero rapping losses. The remaining chambers of the ESP must carry the full load during rapping of the one chamber. Therefore, the effective SCA of the ESP is reduced during rapping. The problems that were encountered in using the model with reduced sneakage are not experienced here, because the sectional model accommodates changes of SCA quite well.

To model full offline rapping, we assume that rapping occurs for half the time, and normal operation for the other half. That is, some chamber of the ESP is assumed to be offline for rapping during half the operating time. This duty cycle might include the time required to shut the damper, operate the rappers repeatedly, and allow the dust cloud to settle or be recollected prior to opening the damper.

The total emission of the ESP under these assumptions would be the average of the normal emission and the emission during rapping. Similarly, the time-averaged penetration would be the average of the normal penetration and the rapping penetration. If the reduction in rapping losses can compensate for the reduced SCA during rapping, then overall performance would improve.

To model the modified offline strategy, we assume normal operation, except for rapping losses in the last section, for 23 out of 24 hours. For the 24th hour, we assume that all chambers will be rapped in close sequence, without rapping losses, while the remaining chambers take up the full gas load. This time assumption might not be realizable for a multichamber ESP and would penalize an ESP with few chambers, but it is made only for comparison purposes.

These offline rapping concepts have been evaluated for four cases, with the number of chambers ranging from 2 to 16. In these cases, the baseline penetration that is shown has been calculated by the model, and is within a factor of 2 of the actual penetration. This has the effect of calibrating the model for each ESP and was done to make the improvement due to offline rapping more realistic.

Case 1. Multi-chamber ESP

This case is the ESP at the Pleasant Prairie station. The ESP has eight independent chambers of eight sections in series, and offline rapping is assumed to take 12.5% of the ESP offline at a time. Its normal operating penetration is 5.0×10^{-4}. When all chambers are on line, not rapping, the calculated penetration is 0.07×10^{-4}. When one chamber is offline for rapping, the remaining 7 chambers have a penetration of 0.16×10^{-4}, for an average value of 0.115×10^{-4}.

The overall improvement here is a factor of 43. This corresponds to an increase of w_k by a factor of 6.6 (k = 0.5, in the Matts-Ohnfeld model; see Reference 2.) This is a significant improvement that comes about partially because the average section penetration for this ESP is 0.39, which means that about half of its emission are due to losses, and the other half due to collection inefficiency. Therefore, reduction of any part of the losses will have a large effect on the total penetration.

In the modified strategy, the normal operating penetration is 4.5×10^{-4} for 23 hours out of 24. During the 24th hour, the penetration of the remaining chambers is 8.8×10^{-4}, for a time averaged penetration of 4.67×10^{-4}. This is a small improvement, a factor of 1.07. Some combination of offline rapping frequency and sections not rapped during online operation may be found to give an acceptably large improvement in operation and infrequent offline conditions.

Case 2. Multi-chamber ESP

This case is the hot-side ESP at the Navajo station (4). The ESP tested has 16 independent chambers of 6 sections in series, and offline rapping is assumed to take 6.25% of the ESP offline at a time. This would be expected to have a minimal effect on the SCA. Its normal operating penetration is 0.0082. When all chambers are on line, not rapping, the calculated penetration is 0.0013. When one chamber is offline for rapping, the remaining 15 chambers have a penetration of 0.0016, for an average value of 0.00145.

The overall improvement here is a factor of 5.6, or a factor of 2.4 in w_k. This is also an outstanding improvement, because the average section penetration is 0.46. Since more than half its emission is due to poor collection, the improvement would not be as great as for Case 1, but the larger number of chambers offsets that difference.

In the modified strategy, the normal penetration is 0.0081 and rises to 0.0093 during the offline rapping period, for a combined penetration of 0.0082. This represents no improvement of the operation.

Case 3. Four-chamber ESP

This is Allen Unit 3, a hot-side ESP (4). With only four chambers of four sections, we would expect that the offline part of the emission would be high. Its normal operating penetration is 0.0050. When all chambers are on line, not rapping, the calculated penetration is 0.00109. When one chamber is offline for rapping, the remaining three chambers have a penetration of 0.00067, for an average value of 0.00088.

The improvement factor is 5.7 and the w_k improvement is 2.4 times. This unit has an average section penetration of 0.28, which makes it a good candidate for improvement by reducing losses. Most of its present level of emission is due to losses, and less than half due to collection inefficiencies. This allows the penetration through the three chambers during rapping to outperform the whole unit under normal operation.

The modified strategy gives an online penetration of 0.0041 and an offline penetration of 0.0063 for a combined penetration of 0.0042. This represents an improvement of 1.19 over normal operation, and shows that multi-section ESPs profit less from the modified rapping strategy than do those with fewer sections in series.

Case 4. Two-chamber ESP

This is the Johnsonville station ESP (4). The ESP has two independent chambers of four sections in series, and offline rapping is assumed to take half the ESP offline at a time. This is a major change in the SCA. Its normal operating penetration is 0.0013. When both chambers are on line, not rapping, the calculated penetration is 0.00025. When one chamber is offline for rapping, the remaining chamber also has a penetration of 0.00031, for an average value of 0.00028.

Even with only two chambers, the model shows an improvement factor of 4.6 in emission and 2.2 in w_k, and the penetration through one chamber without rapping is lower than the penetration through both chambers with rapping. This performance might not be realized in practice, because the gas velocity through the online chamber would double during rapping. Nonetheless, offline rapping shows a potential reduction of emission, even for this two-chamber case.

The modified offline rapping gives an online penetration of 0.00057, an offline rapping penetration of 0.00137, and a combined penetration of factor of 2, with an increase in w_k of 1.4 times. Again, the advantage of the modified strategy lies in having fewer sections in series.

The section penetration for this ESP is 0.19, making its operation almost entirely determined by its losses. Even if the rapping reentrainment were zero, the performance would be bounded by sneakage. Therefore, anything that can be done to reduce its losses will have a direct effect on its emission. Conversely, changes aimed at improving its collection efficiency, such as increased SCA, would have very little effect.

The SCA of this ESP could even be reduced without affecting the performance severely. For example, this ESP would be a good candidate for operation with wide plate spacing. Its operation is not sensitive to SCA, and the increased spacing would reduce its sneakage significantly. The sneakage model shows that the SN fraction varies approximately as the square root of the plate spacing, while the SCA varies inversely with the plate spacing. If the plate spacing were doubled with all other factors held constant, reducing the SCA by a factor of 2, the sectional model predicts that the penetration would rise slightly from 0.0013 to 0.0018. If this slight increase of emission could be tolerated, the ESP could be built at lower cost and have the other advantages of wide-spacing as well.

CONCLUSION

The offline rapping concept shows potential for a major increase in performance. The sectional model results are so startling that they deserve further attention with a more accurate model. The modified strategy shows little improvement over normal operation, suggesting that rapping losses are important throughout the ESP, not only in the last section. Since the goal of the modified offline strategy is to reduce the number of times per day that the chamber dampers would have to be operated, further tradeoffs between frequency of operation and performance improvement should be studied.

SUMMARY

The electrical operation of modern ESPs can be so good that the losses in each section govern the overall performance level. Further substantial improvements of performance can only come from attention to the losses. Even today, some ESPs exhibit quite low loss levels, in comparison with the industry as a whole, and serve as examples to be emulated.

The sectional model gives a good representation of the sneakage and reentrainment losses, accounting for them in physically reasonable ways. It has been used to extrapolate the performance of several existing ESPs with reduced losses, at levels about half the industry average. The results of the extrapolated performance show that average penetrations or emission could be reduced by a factor of 4. Alternatively, for the same emission levels, the SCA could be reduced by an average factor of 2. This shows the promise of controlling the losses, without changing other factors.

Controlling sneakage depends on learning and correcting its causes. One approach has been to determine the pressures driving the sneakage flows and examine the sensitivity of the pressure gradient to various mechanical parameters. Such an analysis leads to recommendations regarding the plate height, length, and spacing, and includes the presence of baffles or stiffeners in the considerations. The analysis also identifies sneakage reduction as a major factor in the preservation of performance when plate spacing is increased. The sectional model does not perform well at low levels of sneakage and should be used with caution in analyzing those situations.

Controlling rapping losses is not as susceptible to detailed analysis as the sneakage problem has been, but the potential of completely eradicating rapping losses has been examined. One possibility is the use of wet-wall ESPs, a solution whose advantages and disadvantages are already known. Another solution proposed is offline rapping, in which a whole chamber can be taken out of the flow stream for rapping. The sectional model is an excellent tool for evaluating this mode of operation. It shows that offline rapping would be advantageous, in terms of emission, for many different ESP configurations.

REFERENCES

1. Okuda, S., and Wada, M., Wet Type Electrostatic Precipitators Installed in Waste Incinerators in Japan. Proceedings of Second International Conference on Electrostatic Precipitation, pp. 726-733. S. Masuda, ed. Kyoto, 1984.

2. Lawless, P.A. and Sparks, L.E. A Review of Mathematical Models for ESPs and Comparison of Their Successes. Proceedings: Second International Conference on Electrostatic Precipitation, S. Masuda, ed., 513-522 (Kyoto, 1984).

3. Yamamoto, T., Lawless, P.A., and Sparks, L.E. Gas and Electrical Sneakage in Electrostatic Precipitators. Presented at the Third International Conference on Electrostatic Precipitation, Padua, Italy (October 1987).

4. Gooch, J.P. and Marchant, G.H. Electrostatic precipitator rapping reentrainment and computer model studies. FP-792. Electric Power Research Institute, Palo Alto, California, 1978.

5. Lawless, P.A. and Sparks, L.E. An Interactive Model for Predicting Electrostatic Precipitator Voltage-Current Curves and Performance, Version 3.0. In preparation. For background, see: Lawless, P.A. and Sparks, L.E. An Interactive Model for Predicting Electrostatic Precipitator Voltage-Current Curves and Performance, Version 1.0. EPA-600/8-86-030 (NTIS PB87-100046/AS) September 1986.

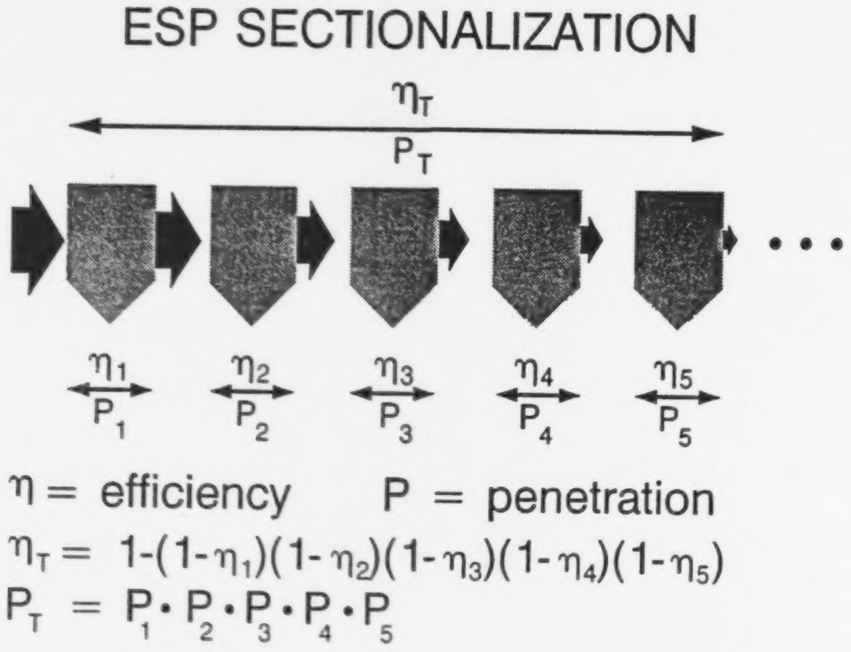

Figure 1. Relation between section efficiency or penetration and total efficiency or penetration.

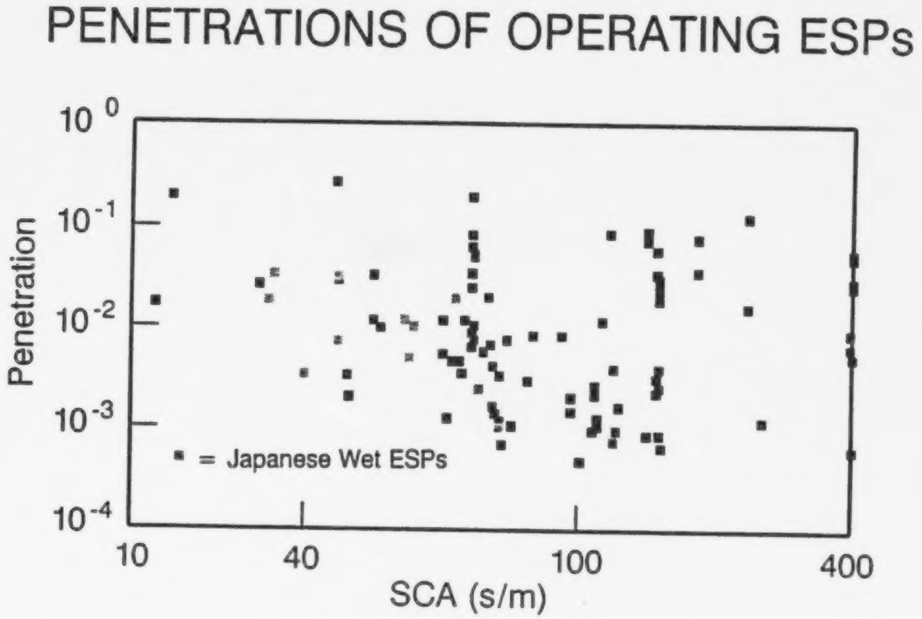

Figure 2. Performance diagram of operating ESPs showing penetration as a function of SCA.

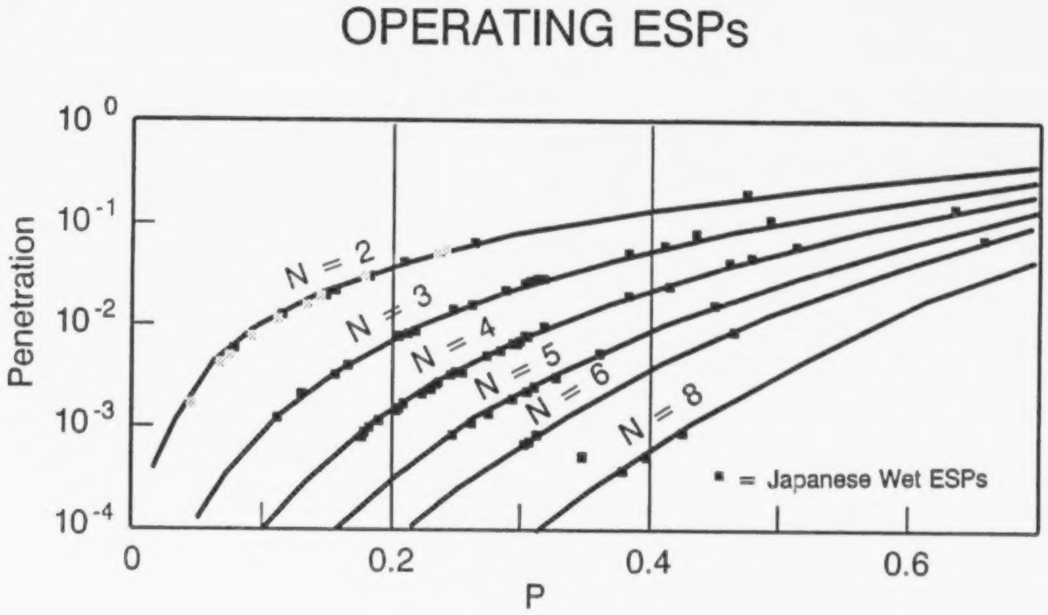

Figure 3. Performance diagram of operating ESPs showing total penetration as a function of average section penetration and number of sections, N.

REDUCTIONS OF SNEAKAGE

- Sneakage flows driven by pressure drop

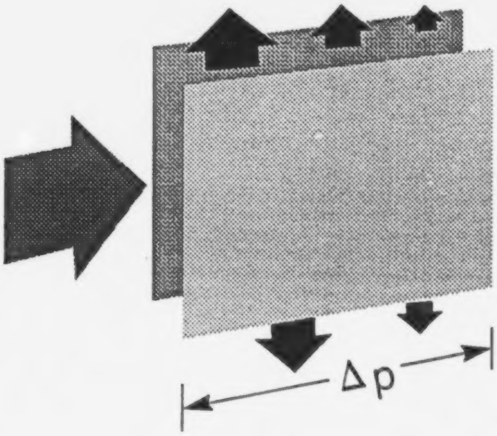

Figure 4. Schematic of sneakage flows driven by the pressure gradient along the length of the section.

OFFLINE RAPPING

(One chamber at a time)

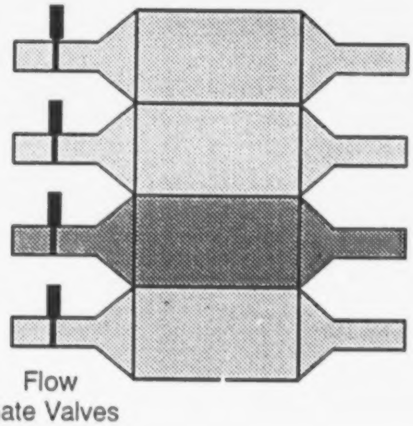

Figure 5. Concept of offline rapping, showing individual control of chamber flows.

Seventh Symposium on Particulate Control Technology

03/22/88-03/25/88

Nashville, TN

List of Attendees

Paul Abbott
Lead Engineer
General Electric Company
200 North 7th Street
Lebanon, PA
717274-7347

Tony J. Ahern
Manager, Systems Engineering
American Elec. Power Service Corp.
1 Riverside Plaza
Columbus, OH 43215
614/223-3260

Francesco Aiello
Engineer
ENEL-CRTN
Centro Ricerca Termica E Nucleare
567100 Pisa, A. Pisano 120
ITALY
050/535950

Don Aikens
Engineering Superintendent
Brunswick Mining & Smelting Corp.
Belledune, New Brunswick
CANADA E0B 1G0
506/522-2100

Carl-Eric Akerlund
Vice President
Flakt Industrial Processes
S-35187 Vaxjo
SWEDEN
+46/470 87403

Charles A. Altin
Project Manager
EBASCO Services, Inc.
145 Technology Park
Norcross, GA 30092
404/662-2347

Ralph Altman
Project Manager
Electric Power Research Institute
516 Franklin Building
Chattanooga, TN 37411
615/899-0072

Marlin H. Anderson, Jr.
Consultant
APCO Services
P.O. Box 1183
Hopkinsville, KY
502/885-5420

William J. Armiger, Jr.
President
EPSCO
325 Mountain View Road
Skillman, NJ 08558
609/466-3488

James Armstrong
Vice President, Operations
ADA Technologies, Inc.
Honeywell Center, Suite 480
304 Inverness Way South
Englewood, CO 80112
303/792-5615

Allan Arnott
Thermal Test Engineer
Ontario Hydro
700 University Avenue
Toronto, Ontario
CANADA
416/592-5931

A. Arstikaitis
Client Manager
Combustion Engineering
P.O. Box 43030
31 Inverness Center Parkway
Birmingham, AL 35243
205/991-2832

William F. Barkowitz
Self-Employed
Consultant
1021 Harrison Street
Lincoln, Park, MI 48146
313/381-8005

Richard Barnes
Research Chemist
BGF Industries
110 Andrews Street
Greensboro, NC 27406
919/379-2867

Charles B. Barranger
Fabric Filter Product Manager
Flakt, Inc.
Environmental Systems Division
P.O. Box 59018
Knoxville, TN 37950-9018
615/693-7550

Don Barton
Environmental Supervisor
Alabama Power Company
Barry Steam Plant
Bucks, AL 36512
205/829-9521

Darrell W. Bayless
Production Engineer
Hoosier Energy REC
P.O. Box 7
Sullivan, IN 47882
812/356-4291

Andrew R. Becker
Manager, Technical Development
Environmental Elements Corporation
P.O. Box 1318
Baltimore, MD 21203
301/625-6048

Roger H. Beckham
Plant Engineer/Manager
Nashville Thermal Transfer Corp.
110 First Avenue S.
Nashville, TN 37201
615/244-3150

Victor H. Belba
Self-Employed
Consultant
4758 Edison Lane
Boulder, CO 80301
303/442-1672

Greg Belland
Metallurgical Engineer
Brunswick Mining & Smelting Corp.
Smelting Division
Belledune, New Brunswick
CANADA E0B 1G0
506/522-5205

Perry Bergman
Chemical Engineer
U.S. Department of Energy
Pittsburgh Energy Technology Ctr.
Pittsburgh, PA 15234
412/892-4521

Peter Bibbo
V.P., Sales & Marketing
Research-Cottrell
P.O. Box 1500
Summerville, NJ 08876
201/685-4299

Roy E. Bickelhaupt
N/A
Bickelhaupt Associates, Inc.
P.O. Box 3532
Carbondale, IL 62902
618/529-5296

Edward B. Bird
Engineer
MPR Associates, Inc.
1050 Connecticut Avenue, N.W.
Washington, DC 20036
202659-2320

Gary M. Blythe
Principal Engineer
Radian Corporation
P.O. Box 201088
Austin, TX 78720-1088
512/454-4797

Wood Bouldin
Regional Manager
Dynatron, Inc.
9020-1 Capitol of Texas Highway N.
Suite 220
Austin, TX 78759
512/346-8069

Keith Bradburn
Product Manager
Flakt, Inc.
Environmental Systems Division
P.O. Box 59018
Knoxville, TN 37950-9018
615/693-7550

Edwin Brailey
Consulting Engineer
New England Service
25 Research Drive
Wes[illegible]rough, MA 01582
617/[illegible]5-9011

Charles Brandt
Assistant Sales Manager
Brandt Environmental Corporation
P.O. Box 148
Tucker, GA 30085-0148
404/496-1946

Robert C. Brandt
President
Brandt Environmental Corporation
P.O. Box 148
Tucker, GA 30085-0148
404/496-1946

Tom E. Britcher
Manager, Sales
Environmental Elements Corporation
P.O. Box 1318
Baltimore, MD 21203
301/368-7290

Theodore G. Brna
Project Officer
U.S. EPA
AEERL/RTP, MD-61
Research Triangle Park, NC 27711
919/541-2683

Vann Bush
Head, Applied Physics Section
Southern Research Institute
P.O. Box 55305
Birmingham, AL 35255-5305
205/581-2269

Tim J. Bushyhead
Engineer
Public Service Co. of Oklahoma
P.O. Box 220
Oologah, OK 74053
918/581-0831

Michael Butts
Senior Engineer
Iowa Power & Light Company
2115 Navajo
Council Bluffs, IA 51501
712/366-5328

Robert Candelaria
N/A
Salt River Project
P.O. Box W
Page, AZ
602/645-8811

Knowlton J. Caplan
Consultant
Pace Laboratories, Inc.
1710 Douglas Drive N.
Minneapolis, MN 55442
612/941-8410

Mike Carlisle
Maintenance Supervisor
Alabama Power Company
Miller Steam Plant
P.O. Box 248
Graysville, AL 35073
205/674-1207

Mary Carpenter
Editor
McIlvaine Company
2970 Maria Avenue
Northbrook, IL 60062
312/272-0010

Robert C. Carr
Mgr., Particulate Control Projects
Electric Power Technologies, Inc.
P.O. Box 307
Menlo Park, CA 94025
415/322-0828

Joe Cavallari
Manager, APC Division
Smogless
Via Mascheroni, 23-M1
ITALY
2/4987651

Ramsay Chang
Project Manager
Electric Power Research Institute
3412 Hillview Avenue
Palo Alto, CA 94304
415/855-2535

Gerald J. Childress
Manager, Southeast Region Sales
United McGill Corporation
1501 Kalamazoo Drive
P.O. Box 909
Griffin, GA 30224
404/228-9864

Dong-Ho Choi
Researh Assistant
Stanford University
Mechanical Engineering Department
Stanford, CA 94305
415/723-1823

John Cochran
Air Quality Engineer
Black & Veatch
P.O. Box 8405
Kansas City, MO 64114
913/339-2190

John R. Cochran
N/A
Black & Veatch
1500 Meadow Lake Parkway
Kansas City, MO 64114
913/339-2000

Byron Corina
Environmental Supervisor
Alabama Power Company
Gaston Steam Plant
P.O. Drawer B
Wilsonville, AL 35186
205/669-4633

Fred Cox
Vice President, Sales
Menardi-Criswell
1853 Milledgeville Road
Augusta, GA 30901
404/724-8241

Donald Creeger
V.P., Business Development
EPSCO
P.O. Box 777
Winburne, PA 16879
814/345-5000

Philip B. Crommelin
Consultant
EPSCO
P.O. Box 38
Stanton, NJ 08885
201/236-2324

Robert Crynack
Mgr., Particulate Control Tchnlgy.
Wheelabrator Air Pollution Control
5100 Casteel Drive
Pittsburgh, PA 15108
412/787-9710

Jeff Cummins
Consulting Engineer
Neundorfer, Inc.
4590 Hamann Parkway
Willoughby, OH 44094
216/942-8990

John D. Cunic
Senior Staff Engineer
Exxon Research & Engineering Co.
P.O. Box 101
Florham Park, NJ 07932
201/765-3986

Kenneth M. Cushing
Head, Fabric Filter Res. Section
Southern Research Institute
P.O. Box 55305
Birmingham, AL 35255-5305
205/581-2381

Bobby E. Daniel
Chemical Engineer & Technician
U.S. EPA
2024 Woodrow Street
Durham, NC
919/541-0908

Wayne T. Davis
Professor/Assistant Dean
University of Tennessee
Civil Engineering Department
Knoxville, TN 37996
615/974-7728

Roger L. Day
V.P., Operations & Engineering
Industrial Resources, Inc.
201 West 3rd Street
Rifle, CO 81650
303/625-1544

Richard Daykin
Marketing Representative
3M
P.O. Box 358
Southfield, MI 48037-0358
313/827-6842

Jose S. DeGuzman
Chemical Engineer
Tennessee Valley Authority
2S 86B Missionary Ridge Place
Chattanooga, TN 37402-2801
615/751-5632

Thomas E. Dixon
President
Dixon Consultants, Inc.
4650 Old Kummer Road
Allison Park, PA
412/367-0881

William DiMarco
Division Vice President, Sales
Midwesco, Inc.
P.O. Box 2075
Winchester, VA 22601
703/667-8500

William Dobbins
Maintenance Superintendent
Nashville Thermal Transfer Corp.
110 First Avenue S.
Nashville, TN 37201
615/244-3150

Richard Dodson
President
DCE, Inc.
11301 Electron Drive
Jeffersontown, CT 40299
502/267-0707

J. R. Donnelly
Chief Development Engineer
Joy Technologies, Inc.
404 East Huntington Drive
Monrovia, CA 91016
818/301-1233

Claude Doucet
Production Coordinator
Brunswick Mining & Smelting Corp.
Belledune, New Brunkswick
CANADA E0B 1G0
506/522-2100

Thomas E. Dowdy
Senior Chemical Engineer
Univ. of Tennessee Space Institute
Tullahoma, TN 37388
615/455-0631

Martin Downey
Regional Manager, Utility Mktg.
Wheelabrator Air Pollution Control
16800 Imperial Valley Drive
Houston, TX 77060
713/591-0742

Delmar J. Doyle
Manager
Wheelabrator Air Pollution Control
441 Smithfield Street
Pittsburgh, PA 15222
412/562-7010

John M. Dudeck
Senior Station Engineer
Pennsylvania Electric Company
P.O. Box K
New Florence, PA 15944
412/235-2711 X216

Patrick Dupuy
Engineer
Central Louisianna Electric Co.
Route 2, P.O. Box 215
Mansfield, LA 71052
318/872-5400

Michael Durham
Vice President
ADA Technologies, Inc.
Honeywell Center, Suite 480
304 Inverness Way South
Englewood, CO 80112
303/792-5615

James L. DuBard
Head, Applied Technology Division
Southern Research Institute
P.O. Box 55305
Birmingham, AL 35255-5305
205/581-2000

James Eckenrode
Project Engineer
ETS, Inc.
3140 Chaparral Drive
Suite C-103
Roanoke, VA 24018
703/774-8999

Jon Emsbo
President
Imtec, Inc.
21 Bryers Lane
Upper Saddle River, NJ 07458
201/825-7070

Heinz L. Engelbrecht
Self-Employed
Consultant
646 Ryland Drive
Pittsburgh, PA 15237-4204
412/366-7479

Glenn England
Manager, Combustion Systems
Energy & Envrnmntl. Research Corp.
18 Mason Drive
Irvine, CA 92718
714/493-8206

David S. Ensor
Director
Research Triangle Institute
Research Triangle Park, NC 27709
919/541-6735

Terry Farmer
Product Manager
Preciptech/A BHA Group Co.
8800 E. 63rd Street
Kansas City, MO 64133
816/356-8400

Arnold Farr
Design Engineer
Combustion Engineering
31 Inverness Center Parkway
P.O. Box 43030
Birmingham, AL 35243
205/991-2832

Greg Faulkner
Senior Physicist
Southern Research Institute
P.O. Box 55305
Birmingham, AL 35255
205/581-2221

Larry G. Felix
Senior Physicist
Southern Research Institute
P.O. Box 55305
2000 9th Avenue, South
Birmingham, AL 35255-5305
205/581-2519

Stephen Felix
Sales Manager
Mount Hope Industrial Fabrics
P.O. Box 390
Niverville, NY 12130
518/784-2247

James J. Ferrigan
V.P., Domestic Sales
Wahlco, Inc.
3600 W. Segerstrom Avenue
Santa Ana, CA 92704
714/979-7300

Mark A. Fiedler
Principal Process Engineer
Flakt, Inc.
P.O. Box 59018
Knoxville, TN 37950-9018
615/693-7550

Susan Fields
Biologist
Radian Corporation
3200 Progress Center
P.O. Box 13000
Research Triangle Park, NC 27709
919/541-9100

Werner Flatt
Mechanical Engineer
Buhler Brothers, Ltd.
Engineering Works
CH-9240 Uzil
SWITZERLAND
073/50 25 83

Robert Frame
General Sales Manager
Field Service Associates, Inc.
2 Enterprise Drive
Shelton, CT 06484
203/926-9949

Peter E. Frankenburg
Research Associate
DuPont Company
Chestnut Run, Building 701
Wilmington, DE 19898
302/999-4858

Joe Fuller
Chemical Technician
Alabama Power Company
Barry Steam Plant
Bucks, AL 36512
205/829-9521

Charles A. Gallaer
Self-Employed
Consultant
1801 Tyburn Lane
Pittsburgh, PA 15241
412/221-1762

Gary Gawreluk
Product Manager
Research-Cottrell
P.O. Box 1500
Somerville, NJ 08876
201/685-4288

Robert P. Gehri
Senior Research Specialist
Southern Company Services
P.O. Box 2625
Birmingham, AL 35202
205/870-6720

Peter Gelfand
Consultant
P. Gelfand Associates
60 Clover Hill Road
Trumbull, CT 06611-2556
203/261-7557

Robert E. Gibbons
Sales Manager
F. L. Smidth & Company
300 Knickerbocker Road
Cresskill, NJ 07626
201/871-3300

Dan V. Giovanni
Program Manager
Electric Power Technologies, Inc.
P.O. Box 5560
Berkeley, CA 94750
415/653-6422

Tom Godbey
Technical Manager
DCE, Inc.
11301 Electron Drive
Jefferson, KY 40299-9990
502/267-0707

Jack Greene
Administrative Manager
U.S. EPA
AEERL/RTP, MD-49
Research Triangle Park, NC 27711
919/541-2905

Gary P. Greiner
Vice President
ETS, Inc.
3140 Chaparral Drive, S.W.
Suite C-103
Roanoke, VA 24018
703/774-8999

James Griffin
Development Engineer
Wheelabrator Air Pollution Control
5100 Casteel Drive
Coraopolis, PA 15108
412/787-9700

Terry Gross
Maintenance Supervisor
Alabama Power Company
Gorgas Steam Plant
Route 2, P.O. Box 201
Parrish, AL 35580
205/686-5029

Theron Grubb
President
Grubb Filtration Testing Services
P.O. Box 1156
Delran, NJ 08075
609/461-1800

John Guffre
Regional Sales Manager
Wahlco, Inc.
3600 W. Segerstrom Avenue
Santa Ana, CA 92704
714/979-7300

H. J. Hall
President
H. J. Hall Associates, Inc.
1250 State Road
Princeton, NJ 08540
609/924-1933

Wallis Harrison
Research Specialist
Southern Company Services
P.O. Box 2625
Birmingham, AL 35202
205/870-6334

Robert Heaphy
Research Engineer
Southern Research Institute
P.O. Box 895
Chattahoochee, FL 32324
904/593-6273

William G. Heard
Design Engineer
C-E Air Preheater
Andover Road
Wellsville, NY 14895
716/593-2700

Arthur G. Hein
Manager, Thermal Power
Hipp Engineering, Ltd.
520 W. 6th Avenue
Vancouver, BRITISH COLUMBIA
V5Z 4J5
604/874-2302

Dennis J. Helfritch
Senior Project Manager
Research-Cottrell
P.O. Box 1500
Somerville, NJ 08876
201/685-4147

Paul D. Hemphill
N/A
CRS Sirrine, Inc.
1177 Westloop South
P.O. Box 22427
Houston, TX 77227
713/552-2000

Robert A. Hewitt
Supervising Engineer
TU Electric
400 N. Olive Street, L.B.-81
Dallas, TX
214/812-8706

David J. Hickey
President
Boiler Equipment Service Company
P.O. Box 80409
Atlanta, GA 30341
404/452-8811

Robert Higgins
Design Specialist
Ontario Hydro
700 University Avenue
Toronto, Ontario
CANADA M5G 1X6
416/592-2680

John W. Hilborn
Envrnmntl./Special Projects Engr.
Ohio Edison Company
76 South Main Street
Akron, OH 44308
216/384-5768

Michael A. Hofacker
Senior Technical Engineer
Montana Power Company
40 E. Broadway
Butte, MT 59701
406/723-5421 X3466

Richard M. Hoffmaster
Area Sales Manager
Lodge-Cottrell/Dresser
601 Jefferson, Suite 2716
Houston, TX 77002
713/750-3764

Gerald Hollinden
Branch Chief
Tennessee Valley Authority
2S 67B Missionary Ridge Place
Chattanooga, TN 37402
615/751-0011

Richard G. Hooper
Principal Engineer
IAM Consulting
7195 So. Chase Court
Littleton, CO 80123
303/933-9610

Kevin M. Hoover
Air Quality Specialist
General Electric Company
1150 Century Circle North
Springdale, OH
513/671-2770

Biff Horvatin
Engineer
Southern California Edison
2244 Walnut Grove
Rosemead, CA 91770
818/302-1522

Louis Hovis
Project Officer
U.S. EPA
AEERL/RTP, MD-4
Research Triangle Park, NC 27711
919/541-3374

Michael Hrycak
Associate
W. L. Gore & Associates, Inc.
P.O. Box 1100
Elkton, MD 21921
301/392-3300

Steve Hudson
Environmental Supervisor
Alabama Power Company
Gorgas Steam Plant
Route 2, P.O. Box 201
Parrish, AL 35580
205/686-5029

Warren Hudson
Filtration Division
Chattanooga Sewing & Sales Co.
2901 Long Street
P.O. Box 2400
Chattanooga, TN 37409
615/756-7067

James P. Huff
Operating Unit Manager
DuPont Company
Textile Fibers Department
P.O. Box 27001
Richmond, VA 27001
804/743-2824

Albert Husdon
Consulting Engineer
EPSCO
7201 Wellington Drive
Knoxville, TN 37919
615/588-0330

Clyde Ingraham
V.P., Technical Service
Westmoreland Coal Company
P.O. Box 1227
Crab Orchard, WV 25827
304/255-4181

Bernard Jackson
Supervisor, Chemical Engineering
Tennessee Valley Authority
2S 87B Missionary Ridge Place
Chattanooga, TN 37402-2801
615/751-5666

Bryan Jankura
Research Engineer
Babcock & Wilcox
1562 Beeson Street
Alliance, OH 44601
216/821-9110 X211

Don Jeanrenaud
Environmental Specialist
Alabama Power Company
Miller Steam Plant
P.O. Box 248
Graysville, AL 35073
205/674-1207

Robert M. Jensen
Self-Employed
Consultant
210 Monte Diablo
San Mateo, CA 94401
415/348-5192

Ken Johnson
Design Engineer
Duke Power Company
P.O. Box 33189, ECI-10
Charlotte, NC 28242
704/373-5989

Michael E. Johnson
Associate
W. L. Gore & Associates, Inc.
P.O. Box 1010
Elkton, MD
301/392-3200

Robert E. Jonelis
President
Midwest Power Corporation
3960 Industrial Avenue
Rolling Meadows, IL 60008
312/870-2400

Morgan D. Jones
Environmental Specialist
Ohio Edison Company
76 South Main Street
Akron, OH 44308
216/384-5449

Allen Jorgensen
Area Sales Manager
Lodge-Cottrell/Dresser
109 Danbury Road
Ridgefield, CT 06877
203/438-9615

Joe Kaminski
Precipitator Specialist
Tampa Electric Company
P.O. Box 111
Tampa, FL 33601
813/247-2629

Glenn Keeling
Senior Engineer
Alabama Power Company
P.O. Box 2641
Birmingham, AL 35291
205/250-4207

Barbara Kelley
Marketing Manager
BHA Group, Inc.
8800 E. 63rd Street
Kansas City, MO 64133
816/356-8400

Tom Kelly
Regional Manager
NWL Transformers
Rising Sun Road
P.O. Box 358
Bordentown, NJ 08505
609/298-7300

Frank S. Kilvinger
President
Boyle Engineering Laboratories
207 N. Woodwork Lane
Palatine, IL 60067
312/991-6200

Bill Kissick
Manager, Utility Marketing
Wheelabrator Air Pollution Control
7240 W. 98th Terrace
Overland Park, KS 66212
913/345-1531

Frank Klopf
Manager
Woagner-Biro U.S.
Liaison Office
105 W. Spring Street
Greenville, SC 29601
803/235-5133

Robert E. Kohl
Mgr., Applications Engineering
Environmental Elements Corporation
P.O. Box 1318
Baltimore, MD 21203
301/368-7375

Henry V. Krigmont
Director, Special Projects
Wahlco, Inc.
3600 W. Segerstrom Avenue
Santa Ana, CA 92704
714/979-7300

Fred Kroll
Sales Manager
Wheelabrator Air Pollution Control
441 Smithfield Street
Pittsburgh, PA 15222
412/562-7300

Jack O. Kuhlman
General Manager
Global Power Company
Route 4
P.O. Box 832
Waverly, TN 37185
615/296-7641

Tony Lamping
Design Specialist
Ontario Hydro
700 University Avenue
Toronto, Ontario
CANADA M5G 1X6
416/592-8179

Carl Landham, Jr.
Head, Precipitator Technology Sec.
Southern Research Institute
P.O. Box 55305
Birmingham, AL 35255-5305
205/581-2000

Joseph B. Landwehr
Project Manager
Burns & McDonnell
4800 East 63rd Street
P.O. Box 41973
Kansas City, MO 64141
816/333-4375

Bill Lane
Engineering Specialist
Bechtel Eastern Power Corporation
Gaithersburg, MD
301/258-4458

William T. Langan
V.P. Product Service
General Electric Company
200 N. 7th Street
Lebanon, PA 17042
717/274-7051

Joel Lantz
Chemical Engineer
Neundorfer, Inc.
4590 Hamann Parkway
Willoughby, OH 44094
216/942-8990

Dennis Laudal
Research Engineer
UND Energy & Mineral Research Ctr.
P.O. Box 8213 University Station
Grank Forks, ND 58201
701/777-5138

Preben Lausen
Chief Engineer
F. L. Smidth & Company
77 Vigersley Alle
DK 2500 Copenhagen
DENMARK
45/1 301166

Phil A. Lawless
Senior Research Physicist
Research Triangle Institute
P.O. Box 12194
Research Triangle Park, NC 27709
919/541-6782

Richard Leuser
Project Director
Roy F. Weston, Inc.
Weston Way
West Chester, PA 19380
215/430-7424

Guy Lewis
Research Engineer
Consolidation Coal Company
4000 Brownsville Road
Library, PA
412/854-6531

Russ LeBeau
Senior Chemical Engineer
Carolina Power & Light Company
P.O. Box 1551
Raleigh, NC 27602
919/836-7221

Daniel A. Lisiecki
Senior Marketing Consultant
F. L. Smidth & Company
300 Knickerbocker Road
Creskill, NJ 07626
201/871-3300

William Z. Looney
Sr. Project Planning Engineer
Southern Company Services
P.O. Box 2625
Birmingham, AL 35202
205/877-7289

Le Lover
Engineer
L.E.C.E.S.
BO 50, Voie Romaine
57210 Raizieres- les-Retz
FRANCE
87/75 30 80

Thomas W. Lugar
Manager, Electrical Subsystems
General Electric Company
200 N. 7th Street
Lebanon, PA 17042
717/274-7221

James E. Lund
Executive Vice President
BHA Group, Inc.
8800 East 63rd Street
Kansas City, MO 64133
816/356-8400

Pat Lynch
Safety Officer
Univ. of Tennessee Space Institute
Tullahoma, TN 37388
619/455-0631 X448

Daniel A. Markley
Fossil Production Engineer
Duke Power Company
P.O. Box 33189, WC-1682
Charlotte, NC 28242
704/373-7206

Henry L. Marschall
Manager, Process Applications
EMCOTEK, Inc.
8220 Doe Avenue
Visalia, CA 93291
209/651-2000

Gregory A. Martel
Senior Engineer
Northeast Utilities
1866 River Road
Middletown, CT 06457
203/638-3175

Brenda Massengill
Administrative Technician
U.S. EPA
AEERL-RTP, MD-49
Research Triangle Park, NC 27711
919/541-2990

Cloyd McAnly
President
C.A. McAnly Associates, Inc.
P.O. Box 395
West Chester, OH 45069
513/779-1377

Joe D. McCain
Senior Physicist
Southern Research Institute
P.O. Box 55305
Birmingham, AL 35255
205/581-2278

Bob McCants
Environmental Supervisor
Alabama Power Company
Greene County Steam Plant
P.O. Drawer P
Demopolis, AL 36732
205/289-1847

Rick McConnell
Spvsr., Air Quality Control Systems
General Electric Company
20 Technology Park
Norcross, GA 30092
404/447-7293

Jack R. McDonald
President
Jack R. McDonald, Inc.
Route 1, P.O. Box 491
Turssville, AL 35173
205/681-0870

Milan McGill
Staff Specialist
Alabama Power Company
600 North 18th Street
P.O. Box 2641
Birmingham, AL 35291-0360
205/250-1376

Marilyn McIlvaine
Managing Editor
McIlvaine Company
2970 Maria Avenue
Northbrook, IL 60067
312/272-0010

Robert McIlvaine
President
McIlvaine Company
2970 Maria Avenue
Northbrook, IL 60067
312/272-0010

John D. McKenna
President
ETS, Inc.
3140 Chaparral Drive, S.W.
Suite C-103
Roanoke, VA 24018-4394
703/774-8999

Bill G. McKinney
Regional Tech Transfer Manager
Electric Power Research Institute
516 Franklin Building
Chattanooga, TN 37411
615/899-0072

Richard D. McRanie
Director, Utility Services
Kilkelly Environmental Associates
P.O. Box 31265
Raleigh, NC 27622
919/781-3150

Patricia Meyer
Director of Marketing
Insitec
2110 Omega Road, Suite F
San Ramon, CA 94583
415/837-1330

H. I. Milde
Staff Scientist
High Voltage Engineering, Inc.
S. Bedford Street
Burlington, MA 01803
617/272-2800

Richard Miller
Senior Engineer
General Electric Company
200 N. 19th Street
Lebannon, PA 17642
717/274-7241

Stan Miller
Senior Research Engineer
University of North Dakota
Energy and Mineral Research Center
P.O. Box 8213, University Station
Grand Forks, ND 58202
701/777-5210

Kevin Mills
Research Engineer
Southern Company Services
P.O. Box 2625
Birmingham, AL 35202
205/877-7324

William Moore
Program Director
U.S. Department of Energy
Germantown, MD 20874
301/353-2901

John G. Musgrove
Supervising Engineer
Bechtel Western Power Company
P.O. Box 2166
Houston, TX 77252-2166
713/235-4365

John C. Mycock
Vice President
ETS, Inc.
3140 Chaparral Drive, S.W.
Suite C-103
Roanoke, VA 24018
703/774-8999

Mike Nelson
Sr. Project Planning Engineer
Southern Company Services
P.O. Box 2625
Birmingham, AL 35202
205/870-6518

George Neundorfer
Product Manager
Neundorfer, Inc.
4590 Hamann Parkway
Willoughby, OH 44094
216/942-8990

Michael Neundorfer
President
Neundorfer, Inc.
4590 Hamann Parkway
Willoughby, OH 44094
216/942-8990

Grady B. Nichols
Dir., Environmental Sciences Res.
Southern Research Institute
P.O. Box 55305
Birmingham, AL 35255-5305
205/581-2361

Charles G. Noll
Director of Technology
United McGill Corporation
2400 Fairwood Avenue
Columbus, OH 43216
614/443-0192

Richard Northrup
Process Control Mechanic
Eastman Kodak Company
1669 Lake Avenue
Rochester, NY 14650
716/722-9577

George Offen
Program Manager
Electric Power Research Institute
3412 Hillview Avenue
Palo Alto, CA 94304
415/855-8942

Gene K. Ogilvie
Vice President, Division Manager
Midwesco, Inc.
P.O. Box 2075
Winchester, VA 22601
703/667-8500

Jim Patterson
V.P., Sales and Marketing
DCE, Inc.
11301 Electron Drive
Jefferson, KY 40299
502/267-0707

John E. Paul
President
PMA, Inc.
P.O. Box 360626
Birmingham, AL 35236-0626
205/988-8192

Rowan P. Perkins
Senior Consultant
E.I. DuPont DeNemours
Engineering Department
P.O. Box 6090
Newark, DE 19714-6090
302/366-2603

John Perry
Supervisor Engineer
Utility Engineering Corporation
P.O. Box 12033
Amarillo, TX 79118
806/378-2448

Herbert Pessl
Engineer
Waagner-Biro A.G.
P.O. Box 1004
A-8021 Graz
AUSTRIA
0316/501-DW 3881

Brian Phelan
Manager
Preciptech/A BHA Group Co.
8800 E. 63rd Street
Kansas City, MO 64133
816/356-8400

Gene Phiefer
Environmental Specialist
Alabama Power Company
Gadsen Steam Plant
Goodyear Avenue
Gadsden, AL 35903
205/546-6317

Walt Piulle
Technical Trans. Administrator
Electric Power Research Institute
3412 Hillview Avenue
Palo Alto, CA 94304
415/855-2470

Norman Plaks
Senior Scientist
U.S. EPA
AEERL/RTP, MD-61
Research Triangle Park, NC 27711
919/541-3084

Wade Ponder
Chief, Air Toxics Control Branch
U.S. EPA
AEERL/RTP, MD-61
Research Triangle Park, NC 27711
919/541-2818

Duane H. Pontius
Head, Physics Division
Southern Research Institute
P.O. Box 55305
Birmingham, AL 35255-5305
205/581-2268

Kjell Porle
Product Manager, Particulates
Flakt Industrial Processes
35187 Vaxjo
SWEDEN
+46/470-87415

Joseph J. Radai
Senior Product Engineer
Lodge-Cottrell/Dresser
601 Jefferson, Suite 2724
Houston, TX 77002
713/750-2356

Geddes H. Ramsey
Project Officer
U.S. EPA
AEERL/RTP, MD-61
Research Triangle Park, NC 27711
919/541-7963

Aldo Ratti
Engineer
Smogless
Vis Mascheroni, 29
Milan, ITALY
02/4987836

Susan Reinhold
Associate Editor
McIlvaine Company
2970 Maria Avenue
Northbrook, IL 60062
312/272-0010

Victor Reyes
Electrical Engineer
F. L. Smidth & Company
Vigerslev Alle' 77
DK-2500 Valby, DENMARK
1/30 11 66

Richard Rhudy
Project Manager
Electric Power Research Institute
3412 Hillview Avenue
Palo Alto, CA 94304
415/855-2421

J.D. Riley
Assistant Vice President
Lurgi Corporation
666 Kinderkamack Road
River Edge, NJ 07661
201/967-4921

George Rinard
Manager, Particulate Control Prog.
University of Denver
Denver, CO 80208
303/871-4370

Phil Rinke
National Sales Manager
Scientific Technology, Inc.
1682 Langley Avenue, Suite 38
Irvine, CA 92714
714/474-9340

Bernd Sandmann
Engineer
Apparatebau Rothemuhle
P.O. Box 5140
D-5963 Wenden 5, Rothemuhle
FEDERAL REPUBLIC OF GERMANY
02762/611 0

Richard J. Savoie
Senior Technologist
Consumers Power Company
1945 Parnall Road
Jackson, MI 49201
517/788-0098

Roger Schaver
Project Engineer
Wisconsin Electric Power Company
333 W. Everett
P.O. Box 2046
Milwaukee, WI 53201
414/221-2291

Hal G. Schildknecht
Sales Manager
Buhler-Miag, Inc.
P.O. Box 9497
1100 Xenium Lane
Minneapolis, MD 55440-9497
612/545-1401

Martin Schiller
President
CSI Engineering
P.O. Box 1515
Fairfield, CT 06430
203/372-8790

Loran T. Schmidt
Vice President
Brandt Environmental Corporation
P.O. Box 148
Tucker, GA 30085-0148
404/496-1946

Susan C. Schreiber
Sales Manager
Global Power Company
Route 4, P.O. Box 832
Waverly, TN 37185
615/296-7641

David Schulz
Regional Power Industry Expert
U.S. EPA
230 S. Dearborn Street
Chicago, IL 60604
312/886-6790

Sidney A. Self
Professor
Stanford University
Mechanical Engineering Department
Stanford, CA 94305
415/723-1745

Emmett Sellers
Senior Engineer
DuPont Company
Textile Fibers Department
P.O. Box 27001
Richmond, VA 23261
804/743-2041

Richard Serrurier
Supervisory Engineer
Southwestern Public Service Company
P.O. Box 1261
Amarillo, TX 79170
806/378-2185

Dan Sheehy
N/A
Cincinnati Milacron
4701 Marburg Avenue
Cincinnati, OH 45209
513/841-8365

A. C. Shelton, Jr.
Chairman
The Drayton Corporation
P.O. Box 820
Jacksonville, AL 36265
205/435-3576

Jeff L. Shelton
President
The Drayton Corporation
P.O. Box 820
Jacksonville, FL 36265
205/435-3576

Fred Simmons
V.P., Engineering
Brandt Environmental Corporation
P.O. Box 148
Tucker, GA 30085-0148
404/496-1946

Rabi K. Sinha
Consulting Engineer
Calgon Corporation
P.O. Box 1346
Pittsburgh, PA 15230
412/777-8864

David Sloat
N/A
Sargent & Lundy
55 E. Monroe Street
Chicago, IL 60603
312/269-2000

David E. Smith
Technical Manager
FMC Corporation
P.O. Box 8
Princeton, NJ 08540
609/452-2300

Jeffrey C. Smith
Executive Director
Industrial Gas Cleaning Institute
1707 L Street, N.W., Suite 570
Washington, DC
202/457-0911

Wallace Smith
Associate Director
Southern Research Institute
2000 9th Avenue, South
Birmingham, AL 35255
205/581-2000

Todd R. Snyder
Research Environmental Engineer
Southern Research Institute
2000 9th Avenue, South
Birmingham, AL 35205
205/581-2000

Leslie Sparks
Project Officer
U.S. EPA
AEERL/RTP, MD-54
Research Triangle Park, NC 27711
919/541-2458

K. Speakman
District Inspector
Inspectorate of Pollution
Woodside Hoeroe
Leeds, ENGLAND
N/A

James P. Spellman
Senior Business Representative
General Electric Company
8101 Stemmons Freeway
Dallas, TX 75247
214/688-6165

H. W. Spencer, III
Executive Vice President
EC&C Technologies
4234 Chevy Chase Drive
La Canada, CA 91011
818/790-7933

Allena Standish
Technician
Weyerhaeuser Company
WTC-1A2
Tacoma, WA 98477
206/924-6549

David H. Stevenson
Design Engineer
Duke Power Company
P.O. Box 33189
Charlotte, NC
704/373-6201

Daniel L. Strein
Particulate Control Engineer
Pennsylvania Electric Company
1001 Broad Street
Johnstown, PA 15907
814/533-8493

Herbert J. Sturm
Division, Vice President
Midwesco, Inc.
P.O. Box 2075
Winchester, VA 22601
703/667-8500

Jack Sturtevant
Senior Plant Maintenance Engineer
Baltimore Gas & Electric Company
P.O. Box 1475
Baltimore, MD 21203
301/787-5528

Thomas C. Sunter
Project Engineer
C-E Air Preheater
Andover Road
Wellsville, NY 14895
716/593-2700

Susan J. Suzuki
Mechanical Engineer
Naval Energy & Envrnmntl. Support
Port Hueneme, CA 93403-5014
805/982-5292

Mike Swink
Market Manager
BGF Industries
P.O. Box 21207
Greensboro, NC 27420
919/379-3248

Robert H. Tetter
Self-Employed
Consultant
Route 1, P.O. Box 156
Mount Holly, NC 28120
704/827-4240

Scott L. Thomas
Maintenance Engineer
Duke Power Company
P.O. Box 2801
Charlotte, NC 28242
704/373-3473

Fred Thomson
General manager
Howden Environmental Systems
5155 East River Road
Minneapolis, MN 55421
612/571-0560

Donald P. Tonn
Principal Engineer
Babcock & Wilcox
20 South Van Buren
Barberton, OH 44203
216/860-1986

Roger Trueblood
Consultant
Stone & Webster Engineering Corp.
245 Summer Street
Boston, MA 02107
617/589-1413

Alexander V. Turchina
Technology Leader
Procter & Gamble Company
6110 Center Hill Road
Cincinnati, OH 45224
513/659-7161

Mohammad Vakili
Power Plant Engineer
Wisconsin Power & Light Company
222 West Washington Avenue
Madison, WI 53701
608/252-3347

John J. Valkiunas
Director of Sales Marketing
Sonic Power Systems, Inc.
P.O. Box 12785
Shawnee Mission, KS 66212
913/764-9111

William B. Van Hooser
Principal Applications Engineer
Environmental Elements Corporation
P.O. Box 1318
Baltimore, MD 21203
301/368-7375

Erik Vogel
N/A
DCE Benelux B.V.
P.O. Box 212
NL-1560 AE Krommenie
75/21 28 81

Tom Waddell
Chemical Engineer
Radian Corporation
P.O. Box 13000
Research Triangle Park, NC 27709
919/541-9100

William I. Walker
President
Clean Air Engineering
207 Woodwork Lane
Palatine, IL 60067
312/991-3300

John W. Walton
Deputy Director
State of Tennessee
701 Broadway Street
4th Floor Customs House
Nashville, TN 37219-5403
615/741-3931

Edwin H. Weaver
Manager of Applications
Belco Pollution Control Corp.
8 Peach Tree Hill Road
Livingston, NJ 07039
201/535-2500

Sandy F. Weinmann
Instrumentation and Controls Engr.
Lodge-Cottrell/Dresser
601 Jefferson Street, 27th Floor
Houston, TX 77002
713/750-2935

Melvin W. Westley
Senior Technical Specialist
DuPont Company
Chestnut Run, Building 713
Wilmington, DE 19898
302/999-3243

Harry L. Wheeler
Principal Development Engineer
Combustion Engineering
31 Inverness Center Parkway
Birmingham, AL 35243
205/991-2832

Jeffrey Williams
Environmental Analyst
Rochester Gas & Electric Company
89 East Avenue
Rochester, NY 14649
716/724-8129

Mike Williams
Product Manager
Neundorfer, Inc.
4590 Hamann parkway
Willoughby, OH 44094
216/942-8990

Thomas Willkomm
Production Engineer
Northern States Power Company
14400 E. Black Dog Road
Burnsville, MN 55337
612/887-1265

Ray Wilson
Research Physicist
Southern Research Institute
2000 9th Avenue South
Birmingham, AL 35255
205/581-2280

Donna Witt
Manager
BHA Group, Inc.
8800 E. 63rd Street
Kansas City, MO 64133
816/356-8400

J. M. Yagen
Maintenance Specialist
Illinois Power Company
500 S. 27th Street
Decatur, IL 62525
217/424-6627

Charlie Yager
Senior Electrical Engineer
Public Service Indiana
1000 East Main Street
Plainfield, IN 46168
317/838-1182

Ronald P. Young
Research Physicist
Southern Research Institute
P.O. Box 55305
Birmingham, AL 35255
205/581-2318